Light-Matter Interactions with Photonic Quasiparticles

by

Nicholas Rivera

B.S., Massachusetts Institute of Technology, 2016

Submitted to the Department of Physics
in partial fulfillment of the requirements for the degree of

Doctor of Philosophy in Physics

at the

MASSACHUSETTS INSTITUTE OF TECHNOLOGY

May 2022

Author . . . . . .
Department of Physics
May 13, 2022

Certified by . . . . . .
Marin Soljačić
Professor of Physics
Thesis Supervisor

Accepted by . . . . . .
Deepto Chakrabarty
Associate Department Head of Physics

Light-Matter Interactions with Photonic Quasiparticles

by

Nicholas Rivera

Submitted to the Department of Physics
on May 13, 2022, in partial fulfillment of the
requirements for the degree of
Doctor of Philosophy in Physics

Abstract

The interactions of matter with electromagnetic fields underlie very many physical phenomena. The physics of these interactions is greatly simplified by their weakness, enabling us to understand them largely at the lowest order in various parameters (e.g., field strength, atomic size, fine-structure constant). This understanding is challenged by recent experiments coupling light to collective electromagnetic excitations in solids ("photonic quasiparticles"), whose strongly confined electromagnetic fields can interact strongly with matter.

This thesis describes how the rules of light-matter interactions are altered when bound and free electrons interact with photonic quasiparticles, and some applications that result. In the first major part of the thesis, I will develop effects arising from the linear optical properties of these excitations, in perturbative and non-perturbative regimes of QED, which give rise to new schemes for generating entangled photons, for X-ray sources, and even for high-energy particle detectors. The second major part of this thesis develops the new physics arising from the nonlinear optical properties of these photonic quasiparticles, and focuses particularly on the development of new non-perturbative nonlinear dissipation and gain phenomena. As an application, I show how these high-order nonlinearity may enable for the first time the deterministic, steady-state generation of large optical Fock and sub-Poissonian states.

Thesis Supervisor: Marin Soljačić
Title: Professor of Physics

Acknowledgments

It's hard to know where to begin. The saying "it takes a village" is probably a good starting point. The work presented in this thesis is the product of collaborations and discussions with many scientists, at every stage of their careers. I am extremely fortunate to have had the opportunity to collaborate with group leaders from all over the world, as well as their postdocs and their students. By working together, I've had the pleasure to work on a wide variety of topical areas in the physics of light-matter interactions (see Chapter 1 for an overview). Within these problems, I've also had the great privilege of experiencing the many different approaches to physics as a whole (e.g., theory vs. experiment, fundamental vs. applied, first-principles vs. phenomenological, and so on). As a result, I have come closer to appreciating the interconnected whole that is the physical world. With that, I would like to acknowledge everyone who I have ever had the opportunity to collaborate with: I have learned from you and certainly become better because of it!

Now, for some specifics. I want to start by thanking my PhD advisor, Marin Soljačić. Who knows where I'd be without his patience, and the broad latitude he has given me throughout my PhD. Beyond that, I've learned a lot from him. There are the obvious things related to research that I can thank him for: like how to choose a problem to work on, how to make sure my work has the most impact, how to work on problems that can have real applications, the important of experiments, starting with very basic questions, knowing when to "turn the crank", exposing myself to a lot of projects, and so on. But there's also the more personal stuff, like teaching me: to work on things that I *really* believe in, how to choose people to work with, and the importance of taking a vacation. There is no doubt that the lessons Marin has taught me will inform my approach to research indefinitely.

Another person who figured very prominently during my PhD is Ido Kaminer. I watched him progress from being a postdoc in our group to being the leader of a thriving group at the Technion. Long past are the days of me going into his office and hijacking his evening with my thoughts about quantum electrodynamics! Nevertheless, I have had the continued fortune to still work with him and "get in on the ground floor", contributing to formative developments in new topical areas with his group such as free-electron quantum optics and

quantum optics in high-harmonic generation. I have always been impressed with Ido's creativity, and I have always inspired by his drive to find "the new in the old" (which I believe has proven fruitful!). Those two traits (among others) inspire a lot of my approach to problems. Beyond this, I have learned many valuable lessons from Ido (largely by example): aim high, and fight hard for what I believe in.

I would be remiss not to also mention John Joannopoulos. I first met him through what is considered a rite of passage for many in our group. Namely, I had results for a potential paper, and it was time for me and my collaborators to make the trek over to the Institute for Soldier Nanotechnology to present them to him, and see what he thought. Since then, JJ has been a reservoir (in the thermodynamic sense) of inspiration, advice, and support for me. He has always encouraged me to maximize the visibility of my work, to broaden my horizons by working with people, to take risks, and to stay true to what I want. It is very likely that I would not be where I am now without him.

I am also enormously grateful for the interactions I've had, and the friendships formed, with students and postdocs in my group and beyond. Special shoutouts go to Jamison Sloan, Charles Roques-Carmes, Yannick Salamin, Thomas Christensen, and Ali Ghorashi. From "being in the trenches" with each of you, I have also managed to learn a lot about myself (as well as physics, of course.)

Finally, it goes without saying, none of this thesis could be possible in a global sense if it weren't for the continuous love and support that my family has provided me with.

Contents

List of Figures

G-1 **Numerical demonstration of transient noise condensation from Eq. (8).** (a) Temporal loss coefficient as a function of photon number. (b) Evolution of the photon statistics in a for different times, assuming an initial Poisson distribution with 70 photons (blue curve). The dynamics largely mirror those presented by the analytical theory in Fig. 2 of the main text. (c) Mean and variance as a function of time, indicating the region where the photon distribution has an uncertainty less than 1. (d) Zoom-in of the small-photon number part of the distribution, showing that part of the distribution moves to smaller photon numbers, somewhat "artificially" diluting the Fano factor. The overall fidelity of generating a 30-photon Fock state in this example is 96%. The parameters for the nonlinear system are $\beta = 5\times10^{-4}$, $\kappa = 10^{-7}$, $\gamma = 10^{-2}$, $\lambda = 0$, and $\omega_d = (1+\delta)\omega_a$ with $\delta = -3\gamma$. 385

G-2 **Numerical demonstration of Fock lasing from steady state of the Liouvillian.** (a) Loss (red) and gain (green) curves for different values of the pump strength. (b) Mean number of photons in the cavity (blue), as well as variance (orange), as a function of pumping rate from the ground state to the upper pumping level. After a threshold, the photon number increases linearly, before going through a nearly discontinuous jump to a low noise state, with noise here 90% below the coherent state level. (c) Fano factor corresponding to the mean and variance in (b), with inset showing the photon probability distribution at the lowest-relative-noise point. Parameters for the nonlinear cavity are the same as Fig. S1 here. Parameters for the gain are: $g = 3\times10^{-4}$, $\gamma_\perp = 10^{-2}, \gamma_{||} = 10^{-4}, \gamma_{12} = 10^{-3}, \gamma_{34} = 1$ (exact value of γ_{34} has little influence insofar as it is much faster than Λ (all units are in units of the frequency of a (e.g., 1.5 eV). 389

G-3 **Systems which could be explored for Fock lasing.** Many options exist for nonlinearity: circuit and cavity QED systems, atomic gases, excitonic strong coupling, and bulk optical materials. Gain media span solid-state, semiconductors, gases, dyes, artificial atoms, and even single atoms (in one-atom lasers). Sources of sharp loss include absorbers, as well as many systems explored in (nano)photonics: photonic crystals, Fano resonances, bound states in the continuum, bistable systems, and coupled cavities. . . . 394

G-4 **Fock lasing in systems with strong optical nonlinearities.** (a) The system of Fig. 3 of the main text is now converted into a "Fock laser" by inclusion of a gain medium. Different transmission profiles for the Fano mirror lead to different losses, and thus different emission-absorption diagrams. Note that t_d is the direct transmission coefficient that controls the Fano lineshape. (b) Evolution of an initial coherent state with different photon numbers (black circles) in the Fock laser. A state to the left of the approximate zero of the loss decays into a thermal state with a very low number of photons, while a state to the right of the zero decays into a steady-state with very low noise, approaching a high-number optical Fock state. (c) Photon number and fluctuations as a function of pump. "S-curves" similar to conventional lasers are observed in the photon number, except they saturate much more strongly, with the photon number hardly changing for increasing pump. Moreover, the photon number fluctuations, rather than increasing according to shot noise, decrease to nearly zero beyond threshold, indicating convergence to a near-Fock state. Different curves indicate different values of the mirror sharpness γ. In this figure, the polaritons have Kerr nonlinear strength $10^{-7}\omega_{\mathrm{LP}}$. The detuning of the mirror from the lower polariton energy (with zero polaritons) is $10^{-3}\omega_0$ and the mirror has a sharpness of $10^{-4}\omega_0$. 396

List of Tables

Chapter 1

Introduction

This thesis first, and foremost, is concerned with fundamental developments in the physics of photonic quasiparticles, and their interaction with matter. The philosophy of this thesis is that this physics, and potential applications, are developed through a broad range of examples. We consider photonic quasiparticles in a broad range of optical materials (dielectrics and metals; bulk and 2D materials; nanophotonic and nanoplasmonic systems), and their interactions with matter systems (both low energy systems such as atoms and low-energy electrons, as well as modestly and ultra-relativistic free-electrons). We consider weak-coupling interactions such as spontaneous emission at different orders in perturbation theory (especially one- and two-photon emission), as well as "non-perturbative effects" associated with the so-called ultra-strong and deep-strong coupling regimes of quantum electrodynamics. It is my view that a diversity of approaches is necessary to begin to appreciate the richness of phenomena and applications of the quantum interactions between matter and electromagnetic fields. The Appendices to the main chapters here tend to reflect this same view; in many cases, the key results of the main chapters are derived by two or even three different theoretical approaches.

The first part of this thesis is focused on providing a high-level, unified, and broad-scope overview of the way that light-matter interactions are fundamentally changed by the presence of material polarization. In materials with optical response, the free electromagnetic field (in vacuum) strongly couples to material polarization to form combined excitations of joint light-matter character. Such photonic quasiparticles run the gamut, subsuming

propagating waves in a bulk transparent dielectric, strongly confined polaritons in van der Waals materials, and fundamentally non-photonic-seeming excitations such as phonons and magnons. Although these excitations seem quite different from each other, they all carry propagating electromagnetic fields which can interact with matter, and these interactions can be quantified using the same techniques. In this chapter, we also introduce a unified theoretical framework, known as *macroscopic quantum electrodynamics* (MQED), which is capable of describing these interactions, and thus, a wide range of known and even currently unexplored physical effects (see Fig. 1 of Chapter 2). We also show how this framework can be used to describe absorption, emission, and strong-coupling phenomena between these photonic quasiparticles and external emitters such as bound electrons (in atoms, molecules, and solids) and even free-electrons. We provide a host of recent examples, primarily experimental, and show how this unified MQED description enables us to understand and quantify these effects. In the Appendix to this chapter, we develop some important results in the theory of MQED. We develop the quantization of the EM field in non-dispersive dielectric media (lossless MQED), and show examples of it in bound and free-electron systems. Many of the examples we develop are sufficiently general to be valid even in the case of dissipative linear media, where the full MQED apparatus is required (which we also develop).

In the second part of the thesis, we provide specific examples of the way in which photonic quasiparticles provide powerful control over spontaneous emission, overcoming some of the limitations coming from the small sizes of quantum emitters. For example, in Chapter 3, we show how the strongly confined and narrow-bandwidth fields associated with phonon polaritons in polar dielectrics enable an unusual type of emitter which prefers to emit entangled pairs of electromagnetic excitations, rather than single quanta, as would naively be expected from perturbation theory based on the typical weakness of light-matter interactions. These effects are maximized in 2D phonon polaritonic systems, which are explored in Chapter 4. At the time of the writing of Chapter 4, 2D phonon polaritons had not been explored or observed, and there had been some remaining questions regarding their fundamental nature. Thus, in Chapter 4, we present the theory of the optical response of phonon polaritons in monolayers of polar dielectrics, providing explicit expressions for the

optical conductivity of phonon polaritons in monolayers, as well as the dispersion of such polaritons − showing the kinds of extreme confinements of electromagnetic energy that are unique to these monolayer systems. We also present experimental measurements of the optical response of hBN monolayers (taken through scanning near-field optical microscopy) which validate the theory presented in this chapter, which were taken in collaboration with the group of Prof. Dmitri Basov.

Much of the emphasis in enhancing light-matter interactions with photonic quasiparticles has largely been focused on the interaction of these photonic quasiparticles with bound electrons, e.g., in saystems of atoms, molecules, or artificial atoms. But many exciting phenomena of light-matter interaction can be realized when the emitter is instead a free electron. Indeed, free-electrons, due to their high kinetic energies and their energy-momentum dispersion, can in principle emit light at very high frequencies (such as X-rays), for which there are typically few mechanisms to produce. Moreover, the spontaneous emission of photonic quasiparticles by free electrons is strongly dependent on the electron velocity, allowing in principle for highly tunable light sources. In Chapter 5, we explore uniquely quantum effects (with no classical description) in light emission arising from the interaction of free electrons with collective excitations in solids. We show a new mechanism of light emission, which we refer to as photon-polariton pair emission, in which a relativistic electron simultaneously can emit two entangled quanta: one highly confined infrared excitation (such as plasmons in graphene, or phonon polaritons in hBN), and one X-ray photon which propagates into the far-field. The power emitted in this process is substantially stronger than expected, especially when the electron is within nanometers of the surface supporting the photonic quasiparticles. This can be understood as a new type of vacuum-induced force acting on charged particles in which the electron Doppler shifts vacuum fluctuating infrared near-fields into X-ray photons. The quantum effect described here also is unique in its ability to entangle infrared and X-ray electromagnetic excitations. The theory here can be thought of as a phenomenon unique to *free-electron quantum optics*, a field which is now starting to develop, and which we provide some additional theoretical foundation for (in the Appendix to Chapter 1).

In Chapter 6, we turn to an application of enhancing spontaneous emission with pho-

tonic quasiparticles; more efficient detectors of high-energy particles such as energetic electrons and X-rays (ionizing radiation). Ionizing radiation is typically detected by the use of *scintillators* which glow (emit photons) upon bombardment by ionizing radiation. By patterning the scintillator on the nanoscale, the dispersion relation of the photonic quasiparticle can be strongly altered (as the photonic excitations are now Bloch photons): the density of optical states can be strongly enhanced and the number of paths coupling emitted photons to the far-field can be strongly increased. In either case, the radiation emission be strongly enhanced, enabling detection of a much lower flux of incident ionizing radiation. At the time of the writing of Chapter 6, neither enhancement of the rate of scintillation through the local density of states, nor large outcoupling enhancements of scintillation, had been observed. Part of the reason for the lack of progress entails a theoretical gap associated with the complex, multiphysics nature of scintillation emission − consisting of several complex parts spanning a wide range of length and energy scales: generation of high-energy carriers by ionizing radiation, "thermalization" to form a non-equilibrium steady state, and radiation by fluctuating currents in inhomogeneous media. The main contribution of Chapter 6 is to provide a theoretical and computational framework to predict nanophotonic scintillation for the first time, integrating all of these parts. The theory developed here shows good agreement with measured spectra of scintillation of photonic crystals bombarded by electrons and X-rays. Many of the complex features as a function of frequency, as well as electron energy, can only be explained by this complete theory.

In the last part of the thesis, we move beyond perturbative effects and consider cases in which the coupling energy between light and matter is comparable to the bare energies of the light and matter subsystems. When the coupling is within an order of magnitude of the bare transition energies, the coupling is said to be in the regime of *ultra-strong coupling*. It has now been experimentally realized in a variety of different systems. This regime differs substantially from the regime of strong-coupling extensively explored in cavity quantum electrodynamics: this is because in strong coupling, the *ground state* is only negligibly altered by the coupling, while in the ultrastrong coupling there is a significant modification of the ground state from the bare ground state (the product of the matter ground state with the photonic quasiparticle vacuum). This fact has motivated exploration of potential appli-

cations in chemistry, materials science and condensed matter, where the ground-state plays a decisive role in the thermodynamic and transport properties of the system. Nevertheless, our theoretical understanding of this regime is limited as there are only two theoretical models for which one can easily (analytically or numerically) diagonalize the Hamiltonian: (1) the Rabi model, describing the coupling of a two-level system to a single mode of the EM field and (2) the Hopfield model, describing the coupling of a harmonic oscillator to a single mode of the EM field. Real systems depart from both of these models. Additionally, the focus of ultra-strong coupling has primarily been on the modification of the matter fields: but it is equally interesting (and arguably equally motivated) to consider the consequences on the electromagnetic fields. In other words, to look at the implications of ultrastrong coupling for *photonics*. In Chapter 7, we address these questions by developing a real-space description of the ground-state of ultra-strongly coupled systems, involving the coupling of multi-level systems to multi-mode optical systems. In doing so, we show how the energy of the ground state, and even the excited states, can be well-described through a factorizable ansatz in which the electromagnetic field modes are strongly modified by the presence of the light-matter coupling.

Taking the ideas of non-perturbative quantum light-matter coupling to their logical extreme is the notion of *deep-strong coupling*, in which the coupling is *larger* than the bare energies of the light and matter. This exotic regime has been recently realized in superconducting flux qubits coupled to microwave resonators, due to the effectively very strong dipole moment associated with the flux qubit architecture. While theoretical studies of this regime are just starting to emerge, they have been primarily focused on ground-state properties, and for good reason. In Chapter 8, we study the properties of excitations in the deep-strong coupling regime. Such excitations ("photons" of the DSC system) are important from the standpoint of quantum nonlinear optics, as they dictate light emission in propagation. We show how the excited-state spectra imply the existence of extremely high-order *electromagnetic nonlinearities* not found in natural optical nature, and how this nonlinearity forms the basis for unique sources of quantum light. In particular, we show how such nonlinearities can form the basis for a type of "LED" (spontaneous emitter) or laser (stimulated emitter) that deterministically produces large Fock states of the system.

The exotic nonlinearity described in Chapter 8 leads, rather directly, to unique possibilities from the standpoint of generating quantum light: one wonders if the theoretical constructs employed can be translated into conventional nonlinear optics (in particular, at optical frequencies). In Chapter 9, we show how the unusual nonlinearity revealed in Chapter 8 is a manifestation a more general phenomenon: in particular, we show how similar phenomena (namely, macroscopic Fock-state generation) can be realized in the presence of a high-order intensity dependent dissipation. We show how in certain systems, the combination of frequency-dependent dissipation and nonlinearity can lead to unique phenomena of nonlinear dissipation that deterministically convert classical light states (such as coherent states) into strongly nonclassical light (such as macroscopic Fock states at optical frequencies of a single mode of light; for which there are no current methods to create even theoretically). This effect forms the basis for a whole new class of optoelectronic devices: for example, lasers employing this intensity-dependent dissipation can produce macroscopically highly number-squeezed states of radiation, which could be employed in metrology applications to get signal-to-noise beyond the quantum limit, as well as applications in quantum simulation where solutions to physical problems are encoded in the dynamical evolution of Fock states. More broadly, the nonlinear dissipation physics introduced here leads to a new route towards deterministically generating quantum light, in a way that can in principle exist in the presence of dissipation.

Chapter 2

Light-matter interactions with photonic quasiparticles

Note: This chapter is heavily based off "Light-matter interactions with photonic quasiparticles" by N. Rivera et al. Nature Reviews Physics (2020).

Interactions between light and matter play an instrumental role in many fields of science, giving rise to important applications in spectroscopy, sensing, quantum information processing, and lasers. In most of these applications, light is considered in terms of electromagnetic plane waves that propagate at the speed of light in vacuum. As a result, light–matter interactions can usually be treated as very weak, and captured at the lowest order in quantum electrodynamics (QED). However, recent progress in coupling photons to material quasiparticles (e.g., plasmons, phonons, and excitons) forces us to generalize the way we picture the photon at the core of every light–matter interaction. In this new picture, the photon, now of partly matter-character, can have greatly different polarization and dispersion, and be confined to the scale of a few nanometers. Such photonic quasiparticles enable a wealth of light–matter interaction phenomena that could not have been observed before, both in interactions with bound electrons and with free electrons. This Review focuses on exciting theoretical and experimental developments in realizing new light–matter interactions with photonic quasiparticles. As just a few examples, we discuss how photonic quasiparticles enable room-temperature strong coupling, ultrafast "forbid-

den" transitions in atoms, and new applications of the Cherenkov effect, as well as breakthroughs in ultrafast electron microscopy and new concepts for compact X-ray sources.

Interactions between light and matter play a crucial role in science and technology. The emission and absorption of light – by bound electrons in atoms, molecules, and solids, as well as by free electrons – form the direct basis for technologies both mature and nascent. Examples include modern spectroscopy, lasers, X-ray sources, LEDs, photo-diodes, solar cells, high-energy particle detectors, and advanced microscopy methods. Light–matter interactions are fundamentally quantum electrodynamical, and in many cases, are described as quantum transitions by electrons, accompanied by the emission, absorption, or scattering of quanta of the electromagnetic field in vacuum (photons). The theory describing photons and their interaction with electrons is nearly as old as quantum mechanics itself, and was first formulated by Dirac in 1927 [3], with an elegant re-formulation (still used today) by Fermi in 1932 [4]. Traditionally, it has been sufficient to describe the electromagnetic quanta as (a) composed of plane waves traveling at the speed of light and (b) having a wavelength much longer than the typical size scales of electron wavefunctions in atoms, molecules, and solids.

This traditional understanding is challenged by recent experiments using near-field microscopes to couple to polaritons in van der Waals materials [5, 6, 7, 8, 9, 10, 11, 12], as well as recent experiments confining light in nano-gaps between metals [13, 14, 15]. In particular, it is now feasible to couple light to extremely confined electromagnetic fields. Such fields – which can be plasmonic, phononic, excitonic, or even magnonic in nature – can be manipulated in many of the same ways as photons. Their close similarity to photons motivates their consideration as part of a more general concept, called photonic quasiparticles (Figs. 1, 2). A photonic quasiparticle, which fundamentally arises as a quantized solution to Maxwell's equations in a medium, is a broad concept that includes not only polaritons, but also photons in vacuum and homogeneous media, photons in cavities and photonic crystals, and even, excitations that seem fundamentally non-photonic, such as bulk plasmons and bulk phonons. As such, these quasiparticles generally differ from photons in vacuum in several key respects like polarization, confinement, and dispersion.

When considering how these excitations are absorbed and emitted by electrons (what we call "light–matter interactions"), one finds that these differences enable many phenomena that are difficult or even impossible to realize with photons in free space.

In systems of bound electrons (e.g., in atoms, molecules, or solids), the confinement of photonic quasiparticles strongly enhances the intrinsic coupling between these electrons and the quantized electromagnetic field. This is because the energy of the quasiparticle, , is confined over a very small volume, leading to correspondingly strong quantized electric and magnetic fields. The enhanced coupling gives rise to greatly enhanced spontaneous emission by excited electrons. For sufficiently confined photonic quasiparticles, the enhanced coupling is strong enough to enable coherent and reversible energy exchange between the electron and the electromagnetic field. The other important effect arising from confinement is the possibility of breaking conventional selection rules governing the types of electronic transitions that can occur. In sum, these effects may enable brighter single-photon sources, highly sensitive sensing and spectroscopy platforms, and potentially even new sources of entangled quasiparticles.

Meanwhile, in systems of free electrons, the spectral and directional properties of spontaneously emitted photonic quasiparticles are sensitive to the dispersion relation of the photonic quasiparticle. Controlling the dispersion relations by using structured media – as photonic crystals, optical nanostructures, or highly confined polaritons – allows one to control "at will" the properties of light emission based on the electron energy. Importantly, the delocalized quantum wave nature of free electrons gives additional opportunities to control light–matter interactions by shaping electron wavefunctions. For example, one can shape the wavefunction to display symmetries which are compatible (or incompatible) with the symmetry of the photonic quasiparticle field, thus leveraging selection rules to control the possible interactions [16]. Additional important effects appear when electrons interact with strong fields of photonic quasiparticles, which enable coherent energy exchange by means of absorption and stimulated emission. In sum, these effects may enable new and enhanced particle detection schemes, compact light sources from infrared to even X-ray frequencies, and breakthrough platforms for electron microscopy with nanometer and femtosecond resolution.

Although free and bound electron phenomena at first appear unrelated, and are typically connected to different fields of research, it is possible, and even illuminating, to take a unified view of these phenomena.

The crux of this unified view is a systematic classification of the types of interactions that can happen between arbitrary electronic systems and arbitrary photonic quasiparticles. This classification is shown in Figs. 1, 2, where we represent different types of elementary light–matter interaction processes between electrons and photonic quasiparticles in terms of Feynman diagrams. These diagrammatic representations emerge naturally from macroscopic quantum electrodynamics (MQED), which describes the interaction of electrons with electromagnetic fields in materials. An especially useful contribution from MQED that we will present in this Review is the quantization of the electromagnetic fields associated with photonic quasiparticles in terms of (classical) solutions of the macroscopic Maxwell equations in a medium.

As can be seen, changing the type of electron or the type of photonic quasiparticle in a particular Feynman diagram leads to fundamentally different phenomena, often seen as disparate physical effects. For example, spontaneous emission by atoms and molecules is loosely analogous to the Cherenkov radiation by free electrons, both being single-photonic-quasiparticle spontaneous emission processes; the Cherenkov effect is analogous to phonon amplification phenomena by electrons in solids solids, being governed by similar energy-momentum conservation rules; the phenomenon of photon-induced near-field electron microscopy is analogous to Rabi oscillations in cavity QED; high harmonic generation by bound electrons is analogous to nonlinear Compton scattering in free electrons. This line of thinking enables knowledge-transfer between different light–matter effects. Ultimately, this perspective enables one to predict and study new types of interactions that have yet to be explored.

Our Review aims to provide details to the picture painted above, by elaborating on the exciting recent theoretical and experimental developments in the field of light–matter interactions in nanophotonics, unifying the different phenomena when possible. The field of light–matter interactions in nanophotonics is broad in scope, and involves many important topics that we touch here only briefly, for which the following representative reviews pro-

vide further insight: polaritons in van der Waals materials [5, 6, 7], plasmonic nano-gaps [15], quantum plasmonics [17], enhanced spontaneous emission phenomena [18], strong coupling physics [19, 20, 21], electron-beam spectroscopy [22], and the theory of macroscopic quantum electrodynamics [23].

2.1 Photonic quasiparticles

2.1.1 Types of photonic quasiparticles

A photonic quasiparticle is a quantized excitation of an electromagnetic mode also called "a photon of a medium" [24, 25]. The mode is formally a time-harmonic solution to Maxwell's equations with frequency ω in an arbitrary medium, subject to boundary conditions. The electromagnetic mode corresponding to this quantized excitation is normalized such that the electromagnetic energy in a single-quasiparticle state is $\hbar\omega$, and its polarization and field-distribution are governed solely by the response functions of the medium: the dielectric permittivity ϵ and magnetic permeability μ. In Fig. 3 (top), we show some of the types of microscopic phenomena that can contribute to the response functions, such as free-electrons (in metals), bound electrons (in simple insulators like glass), optical phonons (in polar dielectrics), magnons (in ferro- and anti-ferromagnets), and excitons (in semiconductors). These microscopic phenomena define the frequency-dependence of the macroscopic response functions of the material. While we have discussed these photonic quasiparticles as contributing to the dielectric function, some, such as excitons, also depend on the dielectric function. For example, excitonic properties depend on the screening encoded by the low-frequency dielectric function. Different materials, as well as different geometries of the materials, lead to qualitatively different kinds of photonic quasiparticles, as shown in Fig. 3 (bottom). Let us now consider a systematic classification of the different types of photonic quasiparticles that exist, based on dimensionality, with an eye towards the effects in light–matter interactions enabled by each type of quasiparticle.

3D translationally invariant photonic quasiparticles

The simplest examples of photonic quasiparticles are those in a 3D translation-invariant bulk, which supports propagating plane waves that are characterized by their frequency, momentum, propagation lifetime, and polarization. The polarization is transverse to the electric displacement $\mathbf{D}$ or magnetic field $\mathbf{H}$, unless $\epsilon(\mathbf{k}, \omega) = 0$ or $\mu(\mathbf{k}, \omega) = 0$ respectively. If $\epsilon(\mathbf{k}, \omega) = 0$ or $\mu(\mathbf{k}, \omega) = 0$, longitudinal modes of Maxwell's equations are allowed, like bulk plasmons and phonons, or bulk magnons in the magnetic case. Even in a homogeneous medium, there exist several distinct kinds of photonic quasiparticles, which include photons in vacuum, photons in a transparent medium (e.g., glass), bulk polaritons, and their quasi-static analogues (e.g., bulk plasmons, bulk phonons, etc.). A key difference between these photonic quasiparticles and photons in vacuum is that some have phase velocities below the speed of light c, with bulk plasmons and phonons having velocities far below the speed of light. These reduced phase velocities enable phenomena such as radiation from uniformly moving charges, e.g., the Cherenkov effect in a dielectric medium [26], bulk plasmon emission processes measured in electron-energy loss spectroscopy [27], and even phonon emission processes by electrons in solids [28].

2D and 1D translationally-invariant photonic quasiparticles

. 2D translation-invariant systems include thin films, slabs, interfaces between two semi-infinite materials, multilayer stacks, and 2D materials. Such systems support several kinds of photonic quasiparticles, including waveguide modes in dielectric slab waveguides and hyperbolic media (such as hexagonal boron nitride), and confined surface modes that evanescently decay from the surface (e.g., surface plasmon polaritons and surface phonon polaritons in conventional media [29, 30]). Because the class of 2D translationally invariant photonic quasiparticles includes both thick and thin films, some examples of photonic quasiparticles such as slab waveguide modes and hyperbolic surface phonon polaritons could be considered as being both surface (due to their evanescent tails) and bulk (due to their propagation in the medium). 2D translationally invariant modes are characterized by their frequency, in-plane momentum, propagation lifetime, and polarization. Waveguide modes

can further have a discrete mode order that determines their out-of-plane field distribution.

From the standpoint of light–matter interactions, the polarization and dispersion of 2D translationally invariant systems lead to many effects that do not occur with photons in vacuum. For example, evanescent modes can have circular polarization in the plane perpendicular to their magnetic field. The chirality is locked to the direction of propagation (spin-momentum locking [31]), so that right-moving and left-moving waves have opposite chirality. Thus, an emitter with a circularly polarized transition dipole moment can only emit waves in one direction, as waves in the opposite direction have zero overlap with the dipole [32]. Relatedly, we note that polaritons in some systems, such as exciton-polaritons [33, 34] and plasmons [35, 36], can take on topological properties inherited from the matter part of the quasiparticle. Such topological properties allow for robust uni-directional polaritonic modes, which in the presence of an emitter could lead to new routes for unidirectional light-matter coupling.

In another example related to polarization, because the polarization of a surface mode is partially out-of-plane, a surface mode overlaps well with a vertically oriented transition dipole associated with a planar emitter such as excitons in a transition metal dichalcogenide [37]. This lies in contrast to free-space, where the transversality of the electromagnetic wave implies that vertically oriented dipoles cannot emit at normal incidence (zero overlap), rendering them optically dark and difficult to detect in the far-field. This enables one to perform spectroscopy with dark excitons based on surface plasmons [37].

Another key difference in light–matter interactions comes from the fact that systems with negative permittivity (polaritonic systems), support surface modes with wavelengths far smaller than that of a photon of the same frequency [38, 9, 8, 10, 39, 40, 11, 12], corresponding to a highly confined out-of-plane field. Such confinement leads to a very high local density of electromagnetic states, and consequently, quantum emitters in the vicinity of these modes can interact quite strongly with them, manifesting in enhanced spontaneous emission, as well as breakdown of selection rules associated with the dipole approximation. These effects are elaborated in Section 2. Experimentally, such quasiparticles have been leveraged for high-resolution nano-imaging of electrons in solids [5, 41, 42], sensitive sensors of vibrational transitions in molecules [43, 44], and enhanced interactions with

quantum emitters [45]. Similar conclusions to those discussed for 2D modes also apply in 1D translation-invariant systems (e.g., fibers and other waveguides) [46, 47, 48].

Importantly, the photonic quasiparticle concept also applies in systems with discrete translation invariance (periodic systems), in any dimension, where it includes photonic crystal modes (Bloch photons) [49].

0D translationally-invariant photonic quasiparticles. Systems with 0D translation-invariance (i.e., that fully break translation-invariance) support localized cavity modes, a distinct type of photonic quasiparticle characterized by its frequency, lifetime, polarization, and field distribution (setting its mode volume). In particular, cavities with high quality factors support photonic quasiparticles such as whispering-gallery modes [50, 51, 52] and photonic crystal defect modes [53, 54], used for example for enhanced sensors and for low-threshold laser interactions. Of importance for this review are cavities with ultra-high quality factors [50, 51, 52, 54] and ultra-small mode volumes (e.g., plasmonic and phonon-polaritonic cavities). Both can enable enhanced spontaneous emission due to the concomitant enhancement of the local-density of states [55, 56, 13, 14]. This feature is similar to highly confined propagating quasiparticles in 1D and 2D. One major difference in 0D systems is that boundary conditions force a quasi-discrete spectrum for the modes, leading to sharp spectral peaks in the local density of states – in contrast to systems with propagating modes, whose spectrum is continuous. Qualitatively, the interaction of quantum emitters with a discrete mode is quite different from that with continuum modes. In the former case, the system resembles two coupled oscillators, allowing new normal modes of the emitter and cavity mode to form (strong coupling). In the latter case, a discrete emitter undergoes irreversible decay into the continuum (enhanced spontaneous emission), provided that the coupling is not too strong.

Special types of photonic quasiparticles that do not fit as neatly into the above categorization can be constructed by superposition of extended modes, which breaks their translation invariance and effectively localizes them. For example, a cylindrically symmetric superposition of surface plasmons creates plasmon vortices characterized by an integral orbital angular momentum (OAM) quantum number. Such 2D vortices have been observed on various metal-insulator surfaces [57, 58, 59] and predicted in graphene and hexagonal

boron nitride [60]. More advanced superpositions can be used to create arrays of vortices with topological features [61]. From the standpoint of light–matter interactions, photonic quasiparticles with OAM are interesting because when an electron absorbs or emits such a quasiparticle, its angular momentum must change by the OAM of the quasiparticle (provided the emitter and vortex are concentric) [62, 63, 64]. Controlling dynamics with OAM-possessing photonic quasiparticles also applies in the case of free-electron absorption and stimulated emission [65, 66].

In this section, we have largely considered photonic quasiparticles in terms of the modes of the linear Maxwell equations: however, photonic quasiparticles are subject to nonlinearities. For example, exciton-polaritons have strong nonlinearities owing to Coulomb interactions between the excitons, leading to phenomena like polariton-polariton scattering. These nonlinearities lead to exciting phenomena such as Bose-Einstein condensation and superfluidity [67, 68, 69, 70, 71, 72] , as have been demonstrated with exciton polaritons, as well as with magnons [73]. For example, in the case of exciton-polariton condensates formed by semiconductors in microcavities, leakage of the photonic part of the polariton from the cavity walls leads to emission in a coherent state (the coherence is derived from that of the condensate), analogous to laser action, and termed accordingly as polariton lasing. Another interesting aspect of these polaritons is that their strong nonlinear interactions lead to intriguing effects such as polarization-sensitive switching effects, which have been proposed for polarization dependent switches and transistors [74, 75, 76, 77].

Example of photonic quasiparticles: Polaritons in van der Waals materials.

An important example of photonic quasiparticles are polaritons in van der Waals and 2D materials – primarily plasmon and phonon polaritons. They are of great recent interest because unlike photons in conventional dielectrics, they can be confined to volumes over a million times smaller than that of a diffraction-limited photon in vacuum, which can enable many new effects in light–matter interactions, as well as enhanced sensors, and enhanced optical nonlinearities. The basic physics of polaritons is well-described in recent reviews (e.g., [78, 5, 6]); our focus is on their unique light–matter interactions, emphasizing the key similarities and differences to free-space photons.

In Fig. 4, we summarize recent experiments probing polaritons in thin films and 2D materials, demonstrating that optics can be performed with polaritons. In planar slabs of polaritonic materials, the polariton has an in-plane wavevector much larger than the wavevector of a photon at the same frequency. Due to the continuous translational symmetry of the slab, photons incident from the far-field cannot couple directly to the slab (ignoring the edges of the slab), necessitating the use of a coupling element that provides momentum to the incident photon, enabling momentum conservation. The most common examples are sharp tips and gratings. A sharp tip fully breaks in-plane translation symmetry, allowing an optical far-field to launch polaritonic waves from the tip, as is central to methods like scanning near-field optical microscopy (SNOM). Such methods are used extensively to measure the complex dispersion relation (wavenumber and propagation length), as well as the spatial distribution of the electric field, in various polaritonic systems: plasmons in graphene [9, 8, 79, 40, 12], phonon polaritons in hexagonal boron nitride (thin films and monolayers) [10, 80, 81, 82], exciton polaritons in molybdenum selenide [83, 84], and newer materials such as hyperbolic phonon polaritons in molybdenum trioxide [85, 86].

Figs. 4a and 4b show direct examples of the highly confined nature of the polaritons. In Fig. 4a, showing a recent example with plasmons in graphene, the plasmon is measured to have a wavelength over 100 times smaller than the wavelength of a photon in vacuum. This is a key difference from photonic quasiparticles in all-dielectric systems. Fig. 4a shows the exceptionally long lifetime that can be achieved with graphene plasmons (roughly 130 optical cycles), which was facilitated by operating at low temperature to suppress losses related to acoustic phonon coupling. The combination of high confinement and low loss is instrumental not only in envisioning optical components based on the propagation of plasmons, but more generally in enhancing light–matter interactions with quantum emitters. Such enhancements depend on the local density of optical states that increase with high confinement and low loss. In Fig. 4b, we show a recent SNOM of highly-confined phonon-polaritons in molybdenum trioxide, whose wave-fronts demonstrate the hyperbolic nature of the polaritons in this material [86], potentially enabling new platforms for hyperbolic optics in the mid-infrared spectral region.

Various antenna structures can also be used to assist the coupling of light into the pho-

tonic quasiparticle mode, as in Fig. 4d, where a gold rod is used to launch phonon polaritons in gratings of hexagonal boron nitride, which act as a hyperbolic metasurface. Due to the opposite signs of in- and out-of-plane permittivities, wavefronts launched from the rod exhibit spatial propagation profile in a clear signature of hyperbolicity [87], enabling one to study light–matter interactions between emitters and hyperbolic quasiparticles. Similar methods using antennas have also been used to launch graphene plasmons [88]. Recently, the reflection and refraction of these hyperbolic polaritons has also been observed [89], at interfaces between hBN and vanadium oxide (VO2), a phase change material. Such observations may enable planar demonstrations of phenomena such as lensing based on photonic quasiparticles.

The interaction with polaritons can also be facilitated with grating structures, as in Fig. 4c, where a grating-cavity consisting of a gold-grating atop a gold mirror sandwiches boron-nitride-encapsulated graphene [11] (encapsulation improves the lifetime of the plasmon, due to suppression of coupling to phonons [90]). The grating couples far field light into the cavity-enhanced graphene plasmons that benefits from the very high reflectivity of gold at the mid-infrared wavelength. While the lifetime is modest, being on the order of ten optical cycles, what is remarkable here is that this cavity achieves out-of-plane confinement of the graphene plasmon to the scale of 1 nm, representing the smallest mode-volume graphene plasmon ever measured, with an estimated mode volume on the order of $10^{-9}\lambda_0^3$. Such small volumes could enable extremely non-perturbative interactions between light and matter, with emerging designs demonstrating potentially even tighter confinement [91].

Example of photonic quasiparticles: plasmons in metallic nanogaps

Another important class of photonic quasiparticles in this Review are plasmons in the "conventional" noble metals such as gold and silver. Confined surface plasmons can be supported in these systems based on thin films and metal-insulator-metal structures. We focus particularly on localized plasmonic cavities as they have been the workhorse of recent experiments in strong quantum light–matter interactions. We leave detailed discussion of the electromagnetic physics of these cavities to dedicated reviews as [15]. Plasmonic nano-

gaps typically involve the geometry of a metallic nano-particle (such as a nano-sphere or nano-disk) separated from a planar metal film by a very small gap, which can be on the order of 1 nm. This geometry is referred to as a nanoparticle-on-mirror (sometimes abbreviated as NPoM) geometry or as a plasmonic nanogap cavity.

Recent experiments have demonstrated the existence of these strongly confined cavity modes based on nanogaps as "large" as 5 nm [55], moving recently to sub-nanometer sizes [13]. A striking recent example of this geometry at its ultimate limit is that of the picocavity [14], which leads to strong field enhancements in a single atom protrusion from a nanoparticle, explained in terms of a type of lightning-rod effect. It is instrumental to note the values of the polarization, lifetime, and mode volume of these types of modes: the polarization is primarily perpendicular to the interfaces, the lifetimes tend to be roughly one to ten optical cycles (with potential improvements coming from hybrid dielectric-metal geometries [92]), and the mode volumes have been estimated to be below 1 nm^3. The extreme confinement of such cavities makes effects related to spatial nonlocality particularly strong [93]; such effects are of considerable importance as they are likely to provide fundamental limitations on applications of nanophotonics and light–matter interactions.

2.1.2 Quantum electrodynamics with photonic quasiparticles

Although the examples above have thus far been understandable from solutions of the classical Maxwell equations, experiments have also demonstrated the underlying quantum nature of the electromagnetic fields of these photonic quasiparticles through quantum optical measurements. Many of these experiments have been in the context of plasmonics. For example, quantum statistics of plasmons were demonstrated [94], along with plasmonic preservation of photon entanglement [95] and two-plasmon quantum interference in a Hong-Ou-Mandel experiment [96].

Perhaps more simply, phenomena like spontaneous emission in any material system already call for a quantized description of the electromagnetic fields associated with each type of photonic quasiparticle. The key theoretical framework that prescribes the quantization of any photonic quasiparticle and the interactions of these quasiparticles with emitters

is called macroscopic quantum electrodynamics (MQED) [23, 97, 98]. It is "macroscopic" because it treats the photonic quasiparticles as being governed by the macroscopic Maxwell equations. i.e., MQED treats the medium in terms of permittivities and permeabilities, taking the microscopic charges and currents in the medium as continuous. As an important point of terminology, since MQED handles the quantization of the EM field in any linear medium, its special cases cover all the effects of "other QEDs" in the literature such as cavity, circuit, waveguide, photonic-crystal, and plasmonic QED.

Quantization of photonic quasiparticles

Pedagogically, it is useful to explain the quantization of the electromagnetic field in two steps: in the first, the fields are quantized in ideal, lossless materials, and in the second, they are quantized in arbitrary absorbing materials. Quantization of electromagnetic fields in lossless materials is long-known, as exposited in [99, 100]. For most cases of interest, the lossless case describes very well the essential physics of the emission and absorption of photonic quasiparticles by emitters, bound or free. With this in mind, we first describe the quantization in lossless materials in a constructive way that introduces the terminology to be used more generally later. The absorbing case is presented in Box 1.

In lossless and non-dispersive materials, we may represent an electromagnetic field operator (such as the vector potential $\mathbf{A}(\mathbf{r},t)$ in the Heisenberg picture) in terms of an expansion over time-harmonic modes $\mathbf{F}_n(\mathbf{r})e^{-i\omega_n t}$. These modes capture all of the details of the frequency, polarization, and field distributions of the photonic quasiparticles described in the previous section (e.g., dispersion relations, polarization properties, and field distributions). In this expansion, each mode, n, is associated with a quantum harmonic oscillator [100], with associated creation $a_n^\dagger$ and annihilation a_n operators, satisfying the canonical bosonic commutation relations: $[a_m, a_n] = [a_m^\dagger, a_n^\dagger] = 0$ and $[a_m, a_n^\dagger] = \delta_{mn}$. The resulting vector potential takes the form:

$$\mathbf{A}(\mathbf{r}) = \sum_n \sqrt{\frac{\hbar}{2\epsilon_0\omega_n}} \left(\mathbf{F}_n(\mathbf{r})a_n e^{-i\omega_n t} + \mathbf{F}_n^*(\mathbf{r})a_n^\dagger e^{i\omega_n t}\right) \tag{2.1}$$

For a non-magnetic medium, the mode satisfies $\nabla \times \nabla \times \mathbf{F}_n = \epsilon k_n^2 \mathbf{F}_n$, with $k_n = \omega_n/c$

[49] and are normalized such that $\int d\mathbf{r}\ \epsilon|\mathbf{F}_n|^2 = 1$. This normalization makes it so that a one-photon state has an electromagnetic energy of $\hbar\omega$ relative to the vacuum state. This mode expansion is immediately applicable to QED

Box 1: Macroscopic quantum electrodynamics (MQED)

In any general material, including lossy ones, we may represent an electromagnetic field operator in terms of a "mode expansion" that decomposes the electromagnetic field in terms of the fields of time-harmonic point dipoles in the medium. These dipoles are parameterized by their location $\mathbf{r}$, frequency ω, and orientation $k = 1, 2, 3$ (or x, y, z). The quantization of the electromagnetic field proceeds by quantizing these dipoles, associating with each $(\mathbf{r}\omega k)$ a quantum harmonic oscillator with associated creation $f_k^\dagger(\mathbf{r}, \omega)$ and annihilation $f_k(\mathbf{r}, \omega)$ operators, satisfying $[f_k(\mathbf{r}, \omega), f_{k'}(\mathbf{r}', \omega')], [f_k(\mathbf{r}, \omega), f_{k'}(\mathbf{r}', \omega')]^\dagger = 0$ and $[f_k(\mathbf{r}, \omega), f_{k'}^\dagger(\mathbf{r}', \omega')] = \delta_{kk'}\delta(\mathbf{r} - \mathbf{r}')\delta(\omega - \omega')$. Using these operators, the EM field Hamiltonian is given by

$$H_{\text{em}} = \int d\mathbf{r} \int_0^\infty d\omega\ \hbar\omega \mathbf{f}^\dagger(\mathbf{r}, \omega) \cdot \mathbf{f}(\mathbf{r}, \omega). \tag{2.2}$$

where we have left out the zero-point energy. The resulting vector potential takes the form (in the Schrodinger picture):

$$\mathbf{A}(\mathbf{r}) = \sqrt{\frac{\hbar}{\pi\epsilon_0}} \int d\omega' \frac{\omega'}{c^2} \int d\mathbf{r}' \sqrt{\text{Im}\ \epsilon(\mathbf{r}', \omega')}\, (\mathbf{G}(\mathbf{r}, \mathbf{r}', \omega') \cdot \mathbf{f}(\mathbf{r}', \omega') + \text{h.c.}) \tag{2.3}$$

where $\mathbf{G}(\mathbf{r}, \mathbf{r}', \omega')$ is the Green's function of the Maxwell equations, which in a non-magnetic medium satisfies $(\nabla \times \nabla \times -\epsilon(\mathbf{r}, \omega)k^2)\mathbf{G}(\mathbf{r}, \mathbf{r}', \omega') = \delta(\mathbf{r} - \mathbf{r}')I$ with $k = \omega/c$. $\epsilon(\mathbf{r}, \omega)$ is the permittivity tensor in a general dispersive, local, anisotropic medium, and I the 3×3 identity matrix. The MQED vector potential for the nonlocal case is shown in Table I. This quantized field operator is a central result of MQED [23], and all the previous expressions for the quantized fields in terms of mode expansions are special cases of this. Note that all of the cases represented in Table 1 assume non-magnetic media. For magnetically polarizable media, as reviewed in [23], additional $\mathbf{f}$ operators must be introduced that correspond to magnetic dipole excitations, which are connected to the field operators through a magnetic Green's function.

Then, the field operators are a sum of terms from electric and magnetic dipoles.

We briefly comment on the physical principles encoded in this formalism. The quantized field is connected to quantized dipoles through the classical Maxwell equations. We give a brief heuristic sketch of how these dipoles are quantized. For simplicity, we will do it here in an isotropic, local medium (which can still be lossy). The idea is to write a current field operator as a sum over bosonic degrees of freedom (point dipoles governed by position, frequency, and direction): $\mathbf{j}(\mathbf{r}) = \int_0^\infty d\omega(N(\mathbf{r},\omega)\mathbf{f}(\mathbf{r},\omega) + \text{h.c.})$ with $N(\mathbf{r},\omega)$ some unknown normalization constant. The normalization is prescribed by both the commutation relations between the $\mathbf{f}$s and the fact that the correlation functions must be in agreement with the fluctuation-dissipation theorem for a linear medium. In particular, for a linear medium, it must be the case that

$$\langle \mathbf{j}(\mathbf{r},\omega) \otimes \mathbf{j}(\mathbf{r}',\omega) = \epsilon_0 \hbar \omega^2 \coth\left(\frac{\hbar\omega}{2kT}\right) \text{Im}\, \epsilon(\mathbf{r},\omega)\delta(\mathbf{r}-\mathbf{r}'). \tag{2.4}$$

Taking the expectation values at zero temperature yields $N(\mathbf{r},\omega) = \sqrt{4\pi\epsilon_0\hbar\omega^2 \text{Im}\, \epsilon(\mathbf{r},\omega)}$. Plugging this in, and convolving the current operator with the $\mu_0\mathbf{G}(\mathbf{r},\mathbf{r}',\omega')$, as per the classical Maxwell equation for the vector potential, gives exactly the vector potential operator above.

phenomena in low-loss cavities, waveguides, and photonic crystals. In practice, mode expansions can also be used in the case of dispersive materials such as the polaritonic materials presented in Fig. 4 (provided the modes kept in the mode expansion are of low loss), by changing the normalization condition (as in Fig. 5 and Box 1). The adjusted normalization condition arises because the energy of the quanta in a dispersive system is governed by the Brillouin energy density formula for dispersive materials [101, 102]. We mention here that these mode expansions are not valid at all frequencies in dispersive materials, because regions of high loss generally exist, particularly in polaritonic materials. The examples shown in Fig. 4 are chosen intentionally to coincide with low enough loss.

2.1.3 Quantum interactions between emitters and photonic quasiparticles

Once photonic quasiparticles are quantized, we now quantitatively describe how these quasiparticles interact with bound and free electrons (collectively referred to as emitters). For this purpose, we consider transitions between electronic states of the emitter that are accompanied by the emission, absorption, or scattering of single or multiple photonic quasiparticles (either real, as in spontaneous emission, or virtual, as in Lamb shifts/Casimir-Polder forces). Examples of these processes for bound and free electrons were shown in Figs. 1, 2, with examples of the relevant photonic quasiparticles shown in Fig. 3 and Section 1.1.

In non-relativistic bound electron systems, these transitions are described by the Pauli-Schrodinger Hamiltonian, or a suitably approximated version of it (see Box 2). In free-electron systems (relativistic or non-relativistic), the transitions are governed by the Dirac Hamiltonian, in cases where electron spin is important, or the Klein-Gordon Hamiltonian, where it is not (see Box 3). In both cases, the transitions are described by a term proportional to $\mathbf{A} \cdot \mathbf{v}$, provided that the electron does not change its energy significantly upon emission or absorption. This term couples the quantized vector potential to the velocity of the electron, described in terms of its momentum by $\mathbf{v} = (\mathbf{p} - q\mathbf{A})/m$, with q the electric charge and m the mass of the electron.

The key element in any calculation of light–matter processes with photonic quasiparticles is the rate of transition between some initial quantum state i and some final quantum state f. See Figs. 1, 2 for examples of initial and final states corresponding to known light–matter interaction processes. This rate of transitions at arbitrary order in the perturbation can be found by an iterative procedure [103]. The most commonly occurring cases are the transition rates at first (1) and second (2) order in QED, which are respectively given as $\Gamma^{(1)} = \frac{2\pi}{\hbar}|V_{fi}|^2\delta(E_f - E_i)$, and $\Gamma^{(1)} = \frac{2\pi}{\hbar}|\lim_{\eta\to 0}\sum_n \frac{V_{fn}V_{ni}}{E_i - E_n + i\eta}|^2\delta(E_f - E_i)$. Here, $V_{ab} = \langle a|V|b\rangle$, with $V = -q\mathbf{A}\cdot\mathbf{v}$ being the interaction Hamiltonian of QED, and n denotes an intermediate (virtual) state to be summed over. The delta functions express the conservation of energy between initial and final states. Energy shifts associated with emission

and re-absorption of virtual photonic quasiparticles (Lamb shifts, Casimir-Polder forces) can be described by time-independent perturbation theory, with the shift in energy δE_i of quantum state i given as $\delta E_i = \lim_{\eta \to 0} \sum_n \frac{|V_{ni}|^2}{E_i - E_n + i\eta}$.

So far, the principles of MQED in its lossless and its lossy varieties have been used with the interaction terms above to describe a plethora of phenomena: atomic spontaneous emission of one and two photons (see e.g., [104, 100, 23, 105, 106, 107, 108, 109]), emission from extended emitters in solids like quantum wells (e.g., [110]), strong-coupling effects in bound emitters (e.g., [23, 111]), cavity / circuit / waveguide / plasmonic / photonic crystal QED phenomena (e.g., [112, 113, 114, 115, 116, 117, 118, 119]), energy shifts due to virtual photon emission and absorption as the Lamb shifts / Casimir-Polder forces (e.g., [120, 121]), Casimir forces (e.g., [122, 23, 123]), and even phenomena associated with emission of photonic quasiparticles by ultra-relativistic electrons [124, 125], as well as electrons driven by strong external fields [126]. Generally, it can be used to describe any of the processes illustrated in Figs. 1, 2.

2.2 Light-matter interactions with photonic quasiparticles in bound electron systems

The bulk of the Review discusses how the photonic quasiparticles described above are used to enhance and control the classical and quantum interactions of electromagnetic fields with electrons in atoms, molecules, solids, and even with free electrons (collectively referred to as "emitters"). For each type of emitter, it is useful to further divide the interactions by whether they are "weak-coupling" effects, such as emission, absorption, and scattering, where the perturbative description of light–matter coupling is valid, or "strong-coupling" effects, where the perturbative description is not valid. We survey both regimes below. In all cases, we consider the effects of different types of photonic quasiparticles.

2.2.1 Controlling bound electron spontaneous emission with photonic quasiparticles

Spontaneous emission with photonic quasiparticles

A key effect arising from photonic quasiparticles is that the spontaneous emission of excited emitters (bound or free) can take place by emission of a photonic quasiparticle different from a photon in vacuum. This effect, first investigated theoretically in the context of nuclear magnetic dipole emission by Edward Purcell in 1946, is today referred to as the Purcell effect. Quantum mechanically, spontaneous emission corresponds to a transition between an excited electron (energy $\hbar\omega_i$) with no photonic quasiparticles $|i,0\rangle$, to a set of final emitter states (energy $\hbar\omega_f$) with one photonic quasiparticle at some mode $\{|f,1\rangle\}$. For a fixed final electron state f, the emission rate Γ_{fi} can be derived by applying Fermi's Golden Rule at first-order in time-dependent perturbation theory, using the quantized electromagnetic field of an arbitrary medium according to MQED [105]:

$$\Gamma_{fi} = \frac{2\mu_0}{\hbar}\int d\mathbf{r}d\mathbf{r}'\,\mathbf{j}^*_{fi}(\mathbf{r})\text{Im}\,\mathbf{G}(\mathbf{r},\mathbf{r}',\omega_{if})\cdot\mathbf{j}_{fi}(\mathbf{r}) \approx \frac{2\mu_0\omega_{fi}^2}{\hbar}\mathbf{d}^*_{fi}\cdot\text{Im}\,\mathbf{G}(\mathbf{r},\mathbf{r},\omega_{if})\cdot\mathbf{d}_{fi}, \quad (2.5)$$

where $\omega_{if} = \omega_i - \omega_f$, and $\mathbf{j}_{fi}(\mathbf{r}) = q\psi^*_f(\mathbf{r})(\mathbf{p}/m)\psi_i(\mathbf{r})$, with $\psi_{i(f)}$ being the initial (final) emitter wavefunction, q the emitter charge, m the emitter mass, $\mathbf{p}$ the momentum operator, and $\mathbf{G}(\mathbf{r},\mathbf{r},\omega)$ the Green's function of the Maxwell equation for the electromagnetic medium of interest. The final formula can also be expressed in terms of ratio the local density of optical states (LDOS) of the medium $\boldsymbol{\rho}(\mathbf{r},\omega_{if}) = \frac{6\omega_{if}}{\pi c^2}\text{Im}\,\mathbf{G}(\mathbf{r},\mathbf{r},\omega_{if})$ as

$$\Gamma_{fi} = (\hat{d}^*_{fi}\cdot\boldsymbol{\rho}(\mathbf{r},\omega_{if})\cdot\hat{d}_{fi}/\rho_0(\omega_{if}))\Gamma_0, \quad (2.6)$$

where $\hat{d}_{fi}$ is the direction of the transition dipole, and $\Gamma_0 = \frac{|\mathbf{d}_{fi}|^2\omega_{if}^3}{3\pi\epsilon_0\hbar c^3}$ the rate of spontaneous emission into photons in vacuum. That the spontaneous emission is proportional to the imaginary part of the Green's function is a manifestation of the fact that spontaneous emission can be seen as emission driven or "stimulated" by vacuum fluctuations of the quantized electromagnetic field. In particular, the fluctuations of the quantized electric field, given by $\langle 0|E_i(\mathbf{r},\omega)E_j(\mathbf{r}',\omega)|0\rangle$ with $|0\rangle$ the vacuum state of the field, are related to the

Green's function via the fluctuation-dissipation relation through $\langle 0|E_i(\mathbf{r},\omega)E_j(\mathbf{r}',\omega)|0\rangle = \frac{\mu_0}{\pi}\hbar\omega^2 \mathrm{Im}G_{ij}(\mathbf{r},\mathbf{r}',\omega)\delta(\omega-\omega')$. More complex phenomena than single-photon spontaneous emission, such as multi-photon spontaneous emission and vacuum energy shifts, are also related to vacuum fluctuations. Consequently, dependences on the imaginary part of the Green's function are ubiquitous in light–matter interactions.

Box 2: Hamiltonians of light–matter interactions in bound-electron systems

We describe the Hamiltonian of light–matter interactions in bound-electron systems. A system of N non-relativistic charges of masses m_i and charges q_i, coupled to the quantized electromagnetic field is described by the Pauli-Schrodinger Hamiltonian H^{PS}:

$$H^{\text{PS}} = \sum_{i=1}^{N} \frac{(\mathbf{p}_i - q_i \mathbf{A}_{\text{ext}}(\mathbf{r}_i) - q_i \mathbf{A}_{\text{q}}(\mathbf{r}_i))^2}{2m_i} + \sum_i q_i \phi_{\text{ext}}(\mathbf{r}_i) + \sum_{i>j}^{N} V(\mathbf{r}_i, \mathbf{r}_j) + H_{\text{em}} \quad (2.7)$$

where $\mathbf{p}_i$ is the momentum operator of the ith particle, $\mathbf{r}_i$ is the corresponding position operator. ϕ_{ext} and $\mathbf{A}_{\text{ext}}$ are the scalar and vector potential of static external fields (e.g., Coulomb atomic field and a DC magnetic field). In certain cases, a strong time-dependent external field, e.g., a high intensity laser, can also be modeled as a classical field and captured by such potentials, which will become time-dependent. $\mathbf{A}_{\text{q}}$ is the quantized electromagnetic field operator. H_{em} is the Hamiltonian of the electromagnetic field. V is the inter-particle (Coulomb) interaction, which depends on the (DC) permittivity of the medium surrounding the particles (screening), provided that electrostatic interactions with a medium are treated at a continuum, rather than atomistic level.

Commonly, the quantized photon fields have spatial variations much longer than the size of the emitter wavefunction, so that $\mathbf{A}_{\text{q}}(\mathbf{r}_i) \approx \mathbf{A}_q(0)$ (long-wavelength approximation), with the emitter being taken to be localized around $\mathbf{r} = 0$ without loss of generality. Under the long-wavelength approximation, it is possible to rigorously transform the interaction Hamiltonian to be specified in terms of the dipole moment ($\mathbf{d} = \sum_{i=1}^{N} \mathbf{d}_i$) and electric field ($\mathbf{E}$). This is the dipole Hamiltonian, given by:

$$H_{\text{dip}} = \sum_{i=1}^{N} \frac{(\mathbf{p}_i - q_i \mathbf{A}_{\text{ext}}(\mathbf{r}_i))^2}{2m_i} + \sum_i q_i \phi_{\text{ext}}(\mathbf{r}_i) + \sum_{i>j}^{N} V(\mathbf{r}_i, \mathbf{r}_j) + H_{\text{em}} - \mathbf{d} \cdot \mathbf{E}(0) + H_{\text{dip}}^{\text{self}} \quad (2.8)$$

where $H_{\text{dip}}^{\text{self}}$, the dipole self-energy, is a term whose precise form depends on how the field is quantized, but in all cases is quadratic in the dipole moment and independent of the field operators. The dipole Hamiltonian is a work-horse in atomic, molecular, and optical physics.

A key simplification arises when two levels of a bound electron system resonantly interacts with a single mode of a low-loss cavity. We may then approximate the quantized electric field in terms of a single mode, i.e., $\mathbf{E}(\mathbf{r}) = i\sqrt{\frac{\hbar\omega}{2\epsilon_0}}\mathbf{u}(0)(a - a^\dagger)$, with $\mathbf{u}(0)$ the cavity mode function at the emitter. We may also approximate the matter as a two-level system, i.e., $H_{\text{TLS}} = \frac{1}{2}\hbar\omega_0\sigma_z$, with σ_z the Pauli z-matrix, and $\mathbf{d} = \mathbf{d}_{fi}\sigma_x$, with $\mathbf{d}_{fi}$ the dipole matrix element of the two-level system. These approximations lead to the Rabi Hamiltonian, which is the key Hamiltonian of cavity QED:

$$H_{\text{Rabi}} = \frac{1}{2}\omega_0\sigma_z + \hbar\omega a^\dagger a + g\sigma_x(a + a^\dagger) \tag{2.9}$$

where we have defined $g = i\sqrt{\frac{\omega}{2\epsilon_0\hbar}}\mathbf{u}(0) \cdot \mathbf{d}_{fi}$ (taking the dipole matrix element and field profile real). The Rabi Hamiltonian includes virtual processes in which the two-level system can be excited while also emitting a photon, as well as those in which the system can be de-excited while also absorbing a photon. If $g \ll \omega$, then these processes can be neglected under the rotating-wave approximation, reducing to the Jaynes-Cummings Hamiltonian:

$$H_{\text{JC}} = \frac{1}{2}\omega_0\sigma_z + \hbar\omega a^\dagger a + g(\sigma^+ a + \sigma^- a^\dagger) \tag{2.10}$$

with $\sigma^\pm$ being the raising $(+)$ and lowering $(-)$ operators of the two-level system.

The quantity $\mathbf{j}_{fi}(\mathbf{r})$ is known as the transition current density, and its introduction reveals that the emission rate is, up to a factor of 2, $W_{fi}/\hbar\omega_{if}$, where W_{fi} is the classical work done on this transition current by its own radiated field. The right-hand side of the equation holds under the dipole approximation (or long-wavelength approximation), i.e., that $\mathbf{j}_{fi}$ is localized over a scale much smaller than that of the optical field, with

$\mathbf{d}_{fi} = \int d\mathbf{r}\ \psi_f^*(\mathbf{r}) q\mathbf{r}\psi_i(\mathbf{r})$ being the transition dipole moment. This formulation allows numerical simulation of the Purcell effect in complex electromagnetic geometries via classical electromagnetic simulations based on e.g., finite-element, finite-difference, or boundary-element methods. The radiated flux to each final state f can be calculated by solving the classical electromagnetic problem for a dipole source $\mathbf{d}_{fi}$ or a more general current source $\mathbf{j}_{fi}(\mathbf{r})$, where each such source is calculated using the quantum mechanical wavefunctions. From the above equation, it can be seen that the validity of such an approach is not limited to dipole emitters but is general to any quantum emitter characterized by its transition current density.

Although the approach here makes use of MQED in lossy media, it conforms with the mode expansions of Section 1.2 by recognizing that in the lossless limit, the imaginary part of the Green's function is given by a mode expansion of the form $\text{Im}\ \mathbf{G}(\mathbf{r}, \mathbf{r}', \omega) = \frac{\pi c^2}{2\omega} \sum_n \mathbf{F}_n(\mathbf{r}) \otimes \mathbf{F}_n^*(\mathbf{r}')\delta(\omega - \omega_n)$ [127], leading to a decay rate in terms of modes given by $\Gamma_{fi} = \frac{\pi q^2}{\epsilon_0 m^2 \hbar \omega_{if}} \sum_n \left| \int d\mathbf{r}\ \psi_f^*(\mathbf{r}) \mathbf{F}_n^*(\mathbf{r}) \cdot \mathbf{p}\psi_i(\mathbf{r}) \right|^2 \delta(\omega_{if} - \omega_n)$. In the dipole approximation, this becomes $\Gamma_{fi} = \frac{\pi \omega_{if}}{\epsilon_0 \hbar} \sum_n |\mathbf{d}_{fi} \cdot \mathbf{F}_n^*|^2 \delta(\omega_{if} - \omega_n)$.

The case of a dipole emitter: the Purcell effect.

One of the most common and instructive examples of the Purcell effect involves the enhancement of spontaneous emission of a dipole emitter in an optical cavity. For a single-mode cavity, the electric field can be expressed as $\mathbf{E}(\mathbf{r}, t) = \mathbf{u}(\mathbf{r}, t) e^{-i\omega t - \Gamma t/2}$ with $\mathbf{u}$ a dimensionless function dictating the spatial mode profile, V the mode volume, and Γ the decay rate of the mode. As there is an arbitrary degree of freedom in defining the mode volume versus the normalization of $\mathbf{u}(\mathbf{r})$, it can be chosen so its maximum value is 1. The imaginary part of the Green's function of this single mode can be written as a Lorentzian [127]: $\text{Im}\ \mathbf{G}(\mathbf{r}, \mathbf{r}, \omega) = \frac{c^2}{V} \frac{\Gamma\omega}{(\omega_{if}^2 - \omega^2)^2 + (\Gamma\omega)^2} \mathbf{u}^*(\mathbf{r}) \otimes \mathbf{u}(\mathbf{r})$. Defining the quality factor $Q = \omega/\Gamma$, the spontaneous emission rate on resonance ($\omega = \omega_{fi}$) immediately follows as:

$$\Gamma_{fi} = \frac{3}{4\pi^2} \frac{Q}{(V/\lambda_0^3)} |\hat{d}_{fi} \cdot \mathbf{u}(\mathbf{r})|^2 \Gamma_0, \tag{2.11}$$

with $\lambda_0 = 2\pi c/\omega_{if}$ the photon wavelength in vacuum. Since Γ_{fi}/Γ_0 is proportional to the LDOS, we see immediately that the LDOS goes as Q/V, i.e., it is enhanced by high quality factors and small modal volumes.

When the transition dipole overlaps perfectly in polarization and is located at the maximum of the mode ($|\hat{d}_{fi}\cdot\mathbf{u}(\mathbf{r})|^2 = 1$), the expression coincides with Purcell's famous formula [128]. Experiments involving the Purcell effect often have many emitters that are not located at the maximum of the mode and whose polarizations do not perfectly overlap with the field polarization – leading to less dramatic enhancements than predicted by the ideal Purcell formula. Another effect that can be appreciated from the Lorentzian dependence of the Green's function is that for an emitter far off-resonance from the cavity, $\Gamma_{fi} < \Gamma_0$, representing an inhibition of spontaneous emission [112].

Typically, the Purcell factor $F_p = \Gamma_{fi}/\Gamma_0$ is either optimized by maximizing Q or by minimizing V. That said, spontaneous emission enhancement need not rely on a cavity, as spontaneous emission can also be enhanced for emitters coupled to waveguides or polaritonic films that support propagating photonic quasiparticles. In such systems, the quality factor of the propagating waves does not play the essential role it plays in cavities, because of the continuous dispersion $\omega(k)$ of the waves. However, the confinement factor $\eta = ck/\omega(k) = \lambda_0/\lambda$ of the modes plays the role of the mode volume, leading to strong enhancement of spontaneous emission into propagating modes that are very sub-wavelength compared to photons in vacuum. In particular, the emission into thin film modes, up to factors of order unity, scales as $\Gamma_{fi} \sim \frac{\eta^2}{(v_g/c)}\Gamma_0$, with v_g the group velocity of the mode. Taking the magnitude of the group and phase velocities to be similar (to order one factors), one then has $\Gamma_{fi} \sim \eta^3\Gamma_0$, stating that the spontaneous emission into surface modes is enhanced by the "volumetric confinement" of the polariton.

Strong Purcell enhancement can be achieved by means of a small modal volume cavity as realized in plasmonic nanogap structures [55] (Fig. 6a). In this experiment, the authors demonstrated directly by time-resolved fluorescence measurements how dye molecules sitting in a few-nm gap between a gold nanocube and gold film (a nanoparticle-on-mirror geometry) emit into the cavity mode far faster than they emit directly into the far-field. This particular experiment shows an increase in the spontaneous emission rate in excess of

1,000, with other experiments in the same geometry showing fluorescence enhancements of 30,000 [129]. Similar enhancements have been proposed with e.g. polaritons in van der Waals materials, such as graphene plasmons or phonon polaritons in hBN. The first to do so was by Koppens et. al., predicting spontaneous emission rate enhancements of one-million-fold in doped nano-disk cavities [130]. The Q/V ratio needed for this level of enhancement has been inferred experimentally in a few graphene-plasmonic systems, and in phonon-polaritonic systems based on hexagonal boron nitride and silicon carbide [131, 132, 11].

So far, such enormous enhancements have yet to be demonstrated, perhaps due to the fact that a suitable emitter has yet to be identified that can be integrated with graphene plasmons, although some recent works along this direction are promising [133]. To that end, experiments with erbium atoms near doped graphene surfaces showed that that relaxation rate of excited erbium atoms was strongly modified in the vicinity of graphene. That work indirectly showed enhancement factor on the order of 1,000, and dependence of the relaxation rate on the doping level in graphene, which enabled several different regimes of decay into electron-hole pairs, plasmons, and photons [45].

Novel spontaneous emission processes enabled by photonic quasiparticles

Transitions associated with emission or absorption are typically associated with emission of a single photonic quasiparticle (per emitter) and typically obey dipole selection rules. However, transitions by other channels are possible: (1) multipolar emission, in which an emitter decays by changing its orbital angular momentum by more than one unit, and (2) multiphoton spontaneous emission (Fig. 6b), where an emitter decays by the simultaneous emission of multiple photonic quasiparticles. The rate of both types of processes is significantly enhanced by photonic quasiparticles in nano-cavities or polaritonic systems, because the field distributions of the quasiparticles becomes highly confined, such that the size of the electromagnetic field more closely matches the size of the wavefunction of the emitter.

The conditions for strong multipolar emission directly arise from the matrix element which appears in Fermi's Golden Rule, $M_{fi} = \int d\mathbf{r}\ \psi_f^*(\mathbf{r})\mathbf{F}_n^*(\mathbf{r}) \cdot \mathbf{p}\psi_i(\mathbf{r})$. Typically, the

spatial extent of the wavefunction, a, is much smaller than the spatial extent of the mode, λ. In that case, we can Taylor expand the mode around the center of the emitter ($\mathbf{r} = 0$), expressing the matrix element as

$$M_{fi} = \int d\mathbf{r}\, \psi_f^*(\mathbf{r})(\mathbf{F}_n^*(\mathbf{0}) + (\mathbf{r}\cdot\nabla)\mathbf{F}_n^*(0) + \frac{1}{2}(\mathbf{r}\cdot\nabla)^2\mathbf{F}_n^*(0) + O((\mathbf{r}\cdot\nabla)^3))\cdot\mathbf{p}\psi_i(\mathbf{r}) \quad (2.12)$$

Each successive term in the series differs from the last by an additional $\mathbf{r}\cdot\nabla$. The first term contains essentially the electric dipole operator (as $\mathbf{p}$ matrix elements are proportional to $\mathbf{r}$ matrix elements), and drives electric dipole (E1) transitions. Note that stopping the expansion at this term is exactly the ubiquitous dipole approximation, and it directly leads to Eq. (2.12) above. The second contains terms that drive electric quadrupole (E2) and magnetic dipole (M1) transitions. The third contains terms that drive electric octupole (E3) and magnetic quadrupole (M2) transitions, and so on.

The magnitude of each successive term, compared to the previous is roughly $|\mathbf{k}\cdot\mathbf{r}_{fi}| \sim ka = 2\pi a/\lambda$, since the typical value of the magnitude of $\mathbf{r}_{fi}$ is the wavefunction size a, and the typical value of the gradient is the inverse of the characteristic length scale, k. Note that for plane wave modes, as in translationally invariant structures considered earlier, this characteristic inverse length scale coincides with the wavenumber when considering the gradient in the direction of invariance. Assuming that different terms in this series do not interfere (a reasonable assumption for small ka), the rates of transitions governed by the nth term scale like $(ka)^{2n}$ relative to the dipole term. Thus, these higher-order transitions can be very strongly enhanced by increasing the wavevector of the mode, e.g., by having a very strongly confined mode – making photonic quasiparticles such as polaritons uniquely suited for probing multipolar transitions (which are typically considered "forbidden" due to their low rates).

Effects associated with multipolar transitions effects have been studied in the past using (metal) plasmonic nanoparticles both theoretically [134, 135, 136, 137] and experimentally [138], with some experiments demonstrating deviations from the classic dipole selection rules in metallic structures [139]. These beyond-dipole corrections were enhanced by the large electronic wavefunctions of the emitters used, namely carbon nanotubes [139] and

mesoscopic quantum dots [138]. In theoretical works, the focus was traditionally on electric quadrupole and magnetic dipole emission, the leading order beyond-dipole transitions, as higher-order decays were still weak relative to typical dipole transition rates. In comparison, effects associated with simultaneous emission of multiple photonic quasiparticles have only been studied in one experiment, which showed an enhanced two-plasmon emission in nanogap structures [140].

Recently, it was predicted (in a unified manner via MQED) that polaritons in van der Waals materials can enable effectively-forbidden transitions due to their high confinement and local density of states. These transitions include high-order electric multipole transitions, singlet-triplet transitions, and even multiplasmon spontaneous emission (Fig. 6b) – all at rates approaching those of dipolar transitions in free space [105]. Similarly, photonic quasiparticles (specifically graphene plasmons) were predicted to enable significant beyond-dipole effects in solid-state emitters such as quantum wells (Fig. 6c) – the emitter can absorb and emit light according to a non-vertical transition, thus changing its momentum significantly [110]. The resulting non-vertical transitions lead to Doppler shifts, and are a manifestation of an induced spatial nonlocality in the quantum well.

Going beyond the above predictions, recent theoretical works have proposed using phonon polaritons to make two-phonon-polariton emission dominate the single-phonon-polariton decay that enables strong quantum nonlinearities [109], using plasmons with orbital angular momentum to control optical selection rules [64, 141], reaching strong coupling effects in multipolar decay [142, 143], showing interference effects between different multipolar channels [144], using surface magnon polaritons to strongly enhance spin relaxation [145], realizing strong Purcell enhancements and strong coupling with exciton polaritons [146, 147], and reaching effects of spatial non-locality on multipolar and multi-plasmon transition enhancement in metals [148, 149]. The last work shows applications of MQED to non-local media [149]. Meanwhile, recent experimental works have investigated selection-rule breakdown based on the polarization of plasmons [37], nonlocal (finite-wavevector) effects in absorption of light by van der Waals quantum wells [150] and by graphene [151], enhancement of quadrupolar transitions with surface plasmons in atomic gases [152], and enhancement of singlet-triplet decays with hyperbolic metamate-

rials [153].

2.2.2 Strong coupling effects with tightly confined photonic quasiparticles

Interaction of photonic quasiparticles with a two-level system: the Rabi Hamiltonian

When emission and absorption are sufficiently enhanced, an emitter is capable of coherently emitting and re-absorbing a photonic quasiparticle before it is lost (e.g., to radiative or dissipative losses) [19, 154, 20, 21]. The emitter and the cavity are then said to be in the strong coupling regime. A simple description of the strong coupling can be derived from the fundamental MQED Hamiltonian in the case where the emitter is strongly coupled to one mode, which is nearly resonant with a transition between two particular levels in the system (see Box 2). In that case, the MQED description becomes equivalent to the Rabi Hamiltonian H_R, i.e., a two-level system coupled to a single harmonic oscillator (the cavity mode):

$$H_R = \frac{1}{2}\hbar\omega_0\sigma_z + \hbar\omega a^\dagger a + \hbar g\sigma_x(a + a^\dagger) \tag{2.13}$$

with $g = \sqrt{\frac{\omega}{2\epsilon_0\hbar V}}\mathbf{d}_{fi}\cdot\mathbf{u}(\mathbf{r})$, where ω_0 is the emitter frequency, ω is the cavity frequency, $\sigma_{z,x}$ are Pauli z- and x-matrices, and $a^{(\dagger)}$ is the annihilation (creation) operator for the cavity photon. The Rabi frequency g, which measures the strength of the interaction between matter and photon, can be found through MQED at different levels of approximation (see Box 2). In the case of a low-loss cavity and a dipole emitter at point $\mathbf{r}$, g can be expressed in terms of the dipole moment of the transition d_{fi}, the mode volume V, and the mode function $\mathbf{u}(\mathbf{r})$. It measures the interaction energy of the dipole with the vacuum(-fluctuation) field of the cavity.

One of the key phenomena encoded in this Hamiltonian is Rabi splitting. In particular, if the emitter and cavity are resonant with each other, and g, then the first two excited states of the system split in energy by an amount $2g$. This Rabi splitting is the hallmark of strong coupling phenomena, and is a key measurement in many works presenting evidence for strong coupling. Typically, this measurement proceeds by sending light at the strongly

coupled system, and recording a scattering (e.g., transmission) spectrum. In the strongly coupled regime, the scattering spectrum will feature two resonances, split by the Rabi splitting (in contrast to a single resonance in the weakly coupled system). The strong coupling regime is manifested experimentally when the splitting is resolvable compared to the widths (related to losses). This condition is mathematically expressed as: $g > \sqrt{\gamma^2 + \kappa^2}$, with κ the photonic quasiparticle loss, and γ the atomic loss. The temporal dynamics associated with this frequency splitting are damped vacuum Rabi oscillations, in which the emitter coherently emits and re-absorbs the photonic quasiparticle multiple times before the quasiparticle decays. Such dynamics have been observed many times in the context of low-loss dielectric cavities [155, 156, 157, 158], but only recently have been observed in plasmonic contexts [13, 159].

In general, there are three ways to achieve strong coupling: by having many (N) emitters couple to the same mode (g becomes enhanced by $\sqrt{N}$), by having many (n) photons pre-populate the cavity mode (g becomes enhanced by $\sqrt{n}$), or by having a single emitter couple to an extremely confined mode with a small mode volume (since $g \sim 1/\sqrt{V}$). The last option represents strong quantum electrodynamical interaction at the single photon level. Any combination of these three methods enhances the coupling further. From the standpoint of this review, the strong confinement of the photonic quasiparticles considered here (polaritons, as well as highly-confined gap plasmons) can enable strong coupling with relatively few emitters and potentially, even a single emitter.

Fig. 6d illustrates this last point, showing a recent experiment demonstrating strong coupling of molecules to a nanoparticle-on-mirror geometry [13]. The authors rely on a nanoparticle-on-mirror-geometry, based on a 0.9 nm gap established by a molecular spacer layer (cucurbit[7]uril) between a gold nanoparticle and a gold film. Beyond the use of cucurbit[7]uril as a spacer, it also intriguingly acts as a "cage" for the emitter used in the experiments, methylene blue, which also allows it to bind to the nanoparticles above. This gap structure supports extremely confined gap modes, which such a small mode volume, that the authors predict that the associated Purcell factors are of 3×10^6. These extreme enhancements are sufficient enough for a few emitters (between one and ten) to experience strong coupling to the cavity mode, as shown through measurements of the Rabi splitting

as a function of the relative concentration of the emitter and the cucurbit[7]uril host. Since the density of molecules change the resonance frequencies of the combined system, the Rabi splitting can act as a measure of their concentration, allowing sensing applications.

Similar Rabi splittings can be observed in scattering spectra even in systems with less drastic (but still large) confinement by means of coupling more emitters to the mode. The Rabi splitting in these macroscopic experiments in some sense are quite classical, as the Rabi splitting can be quantitatively calculated in these many-molecule experiments purely through classical physics. In particular, the Rabi splitting can be obtained by modeling the molecular assembly as a Lorentz oscillator of the appropriate geometry, and solving Maxwell's equations for resonance frequencies in the system of this Lorentz oscillator coupled to the dielectric or metal materials constituting the cavity. Examples of this are shown in Fig. 6(e,f), specifically for 2D material systems: a graphene plasmon-based (bio)sensor [43], and a hexagonal boron nitride phonon-polariton based sensor [44]. In both of these examples, it is the very strong (10 nm scale) field confinement of the polariton, in conjunction with having many emitters, that enables strong coupling. These collective couplings have also been observed in systems of molecular vibrations coupled to resonant systems (e.g., Fabry-Perot cavities) [160, 161, 162, 163]. For high densities of emitters, in order to model the mode splitting based on a Rabi model, counter-rotating terms need to be taken into account, indicative of "ultra-strong coupling". Such systems have been explored with possible applications in controlling chemical reactions [164]. Beyond collective coupling of emitters to cavities, it is also possible to achieve strong (and ultra-strong) coupling between different collective excitations, such as strong coupling of surface phonon polaritons to surface plasmon polaritons in epsilon-near-zero materials [165, 166].

Toward ultrastrong coupling

As an outlook on this section, we mention one last very interesting theoretical possibility, related to single-emitter ultrastrong coupling, that can be achieved as the confinement of the photonic quasiparticle becomes such that it is comparable to the scale of the electronic wavefunction. Strong coupling, as discussed in the previous paragraphs, is maintained when the emitter's decay exceeds the loss rate, which is typically much smaller than the

mode frequency. However, a new regime of quantum light–matter interactions emerges when the decay exceeds the mode frequency [21, 20].

In that case, a number of phenomena emerge that do not occur in strong coupling. Interesting examples include: (1) Rabi oscillation even when an emitter is interacting with a continuum of modes (as in a waveguide, as opposed to a discrete cavity mode) [167]. (2) Considerable changes in the energies of the ground state, due to very strong Lamb shift [168, 167], which could allow changes in macroscopic thermodynamic properties such as chemical reactivity, specific heat, and even dielectric properties. (3) Virtual photons appear as part of the ground state of the coupled system (nonzero expectation values of photon number), which can in principle can be extracted by time-modulating the system, as in the dynamical Casimir effect [169, 170]. (4) Decoupling of light and matter for extreme coupling strengths [171, 172, 173]. The origin of many of these striking new phenomena is the breakdown of the rotating-wave approximation, in which one neglects the effect of virtual (energy non-conserving) processes, such as an emitter both becoming excited and emitting a photon, or an emitter becoming de-excited and absorbing a photon.

To this date, single-emitter ultrastrong coupling has only been observed in systems of superconducting qubits coupled to microwave cavities [174, 175], which works due to the extremely large effective dipole moment of the qubit (which g is proportional to). Looking forward, extremely confined graphene plasmons (as in [11]) may enable bringing single-emitter ultrastrong coupling to the infrared regime, as first suggested in [105] and predicted theoretically to be possible in a graphene–quantum-well stack [111].

2.3 Light–matter interactions with photonic quasiparticles: free electrons

2.3.1 Controlling free electron spontaneous emission with photonic quasiparticles

Much of the focus in the field of quantum light–matter interaction is focused on emission and absorption of photonic quasiparticles based on bound electrons, i.e., emitters which are

spatially confined by some potential in at least one dimension leading to discrete states or bands. However, many researchers are now considering the classical and quantum interactions of emitters based on free electrons. Part of the uniqueness of light–matter interactions of free electrons arises from their energy spectrum being continuous, rather than discrete as with most bound electron systems. This difference results in free-electrons transitions and free-electron radiation sources being tunable. Moreover, free electrons reach much higher (often relativistic) energies, which consequently enables transitions at much higher frequencies than is available for bound electron systems, even allowing emission of X-rays. In this section, we will go into detail on light–matter interactions enabled by free-electrons.

Spontaneous emission by a free electron in a homogeneous medium: the Cherenkov effect

We start by considering the Cherenkov effect, as in some sense, it represents the most basic light–matter interaction possible in free-electron systems. Indeed, the Cherenkov effect can be described as spontaneous emission by a free electron [176, 177]. Historically, the Cherenkov effect (or Cherenkov radiation) has been associated with the radiation emitted when a charged particle (not limited to free electrons) moves faster than the phase velocity of light in a homogeneous dielectric medium [178]. Famously, in a non-dispersive medium, the radiation is emitted into a forward propagating cone centered around the direction of motion of the particle, with an opening angle θ that satisfies $\cos\theta = 1/\beta n$. Here n is the index of refraction of the medium and $\beta = v/c$ is the speed of the particle (v) normalized to the speed of light (c) [179]. Here, the effect is enabled because the photonic quasiparticle, i.e. the photon in a medium, has a phase velocity v_p slower than c.

The scope of the Cherenkov effect goes far beyond charged particles in homogeneous media. For example, consider the relation $\cos\theta = 1/\beta n$. This relation is a specific way of representing a more general phase-matching condition that applies to many free-electron radiation processes beyond the Cherenkov effect. This condition is given by $\mathbf{v} \cdot \mathbf{k} = \omega(\mathbf{k})$, where $\mathbf{v}$ is the charged particle velocity, $\mathbf{k}$ is the wavevector of the photon emitted, and $\omega(\mathbf{k})$ the corresponding frequency of the photon prescribed by the dispersion relation [26, 180, 27, 181]. This phase-matching condition is a result of energy and momentum

conservation. Moreover, as can be seen from this general phase-matching, the emitted photon need not be in a homogeneous medium. The emission can be into a more general photonic quasiparticle, such as a waveguide mode, or surface polaritons such as plasmon and phonon polaritons, or a photonic Bloch mode, provided that the system has a well-defined momentum in some direction (discrete or continuous translation symmetry).

Box 3: Hamiltonians of light–matter interactions in free-electron systems

In general, the interaction of relativistic, spin-½ electrons with the electromagnetic field must be described by the Dirac equation. However, in many cases of interest (e.g., free electrons in microscopes and accelerators), spin weakly influences the dynamics. In such cases, the interaction can be described by the Hamiltonian of spin-less relativistic particles (Klein-Gordon, or scalar QED Hamiltonian). The corresponding Hamiltonian H^{rel} (omitting inter-particle interactions) is given by:

$$\begin{aligned} H^{\text{rel}} &= \sum_{i=1}^{N} \sqrt{m^2c^4 + c^2\left(\mathbf{p}_i - q_i\mathbf{A}(\mathbf{r}_i)\right)^2} + q_i\phi(\mathbf{r}_i) + H_{\text{em}} \\ &\approx \sum_{i=1}^{N} E(\mathbf{p}_i) + q_i\phi(\mathbf{r}_i) - \sum_{i=1}^{N} q_i\mathbf{A}(\mathbf{r}_i)\cdot\mathbf{v}_i + H_{\text{em}} \end{aligned} \tag{2.14}$$

where we have approximated the square root, using the fact that the energy associated with the matter–field coupling is typically much smaller than mc^2. Here, we have also defined $\mathbf{v}_i = \mathbf{p}_i/m\gamma_i$, with $\gamma_i = \left(1 - v_i^2/c^2\right)^{-1/2}$ being the Lorentz factor and $E(\mathbf{p}_i) = \sqrt{m^2c^4 + c^2\mathbf{p}_i^2}$ is the electron kinetic energy.

For relativistic electrons that propagate short enough distances for dispersion to be negligible, and whose dynamics are predominantly in the direction of motion, a simple form of the QED Hamiltonian can be derived. This Hamiltonian can describe phenomena in photon-induced near-field electron microscopy (PINEM) with quantized electromagnetic fields [Kfir2019, DiGiulio2019]. In the absence of dispersion, the electrons can be described within the paraxial approximation. Provided this, and that the electromagnetic momentum $|e\mathbf{A}| \ll mv$, with $\mathbf{A}$ the vector potential and v the magnitude of the electron velocity, the system of a free electron and a quantized radiation field can be described by the following Hamiltonian (up to a constant energy shift)

$$H_{\text{QED}}^{\textbf{el}} = -i\hbar v\partial_z + \sum_n \hbar\omega_n a_n^\dagger a_n - qv\sum_n (A_{nz}(z)a_n + A_{nz}^*(z)a_n^\dagger), \tag{2.15}$$

where $A_{nz} = \sqrt{\frac{\hbar}{2\epsilon_0 \omega_n}} F_{nz}$, defining the z direction as the direction of the velocity.

Writing the interaction Hamiltonian in the interaction picture, it can be shown that

$$V_I(t) = -qv \sum_n A_n(z+vt) a_n e^{-i\omega_n t} + A_n^*(z+vt) a_n^\dagger e^{i\omega_n t} \tag{2.16}$$

has the property that $[V_I(t_1), [V_I(t_2), V_I(t_3)]] = 0$, and thus the state of the system at a given time is $|\psi(t)\rangle = \prod_n e^{\chi_n} e^{S_n} |\psi_0(t)\rangle$. The state $|\psi_0(t)\rangle = e^{-ivt\partial_z - \sum_n i\omega_n t a_n^\dagger a_n}$ describes the time-dependent state of the electron and photon in the absence of electron-photon interactions. The terms in the exponents are

$$\chi_n = -\frac{iq^2}{\hbar^2} \int_{-\infty}^{z} dz_1 \int_{-\infty}^{z_1} dz_2 \mathrm{Im}\left[A_{nz}(z_1) A_{nz}^*(z_2) e^{-i\frac{\omega_n}{v}(z_1 - z_2)} \right] \tag{2.17}$$

$$S_n = e^{i\frac{\omega_n}{v} z} g_n a_n - e^{-i\frac{\omega_n}{v} z} g_n^* a_n^\dagger \tag{2.18}$$

with $g_n = \frac{q}{\hbar\omega_n} \int_{-\infty}^{z} dz' E_{nz}(z') e^{-i\frac{\omega_n}{v} z'}$ and $E_{nz} = i\omega_n A_{nz}$. The g_n derived here, in the limit of $z \to \infty$. is equivalent to the PINEM coupling constant of Eq. (2.21). In the case of electron interaction with a coherent state $a_n \to \alpha_n e^{-i\omega_n t}$ and $a_n^\dagger \to \alpha_n^* e^{i\omega_n t}$,and the resulting wavefunction matches that of the conventional PINEM theory with classical driving fields.

It is also possible for the electron to emit into localized (cavity) modes, analogously to much of the research investigating bound electron coupling to cavities.

Previous work showed how the dispersion relation of the photon distinguishes between variants of the Cherenkov effect. For example, negative index materials [182]. This effect was observed using mathematical analogies simulating the emitting particle by a phased-array antenna [183]. Mathematical analogies were also used to observe a kind of Cherenkov effect involving a directional emission of surface plasmon polaritons, using metasurfaces [184] to simulate the polarization field of a moving electron. Nevertheless, such effects have yet to be observed with true charged particles. Controlling the angular emission properties of Cherenkov radiation is important, particularly in applications such as Cherenkov-

based particle detectors, where it is the emission angles that are used to determine the properties of incident high-energy particles [185].

These interactions can be measured by detecting the electron energy losses associated with the emission (via electron-energy loss spectroscopy EELS) [27], which was also shown to probe the local density of states of the optical structure. That the electrons probe the local density of states can be seen from the general expression for spontaneous emission by a quantum system of Eq. (2.5). The total rate $d\Gamma_i$ of energy loss by an electron in an initial energy eigenstate i (e.g., a plane wave with some momentum $\hbar\mathbf{k}$), into all possible final states, per unit energy-loss $d\omega$, is given by:

$$\frac{d\Gamma_i}{d\omega} = \frac{2\mu_0}{\hbar} \int d\mathbf{r} d\mathbf{r}' \, \mathbf{j}_{fi}^*(\mathbf{r}) \cdot \text{Im}\, \mathbf{G}(\mathbf{r}, \mathbf{r}', \omega) \cdot \mathbf{j}_{fi}(\mathbf{r}') \delta(\omega - \omega_{if}) \tag{2.19}$$

Note that because of the extended nature of a generic free electron, the electron probes a more general quantity than the local density of states, as the electron probes the Green's function at two different locations. However, it is often the case, as in high-resolution electron microscopes, that the emitter is an electron wavepacket which is well-localized around a straight-line trajectory $\mathbf{r} = \mathbf{r}_0 + \mathbf{v}t$. It can then be seen by direct application of Fermi's Golden Rule that the probability dP of the electron of losing energy $\hbar\omega$ per unit frequency $d\omega$ is given by

$$\frac{dP}{d\omega} = \frac{\mu_0 q^2}{\pi\hbar} \int dt dt' \, e^{i\omega(t-t')} \mathbf{v} \cdot \text{Im}\, \mathbf{G}(\mathbf{r}_0 + \mathbf{v}t, \mathbf{r}_0 + \mathbf{v}t, \omega) \cdot \mathbf{v} \tag{2.20}$$

which is the standard EELS formula [27]. Eq. (2.20) thus shows that the electron probes the local density of states along its trajectory, for an arbitrary optical structure [27, 186, 187].

The underlying nature of the Cherenkov effect

The vast majority of the research done on the Cherenkov effect has been based purely on classical electrodynamics, which has accounted perfectly for all known observations thus far. The Cherenkov effect can also be explained through MQED [176, 177] (Fig. 1) simply as the equivalent of spontaneous emission by a free-electron in a medium. This equiva-

lence emphasizes the central place of the Cherenkov effect in the light–matter interactions of free electrons. Moreover, the quantum treatment of Cherenkov radiation leads to corrections originating from the recoil of the emitting particle due to the emission of a single quanta of photonic quasiparticle. The quantum recoil corrections have been predicted to be significant in certain conditions for the Cherenkov effect in regular materials [124] and in graphene [188], and for low energy electrons in the analogous Smith-Purcell effect [189].

Another type of a quantum correction exists in the Cherenkov effect and in other electron radiation phenomena (Fig. 7): the dependence of radiation emission on the wavefunction of the emitting particle. Such phenomena have been predicted for the Cherenkov effect [124], Smith-Purcell effect [190], other spontaneous radiation mechanisms [191], and their stimulated analogues [192]. The first few experiments on this effect have been performed in recent years. One experiment showed no wavefunction dependence [190] because the emission did not depend on characteristics of the photonic quasiparticle, and could be modeled with free-space photons. In contrast, an indirect measurement through EELS showed the first evidence of a wavefunction effect in the other extreme case, of emission into localized surface plasmons [16], where the characteristics of the photonic quasiparticles deviated significantly from those of a free photon. The key difference in these experiments is the nature of the photonic quasiparticle. For the precise shape of the wavefunction to influence the radiation, it must be the case that: two electron states can transition to the same final electron and photon state, so that the transition amplitudes can interfere. In the case of Smith-Purcell radiation of a 1D grating, the photonic quasiparticle has a well-defined momentum (up to a lattice vector), and then strict momentum conservation does not allow two distinct electron states to interfere. In the case of localized quasiparticles (as in [16]) that break translation invariance, such an interference becomes possible due to the relaxation of conservation laws. Therefore, in contrast to previous cases in this Review, where the dispersion, or confinement, or polarization was the root cause of the effects, here it is symmetry.

The Cherenkov effect in condensed matter physics as a test of photonic quasiparticles

Modern incarnations of the Cherenkov effect (Fig. 8) demonstrate the wide applicability of photonic quasiparticles. Specifically, we show that the Cherenkov effect has now been studied with plasmons (Fig. 8a) [193, 194, 195, 196, 188] and with phonons in solids (Fig. 8b) [197, 198], which are the photonic quasiparticles that interact with ultra-slow electrons in solids (in place of relativistic electrons). The emission follows the same phase-matching condition, up to quantum recoil corrections discussed in the previous section. However, in the case of low-energy emitters based on electrons in solids, these quantum recoil corrections can become quite important, allowing emission even when the electron is above the phase velocity of the excitations – such as in the emission of plasmons by hot electrons in graphene [188]. In that sense, the physics of the quantum Cherenkov effect becomes observable and important in condensed matter systems. In these contexts, it is also important to mention that these effects are enabled with electrons in solids because the photonic quasiparticle, the bulk plasmon or phonon, has a phase velocity two-to-four orders of magnitude slower than c.

Taking phonons specifically, their slow velocities enable electrons and holes in solids to emit phonons in a Cherenkov effect, as well as absorb them in an inverse Cherenkov effect. These phenomena can occur in conventional solids [199, 200] and in graphene [197]. Such Cherenkov processes are equivalent to charge carrier relaxation and thermalization by electron-phonon scattering. Nevertheless, treating the process through a Cherenkov formalism proved useful in explaining recently observed phenomena of electron-phonon instabilities and noise amplification in graphene [198]. Beyond these effects with electrons in solids, relativistic free electrons are also used to probe phonons through measuring the energy losses of electrons that spontaneously emit phonons. Such techniques are now used for vibrational spectroscopy [201, 202, 203]. Similar to phonon scattering, even charge carrier scattering (Landau damping) by surface and by bulk plasmons can be connected to a Cherenkov-like process as pointed out by Ginzburg [204]. This similarity between all the excitations helps promote the combined treatment of all photonic quasiparticles with the same concepts and methods of light–matter interactions, as shown in Figs. 1,2. This

combined treatment shows that despite the different microscopic origins of electromagnetic excitations, and despite their varying degree of photon vs. matter composition, they can all be considered as instances of a more general photonic quasiparticle.

Spontaneous emission by a free electron in a periodic medium: the Smith-Purcell effect

Being quite similar in essence to the Cherenkov effect, the Smith-Purcell effect has an electron traveling along a periodic optical system, and emitting light into the far-field [205]. The effect can be understood from the Cherenkov effect, but using a different photonic quasiparticle, which is the Bloch photon mode. Here, the effect is enabled because the photonic quasiparticle, the Bloch photon, has higher momentum components associated with additions of reciprocal lattice vectors. An electron can couple to a Bloch photon if $\mathbf{v} \cdot (\mathbf{k} + \mathbf{G}) = \omega(\mathbf{k})$ (i.e., phase-matching) is satisfied, where $\mathbf{k}$ is the Bloch wavevector inside the first Brillouin zone, and $\mathbf{G}$ is a reciprocal lattice vector [26, 27, 181]. Smith-Purcell radiation arises when this (evanescent) harmonic of wavevector $\mathbf{k}+\mathbf{G}$ diffracts into the far-field. The frequency of the emitted photon depends on the angle of emission, and the periodicity of the crystal by the famous relation $\omega = \frac{\mathbf{v}\cdot\mathbf{G}}{1-\beta\cos\theta}$, showing that emission into gratings with small periods enables high-frequency (even ultraviolet radiation [206]), motivating a push to observe Smith-Purcell effects (and other related free-electron radiation effects) in the interaction of free-electrons with nanostructures [207, 208, 209, 206]. Smith-Purcell radiation is possible for any periodic medium, both metallic gratings where Smith-Purcell was historically studied (and explained in terms of image charges) [205, 210], and dielectric gratings, e.g., silicon [211]. In all cases, by modeling Smith-Purcell radiation as the grating scattering (diffraction) of the electron's near-field into the far-field, one can derive fundamental bounds on the efficiency of Smith-Purcell radiation, as developed and probed experimentally in [212].

As an outlook on the possibility of applying the considerations of Figs. 1, 2 to free-electron processes, we discuss recent theoretical proposals related to free-electron radiation in strong driving fields. Both the strong driving field and the emitted radiation can be modified by the optical environment and lead to new effects. In particular, the electron

can absorb or stimulatedly emit photonic quasiparticles from an external driving field and spontaneously emit another photonic quasiparticle. Typically, due to the relativistic nature of the emitting electron, the spontaneously emitted photon can be at a much different frequency from the original photon. As an example, Fig. 8d shows a proposal to scatter free electrons from a strongly pumped external plasmonic standing wave on the surface of graphene [213]. The free-electron can then undergo a Compton-like process in which it absorbs (or stimulatedly emits) the plasmon and emits a photon. Due to the relativistic nature of the electron and the high optical confinement of the plasmon, the emitted photon can be at hard X-ray frequencies. Compared to other sources of X-rays, this source can produce X-rays using much less relativistic electrons due to the graphene plasmon confinement. That said, the small extent of the evanescent graphene plasmon strongly limits the achievable flux/intensity, with heterostructures having been proposed as a method to mitigate this [214, 215].

Spontaneous emission by free electrons in strong fields of photonic quasiparticles

Interestingly, such radiation processes can in fact take place without any driving field. Fig. 8e considers the case in which a free-electron spontaneously emits both the plasmon and the X-ray photon, which is equivalent to Compton scattering from plasmonic vacuum fluctuations [125]. Strikingly, such a spontaneous process has similar power yields as the stimulated process due to the very strong vacuum fluctuations on the nanoscale, though the emission is far less monochromatic, due to the heavily multimode nature of the process (i.e., spontaneous emission occurs into any available plasmon mode, leading to X-ray emission at a wide spectrum).

So far, all the considered processes were first- or second-order in MQED, but there also exist radiation processes in which many photons are absorbed or stimulatedly emitted (effectively higher-order MQED), followed by spontaneous emission of a single photonic quasiparticle. Such nonlinear Compton scattering processes, are typically very weak, but can become efficient when the emission is into plasmons due to their strong confinement [126]. This enhancement is a manifestation of the Purcell effect, but for strongly driven free electrons (Fig. 8f) instead of bound electrons.

2.3.2 Strong coupling of free electrons and photonic quasiparticles

Stimulated emission and absorption of photonic quasiparticles

Photonic quasiparticles can be used to exert a great deal of control over spontaneous emission by free electrons, in a similar way as for bound electrons. A natural question, extending ideas from bound electron physics, is whether or not strong or ultrastrong coupling (and associated phenomena, such as Rabi oscillations) can also be realized in free-electron systems. Here, some distinction should be made between vacuum strong coupling effects, where the electron-light coupling g is strong enough to induce Rabi oscillations, and stimulated strong coupling effects. In the case of stimulated effects, the coupling is effectively enhanced to $\sqrt{n+1}g$ in the presence of n photonic quasiparticles (see Section 2.2). This enhancement is similar to the case in bound electron systems, where Rabi oscillations in atoms, molecules, and various types of qubits, can be induced by a strong driving field. Vacuum strong and ultrastrong coupling has not yet been observed with free electron systems, though there have been some proposals for strong coupling [216, 217] based on electron-cavity interactions. Other proposals for vacuum ultrastrong coupling involved Cherenkov radiation by heavy ions [218] and Cherenkov radiation of graphene plasmons by electrons in solids [188].

Strong coupling and ultra-strong coupling effects have been observed in non-relativistic systems of particles which are closely related to free electrons. In particular, strong coupling, and the associated phenomena of Rabi splitting in scattering spectra, have been observed in 2D electron gas systems (2DEGs) associated with high-mobility quantum wells immersed in magnetic fields. These systems feature many electrons occupying Landau levels which are collectively coupled to a common resonant cavity mode, typically a terahertz cavity mode associated with a metallic resonator hosting a highly-confined mode [219, 220]. Because strong coupling modifies the energy spectra of the composite system, and because macroscopic properties such as transport and other thermodynamic properties depend on the underlying energy spectra of the system, strong coupling can change the intrinsic properties of the system. This was demonstrated very recently in the context of magnetotransport of electrons in 2DEGs, where the transport properties were strongly mod-

ified by the presence of a terahertz resonator [221]. Similar Rabi splitting effects have also been observed in the coupling of cavities to other free-electron-like systems, such as intersubband transitions in quantum wells (through their electric dipole moments) [222, 223], and even collective excitations of cooper-pairs (Josephson plasma resonances) [224].

Photon-induced near-field optical microscopy (PINEM)

While vacuum strong coupling effects were not observed so far with free electrons, stimulated strong coupling effects have emerged in recent years using pulses of free electrons interacting with pulses of strong laser fields [225]. These results have had immediate applications in ultrafast electron microscopy [226].

The most influential advances in this direction are the results of the new capability called photon-induced near-field electron microscopy (PINEM) [225], in which an electron interacts with a strong field that is coupled to a material. The electron undergoes absorption and stimulated emission of many photons of the driving field in a way that also provides new insight on the material. In particular, by measuring the energy spectrum of electrons undergoing PINEM interactions, it is possible to image the near-field distribution of an excited electromagnetic field with high spatial resolution [225, 227]. PINEM-based techniques reached under 10 nm resolution [228], meV-scale energy resolution [229, 230], and recently also 100fs temporal resolution ([231, 229]), allowing direct measurement of the lifetimes of optical modes. Because PINEM operates based on energetic free electrons, it allows one to also image confined modes "buried" inside materials ([232]). Such capabilities are complementary to other state-of-the-art techniques for imaging near-fields, such as SNOM [8, 9, 29], photo-emission electron microscopy (PEEM) [58, 233, 234, 235] and cathodoluminescence (CL) microscopy [22, 186, 236].

This absorption and emission can be shown to be equivalent to a multi-level quantum system with equally spaced energy levels undergoing quantum Rabi oscillations [227]. The number of photons absorbed and emitted scales with a dimensionless parameter g. This parameter is also equivalent to a quantity used in linear-field laser-acceleration in accelerator physics [237, 238, 239, 240] – the integrated work done by the component of the electric field (E_z) along the trajectory of the particle of charge q, which in our case is normalized

by the energy of the driving photon $\hbar\omega$. For an electron moving with velocity v along the z direction, g equals

$$g = \frac{q}{\hbar\omega} \int_{-\infty}^{\infty} dz e^{-i\omega z/v} E_z(z). \tag{2.21}$$

The PINEM interaction has been observed for a wide-range of photonic quasiparticles, from: localized plasmons [241], surface plasmons [232], free space plane wave scattering off a mirror [242], photonic crystal modes [229] and whispering gallery modes [231], as well as propagating photonic modes in a half-infinite homogeneous medium [239]. In all cases, the presence of matter that modifies the free-space photon is critical, as the equation for g vanishes for any field E in free-space. This result shows the necessity of a strong driving laser pumping an electromagnetic field mode that deviate from that of free-space so that the integral of g does not vanish.

The experimental setups used for such interactions are ultrafast transmission electron microscopes [226], with related effects also observed in ultrafast electron diffraction setups [243, 244] and in other electron-beam setups [245], which show the classical corresponding effects of PINEM. Fig. 9 presents exemplary experimental results in the field, including the extremely nonlinear interaction of a free electron with multiple photons (i.e, ten-photon absorption/stimulated emission Fig. 9b [225]) creating free-electron Rabi oscillations Fig. 9a [227]. This nonlinear interaction has been applied in microscopy for imaging plasmons at buried interfaces [232], presenting meV energy resolution in EELS [230], and imaging plasmons with angular momentum (Fig. 9c) [66]. The latter uses the quantized nonlinear interaction of electrons with the angular-momentum carrying plasmons to create electron vortex beams [246].

2.4 Outlook

In this Review, we have surveyed the broad physics of the interactions between bound/free electron emitters and photonic quasiparticles (photons in media). We showed that by using the photonic quasiparticle concept to describe any electromagnetic field in a medium, we could understand many seemingly disparate phenomena by appealing to either the confine-

ment, symmetry, or dispersion, of the photonic quasiparticle.

We emphasize here that the photonic quasiparticle is rigorously supported by MQED, which allows one to quantize electromagnetic fields in any medium, including non-local ones. One can quantize photons in vacuum, in transparent media, cavity photons, Bloch photons, polaritons in van der Waals materials, and even bulk phonons and plasmons (which are described by non-local response functions). MQED thus serves as a key unifying tool in the physics of light–matter interactions.

From the point of view of MQED fundamentals, many opportunities still remain to be explored in light–matter interactions with photonic quasiparticles. We highlight some of the most ambitious directions here. Many open questions remain on the nature of ultrastrong coupling of emitters to systems with a continuum of modes. Can ultrastrong coupling be used to design new bound states of emitters with photonic quasiparticles? How can strong multiphoton effects be used to design materials with stronger optical nonlinearities? Another interesting direction regards the fact that energy levels of emitters can shift due to virtual absorption and re-emission of photonic quasiparticles, according to the Lamb shift. Can emitters be re-designed at will using Lamb shifts in the ultrastrong coupling regime? Such questions also beget questions regarding renormalization in MQED. The photonic quasiparticle vacuum changes the energy levels of emitters in a way that in principle depend on all modes, even arbitrarily high frequency ones; inviting questions as to how to find correct predictions for energy shifts. See [247] for the case of a homogeneous media. Finally, as an outlook on novel X-ray generation mechanisms, it is of practical interest to explore how/whether these mechanisms can serve as an effective gain medium at X-ray frequencies.

We emphasize here that this field is still in a nascent stage. There are still many theoretical directions to explore, and there are many predictions still waiting to be verified. More than half the experiments in PINEM have been published just in the past few years. Looking forward, it will be of interest to experimentally demonstrate spontaneous (Cherenkov-type) and stimulated (PINEM-type) interactions of free electrons with novel polaritons. In particular, the stimulated PINEM interactions may enable new methods to image the dynamics of highly-confined polaritons with nanometer and femtosecond resolution. The most recent

predictions on strong light–matter interactions with highly confined photonic quasiparticles in 2D materials have not yet been demonstrated experimentally. Thus, one of the most important goals moving forward will to be to test the exciting predictions made regarding enhancing spontaneous emission, realizing forbidden transitions, and achieving strong and even ultrastrong coupling phenomena in new material platforms at optical frequencies. Moreover, it has yet to be shown that enormous spontaneous emission enhancements also extend to two-photon processes. Another exciting experimental direction that we expect to see in the next few years is probing light–matter interactions of bound and free electrons with photonic quasiparticles in Moire systems [248, 249]. Such an experiment will eventually enable to observe strong coupling between twisted bilayer systems and optical cavities, altering the energy spectra of the Moire system, potentially influencing for example their transport and other macroscopic properties [1].

[1] We note here that we cite the following references in Figs. 1, 2 which are not cited in the text [250, 251, 252, 253, 254, 255, 256, 257, 258, 259, 260, 261, 262, 263, 264, 265, 266, 267, 268, 269].

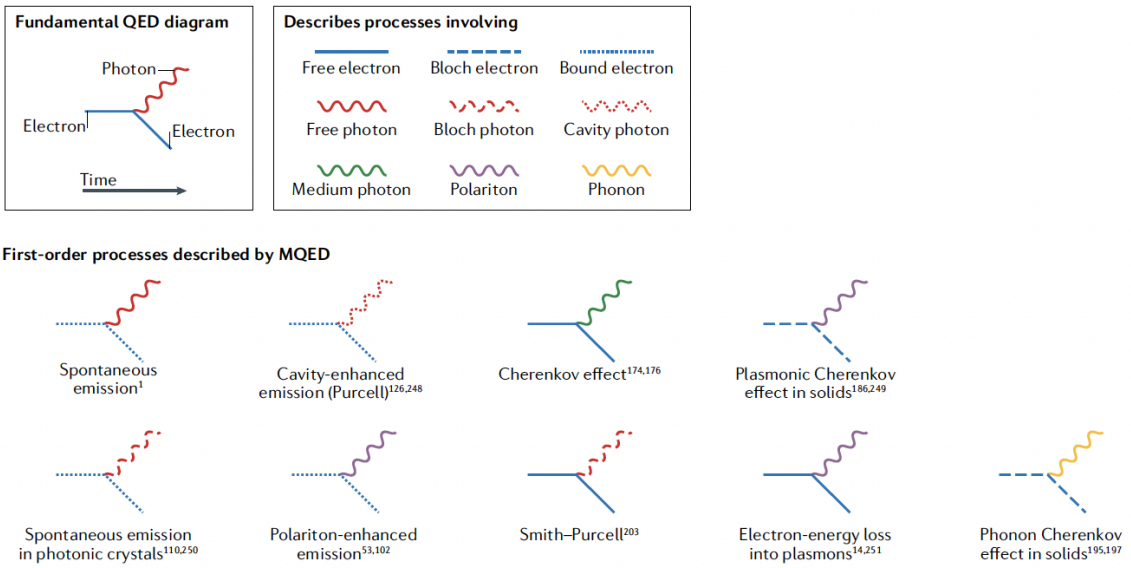

Figure 2-1: **Diagrammatic representation of physical processes contained within macroscopic QED (MQED)**, as they pertain to different types of matter (bound, free, and Bloch electrons), as well as different types of photonic quasiparticles (photons, photons in a homogeneous medium, photonic crystal photons, polaritons (plasmon, phonon, exciton, magnon), and even pure phonons. Each MQED diagram corresponds to a different, sometimes known phenomenon, while others correspond to phenomena which have thus far not been explored. Note that while we represent mostly spontaneous emission effects here, all spontaneous processes also have stimulated processes, as well as absorption (inverse) processes associated with them. For example, corresponding to the Cherenkov effect is the inverse Cherenkov effect, where an emitter absorbs a photon in a medium instead of emitting it. We also note here that in some cases, the emitted quasiparticle has a vacuum far-field component, leading to other effects. For example, a plasmon emitted by an electron can couple to the far-field in nanoparticles, as a mechanism of cathodoluminescence. Or a medium photon associated with an interface can have a vacuum component, leading to transition radiation.

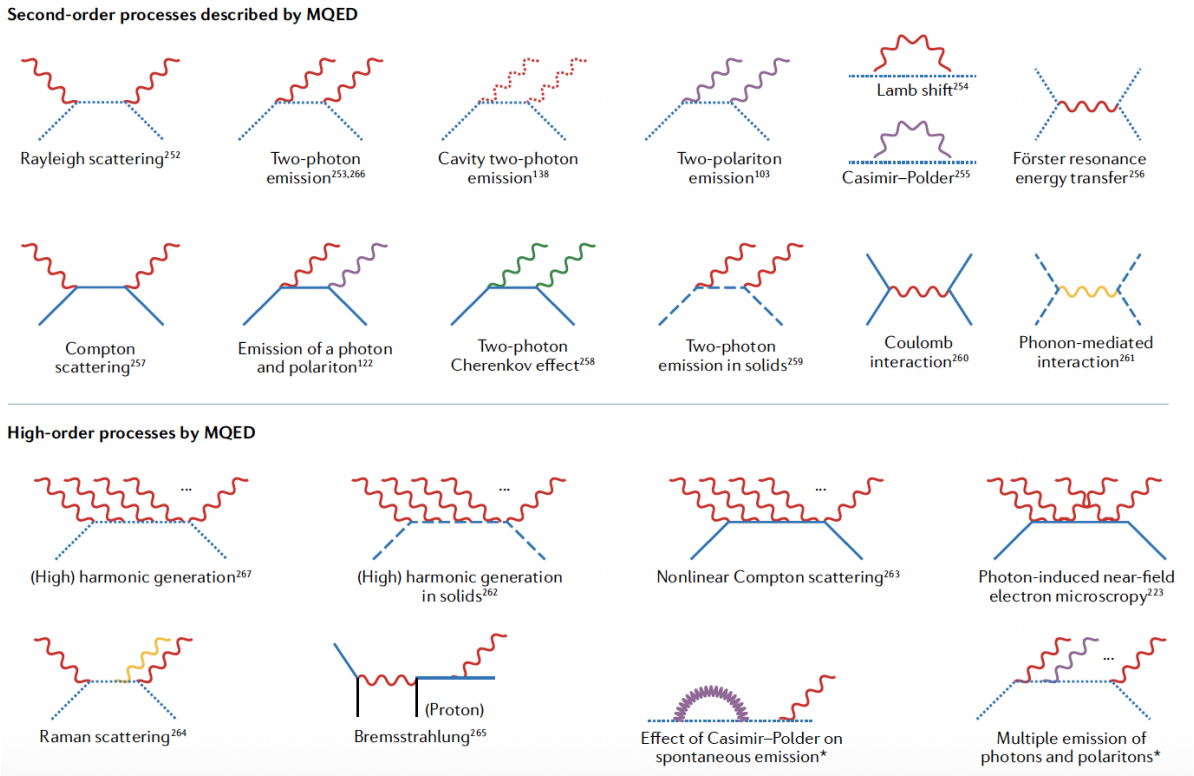

Figure 2-2: **Diagrammatic representation of physical processes contained within macroscopic QED (MQED)**, at higher orders in perturbation theory, revealing a number of effects which have yet to be explored. Processes with no standard or recent reference associated them are marked with a [*].

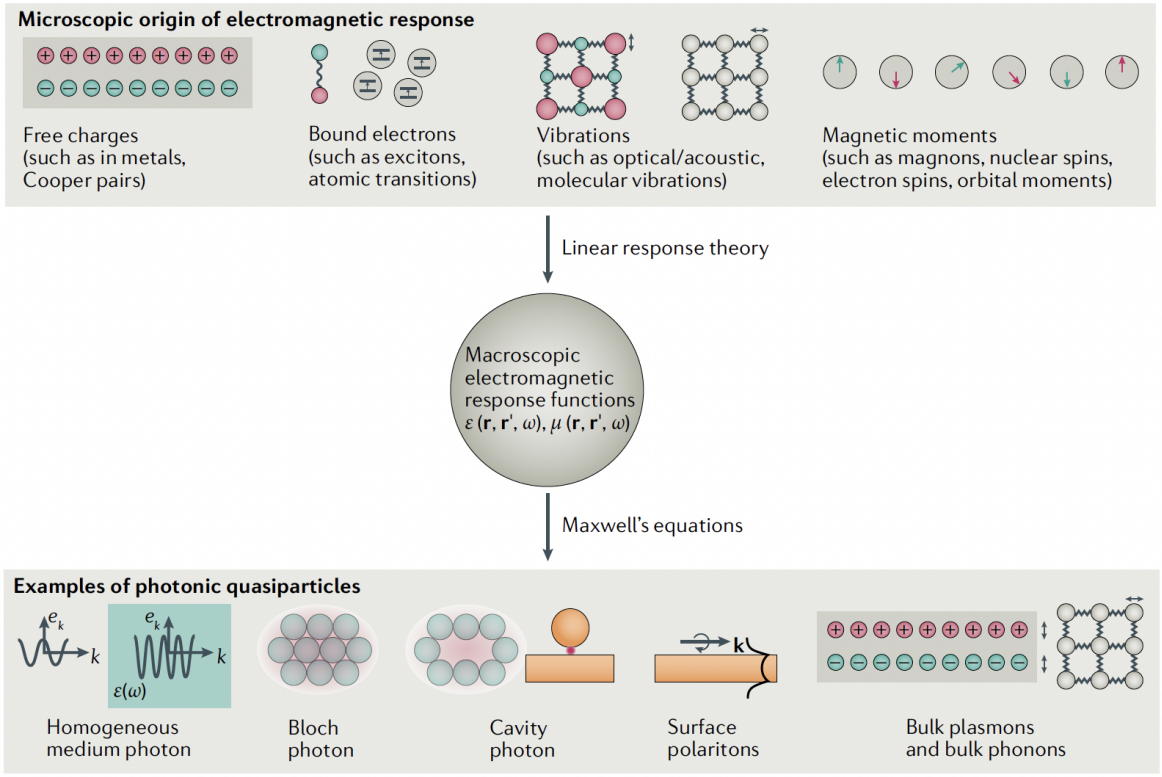

Figure 2-3: **Photonic quasiparticles.** The electromagnetic interactions of bound and free electrons with materials can be unified into a single framework. In this framework, the microscopic origin of the electromagnetic excitations (top) "collapses" into a spatially and temporally dispersive dielectric permittivity and magnetic permeability (middle), which is essentially a black box. The linear electromagnetic response functions can be calculated from the microscopic properties through linear response theory. The material properties, combined with material geometry, give rise to different types of photonic quasiparticles (bottom). Examples of these limits include photons in vacuum and homogeneous media, photonic crystal photons, cavity photons, surface polaritons, and, even bulk plasmon and phonon excitations.

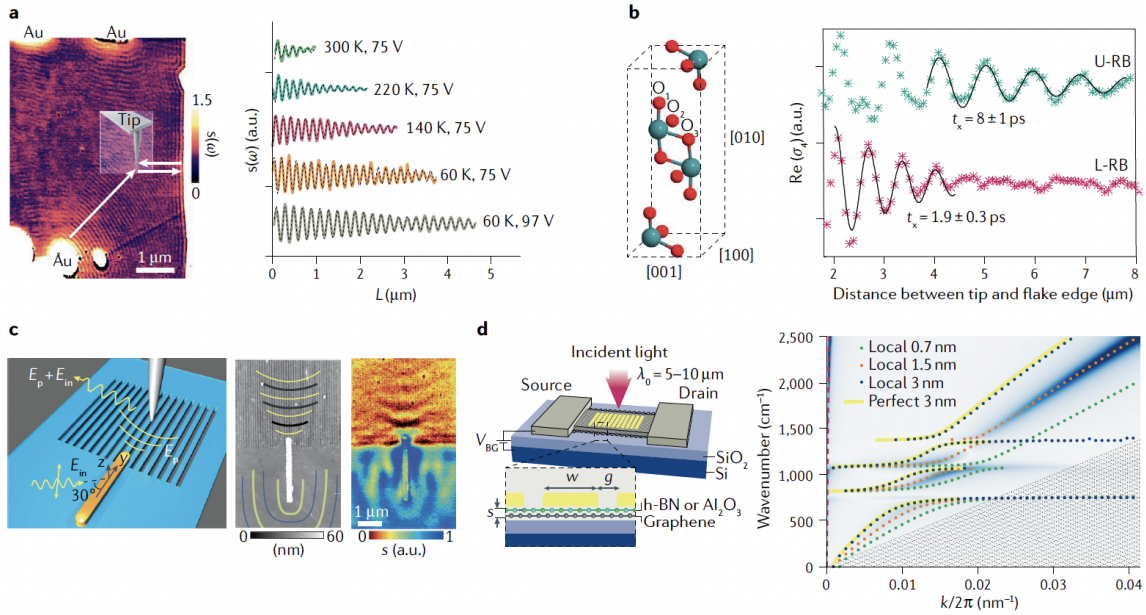

Figure 2-4: **Optics with photonic quasiparticles.** Photonic manipulations (optical excitation, propagation, coupling to structures, and detection of electromagnetic fields), with highly confined polaritons. (a) Propagation of plasmons in graphene at low temperatures, such that the losses are very low. (b) Propagation of phonon polaritons in newly discovered, in-plane hyperbolic material MoO3. (c) Launching hyperbolic phonon polariton waves by an antenna structure, in some sense performing a similar role to the metallic tip in scanning probe microscopy, but allowing strong control over the phase fronts of the polaritonic radiation. (d) Plasmons in a doped graphene situated a nanometer away from a gold grating structure, allowing for confinement of the electromagnetic field on the scale of a few atoms.

Type of medium	Vector potential	Conditions on vector potential
Vacuum	$\sum_{\mathbf{k},\varepsilon_\mathbf{k}} \sqrt{\frac{\hbar}{2\varepsilon_0\omega_\mathbf{k}V}}\left(e^{i\mathbf{k}\cdot\mathbf{r}-i\omega_\mathbf{k}t}\boldsymbol{\varepsilon}_\mathbf{k}a_{\mathbf{k},\varepsilon_\mathbf{k}} + e^{-i\mathbf{k}\cdot\mathbf{r}+i\omega_\mathbf{k}t}\boldsymbol{\varepsilon}_\mathbf{k}^* a_{\mathbf{k},\varepsilon_\mathbf{k}}^\dagger\right)$	$\mathbf{k}\cdot\boldsymbol{\varepsilon}_\mathbf{k}=0; \omega_\mathbf{k}=ck$
Homogeneous, lossless, non-dispersive, isotropic	$\sum_{\mathbf{k},\varepsilon_\mathbf{k}} \sqrt{\frac{\hbar}{2\varepsilon_0\omega_\mathbf{k}n^2V}}\left(e^{i\mathbf{k}\cdot\mathbf{r}-i\omega_\mathbf{k}t}\boldsymbol{\varepsilon}_\mathbf{k}a_{\mathbf{k},\varepsilon_\mathbf{k}} + e^{-i\mathbf{k}\cdot\mathbf{r}+i\omega_\mathbf{k}t}\boldsymbol{\varepsilon}_\mathbf{k}^* a_{\mathbf{k},\varepsilon_\mathbf{k}}^\dagger\right)$	$\mathbf{k}\cdot\boldsymbol{\varepsilon}_\mathbf{k}=0; \omega_\mathbf{k}=ck/n$
Inhomogeneous, lossless, non-dispersive, anisotropic	$\sum_n \sqrt{\frac{\hbar}{2\varepsilon_0\omega_n}}\left(\mathbf{F}_n(\mathbf{r})e^{-i\omega_n t}a_n + \mathbf{F}_n^*(\mathbf{r})e^{i\omega_n t}a_n^\dagger\right)$	$\nabla\times\nabla\times\mathbf{F}_n(\mathbf{r}) = \boldsymbol{\varepsilon}(\mathbf{r})\frac{\omega_n^2}{c^2}\mathbf{F}_n(\mathbf{r});$ $\int d^3r\,\mathbf{F}_n^*\cdot\boldsymbol{\varepsilon}(\mathbf{r})\cdot\mathbf{F}_n = 1$
Inhomogeneous, lossless, weakly dispersive, anisotropic	$\sum_n \sqrt{\frac{\hbar}{2\varepsilon_0\omega_n}}\left(\mathbf{F}_n(\mathbf{r})e^{-i\omega_n t}a_n + \mathbf{F}_n^*(\mathbf{r})e^{i\omega_n t}a_n^\dagger\right)$	$\nabla\times\nabla\times\mathbf{F}_n(\mathbf{r}) = \varepsilon(\mathbf{r},\omega_n)\frac{\omega_n^2}{c^2}\mathbf{F}_n(\mathbf{r});$ $\frac{1}{2\omega_n}\int d^3r\,\mathbf{F}_n^*(\mathbf{r})\cdot\frac{d(\omega^2\varepsilon(\mathbf{r},\omega))}{d\omega}\Big\vert_{\omega_n}\cdot\mathbf{F}_n(\mathbf{r}) = 1$
Inhomogeneous, lossy, dispersive, isotropic, local	$\sqrt{\frac{\hbar}{\pi\varepsilon_0}}\int_0^\infty d\omega\int d^3r'\frac{\omega}{c^2}\sqrt{\mathrm{Im}\,\varepsilon(\mathbf{r}',\omega)}$ $(\mathbf{G}(\mathbf{r},\mathbf{r}',\omega)\mathbf{f}(\mathbf{r}',\omega)e^{-i\omega t} + \mathbf{G}^*(\mathbf{r},\mathbf{r}',\omega)\mathbf{f}^\dagger(\mathbf{r}',\omega)e^{i\omega t})$	$\left(\nabla\times\nabla\times - \varepsilon(\mathbf{r},\omega)\frac{\omega^2}{c^2}\right)\mathbf{G}(\mathbf{r},\mathbf{r}',\omega) = \delta(\mathbf{r}-\mathbf{r}')I$
Inhomogeneous, lossy, dispersive, anisotropic, non-local	$\sqrt{\frac{\hbar}{\pi\varepsilon_0}}\int_0^\infty d\omega\int d^3r'\frac{\omega}{c^2}\sqrt{\mathrm{Im}\,\boldsymbol{\varepsilon}(\mathbf{r},\mathbf{r}',\omega)}$ $(\mathbf{G}(\mathbf{r},\mathbf{r}',\omega)\mathbf{f}(\mathbf{r}',\omega)e^{-i\omega t} + \mathbf{G}^*(\mathbf{r},\mathbf{r}',\omega)\mathbf{f}^\dagger(\mathbf{r}',\omega)e^{i\omega t})$	$\left(\nabla\times\nabla\times - \int d^3r'\,\boldsymbol{\varepsilon}(\mathbf{r},\mathbf{r}',\omega)\frac{\omega^2}{c^2}\right)\mathbf{G}(\mathbf{r},\mathbf{r}',\omega) = \delta(\mathbf{r}-\mathbf{r}')I$

Figure 2-5: **Levels of quantization of the electromagnetic field** showing the quantized vector potential operator under different cases of linear media, starting from the well-known field quantization in vacuum to quantization of the electromagnetic field in a truly arbitrary medium that can be inhomogeneous, anisotropic, lossy, and even spatially non-local.

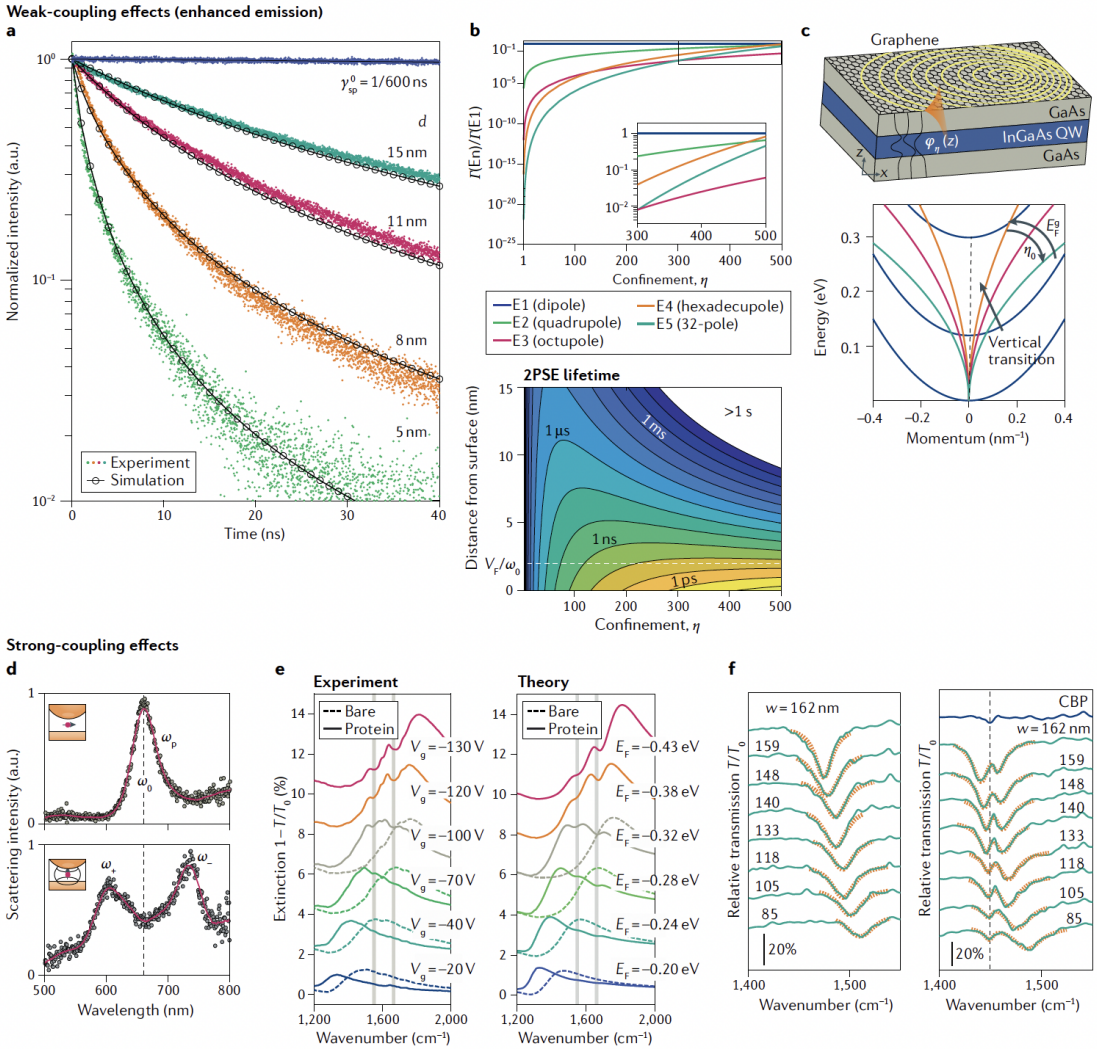

Figure 2-6: **Bound-electron interactions with photonic quasiparticles.** (a) In the visible spectral range, a molecular dye emitter in a plasmonic nanogap can have its spontaneous emission enhanced by nearly four orders of magnitude, reaching picosecond timescales (probed by time-resolved fluorescence). (b) Proposal to use highly confined plasmons to strongly enhance dipole-forbidden transitions and multi-photon emission processes. The strong confinement allows forbidden transitions to compete with conventionally allowed transitions, as well as allows two-plasmon emission processes to become comparable to one-plasmon processes. (c) The high momentum of a graphene plasmon allows significant momentum transfer from the electromagnetic field to electrons in a quantum well. Such a realization of optical nonlocality strongly changes absorption and emission spectral peaks. (d) When the light–matter coupling is strong enough, as in extremely small plasmonic nanogap cavities, even a small number of emitters can reach the strong-coupling regime, leading to Rabi splitting in the scattering spectrum. Strong coupling can also be realized by coupling many emitters (e.g., molecules) to a tightly-confined polariton mode, which can be used for (e) sensing molecules, as demonstrated with graphene plasmons, and (f) infrared spectroscopy, as demonstrated with boron nitride resonators.

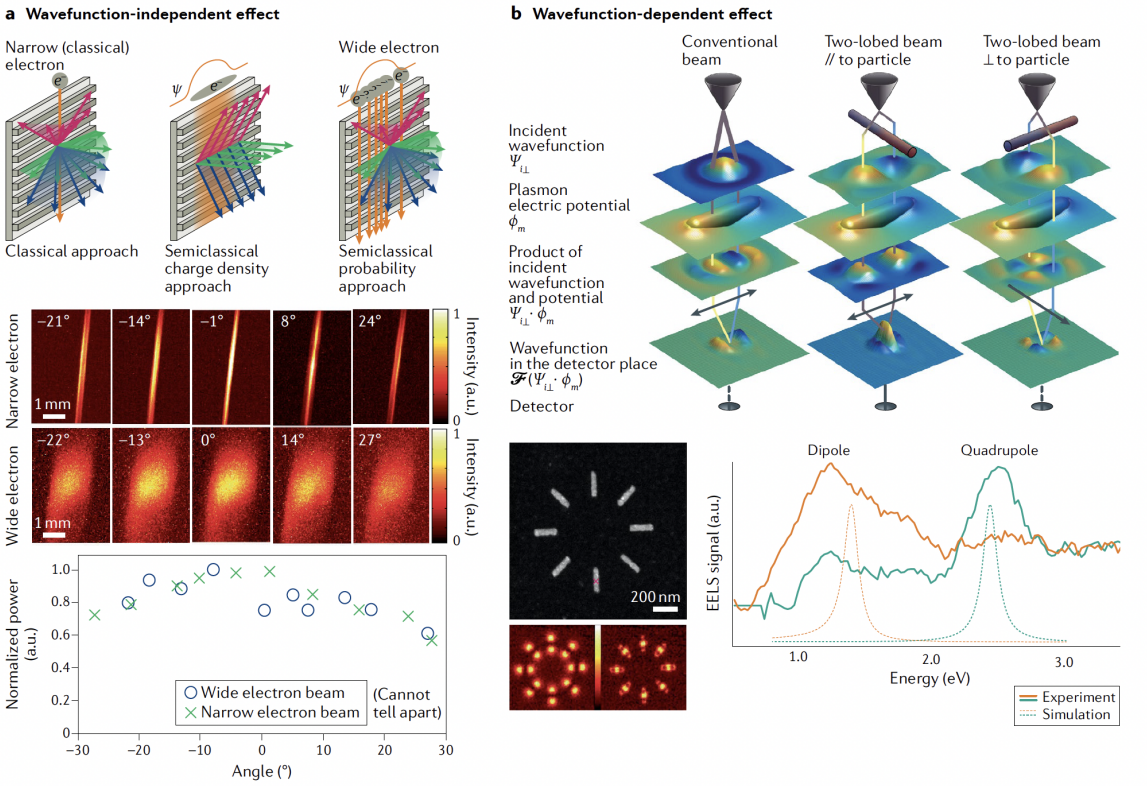

Figure 2-7: **Free-electron spontaneous radiation: quantum wavefunction-dependent effects.** (a) Experiment showing the effect on the coherent size of the electron wavefunction on Smith-Purcell radiation. Comparing a narrow versus wide electron wavefunction, a change is seen in the spatial distribution of the radiation (see color-maps) but no influence is seen on the radiated angular power spectrum. (b) The influence of photonic quasiparticles on electron energy-loss spectroscopy, through symmetry-matching between plasmonic modes and the electron wavefunction, showing how one can control which plasmon modes are coupled to by shaping the electron wavefunction to have a matching symmetry.

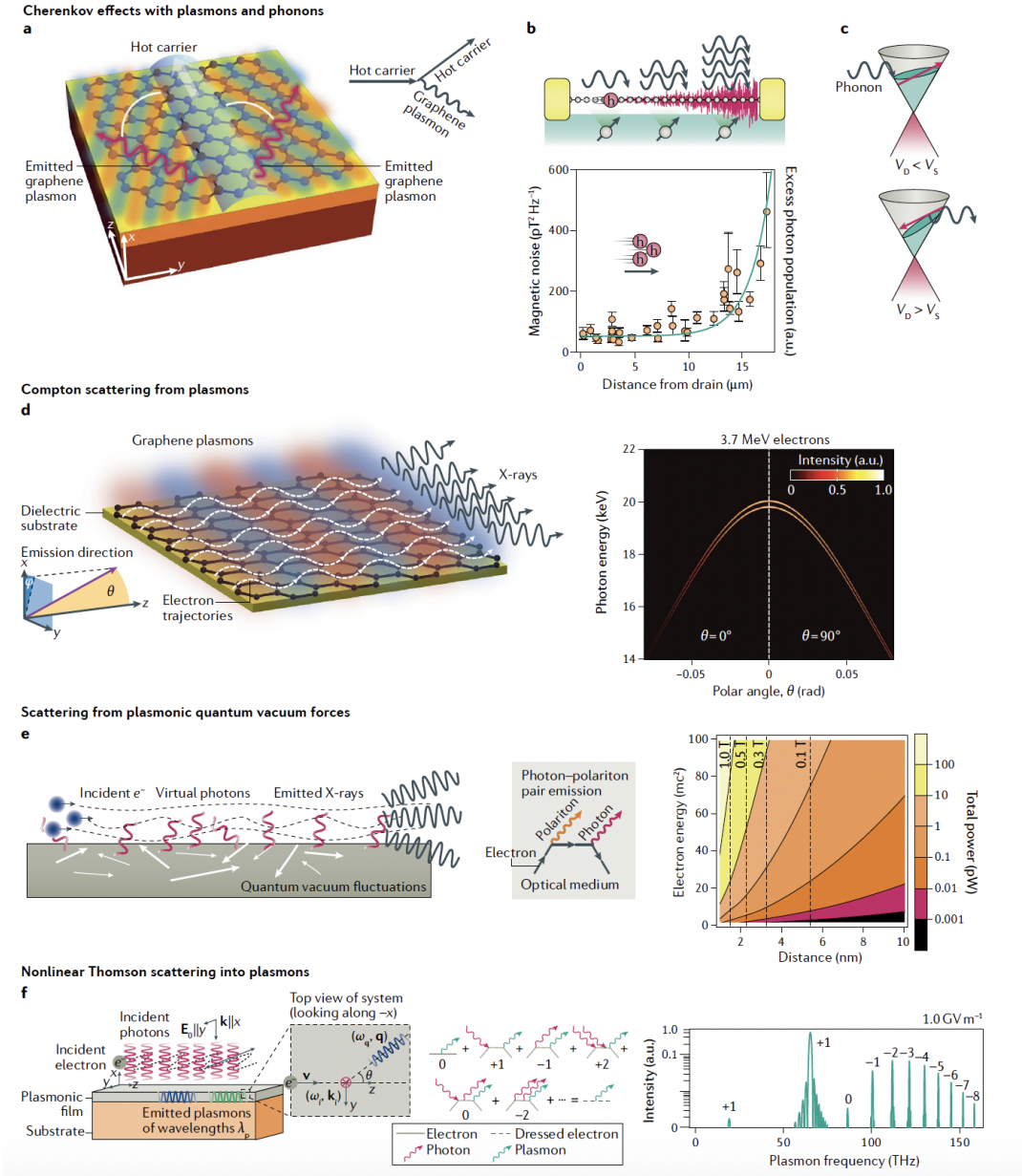

Figure 2-8: **The similarity of electron-photon, electron-plasmon, and electron-phonon interactions: all can be understood as interactions with photonic quasiparticles.** (a) Cherenkov radiation of plasmons in graphene by hot electrons can occur with a very high efficiency compared to Cherenkov radiation in transparent dielectric media. (b) Cherenkov emission of phonons by electrons in ultraclean graphene. (c) Such Cherenkov emission of phonons has been used to explain the amplification of magnetic noise by electrons moving in ultraclean samples of graphene. (d) Proposal of laser-driven photonic quasiparticles, in the form of surface plasmons, that produce X-rays from free electrons via inverse Compton scattering. (e) The phenomenon can even occur without an externally excited plasmon, using strong Casimir-type forces based on vacuum fluctuations of photonic quasiparticles. (f) Proposal to generate high harmonics of photonic quasiparticles, in the form of surface plasmons, by electrons interacting with strong fields.

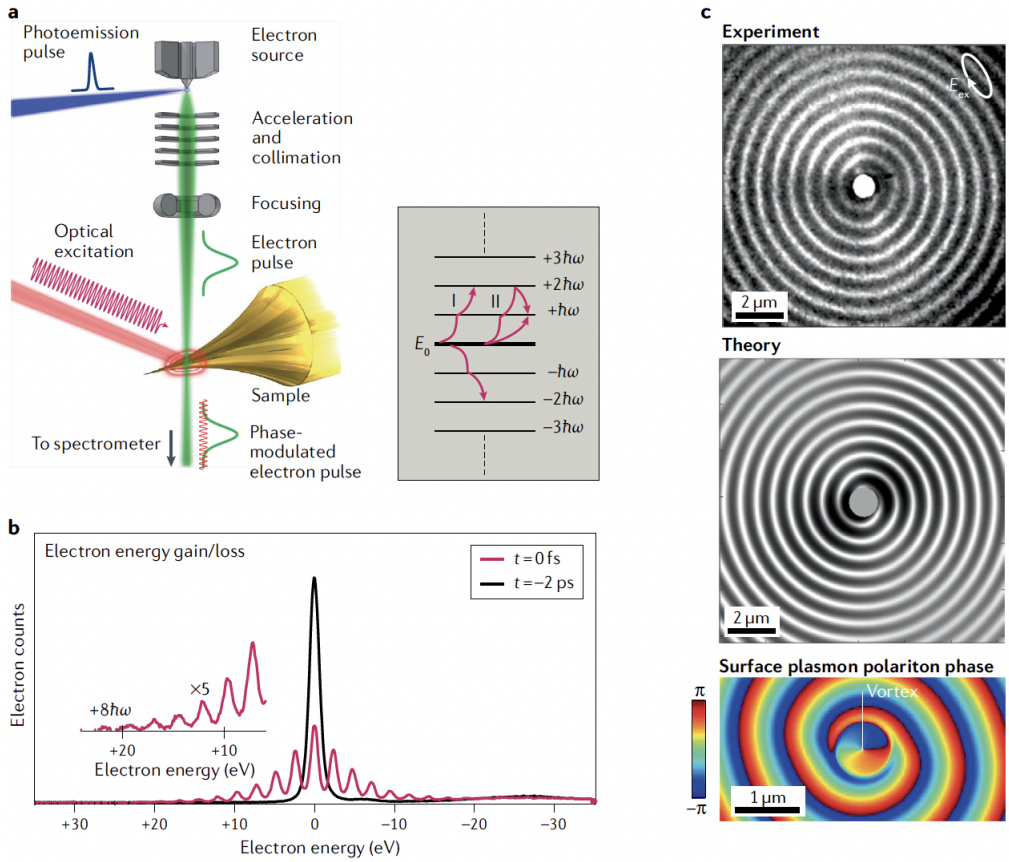

Figure 2-9: **Effects enabled by strong fields of photonic quasiparticles: photon-induced near-field electron microscopy (PINEM).** Stimulated electron-photon interactions when driving laser fields pump a photonic quasiparticle mode, as demonstrated in PINEM. Each electron undergoes stimulated absorption and emission of multiple photons as a result of the PINEM interaction with a strong field, leading to quantized energy gain and loss. (a) The electron can be seen as undergoing a quantum walk on the energy ladder with spacing set by the driving frequency. (b) First demonstration of PINEM. (c) When the electron interacts with a chiral plasmonic field, it imparts orbital angular momentum to the electron, seen in its diffraction pattern.

Chapter 3

Phonon polaritonics in two-dimensional materials

Note: This chapter is heavily based off "Phonon polaritonics in two-dimensional materials" by N. Rivera et al. Nano Letters (2019). It also presents experimental results from "Phonon Polaritons in Monolayers of Hexagonal Boron Nitride" by S. Dai, W. Fang, and N. Rivera, et. al. Advanced Materials (2019).

Extreme confinement of electromagnetic energy by phonon polaritons holds the promise of strong and new forms of control over the dynamics of matter. To bring such control to the atomic-scale limit, it is important to consider phonon polaritons in two-dimensional (2D) systems. Recent studies have pointed out that in 2D, splitting between longitudinal and transverse optical (LO and TO) phonons is absent at the Γ point, even for polar materials. Does this lack of LO–TO splitting imply the absence of a phonon polariton in polar monolayers? To answer this, we connect the microscopic phonon properties with the macroscopic electromagnetic response. Specifically, we derive a first-principles expression for the conductivity of a polar monolayer specified by the wavevector-dependent LO and TO phonon dispersions. In the long-wavelength (local) limit, we find a universal form for the conductivity in terms of the LO phonon frequency at the Γ point, its lifetime, and the group velocity of the LO phonon. Our analysis reveals that the phonon polariton of 2D is simply the LO phonon of the 2D system. For the specific example of hexagonal boron nitride (hBN), we estimate the

confinement and propagation losses of the LO phonons, finding that high confinement and reasonable propagation quality factors coincide in regions which may be difficult to detect with current near-field optical microscopy techniques. Finally, we study the interaction of external emitters with two-dimensional hBN nanostructures, finding extreme enhancement of spontaneous emission due to coupling with localized 2D phonon polaritons, and the possibility of multi-mode strong and ultra-strong coupling between an external emitter and hBN phonons. This may lead to the design of new hybrid states of electrons and phonons based on strong coupling.

Phonon polaritons, hybrid quasiparticles of photons and optical phonons supported in polar materials, hold promise for nanoscale control of electromagnetic fields at mid-infrared and terahertz frequencies. Qualitatively, phonon polaritons share many features with plasmon polaritons in conductors. Recently, it has been shown that phonon polaritons enable confinement of light to volumes $\sim 10^6$ times smaller than that of a diffraction-limited photon in free-space [131, 270, 39, 10, 271, 81, 80, 272, 273, 78, 85, 274, 275, 6, 276, 87, 86]. Due to this remarkable confinement and their relatively high lifetimes—around picoseconds—phonon polaritons open new opportunities for vibrational spectroscopy [44], radiative heat transfer [29], and control of dynamics in quantum emitters [277, 109, 110, 154].

Thus far, extreme confinement of phonon polaritons has been achieved by the use of thin-films (or nanostructuring), which shrink the in- and out-of-plane wavelength of polaritons with decreasing feature size (such as the film thickness) [10, 278]. A monolayer is the ultimate limit of this effect, making it critical to have a fundamental understanding of the optical response of 2D polar materials [279]. Concerning the optical response, the transition from three-dimensional (3D) to two-dimensional (2D) polar materials is nontrivial, however, since in a polar monolayer, the LO–TO splitting that gives rise to phonon polaritons in 3D is absent at the Γ point [280, 281, 282, 283]. This raises a fundamental question about the nature of electromagnetic modes in polar monolayers.

To resolve this question, a connection between the microscopic phonon properties and the macroscopic electromagnetic response is required.

To that end, we develop a first-principles framework for phonon polaritons in polar 2D

materials and illustrate it with quantitative, concrete examples. We derive a universal form for the conductivity of a polar monolayer, which depends solely on the LO and TO phonon frequencies—and their dispersion with momentum—in the 2D system. Using parameters from Ref. [283] for the canonical 2D polar monolayer—hexagonal boron nitride (hBN)—we present the confinement and propagation losses of the 2D phonon polariton modes, identifying the frequency region where they should be most easily detected. Finally, we find that these modes enable extreme light-matter interaction between emitters and polar materials, showing that for atom-like emitters, their spontaneous decay can be enhanced by up to eight orders of magnitude through the emitter–LO phonon coupling. For an infrared emitter with a sufficiently high free-space radiative decay rate ($\gtrsim 10^6 \mathrm{s}^{-1}$), we find that the associated linewidth of the emitter is comparable to the spacing between different phonon polaritonic resonances of an hBN nanostructure. This suggests the possibility of realizing the multi-mode strong coupling and ultra-strong coupling regimes of quantum electrodynamics in a 2D hBN platform. Our results for hBN are particularly relevant due its widespread use in 2D van der Waals heterostructures. In addition to providing functionality as a layer which improves the electrical and optical properties of other 2D materials, e.g.graphene, our results suggest that in these heterostructures, hBN layers could provide a mid-infrared platform for nanophotonics and quantum optics. While we focus on hBN in this manuscript, the salient features of our findings apply to other polar monolayers as well.

3.1 Optical response of optical phonons in two-dimensions

In this section, we develop a theory of electromagnetic response due to optical phonons in 2D systems. The key response function of interest is the conductivity of the monolayer. To that end, we consider the response of the ions of the monolayer due to an electric potential ϕ. For that case, the interaction Hamiltonian is

$$H_{\mathrm{int}} = \int \mathrm{d}^2x \; \rho\phi = -\int \mathrm{d}^2x \; (\nabla \cdot \mathbf{P})\phi, \tag{3.1}$$

with ρ the induced charge density and $\mathbf{P}$ the induced polarization density associated with the ionic motion. Note that boldfaced quantities refer to vectors or tensors as appropriate. Within linear response theory, the polarization density can be straightforwardly evaluated from the displacement $\mathbf{u}_\kappa$ of every atom κ within the unit cell. Specifically, to first order, the polarization density is

$$\mathbf{P} - \mathbf{P}^0 = \sum_\kappa (\mathbf{u}_\kappa \cdot \boldsymbol{\nabla}_{\mathbf{u}_\kappa})\mathbf{P} \equiv \frac{1}{\Omega}\sum_\kappa \mathbf{Z}_\kappa \mathbf{u}_\kappa, \tag{3.2}$$

where $\mathbf{Z}_\kappa \equiv \Omega \boldsymbol{\nabla}_{\mathbf{u}_\kappa}\mathbf{P}$ is the Born effective charge tensor of ion κ and Ω is the unit cell area. $\mathbf{P}^0$ is the equilibrium polarization in the absence of displacements, which is zero here. With this relation between polarization and ionic displacements, the interaction Hamiltonian in Eq. 1 couples the scalar potential and the ionic displacements. We consider the response of the monolayer to a potential of the form $\phi(\mathbf{r}) = \phi(\mathbf{q},\omega)\mathrm{e}^{\mathrm{i}\mathbf{q}\cdot\mathbf{r}-\mathrm{i}\omega t}$, where $\mathbf{q}$ is a 2D wavevector in the plane of the monolayer. Such a potential corresponds to a longitudinal electric field $\mathbf{E}(\mathbf{r}) = \mathrm{i}\mathbf{q}\phi(\mathbf{r})$.

In what follows, we assume the validity of the random-phase approximation (RPA) in calculating Coulombic interactions between ions in the polar lattice. Within the RPA, these Coulombic interactions are accounted for by taking the induced polarization $\mathbf{P}(\mathbf{q},\omega)$ to be proportional *total* electric field, $\mathbf{E}_{\mathrm{tot}}(\mathbf{q},\omega)$, defined to be the sum of the externally applied electric field and the electric field created by the induced polarization. The polarization and total field are connected by the polarization-polarization response (tensor) function $\boldsymbol{\Pi}(\mathbf{q},\omega)$ via

$$\mathbf{P}(\mathbf{q},\omega) = \epsilon_0 \boldsymbol{\Pi}(\mathbf{q},\omega)\mathbf{E}_{\mathrm{tot}}(\mathbf{q},\omega), \tag{3.3}$$

The polarization-polarization response function is related to the conductivity via the relation $\boldsymbol{\sigma}(\mathbf{q},\omega) = -\mathrm{i}\omega\epsilon_0\boldsymbol{\Pi}(\mathbf{q},\omega)$. From the Kubo formula, it follows that the conductivity is

$$\boldsymbol{\sigma}(\mathbf{q},\omega) = \frac{-\mathrm{i}\omega}{\Omega\mathcal{Z}}\sum_{m,n}\frac{\mathbf{P}_{mn}(\mathbf{q})\otimes\mathbf{P}_{nm}(\mathbf{q})}{\hbar\omega + E_{nm} + \mathrm{i}0^+}\left(\mathrm{e}^{-\beta E_m} - \mathrm{e}^{-\beta E_n}\right), \tag{3.4}$$

where m, n are eigenstates in the phononic Fock space of the monolayer, $\mathbf{P}_{mn}(\mathbf{q}) \equiv \sum_\kappa \mathbf{Z}_\kappa \langle m|\mathbf{u}_\kappa(\mathbf{q})|n\rangle$ are matrix elements of the polarization associated with phonon modes

(where $\mathbf{u}_\kappa(\mathbf{q})$ is the Fourier transform of the phonon displacement operator), E_m (E_n) is the energy of state m (n), $\beta \equiv 1/k_\mathrm{B}T$ is the inverse temperature, and $\mathcal{Z}$ is the grand partition function. We now evaluate the contribution of optical phonons to the polarization-polarization response in the low-temperature limit $T \ll \hbar\omega_\mathrm{ph}/k_\mathrm{B}$ with ω_ph a characteristic optical phonon frequency. Considering the long-wavelength (small wavevector) limit, and taking a material with long-wavelength isotropy, such as hBN, we only have to consider the qq-component in the response tensor, where qq denotes a pair of directions parallel to the wavevector. Denoting σ_{qq} as simply σ, we find that the conductivity is given by [284]:

$$\sigma(\mathbf{q},\omega) = \frac{-\mathrm{i}\omega}{\hbar\Omega}\frac{2\omega_{\mathbf{q},\mathrm{L}}}{\omega_{\mathbf{q},\mathrm{L}}^2 - \omega^2 - \mathrm{i}\omega\tau^{-1}}|\hat{\mathbf{q}}\cdot\langle 1_{\mathbf{q},\mathrm{L}}|\mathbf{P}(\mathbf{q})|0_{\mathbf{q},L}\rangle|^2, \tag{3.5}$$

where L-subscripts denote longitudinal polarization, $|0_{\mathbf{q},\mathrm{L}}\rangle$ ($|1_{\mathbf{q},\mathrm{L}}\rangle$) denotes a state with no (one) longitudinal phonon of wavevector $\mathbf{q}$, and $\hat{\mathbf{q}}$ denotes a unit vector in the direction of $\mathbf{q}$. We have also phenomenologically included the phonon dissipation rate τ^{-1}, consistently with a relaxation-time prescription. The frequency $\omega_{\mathbf{q},\mathrm{L}}$ in the denominator, as in the case of bulk phonons, is the frequency of the longitudinal phonon of wavevector $\mathbf{q}$ prior to considering LO–TO splitting [285] (and near the Γ point is approximately equal to the TO phonon frequency). This is consistent with the fact that LO–TO splitting is a collective effect arising from Coulomb interactions and the fact that the equation above represents a single-particle susceptibility. Coulomb interactions are accounted for in the random phase approximation, and to include them in the single-particle response amounts to an uncontrolled double-counting.

Next, we express the polarization matrix element in Eq. 5 in terms of the Born effective charges of the monolayer and the phonon displacement eigenvectors. Considering the longitudinal phonon contribution to the second-quantized ionic displacement, as in Ref. [286], we find that the conductivity within the RPA is given by

$$\sigma(\mathbf{q},\omega) = -\frac{\mathrm{i}\omega}{\Omega}\frac{\left|\hat{\mathbf{q}}\cdot\sum_\kappa \mathbf{Z}_\kappa\boldsymbol{\eta}_\kappa\right|^2}{\omega_{\mathbf{q},\mathrm{L}}^2 - \omega^2 - \mathrm{i}\omega\tau^{-1}}. \tag{3.6}$$

We have defined scaled eigendisplacements $\boldsymbol{\eta}_{\kappa\mathbf{q}} \equiv \hat{\mathbf{e}}_{\kappa\mathbf{q},\mathrm{L}}/\sqrt{M_\kappa}$, where $\hat{\mathbf{e}}_{\kappa\mathbf{q},\mathrm{L}}$ is the unit-

normalized polarization vector of atom κ in the unit cell oscillating according to a longitudinal phonon of wavevector $\mathbf{q}$ and M_κ is the mass of atom κ.

While the conductivity is the main electromagnetic quantity of interest for electrodynamics applications, we briefly state the form of the (2D) permittivity, as its zeros immediately yield the longitudinal modes of the system, which are the LO phonons. The permittivity within the RPA, denoted ϵ_{RPA} is related to the polarization-polarization response function via [38] $\epsilon_{\text{RPA}} = \epsilon_{\text{env}} + \frac{1}{2} q \Pi(q, \omega)$ and the conductivity via $\epsilon_{\text{RPA}} = \epsilon_{\text{env}} + \mathrm{i} q \sigma(q, \omega) / 2\epsilon_0 \omega$. Here, ϵ_{env} is the average permittivity of the bulk above and below the monolayer, and is added to take into account the polarization arising from these bulk materials. Note that we have neglected any intrinsic high-frequency screening in the monolayer itself, which is only relevant for wavevectors comparable to the inverse layer spacing between monolayers. When considering non-local corrections to the conductivity at these large wavevectors, these must be taken into account [287, 279, 283]. Based on Eq. 6, the zeros $\omega_{\mathbf{q}}$ of the RPA dielectric function satisfy:

$$\omega_{\mathbf{q}}^2 - \omega_{\text{TO}}^2 = \frac{V(q)}{e^2} \frac{1}{\Omega} q^2 \left| \hat{\mathbf{q}} \cdot \sum_\kappa \mathbf{Z}_\kappa \boldsymbol{\eta}_\kappa \right|^2, \tag{3.7}$$

where $V(q)$ is the Coulomb interaction in Fourier space, which in two dimensions, is given by $V(q) = e^2 / 2\epsilon_0 \epsilon_{\text{env}} q$. Given that the zeros of the dielectric function are associated with longitudinal modes, one expects that $\omega_{\mathbf{q}}$ is in fact the frequency of the LO phonon mode. This is consistent with the result of Ref. [283], in which it is shown that in 2D polar materials, the extra restoring forces on LO phonons relative to TO phonons, due to the Coulomb interaction, lead to a wavevector-dependent LO–TO splitting and zero LO–TO splitting at the Γ point of the Brillouin zone.

Given these results, we now re-express the conductivity explicitly in terms of the 2D phonon dispersion, and derive a universal form for the conductivity in the local ($q \to 0$) limit specified in terms of three parameters: the LO phonon frequency at the Γ point (i.e., ω_{TO}), the group velocity of the LO phonon at the Γ point, and the damping rate. From

Eq. 7, we can immediately write the conductivity as

$$\sigma(\mathbf{q},\omega) = \frac{-2\mathrm{i}\epsilon_0\epsilon_{\mathrm{env}}\omega}{q}\frac{\omega_{\mathbf{q},\mathrm{LO}}^2 - \omega_{\mathrm{TO}}^2}{\omega_{\mathrm{TO}}^2 - \omega^2 - \mathrm{i}\omega\tau^{-1}}. \tag{3.8}$$

In this expression, ω_{L}, the LO phonon frequency prior to LO–TO splitting, has been renamed as ω_{TO}, the transverse optical phonon frequency, because in the absence of LO–TO splitting, they are degenerate. The RPA zeros $\omega_{\mathbf{q}}$ have also been renamed as $\omega_{\mathbf{q},\mathrm{LO}}$. This is done in order to make the form of the final results more closely resemble their 3D counterparts, in which the dielectric function is expressed in terms of the TO frequency (see for example Eq. 13).

For small q, the Born charges are (to lowest-order) constant, and so the LO phonon dispersion takes the form $\omega_{\mathbf{q},\mathrm{LO}} = \sqrt{\omega_{\mathrm{TO}}^2 + 2v_{\mathrm{g}}\omega_{\mathrm{TO}}q} \simeq \omega_{\mathrm{TO}} + v_{\mathrm{g}}q$, where v_{g}, the LO phonon group velocity, is defined from microscopic parameters through the relation

$$v_{\mathrm{g}} = \frac{\left|\hat{\mathbf{q}}\cdot\sum_\kappa \mathbf{Z}_\kappa\boldsymbol{\eta}_\kappa\right|^2}{4\epsilon_0\epsilon_{\mathrm{env}}\omega_{\mathrm{TO}}\Omega}. \tag{3.9}$$

Thus, in the long wavelength limit, we have the following universal parameterization of the conductivity of a polar monolayer:

$$\sigma(\omega) = \frac{-4\mathrm{i}\epsilon_0\epsilon_{\mathrm{env}}\omega\omega_{\mathrm{TO}}v_{\mathrm{g}}}{\omega_{\mathrm{TO}}^2 - \omega^2 - \mathrm{i}\omega\tau^{-1}}. \tag{3.10}$$

We note that despite its appearance, $\sigma(\omega)$ does not depend on ϵ_{env}, as v_{g} has an opposite dependence on ϵ_{env}. From this relation, it follows that given the properties of the 2D phonons (from experiments or from *ab initio* calculations), one can immediately specify the conductivity. Alternatively, from optical measurements (including far-field measurements) which allow one to extract the conductivity, it becomes possible to extract the group velocity of 2D LO phonons and thus the small-wavevector dispersion of those phonons.

Before moving on to analyze the electrodynamics of 2D phonon polaritons, we make three comments on lack of LO–TO splitting in 2D polar materials. The first is that this situation is in stark contrast to the situation of polar materials in 3D, which have a finite

LO–TO splitting at the Γ point. In the absence of such LO–TO splitting in 3D, there would be no frequency compatible with the existence of a phonon polariton. On the contrary, we will show that in 2D, despite the absence of LO–TO splitting at the Γ point, there persists a strongly confined evanescent electromagnetic mode with a high local density of states which in all respects is similar to a phonon polariton of a thin film, but is in fact the 2D LO phonon of the polar monolayer (thus the phrases 'phonon polariton' and '2D LO phonon' may be used somewhat interchangeably as is the case in plasmonics where the terms 'plasmon polariton' and '2D plasmon' are often used interchangeably).

The second comment is that much of what has been discussed here has a strong analogy with the theory of optical response in electron gases in 2D, and particularly the relation between plasmons in 2D and 3D. To elaborate on this analogy, we take Eq. 7 in the case of a two-atom unit cell (such as hBN), and note that the term in the sum over Born charges can be written as $\left|\hat{\mathbf{q}} \cdot \sum_\kappa \mathbf{Z}_\kappa \boldsymbol{\eta}_\kappa\right|^2 \equiv Q_*^2/M_*$, with Q_* being an effective charge and M_* being an effective mass. Then, the LO–TO splitting can be written as $\omega_{\mathbf{q}}^2 - \omega_{\mathbf{q},\mathrm{TO}}^2 = \frac{Q_*^2}{2\epsilon_0\epsilon_{\mathrm{env}}M_*}q$. Now we note that the RHS is exactly the squared-frequency $\omega_{\mathbf{q}\mathrm{p}}^2$ for a plasma oscillation in a 2D gas of charged particles with charge Q_* and mass M_*. To connect to LO–TO splitting in phonons, this squared frequency $\omega_{\mathbf{q}\mathrm{p}}^2$ can be thought of as the "LP–TP" splitting between longitudinal and transverse plasma oscillations. Of course, there are no transverse plasma oscillations due to the structure-less nature of the electron, and so "ω_{TP}" should be considered equal to zero. In the three-dimensional plasmon case, "$\omega_{\mathrm{TP}} = 0$", but the difference between the squared longitudinal and transverse plasma oscillation frequencies at zero-wavevector is non-zero and given by ω_{p}^2. In other words, the plasma frequency in electron gases is analogous to the LO–TO splitting in polar materials. The change in the dispersion of 3D versus 2D plasmons, like 3D versus 2D LO phonons, arises from the change in dimensionality of the Coulomb interaction from 3D to 2D. This analogy between phononic and plasmonic behavior as a function of dimension is illustrated schematically in Figs. 1b,c in order to help unify the understanding of 2D plasmonics and phononics. These considerations should also extend to the one-dimensional case.

The third comment is that the considerations of this section can be extended to few-layer systems, such as hBN bilayers, which remain two-dimensional from an electromag-

netic perspective for polariton wavelengths large compared to the bilayer thickness. Concretely, the LO–TO splitting in such quasi-2D systems is still given by Eq. 7, provided the appropriate eigendisplacements of the few-layer system are employed, and provided suitable modifications of the Coulomb interaction are made. For N weakly coupled layers, the sum of Born effective charges $\left|\hat{\mathbf{q}}\cdot\sum_\kappa \mathbf{Z}_\kappa\boldsymbol{\eta}_\kappa\right|^2$, which is essentially an oscillator strength, is approximately NQ_*^2/M_*, i.e.enhanced N-fold relative to the monolayer or, equivalently, proportional to the thickness t [283]. For few layers, i.e.for $qt \ll 1$ where the Coulomb interaction remains essentially 2D, this simple geometric effect enhances the LO–TO splitting by a factor N. At larger qt, the Coulomb interaction must eventually approach its 3D limit; to study this transition from monolayer to bulk explicitly, a quasi-2.5D Coulomb interaction [279] can be employed in Eq. 7. Specifically, for a film of thickness t, the interaction is approximately $V_{\text{Q2.5D}}(q) = \frac{e^2}{\epsilon_0\epsilon_\infty q^2 t}\left(1-\frac{2}{qt}e^{-\frac{qt}{2}}\sinh\frac{qt}{2}\right)$, with the static electronic screening ϵ_∞ interpolating between its monolayer value, 1, and its bulk value, ϵ_∞. The $qt\to 0$ and $qt\to\infty$ asymptotics of this interaction are the 2D and 3D interactions—$e^2/2\epsilon_0 q$ and $e^2/\epsilon_0\epsilon_\infty q^2 t$, respectively—which it interpolates between. In the large-thickness or -momentum limit, $qt \gg 1$, the $\propto t$ scaling of the oscillator strength, the $\propto t^{-1}q^{-2}$ scaling of the Coulomb interaction, and the $\propto q^2$ factor in Eq. 7 cancel, producing a thickness- and momentum-independent LO–TO splitting, as expected in the bulk.

Analogously, our considerations can be extended to 1D polar materials, such as BN nanotubes, by employing the 1D Coulomb interaction (and, naturally, the 1D-specific eigendisplacements). For a 1D system of transverse extent R (e.g., the radius of a nanotube), the 1D Coulomb interaction is $e^2K_0(qR)/2\pi\epsilon_0$, where K_0 is the (zeroth order) modified Bessel function of the second kind. Thus, the q-dependence of the (squared) LO–TO splitting in 1D is $q^2K_0(qR) \simeq -q^2\log qR$. This parallels the situation in 1D plasmonics, as expected from the discussion of Fig. 1.

3.2 Electrodynamics of optical phonons in two-dimensions

To relate the conductivity function to the electromagnetic modes supported by a polar monolayer, we solve Maxwell's equations for an evanescent electromagnetic mode sup-

ported by a surface with conductivity σ. We consider the monolayer to be sandwiched by a superstrate of permittivity ϵ_+ and a substrate of permittivity ϵ_-. To strip the analysis to its bare essentials, we consider optical phonon response with in-plane isotropy in the long-wavelength limit arising from in-plane LO oscillations. A relevant example of a system where these conditions are satisfied is in a hexagonal boron nitride monolayer (see Fig. 1a for schematic atomic structure). In a monolayer geometry with translation invariance and in-plane isotropy, the solutions of Maxwell's equations can be decomposed into transverse magnetic (TM) and transverse electric (TE) parts, where the magnetic or electric field respectively is transverse to the in-plane wavevector of the mode. In practice, it is the TM mode which is associated with highly confined electromagnetic waves. We consider without loss of generality a TM mode with wavenumber q along the x-direction in the monolayer and magnetic field $H(z)\mathrm{e}^{\mathrm{i}qx-\mathrm{i}\omega t}$ along the y-direction of the monolayer. The direction transverse to the monolayer is denoted as z. With these definitions in place, the Maxwell equation satisfied by the magnetic field is

$$\left(-\frac{\mathrm{d}^2}{\mathrm{d}z^2}+q^2-\epsilon_\pm\frac{\omega^2}{c^2}\right)H(z)=0, \tag{3.11}$$

where ϵ_+ applies for $z>0$ and ϵ_- applies for $z<0$. We consider a solution of the form $H(z)=h_\pm\mathrm{e}^{\mp\kappa_\pm z}$ with $\kappa_\pm=\sqrt{q^2-\epsilon_\pm\frac{\omega^2}{c^2}}$ with $\pm$ corresponding to $\pm z>0$ respectively. The boundary condition on the magnetic field is $h_+-h_-=-K_x=-\sigma E_x$ where $\mathbf{K}$ is the surface current density, and $\mathbf{E}=-\frac{1}{i\omega\epsilon}\nabla\times\mathbf{H}$ is the electric field. This condition enforces $h_+-h_-=\frac{\sigma}{i\omega\epsilon_+}\kappa_+h_+$. Continuity of the electric field in the x direction enforces $\epsilon_-/\epsilon_+=-\kappa_-h_-/\kappa_+h_+$. Combining the two conditions, we obtain the usual dispersion equation for the TM mode of a polarizable 2D monolayer, namely $\epsilon_+/\kappa_++\epsilon_-/\kappa_-=\frac{\sigma}{i\omega}$. Given the deeply subwavelength nature of 2D phonon polaritons, i.e.since $q\gg\omega/c$ such that $\kappa_\pm\simeq q$, the dispersion equation can be reduced to its quasistatic limit without consequential loss of accuracy:

$$q=\frac{2i\omega\epsilon_0\epsilon_{\mathrm{env}}}{\sigma}, \tag{3.12}$$

with $\epsilon_{\mathrm{env}}\equiv(\epsilon_++\epsilon_-)/2$. This condition, as can be seen from the relation between Π and σ, is equivalent to $\epsilon_{\mathrm{RPA}}=0$. Thus, the condition for phonon polaritons coincides pre-

cisely with the condition for longitudinal optical phonons. One of the main results of our manuscript is that despite the lack of LO–TO splitting at the Γ point, there nevertheless exists a strongly confined evanescent mode in many respects similar to the phonon polaritons of thin films. We now analyze the dispersion relation of phonon polaritons in a specific material, hexagonal boron nitride, in more detail, showing the possibility of highly confined electromagnetic modes with a large local density of states.

In Fig. 2a, we present the conductivity of 2D hBN of Eq. 10, using parameters from Ref. [283] calculated from density functional theory within the local density approximation. In this plot $\epsilon_{\mathrm{env}} = 1$, $\omega_{\mathrm{TO}} = 1387\,\mathrm{cm}^{-1}$ and $v_{\mathrm{g}} = 1.2 \times 10^{-4} c$, with c the speed of light in vacuum.

From the conductivity, the dispersion relation of phonon polaritons on an infinite sheet is given by $q = 2\mathrm{i}\omega\epsilon_0\epsilon_{\mathrm{env}}/\sigma(\omega)$. The dispersion, assuming $\tau = \infty$ and $\epsilon_{\mathrm{env}} = 1$, is shown in Fig. 2c (black line). A key figure of merit for applications involving the propagation of phonon polaritons, is the propagation quality factor, defined by $\mathrm{Re}\, q/\mathrm{Im}\, q = \mathrm{Im}\,\sigma(\omega)/\mathrm{Re}\,\sigma(\omega)$, which is shown in Fig. 2b.

For monolayer hBN, the wavevector grows very rapidly with frequency, due to the extremely low group velocity of 2D LO phonons, which is a remarkable four orders of magnitude slower than the speed of light. In particular, at frequencies of $1450\,\mathrm{cm}^{-1}$, the phonon polariton has a wavelength of about 15 nm, significantly shorter than any phonon polariton measured so far, and, similarly shorter than any plasmonic wavelength, even in graphene. In fact, this short a wavelength well-below that of any polariton in current scattering near-field microscopy (SNOM) measurements. The 2D phonon polariton could in principle be measured by SNOM closer to the TO frequency, where confinement is smaller; unfortunately, as shown in Fig. 2b, near the TO frequency, dissipation is far higher (and corresponding propagation quality factors $\mathrm{Re}\, q/\,\mathrm{Im}\, q$ far lower) due to large $\mathrm{Re}\,\sigma$ (or, equivalently, large $\mathrm{Im}\,\epsilon_{\mathrm{RPA}}$).

These considerations imply that access to the lower-loss and higher-confined portions of the dispersion relation of phonon polaritons, in the absence of a sharper tip, requires a near-field probe such as a free electron probe, as used in electron energy loss spectroscopy (EELS), where slow electrons can be used to probe plasmon wavelengths of just a few

nanometers in monolayer metals, as well as the nonlocal bulk plasmon dispersion in metals [288, 27, 289]. EELS has been recently employed to measure phonon polaritons in ultrathin films of hBN [290]. Another interesting class of near-field probes, with relevance to fundamental physics and quantum optics applications, is a quantum emitter such as an atom, molecule, or artificial atom such as a quantum dot, quantum well, or vacancy center. Recently, it was demonstrated using nanostructures of bulk hBN that the interaction of vibrational emitters with phonon polaritons is on the border of the strong coupling regime [44].

In the rest of this section, we discuss the relation between the dispersion of an hBN monolayer versus the atomically-thick limit of a thin film of a material with hBN's bulk dielectric function. To aid this discussion, in Fig. 2c, we show the dispersion relation of thin films of bulk hBN with film thicknesses of 1, 2, 4, and 8 times the interlayer spacing of bulk hBN, which is roughly 0.33 nm. For these plots, we take hBN to be cleaved such that the optical axis is perpendicular to the plane of the film. The components of the bulk permittivity perpendicular and parallel to the c-axis ($\epsilon_\perp$ and $\epsilon_\parallel$, respectively; indexed by $\alpha \in \{\perp, \parallel\}$ below) are then given by

$$\epsilon_\alpha(\omega) = \epsilon_{\infty,\alpha}\left(1 + \frac{\omega_{\mathrm{LO},\alpha}^2 - \omega_{\mathrm{TO},\alpha}^2}{\omega_{\mathrm{TO},\alpha}^2 - \omega^2}\right), \tag{3.13}$$

with $\epsilon_{\infty,\parallel} = 2.95$, $\omega_{\mathrm{TO},\parallel} = 760\,\mathrm{cm}^{-1}$, and $\omega_{\mathrm{LO},\parallel} = 830\,\mathrm{cm}^{-1}$; and $\epsilon_{\infty,\perp} = 4.87$, $\omega_{\mathrm{TO},\perp} = 1360\,\mathrm{cm}^{-1}$, and $\omega_{\mathrm{LO},\perp} = 1614\,\mathrm{cm}^{-1}$[39, 10]. Losses are ignored in this discussion altogether. In the range between $\omega_{\mathrm{TO},\alpha}$ and $\omega_{\mathrm{LO},\alpha}$, the corresponding component of the permittivity is negative, while the other component is positive. This hyperbolicity leads to a dispersion for hBN thin films that have multiple branches at a given frequency, as can be seen in Fig. 2c. This trend persists even when the thickness of the bulk is taken down to a single layer, albeit pushed to high wavevectors. This is in contrast with the true monolayer, where there is only one LO phonon mode. Given that the phonon polariton of 2D is the LO phonon, there can be only one branch of the dispersion. The bulk dielectric function of Eq. 13 fails to capture this removal of higher-order modes (i.e. hyperbolicity). For a bilayer, however, there is a higher-order LO mode, associated with out-of-phase oscillation

between the two layers. Heuristically, as can be anticipated from the blue higher-order mode in Fig. 2c, this mode would be challenging to observe, given its extremely high confinement and small spectral separation from the TO mode (a few cm^{-1}, comparable to the damping linewidth).

While we have focused on anomalies between the atomically-thin limit of bulk and a true monolayer, a comparison of the monolayer with the fundamental phonon polariton mode of the one-atom-thick thin film suggests that we have a reasonable qualitative understanding of the monolayer dispersion from the one-atom-thick thin film.

This qualitative similarity is to be somewhat expected, as a 2D layer can be considered as a very thin film of bulk material, provided that the microscopic properties of the bulk and monolayer do not deviate substantially. The differences between the $t = t_{\mathrm{2D}} = 0.33\,\mathrm{nm}$ bulk thin-film and monolayer that nevertheless do exist, reflect such microscopic deviations. Occasionally, e.g.for compatibility with standard numerical tools, it is useful to introduce a fictitious, effective bulk material whose fundamental thin-film mode *exactly* matches the monolayer's. The dielectric function of such a "bulkified" monolayer is thickness-dependent and anisotropic: for a film in the xy plane, it is $\boldsymbol{\epsilon}_{\mathrm{Q2D}} = (\hat{\mathbf{x}}\hat{\mathbf{x}} + \hat{\mathbf{y}}\hat{\mathbf{y}})\epsilon_{\mathrm{Q2D},\parallel} + \hat{\mathbf{z}}\hat{\mathbf{z}}\epsilon_{\mathrm{Q2D},\perp}$ with $\epsilon_{\mathrm{Q2D},\perp} = 1$ and

$$\epsilon_{\mathrm{Q2D},\parallel}(\omega) = 1 + \frac{\mathrm{i}\sigma}{\varepsilon_0 \omega t} = 1 + \frac{1}{t}\frac{4\epsilon_{\mathrm{env}}\omega_{\mathrm{TO}} v_{\mathrm{g}}}{\omega_{\mathrm{TO}}^2 - \omega^2 - \mathrm{i}\omega\tau^{-1}}. \tag{3.14}$$

3.3 Strong light-matter interactions enabled by 2D optical phonons

The extreme confinement of electromagnetic fields offered by the 2D phonon polariton presents an opportunity for quantum optical applications in which one seeks to couple an external emitter such as an atom, molecule, defect, or artificial atomic system to electromagnetic fields. Applications of these couplings are ultra-bright single- or two-photon sources, realizing the strong-coupling regime and the associated phenomenology of Rabi oscillations and polaritons, or resolving spectroscopically "forbidden" transitions [130, 44, 105, 109, 110] to achieve near-field spectroscopies with momentum and angular momen-

tum resolution not accessible in far-field spectroscopies.

In Fig. 3, we consider the coupling of a dipole emitter to localized phonon polaritons of nanostructured monolayer hBN. For simplicity, we consider hBN nanostructured as a disk, which leads to the formation of sharp resonances quantized along the azimuthal and radial directions. The disk is taken to have a radii varying from 10 nm to 40 nm and a loss rate $\tau^{-1} = 0.5\,\mathrm{meV}$, which is of the order of the loss rate in bulk hBN [39, 10]. We also show (dashed line) the results for a disk of infinite radius, i.e., a flat sheet of monolayer hBN. We parameterize the coupling between the dipole and phonon polaritons through the rate of spontaneous emission Γ of phonon polaritons by the dipole, normalized to the rate of spontaneous emission in free space Γ_0. It is related to the dyadic Green function $\mathbf{G}$ of the Maxwell equations for the nanostructure via the expression [127]:

$$\frac{\Gamma}{\Gamma_0} = \frac{6\pi c}{\omega}\hat{\mathbf{n}} \cdot \mathrm{Im}\,\mathbf{G}(\mathbf{r}, \mathbf{r}, \omega) \cdot \hat{\mathbf{n}}, \tag{3.15}$$

where $\hat{\mathbf{n}}$ is the orientation of the dipole, $\mathbf{r}$ its position, and ω its frequency.

The dyadic Green function is computed using a quasistatic boundary element method (as in Ref. [291]). In Fig. 3, we plot the enhancement of the spontaneous emission rate Γ/Γ_0 for an external emitter polarized perpendicularly to the plane of the disk and placed 5 nm away from the center of the disk. Due to the orientation and position of the dipole, which maintains the axial symmetry of the disk, the emitter only couples to axially symmetric ($\ell = 0$) modes with zero orbital angular momentum. We find that the rate of spontaneous emission of 2D optical phonons is approximately 8 orders of magnitude larger than the rate of spontaneous emission of photons in the far field at frequencies corresponding to resonant modes of the hBN disk. Such enhancement is much larger than the enhancement presented by an unstructured, infinite sheet at the same frequency, due to the concentration of electromagnetic local density of states around the resonances. Nevertheless, the average spontaneous emission enhancement, defined by the integral of the enhancement over frequencies, is comparable to that of the flat sheet, in keeping with sum rules for spontaneous emission enhancement [23]. We note that in this approach, the coupling of the dipole to phonon polaritons is manifested through the phonon contribution to the conduc-

tivity of the disk. This should be equivalent to an approach that considers the coupling of a bound electron in an emitter to LO phonons in the disk through a 2D Fröhlich coupling—i.e.a coupling of the atomic electron to the electric potential resulting from the polarization associated with an LO phonon mode [287].

In Fig. 3, we show that for an infrared emitter at a transition wavelength of 7 μm with a free-space radiative lifetime of 1 μs, 5 nm away from an hBN disk, the coupling rate to 2D optical phonons (about 65 meV) would be on the same scale as the optical phonon frequency itself (about 180 meV). This rate thus implies coupling between an emitter and the field in the regime of ultra-strong coupling. Moreover, the coupling rate for the 20 nm disk (purple), for an emitter with a far field decay rate of $\gtrsim 3 \times 10^{14}\,\mathrm{s}^{-1}$ would have a sufficient coupling strength to the distinct, radially-quantized resonances in purple for its linewidth to span multiple resonances and thus be in a multi-mode ultra-strong coupling regime. Thus, the extreme confinement of electromagnetic energy associated with LO phonons in two dimensions enables the possibility of realizing ultra-strong coupling of an atom or molecule with optical phonons in a polar material, allowing the potential realization of new coupled states of quantum emitters and phonons such as atom–phonon polariton bound states.

The ability to probe low-loss and highly confined electromagnetic modes associated with optical phonons in 2D polar materials provides a new platform for nanophotonics in the mid- and far-infrared spectral range. The identification of the phonon polariton of bulk and thin-film geometries with the 2D LO phonon made in this manuscript would extend the rich phenomenology of optical phonons to nanophotonic applications. This work also points the way to useful new approaches to study LO phonons, arising from the fact that 2D LO phonons, unlike their 3D counterparts, have their electromagnetic energy extend a considerable distance from the material boundary. Due to the strong electromagnetic interactions between emitters and 2D phonon polaritons shown here, it is now possible to design interesting new hybrid states of matter and phonons based on quantum electrodynamical strong coupling. The highly confined phonon polaritons in polar monolayers may also provide interesting new opportunities in near-field radiative heat transfer, in which it has been long known that thin-film surface phonon polaritons play a critical role. Ad-

ditional opportunities come from considering the near- and far-field optical properties of periodically structured layers involving hBN and other materials such as graphene [292]. An important avenue of future study would be the *ab initio* calculation of lifetimes of 2D LO phonons associated with three-phonon processes [78, 286] and electron-phonon interactions [195, 287, 293]. In further work, it would be of great interest to study the effects of isotopic purification and cryogenic temperatures on reducing the decay rate of these 2D LO phonons [276].

3.4 Experimental observations of 2D phonon polaritons

Scattering near-field optical microscopy. In parallel to the theoretical work reported here, the group of Dmitri Basov at Columbia had performed scattering near-field optical microscope measurements of the dispersion relation of phonon polaritons in monolayer (2D) as well as bilayer (2.5D) hexagonal boron nitride. We worked with them to explain these results in the context of the theory. In Fig. 4, we present those results. The inferred dispersion of the phonon polaritons is displayed in Fig. 4 where we plot frequency ω vs. the confinement factor $\lambda_0/\lambda = k/k_0$. Fig. 4b shows the results for a bilayer (triangles) and Fig. 4c for a monolayer (dots). In both cases, the confinement factor k/k_0 can approach or exceed 60. Accordingly, the mode volume $\lambda^3/2\pi$ of polaritons is reduced compared to the mode volume λ_0^3 of free-space photons by a factor up to 10^6.

Electron energy loss spectroscopy. Since then, other groups have also measured phonon polaritons in monolayer hexagonal boron nitride, providing further tests of the theoretical framework advanced here. One particularly notable recent example was published in 2021 [294], where the highly-confined portion of the dispersion relation was measured. As discussed in the discussion of Fig. 2, the use of scanning near-field optical microscopy is limited to probing relatively longer wavelengths of polaritons (currently $>$ 50 nm, which is set by the tip radius, which dictates the magnitude of evanescent coupling to the polariton near-field). As per Fig. 2, the parts of the dispersion probably by SNOM correspond to points with relatively low propagation quality factors, as consistent with Fig. 4. However, as mentioned above, a near-field probe such as a free-electron can be sensitive to

the high-momentum sector of the dispersion. This is precisely what the 2021 paper did: they measured electron-energy loss of low-energy electrons that pass through suspended monolayers of BN, losing energy by emission of 2D phonon polaritons. They found that the monolayer polaritons indeed support extremely confined excitations (with wavelengths approaching 10 nm): further, the EELS spectra they measure could be well-accounted for by the conductivity of Eq. 10.

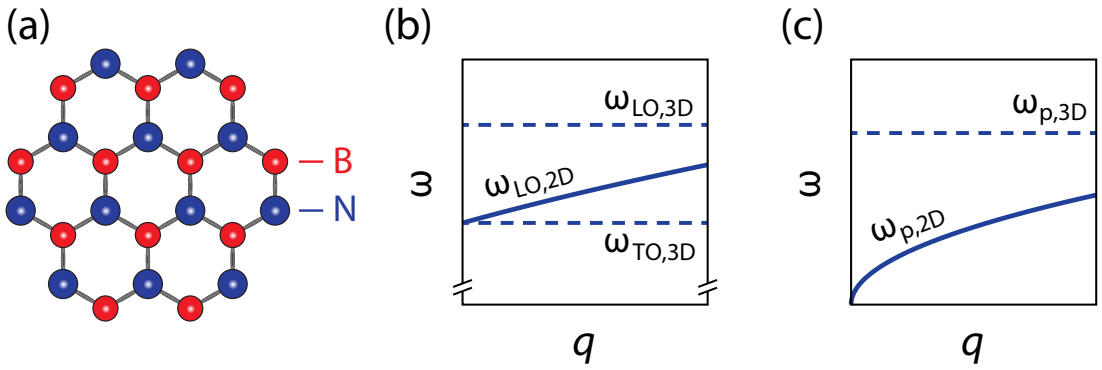

Figure 3-1: **LO phonons as the basic electromagnetic waves of a polar monolayer.** (a) Schematic structure of a polar monolayer such as hexagonal boron nitride. (b) Properties of LO and TO phonons in 3D and 2D. In 3D, there is a finite LO–TO splitting at zero wavevector, while in 2D there is none. Despite this, the 2D LO phonon plays the role of the phonon polariton in 3D and thin films. (c) Analogous physics appears in electron gases in 3D and 2D, where the 3D plasma frequency is similar to the 3D LO–TO splitting. In 2D, the plasma frequency at zero wavevector is zero, but the electromagnetic physics is determined by the dispersion of 2D plasmons, which replace the plasmon polariton of bulk and thin films.

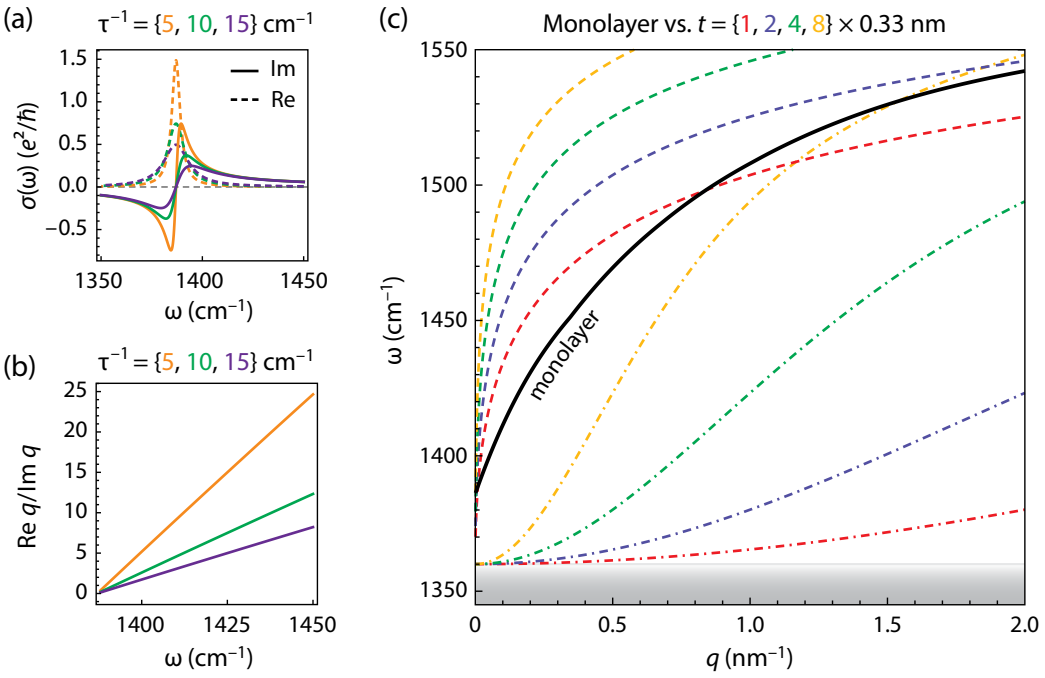

Figure 3-2: **Properties of phonon polaritons in a monolayer of hBN compared to bulk.** (a) Real and imaginary parts of the conductivity of 2D hBN for different values of the loss-rate. (b) Propagation quality factor, which measures the number of wavelengths of propagation of the 2D phonon polariton. (c) Dispersion relation of phonon polaritons in the monolayer (black) and thin films whose thicknesses are taken to be 1, 2, 4, and 8 interlayer spacings in hBN. For the thin-film, the fundamental mode (dashed) and the first higher-order mode (dash-dotted) are plotted.

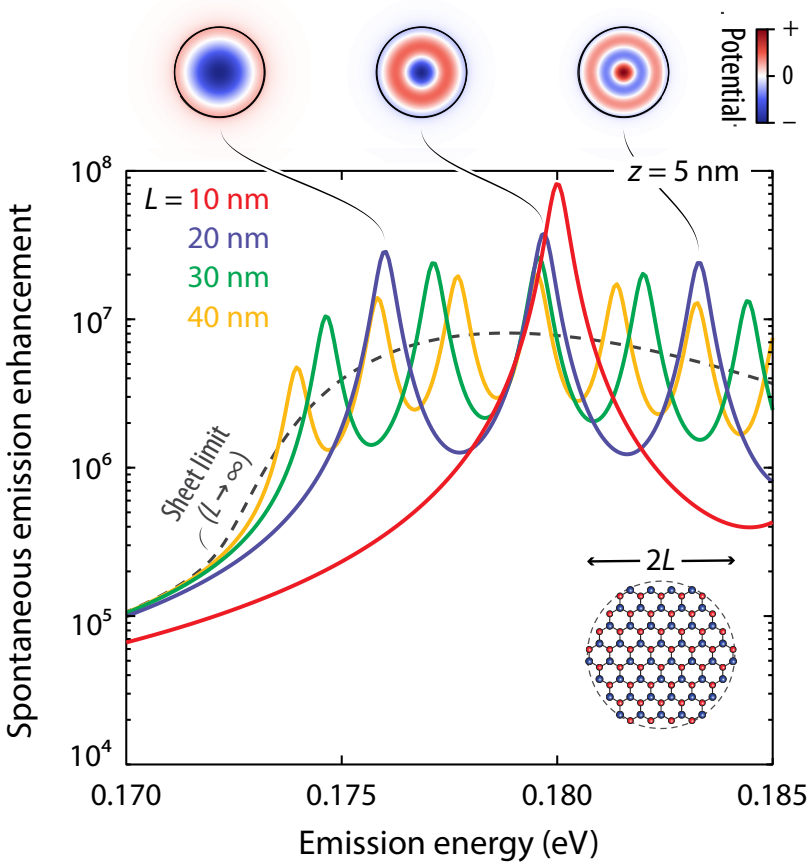

Figure 3-3: **Extreme spontaneous emission enhancement due to 2D phonon polaritons in nanostructured geometries.** Plotted is the enhancement of the spontaneous emission rate for an emitter $z = 5\,\mathrm{nm}$ above the disk's center and oriented normal to its plane ($\hat{\mathbf{n}} = \hat{\mathbf{z}}$). For a disk with a diameter of 20 nm, and assuming a relaxation rate $\tau^{-1} = 0.5\,\mathrm{meV}$, the rate of emission enhancement can be enhanced 100 million-fold. For an emitter with a free-space decay rate of $1 \times 10^6\,\mathrm{cm}^{-1}$ at 7 μm, the emitter would experience a decay rate comparable to the frequency of the disk mode, leading to ultra-strong coupling of an external emitter with 2D phonon polaritons. For reference, we compare the spontaneous emission enhancement in a nanodisk geometry to that of a disk of infinite radius (i.e., a flat sheet), showing clear enhancement relative to the flat sheet due to concentration of local density of states around phonon polariton resonances. Note that $\tau^{-1} = 0.5\,\mathrm{meV}$ is of the order of the loss rate in bulk hBN. Also shown in the figure are maps of the electric potential on the surface of the disk for modes corresponding to selected phonon polariton resonances in the plot.

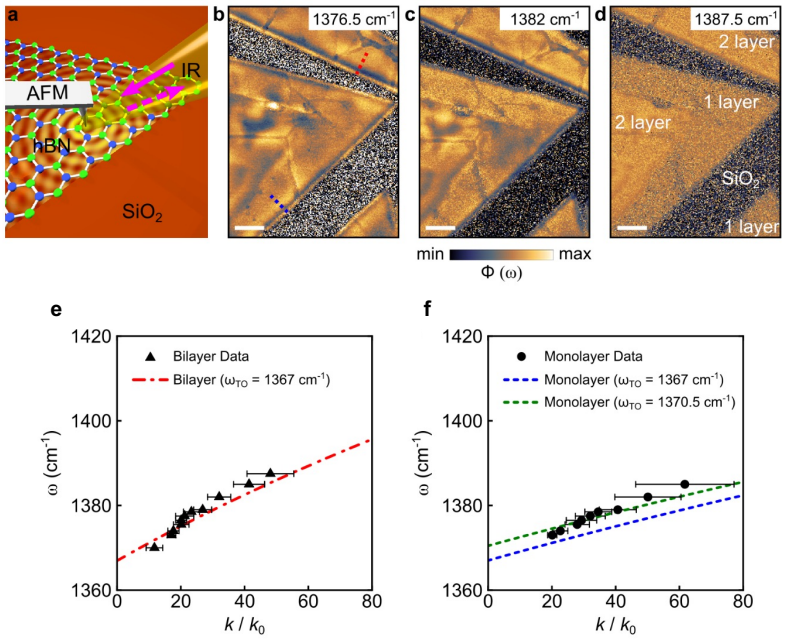

Figure 3-4: **Measurement of 2D phonon polariton dispersion relation by scanning near-field optical microscopy.** (a) Experiment setup. The AFM tip and hBN sample are illuminated by the IR beam (solid magenta arrow) from a quantum cascade laser. Propagating surface phonon polariton waves are launched and detected by the AFM tip (dotted magenta arrow). (b-d) s-SNOM phase images of surface phonon polaritons in monolayer and bilayer hBN at IR frequency ω = 1376.5, 1382 and 1387.5 cm^{-1}. Scale bar: 500 nm. (e,f) Dispersion of surface phonon polaritons in monolayer and bilayer hBN. e), Frequency (ω) – momentum (k / k0) dispersion of surface phonon polaritons in bilayer hBN. f), Frequency (ω) – momentum (k / k0) dispersion of surface phonon polaritons in monolayer hBN. Experimental data (dots for monolayer and triangles for bilayer) are extracted from s-SNOM images in Figure 1. Theoretical results are indicated with blue (ω_{TO} = 1367 $^{-1}$) and green (ω_{TO} = 1370.5 cm^{-1}) dashed curves for monolayer hBN and red (ω_{TO} = 1367 cm^{-1}) dashed-dotted curve for bilayer hBN. Image modified based on Dai, Fang, Rivera, et. al.

Chapter 4

Light emission based on nanophotonic vacuum forces

Note: This chapter is heavily based off "Light emission based on nanophotonic vacuum forces" by N. Rivera et al. Nature Physics (2019).

The vanishingly small response of matter to light above ultraviolet frequencies makes the manipulation of light emission at such frequencies challenging. As a result, state-of-the art sources of high-frequency light are typically active, relying on strong external electromagnetic fields. Here, we present a fundamental mechanism of light emission that is fully passive, relying instead on vacuum fluctuations near nanophotonic structures. This mechanism can be used to generate light at any frequency, including high-frequency radiation such as X-rays. The proposed mechanism is equivalent to a quantum optical two-photon process, in which a free electron spontaneously emits a low-energy polariton and a high-energy photon simultaneously. Although two-photon processes are nominally weak, we find that the resulting X-ray radiation can be significant. The strength of this process is related to the strong Casimir-Polder forces that atoms experience in the nanometer vicinity of materials, with the essential difference that the fluctuating force here acts on a free electron, rather than a neutral, polarizable atom. The light emission can be shaped by controlling the nanophotonic geometry or the underlying material electromagnetic response at optical or infrared frequencies. Our results reveal ways of applying the tools of nanophotonics even at

frequencies where materials have an insubstantial electromagnetic response. The process we study, when scaled up, may also enable new concepts for compact and tunable X-ray radiation.

Since the early days of quantum mechanics, quantum vacuum fluctuations have been a constant source of fascination. The non-zero energy density of the vacuum gives rise to a wide variety of important physical effects that continue to be subjects of intense theoretical and experimental research. In the case of the quantized electromagnetic field, key examples of these effects include spontaneous emission [3], Lamb shifts [256], Casimir (-Polder) and van der Waals forces [295, 296, 297], quantum friction [298], the dynamical Casimir effect [299, 300], and the Unruh effect [301, 302, 303].

A paradigm that has taken hold in recent years is control over these vacuum effects by either nano-structuring of the electromagnetic modes of optical materials [49] or using nano-confined electromagnetic modes in materials with negative permittivity or permeability [5, 6]. This paradigm works because the electromagnetic modes control the spatial and spectral properties of the electromagnetic vacuum. A well-studied example of these concepts is the Purcell effect [128], in which the modification of the local density of states of the electromagnetic field alters light emission by stationary or moving atoms [112, 113] and free electrons [180, 27, 186, 212, 126]. Another example would be the control of Casimir forces and related phenomena, such as near-field radiative heat transfer, which are attributed to fluctuating electromagnetic fields near optical materials. These effects are very strong when two optical materials are a few nanometers away from each other, due to the very large field fluctuations associated with the nanoscale. The large field fluctuations motivate the strong theoretical [304, 305, 306, 307, 308] and experimental [297, 309, 310, 311] push to observe these effects using nanoscale gaps between materials.

Controlling the electromagnetic vacuum ceases to be simple at high frequencies, typically beyond UV [312]. This is a direct consequence of the fact that in almost all known materials, the permittivity approaches that of vacuum at high frequency. As a result, the generation of high-frequency radiation (hard UV through gamma-rays) from emitters relies on the presence of static or dynamic *external fields*, as in inverse Compton scattering, and light-generation processes used in free-electron lasers, synchrotrons and laser undula-

tors [313, 314, 315, 213, 214]. Alternatively, the radiation can come from the weak dielectric response of materials at very high frequencies, as in parametric X-ray generation [316]. The very weak material response at very high frequencies seems to preclude using ideas from nanophotonics and materials physics to influence high-frequency radiation.

Here, we show how vacuum fluctuations at IR-visible frequencies near and inside nanophotonic materials can be used as a means of controlling light emission at very high frequencies, such as X-rays. The mechanism that we propose to exert such control are two-quantum processes involving the spontaneous emission of a photon and a polariton by an energetic free electron (see Fig. 1). Although two-quantum (spontaneous) emission processes are second-order processes in quantum electrodynamics (QED) and are thus considered very weak, the large strength of vacuum forces in the nanoscale vicinity of materials nevertheless leads to a strong per-electron power emitted into high-frequency radiation. In fact, we find that the radiated power is comparable with that emitted by an equal-energy electron moving in an externally applied magnetic field on the order of 1 Tesla. Due to the high spatial confinement of the emitted polariton, the intensity of the emitted light is significant at substantially higher frequencies than in many known light sources, even when modest electron energies are used in our scheme.

For example, in comparison with current X-ray free electron lasers and synchrotrons which utilize GeV-energy electrons to produce few-keV X-rays, X-ray output of 5 keV can be achieved with electron kinetic energies of about 5 MeV and gamma-ray output of 50 MeV can be achieved with electron kinetic energies of around 500 MeV. The emission is broadband, potentially enabling applications in probing physics from UV to hard X-rays (for few-MeV electrons attainable with a table-top RF gun) and gamma-rays (with further electron acceleration). In spite of the output being at such high frequencies, the spatial and temporal properties of the emitted photons can be tailored by controlling the material permittivity at IR frequencies. We illustrate these concepts in tunable nanophotonic materials of current interest such as graphene, a dynamically tunable plasmonic material known to support highly confined and low-loss plasmons at infrared frequencies [38, 8, 9, 11, 12]. Our results may be enabling concepts for novel passive and compact sources of tunable radiation from nanometer to femtometer wavelengths. Our results also suggest a novel

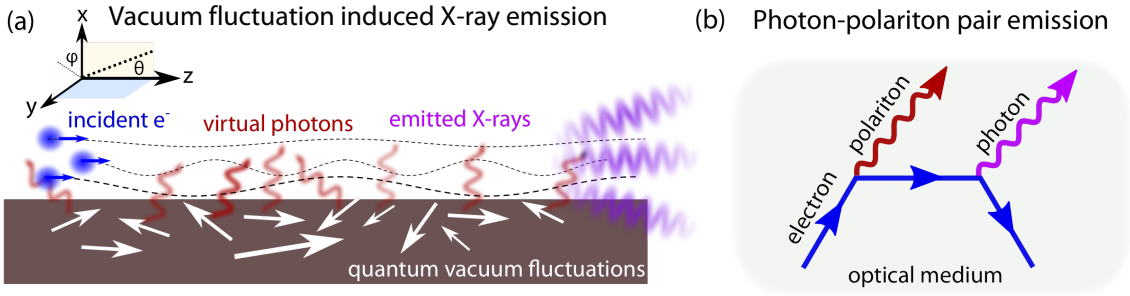

Figure 4-1: **Light emission induced by nanophotonic vacuum fluctuations and spontaneous emission of a photon-polariton pair** (a) Schematic diagram illustrating a beam of electrons traveling in the near-field of a nanophotonic structure. The vacuum fields lead to random modulations of the trajectory with a non-zero variance. These modulations lead in turn to a Doppler shift of the vacuum fluctuations into a higher frequency in the electron's rest frame, resulting in photon output at even higher frequencies. The ratio of the output photon frequency to polariton frequency scales as $\left(\frac{E}{mc^2}\right)^2$, where E is the energy of the electron, resulting in enormous frequency up-conversion factors for relativistic electrons. (b) The complementary description in QED: a second-order two-quantum (spontaneous) emission process involving a mode of the structure (denoted polariton) and a high energy photon.

"nonlinearity" mediated by relativistic electrons that couples "low-frequency" (IR or optical) fields to "high frequency" (UV, X-ray or gamma-ray) fields despite the well-known lack of electromagnetic response at such high frequencies. Our findings may also yield a new way to study the quantized electromagnetic vacuum: through high frequency light emitted into the far field by a relativistic probe.

4.1 Spontaneous emission of a photon-polariton pair by a free electron

Consider a beam of electrons traveling over a photonic structure that permits strong coupling of light and material polarization (Fig. 1a). Examples of such a structure include all-dielectric nanostructures or materials with resonances associated with plasmon-, phonon-, exciton- or magnon-polaritons. For brevity, we will refer to any mode arising from non-trivial optical response as a polariton mode, even those in all-dielectric structures, as the non-trivial optical response is concomitant with strong coupling between light and mate-

rial polarization. The electrons are affected by electromagnetic field fluctuations that arise from the quantum fluctuations of polarization currents inside the material. Although this fluctuating field has zero mean, it has a non-zero variance that leads to the possibility of far-field photon emission by the electron through spontaneous emission. In this spontaneous emission process, a far-field photon and a photonic mode of the nanostructure (a polariton mode) are simultaneously emitted. We henceforth refer to this two-quantum emission as a photon-polariton pair emission. The probability of two-quantum emission processes scale as the square of the fine-structure constant ($\alpha \approx 1/137$), which led to a long delay between prediction and the first direct observation in the specific case of two-photon emission from atoms [255, 268]. However, two-quantum emission can be strongly enhanced by nearby polaritonic media in atomic or low-energy emitters based on bound charges, making these two-polariton emission processes strong or potentially even dominant [261, 140, 105, 109] over single-photon decay channels. Very interestingly, two-photon emission by *free electrons* was suggested by luminaries such as Ilya Frank in his 1958 Nobel Lecture on the Cerenkov effect [260], and was considered as a second-order Cherenkov effect [317, 318].

Fig. 1 summarizes the discussion above by illustrating the two complementary paradigms that can be used to explain the phenomena we study here. The first is the fluctuational electrodynamics paradigm (Fig. 1a) where a free electron radiates as a result of interactions with fluctuations in a nanophotonic vacuum (derived and applied in App. E (referred to as SI) Sections 3 and 4). The second is the quantum electrodynamics paradigm (Fig. 1b), which describes the radiation as part of a second-order quantum process in which a relativistic electron spontaneously emits one photon and one polariton (derived in SI Section 5 via both scalar and Dirac QED, which agree excellently for electron energies below 1 GeV). We show that the quantum electrodynamics approach leads to the same results.

4.2 Methods

In this section, we present a basic overview of the fluctuational electrodynamics formalism used to calculate the spectrum of photon-polariton pair emission. Further details are provided in Sections 3 and 4 of the SI. We emphasize that this formalism, for parameters

considered in the main text, gives precisely the same result as a calculation based on the direct calculation of the emission based on second-order time-dependent perturbation theory (shown in SI Section 5).

From the point of view of fluctuational electrodynamics, it is sufficient here to consider a classical electron traveling initially in a straight line with velocity $\mathbf{v} = c\boldsymbol{\beta}$ and position $\mathbf{r}(t) = \mathbf{r}_0 + \mathbf{v}t$, with $\mathbf{r}_0$ being the position taken at an arbitrarily chosen origin of time $t = 0$, and c is the speed of light. In the presence of an external modulating electric field, this electron will experience an acceleration that leads to subsequent radiation, as prescribed by the Lienard-Wiechert potentials, the essential aspects of which are summarized in the SI. The radiated energy is quadratic in the modulating field. In the spirit of the discussion of Fig. 1a, we identify the modulating field with that associated with the quantum fluctuations of the nanophotonic vacuum at thermal equilibrium. The average power radiated by the electron is governed by the correlation function between different components of the fluctuating electric field at different positions and different times. This correlation function is $\langle E_i(\mathbf{r}, t)E_j(\mathbf{r}', t')\rangle$, where $\mathbf{r}$ and $\mathbf{r}'$ are different points in space, t and t' are different points in time, E_i is the ith component of the quantized electric field operator, and $\langle\rangle$ denotes an ensemble average assuming thermal equilibrium. From the quantum theory of the macroscopic electromagnetic field in an arbitrary dielectric medium, $\langle E_i(\mathbf{r}, t)E_j(\mathbf{r}', t')\rangle$, at zero temperature, is given by [319, 320, 25]:

$$\frac{\hbar}{\pi\epsilon_0 c^2}\int_0^\infty d\omega\ \omega^2 \mathrm{Im}\ G_{ij}(\mathbf{r}(t), \mathbf{r}(t'), \omega)e^{-i\omega(t-t')}, \tag{4.1}$$

with ϵ_0 the permittivity of free space, and $\hbar$ the reduced Planck constant. The non-zero temperature generalization is presented in App. C (referred to as SI). In this equation, the integration variable ω can be interpreted as the angular frequency of a polariton in the nanophotonic structure. In practice, the integral in Eq. (3) is well-approximated by restricting the range of integration to the set of frequencies where the local density of states of the polaritons are high. G_{ij} is the dyadic Green's function of the nanophotonic structure and is dependent on material resonances and material geometry.

To find the energy radiated per unit photon frequency ω' and photon solid angle Ω into

the far-field, $dU/d\omega' d\Omega$, we take the an ensemble average of the radiated power over realizations of the modulating field, thus plugging in Equation (3) for the ensemble averaged modulating field (a detailed derivation is given in SI Section 3). The result of this fluctuational electrodynamics calculation, at zero temperature, is:

$$\frac{dU}{d\omega' d\Omega} = \frac{e^4\hbar}{16\pi^4\epsilon_0^2 m^2 c^5 \gamma^2 (1-\beta\cos\theta)^4} \times \int_{-\infty}^{\infty} dt dt' \int_0^{\infty} d\omega\, \omega^2 \mathrm{Im}\left[e^{-i(\omega+\omega')(1-\beta\cos\theta)(t-t')} \mathrm{tr}\left[\mathbf{T}\mathbf{G}(\mathbf{r}(t),\mathbf{r}(t'),\omega)\mathbf{T}^{\mathrm{T}}\right]\right], \quad (4.2)$$

where $\gamma = (1-\beta^2)^{-1/2}$ is the electron Lorentz factor, θ is the angle of the emitted photon with respect to the direction of electron motion, and t and t' are times which are integrated over the electron's unperturbed linear trajectory. Additionally, we have defined the matrix $\mathbf{T}$, whose components $T_{ij} \equiv (\beta\cos\theta - 1)\delta_{ij} - (\hat{n}_i - \beta_i)\hat{n}_j$, with δ_{ij} a Kronecker delta, $\hat{n}$ a unit vector along the direction of photon emission, and $\mathbf{E}_\gamma = \left(\mathbf{E}_\perp, \frac{E_{||}}{\gamma^2}\right)$ where $\perp$ ($||$) denote directions perpendicular (parallel) to $\mathbf{v}$. The only assumptions made in writing Equation (4) are that the deviations of the electron motion from a straight-line trajectory are fairly small, and that the fluctuating fields are quasi-electrostatic in nature, meaning that effects of the magnetic fields are negligible compared to those of the electric fields, which holds for highly-confined near-fields associated with polaritons in dielectrics and conductors. We note that the assumption of zero-temperature is well-respected even at room temperature, as for the infrared polariton frequencies we consider here, $\frac{kT}{\hbar\omega} \ll 1$. However, at higher temperatures, the emission will be enhanced due to contributions from thermal near-field fluctuations. Equation (4) is the main formal result of this work, and it is applied in the main text. Before doing so, we briefly comment that in the fluctuational electrodynamics paradigm, the effect we describe can be phrased as follows: fluctuating polarization currents in a medium lead to fluctuating acceleration and thus fluctuating dipole moments of an electron, leading to subsequent high-frequency radiation, due to the relativistic speed of the electron. In these terms, the physics is like that of the general Casimir-Polder effect (which has the van der Waals force as its near-field limit), where vacuum fluctuations lead to a force on a bound electron in an atom or molecule. Unlike other often considered

Casimir phenomena, this vacuum force acts on a relativistic free electron and oscillates it, leading to the radiation emission.

4.3 Impact of nano-confinement of polaritons on the emission spectrum

We find that in photon-polariton pair emission by an electron with speed $v = c\beta$ moving along direction $\hat{v}$, the photon and polariton are kinematically related (see SI Section 4). In particular, a photon emitted of frequency ω' along direction $\hat{n}$ is kinematically related to a polariton emitted of frequency ω_q in direction $\hat{q}$ by

$$\omega' = \omega_q \frac{\beta n(\omega_q) \cos\theta_q - 1}{1 - \beta \cos\theta}, \tag{4.3}$$

where $n(\omega_q) = \frac{qc}{\omega_q}$ is the effective mode index of the polariton (with q the magnitude of the polariton wavevector), $\cos\theta_q = \hat{q} \cdot \hat{v}$, and $\cos\theta = \hat{n} \cdot \hat{v}$. Equation (1) reveals two ways by which the photon frequency can be greatly enhanced. The first way to enhance the photon frequency is by minimizing the denominator, which is achieved by using high-energy electrons and collecting photons emitted in the direction of electron motion ($\theta = 0$), as can be seen by the fact that $(1 - \beta\cos\theta)^{-1} \approx 2\gamma^2$ when $\theta = 0$ and $\beta \approx 1$. The second way to enhance the photon frequency is by making use of an optical medium which supports polariton modes of simultaneously high wavevector and high effective mode indices.

The numerator in Eq. (1) reveals a fundamental difference between the process studied here and a potential process in which a photon is emitted and a polariton is absorbed. In this latter case, the numerator of Eq. (1) would change to $vq_{||} + \omega$ (see SI Section 4), implying that strong enhancement of radiated frequency can occur even when $q_{||} = 0$. For a photon-polariton pair emission process, emission is kinematically forbidden for $q_{||} < \frac{\omega}{v}$. This implies that high frequency modes are not necessarily associated with the generation of high-frequency photons in photon-polariton pair emission. Instead, high mode indices are necessary.

The importance of high mode indices to generating high-frequency photons is summa-

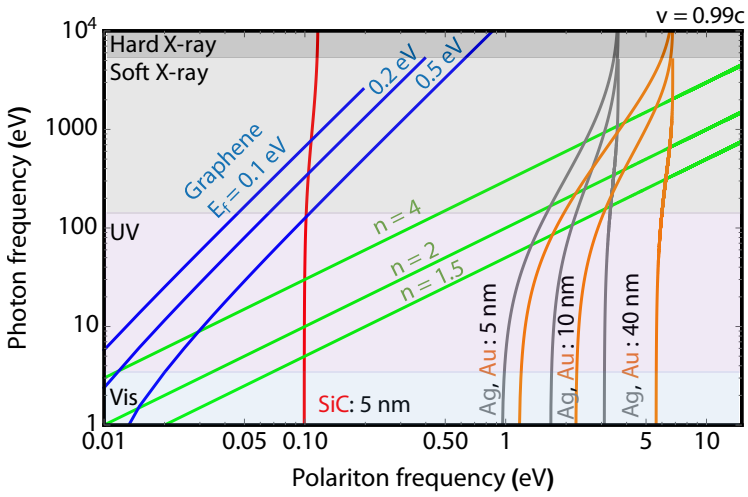

Figure 4-2: **Influence of optical materials on the photon emission spectrum in photon-polariton pair emission.** Radiated photon frequency of Equation (1) for photons emitted along θ = 0, and polaritons emitted along $\theta_q = 0$ (both emitted forward). The photon frequency is shown as a function of polariton frequencies for plasmons in (Drude) gold and silver with different thicknesses, (Drude) graphene with different doping levels, and phonon polaritons in silicon carbide. Also shown are contours corresponding to a constant index of refraction of 1.5, 2, and 4. Despite the very different frequencies of plasmons in graphene, phonon polaritons in silicon carbide, and plasmons in silver and gold, all of these materials are capable of being used for generation of hard X-ray photons.

rized in Fig. 2, where we plot the relationship between the emitted photon frequency and the emitted polariton frequency for different optical materials, in the scenario where both the polariton and photon are emitted in the forward direction by an electron moving at a speed of $0.99c$. We consider plasmonic thin films of gold and silver of varying thickness, 2D plasmonic materials such as graphene, with varying levels of doping, and thin films of phonon polaritonic materials like silicon carbide. As can be seen from Fig. 2, despite the widely different frequencies of the emitted polaritons in these widely different materials, the emitted photons can be at hard X-ray frequencies (frequencies in excess of 5 keV). To summarize this figure: high mode momentum (as long as it comes with a high mode index), leads to high frequency photons.

To highlight further the interplay of electron velocity and polariton mode index on the output photon frequency, we present another example. For graphene, with Fermi energy 0.5 eV, the forward emission of a plasmon of 0.5 eV frequency will be concomitant with

the forward emission of a photon of frequency 110 eV for an electron with velocity $0.7c$ (as from a transmission electron microscope), a photon of frequency 6.7 keV for an electron with velocity $0.995c$ (as from a radio frequency gun), and a photon of frequency 675 keV for an electron with velocity $0.99995c$ (from a linear accelerator). Meanwhile, if the plasmon is replaced by a polariton of frequency 100 eV, but a mode index of 1.01, then for an electron of velocity $0.7c$, it is kinematically forbidden to emit a photon. For an electron of velocity $0.995c$, the outgoing photon has a frequency of 0.099 keV, and for an electron of velocity $0.99995c$, the outgoing photon has a frequency of 20 keV.

4.4 Strong, broadband high-frequency radiation from vacuum fluctuations

Having discussed the kinematics of photon-polariton pair emission, we now move to analyze the angular and frequency correlations of the emitted photon-polariton pairs, as well as the overall strength of the process. To make the discussion concrete, we consider this process when the emitted polariton is a plasmon in graphene, a dynamically tunable plasmonic material known to support plasmons that simultaneously have high mode index, and low-enough losses to be well-defined excitations. Graphene is a very attractive platform for realizing the effect we describe in the manuscript. Besides having highly confined plasmons which propagate for reasonably long distances, it is also tunable, it has a very high surface-to-bulk ratio, and can be produced in suspended form, allowing minimization of background effects. That said, we show (in Figure 4 of SI) that other materials, such as thin films of gold, can give effects of a similar magnitude, as could be anticipated from the utility of conventional plasmonic materials in fields such as near-field radiative heat transfer. The low damping also could allow the intriguing possibility that the emitted polariton could re-interact with the electron beam and lead to feedback and radiation enhancement.

In particular, we consider the photon-polariton pair emission process for a fast electron moving parallel to a sheet of doped graphene, a distance x_0 away from the surface of the graphene. We consider the graphene to be free-standing, although the conclusions of Figs.

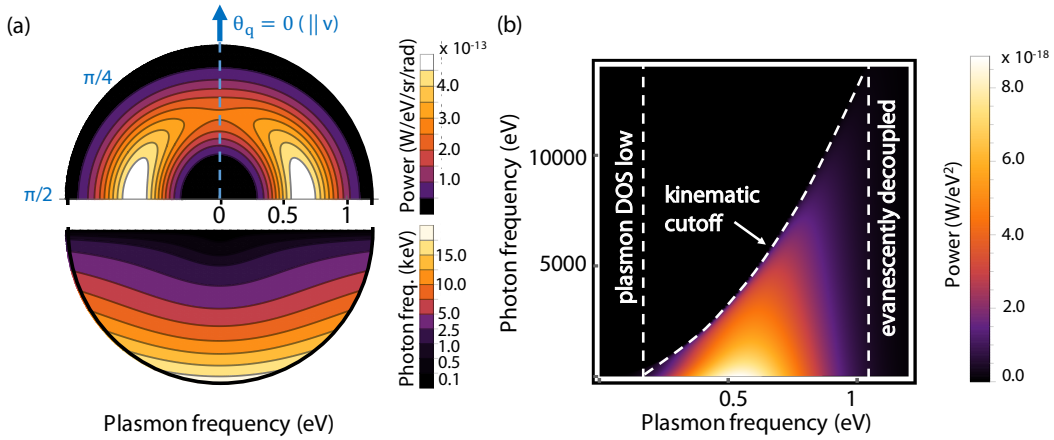

Figure 4-3: **Correlations between emitted infrared polaritons and emitted X-ray photons in photon-polariton pair emission.** (a, top half) Polar plot of emitted photon power in photon-polariton pair emission, when the polariton is a plasmon in doped graphene. The power is per unit plasmon frequency, per unit plasmon angle, and per unit photon angle for forward photon emission $\theta = 0$, plotted as a function of plasmon frequency (radial direction) and plasmon angle (angular direction). A preference exists for plasmons emitted perpendicular to the direction of electron motion due to polarization effects. (a, bottom half) Corresponding frequencies for the forward-emitted photon as a function of plasmon energy and angle. (b) Emitted photon power per unit photon frequency and plasmon frequency, which show a clear correlation between plasmon and photon frequencies. The photon emission is synchrotron-like, extending from UV to X-ray frequencies, having maximum contribution from plasmon frequencies where the local density of states is highest. The electron is taken to have a velocity of $0.99c$, and travels a distance $x_0 = 5$ nm away from the surface of the graphene sheet, which is doped to a Fermi energy of 0.5 eV.

3 and 4 are not qualitatively changed when a transparent substrate is introduced. Note that for simple exposition, we model graphene via a Drude model with an infinite Drude relaxation time. A realistic Drude relaxation time has little effect on the emitted power (see Supplementary Figure 2). We also consider the influence of interband transitions modeled through the local and nonlocal RPA conductivity. The output power in those cases remains similar to the Drude case.

4.4.1 Spectral and angular correlations between the emitted photon and polariton

In photon-polariton pair emission, the fast electron spontaneously emits a photon and a plasmon-polariton, whose spatial and spectral distributions are shown in Fig. 3. In Fig.

3a (upper half-circle), we show the radiated photon energy per unit time (photon power) per unit plasmon frequency, plasmon angle, and photon angle, with fixed photon angle ($\theta = 0$). The electron is taken to have a velocity of $0.99c$. Integrating over these variables gives the total emitted power. The (polar) plot shows this differential power as a function of the plasmon frequency ω_q (radial direction) and plasmon angle θ_q (angular direction). We represent the spectrum this way to show how the emission intensity depends on the kinematical properties of the individual photon-plasmon pairs.

Fig. 3a highlights two main features of photon-polariton pair emission. For one, the plasmons are preferentially emitted into the graphene sheet in a direction perpendicular to the direction of electron motion. This results from the polarization of a highly confined plasmon, which is half in the direction of plasmon propagation, and half perpendicular to the graphene sheet. For a plasmon emitted parallel to the direction of electron motion, half of the plasmon polarization is in the direction of electron motion, which for relativistic electrons, has very little impact on the modulation of the electron trajectory. This component is thus incapable of modulating the electron trajectory and makes little contribution to the emitted power. Meanwhile, for a plasmon emitted perpendicular to the electron motion, every component of the polarization is transverse to the electron's unperturbed trajectory, and thus effectively modulates the trajectory. The second feature is that very little photon emission corresponds to emission of plasmons of frequency less than 0.25 eV or more than 1 eV. The lack of low-frequency plasmons results from the low density of states of the plasmons at low frequency. The lack of high-frequency plasmons results from the fact that their evanescent tails become substantially smaller than x_0, rendering the electron insensitive to those plasmon modes. The lower half-circle shows the photon frequencies which correspond to a particular plasmon angle and plasmon frequency. We see clearly that the emission of plasmons at perpendicular angles corresponds to low photon energies, which follows from Equation (1). As a result of the continuum of plasmon angles and energies in the sheet geometry, the photon emission is quite broadband, spanning from the soft UV to hard X-ray frequencies, similar to synchrotron light.

In Fig. 3b, we elaborate further on the correlated nature of the photon-polariton pair emission by showing the photon power emitted per unit plasmon frequency and photon

frequency, which represents the spectral intensity of plasmon-photon correlations. Integrating over these variables gives the total emitted power. From Fig. 3b, we notice first that the emission of a plasmon with frequencies between 0 and 1 eV is correlated with photon emission from 0 to nearly 10 keV. Higher frequency photons are correlated with higher frequency plasmons, as expected from Equation (1). For a photon of any frequency, it is most correlated with a plasmon which both has a substantial density of states, but is also not evanescently decoupled from the electron, which in the case of Fig. 3b, occurs for plasmons of frequency around 0.5 eV.

For any plasmon frequency, photons have a slight preference to be emitted at lower frequencies (most of the emission is nevertheless in between 1 and 5 keV). This can be understood from the fact that plasmons are preferentially emitted near $\theta_q = \pi/2$, as shown in Fig. 3a. Fig. S1 of the SI shows the same overall phenomena as in Fig. 3 but for different Fermi energy in graphene (and different x_0), which results in a different plasmon dispersion and thus a change in the angular and spectral properties of the emission. This shows that the emitted X-rays can be tuned by changing the modal properties of photons in the IR, whether it be the dispersion relation or polarization properties.

4.4.2 Total radiated power in photon-polariton pair emission

We now evaluate the total power emitted in photon-polariton pair emission. A key result is the total emitted power integrated over all photon and plasmon properties, plotted in Fig. 4a as a function of electron energy and distance between the electron and the surface. The emitted power increases sharply with increasing electron energy (as γ^2) and decreasing distance to the surface (as $x_0^{-7/2}$). This $x_0^{-7/2}$ dependence arises from the Drude model in the quasi-electrostatic limit, and breaks down for distances on the order below 1 nm, when quantum nonlocality becomes significant, and also at distance above about a micron, where retardation becomes signficant. In particular, the expectation value of the squared electric field operator associated with Drude plasmons is given by $\int \frac{dq}{2\pi} \frac{\hbar\omega_{\mathbf{q}} q^2}{2\epsilon_0} e^{-2qx_0} \sim x_0^{-7/2}$ for $\omega_q \sim \sqrt{q}$. Consider a scenario in which a 500 MeV electron travels within 5 nm from the surface of graphene doped to Fermi energy 0.5 eV. The power emitted in the photon

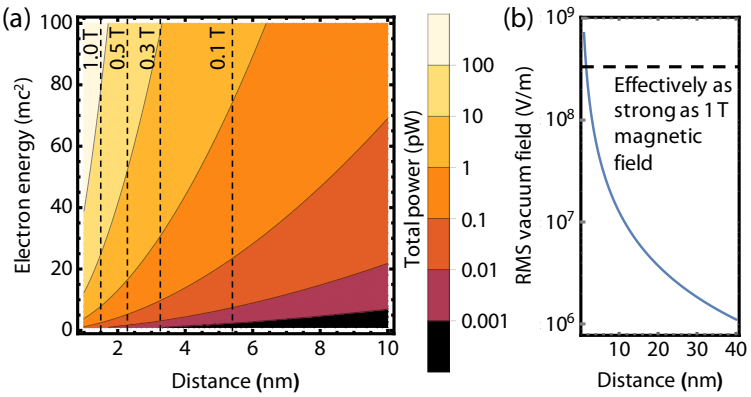

Figure 4-4: **Total emitted power due to nanoplasmonic vacuum fluctuations.** (a) Total photon power as a function of electron energy (in units of the rest mass energy) and distance to a graphene sheet. Vertical dashed lines correspond synchrotron radiation power for different values of a hypothetical driving magnetic field. (b) Dependence of the root-mean-square of the graphene-plasmon contribution to the quantized electric field as a function of the distance to the surface of a sheet of graphene doped to a Fermi energy of 0.5 eV.

component of photon-polariton pair emission is about 1.3 nW. As a point of comparison, we also consider a scenario in which an 500 MeV electron emits synchrotron radiation as a result of traveling in a circular orbit in a 1 T magnetic field. The power emitted via synchrotron radiation is about 15 nW. The closeness of these two powers is a surprising observation given that in the former scenario, vacuum fluctuations drive the radiation, whereas in the latter scenario, a strong applied magnetic field drives the radiation. This finding applies at any electron energy since the emitted powers of photon-polariton pair emission and synchrotron radiation both scale in the same manner with electron energy (as γ^2). We encourage the reader to see SI Section 2 to see more details about the characteristic photon emission rates, methods to scale up the output brightness, and comparison to other miniaturized light sources. Regarding other miniaturized light sources, particularly based on strongly pumping a near-field of a photonic structure, we found that the photon-polariton pair emission, although passive, can lead to as much integrated power as in the situation in which the electron radiates as a result of scattering from an externally pumped near-field containing thousands of quanta.

We now quantitatively explain why the magnitude of this vacuum-induced emission process can be comparable to processes that rely on substantial external driving fields, such

as magnetic fields of 1 T. The starting point for our explanation is an analytical formula for total emitted power P that we obtain in the limit where photon-polariton pair emission is dominated by highly-confined polariton modes. In this limit, the power is given by:

$$P = \frac{e^4\gamma^2(4-\beta^2)}{24\pi\epsilon_0 m^2 c^3}\langle 0|\mathbf{E}^2|0\rangle, \tag{4.4}$$

where $\langle 0|\mathbf{E}^2|0\rangle$ is the expectation value of the quantized electric field associated with plasmonic zero-point fluctuations. Note that we calculate the fluctuations resulting from the medium and remove the contribution free space fluctuations to the squared electric field, as they give zero contribution due to energy-momentum conservation. A detailed derivation of this expression is shown in SI Section 5. Eq. (2) is simply the Larmor formula from classical electrodynamics for a charged particle of acceleration a given in this case by $a = \frac{eE_{\mathrm{RMS}}}{m\gamma}$, with the root-mean square (RMS) electric field defined by $E_{\mathrm{RMS}} \equiv \sqrt{\langle 0|\mathbf{E}^2|0\rangle}$. To see how this explains the high radiated power in photon-polariton pair emission, consider Fig. 4b, which shows the RMS plasmonic field as a function of distance from the graphene surface. The magnitude of the RMS fluctuations 5 nm from the surface is about 50 MV/m, which induces electron acceleration magnitudes that one expects to find for an electron in magnetic field of 0.2 T in a synchrotron. Similarly, the magnitude of the quantum RMS field 1 nm away from the surface is about 300 MV/m, which induces electron acceleration magnitudes that one expects to find for an electron in magnetic field of 1 T. More generally, the power radiated by an electron undergoing synchrotron radiation in a uniform magnetic field B is $P = \frac{e^4\gamma^2 B^2}{6\pi\epsilon_0 m^2 c}$, revealing that the power radiated from photon-polariton pair emission (Eq. (4)) is comparable with that from synchrotron radiation when $\sqrt{\langle \mathbf{E}^2\rangle}$ and cB in the respective processes are comparable. These examples emphasize the strong fields that arise from vacuum fluctuations, and explain the high emitted power we find in Fig. 4a.

4.5 Discussion

One potential method of experimentally demonstrating photon-polariton pair emission would be to send a beam of electrons close to a nanostructure, and at grazing incidence, in a setup capable of detecting very high-frequency radiation (e.g., with energy dispersive (EDS) X-ray detectors [321]), making sure to account for competing Bremsstrahlung by electrons that penetrate the material. Yet another meaningful experimental demonstration would use time-synchronized measurements of coincidences to measure spatiotemporal correlations between the X-ray photon and the emitted polariton. The relevant setup depends on the energy scale. For example, electrons could be accelerated to 200 keV kinetic energy in an electron microscope. MeV electron energies could be achieved by an RF gun or with potential advances in dielectric laser acceleration [238]. GeV electron energies could be achieved with a linear accelerator or potentially with plasma wakefield acceleration [322].

An alternative experimental demonstration could involve the detection – via electron energy loss spectroscopy – of anomalously high energy losses in the electrons that pass a small distance away from the surface at grazing incidence. This would require one to be able to differentiate X-ray losses from core loss transitions in the materials near the surface, which is possible due to the tunability of the photon spectrum (because the EELS peaks from photon-polariton pair emission shift by varying acceleration voltage or nanophotonic geometry as per Equation (1)). In SI Section 2, we discuss briefly methods to minimize background effects that also produce X-rays associated with electrons colliding into the sample.

The concept developed here applies to, and is enriched by, the consideration of alternative materials and structures. Examples include thin films and quasi-2D systems ("transdimensional" systems [323]) of plasmonic materials such as gold, silver, and titanium nitride [324], as well as more general polaritonic materials and metasurfaces. One can consider optimizing various radiation characteristics through optimizing the nanophotonic structure. For example, a structure that could make the radiation more monochromatic would enhance the spectral density, quality, and brightness of the X-ray source. Better monochromaticity could potentially be achieved by structuring a material into a nanograt-

ing, such that the X-ray frequency is selected by reciprocal lattice vectors of the grating. The goal of designing radiation sources through our formalism will benefit from the great computational strides that have been made in calculating fluctuation spectra near complicated arrangements and geometries of optical media [306, 308, 325]. The framework advanced here can also be extended to other charge distributions using results from classical electrodynamics to accommodate radiation from more complicated systems of charges such as moving dipoles or bunched electrons (including periodically bunched electrons which are typical in free electron laser settings). Beyond the possibilities of applying this concept to compact and tunable sources of high-frequency light, the ability to control spontaneous free-electron emission at arbitrarily high frequencies may also ultimately lead to the ability to create synthetic active "nonlinearities" at X-ray [326, 327, 328] and perhaps gamma-ray frequencies controlled by now accessible nano-patterning of photonic systems.

Chapter 5

A framework for scintillation in nanophotonics

Note: This chapter is heavily based off "A framework for scintillation in nanophotonics" by C. Roques-Carmes and N. Rivera* et al. Science (2022).*

Bombardment of materials by high-energy particles often leads to light emission in a process known as scintillation. Scintillation has widespread applications in areas such as medical imaging, x-ray non-destructive inspection, electron microscopy, and high-energy particle detectors. Most research focuses on finding new materials with brighter, faster, and more controlled scintillation. We develop an approach based on integrating nanophotonic structures into scintillators to enhance their emission. We develop a unified theory of nanophotonic scintillators that accounts for the key aspects of scintillation: energy loss by high-energy particles, and light emission by non-equilibrium electrons in nanostructured optical systems. We then demonstrate nearly an order-of-magnitude enhancement of scintillation, in both electron-induced, and x-ray-induced scintillation. Our framework should enable the development of a new class of brighter, faster, and higher-resolution scintillators with tailored and optimized performances.

Scintillation, the process by which high-energy particles (HEP, also known as ionizing radiation) bombarding a material convert their kinetic energy into light, is among the most commonly occurring phenomena in the interaction of ionizing radiation with matter.

It enables a number of technologies, including x-ray detectors used in medical imaging and non-destructive inspection, γ-ray detectors in positron-emission tomography scanners, phosphor screens in night-vision systems, electron detectors in electron microscopes, and electromagnetic calorimeters in high-energy physics experiments [329, 330]. Scintillation appears under many different guises. For example, when the "high-energy" particle is a visible or UV photon, the scintillation is better known as photoluminescence. When the incident particles are energetic electrons, scintillation is also known as incoherent cathodoluminescence. When the high-energy particle is an X- or γ-ray, the phenomenon is almost exclusively referred to as scintillation. [329].

Because of scintillation's broad applications, there is interest in the development of "better scintillators" with greater photon yields, as well as greater spatial and energy resolution. Such enhanced scintillators could translate into enhanced functionalities. One such example is in medicine: brighter and higher-resolution scintillators could enable medical imaging (e.g., computed tomography) with higher resolution and substantially lower radiation dose. Current approaches to improve scintillation are mostly oriented towards the growth of higher-quality materials (e.g., single-crystalline, controlled creation of defect sites) as well as the identification of new materials (e.g., ceramics and metal halide perovskites [331]) with faster and brighter intrinsic scintillation.

We develop a different approach to this problem, which we refer to as "nanophotonic scintillators". By patterning a scintillator on the scale of the wavelength of light, it is possible to strongly enhance, as well as control, the scintillation yield, spectrum, directivity, and polarization response. The motivation for our approach is the observation that the light emitted in scintillation is effectively spontaneous emission [332]. An enormous amount of effort in multiple fields has gone into controlling and enhancing spontaneous emission through the density of optical states [333, 334], with corresponding impact in those fields [335], including photovoltaics [336], sensing [337, 338], LEDs [339, 340], thermal emission [341], and free-electron radiation sources [342, 343, 344, 345, 346, 347, 348, 349, 350, 351]. In the context of scintillation, nanophotonic enhancements could in principle take two forms: (1) through direct enhancement of the rate of spontaneous emission by shaping the density of optical states [332]; or (2) through improved light extraction from

bulk scintillators. Early work demonstrated enhanced light extraction provided by a photonic crystal coating atop a bulk scintillator [352, 353, 354, 355, 356, 357, 358]. Nevertheless, the prospect of enhancing scintillation through the local density of states, as well as the prospect of large scintillation enhancements, by either mechanism, remains unrealized. Moreover, the type of nanophotonic structures that could even in principle realize such effects is unknown.

Part of the reason for the lack of progress in this field so far entails a theoretical gap associated with the complex, multiphysics nature of scintillation emission (Figs. 1a-d). The process of scintillation is composed of several complex parts spanning a wide range of length and energy scales [329]: (1) ionization of electrons by HEP followed by production and diffusion of secondary electrons (Fig. 1b) [359, 22]; (2) establishment of a non-equilibrium steady-state (Fig. 1c) [360, 361]; and (3) recombination, leading to light emission (Fig. 1d). The final step of light emission is particularly complex to model, especially in nanophotonic settings, as it results from fluctuating, spatially-distributed dipoles with a non-equilibrium distribution function which strongly depends on the previous steps of the scintillation process.

5.1 A general theory of nanophotonic scintillation

First, we present a unified theory of nanophotonic scintillators. The theory we develop is ab initio: it can, from first principles, predict the angle- and frequency-dependent scintillation from arbitrary scintillators (established and nascent), taking into account the three steps illustrated in Figs. 1b-d. It takes into account the energy loss dynamics of HEPs through arbitrary materials, the non-equilibrium steady state and electronic structure of the scintillating electrons, and the nanostructured optical environment (i.e., the electrodynamics of the light emission by this non-equilibrium electron distribution).

Consider the situation depicted in Fig. 1a in which a HEP beam deposits energy into a nanophotonic structure (Fig. 1b). The structure may be in proximity of a scintillating material, or integrated with it (as in both cases that we present experiments for). The interaction of the beam with the scintillating material will generally lead to a process of

electron excitation in the scintillator, followed by relaxation into an excited state (Fig. 1c).

Importantly, the occupations of electrons and holes following this relaxation are typically in an approximate equilibrium [361] (referred to as a non-equilibrium steady state). This equilibrium is well-defined since it occurs on picosecond timescales, which are effectively instantaneous compared to the excited state depletion timescales (nanoseconds) [359]. Under these assumptions, the radiative recombination may be described in terms of emission from fluctuating currents in the material, not unlike thermal radiation (in which the electrons are in a true equilibrium). The key difference from thermal radiation is that the occupation functions which determine the current-current correlations (that determine the emission) are no longer governed by the Bose-Einstein distribution, but are instead material and HEP pump-dependent (and therefore spatially dependent).

Despite the non-universality of the current-current correlations, the otherwise strong similarity to thermal radiation inspires a key simplification which also gives rise to simple and powerful numerical methods for modeling and optimizing scintillation. This key simplification is electromagnetic reciprocity, which relates the following two quantities: (1) the emitted scintillation from the structure (at a given frequency ω, direction Ω, and polarization i) and (2) the intensity of the field induced in the scintillator by sending a plane wave at it (of frequency ω, propagating along direction Ω into the structure, and polarization i). The intensity of the field induced in the structure at a given point is proportional to the local absorption, and hence we say that the "emission" (1) is related to "absorption" of a plane wave (2). As a result of this relation, it is possible to calculate the scintillation at some angle and frequency by calculating absorption of light incident from the far-field at that frequency, angle, and polarization. We note that this relation only makes use of the Lorentz reciprocity of Maxwell's equations for the nanophotonic structure, and thus makes no assumption on the electronic transitions responsible for scintillation (we assume that the non-equilibrium electrons only weakly change the material optical properties). Lorentz reciprocity can be broken in several classes of systems, e.g., magnetic, nonlinear, and time-modulated materials [**?**]. Such non-reciprocal photonic structures, which are of great recent interest, require extension of the framework but may allow many new phenomena to be realized, analogously to the case of non-reciprocal effects in thermal radiation (see e.g. Ref.

[**?**]). Direct modeling of light emission by means of calculating the emission from an ensemble of fluctuating dipoles, as considered in the past (e.g., for thermal emission [362]), is extremely resource-intensive from a computational perspective [1]. The effect of the spatial distribution of the scintillating centers is captured by integrating this spatial distribution against the spatially-dependent absorption in the scintillating structure. In this way, the spatial information can be obtained "all-at-once" from a single absorption "map".

We use this simplification to quantify scintillation, which we represent in terms of the scintillation power per unit frequency $d\omega$ and solid angle $d\Omega$ along the ith polarization (e.g., $i = s, p$): $\frac{dP^{(i)}}{d\omega d\Omega}$ (and $\frac{dP}{d\omega d\Omega} = \sum_i \frac{dP^{(i)}}{d\omega d\Omega}$ is the total scintillation power density). In most cases, the current-current correlations in the scintillator are isotropic (a condition that we relax in App. D (referred to as SI)), and we get

$$\frac{dP^{(i)}}{d\omega d\Omega} = \frac{\omega^2}{8\pi^2 \epsilon_0 c^3} \int d\mathbf{r} \frac{\left|\mathbf{E}^{(i)}(\mathbf{r}, \omega, \Omega)\right|^2}{\left|\mathbf{E}^{(i)}_{\text{inc}}(\omega, \Omega)\right|^2} S(\mathbf{r}, \omega), \tag{5.1}$$

where the quantity $\mathbf{E}^{(i)}_{\text{inc}}(\omega, \Omega)$ denotes the electric field of an incident plane wave of frequency ω, incident from a direction Ω, with polarization i. The quantity $\mathbf{E}^{(i)}(\mathbf{r}, \omega, \Omega)$ denotes the total electric field at position $\mathbf{r}$ resulting from the incident field and their ratio is thus the field enhancement. The function $S(\mathbf{r}, \omega)$ in Equation 1 is the spectral function encoding the frequency and position dependence of the current-current correlations, given by $S(\mathbf{r}, \omega) = \frac{1}{3} \sum_{\alpha,\beta} \text{tr}[\mathbf{J}^{\alpha\beta}(\mathbf{r}) \mathbf{J}^{\beta\alpha}(\mathbf{r})] f_\alpha(\mathbf{r})(1 - f_\beta(\mathbf{r}))\delta(\omega - \omega_{\alpha\beta})$. In this spectral function, f_α is the occupation factor of microscopic state α with energy E_α, $\mathbf{J}^{\alpha\beta}$ represents the matrix element of the current density operator ($\mathbf{J} \equiv \frac{e}{m} \psi^\dagger (-i\hbar\nabla)\psi$), $\omega_{\alpha\beta} = [E_\alpha - E_\beta]/\hbar$, and tr denotes matrix trace. Importantly, besides the position dependence of the current density matrix element, the occupation functions can also depend on position, as they depend on the HEP energy loss density (specifically, how much energy is deposited in the vicinity of $\mathbf{r}$). Interestingly, Equation 1 would be proportional to the strength of thermal emission upon substitution of $S(\mathbf{r}, \omega)$ by the imaginary part of the material permittivity, multiplied

[1] This issue is compounded by the sensitivity of the results to assumptions about the spatial and spectral distributions of the dipoles, which are related to the microscopic details of the defect electronic structure, as well as mechanism of high-energy particle energy transfer into the material.

by the Planck function. However here, the primary difference is that $S(\mathbf{r},\omega)$ describes a non-equilibrium state, rather than the thermal equilibrium state of the material.

To better understand the core components of nanophotonic scintillation enhancement, let us simplify it further, by considering the case where the density of excited states is uniform over some scintillating volume V_S (in which case we may drop the spatial dependence of S such that $S(\mathbf{r},\omega) \to S(\omega)$). This volume can be thought of as the characteristic volume over which excited electrons are created (like in Figure 1(b)). Then we may write

$$\frac{dP^{(i)}}{d\omega d\Omega} = \frac{\pi}{\epsilon_0 \omega} \times S(\omega) \times \left[V_{\text{eff}}^{(i)}(\omega,\Omega)/\lambda^3 \right], \tag{5.2}$$

where $V_{\text{eff}}^{(i)}(\omega,\Omega) = \int_{V_S} d\mathbf{r}\ |\mathbf{E}^{(i)}(\mathbf{r},\omega,\Omega)|^2 / |\mathbf{E}_{\text{inc}}^{(i)}(\omega,\Omega)|^2$. Having dimensions of volume, and being proportional to the absorbed power over V_S (in the limit of weak absorption, so as not to perturb the field solutions), we often refer to $V_{\text{eff}}^{(i)}(\omega,\Omega)$ (shortened as V_{eff}) as the effective volume of field-enhancement or the effective volume of absorption. Equation 2 states that the scintillation spectrum, under this approximation, is a simple product of a microscopic factor, set by the non-equilibrium steady-state distribution function $S(\omega)$, and an effective absorption volume V_{eff}, which is set only by the (structured) optical medium surrounding the scintillating medium.

Our framework to calculate scintillation according to Equation 1 consists of three components, as illustrated in Figs. 1b-d, g: energy loss of a beam of HEPs, creation of excited electrons, and subsequent light emission (which is computed by calculating field enhancement from incident plane waves, via electromagnetic reciprocity). As a technical matter, we note that we compute the HEP energy loss density by Monte Carlo simulations of energy loss (as is standard, see Refs. [363]), the electron energy levels and spectral function through density functional theory (DFT), and the nanophotonic field enhancement through finite-difference time-domain and rigorous coupled-wave analysis methods. In principle, these components are coupled together, as described in the SI.

More details on each component of the complete workflow, depicted in Fig. 1g can be found in the Methods and in the SI. The description of scintillation provided here $-$ using calculations of electronic structure, energy-loss, and electromagnetic response $-$ is

to the best of our knowledge, the first to provide an *ab initio* and end-to-end account of scintillation in nanophotonic structures.

5.2 Enhanced electron-beam-induced scintillation

Let us now move to show the theory in action. We first present data from experiments (conducted by Charles Roques-Carmes) probing scintillation from silicon-on-insulator nanophotonic structures due to bombardment by electrons (here, with energies in the range of 10-40 keV). Electrons with a few tens of keV energies are a convenient platform to demonstrate nanophotonic scintillation, as they readily lose almost all of the energy to the nanophotonic structure. Such lower energy particles penetrate materials less deeply, leading to a strong overlap between the spatial region of HEP energy loss density and the region of high field-enhancement (the latter of which is within a few hundred nm of the surface).

The experimental setup that was employed to measure scintillation is based on a modified SEM (an earlier version of which was reported in Refs. [345, 343, 347, 344]), shown in Figs. 2a,e: a focused electron beam of tunable energy (10-40 keV) excites the sample at a shallow ($\sim 1^\circ$) angle and the resulting radiation is collected and analyzed with a set of free space optics. The light is collected by an objective lens which accepts radiation emitted in a cone of half-angle 17.5°. Under the shallow-angle-conditions of electron incidence in our experiments, the effective penetration depth of the electrons is on the scale of a few hundred nanometers (Fig. 2b), far below the nominal mean free paths of 40 keV electrons in silica or silicon, which are on the order of 20 μm. This leads to strong overlap of the energy loss with regions of field enhancement. Control over the incidence angle also enables tuning this overlap between the HEP energy loss density and V_{eff}.

The first structure we consider is a thin film of 500 nm Si atop 1 μm SiO_2 atop a Si substrate. The second structure differs from the first in that the top Si layer is patterned to form a square lattice (design period ∼430 nm; see Fig. 2c) of air holes (diameter ∼260 nm) of various etch depths (∼25, 35, and 45 nm). We refer to them as "thin film" (TF) and "photonic crystal" (PhC) samples of same thicknesses, respectively. Scintillation in these structures occurs in the buried silica layer, and in particular, by a class of commonly

occurring defects called self-trapped holes (STH) [364]. Such defects have been studied extensively due to their consequences for silica fibers. They display distinct emission at red and green wavelengths, which, in addition to our other observations, enable us to attribute our observations to STH defect scintillation (and thus, rule out other mechanisms of electron-beam-induced emission (such as coherent cathodoluminescence; see SI)).

We now show how nanophotonic structures shape and enhance scintillation in silica. The scintillation spectrum of the sample in the visible range, for both TF and PhC samples, is shown in Fig. 2d. The TF scintillation measurements shown in black in Fig. 2f,g display two main sets of features at green ($\sim$ 500 nm) and red ($\sim$ 625 $-$ 675 nm) wavelengths. At red wavelengths, there is a clear double-peak structure, while at green wavelengths, the scintillation spectrum displays multiple peaks. These multiply-peaked spectra differ considerably from prior observations of STH scintillation [364]: while they occur roughly at the same wavelength, prior observations show only one peak at the red and green wavelengths [2]. The multiple peaks of the spectrum (and even its shoulders) are well accounted for at both red and green wavelengths even by the simplified Equation 2, and specifically by multiplying the shape of the STH spectrum in bulk by the V_{eff} calculated for the TF. The bulk spectrum is inferred from previous observations [364] and confirmed by our DFT calculations (see Fig. 3d). The multiply peaked structure of V_{eff} thus arises from thin-film resonances, which enhance the absorption of light in the buried silica layer. The agreement between theory and experiment in Fig. 2f,g unambiguously indicates a strong degree of spectral control over scintillation even in the simplest possible "nanostructure" (namely, a thin film).

In contrast to the TF scintillation, the scintillation from the PhC samples displays very strong and spectrally-selective enhancement. We report an enhancement of the red scintillation peak in the PhC sample, compared to the TF, by a factor of $\sim$ 6 (peak at 674 nm)

[2] In principle, one would want to compare V_{eff} in the TF to a "truly intrinsic" or "bulk" silica case. In that case, one would compare to silica of the same thickness (1000 nm). However, because this reference case is a thin film as well, nanophotonic shaping effects in the spectrum will inevitably be present. Comparing the V_{eff} in the thin film case of Fig. 2 to thin films without (a) the top Si layer, and (b) without both Si layers [see SI Figure 1], one finds that the TF of Fig. 2 presents slightly smaller absorption enhancement at the red peak, possibly due to the high reflectivity of the top Si layer (suppressing the amount of field which can be absorbed by the material). However, the PhC sample still shows strong shaping and enhancement relative to all TF cases.

and of ~ 3 integrated over the main red peak (665 ± 30 nm) as shown in Fig. 2d. This feature is reproduced by our theoretical framework via enhancement of V_{eff} around the red scintillation peak, using the same fitting parameters as those taken from the TF results of Figs. 2f,g. Comparatively, the green peak remains at a value similar to those in the TF spectra. Little enhancement is expected for the green wavelength, due to the high losses at those shorter wavelengths.

The observed enhancement can readily be attributed theoretically to the presence of high-Q resonances at the red wavelength, which lead to enhanced absorption of light in the far-field. Importantly, the positions of the many subpeaks in the scintillation spectra are accounted for by the peaks of V_{eff}. Somewhat larger uncertainties are introduced in the patterned structure because of the strong degree of angular shaping of the radiation associated with certain wavevectors in the PhC bandstructure (see inset of Fig. 2g, showing the predicted scintillation spectrum at normal emission). As a result, the spectrum depends on the exact angular acceptance function of the objective. There is also a more sensitive dependence on the exact distribution of electron energy loss compared to the thin-film case, due to the well-localized nature of the resonances leading to scintillation in the patterned structure.

Having shown scintillation control and enhancement based on nanophotonic structures, we move to show another core element of our general framework for scintillation: the microscopic transition dynamics associated with the scintillation process, their effect on the non-equilibrium occupation functions, and the corresponding effect on observable properties of the scintillation spectrum. In the specific case of silica defects, we can utilize spectral observables such as dependence of the scintillation on the electron energy, as well as the ratio of green to red scintillation peak powers (defined as η) as a function of deposited HEP energy, to test assumptions about the microscopic properties of the scintillation mechanism. We can even infer the energy level structure of the scintillating defects by combining these measurements with *ab initio* electronic-structure calculations and models of the excited electron kinetics (e.g., rate equations).

Fig. 3a shows the evolution of the scintillation spectrum for various energies. At high-energy pumping ($\sim$40 keV), red scintillation in the PhC sample dominates, while we ob-

serve that decreasing the pumping energy results in a gradual increase of the green peak scintillation (and of η). We took similar measurements for high and low-current pumping (at a constant pumping energy of 40 keV) of PhC and TF samples and compiled our results in Figs. 3e. There, one can observe that for the TF sample, the green peak scintillation always dominates ($\eta > 1$), while, for the PhC sample, there is a cross-over for a certain value of the deposited beam power (represented by η crossing unity).

To account for these observations, we consider a description of the defect levels in terms of a three-level Fermi system, featuring two lowest occupied levels (denoted 1 and 2 in Fig. 3c) coupled to an upper "pump" level (denoted 3) through the high-energy electron beam, which acts as a pump. These three levels correspond to energy levels from our electronic structure calculations of the STH defects in silica (based on DFT, see SI). The relative rates of the transitions $3 \rightarrow 1$ (Γ_{31}) and $3 \rightarrow 2$ (Γ_{32}) – which depend on the pump strength and the emission rates (which depend on V_{eff}) – dictate the strength of the green and red emission, respectively. We arrive at the results of Fig. 3e by solving for the steady-state values of these transition rates using rate equations (see Methods) and extracting the corresponding η, as a function of the incident beam power.

The agreement between theory and experiment enables us to understand the crossover as resulting from a combination of (1) the relative enhancement of red transitions from the PhC, and (2) the nonlinear transition dynamics of excited electrons in the defect. In particular, data from both samples indicate that the pump rate for the "green transition", Γ_{13}, is faster than its red counterpart, Γ_{23} (with consistent ratio values of ~ 3.2 for the TF and ~ 3.35 for the PhC). The existence of a cross-over deposited beam power between domains where $\eta > 1$ and $\eta < 1$ translates into an enhancement of the ratio of decay rates Γ_{32}/Γ_{31} in the PhC sample. Comparing model parameters fitting the TF experimental data to models fitting the PhC data, we estimate that the decay rate ratio is enhanced by a factor of $\sim 2.3 \pm 1.0$. This value is in agreement with the V_{eff}-enhancement predicted by our theory and by our observation of enhanced scintillation from the red defects in the experimental data.

By patterning nanophotonic scintillators, one can thus tailor microscopic properties and selectively enhance scintillation from microscopic defects. This also suggests that scintil-

lation rates can be selectively enhanced using nanophotonic structures, a feature that is particularly sought after in some medical imaging modalities [365]. Moreover, our results indicate that the measured scintillation may be used to sort out competing models of the electronic structure, especially in complex defects such as this one, which are hard to model due to self-interaction effects.

5.2.1 Observation of strongly enhanced scintillation induced by x-rays

We now move on to another example of a nanophotonic scintillator designed using our theoretical framework, showing its application to enhancing scintillation induced by high-energy photons such as x-rays. Such HEPs lose their energy much differently from massive charged particles (such as electrons).

In our experimental configuration (Fig. 4a) x-rays traverse a specimen, leading to spatially-dependent absorption of the incident x-ray flux. This absorption pattern is geometrically magnified until it encounters the YAG:Ce scintillator. This absorption pattern is then translated into scintillation photons which are imaged with an objective and a CCD camera. The nanopatterned scintillator is constructed by etching a two-dimensional PhC into YAG (via Focused Ion Beam (FIB) lithography; see Methods), at the surface of the scintillator facing the objective. The PhC period is 430 nm and the total patterned area is 215 μm $\times$ 215 μm (in Fig. 4) or 430 μm $\times$ 430 μm (in Fig. 5).

In the case of YAG:Ce, the intrinsic scintillation properties have been long characterized and our experiments reveal only weak dependence of the scintillation on incident x-ray energy. Thus, the full theoretical apparatus we demonstrate for electron scintillation is not needed to adequately describe our results. Primarily, the electromagnetic response (using reciprocity) is needed to account for the experimental results, and is the part of our general framework that leads us to order-of-magnitude enhancement of x-ray scintillation.

According to the scintillation framework developed in the previous sections, nanophotonic scintillation enhancement is to be expected when the absorption of light is enhanced. In Fig. 4b we show the calculated wavelength-dependent scintillation in YAG:Ce (averaged over the angular acceptance of the objective, as in Fig. 2) for an unpatterned self-standing

thick (20 μm) film, as well as for the PhC sample. Here, the calculated enhancement is by a factor of $\sim 9.3 \pm 0.8$ over the measured scintillation spectrum. In our calculations, we attribute the main error bar to the uncertainty on the hole depth (± 10 nm as can be extracted from our AFM measurements, shown fully in Fig. 4a (right) and in cross-sections in the SI). However, we should note that there are several other sources of uncertainty in the fabricated samples: the hole diameter and periodicity, and the optical absorption of YAG:Ce (taken in our calculations to be the value provided by the wafer supplier). We also measured and compared to our theory scintillation enhancements from multiple nanophotonic scintillators with various thicknesses, hole shapes, depths and patterned areas (see additional experimental data and Table I in the SI).

Here, the x-ray scintillation enhancement originates in light out-coupling enhancement (or by reciprocity, in-coupling enhancement). In particular, the PhC allows more channels (i.e. a plane-wave coupling to a resonance) into the scintillator crystal, compared to a flat interface. The multiple channels translate into sharp resonant peaks in the calculated absorption spectrum. This is to be contrasted with the origin of electron-beam-induced scintillation enhancement in silica, where the enhancement can be tied to the presence of a single, or small number of high-Q resonances. This effect is of the type often leveraged to design more efficient LEDs and solar cells that approach the "Yablonovitch limit" in both ray-optical [366, 367], and nanophotonic [368, 369] settings. There, it is well known that the device efficiency is optimized by designing a structure that leads to strong absorption over the spectral range of the emission [366, 370].

In Fig. 4c, we show the experimentally measured scintillation scanned along a line of the sample. The regions "off" indicate unpatterned regions of the YAG:Ce, while "on" indicates the PhC region. Here, the signal is enhanced on average by a factor of ~ 9.1 over the unpatterned region, consistent with the predictions of Fig. 4b.

To demonstrate the potential of our approach to x-ray imaging, we fabricated a larger-scale pattern on a 50 μm wafer which exhibits a scintillation enhancement of 2.3. We recorded single-shot x-ray scans of biological and inorganic specimens through the PhC, showing no evident decrease in resolution, while increasing the image brightness by the same factor. Equivalently, the required x-ray dose or exposure time to get a given number

of counts on the detector is reduced.

Our framework allows us to further gain understanding of the scintillation mechanism at play, directly leveraging known techniques in absorption enhancement. One could expect even greater scintillation enhancements on the order of $\sim 4n^2$ in the ray-optics approximation [366] or $\sim 4\pi n^2$ for periodic structures on the wavelength scale [368, 369] (where n is the index of refraction). For example, for a high-index material such as doped GaAs, which also scintillates at room temperature [371], enhancements on the order of ~ 50 and ~ 150 could be respectively achieved in the two regimes (over a 2π collection solid angle).

5.3 Discussion

We have presented a general framework to model, tailor, and enhance scintillation by means of nanophotonic structures integrated into scintillating materials (nanophotonic scintillators). While we mainly focused on the demonstration of spectral shaping and enhancement of scintillation, our results could be extended to show angular and polarization control as well. We have demonstrated nanophotonic scintillators enhancing electron-beam-induced and x-ray-induced scintillation. The theoretical framework we used to describe our experimental results combines Monte Carlo simulations of the energy loss density [363] with DFT calculations of the microscopic structure and full-wave calculations of the electromagnetic response of the nanophotonic structures probed in this work.

We note that this type of "full" analysis has to the best of our knowledge not been performed to explain scintillation (nor incoherent cathodoluminescence) experiments, likely due to the prohibitively expensive computations associated with simulating ensembles of dipoles radiating in 3D structures. The reciprocity framework we use (also commonly used in areas of thermal radiation, LEDs, and photoluminescence [361, 372, 373, 374, 375, 376]) strongly simplifies the analysis, and makes a full modeling of the scintillation problem tractable. We conclude by outlining a few promising avenues of future work that are enabled by the results provided here. Further elaboration and initial results, for each of these avenues, is detailed in the SI.

The first area, inspired by our simplified calculations based on reciprocity, is numer-

ical optimization of nanophotonic scintillators. Our framework, which relies on the calculation of V_{eff} (which is relatively amenable, even in 3D), enables the inverse-design of nanophotonic scintillators. The experimentally reported enhancements can be further improved upon by inverse-designing the nanophotonic structure via topology optimization of V_{eff} [377]. In the SI, we show the kind of results that could be expected from topology-optimized nanophotonic scintillators: we find that 10-fold, and even nearly 100-fold selective enhancements of scintillation in topology-optimized photonic structures are possible. By considering different emission linewidths and frequencies, one can selectively design optimized nanophotonic structures which enhance one of the scintillating peaks, at a single-frequency or over the entire scintillation bandwidth. Beyond our reciprocity-based approach, low-rank methods can be utilized for the inverse-design of nanophotonic scintillators with very large angular ranges [378]. Beyond scintillation, our techniques may find applicability in other imaging modalities involving random incoherent emitters, such as surface-enhanced Raman scattering [379].

Another promising area of research enabled by our findings is nanophotonically-enhanced and -controlled UV light sources. In the SI, we show how UV scintillation in materials such as hBN enables strongly enhanced scintillation with a spectrum that can be controlled simply by the position of the electron beam relative to the patterned features in the hBN arising from changes in the overlap between the HEP loss density and V_{eff}. The prospect of realizing optimized and compact nanophotonic UV scintillation sources is particularly exciting for applications in water purification and sanitization [380].

Nanophotonic scintillators provide a versatile approach for controlling and enhancing the performance of scintillating materials for a wide range of applications. The framework developed here applies to arbitrary scintillating materials, nanophotonic structures, and HEPs, solving for the process end-to-end using first-principles methods. The electron-beam and x-ray scintillation experiments provide the proof-of-concept tests of the promising prospects of this field. Our work may open a panoply of exciting applications, from high-resolution, low-dose x-ray imaging to efficient ultraviolet electron-beam-pumped light sources.

We conclude this chapter by acknowledging the contributions of other authors to this multi-disciplinary work. This chapter represents the combined efforts of many authors,

whose contributions are noted here (taken from Ref. 37 of publication list): C. R.-C., N. Ri., N. Ro., I. K., and M. S. conceived the original idea. N. Ri. developed the theory with inputs from C. R.-C. and A. G. C. R.-C. and S. E. K. performed the electron-beam and X-ray experiments. C. R.-C. and N. Ri. analyzed the experimental data and fitted it to the theory. C. R.-C. and S. E. K. built the electron-beam experimental setup with contributions from J. B., A. M., J. S., Y. Ya., I. K., and M. S. N. Ri. performed energy loss calculations. C. R.-C. performed absorption map calculations. A. G. performed DFT calculations. C. R.-C. wrote code for optimizing nanophotonic scintillators with inputs from N. Ri., Z. L. and S. G. J. Y. Yu and C. R.-C. fabricated the X-ray scintillation sample. J. D. J., I. K., S. G. J., and M. S. supervised the project. The manuscript was written by C. R.-C. and N. Ri. with inputs from all authors.

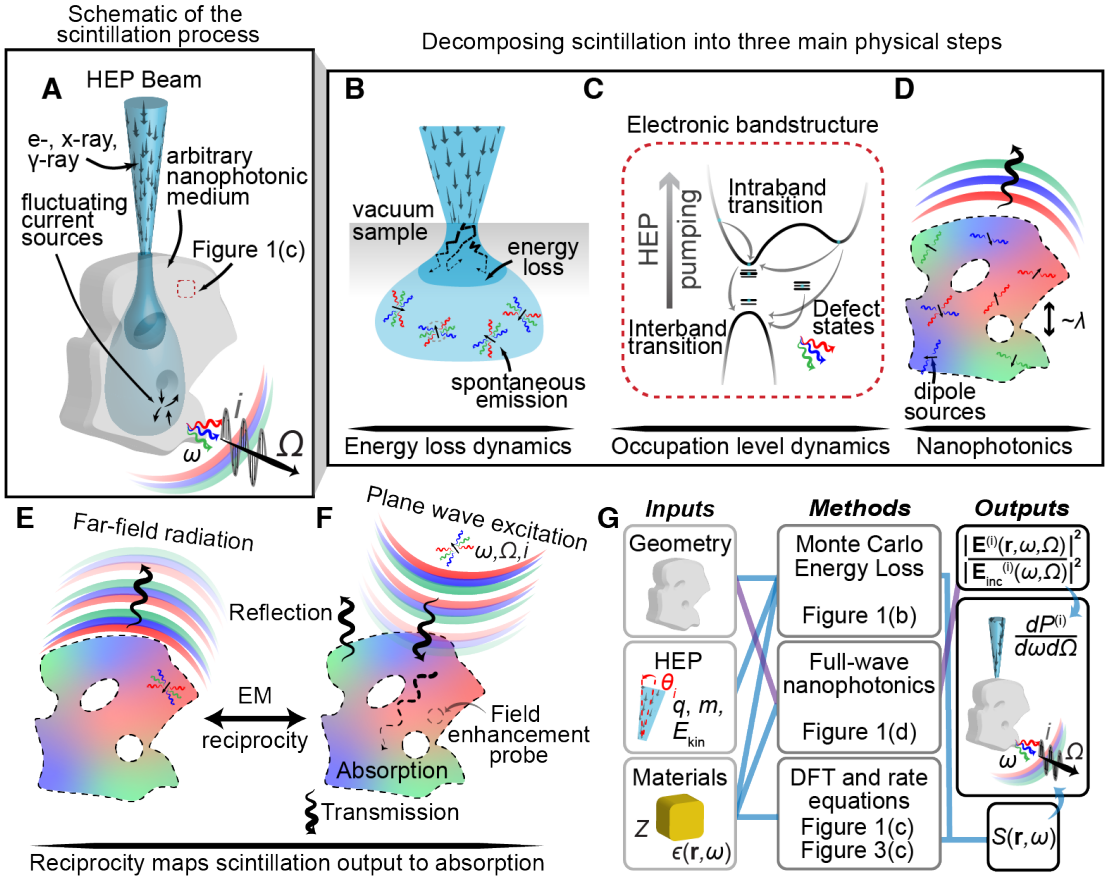

Figure 5-1: **A general framework for scintillation in nanophotonics.** (A) We consider the case of high-energy particles (HEP) bombarding an arbitrary nanophotonic medium, emitting scintillation photons at frequency ω (free-space wavelength λ), propagation angle Ω, and polarization i. (B) Subsequent HEP energy loss results in excitation of radiative sites (darker blue region in sample) which may diffuse before spontaneously emitting photons (lighter blue region in sample). (C) The framework also accounts for different types of microscopic emitters. (D) The emitters may emit in arbitrary nanophotonic environments. (E-F) Electromagnetic reciprocity maps far-field radiation calculations from the stochastic many-body ensemble in a single electromagnetic simulation of plane-wave scattering, by calculating the effective spatially-dependent field enhancement. (G) Summarized framework. Links indicate forward flow of information. The purple links indicate the possibility of backward flow (inverse-design) in our current implementation. $q, m, E_{\text{kin}}, \theta_i$: particle charge, mass, kinetic energy, and incidence angle. $\epsilon(\mathbf{r}, \omega), Z$: material permittivity and effective Z-number. $S(\mathbf{r}, \omega)$: spatially-varying intrinsic scintillation spectral function. $dP^{(i)}/d\omega d\Omega$: scintillation spectral-angular power density at polarization i. An expanded and elaborated version of (g) is presented in the SI.

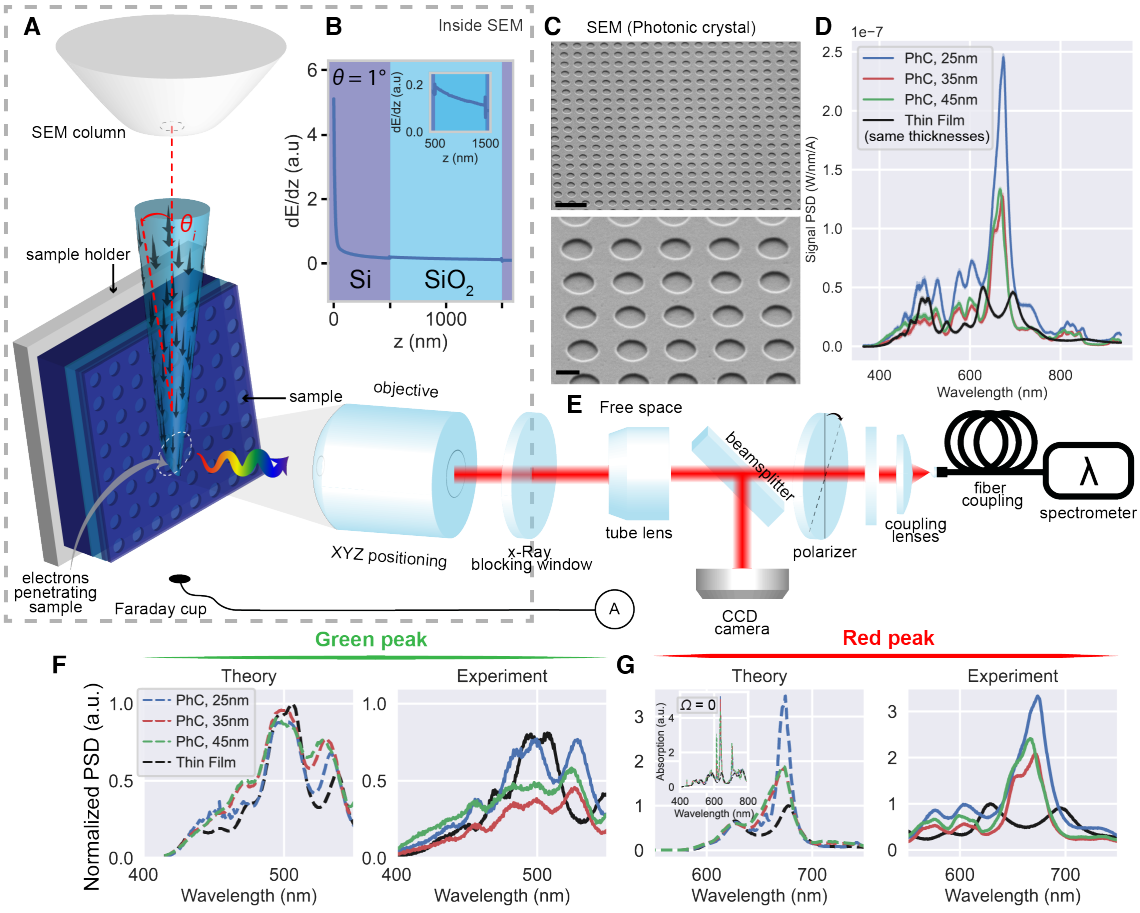

Figure 5-2: **Experimental demonstration of nanophotonic shaping and enhancement of electron-beam-induced scintillation, demonstrating the validity of the general nanophotonic part of the general theory of scintillation.** (A) A modified scanning electron microscope (SEM) is used to induce and measure scintillation from electron beams (10-40 keV) bombarding scintillating nanophotonic structures. (B) Electron energy loss in the silicon-on-insulator wafer is calculated via Monte Carlo simulations. Inset: Zoomed-in electron energy loss in the scintillating (silica) layer. (C) SEM images of photonic crystal (PhC) sample (etch depth 35 nm). Tilt angle 45°. Scale bar: 1 μm (top), 200 nm (bottom). (D) Scintillation spectrum from thin film (TF) and PhC samples with varying etch depths (but same thickness). (E) The scintillation signal is coupled out of the vacuum chamber with an objective and then imaged on a camera and analyzed with a spectrometer. (F-G) Comparison between theoretical (left) and experimental (right) scintillation spectra for green and red scintillation peaks. Inset: Calculated scintillation spectra (per solid angle) at normal emission direction, showing the possibility of much larger enhancements over a single angle of emission. Data collected by Charles-Roques Carmes and Steven Kooi.

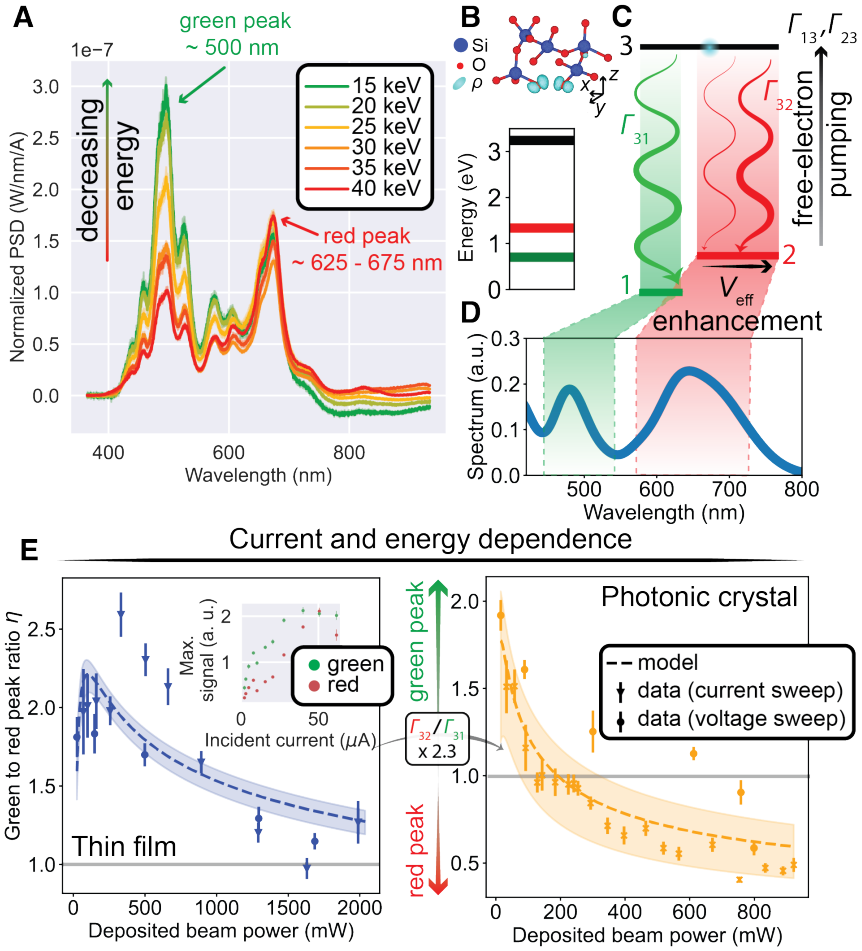

Figure 5-3: **Probing the microscopics of electron-beam-induced scintillation in silica, demonstrating the validity of the combined nanophotonic and microscopic parts of the general theory of scintillation.** (a) Energy-dependent scintillation spectra (PhC sample, etch 25 nm). (b) Top: 3D molecular model of STH defect in silica. Si: Silicon, O: Oxygen, ρ: spin-polarized density. Bottom: Calculated STH defect energy levels via density functional theory (DFT). (c) Simplified three-level system modelling the microscopics of scintillation from STH defect in silica. (d) Bulk scintillation spectrum calculated with DFT (dipole matrix elements). (e) TF (left) and PhC (right) scintillation peak ratios as a function of deposited beam powers through electron pumping. The dashed line corresponds to the mean model prediction and the shaded area to the prediction from the model parameters $\pm$ their standard deviation (TF, PhC: uncertainty on Γ_{31}/Γ_{32}). Inset: Maximum signal of green and red scintillation peaks versus current in TF sample. Data collected by Charles-Roques Carmes and Steven Kooi.

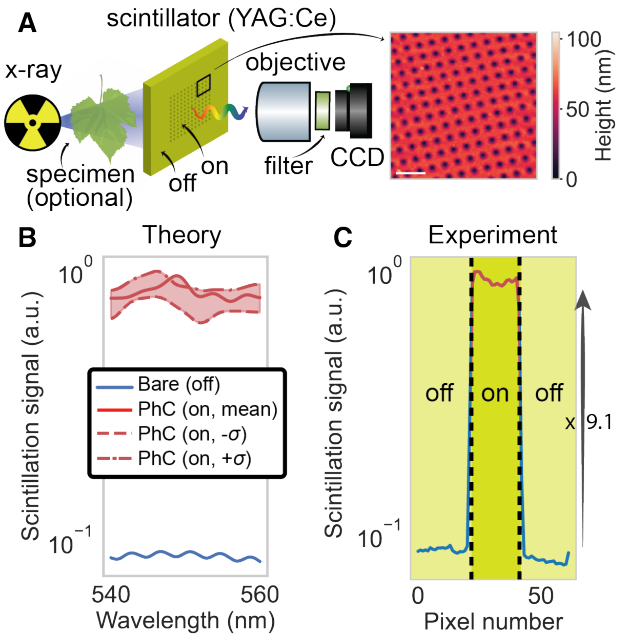

Figure 5-4: **Nanophotonic enhancement of x-ray scintillation, showing how the reciprocity theory enables design of high-brightness scintillators.** (a, Left) x-ray scintillation experimental setup: light generated by x-ray bombardment of a cerium-doped yttrium aluminium garnet (YAG:Ce) scintillator is imaged with a set of free-space optics. A specimen may be positioned between the source and the scintillator to record an x-ray scan of the specimen. (a, Right) Atomic force microscopy image of patterned YAG:Ce scintillator (20 μm thickness). Scale bar: 1 μm. (b) Calculated scintillation spectrum of the PhC, integrated over the experimental angular aperture. Calculations are performed for measured etching depths $\pm$ a standard deviation (corresponding to 40, 50, and 60 nm). The shaded area corresponds to possible scintillation enhancements in between those values. The calculated spectra are convolved with a moving-mean filter of 1.33 nm width (raw signal shown in the SI). (c) Measured scintillation along a line of the sample, including regions on (red) and off (blue) the PhC. The scintillation from the PhC region is on average about $\times 9.1$ higher than the unpatterned region. All signals were recorded with x-ray source settings: 40 kVp, 3 W. Data collected by Charles-Roques Carmes.

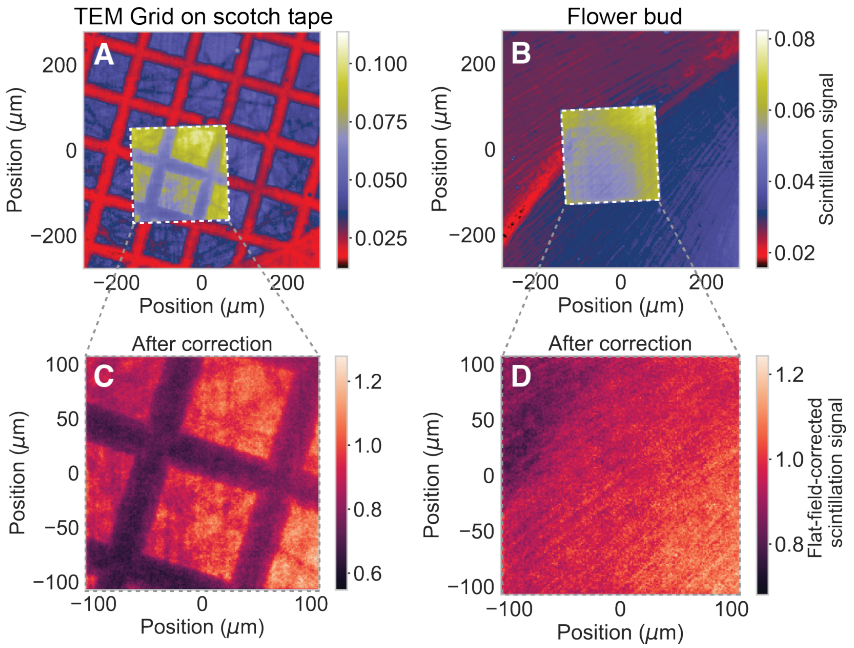

Figure 5-5: **X-ray scintillation imaging with nanophotonic scintillators, showing how the reciprocity theory enables design of high-brightness scintillators.** (a, b) Measured x-ray images of a (a) TEM grid on scotch tape and of a (b) flower bud. The white square delimits the PhC area. (c, d) Flat-field corrected zoom-in of the x-ray image in the PhC area. Geometric magnification on those images is ~ 2. Compared to the unpatterned regions, the images are brighter above the PhC region, and show no evident decrease in resolution. The particular nanophotonic scintillator used for this experiment was patterned over an area of 430×430 μm and resulted in a scintillation enhancement of $\times 2.3$ (measured with respect to unpatterned scintillator of same thickness). All signals were recorded with x-ray source settings: 60 kVp, 5 W. Data collected by Charles-Roques Carmes.

Chapter 6

Variational theory of nonrelativistic quantum electrodynamics

Note: This chapter is heavily based off "Variational theory of nonrelativistic quantum electrodynamics", by N. Rivera et al. Physical Review Letters (2019).

The ability to achieve ultra-strong coupling between light and matter promises to bring about new means to control material properties, new concepts for manipulating light at the atomic scale, and new insights into quantum electrodynamics (QED). Thus, there is a need to develop quantitative theories of QED phenomena in complex electronic and photonic systems. In this Letter, we develop a variational theory of general non-relativistic QED systems of coupled light and matter. Essential to our ansatz is the notion of an effective photonic vacuum whose modes are different than the modes in the absence of light-matter coupling. This variational formulation leads to a set of general equations that can describe the ground state of multi-electron systems coupled to many photonic modes in real space. As a first step towards a new *ab initio* approach to ground and excited state energies in QED, we apply our ansatz to describe a multi-level emitter coupled to many optical modes, a system with no analytical solution. We find a compact semi-analytical formula which describes ground and excited state energies very well in all regimes of coupling parameters allowed by sum rules. Our formulation provides a non-perturbative theory of Lamb shifts and Casimir-Polder forces, as well as suggesting new physical concepts such as the Casimir

energy of a single atom in a cavity. Our method thus give rise to highly accurate non-perturbative descriptions of many other phenomena in general QED systems.

Recent years have brought an explosion of progress in the study of light-matter interactions in the non-perturbative regime of quantum electrodynamics (QED) [381, 382, 383, 384]. Ultra-strong, and even deep-strong coupling has been observed in systems involving superconducting qubits [385, 386, 175, 174, 168, 167], large ensembles of molecules [387, 388, 389, 160, 390, 391, 392, 393], Landau level systems [219, 394], quantum wells coupled to cavities [223, 395], oscillators [396], and even in few-molecule systems [397, 13]. Proposals for new platforms of ultra-strong coupling include emitters coupling to highly confined polaritons in metals and polar insulators [105], heavy ions coupled to optical media via the Cerenkov effect [398], and many more. Proposed applications of ultra- and deep-strong coupling of light and matter are similarly broad, including simulation of many-body systems [383], altering chemical reactivity [387, 390, 393, 399, 400, 401, 402] and electronic transport properties [403] and realizing analogues of nonlinear optical processes with vacuum fluctuations [404]. Concomitantly with these developments are also theoretical developments in the study of QED systems *ab initio*. Through 'reduced quantity theories' such as quantum electrodynamical density functional theory (QEDFT) [405, 406, 407, 408, 409, 410], one is now able to calculate observables in large molecules coupled to realistic optical cavities [411, 410, 409].

In this Letter, we establish a variational framework to analyze complex light-matter systems from first principles. Although *ab initio* methods such as QEDFT are exact in principle and provide access to all observables, a number of practical difficulties arise related to: the lack of simple exchange-correlation functionals to describe the ground state energy, as well as other more involved observables, the difficulty of obtaining real-space information about the photons as they are affected by light-matter coupling, the difficulty of handling excited state energies, and the common use of the long-wavelength (dipole) approximation. A variational framework, as we show, flexibly allows a real-space description of the electrons and photons as they are modified by the coupling and also beyond the dipole approximation. Beyond these advantages, a variational framework also allows conceptual insights, into a simple non-perturbative theory of Lamb shifts, into a quasipar-

ticle description of QED systems, and into the notion of Casimir forces in the limit of one atom. A variational framework also allows compact semi-analytical formulae to describe complex systems which may assist the development of functionals for use in QEDFT.

Motivated by all of these potential advantages, we now develop an ansatz in which the ground state can be considered as a factorizable state of effective matter and effective photon quasiparticles, both in their respective vacuum states. This ansatz − reminiscent to, but qualitatively distinct from, the Hartree-Fock ansatz [412] of electronic structure theory − leads to coupled eigen-equations describing ground and excited states of the light-matter system. We apply our ansatz to describe ground and excited states in a multi-level emitter coupled to many photonic modes. We find that for light-matter couplings that respect sum rules, our method yields ground and excited state energies to a remarkable accuracy of up to 99%, even in deeply non-perturbative coupling regimes. In regimes where our results are accurate, we have found the effective quasiparticle description of the ground state of QED. Our findings also furnish a non-perturbative theory of the position-dependent energy (Lamb) shifts of ground and excited states that give rise to Casimir-Polder forces. The variational method developed in this manuscript is particularly suited for analyzing QED systems in the ultrastrong coupling regime, in which the rotating-wave approximation no longer holds, and subsequently methods based on the Jaynes-Cummings model such as dressed state approaches [413] are no longer accurate.

In general, the QED Hamiltonian is given by $H = H_{\rm mat} + H_{\rm em} + H_{\rm int}$ where $H_{\rm mat}$ describes the matter in the absence of the quantized electromagnetic field, $H_{\rm em}$ describes the photons in the absence of the matter, and $H_{\rm int}$ describes the coupling between light and matter. The matter Hamiltonian takes the form:

$$\begin{aligned} H_{\rm el} = &\int d^3x\, \psi^\dagger(\mathbf{x}) \left(-\frac{\hbar^2\nabla^2}{2m} + v_{\rm ext}(\mathbf{x}) \right) \psi(\mathbf{x}) \\ &+ \frac{1}{2} \int d^3x d^3x'\, \psi^\dagger(\mathbf{x}) \psi^\dagger(\mathbf{x}') V(\mathbf{x}-\mathbf{x}') \psi(\mathbf{x}') \psi(\mathbf{x}), \end{aligned} \tag{6.1}$$

where $v_{\rm ext}$ is the one-body external potential, $V(\mathbf{x}-\mathbf{x}')$ is the two-body interaction kernel, and ψ is the second-quantized electron field.

Parameterizing the electromagnetic field purely in terms of a vector potential: $\mathbf{E} =$

$-\partial_t \mathbf{A}$ and $\mathbf{B} = \nabla \times \mathbf{A}$ renders the free electromagnetic Hamiltonian as

$$H_{\text{em}} = \frac{\epsilon_0}{2} \int d^3x \, \epsilon (\partial_t \mathbf{A}(\mathbf{x}))^2 + \mathbf{A}(\mathbf{x}) \cdot (\nabla \times \mu^{-1} \nabla \times \mathbf{A}(\mathbf{x})), \tag{6.2}$$

where ϵ and μ represent a non-dispersive and positive dielectric and magnetic background that the matter and photon occupy. For cases we consider in this work, these will be taken to be unity.

The interaction Hamiltonian takes the form:

$$\begin{aligned} H_{\text{int}} = & \frac{-i\hbar e}{2m} \int d^3x \, \psi^\dagger(\mathbf{x}) (\mathbf{A}(\mathbf{x}) \cdot \nabla + \nabla \cdot \mathbf{A}(\mathbf{x})) \psi(\mathbf{x}) \\ & + \frac{e^2}{2m} \int d^3x \, \psi^\dagger(\mathbf{x}) \psi(\mathbf{x}) \mathbf{A}^2(\mathbf{x}). \end{aligned} \tag{6.3}$$

The full Hamiltonian H, which depends on the fields ψ and $\mathbf{A}$ is parameterized in terms of an orthonormal set of electron single-particle wavefunctions (orbitals) $\{\psi_n\}$, and in terms of a set of photonic mode functions (orbitals) $\{\mathbf{F}_i\}$. The electron field operator takes the form $\psi(\mathbf{x}) = \sum_n \psi_n(\mathbf{x}) c_n$. The c_n is an annihilation operator for an electron corresponding to state n. The electromagnetic field operator takes the form $\mathbf{A}(\mathbf{x}) = \sum_i \sqrt{\frac{\hbar}{2\epsilon_0 \omega_i}} \left(\mathbf{F}_i(\mathbf{x}) a_i + \mathbf{F}_i^*(\mathbf{x}) a_i^\dagger \right)$, where the $a_i^{(\dagger)}$ annihilate (create) a photon in mode i.The electromagnetic field operator is parameterized by both mode functions and frequencies. The normalization chosen for the electron wavefunctions is $\int d^3x \, \psi_m^* \psi_n = \delta_{mn}$ while for the photon mode functions, it is $\int d^3x \, \epsilon \mathbf{F}_i^* \cdot \mathbf{F}_j = \delta_{ij}$ [49]. Assumptions behind the form of the Hamiltonian are stated in Supplementary Materials, page 2.

Given an ansatz $|\Omega\rangle$ for the ground state of H, the variational theorem ensures that $\langle \Omega | H | \Omega \rangle$ is an upper bound for the ground state energy. We choose as our ansatz

$$|\Omega\rangle = \left(\prod_n c_n^\dagger |0_n\rangle \right) \otimes \left(\bigotimes_i |0_i\rangle \right). \tag{6.4}$$

where, $\prod_n c_n^\dagger |0_n\rangle$ represents a 'filled Fermi sea' for effectively non-interacting electrons, and $(\bigotimes_i |0_i\rangle)$ represents a 'photonic vacuum' for effectively non-interacting photons (see Fig. 1). Implicitly, this ansatz, once we take the expectation value $\langle \Omega | H | \Omega \rangle$, denotes a

family of ansatzes labeled by all possibilities for the electron wavefunctions, photon mode functions, and photon mode frequencies. Thus, we minimize the expectation value with respect to $\psi_n, \psi_n^*, \mathbf{F}_i, \mathbf{F}_i^*$, and ω_i. We enforce that the matter and photon remain normalized by constructing the Lagrange function:

$$\begin{aligned}\mathcal{L}[\{\psi_n, \psi_n^*\}, \{\mathbf{F}_i, \mathbf{F}_i^*, \omega_i\}] &= \langle\Omega|H|\Omega\rangle \\ &- \sum_n E_n \left(\int d^3x \; \psi_n^* \psi_n - 1 \right) - \sum_i \frac{\hbar\lambda_i}{2} \left(\int d^3x \; \epsilon \mathbf{F}_i^* \cdot \mathbf{F}_i - 1 \right),\end{aligned} \tag{6.5}$$

with the E_n and $\frac{\hbar\lambda_i}{2}$ being the Lagrange multipliers that enforce the normalization conditions. Evaluating the expectation value of the Hamiltonian, and minimizing the Lagrange function immediately yields:

$$\left(\frac{\mathbf{p}^2}{2m} + v_{\text{ext}}(\mathbf{x}) \right) \psi_i(\mathbf{x}) + F[\{\psi\}] + \frac{\hbar e^2}{4m\epsilon_0} \left(\sum_n \frac{1}{\omega_n} |\mathbf{F}_n|^2 \right) \psi_i(\mathbf{x}) = E_i \psi_i(\mathbf{x}), \tag{6.6}$$

for the electron orbitals and energies, where $F[\{\psi\}]$ represent Hartree-Fock terms (see App. E, referred to as SI). Here the effect of the QED coupling is to add a one-body ponderomotive potential.

For the photon orbitals and energies, the minimization yields:

$$\left(\nabla \times \nabla \times - \frac{\omega_i^2}{c^2} \left(1 - \frac{\omega_p^2(\mathbf{x})}{\omega_i^2} \right) \right) \mathbf{F}_i = 0, \tag{6.7}$$

where $\omega_p^2(\mathbf{x}) = \frac{e^2}{m\epsilon_0} \sum_{n=1}^{N} |\psi_n(\mathbf{x})|^2$ is a position-dependent squared-plasma frequency which will push the photon orbitals out of the region where the emitter is located. Equations (6) and (7) are main results and can be used to describe ultra-strongly coupled systems in three dimensions, in an arbitrary photonic system, and with multi-electron matter. Excited states in this framework can be identified with matter and photon quasiparticle excitations. Taking the divergence of Eq. (7), we see that $\nabla \cdot (1 - \frac{\omega_p^2(\mathbf{x})}{\omega^2})\mathbf{F}(\mathbf{x}) = 0$, which is a generalized Coulomb gauge condition on the modes [100]. For more discussion, see Supplementary Information, page 2.

Note that term in the interaction Hamiltonian linear in the vector potential (the "$A \cdot p$

term“) makes no contribution to the expectation value of the ground state of the energy in this ansatz. Physically, this term will mix the factorizable ground state of Eq. (4) with states that have virtual excitations of the matter and the electromagnetic field. The resulting state is non-factorizable and thus, the $A \cdot p$ term leads to *correlations* in the system, and contributes wholly at lowest order to the correlation energy of QED ground and excited states [1].

We capture the effect of correlations perturbatively. For the ground state, we consider the second-order correction δE to the ground state energy arising from the $A \cdot p$ term. That correction is given by

$$\delta E = \frac{e^2\hbar^2}{8m^2\epsilon_0} \sum_{i=1}^{\infty} \sum_{n=N_\sigma+1}^{\infty} \sum_{m=1}^{N_\sigma} \frac{\left| \int d^3x \, \mathbf{F}_i^* \cdot \mathbf{j}_{nm} \right|^2}{\omega_i(\omega_{mn} - \omega_i)}, \tag{6.8}$$

where $\mathbf{j}_{nm} = \psi_n^* \nabla \psi_m - (\nabla \psi_n^*)\psi_m$, $\omega_{mn} = \omega_m - \omega_n$, and N_σ is the number of occupied orbitals, equal to the number of electrons. In a method without self-consistency, the electron and photon orbitals and eigenvalues are those obtained from Eqs. (6) and (7), and then the electron energies and orbitals as well as the photon frequencies and orbitals, are plugged into Eq. (8). By considering an ansatz for an excited state, correlation corrections to excited states can also be found. In the SI, we derive a set of equations for the matter orbitals and photonic mode functions which self-consistently takes into account the correlation energy associated with Eq. (8). These equations take into account the spatially varying wavefunctions to the spatially varying mode functions, just like Eqs. (6) and (7), and therefore do not assume the dipole approximation.

In what follows, we provide a proof-of-concept demonstration of the accuracy and content of the variational theory derived here. We consider the QED Hamiltonian corresponding to a single emitter placed at position $z = d$ in a one-dimensional cavity whose axis is along the z-direction. As the cavity is considered for simplicity to be one-dimensional, the electric field is oriented along a single direction, denoted x, while the magnetic field is

[1] The behavior of the $A \cdot p$ and A^2-term is similar to the $r \cdot D$ and r^2 term in the length-gauge reported in recent work on the optimized effective potential [414, 411] method for QEDFT including one-photon processes.

oriented along a direction transverse to both the electric field and the cavity length, denoted y. Working under the long-wavelength (dipole) approximation, the Hamiltonian can then be written as:

$$H = H_{\text{matter}} + \frac{\epsilon_0 S}{2}\int dz\,(E^2 + c^2B^2) + \frac{q}{m}A(d)p + \frac{q^2}{2m}A^2(d), \tag{6.9}$$

with the emitter charge now expressed as q, E, B, and A being the electric field, magnetic field, and vector potential, and S being a normalization area of the cavity in the xy plane. The fields can be expressed as a mode expansion, where for a cavity of length L, the modes are given by $F_n(z) = \sqrt{\frac{2}{L}}\sin\left(\frac{n\pi z}{L}\right)$ and the corresponding mode frequencies are $\omega_n = \frac{n\pi c}{L}$. The matter Hamiltonian we take to be a multilevel system with N_a levels. The matter system we describe can thus be mapped to an N_a site system, which be considered as a simplified model of a molecule within a tight-binding description. Thus we parameterize the general family of matter Hamiltonians as $H_{\text{matter}} = \sum_{i=1}^{N_a-1} V_i|i\rangle\langle i| + t(|i\rangle\langle i+1| + |i+1\rangle\langle i|)$. The momentum operator, we write as $p = \frac{-i\hbar}{R}\sum_{i=1}^{N_a-1}(|i\rangle\langle i+1| - |i+1\rangle\langle i|)$, where R is a constant with units of length representing roughly the difference in positions between sites. This physical interpretation however is rough: it is also a function of the hopping elements t, because we choose R in this work such that the Thomas-Reiche-Kuhn (TRK) sum rule is enforced: $\frac{2}{m}\sum_{i=2}^{N_a}\frac{|p_{ig}|^2}{E_i - E_a} = 1$, where $p_{ig} = \langle i|p|g\rangle$ are momentum matrix elements between different matter states [413]. Although the sum rule is based on a full electronic real-space description, a discrete system which has $\frac{2}{m}\sum_{i=2}^{N_a}\frac{|p_{ig}|^2}{E_i - E_a} > 1$ cannot exist physically. The TRK sum rule places a bound on how strong the effect of the $A\cdot p$ term can be. The net effect is that the value of R we choose is on the order of $\sqrt{\frac{\hbar}{2mt}}$.

Derivations of the energies of states via the formalism introduced here are shown in the SI. Here, we present the main results. Using a one-dimensional version of Eqs. (6) and (7), we calculate the electron orbitals, photon orbitals, and photon frequencies in the absence of correlations. In the absence of correlations, we found that the energy of any matter state a with no photonic quasiparticles is given by:

$$E_a = E_a^0 + \frac{1}{2}\sum_{n=1}^{\infty}(\hbar\omega_n - \hbar\omega_n^0), \tag{6.10}$$

where E_a^0 is the energy of the matter state in the absence of coupling, ω_n are found in our framework, $\omega_n^0 = \frac{n\pi c}{L}$. The modes found in our framework have their frequencies given by

$$\cot\left(\frac{\omega_n}{c}d\right) + \cot\left(\frac{\omega_n}{c}(L-d)\right) = -\frac{q^2}{m\epsilon_0\omega_n c}. \tag{6.11}$$

The corresponding 'interacting' field mode profiles, shown in Fig. 2b, are given by compact expressions shown in the SI.

The result of Eq. (10) says that in the absence of correlations, the energy of the system is the Casimir energy of the system. In particular, it has long been known that when two conducting plates are placed near each other, there is a Casimir energy associated with the fact that the zero-point energy of the nearby plates is different than the zero-point energy of plates infinitely apart. This Casimir energy is simply the difference between the interacting and non-interacting zero-point energies [415, 295]. This logic can be applied to any arrangement of macroscopic polarizable objects. What is notable about the result of Eq. (10) is it implies that the same logic about zero-point energy differences can be applied to find the interaction energy of a *single atom* placed near a cavity.

In the presence of correlations we must add to the energy a contribution of the form of Eq. (8), specialized to the case of an emitter in a one-dimensional cavity. We apply the correlation correction to excited states as well, calculating excited-state energy shifts within second-order perturbation theory. In Fig. 2a, we show the result of this procedure when applied to calculate ground- and excited- state energies for few-level systems coupled to a one-dimensional cavity. The relevant parameters for Fig. 2(a) are listed in the SI. For the largest couplings considered here, the magnitude of the energy shift associated with the $A \cdot p$ term predicted from perturbation theory is larger than the energy separation between bare emitter levels, signaling the ultrastrong coupling regime.

In all cases, the agreement between our variational approach and numerical diagonalization is excellent, suggesting that our variational method is sufficiently flexible to capture ground states and excited states. The accuracy as a function of number of levels suggests that the breakdown of gauge invariance associated with few-level systems is not crucial to the good agreement between variational and numerical results [416]. Perturbation theory

in the bare matter and photon states can both strongly over- and underestimate the energies. Strong disagreement arises in the case of the two-level system (top panel). For the two-level system considered here, the variational result agrees very well with numerical diagonalization, while perturbation theory predicts an energy which evolves with coupling in the wrong direction and is off from the true energy by over 100% for the largest coupling.

Perturbation theory fails for first excited state because the first bare cavity mode is nearly resonant with the transition between ground and excited emitter states, leading to a very large negative contribution from the $A \cdot p$ term of nearly 2 eV, which is far larger than the spacing of the bare emitter levels. In contrast, no such near-resonance is found in the variational framework because the plasma term in Eq. (7) blue-shifts all of the photon frequencies. For the largest coupling considered in Figure 2, we find that the lowest photon frequency is shifted to 0.99 eV (from 0.62 eV), far off-resonance from the bare emitter transition. The plasma term also strongly reduces the coupling between light and matter by a mechanism in which the field modes obtained from Equation (7) are screened out of the emitter, thus self-consistently reducing the strength of the coupling between matter and field (see Fig. 2b). This is a light-matter decoupling effect, which was proposed in Ref. [417], where, on the basis of photodetection probabilities for exactly-obtained excited polaritonic eigenstates in a Hopfield model, "effective field mode profiles" are obtained with a strong dip in the location of the emitter, in qualitative agreement with what we report here.

This light-matter decoupling is also reflected in Fig. 3, where we calculate a correlated ground state observable such as $\langle A \cdot p \rangle$, which is a measure of entanglement between the ground state and excitations of the photon and matter (details shown in SI). As shown in Fig. 3, numerical and variational methods capture a saturation and then decrease of this expectation value. The results of Figs. 2 and 3 demonstrate not only the accuracy of our ansatz, but provides insight into the mechanisms by which light-matter coupling saturates in the nonperturbative QED regime. The results of Figs. 2 and 3 also show that despite correlations being treated perturbatively, it remains possible for correlated observables (and energies) to be predicted with high accuracy.

Our results also demonstrate a non-perturbative theory of the Lamb shift and conse-

quently Casimir-Polder forces. In particular, it is long known that energy levels of emitters can shift as a result of virtual photon emission and re-absorption. These energy shifts, called Lamb shifts, depend on the particular position of the emitter in the photonic structure it is embedded in. These shifts not only lead to changes in the transition frequencies of the emitter, but the position dependence of these energy shifts also implies forces on the emitter, often called Casimir-Polder forces. Such forces are calculated by applying second-order perturbation theory in the form of Eq. (8) using *bare* atomic and photonic properties [320]. Our calculation of the Lamb shifts via Eq. (8) says that the shifts result from virtual emission and re-absorption of the photonic quasiparticles (the *interacting* modes), which are dependent on properties of the matter. As these interacting photon modes differ greatly from the bare modes and frequencies in the non-perturbative regime, Eq. (8) using interacting modes provides a compact, and conceptually simple extension of the theory of Lamb shifts and Casimir-Polder forces to the non-perturbative regime.

The theory posed here could form the basis of an understanding of Lamb shift, Casimir forces, and potentially many other phenomena in the ultrastrong coupling regime for complex QED systems beyond current analytical and numerical methods.

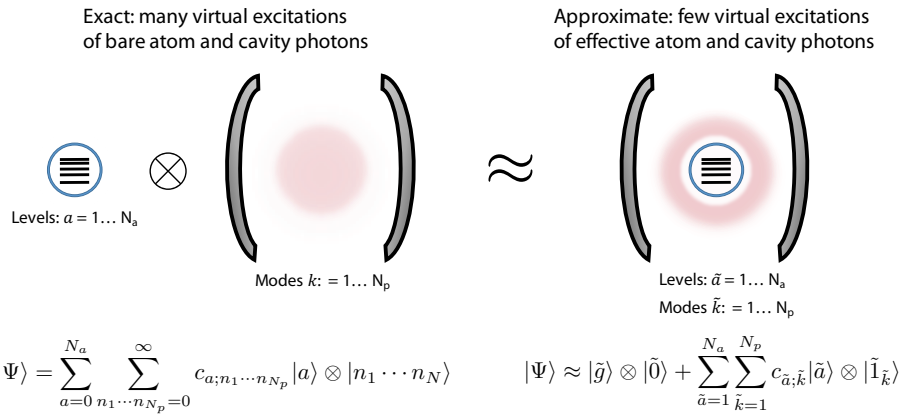

Figure 6-1: **Ground-state ansatz applied to matter in a cavity: effectively decoupled matter and photons.** (Left) Bare description of the coupled light-matter ground state in terms of many virtual excitations of the emitter state and the bare cavity photons. (Right) Quasiparticle description of the coupled system as a factorizable state of an effective emitter in its ground state and the vacuum of an effective photonic degree of freedom.

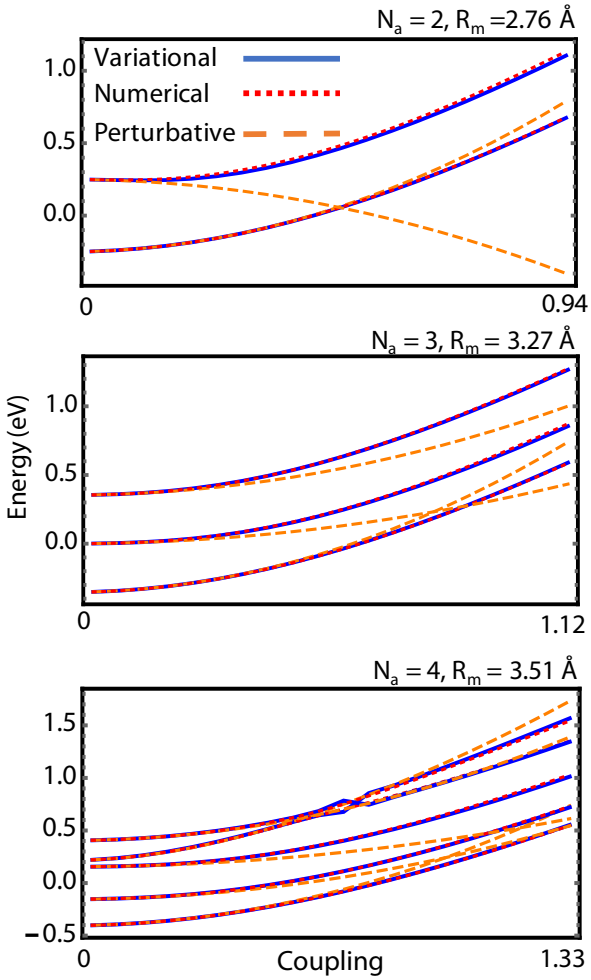

Figure 6-2: **Variational theory of ground and excited states in non-perturbative QED.** (a) Lowest few energy levels of a two (top), three (middle), and four (bottom) level system embedded in the middle of a one-dimensional cavity. The results of the variational method (blue) are compared to perturbation theory (orange), as well as numerical diagonalization (red) with the Fock space truncated to fifty cavity modes with no more than four photons. (Inset) The fourth and fifth energy levels show a weak anti-crossing behavior which is reproduced by the variational theory. (b) Mechanism of overestimation of couplings and resonances in perturbation theory: modes derived from the variational theorem are suppressed in the vicinity of the emitter, self-consistently decreasing light-matter coupling.

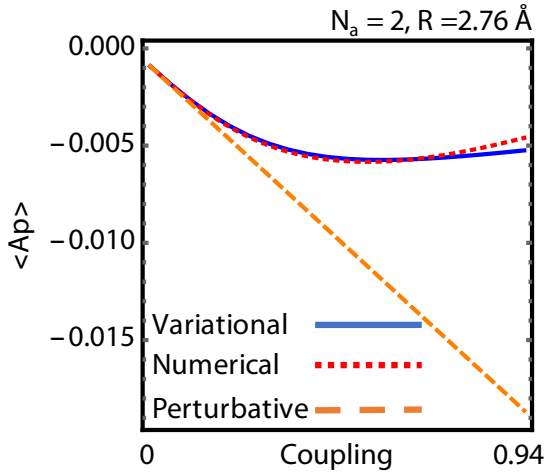

Figure 6-3: **Expectation value of the correlated observable $\langle A \cdot p \rangle$ as a function of coupling.** Parameters are identical to those of the top panel of Fig. 2a. Despite correlations being treated perturbatively, this observable is in excellent agreement with exact diagonalization, while in poor agreement with perturbation theory in the bare photonic modes.

Chapter 7

Nonperturbative quantum nonlinearities and Fock-state lasers based on deep-strong coupling of light and matter

Note: This chapter is heavily based off "Nonperturbative quantum nonlinearities and Fock-state lasers based on deep-strong coupling of light and matter", by N. Rivera et. al. arXiv:2111.07010

Light and matter can now interact in a regime where their coupling is stronger than their bare energies. This deep-strong coupling (DSC) regime of quantum electrodynamics promises to challenge many conventional assumptions about the physics of light and matter. Here, we show how light and matter interactions in this regime give rise to electromagnetic nonlinearities dramatically different from those of naturally existing materials. Excitations in the DSC regime act as photons with a linear energy spectrum up to a critical excitation number, after which, the system suddenly becomes strongly anharmonic, thus acting as an effective intensity-dependent nonlinearity of an extremely high order. We show that this behavior allows for *N-photon blockade* (with $N \gg 1$), enabling qualitatively new kinds of quantum light sources. For example, this nonlinearity forms the basis for a new type of gain medium, which when integrated into a laser or maser, produces large Fock states (rather than coherent states). Such Fock states could in principle have photon numbers orders of

magnitude larger than any realized previously, and would be protected from dissipation by a new type of equilibrium between nonlinear gain and linear loss. We discuss paths to experimental realization of the effects described here.

Recent successes in the coupling of matter and light now make it possible to realize regimes of light-matter interactions in which the coupling between light and matter can be much stronger than in established optical technologies. Because of the central role the physics of light and matter plays in many fields, these new coupling regimes are being intensely explored. One such example is the ultra-strong coupling regime, where the coupling energy is within an order of magnitude of the bare energies of the light and matter [21]. Such regimes promise to give rise to new chemical processes [418, 154, 419, 164], strong modifications of transport and thermodynamic properties of materials [420, 221], new phases of matter, quantum simulators, and quantum technologies more broadly [21, 20].

Taking these ideas to their logical extreme is the so-called *deep-strong coupling regime* (DSC), where the strength of the coupling is *greater* than the bare energies of the light and matter. In the past few years, the first experiments in this regime have emerged [168, 167]. Much of the interest in ultra-strong and deep-strong coupling is focused on the properties of the ground state of either one or many emitters coupled to a cavity mode, leading to many interesting new phenomena such as light-matter decoupling [171, 173], population collapses and revivals [421], large Lamb shifts leading to inversion of qubit energy levels [168, 422], and renormalization of qubit energy levels by a photonic continuum [167]. Likely, many of the potential applications of this regime have yet to be identified.

Here, we consider the opportunities afforded to us by the excited states of a DSC system, which are important from the perspective of quantum and nonlinear optics. For example, the emission of light in such systems probes the excited states. First, we show that deep-strong coupling of a two-level system to a resonant cavity leads to the formation of excitations ("photonic quasiparticles" [423], which we refer to as "DSC photons") with nonlinear properties much different than those in any known system. Then, we analyze the coupling of an emitter to this nonlinear photonic quasiparticle. We find that the coupling of an excited two-level system to this nonlinear system enables a phenomenon of N-photon blockade in which N excitations can be populated, but $N+1$ cannot. We show that a laser

or maser based on stimulated emission of DSC photons behaves fundamentally differently from a conventional maser or laser. Specifically, this maser produces close approximations to Fock states in its steady-state, rather than coherent states, as in conventional lasers. They could have a few hundred photons, thus being orders of magnitude larger than any Fock states realized thus far. Moreover, Fock states produced by this mechanism are stable against dissipation as they arise from a new type of equilibrium between nonlinear gain and linear loss. Our results may thus help to address the long-standing problem in quantum science of generating Fock states. Finally, we discuss how the concept developed here can be implemented in superconducting qubit platforms.

7.1 Nonlinear photonic quasiparticles based on deep strong light-matter coupling

Fundamental to our results is the spectrum of a two-level system (qubit) interacting with a single-mode cavity (schematically illustrated in Fig. 1a), which we review here [424]. The Hamiltonian, referred to as the (generalized) Rabi Hamiltonian, is given by

$$H_{\text{Rabi}}/\hbar = \frac{1}{2}\left(\omega_0\sigma_z + \lambda\sigma_x\right) + \omega a^\dagger a + \tilde{g}\sigma_x(a + a^\dagger). \tag{7.1}$$

Here, ω_0 is the transition frequency of the two-level system, $\sigma_{x,z}$ are the x and z Pauli matrices, ω is the cavity frequency, $a^{(\dagger)}$ is the cavity annhilation (creation) operator, and $\tilde{g}$ is the Rabi frequency. It will be convenient to non-dimensionalize the coupling as $g = \tilde{g}/\omega$. We have also generalized the standard Rabi Hamiltonian by including a term $\lambda\sigma_x$ which is relevant in contexts of superconducting qubits with applied bias fluxes [168]. For simplicity of presentation, we consider the case of $\lambda = 0$, which leads to approximately degenerate spin states (and in which case the qubit frequency is ω_0). In the Appendix (App. F, referred to as SI), and in various numerical results, we do consider the effect of a finite λ term, which yields the same qualitative conclusions.

While the Rabi Hamiltonian cannot be analytically diagonalized in general, an approximate spectrum can be found for the regime $g \gg 1$, which forms the basis for our analytical

theory. In the SI, it is shown that the approximate eigenstates are labeled by an oscillator quantum number $n = 0, 1, 2, \ldots$ and a spin quantum number $\sigma = \pm 1$. These eigenstates $|n\sigma\rangle$ and corresponding energies $E_{n\sigma}$, for $g \gg 1$, are given by

$$|n\sigma\rangle = \frac{1}{\sqrt{2}}\left(D^\dagger(g)|n, x+\rangle + \sigma D^\dagger(-g)|n, x-\rangle\right)$$
$$E_{n\sigma}/\hbar = \omega(n + \frac{\sigma}{2}e^{-2g^2}L_n(4g^2)), \tag{7.2}$$

where $D(z) \equiv \exp\left[z(a^\dagger - a)\right]$ is the displacement operator, and L_n is the Laguerre polynomial of order n. The state $|n\rangle$ on the right-hand side refers to the Fock basis of the cavity, while the states $|x\pm\rangle$ refer to the x-polarized spin states of the qubit. The spectrum is plotted in Fig. 1b (adding an g-dependent offset $\hbar\omega g^2$ for convenience). As seen in Eq. (2), the spectrum in the DSC regime is organized into two oscillator-like ladders (one for each spin). Moreover, for large g, the spectrum appears almost completely harmonic, indicating the existence of an effective photon (or photonic quasiparticle, which we will sometimes call a DSC photon). To understand this, we note that for $g \gg 1$, the σ_z acts as a perturbation to the remaining Hamiltonian, $H_{\text{DSC}}/\hbar \equiv \omega a^\dagger a + g\sigma_x(a + a^\dagger) = \omega(b^\dagger b - g^2)$, where $b = D^\dagger(g\sigma_x)aD(g\sigma_x) = a + g\sigma_x$. This approximate Hamiltonian admits a harmonic spectrum, in which the new oscillator variables b obey canonical commutation relations $[b, b^\dagger] = 1$, and excitations are constructed by applying further $b^\dagger$ operators. In other words, the eigenstates of H_{DSC} are Fock states of b, or equivalently, displaced Fock states of a.

The σ_z term breaks the even spacing of the ladder, leading to an anharmonicity (equivalently, nonlinearity) which we now quantify. Without loss of generality, we will focus on the lower-energy $\sigma = -1$ ladder, enabling us to omit the spin index in our notation. We assess the "harmonicity" of the spectrum by plotting successive excitation energies $E_{n+1} - E_n$ as a function of n, as in Fig. 1c (in units of $\hbar\omega$). We will refer to n as the "photon number." For strong and ultrastrong coupling, the spectrum is anharmonic at the level of a single photon, leading to the familiar phenomenon of photon blockade. For deep-strong coupling, the behavior is quite different: the spectrum is harmonic up to some critical excitation number ($n_c \sim g^2$), and then rapidly becomes anharmonic. This may be seen directly from the properties of $L_n(x)$.

To understand the relation of this strong anharmonicity to existing nonlinear optical systems, recall that a single-mode cavity with an embedded Kerr nonlinear medium can be described by a Hamiltonian of the form $H_{\text{Kerr}} = \hbar\omega\left(a^\dagger a + \beta a^{\dagger 2} a^2\right)$ [425, 426], with β a (typically small) dimensionless coefficient. In such a system, the energy to add an excitation is $E_{n+1} - E_n = \hbar\omega(1 + 2\beta n)$, meaning that the deviation from harmonic behavior is linear in the intensity (proportional to photon number). Thus, the plots of 1(c), for a photon in a Kerr medium, would be straight lines with slope 2β. This linear dependence arises from a low-order expansion of the nonlinear medium polarization in the cavity electric field: in this case third order, leading to a refractive index dependent on intensity. Here, in the case of DSC, the difference is that the excitation energies are not linear in intensity, but instead are high-order near the critical photon number (more or less growing exponentially before oscillating, as in Fig. 1c), as if the effective polarization had a non-perturbative, or infinite-order, dependence on intensity (as if the system were described in terms of $\chi^{(n)}$s where $n \gg 1$).

7.2 Light emission in the deep-strong coupling regime

The nonlinearity perspective presented here, although not previously noted in the literature, is largely based on the known spectrum of DSC systems. We now use this perspective to develop the main new results of this paper. Specifically, we study how light emission is modified by these photonic quasiparticles. Unlike most studies of light emission with photonic quasiparticles (reviewed for example in [423]), here we look at the unique modifications coming from the nonlinear properties. Consider an external qubit (denoted 'em', for emitter) coupled to this DSC photon. The exact form of the coupling depends on the circuit implementation. To keep the discussion concrete, we will consider a simple coupling Hamiltonian of the type

$$\begin{aligned} H &= H_{\text{Rabi}} + \frac{\omega_0^{\text{em}}}{2}\sigma_z^{\text{em}} + V \\ V/\hbar &= \epsilon\sigma_x^{\text{em}}(b + b^\dagger) \approx \epsilon(\sigma_+^{\text{em}} b + b^\dagger \sigma_-^{\text{em}}), \end{aligned} \tag{7.3}$$

which couples the emitter directly to the DSC photon. Regarding the assumed form of the Hamiltonian, we note that our conclusions are not particularly sensitive to the exact form of the interaction [1]. What we do assume however is that ϵ is small, so that the coupling of the external emitter to the DSC system is weak ($\epsilon \ll \omega$). Thus, the system in mind is a single resonator coupled to two qubits, one with weak coupling and one with deep strong coupling, as illustrated in Fig. 2a.

To understand emission and absorption of DSC photons, consider the case in which the qubit is in its excited state $|e\rangle$ and there are n DSC photons present of spin -1 (e.g., occupying the state $|n,-1\rangle$ of Eq. (2)). If the qubit is at frequency ω (same as in Eq. (2)), then the qubit transition will be nearly resonant with the transition $n \to n+1$ of the DSC photon, provided $n \lesssim n_c$. The dynamics can be restricted to the subspace $\{|e,n\rangle, |g,n+1\rangle\}$, and the probability of (stimulated) emission $P(n+1)$ is simply given by

$$P(n+1) = \frac{(n+1)\epsilon^2}{\Delta_{n+1}^2 + (n+1)\epsilon^2} \sin^2\left(\sqrt{\Delta_{n+1}^2 + (n+1)\epsilon^2}t\right)$$
$$\Delta_{n+1} = \frac{\omega}{2}\left(\delta - \frac{1}{2}e^{-2g^2}(L_n(4g^2) - L_{n+1}(4g^2))\right). \tag{7.4}$$

Here, δ is the dimensionless detuning of the emitter and ω, such that $\omega_0^{\text{em}} - \omega \equiv \omega\delta$. Eq. (4) is the direct consequence of the Jaynes-Cummings dynamics of a two-level system (emitter) with a boson (DSC photon) with some detuning. The detuning depends on excitation number due to the nonlinearity of the DSC photon, and the detuning sharply rises near n_c (Fig. 1c). In Fig. 2a, we plot the stimulated emission probability as a function of n after a small evolution time $t \ll \epsilon^{-1}$ and for $\delta = 0$. For $n < n_c$, $\Delta_{n+1} \approx 0$, that probability is simply $(n+1)(\epsilon t)^2$, corresponding to stimulated emission proportional to $n+1$, as expected for conventional photons. For $n \gtrsim n_c$, the emission probability drops rapidly, because of

[1] The term $\sigma_x^{\text{em}}(b + b^\dagger)$ contains an interaction between the dipole moment of the emitter and that of the qubit. Such interactions are to be generically expected, as especially emphasized in recent works on superradiant phase transitions, as well as gauge invariance in ultrastrong coupling cavity and circuit quantum electrodynamics [427, 428, 429, 430, 431]. We could write the term in question as $\alpha\sigma_x^{\text{em}}\sigma_x$. Here, $\alpha = 2\epsilon g$. Because this dipole-dipole term leads only to changes in spin quantum number, and not changes in excitation number (see SI), and because the spins are not separated by ω, these terms have little effect on the dynamics of the photon number probabilities that we consider. For example, we find that ignoring this term altogether leads to the same conclusions. Hence, for the purposes of the manuscript, we have taken a simple coupling that illustrates the physics best (emission of a "b" particle by an emitter).

the corresponding rapid increase in Δ_n. This can be understood as a type of N-photon blockade, in which a system can readily accept N excitations, but not $N+1$. For $N=1$, this corresponds to the conventional photon blockade observed and discussed extensively in strong coupling cavity QED.

7.2.1 A new type of laser

Eq. (4) displays one of the main results: that the high-order nonlinearities arising from non-perturbative quantum electrodynamical coupling lead to a type of gain (stimulated emission) that is correspondingly non-perturbative in intensity. One may imagine that this type of nonlinear stimulated emission would have implications for lasers – or in this case, masers, given that the most imminent implementations, based on circuit QED, would be at microwave frequencies. We will stick to the term "laser" since it has largely subsumed masers. In this section, we show that the DSC-based gain discussed before creates lasing into high-order Fock states (rather than coherent states).

We now show how the nonlinear gain provided by the coupling of an excited two-level system to DSC photons can result in a laser with new steady state photon statistics. To capture the resulting lasing dynamics in a quantum mechanical way, we shall find an equation of motion for the reduced density matrix ρ of the DSC photon (tracing out the gain medium). This equation takes into account both the stimulated emission dynamics and the loss dynamics associated with, for example, leakage from the cavity (which we take here for simplicity as the primary loss mechanism for the DSC photon). In the SI, we derive the equation using several methods, all in agreement with each other. Here, we focus on the equation for the DSC photon occupation probabilities, ρ_{nn}. Assuming that excited states of the gain medium are pumped at rate r, the equation of motion for the DSC photon density matrix is found to be:

$$\begin{aligned}\dot{\rho}_{nn} = {} & R_n n \rho_{n-1,n-1} - (R_{n+1}(n+1)\rho_{nn} + \kappa_n n \rho_{nn}) \\ & + \kappa_{n+1}(n+1)\rho_{n+1,n+1}\end{aligned} \tag{7.5}$$

Here, $R_n = \frac{2r\epsilon^2}{\Gamma^2 + F_n}$ is the stimulated emission coefficient, with the quantity $F_n \equiv 4n\epsilon^2$

$+\frac{1}{4}\omega^2 e^{-4g^2}(L_n(4g^2) - L_{n-1}(4g^2))^2$. The R_n are plotted (green curves) in Fig. 2b for different coupling strengths. For weak coupling, it is simply saturable gain $R(n) \sim 1/(1 + n/n_s)$ with n_s the saturation photon number. For DSC, we see that the gain coefficient is given by the standard saturable form for $n < n_c$ and then rapidly decays for $n \gtrsim n_c$ (with occasional oscillations arising from the oscillatory behavior of the Laguerre polynomials). Here, $\kappa_n = \kappa|\langle n-1|a + a^\dagger|n\rangle|^2$, with κ the decay rate of the cavity in the absence of DSC (see App. F for derivation). We note that for simplicity, the gain medium has been taken to have population and coherence decay rates arising from the same source (so that $\Gamma = 1/T_1 = 2/T_2$). This simplifies the calculations but does not qualitatively change our conclusions.

The steady state photon probability distribution is entirely different from that of a traditional laser, which produces a dephased coherent state. To quantify this, we solve a recursion relation to obtain the steady-state probability distribution $\rho_{n,n} = Z^{-1} \prod_{m=1}^{n} R_m/\kappa_m$, with Z a normalization coefficient enforcing $\sum_n \rho_{n,n} = 1$. In Fig. 2c, we show the intracavity photon number and photon fluctuations for DSC in comparison with weak coupling. We also present the corresponding photon statistics. In the weak coupling regime, the photon number as a function of pump follows the canonical "S-curve" relating the input pump and output intensity of a laser. The output intensity grows sharply for pump beyond the threshold pump level, $r_{\text{th}} = \kappa\Gamma^2/2\epsilon^2$. The fluctuations below threshold are essentially those of a thermal state, and far above threshold, grow according to shot-noise (as $\sqrt{n}$, as for a Poissonian distribution corresponding to a randomly-phased coherent state): this is the textbook result of the laser theory of Lamb and Scully [432, 433]. In contrast, the "Fock laser" ($g = 5, 10, 18$), saturates (at $n_c \sim g^2$), and the photon number fluctuations go to zero, leading to the quantum statistics of a Fock state (Fig. 2c, right) as the pump increases. Fig. 2c (bottom) further shows how the photon statistics evolve with pump and coupling (taken for $g = 10$; additional results shown in SI). Beyond threshold, the distribution of photons (for DSC) approaches that of a thermal state of negative temperature. Such states, as the pump is increased (and $T \to 0^-$), approach states where only the highest-most level is filled, with minimal spread, which closely approximates a Fock state of n_c DSC photons.

To understand this Fock lasing effect, it is helpful to refer to the gain and loss curves of

Fig. 2b, as well as the steady-state distribution $\rho_{n,n} = Z^{-1} \prod_{m=1}^{n} R_m/\kappa_m$. The steady-state distribution has the property that the probabilities are maximized where gain equals loss, and probabilities are suppressed if one of gain or loss far exceeds the other. In particular, the larger the angle between the gain and loss curves (at the crossing point), the tighter the concentration of probabilities about the mean. Increasing the pump rate r further will scale the gain curve up, leading to a steeper slope and further suppression of photon number fluctuations, leading asymptotically to a Fock state.

Beyond these close approximations to high-photon-number Fock states, other unusual states can arise from the equilibrium between gain and loss, due to this sudden anharmonicity for $n \gtrsim n_c$. For example, near threshold, where the number fluctuations increase dramatically, the resulting distribution is nearly step-like, going to zero rapidly for n_c. This anharmonicity provides a "wall" for the photon probability distribution that is too hard to pass through, even as the fluctuations get very large near threshold. These effects also depend on the decay rate of the gain medium: if the decay rate is high, then it provides gain over a large bandwidth, and so changes in the DSC photon frequency have a reduced effect on the stimulated emission rate R_n. As a result, for increasing pump, the distribution can "tunnel" through the wall, leading to states that interpolate between Fock and coherent states, as well as pure coherent states for large enough pump.

7.3 Discussion and outlook

Recent work on realizing deep-strong coupling of superconducting qubits to a microwave (LC) resonator, as in [168, 422], provides a path to observing the effect predicted here. It is already possible to have control over g from weak coupling to a value of nearly 2. With a g of 2, one can see from Fig. 1 that a Fock state of three or four excitations could be pumped. For smaller g, in the ultra-strong coupling regime where $0.1 < g < 1$, only one excitation can be created, as a manifestation of the conventional photon blockade effect [434, 435]. Thus, the behavior of our model from weak to (modest) deep strong coupling can already be realized.

Regarding the gain medium, it is important to point out that while a typically gain

medium consisting of many emitters, the physics can also be realized by a gain medium consisting of a single qubit. The qubit should be weakly coupled to the same cavity as the strongly coupled qubit, and will lase, provided that the gain from this one qubit is above threshold [433]. Single-qubit gain is responsible for much of the exciting experiments on "one-atom lasers" (in real [436, 437] and artificial atoms [438, 439, 440]), in which a single atom or artificial atom provides enough gain to lase.

Thus, a conceptually simpler − and perhaps more attractive − approach to realize our predictions is to consider a gain medium consisting of a continuously pumped superconducting qubit which is *weakly* coupled to the same resonance as the strongly coupled qubit (which for example happens if $\epsilon \ll \kappa$). In Fig. 2, we took $\epsilon = 10^{-5}\omega$, and $\Gamma = 10^{-3}\omega$. Thus, for a single gain qubit, threshold is reached provided the quality factor of the resonator is above 5×10^6. There are two advances that would support reaching larger g values: the rapidly increasing coupling constants that have been realized with superconducting qubits (see Fig. 1 of [20]), and early estimates in this field suggesting the possibility of g values of roughly 20 [441]. Another important point is that while we have focused in this paper on incoherent pumping (based on emission from two-level systems), the nonlinear emission physics described in this manuscript could also be extended to coherent pumping of the DSC photon by an external microwave signal. In that case, we expect that by combining the high-order nonlinearity of the DSC photon with a frequency-dependent leakage loss (e.g., loss coming from a reflection filter), one could engineer a highly nonlinear loss which would be "dual" to the highly nonlinear gain introduced in Fig. 2.

Summarizing, we have shown a physical principle – using non-perturbative photonic nonlinearity – which could enable lasers that produce deterministic, macroscopic quantum states of light, such as Fock states. Part of the new physics uncovered here, related to lasing in systems with sharply nonlinear gain, could in principle also be extended into the optical regime. In fact, in [442] − inspired by the developments in this manuscript − we discuss how trying to mimic the new "Fock lasers" predicted here, but at *optical frequencies*. This is done essentially by combining a highly frequency-dependent loss with Kerr nonlinearities to get an effectively non-perturbatively nonlinear loss. Thus, the principles established here, independently of deep-strong coupling, should also give rise to new ideas

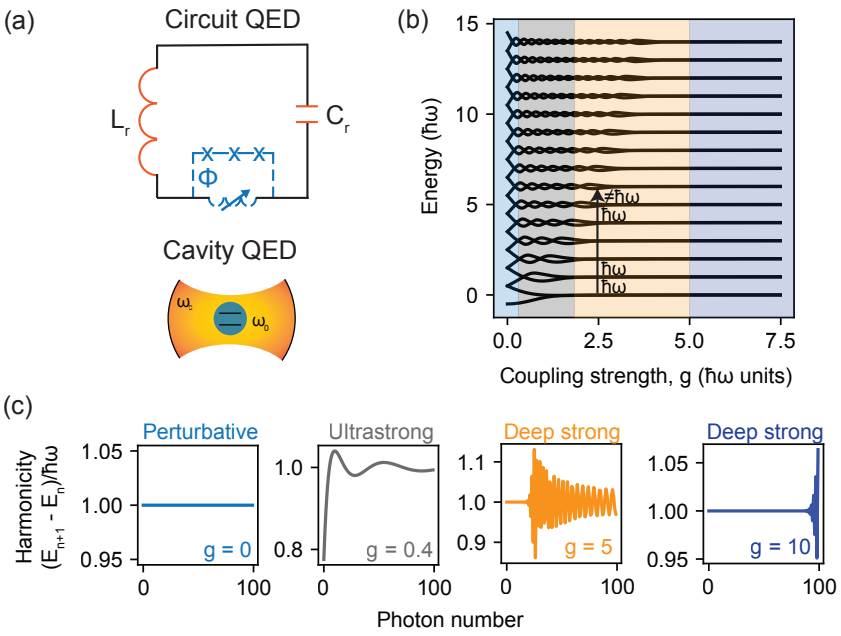

Figure 7-1: **High-order nonlinearities in deep strong coupling of light and matter.** (a) Schematic of a two-level system coupled to a single resonator mode, as in circuit or cavity QED. (b) Spectrum of the system from weak ($g = \tilde{g}/\omega \ll 1$) to deep-strong coupling ($g \gg 1$). Here, $\lambda = 0$. (c) Successive excitation energies for a single spin sector for different coupling values. For $g \gg 1$ the excitation energies are constant, as for a bare photon. At large photon number, they deviate rapidly and nonlinearly from harmonicity, akin to a photon with a strongly intensity-dependent nonlinearity.

and experiments in the optical domain.

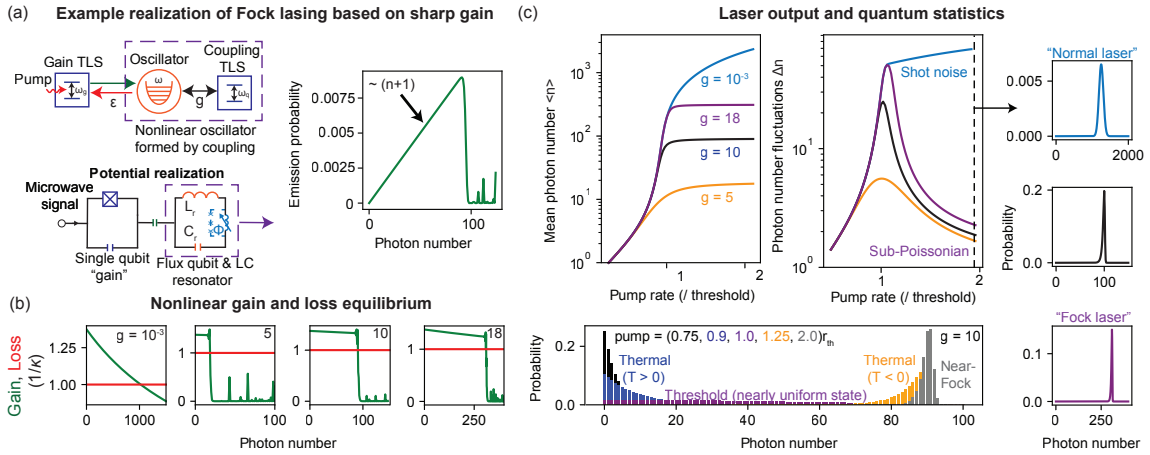

Figure 7-2: **Fock lasing due to equilibrium between high-order nonlinearity and dissipation.** (a) Light emission of DSC photons can be understood in terms of the coupling of an emitter (e.g., a probe qubit) weakly coupled to the DSC system, as might be realized by coupling a superconducting qubit to a flux-qubit-LC-resonator system. The probability to stimulatedly emit DSC photons scales as $n+1$ for small n, and then sharply decreases due to the sudden anharmonicity for $n > n_c \sim g^2$. "TLS" denotes two-level system. (b) This behavior leads to a gain medium whose gain coefficient (green lines) is highly nonlinear. The quantum state of DSC photons will depend on how this nonlinear gain comes into equilibrium with the loss (red lines). (c) Steady-state intensity and power fluctuations of lasers in different coupling regimes as a function of pump intensity. For the "harmonic" regimes (weak, and deep-strong), a rapid growth in intensity at threshold is seen. In contrast to the weak coupling regime (as in a "normal" laser; light blue curve), a laser operating in the deep-strong coupling regime has its intensity saturate, and its fluctuations vanish at high pump, converging to a high-number Fock state (dark blue and purple curves), leading to Fock-like statistics (right). (c, bottom) Statistics for different pump strengths for a single coupling, showing evolution from thermality to Fock-like statistics.

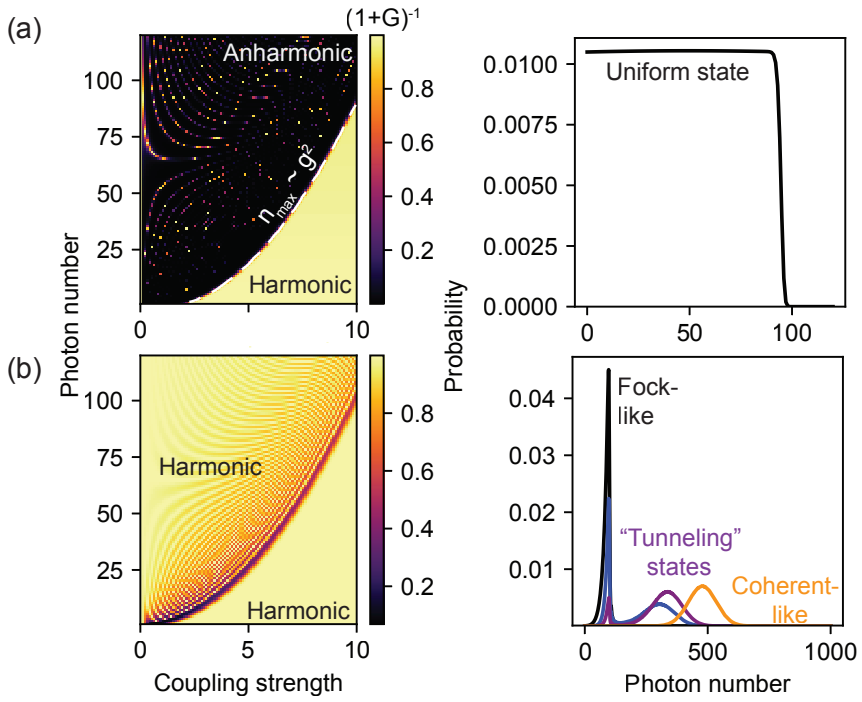

Figure 7-3: **Uniform and tunneling states arising at the harmonic-to-anharmonic crossover.** (a) The function $(1 + G_n))^{-1}$ which propagates the photon probability distribution from n to $n + 1$, plotted as a function of coupling strength and photon number ($G_n = F_n/\Gamma$). A harmonic-to-anharmonic crossover occurs for a maximum photon number $n_{\text{max}} \sim g^2$ for which the propagation function goes to zero. When this happens, the probability of having photons larger than n_{max} vanishes. Near threshold (where the effective temperature of the photon goes to infinity), this leads to nearly uniform states of the electromagnetic field sharply cutoff at the maximum photon number (right panel). (b) When the decay rate of the gain medium is large, the anharmonic region becomes narrower (bottom left), and for sufficient pump intensity, the photon distribution can "tunnel" through the barrier, evolving effectively as a coherent state. In this tunneling regime, the distribution becomes bimodal, taking on the characteristics of the Fock and coherent states for some pump parameters (bottom right).

Chapter 8

Complete condensation of photon noise in nonlinear dissipative systems

Note: This chapter is heavily based off "Complete condensation of photon noise in nonlinear dissipative systems", by N. Rivera et. al. arXiv:2111.03099

Macroscopic non-Gaussian states of light are among the most highly-coveted "holy grails" in quantum science and technology. An important example is that of macroscopic number (Fock) states of light, which, being the most fundamental states of radiation, are considered an important resource for many quantum tasks including metrology, communication, simulation, and information processing. However, the deterministic creation and stabilization of even approximate large-number Fock states remains an open problem. This is especially so at optical frequencies, where it is difficult to produce Fock states with more than a single photon, let alone at macroscopic scales. Here, we introduce a mechanism to deterministically generate macroscopic Fock states and close approximations – at optical frequencies. The mechanism is based on a new type of intensity-dependent (nonlinear) dissipation in which: a nonlinear resonance is dissipationless when it has a particular number of photons inside it, and is lossy otherwise. We show that an initially noisy quantum state of photons, undergoing this dissipation, can experience *complete* condensation of intensity noise, such that over time, the noisy state evolves into a large Fock state. We further show that even in the presence of external destablizing effects (like linear loss), extremely

low-noise states can be stabilized in time. This is done by building a laser (called the "Fock laser") which stabilizes the macroscopic quantum state in an equilibrium between gain and the introduced nonlinear dissipation. Throughout the text, we present examples showing the types of systems that could realize these effects. In one, we show how strongly-coupled systems, with their strong nonlinearities, could be used to create optical Fock states of $n = 1000$. In another, we show how standard laser architectures could be leveraged to generate macroscopic light ($> 10^{12}$ photons) with extreme levels of broadband photon-number squeezing (nearly 95% less noise than the standard quantum limit). When realized, our results could enable many of the previously envisaged applications of optical number states for quantum algorithms, simulation, metrology, and spectroscopy. Moreover, because the effects we introduce here are general to nonlinear bosonic systems beyond optics, we expect the physics introduced here to enjoy wide application in many other fields.

Much of the current focus in quantum optics is on the generation and application of quantum states of light, such as single-photons, entangled photon pairs, cluster states, and quadrature-squeezed light [443, 444, 445, 446, 447, 448]. Such states enable the extension of important applications − such as information processing, simulation, precision measurement, and communication − beyond the limits imposed by classical physics.

While these states are already useful, a complete transformation of the quantum landscape is expected if macroscopic non-Gaussian states of light, which offer the most unique degree of quantum advantage, could be deterministically realized. As one concrete example, consider what would happen if one could realize an extremely nonclassical state, such as a large Fock state of light. Such states have long been eyed in quantum metrology because they have a perfectly defined intensity that would enable measurements without shot noise [449, 450, 451]. They are also considered valuable in simulation and information processing tasks. Perhaps one of the highest-profile applications of large Fock states would be for a quantum algorithm such as boson sampling (or gaussian boson sampling) [452, 453, 454, 455, 456, 457]: a "modest" (multimode) Fock state of even 100 photons enables computations of matrix permanents at least fifteen orders of magnitude larger than could be handled by even the largest supercomputers today [458], and could resoundingly

bring the promise of quantum computation to reality.

Despite the potential rewards, deterministic generation of macroscopic Fock states of light, in *any* setting, remains an open problem, limiting the attainable benefit in applications. Part of the reason is that the well-established interactions between light and matter do not naturally select for large-n Fock states. This is in contrast to, say, states like coherent states and quadrature-squeezed states, which can be macroscopically produced by means of lasers or nonlinear media [433]. The other key issue is that Fock states are fragile and destabilize in the presence of dissipation [459]. Due to these challenges, the approach that has led to record Fock states (about 15 microwave photons) is based on transient accumulation of photons in a cavity at precise times using cavity quantum electrodynamical interactions with superconducting qubits, as demonstrated in [459, 460]. Fock states generated this way could then be used as a resource state to simulate vibronic excited-state spectra of molecules [461]. It is important in these techniques that the photons are built up before losses set in, setting the maximal Fock state that is generated. Other exciting schemes applied at microwave frequencies include the "micromaser" [433, 462, 463] and quantum feedback protocols [464]. Such techniques cannot at present be extended to optics: thus, generating Fock states of more than one photon is difficult (one-photon states are generated by quantum emitters and also by heralding photon pairs produced by parametric down-conversion [157]). Fock states can also be non-deterministically generated by collapsing the wavefunction in the number basis [465, 466] or via quantum non-demolition measurement [467].

Here, we introduce a fundamentally new physical effect that enables the generation of macroscopic optical Fock states and close approximations thereof. We will show how existing systems can potentially be leveraged to produce Fock states of light with photon numbers orders of magnitude above what has been realized, or even predicted. Even when exact Fock states are not produced, the resulting states can have very low photon noise (extreme squeezing) that often exceeds that available in all known schemes for reducing photon noise. Central to the developments in this paper is a new type of dissipative nonlinearity that we identify (and show how to construct), which naturally produces Fock states.

We start by describing the new effects and the intuition behind them. Consider a non-

linear resonance with dissipation (e.g., a leaky mode of a nonlinear cavity), as illustrated in Fig. 1a. Suppose that the loss rate, $\kappa(n)$ of the mode depends on the number of photons in the cavity, n, in the way shown in Fig. 1b. Namely, the nonlinear loss should have regions where the loss increases rapidly with intensity. Ideally, the loss also has a zero for some special photon number n_0. In such a system, Fock and highly photon-number-squeezed (or "sub-Poissonian") quantum states of light can be created. To see how, consider the time evolution of the probability $p(n)$ that the resonance has n photons. If the distribution is concentrated above the minimum of the loss at time t_0 (pictured in Fig. 1b), it will eventually fall through the region of sharply increasing loss. This will cause the probability distribution to condense, because the tail of the distribution on the high-number side moves towards lower photon numbers faster than the tail on the low-number side (see Fig. 1c). On the other hand, if the distribution falls through a region of decreasing loss, the distribution will expand (by similar reasoning). If the loss has an exact zero at photon number n_0, then Fock states of photon number n_0 are created because the probability distribution will get stuck: it cannot move towards lower photon numbers, while the high-number tail gets pushed towards the zero. The special nonlinear loss required to realize the effect can arise by a combination of (1) frequency-dependent loss (for example, if an element of the cavity has frequency-dependent transmission out of the cavity) and (2) Kerr nonlinearity, which leads to a photon-number-dependent resonance frequency (because the index of refraction, and thus the resonance frequency of the cavity depends on the intensity or equivalently the cavity photon number). As we will show rigorously, the frequency-dependent "loss" and the photon-number-dependent "frequency" compose (in the sense of function composition) to create just the right number-dependent loss (as illustrated schematically in Fig. 1d). For example, for a certain number of photons n_0 in the cavity, the resonance frequency $\omega(n)$ will be exactly ω_0, corresponding to the zero of the transmission in Fig. 1d, and thus at n_0 photons, the cavity becomes lossless. As we shall discuss later (in Figs. 3 and 4), this nonlinear loss can be then used in place of conventional linear loss in any device that establishes equilibrium between pumping and damping (e.g., a pumped cavity, or a laser). For example, when the nonlinear loss of Fig. 1b is used in place of linear loss in a laser, the equilibrium state of the cavity photons that is established has very low intensity noise

(approaching a Fock state).

In what follows, we provide details to the picture painted above. We start by identifying a broad class of physical systems, of the form schematically illustrated in Fig. 1e, that can implement the proposed nonlinear loss and noise condensation effects. We explicitly show, on the basis of a quantum optical theory of nonlinear dissipation, how the described effects arise in this class of systems. Although the effect illustrated in Figs. 1a-c can appear in many more systems than the one shown in Fig. 1e, focusing on the particular type of system shown in Fig. 1e has the benefit of allowing us to rigorously prove the existence of the effect in a way that makes the assumptions and approximations clear. In the main text, we summarize those key results of the theory that underlie the analysis of the examples that we discuss. The Supplementary Information (Appendix G of this thesis; referred to as SI) systematically develops the theory in detail, showing how the effects can be derived from several approaches, all of which are in agreement: master equation methods, quantum Langevin methods, and exact numerical solutions.

8.1 A quantum nonlinear loss which naturally produces macroscopic Fock states

A broad class of physical systems which displays these effects is schematically illustrated in Fig. 1e: one nonlinear oscillator (with annihilation operator a), and one linear oscillator (annihilation operator d and frequency ω_d), coupled to a common continuum of bath oscillators (annihilation operators b_k and frequencies ω_k; k indexing the continuum). The couplings of a and d to the continuum are respectively g_k and v_k. The Hamiltonian of this general class of systems is:

$$\begin{aligned} H/\hbar = \Omega(a^\dagger a) + \omega_d d^\dagger d + \left(\lambda a d^\dagger + \lambda^* a^\dagger d\right) \\ + \sum_k \omega_k b_k^\dagger b_k + \sum_k \left(X_k b_k^\dagger + X_k^\dagger b_k\right), \end{aligned} \tag{8.1}$$

where we have considered the case of an intensity-dependent nonlinear resonance in which the energy of n excitations (photons) is given by $\Omega(n)$. For a Kerr nonlinear system,

$\Omega(a^\dagger a) = \omega_a((1-\beta)a^\dagger a + \beta(a^\dagger a)^2)$, with $\beta\omega_a$ the nonlinear strength of a single photon. The operator $X_k = g_k a + v_k d$ appearing in the Hamiltonian reflects the coupling of a, d to the common continuum. We consider the standard case in which the bath has negligible memory and may be taken to be in the vacuum state. Let us further consider systems for which the response time of the linear resonance ($\gamma = 2\pi\rho_0 v^2$, with ρ_0 the density of bath states) is much shorter than that of the nonlinear resonance ($\kappa = 2\pi\rho_0 g^2$): then, d can be adiabatically eliminated, admitting a simple equation for the dynamics of a alone.

A key result is the equation of motion for the reduced density matrix of a (denoted ρ) (see SI for derivation):

$$\begin{aligned}\dot{\rho} = &-\sum_{n=0}^{\infty} n(\mu_n T_{n,n}\rho + \mu_n^* \rho T_{n,n}) \\ &+ \sum_{m,n=0}^{\infty} \sqrt{m(n+1)}(\mu_m + \mu_{n+1}^*) T_{m-1,m}\rho T_{n+1,n},\end{aligned} \tag{8.2}$$

where $T_{m,n} \equiv |m\rangle\langle n|$, $\mu_n = \frac{1}{2}\kappa - \frac{G_+ G_-}{i(\omega_d - \omega_{n,n-1}) + \gamma/2}$, $G_- \equiv i\lambda + \frac{1}{2}\sqrt{\kappa\gamma}$, $G_+ \equiv i\lambda^* + \frac{1}{2}\sqrt{\kappa\gamma}$, and $\omega_{n,n-1} = \Omega(n) - \Omega(n-1)$. While Eq. (2) governs the entire evolution of a, we focus here on the the probability $p(n) \equiv \langle n|\rho|n\rangle$ that the nonlinear resonance has n photons. Such probabilities, when more tightly concentrated than the Poisson distribution (so that the variance $(\Delta n)^2 < \bar{n}$, with $\bar{n}$ the mean number of photons), correspond to sub-Poissonian (number-squeezed) states of light that have no classical analog [468, 450, 426] ($\Delta n = 0$ corresponds to a Fock state). The probabilities evolve as:

$$\dot{p}(n) = -L(n)p(n) + L(n+1)p(n+1), \tag{8.3}$$

where $L(n) \equiv 2n\text{Re}\ \mu_n$, the rate of transitions from the cavity state with n photons to that with $n-1$ photons, is given by

$$L(n) = n\left(\frac{\kappa\delta_n^2 + \gamma|\lambda|^2 + 2\sqrt{\kappa\gamma}\delta_n \text{Re}\ \lambda}{\delta_n^2 + \gamma^2/4}\right) \equiv n\kappa(n), \tag{8.4}$$

where $\delta_n = \omega_{n,n-1} - \omega_d$. Eqs. (3) and (4) describe a process of nonlinear dissipation in which excitations decay at a rate $\kappa(n)$ which depends on the number of excitations.

The resulting intensity-dependent loss curve $\kappa(n)$ is exactly of the form shown in Fig. 1b. The loss displays a zero for some photon number n_0. As one moves away from n_0, the loss sharply increases. Much of the behavior of Eq. (4) can be understood from the *linear* equation for the mean values of a and d, denoted $\bar{a}$ and $\bar{d}$, which reads (see SI pages 14-15):

$$\begin{pmatrix} \dot{\bar{a}} \\ \dot{\bar{d}} \end{pmatrix} = \left[-i\omega_d - \begin{pmatrix} i\delta + \frac{1}{2}\kappa & i\lambda^* + \frac{1}{2}\sqrt{\kappa\gamma} \\ i\lambda + \frac{1}{2}\sqrt{\kappa\gamma} & \frac{1}{2}\gamma \end{pmatrix} \right] \begin{pmatrix} \bar{a} \\ \bar{d} \end{pmatrix}. \tag{8.5}$$

The dissipation rates of the two coupled modes, for $\kappa \ll \gamma$, are of order κ and γ, as expected. The coupled mode with decay rate $O(\gamma)$ decays very rapidly, and can be ignored. The other mode (which is a, to order $\sqrt{\kappa/\gamma}$), has a decay rate which is simply the $\kappa(n)$ of Eq. (4), taking $\delta \to \delta_n$. The problem of two *linear* resonances coupled to a common continuum, as formulated in Eq. (5), is known to yield vanishing losses for one of the eigenvalues, resulting from interference of two leakage paths for a: one in which a passes directly to the continuum, and one in which a transits through d before going to the continuum. This is connected to effects of appreciable recent interest in photonics, such as the Fano effect [1, 469, 470] and bound states in the continuum [471, 472]. Further support for this connection is provided in SI, pages 13-16. The role of nonlinearity is to bind the leakage amplitudes to the excitation number in a, such that: for some "magic" number of excitations n_0 in a, the interference is perfect and a is lossless (vaguely reminiscent of electromagnetically-induced transparency [473]). Stated quantitatively, in the limit $\kappa \ll \gamma$, the Fano transmission profile and the nonlinear Kerr shift "compose" (as illustrated in Fig. 1d), converting a linear loss − which introduces intensity fluctuations − into a nonlinear loss, which is known to allow for the possibility of number squeezing [474, 475, 476, 477]. What will distinguish the nonlinear loss of Fig. 1b from previously explored nonlinear losses (e.g., based on multi-photon absorbers [478, 479, 480, 481]), as well as other nonlinear effects such as squeezing in parametric oscillators [482, 443, 483], is that the number squeezing can in principle be complete, yielding a Fock state of n_0 photons.

There are many physical systems that can realize the type of loss derived here, yielding many opportunities. For example, the loss of Eq. (4) could be realized in a Kerr-nonlinear cavity formed by one perfectly reflecting mirror and one mirror with a frequency-dependent

transmission (as for example in a photonic crystal mirror or an etalon): see SI for further discussion. The source of the loss does not need to be transmission: it can also arise due to internal absorption. Absorbers with more complex frequency-dependent absorption lineshapes (such as from electromagnetically induced transparency) may also display the type of zeros which would be amenable to the effects described here [473]. Our theory is also readily extendable to the case of more general filters with more complex transmission profiles (e.g., a Bragg mirror): in that case, the nonlinear loss is dictated by the frequency-dependent transmission of that system, evaluated at the nonlinear resonator frequency.

8.2 Complete condensation of optical noise

The unique form of this nonlinear dissipation leads directly to the new quantum statistical effects reported here. One such effect is transient noise condensation. Consider the evolution of the photon probability distribution $p_n(t)$ due to free nonlinear dissipation. We consider initial conditions which are purely diagonal, corresponding to de-phased light, so that the density matrix is specified at all times by the probabilities. For concreteness, consider an initially Poissonian distribution of light (as from e.g., an ideal laser pumped well-above threshold). As per the discussion surrounding Figs. 1a,b, we expect that an initially Poissonian distribution with mean photon number above n_0 should rapidly squeeze and approach a Fock state $-$ in stark contrast to the textbook case of linear loss ($\kappa(n) = \kappa$) [1]. Meanwhile an initial distribution below n_0 should expand and eventually become Poissonian.

These intuitions are confirmed by direct solution of Eq. (3) for the photon probabilities. In Fig. 2, we show the time-evolution of the photon probability distribution, as well as the mean and variance, for an example system. The parameters taken are characteristic of systems of exciton-polaritons (arising from strong coupling of a quantum well to a cavity), which have been shown to realize dissipative Kerr Hamiltonians similar to Eq. (1) (without "d") [484, 485]. The strong nonlinearities characteristic of such systems derive from

[1] In the case of linear loss, an initially Poissonian photon probability distribution will stay Poissonian, while a Fock state will have its relative fluctuations (measured by its Fano factor, $F = (\Delta n)^2/\bar{n}$) increase over time. In particular, a Fock state will evolve into a binomial distribution (with success probability $e^{-\kappa t}$, such that $F = 1 - e^{-\kappa t}$ goes to 1 (the Poisson value) as $t \to \infty$).

Coulomb interactions between excitons. By coupling the polaritons (representing "a") to a frequency-dependent loss, the system of Eq. (1) may be realized. This may be done e.g., by coupling the system to a resonator-waveguide system, introducing an absorber, or having one of the cavity mirrors be frequency-dependent (all possible manifestations of "d"). The evolution is shown for two distinct (Poissonian) initial conditions: one in which the mean photon number is below $n_0 = 1000$, and one in which it is above. The case where $\bar{n}(0) < n_0$ does not lead to any noise reduction: after becoming slightly super-Poissonian, the statistics become Poissonian as the amplitude decays to zero. In contrast, when $\bar{n}(0) > n_0$, the variance decays much faster than the mean, ultimately approaching a Fock state of $n_0 = 1000$ photons (Fig. 2c, inset).

It is important to understand that, due to the "one-way" nature of loss, residual linear loss, as well as any external effects that cause coupling to lower-photon number states, will destabilize the trapped state and limit the noise condensation. However, even when there is no longer a zero of the loss, heavily sub-Poissonian states can result – provided that the distribution falls through a region where the loss is sharply increasing (see SI Fig. S5). Such states can still fall far below the classical noise limit (beyond number-squeezing experimentally realized thus far), and are still useful for some of the applications described earlier. To explain this, we refer to the equation of motion for the mean and the variance. In the approximation where $\Delta n \ll \bar{n}$:

$$\begin{aligned} \dot{\bar{n}} &= -L(\bar{n}) \\ \dot{(\Delta n)^2} &= L(\bar{n}) - 2L'(\bar{n})(\Delta n)^2, \end{aligned} \tag{8.6}$$

where $L' \equiv dL/dn$. When $L'(\bar{n}) > \kappa(\bar{n})$, the variance will decay faster than the mean, and Poissonian light can become sub-Poissonian. This inequality can be achieved by means of a sharply increasing loss (left-hand side of Eq. (6)) and/or a loss coefficient which goes to zero (right-hand side).

8.3 Fock lasers

It is of great interest to stabilize large Fock or sub-Poissonian states in time. This can be achieved by establishing an equilibrium between a pump of energy (e.g., gain) and the nonlinear dissipation. This line of thinking motivates us to introduce and analyze the "Fock laser," shown in Fig. 3a, b: it consists of a pumped gain medium with feedback from an optical resonator. Unlike a conventional laser, the Fock laser uses a resonator with the dissipation of Eq. (4). This loss introduces a new saturation mechanism for the laser which fundamentally differs from that provided by saturable gain. In particular, we will show conditions under which the new saturation leads to steady states with far lower noise (even approaching Fock states) than would be expected (e.g., from an ideal conventional laser, with Poissonian fluctuations of cavity photon number). The number-squeezing can be quite extreme, with examples in the main text displaying nearly 15 dB squeezing over *all* frequencies and over 20 dB squeezing at low frequencies. In the SI (Fig. S4), we show how a laser with this nonlinear loss could present over 30 dB all-frequency squeezing. The theory of lasers with nonlinear loss of the type introduced here is developed in the SI.

The operating principle of the Fock laser is illustrated in Fig. 3c, where we plot the gain and loss coefficients as a function of cavity photon number for a conventional laser (with linear dissipation) versus a Fock laser (with nonlinear dissipation). We consider the ideal case of a single-mode laser in which technical noise due to pump, mechanical, and thermal fluctuations is negligible (due to e.g., active stabilization [486]). The mean photon number $\bar{n}$ in the cavity corresponds to where gain balances loss. Thus, the photon probability distribution will be centered around $\bar{n}$. The fluctuations will differ in the two cases, even when the magnitude of the gain and loss (at $\bar{n}$) are identical. The fluctuations are related to the angle of intersection between the gain and loss curves. If the curves intersect steeply, then a small change in photon number leads to a large differential between gain and loss (in absolute value). It is expected that the laser will not occupy such states with high probability, preferring states in equilibrium between gain and loss. Thus, a sharply increasing loss (and/or sharply decreasing gain; illustrated in Fig. 3c but not explored further) leads to suppression of fluctuations beyond those of the conventional laser. This

pictorial intuition becomes quantitative in the case of a gain medium where the inversion decay time is fast compared to cavity losses. Then, the equilibrium photon probability distribution is approximately $p(n) \approx e^{-\frac{(n-\bar{n})^2}{2(\Delta n)^2}}/\sqrt{2\pi(\Delta n)^2}$, where (see SI):

$$\Delta n = \frac{1}{\sqrt{-\frac{d}{dn}\frac{G(n)}{\kappa(n)}\Big|_{\bar{n}}}} \approx \frac{1}{\sqrt{\kappa'(\bar{n})/\kappa(\bar{n})}}. \tag{8.7}$$

Here, $G(n)$ is the temporal gain coefficient, and the approximation holds when the loss varies much more sharply than the gain. This equation confirms that: if κ sharply increases relative to its equilibrium value, the photon noise will be suppressed, and thus, the loss introduced in Fig. 1b facilitates the generation of low-loss equilibrium states. It is interesting to point out that the condition for non-classicality $F = (\Delta n)^2/\bar{n} < 1$, corresponds to $\kappa(\bar{n})/(\bar{n}\kappa'(\bar{n})) \approx \kappa(\bar{n})/L'(\bar{n}) < 1 \implies L'(\bar{n}) > \kappa(\bar{n})$, which was precisely the condition for transient noise condensation (see Eq. (6)). An important corollary of Eq. (7) is that in order to have $\Delta n \sim 1$, one requires the loss coefficient to change by an amount comparable to itself, over a variation of one photon.

An example of the output characteristics of a Fock laser is shown in Figs. 3(d-f), for a nonlinear resonator similar to that of Fig. 2, integrated with a gain medium (for concreteness, parameters describing the gain are those characteristic of molecular dyes). Much can be understood from the gain-loss curves, plotted in Fig. 3d, where the gain coefficient is shown for different pump intensities. Crudely speaking, stable equilibria exist at values $\bar{n}$ where $G(\bar{n}) = \kappa(\bar{n})$ and $G(\bar{n}^+) < \kappa(\bar{n}^+)$. Characteristic of these non-monotonic loss profiles are (1) multiple stable equilibria (here, at most two) and (2) stable lasing equilibria with finite photon number even when the pump is below threshold (in other words, when $G(0) < \kappa(0)$, so that the system, started from vacuum, cannot have its photon number increase). These multiple equilibria lead to distinct input-output relations between the pump and the steady-state photon number. Above a threshold pump strength P_{th}, the mean photon number increases linearly with pump strength, and the noise is substantially higher than the Poisson level, as expected for a laser weakly above threshold. At a certain intensity (here, about $1.55P_{\text{th}}$), the system discontinuously jumps to a new steady state with much larger

photon number, as well as very low noise (about 95% lower than the standard quantum limit expected from an ideal laser). If we start from this "low noise branch" and then lower the pump intensity, the system will follow the purple curve in Fig. 3e, and, as the pump goes down to zero, the stable equilibrium approaches the zero-loss point (see inset of Fig. 3d). This point, in a similar manner to Fig. 2, is accompanied by a low noise equilibrium state, which tends to a Fock state as the zero of the loss is approached. For example, for a pump strength of $0.01P_{\text{th}}$, the noise is 20 dB below the shot noise level, and the photon number uncertainty is roughly 3.

The Fock laser principle can also be fruitfully extended to truly macroscopic regimes, e.g., "conventional laser architectures" employing bulk nonlinearities to generate highly intense sub-Poissonian light. In this case, because the single-photon nonlinear shifts are quite small, one would not be able to generate a state with $\Delta n = O(1)$. However, it is in principle still possible to reduce the noise by a large fraction compared to the standard quantum limit, which, if observed, would yield record squeezing both at a single noise frequency (> 20 dB) and integrated over all frequencies (> 10 dB). An example is presented in Fig. 4 (here, parameters are characteristic of a rare-earth gain medium such as Nd:YAG). Evaluating noise spectra for the cavity photon number for two different intensities, we see that the photon noise (integrated over all frequencies) can drop nearly 95% below the shot noise limit, but at photon numbers of 10^{12}, which are clearly macroscopic. Such effects follow directly from Eq. (7), being assisted by a loss which is both sharp and small in magnitude (it is comparable to that offered by state-of-the-art supermirrors [487].)

8.4 Discussion

We have shown that a suitably designed nonlinear dissipation leads to the deterministic generation of macroscopic quantum states of light, such as Fock and heavily photon-number-squeezed (sub-Poissonian) states. The key to deterministically generating such states is a loss which sharply increases away from a minimum (of ideally zero loss). This type of nonlinear dissipation is effectively non-perturbative in intensity, in the sense that it cannot be represented as a low-order Taylor expansion about zero intensity (in the way that the loss

associated with two- or few-photon absorption can be). Although such a non-perturbative dissipation is not naturally realized in absorbing materials, we have shown rigorously in a specific class of systems (with the Hamiltonian of Eq. (1)) that the desired nonlinear loss can be constructed by combining frequency-dependent losses with Kerr nonlinearities. This effectively converts a linear loss, which spoils photon-number squeezing, into a nonlinear loss, which can induce it (through the mechanism illustrated in Figs. 1a-d). This composition of frequency-dependent loss and nonlinearity, illustrated in Fig. 1d, suggests a recipe for mitigating the effect of loss in existing experiments: the prescription is to take the dominant loss, and "make it nonlinear". The physics described by Eq. (1), namely: dissipative coupling between a linear and a nonlinear resonance, can be realized in a large class of systems both in optics and beyond $-$ implying a great variety of systems to which the physics introduced here can apply.

In this work, we have focused on the creation of single-mode Fock states, as appropriate to a mode of a resonant cavity. Such cavity fields can be directly employed for quantum spectroscopy and metrological applications (by coupling the sample to the intracavity fields, as is done in various spectroscopies) [488, 489, 490]. The intracavity states can also be directly used to realize new light-matter interactions: the strong intracavity fields could be used to strongly couple to atoms as well as pump nonlinear processes with quantum light [491, 492]. For many applications, it will be useful to couple the Fock states into the far field. The intracavity states can be emitted into the far-field by means of a fast loss modulation (cavity dumping in the gain-less case of Fig. 2, and Q-switching in the gain-ful cases of Fig. 3, 4). In either case, the cavity transmission is suddenly increased (e.g., by electro-optic modulation) relative to the (relatively long) loss rate of a (μs to ns). In that case, the field is converted into a far-field pulse of n photons.

In optics, the realization of the nonlinear loss of Fig. 1 is perhaps especially addressable now, given recent advances in nanophotonics focusing on the engineering of radiative loss (including dissipative coupling of resonances [493]). For example, recent work on Fano states and bound states in the continuum (summarized e.g., in [472, 470]), when combined with Kerr nonlinearities, may enable realization of the Hamiltonian of Eq. (1) and the loss of Fig. 1b. Nanophotonic systems more broadly (exploiting coupled cavities based on high-

Q ring resonators and microspheres [52], or photonic crystal cavities [53]) should enable the construction of almost arbitrary nonlinear losses. Our proposal is also timely in light of a considerable volume of work on "non-Hermitian" optical systems with highly-engineered gain and loss [494, 495], even including nonlinearity [496].

Compared to other nonlinear loss effects that have been explored for noise suppression (e.g., multi-photon absorbers [478, 479, 480, 481, 497], amplitude-phase coupling [474, 475], optical bistability [425], soliton squeezing [498, 499]) − and even compared to squeezing from second-order nonlinearities (+ coherent displacement) [483, 482] − the nonlinear loss here is the only one we are aware of that can create Fock states. Even in cases where Fock states are not generated, the squeezing often exceeds the theoretical maximum for all of these cases. Another related approach is that used in so-called lasers with "quiet pumping" [500, 501, 502, 503], where a low-noise pump current is used to reduce the low-frequency noise of a laser. Such approaches lead to at most 50% noise reduction in the cavity [426]. As compared to other schemes for optical Fock state generation (such as schemes using photon blockade [157], "unconventional" photon blockade [504], or engineered driving terms [505]), our proposal addresses macroscopic Fock states.

That said, the ideas presented here may also be employed to create one- and few-photon Fock states, by combining single-photon-scale nonlinearities (e.g., using strong coupling [19] or Rydberg atoms [506]) with Fano interference in a way such that such that n_0 (of Fig. 1) is of order one. Such results would represent an exciting milestone in quantum nonlinear optics. All of the present work on creating single-photon scale nonlinearities is also more generally useful in realizing large Fock and sub-Poissonian states, as strong changes in loss over the scale of one photon are needed to get to the ultimate Fock-state limit (as per Eq. (7)). Our scheme can also be applied in the microwave regime, especially in superconducting qubit systems, where reservoirs can be engineered with greater facility and nonlinearities are quite strong [507, 21, 20].

Let us also summarize the experimental state of the art: in optics, only one-photon Fock states can be deterministically created thus far [508] (using e.g., heralded parametric down conversion, photon blockade, or quantum emitters). Fock states can also be non-deterministically generated by collapsing the wavefunction in the number basis [465, 466].

At microwave frequencies, more is possible, and approximate Fock states of around 15 photons have been generated. This is done using cavity quantum electrodynamical interactions with superconducting qubits (essentially adding photons to a cavity "one at a time" until linear loss sets in [459, 460]). Other schemes applied at microwave frequencies include the "micromaser" [433, 462, 463] and quantum feedback protocols [464].

Regarding experimental realization of the effects in optics on macroscopic scales, the systems we discussed (especially Fock lasers) entail a huge design space (see the table on SI pg. 37 to get a sense). It is almost certain that there are better platforms than ones discussed here to realize the physics proposed in this work. The systems we chose were mainly taken for the sake of illustration: to show what would be needed. For the gain medium, an obvious choice to consider is semiconductor gain media which need not be laser pumped, and can provide rather high gain over a very broad frequency range, enabling compatibility with many different nonlinear materials. Another important advantage of semiconductor gain media is that they could be integrated into nanophotonic platforms which present high nonlinearities (β at least 10 orders of magnitude higher than the bulk realizations presented, due to the reduced mode volumes [509]).

Given the generality of the effects introduced here, we expect that the theoretical and experimental development of physical platforms to realize them will provide a great deal of exciting new areas for discovery.

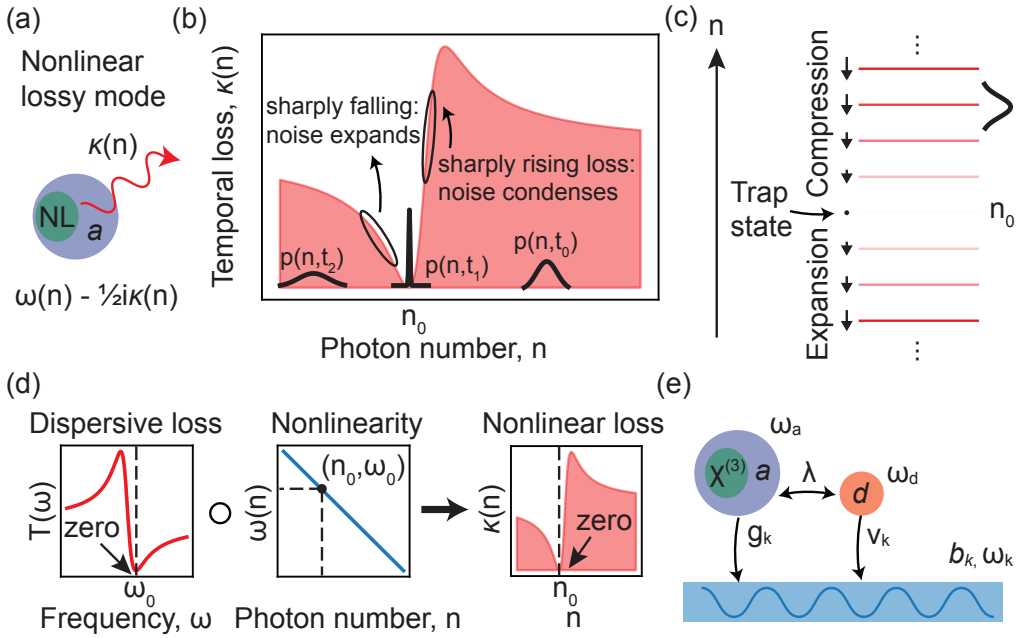

Figure 8-1: **Photon noise condensation and Fock state generation in systems with sharply nonlinear loss.** (a) A nonlinear resonance whose loss rate $\kappa(n)$ depends on photon number n. (b) For the nonlinear loss as plotted in the red curve, the resonance will have its photon number fluctuations compress as it decays, if it falls through a region of sharply rising loss. This is represented by the temporal evolution of the photon probability distribution (black) for different times (with $t_0 < t_1 < t_2$). If the loss has a zero for some photon number n_0, the noise condensation is perfect and the system approaches a Fock state of n_0 photons. (c) This can be understood through the n-dependent rate of transitions from n to $n-1$ photons (arrows denote magnitudes, lines denote states on the Fock ladder). The gradient of the rates (loss "sharpness") dictates the magnitude of compression, expansion, or trapping of the distribution. (d) The requisite nonlinear loss can be understood as arising from a "composition" of a frequency-dependent loss and an intensity-dependent cavity resonance frequency (e.g., due to Kerr nonlinearity). (e) Example of one of the many systems that could realize a loss of the form shown in (a): two resonances coupled to a common continuum, in which one is linear (d) and one is nonlinear (a). A zero surrounded by a region of sharp loss arises due to destructive (Fano) interference between two leakage pathways for a which can become perfect for a precise number of photons in a (namely, n_0).

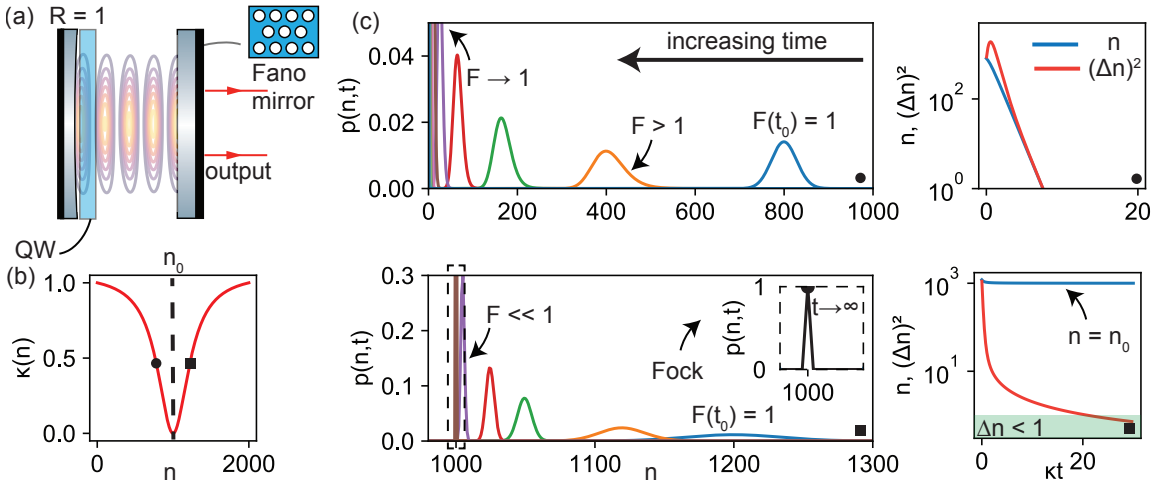

Figure 8-2: **Photon noise condensation in systems with sharply nonlinear loss.** (a) Example system to realize the effect of interest: a nonlinear resonance (e.g., an exciton polariton) coupled to a mirror with an internal resonance (a "Fano mirror" [1]) with a single loss channel (temporal loss shown in (b)). (c) Time-dependent photon probability distributions for $\bar{n}(0) = 800$ (top) and $\bar{n}(0) = 1200$ (bottom), as well as mean and variance. For $\bar{n}(0) = 800$, the system tends to the vacuum state, while for $\bar{n}(0) = 1200$, the system tends to a Fock state of 1000 photons. In this example: $\beta = 5 \times 10^{-7}, \kappa = 10^{-5}, \gamma = 5 \times 10^{-4}, \omega_d = (1 + \delta)$, with $\delta = 10^{-3}$, in units of the lower polariton frequency, 1.47 eV.

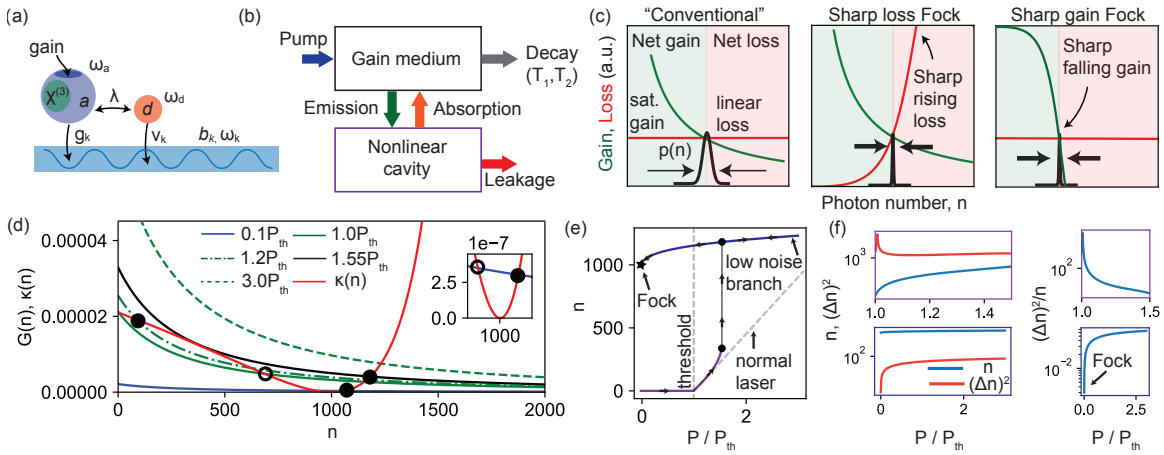

Figure 8-3: **The Fock laser.** (a) Components of a general Fock laser, which consists of a pumped gain medium and a nonlinear cavity, interacting via absorption and emission of cavity photons by the gain medium. (b) Energy flows between components of the Fock laser. The cavity leakage is of the sharp form in Fig. 1b. (c, left) Saturable gain and linear loss (corresponding to a conventional laser) leads to Poissonian photon statistics well-above threshold. (c, middle) On the other hand, saturable gain, combined with sharply rising loss, leads to condensation of the photon probability distribution, as in Fig. 1, except now in the steady-state. (c, right) The same condensation also holds when the gain sharply decreases and the loss is linear. (d) Gain and loss curves for a Fock laser for different values of the pump intensity. (e) Mean value of the intracavity photon number as a function of pump strength, relative to threshold. (f) Mean and variance, as well as Fano factor, for the two branches of the input-output curve of (e). Parameters used in this plot are $\beta = 5 \times 10^{-5}, \kappa = 10^{-5}, \gamma = 2 \times 10^{-3}, \omega_d = (1 + \delta)$, with $\delta = 0.04$ (in units of the lower polariton frequency ω_{LP}). Detailed gain and cavity parameters are provided in the SI, pg. 37.

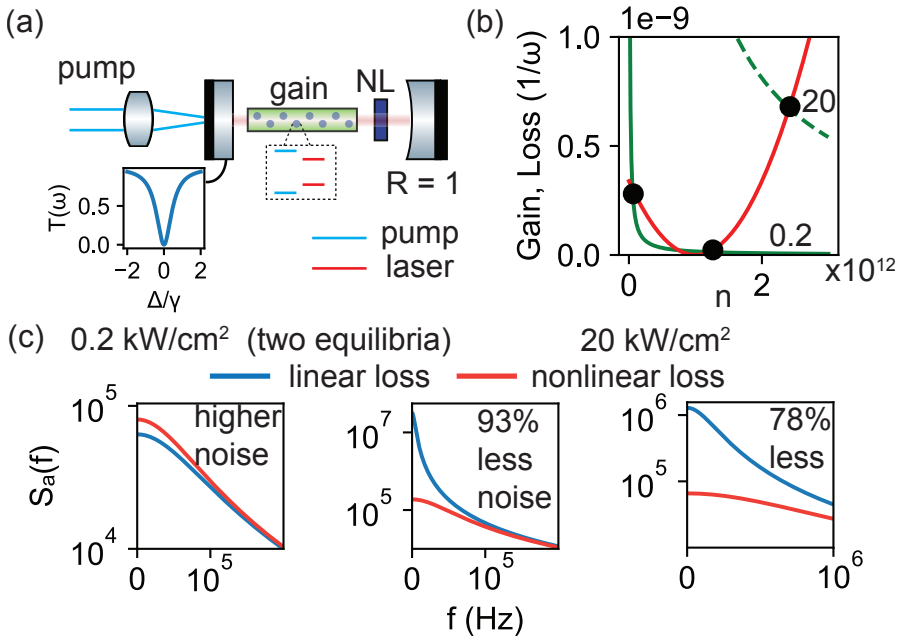

Figure 8-4: **Fock lasers in the macroscopic regime and large suppression of photon noise in a common laser architecture.** (a) A macroscopic implementation of a Fock laser based on a diode-pumped solid-state laser with a sharply-varying transmissive element and a nonlinear crystal. (b) Gain-loss diagrams with black circles showing stable equilibria for different pump intensities. (c) Cavity amplitude-noise spectra as a function of frequency for different pump intensities. For intermediate pump intensities, the overall noise reduction can be nearly 95% of the shot-noise limit with 10^{12} photons. The frequency-dependent noise can be reduced by as much as 100-fold for low frequencies. Parameters used in this plot are $\beta = 5 \times 10^{-18}, \kappa = 8 \times 10^{-5}, \gamma = 10^{-2}, \omega_d = (1 + \delta)$, with $\delta = -10^{-5}$ (in units of the lasing frequency, 1.17 eV). Detailed gain and cavity parameters are provided in the SI, pg. 37.

Chapter 9

Summary and outlook

In this thesis, we have studied the types of new phenomena that can arise when light interacts with collective excitations in materials. Simply put, we explored the interactions of various "matter" systems (e.g., two- and multi-level atoms, superconducting qubits, relativistic free electrons, optical phonons) with photonic quasiparticles of all types (e.g., free photons, plasmons, polaritons, and cavity photons).

We have found that these interactions can form the basis for extremely confined low-loss electromagnetic fields in the mid-IR (based on 2D optical phonons; Chapter 3), new types of vacuum forces acting on charged particles and new forms of entanglement between high-frequency (X-ray) and low-frequency (IR) excitations (Chapter 4), and even to new and highly sensitive high-energy particle detectors (Chapter 5). Such phenomena result from essentially *weak coupling* of light and matter. When their coupling gets strong, or even very strong, we showed how the energy-level structure of such systems (both ground and excited states) could be very well-accounted for by the formation of new photonic quasiparticles with spatially re-structured vacuum electromagnetic fields (Chapter 6). These strong interactions, in the regimes of the strongest couplings, e.g., *deep strong coupling* lead to very interested effects in excited-state spectra, and unique quantum nonlinearities that operate at the level of many photons, rather than single photons. Such quantum nonlinearities form the basis for new optoelectronic devices, such as lasers that produce macroscopic non-classical light states, such as large Fock states, which are currently infeasible to produce (especially deterministically) (Chapter 7). The N-photon

quantum nonlinearities discovered here were found to be part of a larger class of *dissipative nonlinearities* that could produce such macroscopic quantum states. In particular, we showed how engineering dissipation (e.g., radiative losses) in the presence of nonlinearity could lead to highly correlated dissipation phenomena that could also in principle produce large Fock states of light, but at optical frequencies (Chapter 8).

A great number of questions remain, and we believe there are many exciting directions that could ultimately be probed, using the developments presented here as a starting point. We will largely go through them in a chronological, chapter-by-chapter basis. In Chapter 3, we examined the theory of the interaction of light with optical phonons in materials to study the properties of phonon polaritons in 2D materials. Some important phononic effects we had not taken into account were (1) phonon nonlocality; essentially the dependence of the Born effective charges and phonon lifetimes on wavevector. Such effects are crucial when taking the phonon confinement down to the atomic limit, and are important from the standpoint of maximizing light-matter interactions. We also did not take into account (2) phonon nonlinearities (anharmonicity), which can in principle be substantial, unlike photons in bulk nonlinear media.

In Chapter 4, where we studied X-ray production by electrons traversing a nanophotonic vacuum, we claimed from energy-momentum conservation that the infrared plasmon and X-ray photon produced would feature entanglement. It would be of interest to pursue this entanglement and correlation in greater detail: what would be the properties of the second-order correlations $g^{(2)}(\mathbf{r}, \mathbf{r}', t, t')$ associated with this highly broadband infrared/X-ray photon wavepacket? Moreover, could the effect here provide the basis for a new type of two-photon gain? By having one of the two photons (e.g., the infrared) be in a high-quality-factor cavity, could this lead to a type of self-induced X-ray emission (by building up an infrared field which further stimulates X-ray production)?

In Chapter 5, we studied nanophotonic scintillators. There are natural questions about maximizing the effects predicted and demonstrated there: what structures provide maximal scintillation enhancement, either by density of states enhancement, or increasing the light outcoupling? Another interesting future perspective relates to the non-equilibrium nature of scintillation: could the use of strongly interacting electrons, or electrons in topologi-

cal bands, or 2D materials impart new properties on the scintillation photons? Moreover, it would be of interest to use our general formulation for scintillation *in reverse*: given the output scintillation, could we infer the non-equilibrium spectral function, giving information both on the non-equilibrium occupation factors and various oscillator strengths in material systems?

In Chapter 6, we presented a variational theory of strongly interacting light-matter systems. For reasons of concreteness, we developed this theory in the velocity gauge, writing the Hamiltonian in terms of the vector potential: the key item of interest would be generalizing these considerations to the length gauge Hamiltonian, which is more commonly used in practice due to its reduced sensitivity to Hilbert space truncation, and simpler interpretation of many observables.

In Chapter 7, where we presented quantum nonlinearities arising from deep-strong light-matter coupling, we considered the canonical Rabi model in the deep-strong coupling regime. Such a model describes the deep-strong coupling of a two-level system to a resonant cavity. Nevertheless, it would be of interest to describe the coupling of multi-level systems to resonant cavities, as well as cavities with multiple modes. Moreover, it is well-known that coupling can be strongly enhanced by coupling many two-level systems to a common mode - such considerations enable ultrastrong coupling in the infrared and optical domain. A natural question regards the nonlinear properties of many emitters collectively coupled a single resonance mode in this coupling regime. Moreover, while we considered incoherent pumping (associated with stimulated emission), it would be of interest to study the quantum states that could be produced without gain, e.g., by coherently driving the cavity with an external signal (e.g., by connecting it to a transmission line with an injected signal).

In Chapter 8, we developed the theory of nonlinear dissipation in systems where strong frequency-dependent loss is coupled to nonlinearity. Such effects were shown, by a wide range of theoretical approaches, to lead to sub-Poissonian and even large Fock state generation. A natural question, as in Chapter 7, concerns the pumping of these nonlinear dissipative cavities with external signals. Could this coherent pumping also lead to large sub-Poissonian state generation? From an experimental perspective, such systems could

prove much simpler and more versatile. A more detailed list of next theoretical steps that follow from this work is presented in the Appendix of Chapter 8, as well as at the end of Chapter 8 itself.

Appendix A

List of Publications

40. **N. Rivera**, J. Sloan, I. Kaminer, and M. Soljačić. ”Fock lasers based on deep-strong coupling of light and matter.“ arXiv:2111.07010.

39. **N. Rivera**, J. Sloan, Y. Salamin, and M. Soljačić. ”Macroscopic condensation of photon noise in sharply nonlinear dissipative systems.“ arXiv:2111.03099.

38. A. Pizzi, A. Gorlach, **N. Rivera**, A. Nunnenkamp, and I. Kaminer. ”Light-emission from strongly driven many-body systems.“

37. C. Roques-Carmes*, **N. Rivera***, A. Ghorashi, S. Kooi, Y. Yang, Z. Lin, J. Beroz, N. Romeo, J. D., Joannopoulos, I. Kaminer, S. G. Johnson, and M. Soljačić. A framework for scintillation in nanophotonics.” **Science** (2022).

36. J. Sloan, **N. Rivera**, J. D. Joannopoulos, and M. Soljačić. “Two-photon emission from superluminal and accelerating index perturbations.” **Nature Physics** (2021).

35. A. Karnieli, **N. Rivera**, A. Arie, and I. Kaminer. “Super-and subradiance by entangled free particles.“ **Physical Review Letters** (2021).

34. J. Sloan, **N. Rivera**, J. D. Joannopoulos, and M. Soljačić. ”Casimir light in dispersive nanophotonics.“ **Physical Review Letters** (2021).

33. R. Ruimy, A. Gorlach, C. Mechel, **N. Rivera**, I. Kaminer. “Towards atomic-resolution quantum measurements with coherently-shaped free electrons.” **Physical Review**

Letters (2021).

32. A. Karnieli, **N. Rivera**, A. Arie, and I. Kaminer. "The coherence of light is fundamentally tied to the quantum coherence of the emitting particle." **Science Advances** (2021).

31. S. Ghosh, **N. Rivera**, G. Eisenstein, and I. Kaminer. "Creating heralded hyperentangled photons using Rydberg atoms." **Light: Science & Applications** (2021).

30. L. J. Wong, **N. Rivera**, C. Murdia, T. Christensen, J. D. Joannopoulos, M. Soljačić., and I. Kaminer. "Control of quantum electrodynamical processes by shaping electron wavepackets." **Nature Communications** (2021).

29. A. B. Hayun, O. Reinhardt, J. Nemirovsky, A. Karnieli, **N. Rivera**, and I. Kaminer. "Shaping quantum photonic states with free electrons." **Science Advances** (2021).

28. C. Mechel, Y. Kurman, A. Karnieli, **N. Rivera**, A. Arie, and I. Kaminer. "Quantum correlations in electron microscopy." **Optica** (2021).

27. **N. Rivera**, and I. Kaminer. "Light-matter interactions with photonic quasiparticles." **Nature Reviews Physics**. (2020). Featured on journal cover.

26. A. Gorlach, O. Neufeld, **N. Rivera**, O. Cohen, I. Kaminer. "On the quantum optical nature of high-harmonic generation." **Nature Communications** (2020).

25. R. Sundararaman, T. Christensen, Y. Ping, **N. Rivera**, J. D. Joannopoulos, M. Soljačić, and Narang. P. "Plasmonics in argentene." **Physical Review Materials** (2020).

24. A. Gorlach, **N. Rivera**, and I. Kaminer. " Making materials mimic each other" **Physics [Viewpoint]**. (2020).

23. S. Fisher, C. Roques-Carmes, **N. Rivera**, L. J. Wong, I. Kaminer, and M. Soljačić. "Monochromatic X-ray source based on scattering from a magnetic nanoundulator." **ACS Photonics** (2020).

22. P. A. D. Goncalves, T. Christensen, **N. Rivera**, A. P. Jauho, N. A. Mortensen, and M. Soljačić. "Plasmon-emitter interactions at the nanoscale." **Nature Communications** (2020).

21. J. Sloan*, **N. Rivera***, J. D. Joannopoulos, I. Kaminer, and M. Soljačić. "Controlling spins with surface magnon polaritons." **Physical Review B** (2019).

20. **Rivera N.**, L. J. Wong, J. D. Joannopoulos, M. Soljačić, and I. Kaminer."Light emission based on nanophotonic vacuum forces". **Nature Physics** (2019).

19. R. Dangovski, **N. Rivera**, M. Soljačić, and I. Kaminer. "Shaping long-lived electron wavepackets for customizable optical spectra." **Optica** (2019).

18. S. Dai, Y. Stehle, **N. Rivera**, W. Fang, R. Tay, C. Ciccarino, Q. Ma, D. Rodan-Legrain, P. Jarillo-Herrero, M. Fogler, E. H. T. Teo, J. Kong, P. Narang, and D. N. Basov. "Phonon polaritons in hexagonal boron nitride at the atomic-scale limit." **Advanced Materials** (2019).

17. **N. Rivera**, J. Flick, and P. Narang. "Variational theory of non-relativistic quantum electrodynamics." **Physical Review Letters** (2019).

16. **N. Rivera**, T. Christensen, and P. Narang."Phonon polaritonics in two-dimensional materials'. **Nano Letters** (2019).

15. **N. Rivera**, L. J. Wong, M. Soljačić, and I. Kaminer. "Ultrafast multiharmonic plasmon generation by optically dressed electrons'. **Physical Review Letters** (2019).

14. C. Roques-Carmes, **N. Rivera**, J. D. Joannopoulos, M. Soljačić, and I. Kaminer. "Nonperturbative quantum electrodynamics in the Cherenkov effect". **Physical Review X** (2018).

13. G. Rosolen, L. J. Wong, **N. Rivera**, B. Maes, M. Soljačić, and I. Kaminer. "Metasurface based multi-harmonic light source". **Light: Science & Applications** (2018).

12. J. Flick, **N. Rivera**, and P. Narang."Strong light-matter coupling in quantum chemistry and quantum photonics." **Nanophotonics** (2018).

11. F. Machado*, **N. Rivera***, H. Buljan, M. Soljačić, and I. Kaminer. "Shaping polaritons to reshape selection rules". **ACS Photonics** (2018).

10. Y. Kurman, **N. Rivera**, T. Christensen, S. Tsesses, J. D. Joannopoulos, M. Soljačić, M. Orenstein, and I. Kaminer. "Control over semiconductor emitter frequency with polariton momenta." **Nature Photonics** (2018).

9. J. J. Lopez, A. Ambrosio, S. Dai, C. Huynh, D. C. Bell, X. Lin, **N. Rivera**, S. Huang, Q. Ma, S. Eyhusen, I. Kaminer, K. Watanabe, T. Taniguchi, J. Kong, D. N. Basov, P. Jarillo-Herrero, and M. Soljačić. Large photothermal effect in sub-40 nm hBN nanostructures patterned via high-resolution ion beam. **Small** (2018).

8. Sloan J., **N. Rivera**, M. Soljačić, and I. Kaminer. "Tunable UV emitters through graphene plasmonics." **Nano Letters** (2018).

7. **N. Rivera**, G. Rosolen, J. D. Joannopoulos, I. Kaminer, and M. Soljačić. "Extreme light-matter interactions with phonon-polaritons in the mid-IR: making two-photon processes dominate one-photon processes". **Proceedings of the National Academy of Sciences** (2017).

6. G. T. Papadakis, P. Narang, R. Sundararaman, **N. Rivera**, H. Buljan, N. Engheta, and M. Soljačić. "Ultra-light Å-scale Optimal Optical Reflectors." **ACS Photonics** (2017)

5. C. H. Chang, **N. Rivera**, J. D. Joannopoulos, M. Soljačić, and I. Kaminer. "Designer atoms through resonant lamb shifts in graphene." **ACS Photonics: Special Issue on 2D Nanophotonics.** (2017)

4. X. Lin, Y. Yang, **N. Rivera**, J. J. Lopez, Y. Shen, I. Kaminer, H. Chen, B. Zhang, J. D. Joannopoulos, and M. Soljačić. "All-angle negative refraction of highly squeezed plasmon and phonon polaritons in graphene boron nitride heterostructures." **Proceedings of the National Academy of Sciences** (2017).

3. X. Lin, **N. Rivera**, J. J. Lopez, I. Kaminer, H. Chen, and M. Soljačić. "Tailoring the energy distribution and loss of 2D plasmons." **New Journal of Physics** (2016).

2. **N. Rivera**, C. W. Hsu, B. Zhen, H. Buljan, J. D. Joannopoulos, and M. Soljačić. "Controlling directionality and dimensionality of radiation through separable bound states in the continuum." **Scientific Reports** (2016).

1. **N. Rivera***, I. Kaminer*, B. Zhen, J. D. Joannopoulos, and M. Soljačić. "Shrinking light to allow forbidden transitions on the atomic scale." **Science** (2016).

Appendix B

Appendix for: Light-matter interactions with photonic quasiparticles

In this Appendix, we provide a technical overview of the main theoretical tools used throughout this thesis to describe light-matter interactions with photonic quasiparticles. It is organized as follows:

1. First, we rigorously, starting from a Lagrangian framework, develop the theory of electromagnetic field quantization in inhomogeneous, lossless dielectrics. We also rigorously develop the description of the interaction of these quantized fields with external charges (e.g., atoms, molecules, electrons, etc.).

2. From this general description of light-matter interactions, we establish a number of key Hamiltonians used for simplified reduced descriptions of light-matter interactions: the Rabi and Jaynes-Cummings models, the Hopfield model, and a quantum model of the interaction of a moving free charge (such as an electron) with light (the so-called QPINEM Hamiltonian). We use this as an opportunity to also introduce concepts such as polaritons, quantum nonlinearity, strong coupling, and relativistic light-matter Hamiltonians.

3. We then discuss the role of dissipation, presenting complementary treatments of the effect of dissipation in terms of a reservoir approach (which informs many modern works in quantum state engineering) and fluctuating (Langevin) forces, the latter of

which is a very powerful framework. This discussion enables us to then move to the topic of field quantization in *absorbing* linear and inhomogeneous dielectrics. This establishes the framework of macroscopic quantum electrodynamics in full generality.

We should note that while much of this treatment is meant to be introductory and to provide an "overview" of effects in light-matter interaction (much in the style of a seminar on light-matter interactions), we do go into rigorous technical details in a few places. One is a derivation of the Hamiltonian description of light-matter interaction, with key results being Eqs. (63) and (74). The Hamiltonians of light-matter interactions in the velocity gauge (Eq. (63)) and in the length gauge (Eq. (74)) form the rigorous basis for most studies on light-matter interaction, and accordingly have appeared in some form (typically with approximations) in most of our work (see various publications in App. A). Thus, we have elected to derive these Hamiltonians quite rigorously, showing the role that gauge choice plays. Compared to other treatments, we have not seen a general derivation of mode quantization in arbitrary lossless media that includes the modifications of the Coulomb interaction coming from the inhomogeneous dielectric, and we have not seen a general proof of the cancellation of the dipole-self energy. This full derivation also clarifies the role played by generalized Coulomb gauge. We should note that many of these results and interpretations have however been worked out in specific cases (e.g., near a perfectly conducting mirror [120]) and also in QED in vacuum [413]. The primary utility of this section is to generalize these results to an arbitrary medium in an end-to-end manner and have it all presented in one treatment.

B.1 Lagrangian and Hamiltonian formulation of classical electromagnetism in dielectrics

In this section, we develop the theory of quantum electrodynamics for non-relativistic charges coupled to electromagnetic fields in materials. We are especially interested in situations in which the charges are coupled to fields in inhomogeneous dielectric (such as

photonic cavities, photonic crystals, waveguides, bulk dielectrics, and so on). To quantize the system means essentially to turn all observable quantities describing the system into operators. Thus, the positions and velocities of the matter (charges) become operators, as do the electric and magnetic fields. Additionally, we will need to find a Hamiltonian operator which generates the time-evolution of the light-matter system.

We already know how to quantize the charges, as this is just conventional quantum mechanics – thus the essential new element is the quantization of the electromagnetic field. In general, the strategy is as follows:

1. Start from a Lagrangian whose equations of motion (Euler-Lagrange equations) are classical equations that we already know (the Maxwell equations for the fields in a dielectric, the Newton equations for the charges)

2. Turn the Lagrangian into a Hamiltonian through the standard Legendre transform

3. For matter described by positions and velocities, we quantize as usual, converting the position into the position operator, and the momentum into the momentum operator $\mathbf{p} = -i\hbar\nabla$. For fields, which possess an infinite number of degrees of freedom (to describe the field at all points in space), we will find that degrees of freedom of the EM field can be conveniently cast in terms of the amplitudes of the normal modes of the field. We will find that, as is typical in quantum field theory, the independent field modes act as independent harmonic oscillators, which lead then to a simple and straightforward quantization.

Let us start by finding the Lagrangian of the system of matter and fields. We will do this in three steps: we will first introduce the Lagrangian of a system of matter in an external electromagnetic field. Then, we will introduce the Lagrangian of the electromagnetic field in the absence of charges. Finally, we will derive the Lagrangian describing the interaction between the charges and the fields.

B.1.1 Lagrangian of matter in an external field

We start by considering the Lagrangian describing a single particle in an external field, described by the scalar potential $\phi(\mathbf{r}, t)$ and the vector potential $\mathbf{A}(\mathbf{r}, t)$. We are looking to find a Lagrangian $L(\mathbf{r}(t), \dot{\mathbf{r}}(t), t)$ (dots here denote time-derivative) such that when the associated action functional

$$S[\mathbf{r}(t), \dot{\mathbf{r}}(t); t_i, t_f] \equiv \int_{t_i}^{t_f} dt\ L(\mathbf{r}(t), \dot{\mathbf{r}}(t), t) \tag{B.1}$$

is stationary, it reproduces the Newtonian equation of motion for the particle in an external electromagnetic field. By stationary, we mean with respect to a change of the functions $\mathbf{r}(t), \dot{\mathbf{r}}(t)$. To minimize the action, let us consider a small variation of the trajectory $\mathbf{r}(t) \to \mathbf{r}(t) + \delta\mathbf{r}(t)$, where $|\delta\mathbf{r}| \ll |\mathbf{r}|$. We can expand the action in this small variation as

$$\begin{aligned} S[\mathbf{r}(t) + \delta\mathbf{r}(t), \dot{\mathbf{r}}(t) + \delta\dot{\mathbf{r}}(t); t_i, t_f] &= \int_{t_i}^{t_f} dt\ L(\mathbf{r}(t) + \delta\mathbf{r}(t), \dot{\mathbf{r}}(t) + \dot{\delta\mathbf{r}}(t), t) \\ &\approx \int_{t_i}^{t_f} dt\ \left(L(\mathbf{r}(t), \dot{\mathbf{r}}(t), t) + \delta\mathbf{r} \cdot \nabla_{\mathbf{r}} L + \delta\dot{\mathbf{r}} \cdot \nabla_{\dot{\mathbf{r}}} L\right). \end{aligned} \tag{B.2}$$

The corresponding change in the action is then

$$\delta S = \int_{t_i}^{t_f} dt\ \left(\delta\mathbf{r} \cdot \nabla_{\mathbf{r}} L + \delta\dot{\mathbf{r}} \cdot \nabla_{\dot{\mathbf{r}}} L\right). \tag{B.3}$$

To simplify this further, expressing everything in terms of the change in $\mathbf{r}$, we may use the fact that $\dot{\delta\mathbf{r}} = \delta\dot{\mathbf{r}}$, and perform integration by parts to get

$$\delta S = \delta\mathbf{r} \cdot \nabla_{\dot{\mathbf{r}}} L \Big|_{t_i}^{t_f} + \int_{t_i}^{t_f} dt\ \delta\mathbf{r} \cdot \left(\nabla_{\mathbf{r}} L - \frac{d}{dt} \nabla_{\dot{\mathbf{r}}} L\right). \tag{B.4}$$

The boundary terms vanish, as the trajectory that makes the action stationary must respect the boundary conditions of the problem: that we know the position and velocity at the initial

and final times. Therefore, if the stationary trajectory respects these boundary conditions, the variation in the trajectory must be zero so that any variation also respects the boundary conditions. Stated mathematically: $\delta\mathbf{r}(t_i) = \delta\mathbf{r}(t_f) = 0$. For the action to be stationary, we therefore must have:

$$0 = \int_{t_i}^{t_f} dt\ \delta\mathbf{r} \cdot \left(\nabla_{\mathbf{r}} L - \frac{d}{dt} \nabla_{\dot{\mathbf{r}}} L \right). \tag{B.5}$$

This equation must hold for *any* variation $\delta\mathbf{r}$. The only way this is possible is if the integrand is zero throughout the integration domain. To see this, consider $\delta\mathbf{r} = (1,0,0)\delta(t - t_0)$, with $t_i < t_0 < t_f$. Then we get $0 = \partial_x L(t_0) - \frac{d}{dt}\partial_{\dot{x}} L(t_0)$. This holds for any time, and also for a y or z-directed unit vector weighting the delta function. Therefore,

$$\nabla_{\mathbf{r}} L = \frac{d}{dt} \nabla_{\dot{\mathbf{r}}} L, \tag{B.6}$$

which is the Euler-Lagrange equation.

To find the Lagrangian of a given system is essentially trial-and-error: guess a Lagrangian and show that the Euler-Lagrange equations result in the equations of motion for the system. For example, for a single particle of charge q and mass m in an electromagnetic field, the Lagrangian is given as:

$$L = \frac{1}{2} m\dot{\mathbf{r}}^2 - q\phi(\mathbf{r}(t)) + q\mathbf{A}(\mathbf{r}(t), t) \cdot \dot{\mathbf{r}}. \tag{B.7}$$

To show this is the correct Lagrangian, let us evaluate the corresponding Euler-Lagrange equation, showing that it reduces to the Newtonian equation of motion for a charged particle subject to the Lorentz force law. The left-hand side of the Euler-Lagrange equation is simply

$$\nabla_{\mathbf{r}} L = -q\nabla\phi + q(\nabla_{\mathbf{r}}\mathbf{A}) \cdot \dot{\mathbf{r}}, \tag{B.8}$$

where it is understood that the dot-product refers to the indices of $\mathbf{A}$ and $\mathbf{r}$. The right-hand side of the Euler-Lagrange equation is given by

$$\frac{d}{dt} \nabla_{\dot{\mathbf{r}}} L = m\ddot{\mathbf{r}} + \frac{d}{dt}\mathbf{A}(\mathbf{r}(t), t) \cdot \nabla_{\dot{\mathbf{r}}}\dot{\mathbf{r}} \tag{B.9}$$

which, by application of the chain-rule, gives

$$\frac{d}{dt}\nabla_{\dot{\mathbf{r}}}L = m\ddot{\mathbf{r}} + q\partial_t\mathbf{A} + q(\dot{\mathbf{r}}\cdot\nabla)\mathbf{A}, \tag{B.10}$$

where we have omitted the functional dependence of $\mathbf{A}$, as we will not need to think about it anymore. We can very clearly see how the electric field arises in this equation, given that $\mathbf{E} = -\nabla\phi - \partial_t\mathbf{A}$. We need to however expose the dependence on the magnetic field. Let us look at the term $q(\nabla_{\mathbf{r}}\mathbf{A})\cdot\dot{\mathbf{r}}$ in more detail. Writing the i-component of this in repeated index notation, we have that

$$q(\nabla_{\mathbf{r}}\mathbf{A})\cdot\dot{\mathbf{r}} = q(\partial_i A_j - \partial_j A_i)\dot{r}_j + q(\partial_j A_i)\dot{r}_j. \tag{B.11}$$

To proceed, it is useful to cast the term we want $(\dot{\mathbf{r}}\times(\nabla\times\mathbf{A}))_i$ in a form that resembles what we have just derived. We may write

$$\begin{aligned}(\dot{\mathbf{r}}\times(\nabla\times\mathbf{A}))_i &= \epsilon_{ijk}\dot{r}_j\epsilon_{klm}\partial_l A_m \\ &= \epsilon_{kij}\epsilon_{klm}\dot{r}_j\partial_l A_m \\ &= (\delta_{il}\delta_{jm} - \delta_{im}\delta_{jl})\dot{r}_j\partial_l A_m \\ &= \dot{r}_j(\partial_i A_j - \partial_j A_i),\end{aligned} \tag{B.12}$$

exactly equal to a term we got from the Euler-Lagrange equation. Therefore $q(\nabla_{\mathbf{r}}\mathbf{A})\cdot\dot{\mathbf{r}} = q\dot{\mathbf{r}}\times\mathbf{B} + q(\dot{\mathbf{r}}\cdot\nabla_{\mathbf{r}})\mathbf{A}$. Equating the left and right hand sides of the Euler-Lagrange equations then yields

$$m\ddot{\mathbf{r}} = q(\mathbf{E} + \dot{\mathbf{r}}\times\mathbf{B}), \tag{B.13}$$

as desired.

In many cases, we have not just one particle, but many (N), in external electromagnetic fields. The arguments of this section can easily be generalized to show that the Euler-Lagrange equations still apply for each particle independently, and that the Lagrangian is

the sum of the Lagrangians of each individual particle. In other words

$$L = \sum_{i=1}^{N} \frac{1}{2} m_i \dot{\mathbf{r}}_i^2 - q_i \phi(\mathbf{r}_i, t) + q_i \mathbf{A}(\mathbf{r}_i, t) \cdot \dot{\mathbf{r}}_i \tag{B.14}$$

B.1.2 Lagrangian of the fields without sources

We now move to derive the Lagrangian of the free electromagnetic field. Let us consider for simplicity the electromagnetic field in the absence of sources. Unlike matter, which have well-defined locations, fields are extended over some space (usually infinite). As a result, the Lagrangian of some field, ϕ, is typically expressed in terms of a Lagrangian density, $\mathcal{L}$ via

$$L[\phi] = \int d^3r \; \mathcal{L}[\phi(\mathbf{r}, t), \partial_\mu \phi(\mathbf{r}, t)], \tag{B.15}$$

where we have taken the field to be in three spatial dimensions, as is the most common scenario. We have assumed the Lagrangian to be a function of both the field itself and its derivatives, labeling a generic derivative (time or space), as $\partial_\mu \phi$. The corresponding action is expressed as

$$S[\phi] = \int d^4x \; \mathcal{L}[\phi(\mathbf{r}, t), \partial_\mu \phi(\mathbf{r}, t)], \tag{B.16}$$

with $d^4x \equiv d^3r dt$. Fields, like matter, are also subject to a principle of stationary action. Thus, the field is that which leads to $\delta S = 0$. Let us consider an arbitrary variation of the field $\phi \to \phi + \delta\phi$. The action can then be expanded in this variation to first order as

$$\begin{aligned} S[\phi + \delta\phi] &= \int d^4x \; \mathcal{L}[\phi(\mathbf{r}, t) + \delta\phi, \partial_\mu \phi(\mathbf{r}, t) + \delta(\partial_\mu \phi)] \\ &\approx S[\phi] + \int d^4x \left(\delta\phi \frac{\partial \mathcal{L}}{\partial \phi} + \delta(\partial_t \phi) \frac{\partial \mathcal{L}}{\partial(\partial_t \phi)} + \delta(\nabla_{\mathbf{r}} \phi) \cdot \frac{\partial \mathcal{L}}{\partial(\nabla_{\mathbf{r}} \phi)} \cdot \right), \end{aligned} \tag{B.17}$$

where

$$\frac{\partial \mathcal{L}}{\partial(\nabla_{\mathbf{r}} \phi)} \equiv \left(\frac{\partial \mathcal{L}}{\partial(\partial_x \phi)}, \frac{\partial \mathcal{L}}{\partial(\partial_y \phi)}, \frac{\partial \mathcal{L}}{\partial(\partial_z \phi)} \right) \tag{B.18}$$

in Cartesian coordinates. To proceed, we need to consider boundary conditions for the fields. Regarding spatial boundary conditions, let us assume that the fields either vanish at infinity, or that the fields are enclosed in a large box with periodic boundary conditions.

Similarly, we will apply the same temporal boundary conditions. Whether the fields vanish or are periodic, one can show that the boundary terms in the integration by parts vanish. Therefore, it immediately follows that the variation in the action is

$$\delta S = \int d^4x \, \delta\phi \left(\frac{\partial \mathcal{L}}{\partial \phi} - \partial_t \frac{\partial \mathcal{L}}{\partial(\partial_t \phi)} - \nabla_{\mathbf{r}} \cdot \frac{\partial \mathcal{L}}{\partial(\nabla_{\mathbf{r}} \phi)}. \right) \tag{B.19}$$

By an argument similar to the one used to derive the Euler-Lagrange equations for matter, it follows that for the action to be stationary for *any* $\delta\phi$, it must be that

$$\frac{\partial \mathcal{L}}{\partial \phi} - \nabla_{\mathbf{r}} \cdot \frac{\partial \mathcal{L}}{\partial(\nabla_{\mathbf{r}} \phi)} = \partial_t \frac{\partial \mathcal{L}}{\partial(\partial_t \phi)}, \tag{B.20}$$

which is the Euler-Lagrange equation for fields.

Let us now apply this to the case of electromagnetism in (non-magnetic, non-dispersive) material media. The Lagrangian of the electromagnetic field, described by a scalar and vector potential, turns out to be

$$L[\phi, \mathbf{A}, \partial_\mu \mathbf{A}] = \frac{\epsilon_0}{2} \int d^3r \, \epsilon \mathbf{E}^2 - c^2 \mathbf{B}^2 = \int d^3r \, \epsilon (\nabla\phi + \partial_t \mathbf{A})^2 - c^2 (\nabla \times \mathbf{A})^2. \tag{B.21}$$

This Lagrangian looks considerably more complicated than the one we derived above for a single-component field due to the dependence on multiple fields (ϕ, $\mathbf{A}$), as well as due to the vectorial nature of the vector potential. However, from the standpoint of the derivation of the Euler-Lagrange equation, all that has happened is that the number of degrees of freedom is larger. We can think of the Lagrangian as

$$L[\phi, \partial_\mu \phi, A_x, \partial_\mu A_x, A_y, \partial_\mu A_y, A_z, \partial_\mu A_z]. \tag{B.22}$$

And the Euler-Lagrange equations will apply separately to ϕ, A_x, A_y, A_z.

First, let's find the equation for the scalar potential. Noticing that the Lagrangian does not depend on ϕ or $\partial_t \phi$, but does depend on its spatial gradient, we see that the Euler-

Lagrange equation generated from the potential is

$$\nabla \cdot \epsilon \nabla \phi + \partial_t \nabla \cdot (\epsilon \mathbf{A}) = 0, \tag{B.23}$$

which coincides with the expected classical equation for the scalar potential in the absence of free charges or currents [1].

Now, we need to obtain the equations from differentiation with respect to the vector potential and its derivatives. There is no dependence on the vector potential itself, only its derivatives. Differentiating with respect to the time-derivative of A_s, the s-component of $\mathbf{A}$, gives

$$\frac{\partial \mathcal{L}}{\partial(\partial_t A_s)} = \epsilon_0 \epsilon(\partial_t A_s + \partial_s \phi) = -\epsilon_0 \epsilon E_s = -D_s, \tag{B.26}$$

with $\mathbf{D}$ the displacement field.

Now, we must differentiate the Lagrangian with respect to the spatial derivatives, which is complicated by the presence of curls. The term to evaluate for the equation for A_s is

$$\partial_r \frac{\partial \mathcal{L}}{\partial(\partial_r A_s)}. \tag{B.27}$$

In repeated-index notation, the term in the Lagrangian density associated with the magnetic field (modulo $\epsilon_0 c^2$) is

$$-\frac{1}{2}\epsilon_{ijk}\epsilon_{ilm}(\partial_j A_k)(\partial_l A_m). \tag{B.28}$$

Noting that the $\partial_i A_j$ are independent degrees of freedom, it follows that $\frac{\partial(\partial_i A_j)}{\partial(\partial_r A_s)} = \delta_{ir}\delta_{js}$.

[1] Maxwell's equations in an inhomogeneous, non-dispersive medium are typically stated for the fields rather the potentials. Yet, from the standpoint of field quantization, the potentials take precedence. Thus, we briefly derive the equations for the potentials. Recall. that $\mathbf{E} = -\nabla\phi - \partial_t \mathbf{A}$ and $\mathbf{B} = \nabla \times \mathbf{A}$. Then, Gauss's law, $\epsilon_0 \nabla \cdot \epsilon \mathbf{E} = \rho_f$, with ρ_f the free charge density, becomes:

$$\nabla \cdot \epsilon \nabla \phi + \nabla \cdot \epsilon \partial_t \mathbf{A} = -\rho_f/\epsilon_0. \tag{B.24}$$

Meanwhile, the Ampere's law, $\nabla \times \mathbf{B} = \mu_0 \mathbf{J}_f + \frac{\epsilon}{c^2}\partial_t \mathbf{E}$ can be expressed as

$$\nabla \times \nabla \times \mathbf{A} + \frac{\epsilon}{c^2}\partial_t^2 \mathbf{A} + \frac{\epsilon}{c^2}\partial_t \nabla \phi = \mu_0 \mathbf{J}_f. \tag{B.25}$$

It follows that the derivative (Eq. 5.1.25) of Eq. (5.1.26) is simply

$$\epsilon_{sri}\epsilon_{ilm}\partial_r\partial_l A_m = (\nabla \times \nabla \times \mathbf{A})_s. \tag{B.29}$$

Therefore, the equation for the vector potential is

$$\nabla \times \nabla \times \mathbf{A} + \frac{\epsilon}{c^2}\left(\partial_t^2 \mathbf{A} + \nabla\partial_t\phi\right) = 0, \tag{B.30}$$

which also coincides with the expected classical equation for the vector potential in the absence of free charges or currents. We have thus proven that the Lagrangian of Eq. (21) is in fact the correct Lagrangian of the field.

B.1.3 Interaction Lagrangian

Now let's consider the influence of interactions between matter and light. In Section 1.2. we derived the Lagrangian describing matter in electromagnetic fields, thus implicitly taking into account the interactions between matter and fields. The only real change is one of perspective: the fields are now degrees of freedom, rather than fixed, external entities, and therefore are subject to time-evolution. The Lagrangian of a system of N matter in an electromagnetic field is thus

$$\boxed{L = \sum_{i=1}^{N} \frac{1}{2} m_i \dot{\mathbf{r}}_i^2 - q_i\phi(\mathbf{r}_i, t) + q_i\mathbf{A}(\mathbf{r}_i, t)\cdot\dot{\mathbf{r}}_i + \int d^3r\ \epsilon(\nabla\phi + \partial_t\mathbf{A})^2 - c^2(\nabla\times\mathbf{A})^2}. \tag{B.31}$$

This Lagrangian does not change the equations of motion for the matter, as the field Lagrangian does not depend on the particle degrees of freedom. However, the term representing the interaction between matter and fields: $-q_i\phi(\mathbf{r}_i, t) + q_i\mathbf{A}(\mathbf{r}_i, t)\cdot\dot{\mathbf{r}}_i$ do change the equation for the fields. To find the change to the field equations however, we need to find the Lagrangian density associated with the interaction terms, and cast these terms as

integrals. This is done by introducing integrals, so that the interaction terms become

$$\begin{aligned}&\int d^3r - q_i\phi(\mathbf{r}_i,t)\delta(r-r_i(t)) + q_i\mathbf{A}(\mathbf{r}_i,t)\cdot\dot{\mathbf{r}}_i\delta(r-r_i(t))\\&= \int d^3r \ -\rho(\mathbf{r},t)\phi(\mathbf{r},t) + \mathbf{j}(\mathbf{r},t)\cdot\mathbf{A}(\mathbf{r},t),\end{aligned} \tag{B.32}$$

where we have introduced the charge and current densities.

Differentiating the Euler-Lagrange equations for the fields gives

$$\nabla\cdot\epsilon\nabla\phi + \partial_t\nabla\cdot(\epsilon\mathbf{A}) = -\rho/\epsilon_0 \tag{B.33}$$

for the scalar potential equation and

$$\nabla\times\nabla\times\mathbf{A} + \frac{\epsilon}{c^2}\left(\partial_t^2\mathbf{A} + \nabla\partial_t\phi\right) = \mu_0\mathbf{j} \tag{B.34}$$

for the vector potential equation. These are exactly the same as the Maxwell equations with sources that we derived earlier. With this, we have the full *Maxwell-Newton-Lorentz* system of equations that classically describes light and matter

$$\begin{aligned}&m\ddot{\mathbf{r}} = q(\mathbf{E} + \dot{\mathbf{r}}\times\mathbf{B})\\&\nabla\cdot\epsilon\nabla\phi + \partial_t\nabla\cdot(\epsilon\mathbf{A}) = -\rho/\epsilon_0\\&\nabla\times\nabla\times\mathbf{A} + \frac{\epsilon}{c^2}\left(\partial_t^2\mathbf{A} + \nabla\partial_t\phi\right) = \mu_0\mathbf{j}.\end{aligned} \tag{B.35}$$

B.1.4 Hamiltonian of the matter and the fields

As our ultimate goal is a quantum theory of matter and electromagnetic fields, as because the Hamiltonian is the central quantity of that theory, we must derive the Hamiltonian corresponding to this Lagrangian. The Hamiltonian $H(p,q)$ corresponding to a Lagrangian $L(q,\dot{q})$, for a system with a single canonical position, is obtained by the Legendre transform:

$$H = p\dot{q} - L, \tag{B.36}$$

where p, the canonical momentum, is defined as

$$p = \frac{\partial L}{\partial \dot{q}}. \tag{B.37}$$

For the matter, the canonical momentum can easily be seen to be

$$\mathbf{p} = m\mathbf{v} + q\mathbf{A}. \tag{B.38}$$

Meanwhile, for the fields, the canonical momentum is

$$\mathbf{\Pi}(\mathbf{r}) = \frac{\partial L}{\partial \dot{\mathbf{A}}} = -\mathbf{D}. \tag{B.39}$$

The Hamiltonian then follows immediately as

$$H = \sum_{i=1}^{N} \frac{(\mathbf{p}_i - q_i \mathbf{A}_i(\mathbf{r}_i))^2}{2m_i} + q_i\phi(\mathbf{r}_i, t) + \frac{\epsilon_0}{2}\int d^3r\, \frac{\mathbf{\Pi}^2}{\epsilon} + c^2(\nabla \times \mathbf{A})^2. \tag{B.40}$$

While this answer looks quite clean, it has a serious complication associated with it. It has to do with the fact that matter and field degrees of freedom are mixed together. For example, the vector and scalar potentials in Eq. (34) are mixed together. Additionally, the Hamiltonian of the field mixes the scalar and vector potentials through $\mathbf{\Pi}$ (which, being the electric displacement, mixes the electric field and the matter polarization). This complicates analysis greatly, and thus we shall now make a choice of gauge that eliminates this mixing.

From now on, we will work in the so-called *generalized Coulomb gauge*, so that

$$\boxed{\nabla \cdot \epsilon \mathbf{A} = 0}. \tag{B.41}$$

This choice of gauge leads to two major simplifications. The first is that the scalar potential is completely determined by the matter (as there are no homogeneous solutions to $\nabla \cdot \epsilon\nabla\phi = -\rho/\epsilon_0$ that carry an electric field). Therefore, the scalar potential is actually a particle degree of freedom. This is exactly like the case of field-quantization in vacuum, where $\nabla \cdot \mathbf{A} = 0$. The scalar potential is given in terms of the Green's function of the

Laplace equation as

$$\phi(\mathbf{r}) = -\sum_{i=1}^{N} q_i G_\phi(\mathbf{r}, \mathbf{r}_i). \tag{B.42}$$

In vacuum, the Green's function of the Laplace equation, defined such that $\nabla\cdot\epsilon\nabla G_\phi(\mathbf{r}, \mathbf{r}_i) = -\delta(\mathbf{r} - \mathbf{r}_i)$, would simply be $-1/|\mathbf{r} - \mathbf{r}_i|$, saying that the potential is given by the (instantaneous) Coulomb's law $-$ as expected. The second thing is that we can define the canonical field momentum without the scalar potential. This is because the canonical field momentum came from deriving a term like

$$\int d^3r\ \epsilon((\partial_t \mathbf{A})^2 + 2\mathbf{A}\cdot\nabla\phi + (\nabla\phi)^2). \tag{B.43}$$

But, if $\epsilon\nabla\cdot\epsilon\mathbf{A} = 0$, then $\int d^3r\ \mathbf{A}\cdot\nabla\phi = 0$ because it is an integral of a dot product between a curl-less and divergence-less function. Meanwhile, we can write the third term as

$$\int d^3r\ \epsilon\nabla\phi\cdot\nabla\phi = \int d^3r\ -\phi\nabla\cdot\epsilon\nabla\phi = \int d^3r\ \rho\phi. \tag{B.44}$$

Therefore, re-defining the canonical momentum for the field as $\mathbf{\Pi} = \epsilon_0\epsilon(\partial_t\mathbf{A})$, we can write the Hamiltonian as:

$$H = \sum_{i=1}^{N} \frac{(\mathbf{p}_i - q_i\mathbf{A}_i(\mathbf{r}_i))^2}{2m_i} + \frac{1}{2}\sum_{i,j=1}^{N} q_i q_j G_\phi(\mathbf{r}_i, \mathbf{r}_j) + \frac{\epsilon_0}{2}\int d^3r\ \frac{\mathbf{\Pi}^2}{\epsilon} + c^2(\nabla\times\mathbf{A})^2. \tag{B.45}$$

This is the final form of the Hamiltonian of light and matter. As a note, while the Hamiltonian "should" be written in terms of position and momenta, as we have above, it is very common to see the Hamiltonian with the field momentum expressed in terms of the vector potential, in order to keep a small number of variables in the Hamiltonian. Thus, the form we will state in practice is

$$\boxed{H = \sum_{i=1}^{N} \frac{(\mathbf{p}_i - q_i\mathbf{A}_i(\mathbf{r}_i))^2}{2m_i} - \frac{1}{2}\sum_{i,j=1}^{N} q_i q_j G_\phi(\mathbf{r}_i, \mathbf{r}_j) + \frac{\epsilon_0}{2}\int d^3r\ \epsilon(\partial_t\mathbf{A})^2 + c^2(\nabla\times\mathbf{A})^2}. \tag{B.46}$$

Generality, caveats, and potential pitfalls

It is worthwhile to note that this simple Hamiltonian is quite general, and forms the basis for the description of most of the light-matter interaction phenomena we treat in this thesis. It is worth mentioning that this Hamiltonian is deceptively simple, and seemingly innocuous manipulations can lead to errors. We state some of them here, along with some common pitfalls and misconceptions. The purpose of this list is not to be exhaustive, but simply to review some of the subtleties of quantum electrodynamics that have been uncovered through decades of rigorous investigations. Many of these listed below are common points of confusion for newcomers. We should also note that some subtleties are only starting to get elucidated with new work that is enabled in the regime where the light-matter coupling terms are especially strong.

1. This form of the Hamiltonian has been specifically derived in the generalized Coulomb gauge. It is only in that gauge that the scalar potential becomes manifestly a matter degree of freedom (and the vector potential a purely radiation degree of freedom). In other gauges, both potentials take a mixed character and are much harder to interpret.

2. This Hamiltonian is invariant under unitary transformations (frame transformations), in the sense that performing a frame transformation will not change any predicted observables. But, simple truncation of the Hilbert space (e.g., by restricting the matter Hilbert space to two levels, as in cavity quantum electrodynamics) will generally break gauge invariance $-$ and lead to different predictions in different frames. Some frames "do better" than others in this case, such as the "dipole frame" (also called the "length gauge") to be introduced in the next section. We note also as a point of terminology that this representation of the Hamiltonian in terms of the vector potential is called the "velocity gauge".

3. This Hamiltonian is also invariant under gauge transformations. The potentials can be re-defined such that for some gauge function χ, $\phi \to \phi + \partial_t \chi$ and $\mathbf{A} \to \mathbf{A} - \nabla\chi$. But in quantum mechanics, this means that the wavefunctions of the matter must also transform. For calculations of transition amplitudes between stable asymptotic

states of the non-interacting Hamiltonian, one may prove that the amplitudes are independent of this wavefunction transformation [413].

4. Often, a gauge called the Weyl gauge is invoked. The Weyl gauge is the one in which the scalar potential is eliminated (thus, the vector potential is no longer transverse (transverse in real-space, meaning $\nabla \cdot \epsilon \mathbf{A} = 0$), it has some electrostatic (or really, longitudinal) components). It is commonly used in order to "ignore" consideration of the scalar potential. This is not valid, but this only becomes apparent when looking at higher-order corrections (e.g., energy shifts) or in non-perturbative regimes. It should also be noted that often, the way this Hamiltonian in the "Weyl gauge" is actually used is often closer to the generalized Coulomb gauge.

5. The term involving the Green's function of the Laplace equation is a pure matter term in the generalized Coulomb gauge. It can thus be diagonalized with the other matter terms (e.g., the kinetic energy) in order to define the matter Hamiltonian. For example, Coulomb interactions lead to an atomic potential that leads to the formation of bound states. However, it is important to realize that *in this frame*, the "Coulomb potential" also depends on the medium. As a trivial example, for electron in a bulk medium with dielectric constant ϵ, the Coulomb interaction is significantly screened, leading to in principle a large change in the unperturbed energies.

B.1.5 Electromagnetic modes as degrees of freedom of the radiation

The Hamiltonian form of classical electrodynamics exposes that the non-redundant degrees of freedom are the system are the positions and momenta of the matter, the vector potential, and its time-derivative. The vector potential carries an infinite number of degrees of freedom, as a result of the fact that the fields are defined at every point in space. This is cumbersome, and it would be ideal to have a simpler (but still infinite) set of degrees of freedom by which to describe the electromagnetic field. The normal modes of the free electromagnetic field in a medium enable just that.

Recall that for a time-dependent potential satisfying the generalized Coulomb gauge condition, we may expand the potential in terms of the modes of the source-free Maxwell

equations as (see the Box on the next page for details on the mode expansion):

$$\mathbf{A}(\mathbf{r},t) = \sum_n A_n(t)\mathbf{F}_n(\mathbf{r}). \tag{B.47}$$

Here, we will take $A_n(t)$ to be purely real coefficients, and $\mathbf{F}_n(\mathbf{r})$ to be real-valued modes. This can be done without loss of generality in lossless non-magnetic systems[2] Later, we will show that this assumption was unnecessary, and that everything we will derive will hold for complex modes as well. But this makes the derivations easy.

Let us see how the Lagrangian and Hamiltonian of the electromagnetic field without sources looks like under this mode expansion. Plugging this into the Lagrangian, and using orthonormality, we immediately find that:

$$L = \frac{\epsilon_0}{2}\sum_n \left(\dot{A}_n^2 - \omega_n^2 A_n^2\right). \tag{B.48}$$

The second term arose from moving one of the curls to the other side and making use of the Maxwell eigenproblem. The Lagrangian has now been recast as a function of A_n and $\dot{A}_n$,, suggesting that the mode coefficients, A_n, are the canonical coordinates of the electromagnetic field. For each n, then we have as the corresponding Euler-Lagrange equation:

$$\ddot{A}_n + \omega_n^2 A_n = 0, \tag{B.49}$$

The corresponding Hamiltonian is:

$$H = \frac{\epsilon_0}{2}\sum_n \left(\dot{A}_n^2 + \omega_n^2 A_n^2\right). \tag{B.50}$$

Expressing H in terms of the canonical position A_n and momentum $\epsilon_0\dot{A}_n$, we have that

$$H = \sum_n \left(\frac{p_n^2}{2\epsilon_0} + \frac{1}{2}\epsilon_0\omega_n^2 q_n^2\right). \tag{B.51}$$

[2]It is a consequence of ϵ being real that all of the modes can be chosen *real*. It can be immediately seen that if $\mathbf{F}$ is a mode of Maxwell's equations with frequency ω, it is also the case that $\mathbf{F}^*$ is also a mode with the same frequency, meaning that $\mathbf{F} \pm \mathbf{F}^*$ are both modes, which are purely real. This also means that for a non-degenerate mode, it is real. While for a complex mode, it must have a degenerate partner which is its conjugate. This situation also happens in the Schrodinger equation.

This is clearly the Hamiltonian of a set of harmonic oscillators associated with each mode. The frequencies of the oscillators are the modal frequencies ω_n and a "mass" ϵ_0.

Normal mode expansion of the vector potential

Consider Maxwell's equations (in frequency-domain) in the absence of sources: $\mathbf{J} = 0$ and $\rho = 0$. The scalar potential equation is solved by $\phi = c$ with c a constant. As we can always perform a gauge transformation that removes this constant, we may simply say $\phi = 0$. Thus, the only equation of interest is that for the vector potential, which simplifies to (for an isotropic linear medium)

$$\nabla \times \nabla \times \mathbf{A}(\mathbf{r}, \omega) = \epsilon(\mathbf{r}, \omega) \frac{\omega^2}{c^2} \mathbf{A}(\mathbf{r}, \omega). \tag{B.52}$$

The equation for the vector potential on the other hand does have non-zero solutions for $\omega \neq 0$. For example, if $\epsilon = 1$, then a plane transverse wave of wavevector magnitude k satisfies this equation when $\omega = ck$. In what follows, we will consider a *non-dispersive*, but *inhomogeneous* dielectric medium, so that $\epsilon(\mathbf{r}, \omega) = \epsilon(\mathbf{r})$. We will also only consider *lossless* media for the present, such that ϵ is real-valued. A number of powerful general results emerge simply in this case. The resulting equation is a *generalized eigenproblem*, in which an operator ($\nabla \times \nabla \times$), acting on a (vector) function ($\mathbf{A}$), gives that same function, up to an eigenvalue ($\frac{\omega^2}{c^2}$), and a function (ϵ). In the absence of this additional function, this would be a standard eigenproblem. Nevertheless, many results from standard eigenproblems carry over with minimal modification. Here, we enumerate the basic properties of this generalized eigenproblem, and its consequences. These consequences will be critical in the quantization of the electromagnetic field. Some of these properties are developed in more detail and used extensively in treatments of nanophotonics, see for example [49]. To derive basic properties of the Maxwell eigenproblem, we will need to define an inner product between vector functions. In particular, we define

$$\langle \mathbf{X}, \mathbf{Y} \rangle \equiv \int d^3r \, \mathbf{X}^* \cdot \mathbf{Y}. \tag{B.53}$$

Given this inner product, we may state the following properties of the Maxwell equations, its eigenfunctions (or eigenmodes) $\mathbf{F}_n(\mathbf{r}) \equiv \mathbf{A}(\mathbf{r}, \omega_n)$, and its corresponding eigenfrequencies ω_n:

1. **The eigenproblem is Hermitian.** In particular $\langle \mathbf{X}, \nabla \times \nabla \times \mathbf{Y} \rangle = \langle \nabla \times \nabla \times \mathbf{X}, \mathbf{Y} \rangle$.

2. **The eigenvalues are real if ϵ is positive.**

3. **The eigenfunctions can be made orthonormal according to a modified inner product**. Eigenfunctions of different eigenvalues are manifestly orthogonal (and then normalized to be orthonormal) with respect to a new inner product $(\mathbf{X}, \mathbf{Y}) \equiv \int d^3r \; \epsilon \mathbf{X}^* \cdot \mathbf{Y}$. Degenerate eigenfunctions can be made orthonormal by the Gram-Schmidt procedure, just as in quantum mechanics.

4. **The eigenfunctions span the space of divergenceless functions.** Consider a divergenceless (transverse) function $\mathbf{X}$, such that $\nabla \cdot \mathbf{X} = 0$. Then it may be expanded in terms of the eigenfunctions via:

$$\mathbf{X} = \sum_n c_n \epsilon \mathbf{F}_n, \tag{B.54}$$

   with c_n the expansion coefficients, given by $c_m = \int d^3r \; \epsilon \mathbf{F}_m^* \cdot \mathbf{F}_n$. You can see that the divergence of each individual term is zero (from the generalized Coulomb gauge condition), so that the divergence of the overall function is zero.

It then follows that we may write an any time-dependent vector potential in the generalized Coulomb gauge by using a mode expansion, as

$$\mathbf{A}(\mathbf{r}, t) = \frac{1}{2} \sum_n \alpha_n \mathbf{F}_n(\mathbf{r}) e^{-i\omega_n t} + \alpha_n^* \mathbf{F}_n^*(\mathbf{r}) e^{i\omega_n t}, \tag{B.55}$$

where α_n are arbitrary coefficients.

The result we arrived at, although very simple, is extremely important. It says: the time-dependent amplitudes of the modes behave in exactly the same way as a harmonic oscillator. In the quantum theory, the mode amplitudes act as independent quantum harmonic oscillators. This point holds not just for electromagnetism, but other wave equations, such as acoustic wave equations, hydrodynamic wave equations, and relativistic wave equations for fundamental particles.

B.2 Quantization of the electromagnetic field in the absence of charges

We have shown at least classically that the free electromagnetic field is dynamically equivalent to a set of harmonic oscillators. Therefore, we quantize it in the same way we quantize a particle on a spring. The canonical position and momenta of the different modes are promoted to Hermitian operators satisfying a canonical commutation relation where $[p_m, q_n] = i\hbar\delta_{mn}$. In quantum field theory, it is not common to make too much reference to this commutator. Instead, it is more useful to recast this commutator as one in terms of creation and annihilation operators. Then the canonical commutation relation will be formulated as the usual $[a_m, a_n^\dagger] = \delta_{mn}$. Let us define creation and annihilation operators

$$a_n = \sqrt{\frac{\epsilon_0}{2\hbar\omega_n}}\left(\omega_n q_n + \frac{i}{\epsilon_0}p_n\right), \quad a_n^\dagger = \sqrt{\frac{\epsilon_0}{2\hbar\omega_n}}\left(\omega_n q_n - \frac{i}{\epsilon_0}p_n\right). \tag{B.56}$$

It follows immediately that

$$q_n = \sqrt{\frac{\hbar}{2\epsilon_0\omega_n}}\left(a_n + a_n^\dagger\right), \quad p_n = -i\sqrt{\frac{\hbar\omega_n\epsilon_0}{2}}\left(a_n - a_n^\dagger\right). \tag{B.57}$$

Expressing the canonical degrees of freedom in terms of the creation and annihilation operators, we have that

$$H = \sum_n \frac{\hbar\omega_n}{2}\left(a_n^\dagger a_n + a_n a_n^\dagger\right) = \sum_n \hbar\omega_n\left(a_n^\dagger a_n + \frac{1}{2}\right). \tag{B.58}$$

To complete the quantization of the field, the last thing we need to do is write the operator form of the vector potential. That follows from the mode expansion and the fact that $q_n = A_n$. Expressing the q_n in terms of the creation and annihilation operators, we automatically have

$$\mathbf{A} = \sum_n \sqrt{\frac{\hbar}{2\epsilon_0 \omega_n}} (a_n + a_n^\dagger) \mathbf{F}_n. \tag{B.59}$$

In the quantization of the fields, we assumed that the modes were real. This is not necessary. If we express the vector potential in terms of complex modes, then the Hamiltonian is the same as before (just keeping in mind that the creation and annihilation operators are associated with different modes from before). The vector potential on the other hand, takes the form:

$$\mathbf{A}(\mathbf{r}) = \sum_n \sqrt{\frac{\hbar}{2\epsilon_0 \omega_n}} \left(\mathbf{F}_n(\mathbf{r}) a_n + \mathbf{F}_n^*(\mathbf{r}) a_n^\dagger \right). \tag{B.60}$$

To see that this form can be arrived at from an expansion in real modes, consider a case in which the vector potential has two degenerate real modes of frequency ω. As we argued before, since any complex mode has a degenerate partner which is the conjugate, we can always construct two real degenerate modes as the real and imaginary parts of one of the complex modes. Let us call these modes $\mathbf{F}_1$ and $\mathbf{F}_2$, their associated annihilation operators a_1 and a_2 and then consider the contribution of those two modes to the vector potential. Let us now do a change of variables. Let us define two new annihilation operators $b_1 \equiv \frac{a_1 - i a_2}{\sqrt{2}}$ and $b_2 \equiv \frac{a_1 + i a_2}{\sqrt{2} i}$. Let us also define two new modes $\mathbf{G}_1 = \frac{\mathbf{F}_1 + i \mathbf{F}_2}{\sqrt{2}}$ and $\mathbf{G}_2 = \frac{i \mathbf{F}_1 + \mathbf{F}_2}{\sqrt{2}}$. With these definitions, one can show that

$$\omega(a_1^\dagger a_1 + a_2^\dagger a_2) = \omega(b_1^\dagger b_1 + b_2^\dagger b_2) \tag{B.61}$$

and

$$(a_1 + a_1^\dagger)\mathbf{F}_1 + (a_2 + a_2^\dagger)\mathbf{F}_2 = \mathbf{G}_1(\mathbf{r}) b_1 + \mathbf{G}_1^*(\mathbf{r}) b_1^\dagger + \mathbf{G}_2(\mathbf{r}) b_2 + \mathbf{G}_2^*(\mathbf{r}) b_2^\dagger. \tag{B.62}$$

It is always possible to go from a purely real form of the mode expansion of the vector potential operator to a complex form.

B.2.1 Hamiltonian of quantum electrodynamics for non-relativistic matter

We have now quantized the electromagnetic field in the absence of currents and charges. However, most problems that we will be interested in involve the interaction of bound and free electrons with electromagnetic fields. These bound and free electrons represent free charges and currents (which we call matter), and therefore the electromagnetic field is no longer free. We are therefore interested in the Hamiltonian that describes the interaction of light and matter. To construct it, all we need to do is take the Hamiltonian of Eq. (46) and replace the free electromagnetic field part by the expansion in Harmonic oscillators. The final Hamiltonian is

$$\boxed{H = \sum_{i=1}^{N} \frac{(\mathbf{p}_i - q_i \mathbf{A}(\mathbf{r}_i))^2}{2m_i} - \frac{1}{2\epsilon_0} \sum_{i,j=1}^{N} q_i q_j G_\phi(\mathbf{r}_i, \mathbf{r}_j) + \sum_n \hbar\omega_n \left(a_n^\dagger a_n + \frac{1}{2}\right)}. \quad \text{(B.63)}$$

B.2.2 Dipole approximation and dipole Hamiltonian

In many situations in quantum electrodynamics, the wavelength of the photons which the matter interacts with is much larger than the spatial extent of the system of charges. It follows then that the modes of the vector potential vary negligibly over the extent of the electronic wavefunctions. In that case, we may simply replace the $\mathbf{r}_i$ in the vector potential by $\mathbf{r}_0$, which can be thought of as the center of the distribution of charges. This approximation is called the *long-wavelength approximation*, and also the *dipole approximation*, as the result of the approximation is that the interaction between matter and light is well described as an interaction of the quantized electric field with the dipole moment of the system of charges. In this section, we will do a unitary transformation of the Hamiltonian to a much simpler form that is exactly equivalent in the dipole approximation.

Consider the following unitary transformation of the Hamiltonian prescribed by the operator $U = e^{\frac{i}{\hbar}\mathbf{d}\cdot\mathbf{A}(\mathbf{r}_0)}$, where $\mathbf{d} = \sum_{i=1}^{N} q_i \mathbf{r}_i$ is the total dipole moment associated with the charges. We would like to calculate $U^\dagger H U$. To do this, we will make heavy use of the

Baker-Campbell-Hausdorff (BCH) formula:

$$e^A B e^{-A} = A + [A, B] + \frac{1}{2!}[A, [A, B]] + \frac{1}{3!}[A, [A, [A, B]]] + \dots . \tag{B.64}$$

Let's start by evaluating the unitary rotation of $\mathbf{p}_i$, $\mathbf{A}(\mathbf{r}_i)$, and a_n. No unitary rotation needs to be done on the scalar potential terms, as they are functions of the position operators, which commute with the position operators in the argument of the exponential of U. According to BCH, for the kth component of the momentum $\mathbf{p}_i$:

$$U^\dagger p_{ik} U = p_{ik} - \frac{i}{\hbar}\sum_j q_j [r_{jk'} A_{k'}(\mathbf{r}_0), p_{ik}] + \dots = p_{ik} - \frac{i}{\hbar}\sum_j q_j A_{k'}(\mathbf{r}_0)(i\hbar\delta_{ij}\delta_{kk'}) + \dots , \tag{B.65}$$

where $\dots$ denotes the remaining terms of the expansion. We are using repeated index notation. The remaining terms are zero, as the second term is a multiple of the identity in the particle space, which will commute with p_{ik}. Therefore, we have

$$U^\dagger p_{ik} U = p_{ik} + q_i A_k(\mathbf{r}_0). \tag{B.66}$$

Now let's look at the unitary rotation of the vector potential.

$$U^\dagger A_k(\mathbf{r}_0) U = A_k(\mathbf{r}_0) - \frac{i}{\hbar}\sum_j q_j [r_{jk'} A_{k'}(\mathbf{r}_0), A_k(\mathbf{r}_0)] + \dots = A_k(\mathbf{r}_0). \tag{B.67}$$

This is obvious, as the terms of vector potential are analogous to the position operator of the harmonic oscillator. And we know that the components of the position operator commute with themselves. Thus, the vector potential is unchanged by the rotation. But if that's the case, then we have that

$$U^\dagger \sum_{i=1}^{N} \frac{(\mathbf{p}_i - q_i \mathbf{A}(\mathbf{r}_0))^2}{2m_i} U = \sum_{i=1}^{N} \frac{\mathbf{p}_i^2}{2m_i}. \tag{B.68}$$

To conclude the transformation, we need to transform the creation and annihilation opera-

tors. Let's examine the unitary rotation of the creation operator

$$U^\dagger a_n^\dagger U = a_n^\dagger - \frac{i}{\hbar}\sum_j q_j[r_{jk}A_k(\mathbf{r}_0), a_n^\dagger] + \cdots = a_n^\dagger - \frac{i}{\hbar}\sum_j q_j \mathbf{r}_j \sqrt{\frac{\hbar}{2\epsilon_0\omega_n}}\mathbf{F}_n^*(\mathbf{r}_0)$$
$$= a_n^\dagger - \frac{i}{\hbar}\sqrt{\frac{\hbar}{2\epsilon_0\omega_n}}\mathbf{d}\cdot\mathbf{F}_n^*(\mathbf{r}_0). \tag{B.69}$$

Again, the second term is a multiple of the identity (this time on the photon space), and so the other terms in the series are zero. It follows by Hermitian conjugation that

$$U^\dagger a_n U = a_n + \frac{i}{\hbar}\sqrt{\frac{\hbar}{2\epsilon_0\omega_n}}\mathbf{d}\cdot\mathbf{F}_n(\mathbf{r}_0). \tag{B.70}$$

The number operator then transforms as

$$U^\dagger a_n^\dagger a_n U = \left(a_n^\dagger - \frac{i}{\hbar}\sqrt{\frac{\hbar}{2\epsilon_0\omega_n}}\mathbf{d}\cdot\mathbf{F}_n^*(\mathbf{r}_0)\right)\left(a_n + \frac{i}{\hbar}\sqrt{\frac{\hbar}{2\epsilon_0\omega_n}}\mathbf{d}\cdot\mathbf{F}_n(\mathbf{r}_0)\right). \tag{B.71}$$

Combining this with the $\hbar\omega_n$ and the summation, we have that the free-field Hamiltonian transforms into

$$\hbar\omega_n\left(a_n^\dagger a_n + \frac{1}{2}\right) - \mathbf{d}\cdot\left(i\sum_n\sqrt{\frac{\hbar\omega_n}{2\epsilon_0}}\left(\mathbf{F}_n a_n - \mathbf{F}_n a_n^\dagger\right)\right) + \frac{1}{2\epsilon_0}\sum_n\left|\mathbf{d}\cdot\mathbf{F}_n(\mathbf{r}_0)\right|^2. \tag{B.72}$$

Noting that the modal sum in parentheses in the second term is simply the electric field operator $\mathbf{E}(\mathbf{r}_0)$, we may write the QED Hamiltonian as

$$H = \sum_{i=1}^N \frac{\mathbf{p}_i^2}{2m} - \frac{1}{2\epsilon_0}\sum_{i,j=1}^N q_i q_j G_\phi(\mathbf{r}_i,\mathbf{r}_j) + \sum_n \hbar\omega_n\left(a_n^\dagger a_n + \frac{1}{2}\right)$$
$$- \mathbf{d}\cdot\mathbf{E}(\mathbf{r}_0) + \frac{1}{2\epsilon_0}\sum_n\left|\mathbf{d}\cdot\mathbf{F}_n(\mathbf{r}_0)\right|^2 \tag{B.73}$$

There are several main advantages of the dipolar Hamiltonian with respect to the Hamiltonian written in terms of the momentum. For one, the quadratic term in the vector potential has gone, leading to only a single interaction term between light and matter, in terms of the physical electric field. Another major advantage of this Hamiltonian relates to the meanings of the various operators. In particular, in the old frame (called the velocity frame from

now on), the velocity is given by $\mathbf{v} = (\mathbf{p} - q\mathbf{A})/m$, meaning that the physical velocity of the particle is tied to the quantized field, making it difficult to interpret. Moreover, the momentum operator does not have a direct physical significance in this gauge. In the dipolar gauge, the velocity transforms to $U^\dagger \mathbf{v} U = \mathbf{p}/m$, making the physical velocity independent of the quantized field – and allowing much simpler and more intuitive interpretation of what the particles do versus what the photons do. There is a third reason, which has to do with the last term in the Hamiltonian, which is called the *dipole self-energy*, which we will elaborate on below.

As a rule then, when the long-wavelength approximation is valid, we will use the dipolar Hamiltonian.

Cancellation of the dipole self-energy with parts of the Coulomb Hamiltonian

In this section, we elaborate on the form of the dipolar self-energy, showing that it is completely cancelled by part of the Coulomb term (the second term) of Eq. (46). As a result, the final Hamiltonian describing the system of charges in the dipole gauge is

$$\boxed{H = \sum_{i=1}^{N} \frac{\mathbf{p}_i^2}{2m} + \sum_{i,j=1}^{N} \frac{q_i q_j}{8\pi\epsilon_0 |\mathbf{r}_i - \mathbf{r}_j|} + \sum_n \hbar\omega_n \left(a_n^\dagger a_n + \frac{1}{2}\right) - \mathbf{d}\cdot\mathbf{E}(\mathbf{r}_0)}. \tag{B.74}$$

In the remainder of this section, we prove this remarkable simplification. But a reader interested primarily in applying this Hamiltonian to solve problems may skip this section without loss of continuity. This cancellation implies that there is a connection between the radiation modes $\mathbf{F}$ and the solutions of the Poisson equation (which are connected to G_ϕ). They are connected by completeness: any radiation field can be expanded in the $\mathbf{F}$ functions, while any electrostatic field can be expanded in eigenfunctions ϕ of the Laplace equation. Together then, any electric field whatsoever can be expanded in terms of the $\mathbf{F}$s and the ϕs. Let's now make this connection more precise.

To this end, let us define two tensorial projection functions, $\mathbf{P}^{\epsilon,\perp}(\mathbf{r},\mathbf{r}'), \mathbf{P}^{\epsilon,||}(\mathbf{r},\mathbf{r}')$ as

$$\begin{aligned}\mathbf{P}^{\epsilon,\perp}(\mathbf{r},\mathbf{r}') &= \sum_n \epsilon(\mathbf{r}')\mathbf{F}_n^*(\mathbf{r}')\mathbf{F}_n(\mathbf{r}) \\ \mathbf{P}^{\epsilon,||}(\mathbf{r},\mathbf{r}') &= -\sum_n \epsilon(\mathbf{r}')\nabla'\phi_n^*(\mathbf{r}')\nabla\phi_n(\mathbf{r})/\lambda_n,\end{aligned} \tag{B.75}$$

where the functions ϕ_n are eigenfunctions of the Laplace equation in a medium, with eigenvalue λ_n, defined by

$$\nabla\cdot\epsilon\nabla\phi_n = \lambda_n\phi_n \tag{B.76}$$

We have defined the second projection function with a minus sign as a matter of convenience. It is easy to show that the Laplace eigenfunctions, for a real permittivity, are orthonormal.

We have referred to these two functions as projection functions. Let us now show that they are. The claim is that $\mathbf{P}^{\epsilon,\perp}(\mathbf{r},\mathbf{r}')$ projects a function onto the space spanned by the radiation modes, while $\mathbf{P}^{\epsilon,||}(\mathbf{r},\mathbf{r}')$ projects a function onto the space spanned by the Laplace eigenfunctions. Let us start by projecting $\mathbf{P}^{\epsilon,\perp}(\mathbf{r},\mathbf{r}')$ onto functions like $F_m(\mathbf{r})$ and $\nabla\phi_m(\mathbf{r})$, as follows:

$$\begin{aligned}\int d^3r'\ \mathbf{P}^{\epsilon,\perp}(\mathbf{r},\mathbf{r}')\cdot\mathbf{F}(\mathbf{r}') &= \mathbf{F}_m(\mathbf{r}) \\ \int d^3r'\ \mathbf{P}^{\epsilon,\perp}(\mathbf{r},\mathbf{r}')\cdot\nabla\phi_m(\mathbf{r}') &= 0.\end{aligned} \tag{B.77}$$

In the first, we have used the orthonormality of the radiation mode eigenfunctions. In the second, we have used the fact that the dot product of a divergenceless function and a curl-less function integrates to zero.

Meanwhile, projecting $\mathbf{P}^{\epsilon,||}(\mathbf{r},\mathbf{r}')$ onto functions like $F_m(\mathbf{r})$ and $\nabla\phi_m(\mathbf{r})$, as follows:

$$\begin{aligned}\int d^3r'\ \mathbf{P}^{\epsilon,||}(\mathbf{r},\mathbf{r}')\cdot\mathbf{F}(\mathbf{r}') &= 0 \\ \int d^3r'\ \mathbf{P}^{\epsilon,||}(\mathbf{r},\mathbf{r}')\cdot\nabla\phi_m(\mathbf{r}') &= \nabla\phi_n(\mathbf{r}).\end{aligned} \tag{B.78}$$

In the first line, we have used the fact that the dot product of a divergenceless function and

a curl-less function integrates to zero. In the second, we have used integration by parts and the orthonormality of the Laplace eigenfunctions. Notice that the minus sign, as well as the division by the eigenvalue were necessary to get the projection to come out to just the gradient of the Laplace eigenfunction. Suppose we decompose the electric field into radiation and electrostatic parts, as:

$$\mathbf{E}(\mathbf{r}) = \mathbf{E}^{\epsilon,\perp}(\mathbf{r}) + \mathbf{E}^{\epsilon,||}(\mathbf{r}), \tag{B.79}$$

with

$$\begin{aligned} \mathbf{E}^{\epsilon,\perp}(\mathbf{r}) &= \sum_n A_n \mathbf{F}_n(\mathbf{r}) \\ \mathbf{E}^{\epsilon,||}(\mathbf{r}) &= -\sum_n B_n \nabla\phi_n(\mathbf{r}). \end{aligned} \tag{B.80}$$

Then it immediately follows from the projection operators above that

$$\begin{aligned} \int d^3r' \, \mathbf{P}^{\epsilon,\perp}(\mathbf{r},\mathbf{r}') \cdot \mathbf{E}^{\epsilon,\perp}(\mathbf{r}') &= \mathbf{E}^{\epsilon,\perp}(\mathbf{r}) \\ \int d^3r' \, \mathbf{P}^{\epsilon,\perp}(\mathbf{r},\mathbf{r}') \cdot \mathbf{E}^{\epsilon,||}(\mathbf{r}') &= 0. \end{aligned} \tag{B.81}$$

and

$$\begin{aligned} \int d^3r' \, \mathbf{P}^{\epsilon,||}(\mathbf{r},\mathbf{r}') \cdot \mathbf{E}^{\epsilon,\perp}(\mathbf{r}') &= 0 \\ \int d^3r' \, \mathbf{P}^{\epsilon,||}(\mathbf{r},\mathbf{r}') \cdot \mathbf{E}^{\epsilon,||}(\mathbf{r}') &= \mathbf{E}^{\epsilon,||}(\mathbf{r}). \end{aligned} \tag{B.82}$$

Of course, from which it follows that

$$\int d^3r' \, (\mathbf{P}^{\epsilon,\perp}(\mathbf{r},\mathbf{r}') + \mathbf{P}^{\epsilon,||}(\mathbf{r},\mathbf{r}')) \cdot \mathbf{E}(\mathbf{r}') = \mathbf{E}(\mathbf{r}), \tag{B.83}$$

meaning that in the space of electric field functions,

$$\mathbf{P}^{\epsilon,\perp}(\mathbf{r},\mathbf{r}') + \mathbf{P}^{\epsilon,||}(\mathbf{r},\mathbf{r}') = \delta(\mathbf{r}-\mathbf{r}')I, \tag{B.84}$$

with I the 3×3 identity matrix.

To proceed, we need to understand the electrostatic projection function, $\mathbf{P}^{\epsilon,||}(\mathbf{r}, \mathbf{r}')$, better. It can be immediately shown that

$$\mathbf{P}^{\epsilon,||}(\mathbf{r}, \mathbf{r}') = -\epsilon(\mathbf{r}')\nabla\nabla' G_\phi(\mathbf{r}, \mathbf{r}'). \tag{B.85}$$

To see this, let us consider the defining equation for the Green's function

$$\nabla \cdot \epsilon\nabla G_\phi(\mathbf{r}, \mathbf{r}') = \delta(\mathbf{r} - \mathbf{r}'). \tag{B.86}$$

Let us expand the delta function in terms of the Laplace eigenfunctions, similarly to what we did when finding the mode-expansion of the Green's function of the Maxwell equations in Chapter 3. Suppose we define

$$\begin{aligned} G_\phi(\mathbf{r}, \mathbf{r}') &= \sum_n G_n \phi_n(\mathbf{r}) \\ \delta(\mathbf{r} - \mathbf{r}') &= \sum_n \delta_n \phi_n(\mathbf{r}). \end{aligned} \tag{B.87}$$

By taking inner products, it can immediately be seen that $\delta_n = \phi_n^*(\mathbf{r}')$. Plugging these expansions into Eq. (86) yields

$$G_\phi(\mathbf{r}, \mathbf{r}') = \sum_n \phi_n^*(\mathbf{r}')\phi_n(\mathbf{r})/\lambda_n, \tag{B.88}$$

immediately proving the claim of Eq. (85).

Let us now consider the implications of Eq. (85) for Eq. (84). Eq. (84) then states

$$\sum_n \epsilon(\mathbf{r}')\mathbf{F}_n^*(\mathbf{r}')\mathbf{F}_n(\mathbf{r}) = \delta(\mathbf{r} - \mathbf{r}')I + \epsilon(\mathbf{r}')\nabla\nabla' G_\phi(\mathbf{r}, \mathbf{r}'). \tag{B.89}$$

As we see here, the radiation modes are in fact connected to the electrostatic interactions encoded in G_ϕ.

With Eq. (89) in place, we can now consider the dipole self-energy term. Let us consider it in the context of a neutral system of charges (i.e., no ions) in a region where $\epsilon = 1$,

for simplicity. If they are not, then additional complications related to *local field effects* arise. In accord with the long-wavelength approximation, the charges are also assumed to localized around position $\mathbf{R}$ with positions $\mathbf{R}+\mathbf{r}_i$. Defining the dipole moment $\mathbf{d} = \sum_i q_i \mathbf{r}_i$, we have that the dipole self-energy term is

$$\frac{1}{2\epsilon_0} \sum_{i,j} q_i q_j \mathbf{r}_i \cdot (\sum_n \mathbf{F}_n^*(\mathbf{R}) \mathbf{F}_n(\mathbf{R})) \cdot \mathbf{r}_j. \tag{B.90}$$

From Eq. (5.34), we see that this term is

$$\frac{1}{2\epsilon_0} \sum_{i,j} q_i q_j \mathbf{r}_i \cdot (I\delta(0) + \nabla\nabla' G_\phi(\mathbf{R}, \mathbf{R})) \cdot \mathbf{r}_j. \tag{B.91}$$

The first term is clearly infinite, but also has no dependence on the medium whatsoever. This term thus also appears in the free-space QED Hamiltonian. In the context of the free-space Hamitonian, that this first term is an infinite (non-identity) operator presents a problem, as it shifts the energy levels of the system by different infinite amounts (leading to infinite energy differences between states). This is clearly unacceptable, as is. It is however solvable by the program of *renormalization*. The resolution is that this term, in addition to other infinite contributions, lead to a *slight* change or renormalization of the energy levels of the matter in the absence of the electromagnetic field. Thus, functionally, this term is ignored, and we consider it as slightly changing the energy levels of the unperturbed system.

The second term however, looks quite a lot like another term in the Hamiltonian: the Coulomb interaction, given by

$$V_{\text{coul}} = -\frac{1}{2\epsilon_0} \sum_{i,j=1}^{N} q_i q_j G_\phi(\mathbf{r}_i, \mathbf{r}_j). \tag{B.92}$$

In fact, it is tempting to Taylor expand the Green's function, so that

$$V_{\text{coul}} \approx -\frac{1}{2\epsilon_0} \sum_{i,j=1}^{N} q_i q_j (G_\phi(\mathbf{R}, \mathbf{R}) + \mathbf{r}_i \cdot \nabla\nabla' G_\phi(\mathbf{R}, \mathbf{R}) \cdot \mathbf{r}_j). \tag{B.93}$$

The second term would exactly cancel the second term in the dipole self-energy. However,

the Green's function has a rapidly varying part like $1/|\mathbf{r}_i - \mathbf{r}_j|$ associated with the free-space Coulomb interaction, making it un-justified to Taylor expand the Green's function this way. To solve this however, we can *split* the Green's function in two parts, as:

$$G(\mathbf{r}, \mathbf{r}') = -\frac{1}{4\pi|\mathbf{r} - \mathbf{r}'|} + G^{\text{ind}}(\mathbf{r}, \mathbf{r}'). \tag{B.94}$$

We claim that this second term varies *slowly* over the scale of the system of charges, provided that the system is far from the interface with a medium (compared to the extent of the emitter). This can be understood from the principle of superposition in electrostatics. When we place a charge near a medium, the total electrostatic potential is the sum of the potential of the charge, and the potential of the bound charges in the medium *induced* by the charge. In other words, the field created by a charge of magnitude q at position $\mathbf{r}'$ is

$$\phi = \frac{q}{4\pi\epsilon_0|\mathbf{r} - \mathbf{r}'|} + \int d\mathbf{s}\, \frac{\rho^{\text{ind}}(\mathbf{s})}{4\pi\epsilon_0|\mathbf{r} - \mathbf{s}|}. \tag{B.95}$$

The first term corresponds to the free-space part of the Green's function, while the second corresponds to $G^{\text{ind}}(\mathbf{r}, \mathbf{r}')$. Suppose distance of the system of charges to the medium (where induced charges are) is d and the extent of the system of charges is a. Then, it is clear from the previous equation that the potential of the induced charges varies slowly over a provided $a \ll d$, and can thus be Taylor expanded around the center of the system of charges. Therefore, we may write the Coulomb interaction as:

$$V_{\text{coul}} = \sum_{i,j=1}^{N} \frac{q_i q_j}{8\pi\epsilon_0|\mathbf{r}_i - \mathbf{r}_j|} - \frac{1}{2\epsilon_0} \sum_{i,j=1}^{N} q_i q_j (G^{\text{ind}}(\mathbf{R}, \mathbf{R}) + \mathbf{r}_i \cdot \nabla\nabla' G^{\text{ind}}(\mathbf{R}, \mathbf{R}) \cdot \mathbf{r}_j). \tag{B.96}$$

For a neutral system of charges, $\sum_i q_i = 0$, simplifying the Coulomb interaction to

$$V_{\text{coul}} = \sum_{i,j=1}^{N} \frac{q_i q_j}{8\pi\epsilon_0|\mathbf{r}_i - \mathbf{r}_j|} - \frac{1}{2\epsilon_0} \sum_{i,j=1}^{N} q_i q_j \mathbf{r}_i \cdot \nabla\nabla' G^{\text{ind}}(\mathbf{R}, \mathbf{R}) \cdot \mathbf{r}_j. \tag{B.97}$$

Meanwhile from Eq. (91), we get (ignoring the $\delta(0)$ term)

$$\frac{1}{2\epsilon_0}\sum_{i,j} q_i q_j \mathbf{r}_i \cdot \left(-\nabla\nabla' \frac{1}{4\pi|\mathbf{r}-\mathbf{r}'|}\Big|_{\mathbf{r}=\mathbf{r}'=\mathbf{R}} + \nabla\nabla' G^{\text{ind}}(\mathbf{R},\mathbf{R}) \right) \cdot \mathbf{r}_j. \tag{B.98}$$

The first term is an infinite self-energy which doesn't depend on the medium, and can also functionally be ignored. The second term however, which is medium-dependent is cancelled by a term of opposite sign in V_{coul}. Therefore, neglecting infinite self-energy terms which don't affect subsequent calculations, the Hamiltonian reduces to:

$$H = \sum_{i=1}^{N} \frac{\mathbf{p}_i^2}{2m} + \sum_{i,j=1}^{N} \frac{q_i q_j}{8\pi\epsilon_0|\mathbf{r}_i - \mathbf{r}_j|} + \sum_n \hbar\omega_n \left(a_n^\dagger a_n + \frac{1}{2} \right) - \mathbf{d}\cdot\mathbf{E}(\mathbf{r}_0), \tag{B.99}$$

completing the proof of this remarkable cancellation.

B.3 Common Hamiltonians of light-matter systems and key effects in light-matter interaction

The vast majority of the literature − past and current − on light-matter interactions is based on the Hamiltonians of Eq. (63) (in the velocity gauge) and Eq. (74) (in the length gauge). These Hamiltonians are sufficiently general to describe general matter systems (e.g., many-electron systems in real space) interacting with electromagnetic fields in arbitrary dielectric structures (for which many photon modes can in principle interact with the matter). In many cases, the full Hamiltonians are not amenable to direct solution of the time-dependent Schrodinger equation. There are however key simplifications that arise in many case of light-matter interaction that lead to much simpler model Hamiltonians that may either be (a) directly diagonalized or (b) readily numerically solved. Here, we review some of those Hamiltonians, and the key phenomena that arise from them.

A bound electron system in an optical cavity and the Rabi Hamiltonian. One of the most common situations considered in light-matter interactions is that of a bound system of charges (with matter Hamiltonian H_{mat}) coupled to a cavity with a low-loss resonant optical mode of frequency ω. If ω is similar to a transition energy of the matter system (and

the transition is dipole-allowed), then the dynamics can be very well-understood by treating the matter system as a two-level system. The corresponding Hamiltonian, describing the coupling of a two-level system of frequency ω_0 to a cavity mode of frequency ω, is referred to as the *Rabi Hamiltonian* and is given as

$$H_R/\hbar = \frac{1}{2}\omega_0\sigma_z + \omega a^\dagger a + g\sigma_x(a + a^\dagger), \tag{B.100}$$

where $\sigma_{x,z}$ are the usual Pauli matrices, and g is the coupling energy and is given by (in the dipole approximation) $\sqrt{\frac{\omega}{2\epsilon_0\hbar}}\mathbf{d}\cdot\mathbf{F}(0)$, where $\mathbf{F}(0)$ is the mode function for the cavity mode at the location of the two-level system (we've taken the mode function real without loss of generality). Intriguingly, this Hamiltonian, while simple, is not analytically diagonalizable. However, in a great many cases, the coupling is very weak compared to the cavity frequency, $g \ll \omega$. In this case, processes involving simultaneous (de-)excitation of the two-level system and (de-)excitation of the cavity would be expected to have very low amplitude (due to energy conservation). In this *rotating wave approximation*, one may approximate $\sigma_x(a + a^\dagger) \approx \sigma^+ a + \sigma^- a^\dagger$, with $\sigma^\pm$ are the usual two-level raising and lowering operators. The resulting Hamiltonian, H_{JC} given by

$$H_{JC}/\hbar = \frac{1}{2}\omega_0\sigma_z + \omega a^\dagger a + g(\sigma^+ a + \sigma^- a^\dagger), \tag{B.101}$$

is known as the *Jaynes-Cummings Hamiltonian* and is amenable to direct solution. Let us solve it to get a sense of the type of phenomena to be expected in light-matter interaction. Upon writing the Hamiltonian matrix, one sees a block-diagonal structure involving blocks in the subspace span$\{|e,n\rangle, |g,n+1\rangle\}$ with Hamiltonian $H = \frac{1}{2}(\omega_0+\omega)I + \frac{1}{2}(\omega_0-\omega)\sigma_z + g\sqrt{n+1}\sigma_x \equiv \frac{1}{2}\bar{\omega}I + \mathbf{V}\cdot\boldsymbol{\sigma}$, with $\bar{\omega} = \frac{1}{2}(\omega_0+\omega)$ and the vector $\mathbf{V} = (g\sqrt{n+1}, 0, \frac{1}{2}\Delta)$ with $\Delta = \omega_0 - \omega$. This is merely the Hamiltonian of a two-level system, thus we may immediately read off the dynamics. For example, an initial σ_z eigenstate such as $|e,n\rangle$ will precess around the Bloch sphere (around the vector V). If $\Delta = 0$ (resonance), then a point on a pole of the Bloch sphere will reach the other pole after time $\pi/g\sqrt{n+1}$ and eventally return - a phenomenon known as Rabi oscillation. The number of photons will oscillate between n and $n+1$ over time and the atom will similarly oscillate between excited and

de-excited.

Photon blockade and quantum nonlinearity Much can also be understood from the spectrum of the Jaynes-Cummings Hamiltonian. The energies are divided into two-state manifolds labeled by n

$$E_{n\pm} = n\omega + \frac{1}{2}\bar{\omega} \pm \sqrt{\frac{1}{4}\Delta^2 + (n+1)g^2}. \tag{B.102}$$

for $n = 0, 1, 2, ...$ (note that the state $|g, 0\rangle$ is the only one not in a doublet, it's energy is simply $E_0 = -\omega_0/2$). For $g = 0$, there are two ladders of states which are equally spaced by ω. When $g \neq 0$, the ladders are no longer evenly spaced. This *anharmonicity* leads to an interesting phenomenon of photon-blockade. To see it, consider what happens when the atom-cavity system is pumped by photons of frequency Ω resonant with a transition of the combined atom-cavity system. Suppose for example that $\Omega = E_{1+} - E_0$. Then the system will efficiently be pumped into the state $|1+\rangle$. Were the states $|1+\rangle$ and $|2+\rangle$ equidistant, the system could move into the next state. But it cannot, this transitions is off-resonance with Ω and therefore the incident photon will be reflected from the cavity. There will never be more than one excitation in the cavity. This phenomenon is known as *photon blockade*.

This photon blockade arises directly from the anharmonicity of the spectrum. This anharmonicity can be understood as a type of unusual optical nonlinearity which is operable at the level of a single-photon. To understand the connection to optical nonlinearities, consider the electromagnetic field in a third-order nonlinear medium, with third-order susceptibility $\chi^{(3)}$. In a material with such an optical nonlinearity, the material polarization in response to an applied electric field has a cubic contribution, leading to a term in the Hamiltonian which is quartic in the electric field. For example, with a cavity with a medium with a nonlinear index inside of it, the resulting cavity Hamiltonian can be written in the form $H_{\text{Kerr}} = \hbar\omega a^\dagger a + \frac{1}{6}\beta\hbar\omega : (a - a^\dagger)^4 :$, where β is a nonlinear coupling constant, and :: denotes normal ordering. In the rotating-wave approximation (i.e., ignoring terms with unbalanced numbers of creation and annihilation operators), the Kerr nonlinearity takes the more commonly stated form $H_{\text{Kerr}} = \hbar\omega\left((1+\beta)a^\dagger a + \beta(a^\dagger a)^2\right)$ [425, 426]. The cavity eigenstates are Fock states of n photons with with energy $E_n \equiv \hbar\omega_n = \hbar\omega\left[(1+\beta)n + \beta n^2\right]$. Thus,

the energy to add a photon depends on the number of photons present and so the energy ladder becomes evenly spaced. Therefore, a single-frequency pump can become progressively more or less efficient at pumping the cavity as photons build up, leading to known phenomena such as optical bistability, and even some new phenomena, such as Fock lasing, introduced in Chapter 8. The nonlinearity coming from the Jaynes-Cummings model is particularly extreme because of its strength. If the nonlinearity is sufficiently strong (compared to dissipation), then the anharmonicity becomes effective at the level of one photon. In nonlinear optical materials, the nonlinear shift per photon (measured by β) is typically exceptionally weak.

We conclude this section by noting that all of this analysis is predicated on $g \ll \omega$. When this is no longer true, the system enters the *ultrastrong* and *deep strong* coupling regimes in which the light-matter wavefunctions substantially change, the ground-state energy is modified (and thus many thermodynamic and chemical properties), and new types of nonlinearities can emerge. In Chapter 6, we explore the development of accurate descriptions of ground- and excited-state energies in ultrastrong coupling based on photonic quasiparticle ansatzes, while in Chapter 7, we explore an unusual form of nonlinearity arising from the spectrum of the Rabi model. It behaves almost perfectly linearly for excitations below a critical excitation number N, and then anharmonically beyond this point (almost like an $N-$level system). Such a system facilitates the creation of N-excitation Fock states.

One or more harmonic oscillators coupled to the radiation field. Although we do not analyze this example in great detail in this thesis, it is a key model in the physics of light-matter interaction (with many appearances in current work), and it does effectively appear in Chapter 3 where we discuss the linear response of 2D phononic materials $-$ in which we consider the coupling of light to a continuum of optical phonons in a 2D material, which represent a continuum of harmonic oscillators. For a harmonic oscillator coupled to a radiation field described by the dipole Hamiltonian, the simplified Hamiltonian, called the *Hopfield Hamiltonian* will read something like

$$H_{\text{Hopfield}} = \omega_0 b^\dagger b + \omega a^\dagger a + ig(b + b^\dagger)(a - a^\dagger). \tag{B.103}$$

A moving free charge coupled to the radiation field. The Hamiltonian of free-electrons and light is generally given as

$$H = H_{\text{el}} + H_{\text{em}} + H_{\text{int}}, \tag{B.104}$$

with H_{el} the Hamiltonian of the electrons, H_{em} the Hamiltonian of the electromagnetic field, and H_{int} the interaction between them.

For a system of N relativistic (spin-less) electrons, their Hamiltonian is given as the Klein-Gordon one,

$$H_{\text{el}} = c\sqrt{m^2c^2 + \mathbf{p}^2}. \tag{B.105}$$

In the presence of an electromagnetic field described by its vector potential $\mathbf{A}(\mathbf{r}_i)$, the Hamiltonian, under a minimal coupling transformation, contains both the pure electron part of the Hamiltonian and the interaction. In particular:

$$H_{\text{el}} + H_{\text{int}} = c\sqrt{m^2c^2 + (\mathbf{p} + e\mathbf{A}(\mathbf{r}))^2}. \tag{B.106}$$

Making the very-well-respected approximation that $|e\mathbf{A}| \ll \sqrt{m^2c^2 + \mathbf{p}^2}$, we can perform a Taylor expansion of the square root to arrive at:

$$c\sqrt{m^2c^2 + \mathbf{p}^2} + \frac{ec}{\sqrt{m^2c^2 + \mathbf{p}^2}}\mathbf{A}(\mathbf{r}) \cdot \mathbf{p}, \tag{B.107}$$

where we have ignored the so-called *diamagnetic term* proportional to $\mathbf{A}^2$, and the non-commutability of $\mathbf{p}$ and $\mathbf{A}$[3]. The Hamiltonian can also be simplified further in the case when we treat the electron under the paraxial approximation, which results from linearizing the dispersion relation of the electron around its central momentum. For fast-moving electrons in transmission electron microscopes where these effects are typically observed, this approximation is well-respected as the speed of the energetic electron is hardly changed by its interaction. Put more rigorously, we will restrict the electron Hamiltonian to the space

[3]This is justifiable when the electron propagates always in regions of constant permittivity. This is because the vector potential and Hamiltonian above are derived under the generalized Coulomb gauge for which $\nabla \cdot \epsilon\mathbf{A} = 0$ and so if epsilon is constant, then the vector potential is divergenceless.

of functions of the form $\psi = e^{i\mathbf{k}_0\cdot\mathbf{r}}f$, where f is slowly varying ($|\nabla f| << |kf|$). In that case, the action of the electron Hamiltonian (taken for a single electron WLOG) on the state is

$$H_{\text{el}}\psi = c\sqrt{m^2c^2 - \hbar^2\nabla^2}e^{i\mathbf{k}_0\cdot\mathbf{r}}f \approx e^{i\mathbf{k}_0\cdot\mathbf{r}}c\sqrt{m^2c^2 + \hbar^2\mathbf{k}_0^2 - 2i\hbar^2\mathbf{k}_0\cdot\nabla}f \tag{B.108}$$

Taylor expanding, and noting that in relativity $p/E = v/c^2$, we have

$$e^{i\mathbf{k}_0\cdot\mathbf{r}}(c\sqrt{m^2c^2 + \hbar^2\mathbf{k}_0^2} + \frac{\hbar c\mathbf{k}_0\cdot(-i\hbar\nabla)}{\sqrt{m^2c^2 + \hbar^2\mathbf{k}_0^2}})f = e^{i\mathbf{k}_0\cdot\mathbf{r}}(E_0 - i\hbar\mathbf{v}\cdot\nabla))f, \tag{B.109}$$

with $E_0 = \sqrt{m^2c^4 + \hbar^2c^2\mathbf{k}_0^2}$. We may thus approximate H_{el} as $-i\hbar\mathbf{v}\cdot\nabla$ [4] Therefore, our final electron Hamiltonian is $H_{\text{el}} \approx -i\hbar\mathbf{v}\cdot\nabla$. Taking the electron velocity to dominantly be in the z-direction WLOG, we have that the Hamiltonian of *free-electron quantum optics* (also called the *quantum PINEM Hamiltonian* (PINEM stands for photon-induced near-field electron microscopy, see Chapter 2) is given by:

$$H = -i\hbar v\partial_z + \sum_n \hbar\omega_n a_n^\dagger a_n + \sum_n W_n(z)a_n + W_n^*(z)a_n^\dagger \equiv H_0 + V, \tag{B.110}$$

with $H_0 = -i\hbar v\partial_z + \sum_n \hbar\omega_n a_n^\dagger a_n$, and we have defined $W_n = ev\sqrt{\frac{\hbar}{2\epsilon_0\omega_n}}F_{nz}(z)$. This Hamiltonian describes the interaction of a relativistic electron with the electromagnetic field in the paraxial approximation. Intriguingly, it is exactly solvable. Using the Magnus expansion (see [423]), one can show that an initial wavefunction of the electron and light evolves as:

$$|\psi(t)\rangle = e^{\sum_n \chi_n} e^{\sum_n S_n} U_0|\psi(0)\rangle, \tag{B.111}$$

with

$$\chi_n = -\frac{i}{\hbar^2 v^2}\int_{-\infty}^{z} dz_1 \int_{-\infty}^{z_1} dz_2 \,\text{Im}\left[W_n(z_1)W_n^*(z_2)e^{-i\frac{\omega_n}{v}(z_1-z_2)}\right], \tag{B.112}$$

$$S_n = e^{-i\frac{\omega_n}{v}z}g_n^* a_n^\dagger - e^{i\frac{\omega_n}{v}z}g_n a_n, \tag{B.113}$$

[4] This is because they are the same on this space of states up to the identity. In particular $H_{\text{el}}\psi - (-i\hbar\mathbf{v}\cdot\nabla)\psi = e^{i\mathbf{k}_0\cdot\mathbf{r}}(E_0 - \hbar\mathbf{k}_0\cdot\mathbf{v})f = (E_0 - \hbar\mathbf{k}_0\cdot\mathbf{v})\psi$ clearly differing only by a constant multiple of the identity, since $\mathbf{v}$ and $\mathbf{k}$ are constants for every state.

$$g_n = \frac{i}{\hbar v} \int_{-\infty}^{z} dz'\, W_n(z') e^{-i\frac{\omega_n}{v}z'}, \tag{B.114}$$

and

$$U_0 = e^{-\frac{iH_0 t}{\hbar}} = e^{-vt\partial_z - it\sum_n a_n^\dagger a_n}. \tag{B.115}$$

A few comments are in order. Ignoring the χ, we see that the evolution of the electron-light wavefunction has two main contributions: one is the unperturbed evolution U_0, corresponding to a translation of the electron wavefunction (by vt) and free-evolution of the field oscillators. The other is associated with the term $\exp[e^{-i\frac{\omega_n}{v}z} g_n^* a_n^\dagger - e^{i\frac{\omega_n}{v}z} g_n a_n]$. The operator $e^{\pm i\frac{\omega_n}{v}z}$ raises (lowers) the momentum by $\hbar\omega_n/v$ and the energy (and energy, given linear dispersion, by $\hbar\omega_n$). Thus, the plane wave factors are electron raising and lowering operators. We may thus write the term S_n as a beam-splitter-type interaction $\exp[g_n^* b_n a_n^\dagger - g_n b_n^\dagger a_n]$, evocative of the Hopfield model. Interestingly, the electron raising and lowering operators are *not* like oscillator operators at all, despite moving the system up and down and evenly spaced ladder of states. This is because $[b_n, b_m^\dagger] = 0$ (and of course $[b_n, b_m]$ and $[b_n^\dagger, b_m^\dagger] = 0$), as the ladder operators are functions of the position operator only. Thus, the model of a swift electron of constant velocity, coupled to a field, is that of an effectively *classical oscillator* coupled to the field.

Let us briefly highlight some results of this Hamiltonian related to the quantum states of light that can be generated, following our treatment in Ref. 29 of App. A. For mono-energetic electrons $|E_0\rangle$ coupled to a single field mode with $|\ell_0\rangle$ photons initially, the system evolves into an entangled state of fixed excitation number $|\psi\rangle \to \sum_\ell c_\ell |E_0 - \ell\hbar\omega, \ell\rangle$. Another interesting case is one in which the electron is in an eigenstate of z, thus having a perfectly defined position. In this case, $b_n \to \beta_n \equiv e^{-i\omega_n z/v}$ and S_n corresponds exactly to a displacement transformation on the field. In this case, the electron acts as a true "classical current" and displaces the any field state, in principle allowing for the creation of displaced squeezed states, displaced Fock states, and true coherent states (acting like an optical frequency antenna).

To close this section, we should also note that this Hamiltonian is purely one-dimensional, and neglects effects from spin, as well as quantum recoil (changes in the velocity of the

electron) (as well as a large class of multi-photon emission effects involving simultaneous emission of two photons (as opposed to sequential emission)). In Chapter 5, we consider a more general interaction Hamiltonian between a relativistic spinor electron and quantized fields in materials (e.g., 2D materials supporting plasmons). In those cases, the relevant Hamiltonian is the Dirac Hamiltonian (see Appendix corresponding to Chapter 5). The scalar QED Hamiltonian (for a relativistic, spinless charge) also describes many of the effects we consider when the emitted photons have energies much smaller than that of the electron.

B.3.1 The effect of dissipation

The Hamiltonians described in the previous paragraphs all describe closed systems – of a matter system with some number of optical modes. In reality, these Hamiltonians often neglect the fact that the matter and/or the radiation (say, in the cavity) are in general coupled to more than each other. For example, if one of the mirrors of the cavity has partial transmission, then a photon in the cavity can escape into the outside of the cavity. This outside world, being infinite (or large enough) in extent, supports a continuum of propagating modes. Therefore light in the cavity (generally) will irreversibly leak out, and the outside continuum acts as a reservoir in the thermodynamic sense: although the continuum becomes populated with cavity excitations, the state of the continuum can effectively be thought to be unchanged by this small number of excitations. Although all of these interactions are entirely conservative (the net energy of the cavity+reservoir is unchanged), when we look at the cavity only, as is very often the case, the state of the cavity appears to undergo damping. We should note that similar phenomena arise for matter as well. An excited electron in an atom immersed into a cavity may spontaneously emit into many other photon modes (or other excitations, like phonons) besides those from the cavity, causing irreversible transfer population from an atomic excited state to an atomic ground state. This will appear as atomic damping if we only consider the atom and cavity. Intriguingly, one can also have damping without population transfer, as in *pure dephasing*, where for example, a system can emit low-frequency excitations (like phonons), changing perhaps its

vibrational state but not its electronic state. If we consider only the electronic state, this dephasing will result in decay of electronic superpositions (like coherence between the excited and ground states, which leads to a dipole moment). These effects manifest as decay of the off-diagonal components of the atomic density matrix.

Because it is fundamentally impractical to follow the continuum of far-field modes along with the cavity, we now outline the description of damping in light-matter interactions. We outline the effect of damping on the density matrix, as well as on Heisenberg operators of the system. We then use the results from the Heisenberg treatment to develop a description of field quantization in dissipative media. This treatment is meant to be expository and somewhat more heuristic in places. The more rigorous framework for the density matrix treatment of damping is very well-covered in introductory texts such as [433], and is also used in Chapters 7 and 8 of the thesis. In the thesis we also extend the density matrix treatment to more complex cases with nonlinearities and multiple resonances, as well as more general systems (such as photonic quasiparticles arising from deep-strong light-matter coupling). We will consider damping here only for a harmonic oscillator (such as a cavity mode) for the purposes of demonstration.

Dissipation as a reservoir on a single-mode

Let us develop a heuristic treatment of damping (we will get the right answer, but not in a particularly rigorous way). Suppose we have a cavity mode with annihilation operator a coupled to an *single* oscillator with harmonic oscillator b at the same frequency (taken to be in the vacuum state). And suppose we want an equation of motion for the density matrix of a alone. To proceed, let us calculate the density matrix of the joint system after a short time dt. In the interaction picture, the density matrix evolves according to $\rho(t+dt) = e^{-iV(dt)}\rho(t)e^{iV(dt)}$, where $V = g(ab^\dagger + a^\dagger b)$, with g the Rabi frequency. We shall expand the exponentials, retaining terms up to second order in V, which will be the leading-order change to the density matrix of a (the first-order term will vanish). Doing so yields

$$\rho(t+dt) = \rho(t) - i[V,\rho(t)](dt) - \frac{1}{2}(V^2\rho(t) + \rho(t)V^2 - 2V\rho(t)V)(dt)^2. \qquad \text{(B.116)}$$

Now, we take the partial trace with respect to b to get the reduced density matrix of a. In what follows, I will make use of the fact that when b is in the vacuum state, we have $\mathrm{tr}_b(b) = \mathrm{tr}_b(b^\dagger) = \mathrm{tr}_b(b^2) = \mathrm{tr}_b(b^{\dagger 2}) = \mathrm{tr}_b(b^\dagger b) = 0$, and $\mathrm{tr}_b(bb^\dagger) = 1$. Using this, we immediately arrive at, defining $\rho_a = \mathrm{tr}_b(\rho)$:

$$\rho_a(t+dt) = \rho_a(t) - \frac{1}{2}(gdt)^2(a^\dagger a\rho_a(t) + \rho_a(t)a^\dagger a - 2a\rho_a(t)a^\dagger). \tag{B.117}$$

Since gdt is simply the probability of de-excitation of a one-photon state in the cavity, we shall make the following extrapolation of the theory here. In the case where the cavity is instead coupled to a continuum of b modes, we expect decay at some rate κ, such that the probability of de-excitation of a one-photon state becomes κdt. Making this substitution ($(gdt)^2 \to \kappa dt$), we may now write

$$\dot{\rho}_a = -\frac{\kappa}{2}(a^\dagger a\rho_a + \rho_a a^\dagger a - 2a\rho_a a^\dagger). \tag{B.118}$$

This equation holds at all times because the state of the reservoir can be approximated as vacuum at all times. It is as if we threw away the far-field photon after an infinitesimal time, which to some extent is true in a leaky cavity.

Dissipation in the Heisenberg picture and quantum Langevin forces

Now, we will show that there is an equivalent perspective to the problem of damping, formulated not for the density matrix, but for the Heisenberg operators of the system. In this picture, damping will be understood as concomitant with the action of a random force (called a (quantum) Langevin force) on the cavity. Here, we shall opt to be less heuristic than the previous section, because we would like to use it in the next section as the basis for field quantization in dissipative media. Let us consider the coupling of our cavity mode to an *continuum* of reservoir modes b_k, with k indexing over the continuum. The Hamiltonian is now

$$H/\hbar = \omega a^\dagger a + \sum_k \omega_k b_k^\dagger b_k + \sum_k g_k(ab_k^\dagger + a^\dagger b_k). \tag{B.119}$$

Let us develop a Heisenberg picture description of the evolution of a. The Heisenberg equations for a and b_k are

$$\begin{aligned}\dot{a} &= -i\omega a - i\sum_k g_k b_k \\ \dot{b}_k &= -i\omega_k b_k - i g_k a. \end{aligned} \tag{B.120}$$

To proceed, let us formally eliminate b_k as $b_k(t) = b_k(0)e^{-i\omega_k t} - ig_k \int^t dt' e^{-i\omega_k(t-t')}a(t')$. Inserting this into a, we have

$$\dot{a} = -i\omega a - i\sum_k g_k b_k(0)e^{-i\omega_k t} - i\sum_k g_k^2 \int^t dt' e^{-i\omega_k(t-t')}a(t'). \tag{B.121}$$

Taking the coupling constants to vary slowly over the typical decay constant of the field ($\kappa = 2\pi\rho g^2$ with ρ the density of continuum states and g the coupling constant at the cavity frequency), we make make a so-called *white-noise approximation*, $g_k \approx g$ – referred to as such because all continuum modes (fluctuations) get the same weight. In this white noise approximation, and taking the sum into an integral $\sum_k \to \int d\omega_k \rho$, we have

$$\dot{a} = -i\omega a - \frac{1}{2}\kappa a + F, \tag{B.122}$$

where

$$F = -i\sum_k g_k b_k(0)e^{-i\omega_k t}, \tag{B.123}$$

is the so-called quantum Langevin force. We see that as expected, the equation of motion for the cacvity operator decays at the expected (amplitude) decay rate of $\kappa/2$. However, there is this additional fluctuating force. It's role is to add fluctuations in a way to preserve $[a, a^\dagger] = 1$ at all times. Without the Langevin force, the commutator would decay in time as $[a, a^\dagger] \to e^{-2\kappa t}$, which is unphysical. If the commutator decays, then there could be violations of the Heisenberg uncertainty principle, which is fundamental (recall that the uncertainty product of conjugate operators is bounded by the expectation value of a commutator, so if $[a, a^\dagger] \to 0$, then $[x, p] \to 0$, which is evidently unphysical). This force can be understood as a "random" force, as the operators $b(0)$ essentially represent vacuum

fluctuations which are present at all times, including at asymptotic $-\infty$.

Thus, in the Heisenberg picture, the description of damping is that in which the operators decay at the classically expected rate, up to a fluctuating force term which preserves the commutation relations. Calculations can be performed by treating the force as a source term, and the calculation of expectation values of correlation functions of a goes through the correlators of the force. For example, we may at once say that in a damped cavity, the Heisenberg operator for the cavity is

$$a = a(0)e^{-i\omega t-\kappa t/2} + \int^t dt' e^{-(i\omega+\kappa/2)(t-t')}F(t'). \tag{B.124}$$

Notice that if the initial time goes to $-\infty$, then only the force term remains. To evaluate expectation values, one can use results like $\langle F\rangle = 0, \langle F^\dagger(t)F(t')\rangle = 0$ (for a vacuum reservoir) and $\langle F(t)F^\dagger(t')\rangle = \kappa\delta(t-t')$ (see [426] for more information).

This Langevin framework is developed and extended in extensive detail for applications in quantum nonlinear optics in Chapter 8. There, we extend the Langevin framework to nonlinear cavities, in which the dissipation depends on the number of photons in the cavity (so it is a highly correlated *nonlinear* dissipation process). Using this framework we show how highly non-classical macroscopic states (such as Fock states) can be created using lasers.

B.4 Quantization of the EM field in absorbing media

We now use these developments to show how the electric field can be quantized in a linear *absorbing* medium (with ϵ complex instead of real). In previous sections, we considered field quantization in non-dissipative media, where one could write the vector potential as an expansion over orthonormal modes with some expansion coefficients. These expansion coefficients were essentially identified as the creation and annihilation operators. This procedure cannot be extended in dissipative media, as although there are still eigenvectors of the Maxwell eigenequation, they are not necessarily complete, and so an arbitrary vector potential may not be expressed in terms of them. We now show that it is possible to write

a quantized operator for the field purely in terms of the Langevin force operators of the reservoirs that lead to this damping.

Consider a medium with damping coupled to the transverse electromagnetic field in vacuum. The Hamiltonian of the system, in the Coulomb gauge, is

$$H = H_{mat} + \frac{\epsilon_0}{2}\int d^3r\, \mathbf{E}^2 + c^2\mathbf{B}^2 - \int d^3r\, \mathbf{j}\cdot\mathbf{A} = H_0 - \int d^3r\, \mathbf{j}\cdot\mathbf{A} = H_0 + V, \quad \text{(B.125)}$$

where H_{mat} is the Hamiltonian of the underlying matter (for example, of N atoms with Z protons and electrons arranged according to some crystal lattice interacting Coulombically). The Heisenberg equation of motion for $\mathbf{A}$ can be shown to just be the Maxwell equation (in operator form; as this is expected, we do not derive it here). In particular, we have that in frequency-domain (Fourier transform the Heisenberg equation)

$$\left(\nabla\times\nabla\times - \frac{\omega^2}{c^2}\right)\mathbf{A}(\mathbf{r},\omega) = \mu_0\mathbf{j}(\mathbf{r},\omega). \quad \text{(B.126)}$$

To proceed to find the equation of motion for $\mathbf{j}$, we will consider the lowest-order effect of $\mathbf{A}$ on $\mathbf{j}$. This may be done by writing the Heisenberg picture $\mathbf{j}$ (I subscript denotes interaction picture)

$$\mathbf{j}(\mathbf{r},t) = U^\dagger\mathbf{j}(\mathbf{r})U = \left(\mathrm{T}e^{-\frac{i}{\hbar}\int^t d^4x'\mathbf{j}_I(x')\cdot\mathbf{A}_I(x')}\right)e^{iH_0t/\hbar}\mathbf{j}(\mathbf{r})e^{-iH_0t/\hbar}\left(\mathrm{T}e^{\frac{i}{\hbar}\int^t d^4x'\mathbf{j}_I(x')\cdot\mathbf{A}_I(x')}\right), \quad \text{(B.127)}$$

with $\int^t d^4x = \int^t dt'\int d^3r'$ and $x = (\mathbf{r}', t')$. Expanding in the interaction as:

$$\mathbf{j}(\mathbf{r},t) = \left(1 - \frac{i}{\hbar}\int^t d^4x'\mathbf{j}_I(x')\cdot\mathbf{A}_I(x')\right)\mathbf{j}_I(\mathbf{r},t)\left(1 + \frac{i}{\hbar}\int^t d^4x'\mathbf{j}_I(x')\cdot\mathbf{A}_I(x')\right), \quad \text{(B.128)}$$

we may write (to first order in the interaction)

$$j_i(\mathbf{r},t) = j_{iI}(\mathbf{r},t) - \frac{i}{\hbar}\int d^3\mathbf{r}'dt'\,\theta(t-t')[j_{Ij}(\mathbf{r}',t'), j_{Ii}(\mathbf{r},t)]A_{jI}(\mathbf{r}), \quad \text{(B.129)}$$

where we have extended the upper limit of the time integration by adding a heaviside function. Thus, in frequency domain, we have (for a time-translation-invariant system, where

the commutator must be a function of $t - t'$)

$$j_i(\mathbf{r},\omega) = j_i^{(0)}(\mathbf{r},\omega) + \int d^3r' \chi_{ij}(\mathbf{r},\mathbf{r}',\omega) A_j(\mathbf{r}',\omega), \tag{B.130}$$

where we have dropped the I subscript upon Fourier transformation, and identified $j_i^{(0)}(\mathbf{r},\omega)$ as the Fourier transform of the the interaction-picture current in the absence of interactions. In addition, we have also defined the current-current susceptibility or response function:

$$\chi_{ij}(\mathbf{r},\mathbf{r}',\omega) = \int d(t-t') e^{i\omega(t-t')} \left(\frac{i}{\hbar} \theta(t-t') [j_{Ii}(\mathbf{r},t), j_{Ij}(\mathbf{r}',t')] \right), \tag{B.131}$$

which is just the susceptibility that is expected from the Kubo formula from linear response theory (similar formulae are manipulated in Chapter 4 to calculate the electromagnetic response of optical phonons in 2D materials). This susceptibility is proportional to the optical conductivity of the material, from standard linear response considerations (see for example [510]). In particular, $\chi_{ij}(\mathbf{r},\mathbf{r}',\omega) = i\omega\sigma(\mathbf{r},\mathbf{r}',\omega)$. It is important to understand that the $\mathbf{A}$ which appears in the equation for $\mathbf{j}$ is in the absence of interactions, and not the full Heisenberg operator. In fact, we expect the current to respond to not the non-interacting field, but the total field, which can be very different from the "applied" field in a dense medium. As a trivial example, a dense medium can have an index of refraction that strongly changes the quantized field operator! However, we shall invoke the so-called *random-phase approximation* (RPA) used in classical linear response theory and say that $\mathbf{j}$ really interacts with the Heisenberg $\mathbf{A}$. In this so-called *quantum electrodynamical RPA*, we simply take $\mathbf{A}$ in the equation for $\mathbf{j}$ as the same Heisenberg operator which appears in the Maxwell equation for $\mathbf{A}$. Plugging this expression for the current back into the Maxwell equation, we have

$$\left(\nabla \times \nabla \times - \frac{\omega^2}{c^2} \right) \mathbf{A}(\mathbf{r},\omega) = \mu_0 \mathbf{j}^{(0)}(\mathbf{r},\omega) - i\omega\mu_0 \int d^3r' \sigma(\mathbf{r},\mathbf{r}',\omega) \cdot \mathbf{A}(\mathbf{r}',\omega). \tag{B.132}$$

To make things more recognizable, we consider the most standard case of a local conductivity: $\sigma(\mathbf{r},\mathbf{r}') \to \sigma(\mathbf{r})\delta(\mathbf{r}-\mathbf{r}')$ (the following derivations can be easily generalized). Thus

we have instead

$$\left(\nabla \times \nabla \times -\frac{\omega^2}{c^2}\right) \mathbf{A}(\mathbf{r},\omega) = \mu_0 \mathbf{j}^{(0)}(\mathbf{r},\omega) - i\omega\mu_0\sigma(\mathbf{r},\omega)\cdot\mathbf{A}(\mathbf{r}',\omega). \tag{B.133}$$

Recalling that the conductivity and permittivity are related as $-i\omega\epsilon_0(\epsilon-1)=\sigma$, we may write the Maxwell equation instead as:

$$\left(\nabla \times \nabla \times -\frac{\omega^2}{c^2}\boldsymbol{\epsilon}(\mathbf{r},\omega)\right) \mathbf{A}(\mathbf{r},\omega) = \mu_0 \mathbf{j}^{(0)}(\mathbf{r},\omega). \tag{B.134}$$

The left-hand side is merely the Maxwell equation in an inhomogeneous dielectric medium (the matter). The right-hand side indicates the existence of a source current which exists *in the absence* of the vector potential and is in fact related to the time-evolution of the non-interacting current. This term is exactly the same in spirit as the quantum Langevin equation for a damped cavity. There, we had a source term related to the time-evolution of the non-interacting reservoir modes. Here, our reservoir represents the matter spread out over a continuum of positions and frequencies.

We are now in position to derive a quantized vector potential operator. To do so, we merely solve the inhomogeneous Maxwell equation as

$$\mathbf{A}(\mathbf{r},\omega) = \mathbf{A}^{(0)}(\mathbf{r},\omega) + \mu_0 \int \mathrm{d}^3 r' \; \mathbf{G}(\mathbf{r},\mathbf{r}',\omega)\cdot\mathbf{j}^{(0)}(\mathbf{r},\omega), \tag{B.135}$$

with $\mathbf{G}(\mathbf{r},\mathbf{r}',\omega)$ the dyadic Green's function of the Maxwell equations (used for various applications in this text from one- and two-photonic quasiparticle emission rates, scintillation theory, and so on). The first term is the Fourier transform of the non-interacting field (in a dissipative medium). It is the homogeneous solution to the problem and is solved by the complex eigenfrequencies. Because this operator is a vacuum field operator, it plays no role in the evaluation of normally-ordered correlation functions (related for example to probabilities of generating one or more photonic quasiparticles). We thus ignore it. The

resulting time-domain field operator is

$$\mathbf{A}(\mathbf{r},t) = \mu_0 \int_{-\infty}^{\infty} \frac{d\omega}{2\pi} e^{-i\omega t} \int \mathrm{d}^3 r' \; \mathbf{G}(\mathbf{r},\mathbf{r}',\omega)\cdot\mathbf{j}^{(0)}(\mathbf{r},\omega). \tag{B.136}$$

To calculate observables related to the field, we need to know the correlation functions of $\mathbf{j}^{(0)}$. As before, let us keep our discussion restricted to zero temperature (it is readily generalized to finite temperatures (see e.g. [23]), but here we merely want to show the core physics). In the ground state, we have $\langle j\rangle = \langle j^\dagger\rangle = 0$ (for positive ω). To see this, note that the Fourier transform of the interaction picture operator may be written as

$$\mathbf{j}^{(0)}(\mathbf{r},\omega) = 2\pi \sum_{\alpha,\beta} = \mathbf{j}^{\alpha\beta}(\mathbf{r})\delta(\omega-\omega_{\alpha,\beta})|\alpha\rangle\langle\beta|, \tag{B.137}$$

where $\mathbf{j}_{\alpha\beta} = \langle\alpha|\mathbf{j}^{(0)}|\beta\rangle$ and $\omega_{\alpha,\beta} = (E_\alpha - E_\beta)/\hbar$, and α,β label energy eigenstates of the matter Hamiltonian. Let us define positive- and negative-frequency operators as

$$\mathbf{j}^{(+)}(\mathbf{r},\omega) = 2\pi \sum_{\alpha<\beta} = \mathbf{j}^{\alpha\beta}(\mathbf{r})\delta(\omega+\omega_{\alpha,\beta})|\alpha\rangle\langle\beta|, \tag{B.138}$$

and

$$\mathbf{j}^{(-)}(\mathbf{r},\omega) = 2\pi \sum_{\alpha>\beta} = \mathbf{j}^{\alpha\beta}(\mathbf{r})\delta(\omega+\omega_{\alpha,\beta})|\alpha\rangle\langle\beta|, \tag{B.139}$$

with $\mathbf{j}^{(+)} = \mathbf{j}^{(-)\dagger}$. Thus $\mathbf{j} = \mathbf{j}^{(+)} + \mathbf{j}^{(-)}$ (terms with $\alpha = \beta$ are ignored as we are interested in the AC response). The positive-frequency current lowers microscopic states and is a lowering operator, while the negative does the reverse. From these definitions, it is clear that $\langle j^{(-)j^{(+)}}\rangle = 0$. The only non-vanishing correlator is

$$\begin{aligned}\langle j_i^{(+)}(\mathbf{r},\omega) j_j^{(-)}(\mathbf{r}',\omega')\rangle &= (2\pi)^2 \sum_n (j_i^{0n}(\mathbf{r}))^* (j_j^{n0}(\mathbf{r}'))\delta(\omega-\omega_{n0})\delta(\omega'-\omega_{n0}) \\ &= (2\pi)^2\delta(\omega-\omega')\sum_n (j_i^{0n}(\mathbf{r}))^* (j_j^{n0}(\mathbf{r}'))\delta(\omega-\omega_{n0}) = (2\pi)^2 \frac{\epsilon_0\hbar\omega^2}{\pi}\delta(\omega-\omega')\mathrm{Im}\;\epsilon_{ij}(\mathbf{r},\mathbf{r}',\omega).\end{aligned} \tag{B.140}$$

where we have used the fact that the matter is in state 0 (its ground state; the finite-

temperature generalization amounts to weighting excited state contributions by thermal factors). The last equality is a standard result of linear response theory [127]. Let us stick to the local and isotropic case to make the following math simpler. In that case, the correlator is $\frac{\epsilon_0 \hbar \omega^2}{\pi} \text{Im } \epsilon(\mathbf{r}, \omega) \delta(\omega - \omega') \delta(\mathbf{r} - \mathbf{r}') \delta_{ij}$. These correlators are exactly identical to those for a set of independent bosonic oscillators $f_i(\mathbf{r}, \omega)$ for each orientation, position, and frequency. In that case, one would expect the only nonvanishing correlation function to be $\langle f_i(\mathbf{r}, \omega) f_j^\dagger(\mathbf{r}, \omega') = \delta_{ij} \delta(\mathbf{r} - \mathbf{r}') \delta(\omega - \omega')$. Thus, defining

$$\mathbf{j}(\mathbf{r}, \omega) = 2\pi \sqrt{\frac{\epsilon_0 \hbar \omega^2}{\pi} \text{Im } \epsilon(\mathbf{r}, \omega)}, \tag{B.141}$$

we finally may write the final expression of macroscopic quantum electrodynamics for the field in a dissipative linear media. We have:

$$\mathbf{A}(\mathbf{r}, t) = \sqrt{\frac{\hbar}{\pi \epsilon_0}} \int_{-\infty}^{\infty} d\omega e^{-i\omega t} \frac{\omega}{c^2} \int \mathrm{d}^3 r' \sqrt{\text{Im } \epsilon(\mathbf{r}', \omega)} \ \left(\mathbf{G}(\mathbf{r}, \mathbf{r}', \omega) \cdot \mathbf{f}(\mathbf{r}, \omega) + \text{h.c} \right). \tag{B.142}$$

Thus, the quantized field in a linear and dissipative medium can be thought of as a type of mode expansion: not over modes of the Maxwell equations, but instead over time-harmonic point dipoles that span the possible current excitations in a material medium. These dipoles correspond essentially to Langevin currents / forces. To make the transition to calculations of decay rates at first and second order perturbation theory (for example as discussed in Ch. 1 and Ch. 5 of the thesis, as well as many of the references in the publication list): one simply uses this form of the vector potential and takes it to interact with the momentum (of say an excited electron in a potential, or even a free electron). This procedure, in the lossless limit, reproduces all known effects arrived at from modal quantization, and predicts effects with losses in agreeement with classical limits where such are known.

Appendix C

Appendices for: Light emission based on nanophotonic vacuum forces

Note: This chapter is heavily based off "Light emission based on nanophotonic vacuum forces" by N. Rivera et al. Nature Physics (2019).

C.1 Supplementary Figures

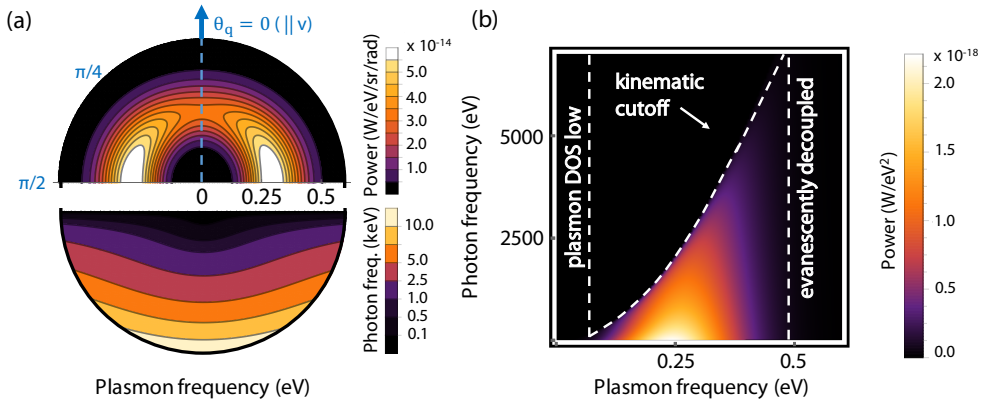

Figure C-1: **Correlations between infrared polaritons and X-ray photons in photon-polariton pair emission.** Same as Figure 3 of the main text, except that the electron now travels 10 nm away from the surface of the graphene sheet, and it is doped to a Fermi energy of 0.25 eV.

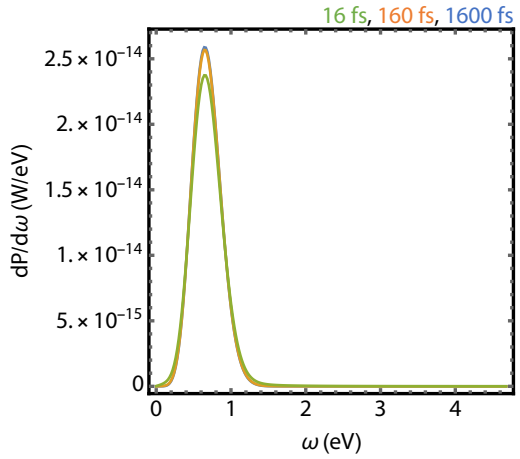

Figure C-2: **Influence of Drude losses on photon emission.** Emitted power (into photons) per unit frequency of polaritons for the case of an electron of velocity $0.99c$ traveling 5 nm away from a sheet of Drude graphene doped to a Fermi level of 0.5 eV for Drude relaxation times of 1600 fs, 160 fs, and 16 fs. The Drude time has a weak influence on the emitted power.

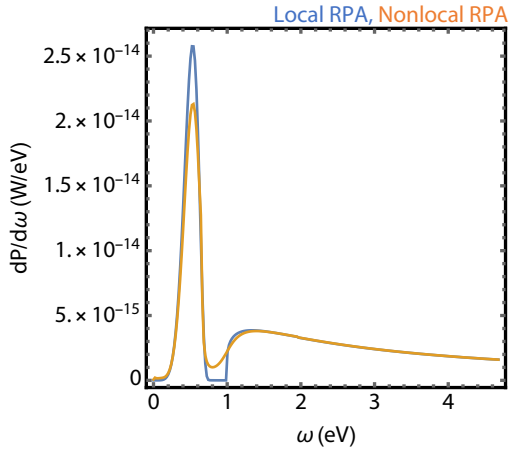

Figure C-3: **Influence of interband damping on photon emission.** Emitted power (into photons) per unit frequency of polaritons for the case of an electron of velocity $0.99c$ traveling 5 nm away from a sheet of graphene doped to a Fermi level of 0.5 eV with a Drude relaxation time of 1600 fs. Graphene is modeled here through both the local and nonlocal RPA. Interband damping has a stronger influence on the emitted power, which stays in the same order of magnitude. The power emitted is about 15 fW, compared to 12 fW in the Drude case.

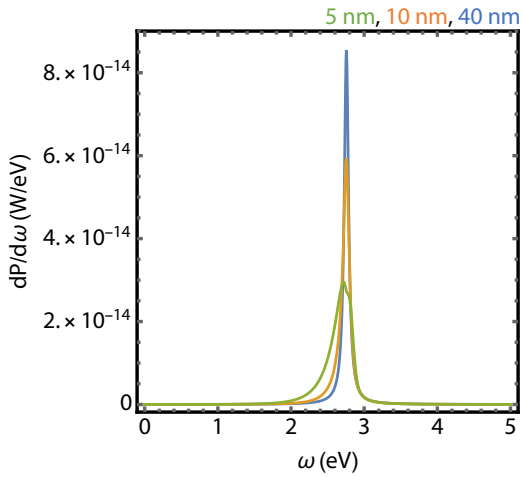

Figure C-4: **Photon-polariton emission for electrons near gold films.** Emitted power (into photons) per unit frequency of polaritons for the case of an electron of velocity $0.99c$ traveling 5 nm away from a thin film of Drude gold of varying thicknesses. The underlying emission power stays similar to the case of Fig. S3, varying from 9.9 fW per electron for 40 nm gold to 11 fW per electron for 5 nm gold.

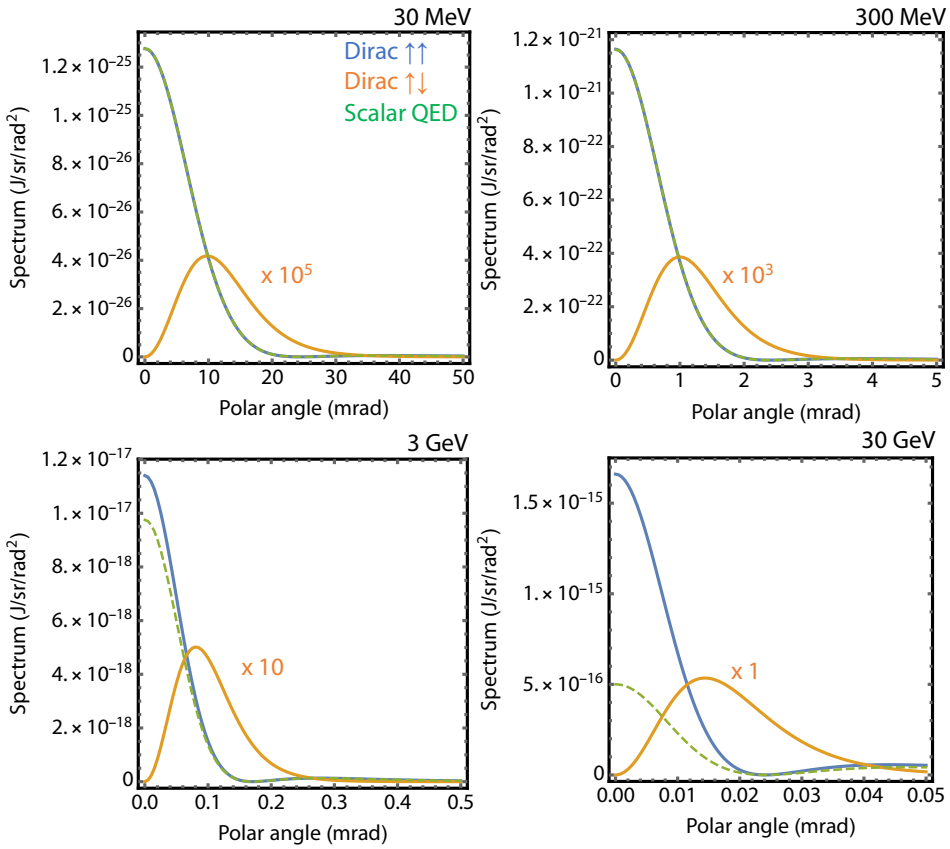

Figure C-5: **Influence of the electron spin on photon-polariton pair emission.** Emitted power (into photons) per unit photon angle, plasmon frequency, and plasmon angle in scalar QED versus fermion QED. The contribution to the emission in fermion QED from transitions that conserve the electron spin is shown in blue. Spin-flipping contributions are shown in orange, and the scalar QED prediction is shown in green. The plasmon is emitted in the direction of the electron motion with frequency equal to the Fermi energy of 0.5 eV. The electron is assumed to travel 5 nm away from the surface of graphene. The electron energies considered are 30 MeV (top left), 300 MeV (top right), 3 GeV (bottom left), and 30 GeV (bottom right). As these plots show, the scalar QED results are in excellent agreement with the spin-conserving results of fermion QED for electron kinetic energies below 3 GeV, and continue to predict similar trends as a function of polar angle even at larger electron energies.

C.2 Experimental considerations for realizing photon-polariton pair emission

In this section, we briefly discuss a few considerations important to experimentally realizing the photon-polariton pair emission effect discussed in this work. We discuss (a) the rate of photon emission associated with photon-polariton pair emission for a realistic electron beam, as achievable by a transmission electron microscope, (b) comparison to other high-energy light sources that are driven by electromagnetic fields, and (c) mitigation of X-ray producing background effects associated with the electron beam impinging the sample.

C.2.1 Photon emission rates

The characteristic photon emission rates per electron are on the order of 10^2-10^4 photons per second per electron, for electrons traveling 1-10 nm above the graphene sheet, and a graphene Fermi level between 0.1-1 eV. The corresponding emission length is on the order of 10-1000 km. These numbers are similar to other compact lab-scale photon sources based on high-energy electrons, as can be verified directly from the Larmor formula for a typical example of 5 MeV electrons interacting with 100 MV/m electric fields to produce keV frequency photons. The fact that both the emitted power and the average photon energy scale as γ^2 allows us to infer that the photon emission rate (given by emitted power divided by photon energy) is somewhat insensitive to electron energy. For electron beam currents of 100 nA to 100 μA and an interaction length of 100 μm, the expected rate of photon emission for electrons 5 nm from the surface is about $10^3 - 10^6$ photons per second, the higher values in this range being comparable to X-ray yields from high-harmonic generation [511]. Our scheme also has an advantage that with increasing electron energy, the brightness can be improved, and harder X-rays or even gamma ray energies could eventually be reached. With multilayer structures [512], and pre-bunching via emittance exchange techniques [513, 514], laser-plasma interactions [515], or electromagnetic intensity gratings [516], the photon yields, and spectral brightness can be scaled up by several orders of magnitude.

C.2.2 Comparison to x-ray sources based on strongly excited plasmons

We mention one other point of comparison with regards to the emitted power. Consider an electron interacting with an externally pumped graphene plasmon, with a surface field strength of 1 GV/m as was proposed in Ref. [213]; the excitation is approximately monochromatic and can be described by a single plasmon mode. Let us assume that the plasmon frequency is 0.8 eV and that its confinement factor is 100 so that plasmon wavelength is 15 nm. The time-averaged radiation power as a result of an electron scattering off this plasmon mode, calculated through the Larmor formula, is 1.3 nW - about the same value as the *spontaneously* generated power in a photon-polariton pair emission. This is surprising given that a 1 GV/m field in the stimulated emission case corresponds to a large number of plasmons, whereas the spontaneous pair-emission we present here does not involve any driving plasmons. For instance, a 50 nm $\times$ 50 nm excitation area already requires 1000 plasmons to support a 1 GV/m field. This unexpected result – that spontaneous pair-emission can produce as much radiated power as a stimulated emission scenario that uses a large number of plasmons – is explained by the fact that the electron in the spontaneous pair-emission case is "driven" by a highly multi-mode field and experiences the field of effectively half of a polariton for each mode (as a result of the zero-point polariton energy being half the energy of a polariton). The outgoing radiation is consequently also much more spectrally broad compared to the single-mode case.

C.2.3 Mitigation of background effects

Regarding background effects (particularly, background effects that produce X-rays) from the electron crossing the sample, the experimental capabilities needed to minimize such effects are present. For example, it is not uncommon in transmission electron microscopes to have an electron beam of size below one nanometer. It is also possible to keep the beam divergence small, such that after about 10-100 microns of propagation (characteristic sample size), the divergence is on the order of a few nanometers. At that level of divergence, most of the electron beam will not penetrate the sample. Background effects can

be even further minimized by using porous substrates or by using suspended 2D materials, such as graphene, or hexagonal boron nitride, which can be produced. In this case, there is as high a vacuum-to-solid ratio as possible, and the electrons spend most of their time interacting with vacuum fluctuations. Yet another interesting approach being actively developed, which could be used to both minimize background effects, as well as maximize the X-ray signal from this process, is to use "flat" electron beams with a very high aspect ratio [517, 518, 519]. Low-emittance electron beams of aspect ratios of 100 have been realized experimentally [518]. Such an approach would not only allow the electrons to exist in the nanometer vicinity of the sample surface with minimal spread, but the number of electrons interacting with the sample could be further enhanced. Another consideration for experimental verification, particularly in graphene, is that graphene is not perfectly flat, which will average the spectrum over the distribution of distances between the electron and the graphene surface. Although graphene is known to be not perfectly flat, these "defects" can occur at sufficiently low densities, such that the average height of the electron above the graphene surface is only changed by an amount on the order of a percent [520, 521], leading to photon-polariton pair emission with similar intensity (different by a few percent). With rapid advancement in graphene fabrication techniques, new methods to smoothen wrinkles in graphene continue to emerge, based on the use of boron nitride substrates [522], or paraffin-based transfer [523], both of which can lead to highly smooth graphene. Additionally, given the high resolution of transmission electron microscopes, a preferred area of interaction could be chosen so that such effects can be further mitigated.

C.3 Fluctuational theory of high energy emission by electrons near photonic structures

In the remainder of this Supplement, we derive in detail the theory of two-photon emission by a free electron moving through an arbitrary photonic structure. First (Sections 3 and 4), we develop a "fluctuational theory", in which we treat the two-photon emission process as effectively a one-photon process, in which the vacuum fluctuations of a photonic

structure act as an external field which scatters the electron, leading to far-field photon emission. Then (Section 5), we then develop a more direct theory of the two-photon process by calculating simultaneous emission of a low-energy photon in the photonic structure and a high-energy photon, within the framework of relativistic quantum field theory. We from now on refer to the low-energy photon in the photonic structure as a "polariton", as the nontrivial spatial and spectral properties of photons in complex structures arise from the complex interplay of electromagnetic fields with polarization charges and currents (i.e., matter). We conclude by showing that these two theories make the same predictions and exemplify it with the specific case of the polariton being a plasmon polariton of a two-dimensional electron gas. We explain why the fluctuational theory and the direct theory should be equivalent for any structure.

We consider an electron moving near a nanophotonic structure. Due to electromagnetic fluctuations of the photonic structure, the electron on average feels a mean-square driving field and may radiate either back into the structure or into the far field. Here, we focus specifically on the case in which the electron radiates into the far-field, as we are interested in the spectrum of hard-UV, X-ray, and gamma ray photons emitted by a relativistic electron. At these frequencies, the material response is negligible.

To develop this theory, we first review a general expression from electrodynamics relating far-field radiation to the acceleration of moving charges. Then from relativistic mechanics, we parameterize the acceleration of the charge in terms of a driving field. Last we find the driving field associated with electromagnetic vacuum fluctuations in the material. This way, we relate the far-field radiation to the vacuum fluctuations that oscillate the electron. These steps lead to a general expression allowing one to determine the far-field radiation at any frequency, by charged particles of any velocity, induced by quantum vacuum fluctuations in any photonic structure.

C.3.1 Radiation by a moving charge

The time-averaged power P per unit solid angle Ω, $\frac{dP}{d\Omega}$, emitted by a system of charges at a position $\mathbf{R}$, far from the origin of coordinates, is related to the time-averaged Poynt-

ing vector $\mathbf{S}$ by $\frac{dP}{d\Omega} = R^2 \hat{n} \cdot \mathbf{S}$, where $\hat{n}$ is the unit vector in the direction of observation. Expressing the time-dependent fields in Fourier domain using the convention $\mathbf{E}(\mathbf{r}, t) = \int_{-\infty}^{\infty} d\omega' \; e^{-i\omega' t} \mathbf{E}(\mathbf{r}, \omega')$, the single-sided (positive-frequency) time-averaged energy U radiated per unit frequency ω' per unit solid angle can be written as

$$\frac{dU}{d\omega' d\Omega} = \frac{4\pi R^2}{\mu_0} \hat{n} \cdot \text{Re} \left[\mathbf{E}(\mathbf{r}, \omega') \times \mathbf{B}^*(\mathbf{r}, \omega') \right], \tag{C.1}$$

where μ_0 is the permeability of free space. From Maxwell's equations in the far-field, we have that the frequency-domain magnetic field is related to the frequency-domain electric field by $\mathbf{B}(\mathbf{r}, \omega') = \frac{\hat{n}}{c} \times \mathbf{E}(\mathbf{r}, \omega')$, meaning that we may write Equation (1) purely in terms of $\mathbf{E}(\mathbf{r}, \omega')$ as

$$\frac{dU}{d\omega' d\Omega} = \frac{4\pi R^2}{\mu_0 c} \left(\left| \mathbf{E}(\mathbf{r}, \omega') \right|^2 - \left| \hat{n} \cdot \mathbf{E}(\mathbf{r}, \omega') \right|^2 \right) = \frac{4\pi R^2}{\mu_0 c} \left| \mathbf{E}(\mathbf{r}, \omega') \right|^2, \tag{C.2}$$

where the last equality applies when only the radiative component is considered.

We now consider the specific case of the fields of a moving electron of charge $-e$ with a general trajectory corresponding to position $\mathbf{r}(t)$ and velocity $\dot{\mathbf{r}}(t) = \mathbf{v}(t) = c\boldsymbol{\beta}(t)$, with c the speed of light. From the Lienard-Wiechert potentials [312], the frequency-domain electric field of the moving electron is given by

$$\mathbf{E}(\mathbf{r}, \omega') = \int \frac{dt'}{2\pi} \, e^{i\omega' t'} \frac{-e}{4\pi\epsilon_0 R c (1 - \hat{n} \cdot \boldsymbol{\beta}(t'))^3} \left(\hat{n} \times \left((\hat{n} - \boldsymbol{\beta}(t')) \times \dot{\boldsymbol{\beta}}(t') \right) \right), \tag{C.3}$$

where ϵ_0 is the permittivity of free space. We note that in this expression, a primed time variable denotes the retarded time of the electron for the observer at distance R and is given by $t' = t - \frac{R(t)}{c}$. Time-derivatives are calculated with respect to t'. We can change the integration variable in (3) to the non-retarded time t by making a change of variables $t' = t(1 - \hat{n} \cdot \boldsymbol{\beta})$. Plugging Equation (3) into Equation (2) yields a general expression connecting the acceleration of the electron to the far-field radiation spectrum.

In physical situations involving radiation by accelerated electrons [524], it is common for the modulation of the electron trajectory by a driving field to be very weak, meaning that deviations of the electron from an initial straight line motion in the absence of a driving

field are small. This is also the case in all cases considered in this manuscript, in which the driving fields are quantum fluctuations of a nanophotonic vacuum. Thus, we approximate (3) to lowest order in the electron modulation by taking $(1-\hat{n}\cdot\boldsymbol{\beta}(t'))\approx(1-\hat{n}\cdot\boldsymbol{\beta})$ and $\hat{n}-\boldsymbol{\beta}(t')\approx\hat{n}-\boldsymbol{\beta}$, where $\boldsymbol{\beta}$ without explicit time-dependence represents the initial velocity of the electron, normalized to c. Applying this approximation, the angular and frequency spectrum of radiation is given by

$$\frac{dU}{d\omega' d\Omega}=\frac{e^2}{16\pi^3\epsilon_0 c(1-\beta\cos\theta)^4}\left|\int dt\, e^{-i\omega'(1-\beta\cos\theta)t}\hat{n}\times\left((\hat{n}-\boldsymbol{\beta})\times\dot{\boldsymbol{\beta}}(t)\right)\right|^2, \quad \text{(C.4)}$$

where $\theta=\cos^{-1}\left(\hat{n}\cdot\hat{\beta}\right)$ is the angle of radiation emission relative to the initial direction of electron motion $\hat{\beta}=\frac{\boldsymbol{\beta}}{\beta}$ (with β the magnitude of $\boldsymbol{\beta}$). Small deviations of the trajectory $R(t)$ from the unperturbed linear trajectory are neglected in the exponential, as such corrections yield corrections at second-order in the trajectory modulation. We have also replaced the quantity inside the modulus-squared by its complex conjugate, without loss of generality, for reasons that will be apparent later. We now proceed to relate the normalized acceleration $\dot{\boldsymbol{\beta}}(t)$ to external fields that the electron experiences.

C.3.2 Modulation of the trajectory of a charged particle by an electromagnetic field

Consider external (driving) electric and magnetic fields $\mathbf{E}$ and $\mathbf{B}$. The acceleration of the electron of mass m is governed by the Newton-Lorentz equation of motion:

$$mc(\gamma(t)\dot{\boldsymbol{\beta}}(t))=-e[\mathbf{E}(t)+c\boldsymbol{\beta}(t)\times\mathbf{B}(t)], \quad \text{(C.5)}$$

where the Lorentz factor $\gamma(t)=(1-\beta^2(t))^{-1/2}$ accounts for the electron's relativistic motion. As in the previous section, we apply the approximation that the trajectory of the electron is weakly perturbed from its initial trajectory $\mathbf{r}(t)=\mathbf{r}_0+\mathbf{v}t$. In this case, we may assume that $\gamma(t)$ is determined only by the velocity component parallel to $\mathbf{v}$. Taking this velocity component without loss of generality to be along the z-direction of a Cartesian system of coordinates, we approximate $\gamma(t)\approx(1-\beta_z^2(t))^{-1/2}$. In expressions where we

do not take its time derivative, it can be approximated as constant: $\gamma \approx (1-\beta^2)^{-1/2}$, where functions without explicit time-dependence represent initial values. In that case, Newton's equations of motion for the z-directed velocity can be shown to reduce to:

$$\dot{\beta}_z(t) = -\frac{e}{\gamma^3 mc} E_z(t). \tag{C.6}$$

For components of the acceleration perpendicular to the initial velocity, the equation of motion reduces to

$$\dot{\boldsymbol{\beta}}_\perp(t) = -\frac{e}{\gamma mc}\left(\mathbf{E}_\perp(t) + (\mathbf{v}\times\mathbf{B}(t))_\perp\right). \tag{C.7}$$

In what follows, we make our final approximation with regards to the electron motion, which is that the driving fields we consider are quasi-electrostatic and approximately satisfy the Laplace equation. As such, the magnetic part of the quasi-static field is neglected. This approximation is justified when the electromagnetic driving field is highly spatially confined, meaning that the length scale of the spatial variations of the field λ, are much smaller than the free-space wavelength of light, $\lambda = \frac{2\pi c}{\omega}$, at the same frequency ω (i.e., $\lambda \ll \frac{2\pi c}{\omega}$). This approximation is accurate in the systems we consider, because such highly confined fields are also advantageous for generating X-rays and gamma rays with relatively low energy electrons [213]. In that case, the acceleration is completely specified in terms of the electric field as $\dot{\boldsymbol{\beta}}(t) = -\frac{e}{\gamma mc}\left(\mathbf{E}_\perp(t), \frac{E_z(t)}{\gamma^2}\right) \equiv -\frac{e}{\gamma mc}\mathbf{E}_\gamma(t)$. Plugging this expression for the acceleration into Equation (4) yields

$$\frac{dU}{d\omega' d\Omega} = \frac{e^4 T_{ij} T_{ik}}{16\pi^3 \epsilon_0 m^2 \gamma^2 c^3 (1-\beta\cos\theta)^4} \int dt dt'\; e^{-i\omega'(1-\beta\cos\theta)(t-t')} E_{\gamma,j}(\mathbf{r}(t)) E_{\gamma,k}(\mathbf{r}(t')), \tag{C.8}$$

where for brevity, we have defined the tensor T_{ij} as the ij-component of linear operation $\hat{n}\times((\hat{n}-\boldsymbol{\beta})\times)$, and we are using Einstein repeated-index notation.

Having parameterized the far-field radiation in terms of the driving field, we now consider a situation in which this driving field is a fluctuating field of a nanophotonic structure in thermal equilibrium, so that the fluctuations are Bose-Einstein distributed in frequency. These fluctuations have both a quantum component and a thermal component. Only the quantum component persists at zero temperature. To find the average power radiated by

electrons in this fluctuating field, we take the (quantum) ensemble average of Equation (8) over all realizations of the field. The resulting "master formula" connecting fluctuating electric fields to far-field radiation is then:

$$\frac{d\langle U\rangle}{d\omega' d\Omega} = \frac{e^4 T_{ij} T_{ik}}{16\pi^3 \epsilon_0 m^2 \gamma^2 c^3 (1-\beta\cos\theta)^4} \int dt dt' \; e^{-i\omega'(1-\beta\cos\theta)(t-t')} \langle E_{\gamma,j}(\mathbf{r}(t)) E_{\gamma,k}(\mathbf{r}(t'))\rangle, \tag{C.9}$$

where $\langle(\cdots)\rangle$ is the ensemble average of $(\cdots)$. To complete the fluctuational theory of photon-polariton pair emission, we require the ensemble average of a product of two electric fields in the vacuum state of an arbitrary photonic structure. From the quantum theory of the macroscopic electromagnetic field, one finds that such an ensemble average is given by:

$$\langle E_i(\mathbf{r},t) E_j(\mathbf{r}',t')\rangle = \frac{\hbar}{\pi\epsilon_0 c^2} \int_0^\infty d\omega \; \omega^2 \text{Im}\, G_{ij}(\mathbf{r},\mathbf{r}',\omega) \left(n_\omega e^{i\omega(t-t')} + (n_\omega+1) e^{-i\omega(t-t')} \right), \tag{C.10}$$

where $\hbar$ is the reduced Planck constant, G_{ij} is the Dyadic Green's function of the medium, and $n_\omega = (e^{\frac{\hbar\omega}{kT}} - 1)^{-1}$ is a Bose-Einstein occupation factor evaluated at temperature T.

Given the result of Equation (10), Equation (9) can be expressed as:

$$\frac{dU}{d\omega' d\Omega} = \frac{e^4 \hbar}{16\pi^4 \epsilon_0^2 m^2 c^5 \gamma^2 (1-\beta\cos\theta)^4} T_{ij} T_{ik} \int dt dt' \times$$
$$\int_0^\infty d\omega \; \omega^2 e^{-i\omega'(1-\beta\cos\theta)(t-t')} \text{Im}\, G_{\gamma,jk}(\mathbf{r}(t),\mathbf{r}(t'),\omega) \left(n_\omega e^{i\omega(t-t')} + (n_\omega+1) e^{-i\omega(t-t')} \right), \tag{C.11}$$

where $G_{\gamma,jk}$ differs from G_{jk} by a factor of γ^{-2} if one component is along z, and by a factor of γ^{-4} if both components are along z. In other words: $G_{\gamma,jk} = c_j c_k G_{jk}$, where $c_j = \gamma^{-2}$ if j refers to the z-component, and $c_j = 1$ otherwise. We have reintroduced here the convention that repeated indices are summed. Equation (11) can be written in a more compact form for material systems which are reciprocal. In particular, Equation (11) can

be re-expressed as

$$\frac{dU}{d\omega' d\Omega} = \frac{e^4\hbar}{16\pi^4\epsilon_0^2 m^2 c^5 \gamma^2 (1-\beta\cos\theta)^4} \int dt dt' d\omega\, \omega^2 \Theta(\omega) \\ \text{Im}\left[e^{-i\omega'(1-\beta\cos\theta)(t-t')}\left(n_\omega e^{i\omega(t-t')} + (n_\omega+1)e^{-i\omega(t-t')}\right)\text{tr}\left[\mathbf{TG}(\mathbf{r}(t),\mathbf{r}(t'),\omega)\mathbf{T}^{\mathrm{T}}\right]\right], \tag{C.12}$$

where bolded versions of quantities that originally had indices denote matrices. Additionally, we have included a Heaviside step function ($\Theta(\omega) = 1$ if $\omega > 0$ and $\Theta(\omega) = 0$ otherwise) to extend the domain of the frequency integration from $-\infty$ to ∞.

Before proceeding to evaluate these expressions for specific material systems, we comment that the replacement of deterministic fields by their quantum averages is a key step in any calculation in the framework of fluctuational electrodynamics (see for example Refs. [319, 525, 305, 308, 127] and references therein). This framework has thus far been used to predictively calculate phenomena such as near- and far-field heat transfer, Casimir forces, Casimir-Polder and van der Waals forces. In what follows, we briefly describe how the concept that led us to Equation (9) has been used to develop successful theories of Casimir forces and near-field radiative heat transfer.

Within fluctuational electrodynamics, the step that led to Equation (9) (constructing a classical model, and then taking quantum averages), is ubiquitous. For example, this step is used in Casimir force between two polarizable bodies. In the calculation, one calculates the classical Lorentz force felt by a polarizable structure due to a field [23, 127]. The expression for the Lorentz force becomes an expression in terms of the permittivity and permeability of the structure, as well as the (vacuum) fields felt by the structure. Then, to account for the fluctuating nature of the fields that generate Casimir forces, one replaces the fields by their ensemble average in the electromagnetic vacuum. In another example of such a replacement of fields by their ensemble averages, when one is interested in radiative heat transfer between two bodies, one calculates the Poynting flux over the surface of a body due to fluctuating currents in the bodies, and then replaces the fields by their ensemble average taking into account the finite temperatures of the bodies [305].

We also briefly comment about the physical significance of the n_ω and $n_\omega + 1$ factors.

The term which has n_ω represents physically a situation in which a polariton (i.e., low frequency photon of the photonic structure) at frequency ω is absorbed, while the term with $n_\omega + 1$ represents emission of a polariton. When $n_\omega = 0$, as is the case at zero-temperature, only the "1" contribution remains, which by the general principles of quantum mechanics, corresponds to the spontaneous emission of a polariton. The photon emission at frequency ω' is already spontaneous, as it is considered in the absence of additional photons at frequency ω'. It therefore follows that at zero temperature, *the emission due to vacuum fluctuations derived here corresponds to a two-quanta spontaneous emission process in which a photon and a polariton are emitted.* When $n_\omega \gg 1$, both terms contribute approximately equally, resulting in a combined effect of stimulated emission and absorption. Together, they reproduce the classical effect of polariton-driven (inverse) Compton radiation as was derived classically in [213]. This match further corroborates our findings in these formulas. Furthermore, in the final section of the SI we derive results equivalent to those of Equation (12) at zero temperature from a direct application of Fermi's golden rule, without using any classical or fluctuational electrodynamics arguments. To summarize this section, Formula (25) produces both the two-photon emission and inverse-Compton scattering, both at zero temperature and at a finite temperature. Formula (12) may be seen as the master formula for any future calculation which seeks to understand fluctuation-induced far-field emission from free electrons.

C.4 Application to a planar interface

We now consider the case when the electromagnetic quantum fluctuations that interact with a relativistic electron are those of a structure with translational invariance in two dimensions. For simplicity, we also consider the case in which the electron flies parallel to the plane of translational invariance, defined as the yz-plane. For the example of a thin film of thickness d with permittity $\epsilon(\omega)$ surrounded by infinite dielectric of permittivities ϵ_1 ($x > d/2$) and ϵ_2 ($x < -d/2$), the Green's function above the slab (in the ϵ_1 region) can be

written as as a sum of contributions from p- and s-polarized plane waves as [127]:

$$G_{ij}(\mathbf{r},\mathbf{r}',\omega) = \frac{i}{2}\int \frac{d^2q}{(2\pi)^2}\ \left(C_{ij}^{p}(\mathbf{q},\omega) + C_{ij}^{s}(\mathbf{q},\omega)\right) e^{i\mathbf{q}\cdot(y-y',z-z')}e^{-\kappa_q(x+x')}, \tag{C.13}$$

where $\kappa_q = \sqrt{q^2 - \epsilon_1\frac{\omega^2}{c^2}}$, and $C_{ij}^{p,s}(\mathbf{q},\omega)$ are tensors that take into account the differences in polarizations and reflectivities of p- and s- polarized waves [127]. The strength of contributions from p- and s- polarized waves differs substantially in the near-field zone (i.e., high wavenumbers q) where $\frac{cq}{\omega} \gg 1$. In particular, p- polarized contributions dominate by a factor of $\left(\frac{cq}{\omega}\right)^2$, as shown in [130, 105, 526]. As we are interested in high-frequency radiation, which we will show (in Equation (21)) comes from high-wavevector polariton modes, we may approximate the Green's function by its p-polarized part in the electrostatic limit, with $C_{ij}^{p}(\mathbf{q},\omega)$ given by

$$C_{ij}^{p}(\mathbf{q},\omega) = -2i\frac{c^2q}{\omega^2}r_p(\mathbf{q},\omega)\hat{\epsilon}_i(\mathbf{q})\hat{\epsilon}_j^*(\mathbf{q}), \tag{C.14}$$

with $\hat{\epsilon}(\mathbf{q}) \equiv \frac{\hat{q}+i\hat{x}}{\sqrt{2}}$ and $r_p(\mathbf{q},\omega)$ being the reflectivity of a p- polarized wave of wavevector $\mathbf{q}$ and frequency ω. Thus, for a general planar interface, treated in the electrostatic limit, the radiated photon spectrum is given by (substituting Equations (13) and (14) into (12))

$$\frac{1}{T_0}\frac{d\langle U\rangle}{d\omega' d\Omega} = \frac{e^4\hbar}{8\pi^3\epsilon_0^2m^2c^3\gamma^2(1-\beta\cos\theta)^4}\int \frac{d^2q}{(2\pi)^2}d\omega\ \theta(\omega)q|\mathbf{T}\hat{\epsilon}_\gamma(\mathbf{q})|^2\text{Im}\ r_p(\mathbf{q},\omega)e^{-2qx_0}\times$$
$$(n_\omega\delta(\omega'(1-\beta\cos\theta) - q_zv - \omega) + (n_\omega+1)\delta(\omega'(1-\beta\cos\theta) - q_zv + \omega)) \tag{C.15}$$

where $\hat{\epsilon}_\gamma(\mathbf{q}) = \frac{1}{\sqrt{2}}(i, \sin\chi_{\mathbf{q}}, \frac{\cos\chi_{\mathbf{q}}}{\gamma^2})$, T_0 is the interaction time, β is the magnitude of the velocity, $\chi_{\mathbf{q}}$ is the angle made by $\mathbf{q}$ to the z-axis, and x_0 is the position of the electron in the x-direction, transverse to the sheet. Henceforth, although we assume a finite temperature, and so $n_\omega \neq 0$, no explicit reference to variables involving temperature will be made. The dependence on temperature of the expressions was explained in the previous section. Additionally, since $\frac{d\langle U\rangle}{T_0}$ has the dimensions of power, we will now refer to it as dP (with no angle brackets, for brevity).

We note that the assumptions in writing the Green's function can straightforwardly be generalized beyond the electrostatic limit, which means including s-polarized contributions

as well as including retardation effects (i.e., effects from $q \sim \frac{\omega}{c}$) in the the p- polarized contributions. When doing this, one must remember that the electrostatic limit was also employed in deriving Equation (9), where magnetic forces have been neglected when considering the Lorentz force. Therefore, one must restore magnetic contributions to the field fluctuations in order to employ a fully-retarded Green's function.

C.4.1 Energy-momentum conservation

We briefly note that the arguments of the delta functions reflect energy-momentum conservation. In particular, the first delta function condition: $\omega'(1 - \beta\cos\theta) - q_z v - \omega = 0$, must be satisfied in order for energy-momentum conservation to be satisfied in a process in which a polariton is absorbed and a photon is emitted. The second delta function condition $\omega'(1-\beta\cos\theta)-q_z v+\omega = 0$ must be satisfied in order for energy-momentum conservation to be satisfied in a process in which both the polariton and the photon are emitted.

To impose energy-momentum conservation in a compact way, we collect the energy and momentum of the incident and final particles into four-vectors, in which the first component is the energy and the other three components are the 3-momenta. The relevant momenta are:

$$\begin{aligned} p_i^\mu &= \left(\frac{E_i}{c}, \mathbf{p}_i\right) \\ p_f^\mu &= \left(\frac{E_f}{c}, \mathbf{p}_f\right) \\ k^\mu &= \hbar\left(\frac{\omega'}{c}, \mathbf{k}\right) \\ q^\mu &= \hbar\left(\frac{\omega}{c}, \mathbf{q}\right), \end{aligned} \tag{C.16}$$

where $p_{i(f)}$ denotes the four-momentum of the initial (final) electron, k denotes that of the emitted photon, and q denotes that of the polariton. Here and henceforth, a Greek sub- or superscript denotes a four-vector. It is important to note that due to the evanescent nature of the polariton in the direction perpendicular to the polaritonic film, the momentum component in that direction is not a good quantum number of the polariton mode. Instead, it should be thought as variable, and sampled from a momentum probability distribution

that roughly-speaking, is a squared Lorentzian. This squared Lorentzian form results from the fact that the momentum probability distribution for an evanescent wave would be the square of the Fourier transform of $e^{-q|z|}$, which is Lorentzian. When the incident electron moves in a direction with components along this direction, the variable momentum of the polariton in this direction broadens the phase space of emission. In the main text, we consider electrons moving parallel to a 2D plasmonic film. As a result, we will see that the effect of the momentum in transverse directions is essentially negligible.

The equation for conservation momentum in a process where a photon is emitted and a polariton is absorbed (+) or emitted (−) are:

$$p_i^\mu \pm q^\mu = p_f^\mu + k^\mu \tag{C.17}$$

Squaring both sides of this equation, in the Minkowski sense, so that $a^\mu b_\mu = a_0 b_0 - \mathbf{a}\cdot\mathbf{b}$, we have that

$$\pm 2p_{i,\mu}q^\mu + q_\mu q^\mu = 2p_{f,\mu}k^\mu = 2(p_{i,\mu} \pm q_\mu - k_\mu)k^\mu = 2p_{i,\mu}k^\mu \pm 2q_\mu k^\mu \tag{C.18}$$

where we have used that the square of any electron momentum is m^2c^2 and that the square of the momentum of a photon is zero. Further noting that for all situations considered in this text, $\hbar\omega' \ll E_i$, $\hbar\omega \ll E_i$, $\hbar|\mathbf{k}| \ll |\mathbf{p}_i|$ and $\hbar|\mathbf{q}| \ll |\mathbf{p}_i|$, it follows that to leading order:

$$\pm p_{i,\mu}q^\mu = p_{i,\mu}k^\mu. \tag{C.19}$$

Expanding the Minkowski dot products yields:

$$\pm(\omega - \mathbf{q}\cdot\mathbf{v}) = (\omega' - \mathbf{k}\cdot\mathbf{v}), \tag{C.20}$$

with $\mathbf{v}$ the electron velocity. Taking this velocity to be in the arbitrarily chosen z-direction, and defining the angle of far-field photon emission θ to be relative to the z-direction, one immediately has that

$$\omega'(1 - \beta\cos\theta) \pm q_z v \mp \omega = 0. \tag{C.21}$$

The $(-)$ branch of the equation $\omega'(1-\beta\cos\theta) - q_z v + \omega = 0$, which describes emission, corresponds to the argument of delta function multiplying the $n_\omega + 1$ term, which is consistent with that term in Equation (15) describing emission. The $(+)$ branch of the equation $\omega'(1-\beta\cos\theta) + q_z v - \omega = 0$, describes absorption of a polariton which is moving in the same direction as the electron. If the sign of q_z is flipped, it describes absorption of a polariton colliding head-on with the electron. Thus, in the argument of the delta function multiplying the n_ω term of Equation (28), positive q_z corresponds to absorption of a polariton whose z-velocity is opposite that of the electron. Negative q_z, which is also included in the integration, corresponds to absorption of a plasmon whose z-velocity is in the same direction as that of the electron.

C.4.2 Emission spectrum for different materials and different material geometries

In the main text, we show the result of Equation (15) for the frequency spectrum associated with far-field emission of high energy photons. The only material-specific data needed to calculate the emission from different materials is the p-polarized reflectivity. We consider three basic geometries: a semi-infinite slab geometry, a thin-film geometry, and a two-dimensional material geometry (such as graphene, which is considered in the main text (Figures 2 and 3)). In all cases, we consider the quasi-electrostatic limit of the expressions for the reflectivity, in keeping with the approximations that led to Equation (9).

For an isotropic semi-infinite slab of permittivity $\epsilon(\omega)$ surrounded by vacuum, the p-polarized reflectivity is given by the simple expression:

$$r_p(\omega) = \frac{\epsilon(\omega) - 1}{\epsilon(\omega) + 1}. \tag{C.22}$$

For a thin film of of permittivity $\epsilon(\omega)$ and thickness d surrounded by vacuum on the top side and a substrate of permittivity ϵ_s, the p-polarized reflectivity is given by:

$$r_p(q,\omega) = \left(\frac{\frac{\epsilon(\omega)-1}{\epsilon(\omega)+1} - \frac{\epsilon(\omega)-\epsilon_s}{\epsilon(\omega)+\epsilon_s} e^{-2qd}}{1 - \frac{\epsilon(\omega)-1}{\epsilon(\omega)+1}\frac{\epsilon(\omega)-\epsilon_s}{\epsilon(\omega)+\epsilon_s} e^{-2qd}} \right). \tag{C.23}$$

For a two-dimensional material of surface conductivity $\sigma(\omega)$ surrounded by vacuum on the top side and a substrate of permittivity ϵ_s, provided that the mode wavelength is much longer than the thickness of the atomic layer, one has:

$$r_p(q,\omega) = \frac{(\epsilon_s - 1)i - \frac{q\sigma(\omega)}{\omega\epsilon_0}}{(\epsilon_s + 1)i - \frac{q\sigma(\omega)}{\omega\epsilon_0}}. \tag{C.24}$$

As an example of a usage of the reflectivity of a monolayer, we use this in the results of the main text when considering plasmons in a sheet of graphene in the local limit modeled by a 2D Drude conductivity (with no dissipation).

In what follows, we discuss a few applications of Equations (15) which both reaffirm and enrich the discussion and conclusions of the main text. We consider the influence of a finite Drude relaxation time, as well as the influence of interband damping [38, 130]. We also discuss the power spectrum from alternative materials.

C.4.3 Influence of Drude relaxation and interband damping in graphene

In Supplementary Figure 2, we calculate the emitted photon power per unit frequency of electromagnetic fluctuations in the surface. Integrating over frequency of fluctuations yields the total power emitted into high-frequency radiation, the kind of quantity we consider in Figure 4 of the main text. Unlike the discussion in the main text, we include a finite Drude relaxation time, which varies from 16 to 1600 fs, the longest value corresponding to observations reported in Ref. [12]. As one can see from Supplementary Figure 2, despite the fact that the relaxation time varies by three orders of magnitude, the intensity of emitted photons remains essentially the same.

In Supplementary Figure 3, we calculate the emitted photon power per unit frequency of electromagnetic fluctuations in the surface, but now for graphene modeled in the local and nonlocal RPA. For graphene modeled through either the local RPA or the non-local RPA (both giving similar results), there are additional contributions to the spectrum of fluctuations coming from interband transitions. Qualitatively, the main effect one sees in Supplementary Figure 3 is that below the Fermi frequency, the power spectrum is largely the same, with some red-shift of the peak (due to the plasmon red-shift in interband mod-

els), and some slight reduction of the peak in the nonlocal RPA case. Between the Fermi frequency and twice the Fermi frequency, the spectrum is reduced, with the local RPA overestimating the extent of the dip. These behaviors are similar to those seen in previous work on Purcell enhancement of quantum emitters near graphene [130]. Above twice the Fermi frequency, there is a new contribution to the power which does not appear in the Drude model, which arises from electromagnetic fluctuations concomitant with interband damping (from the fluctuation-dissipation theorem). Unlike the Drude case, the emitted "polariton" above twice the Fermi frequency does not propagate, and thus the polaritonic character of the radiation is quite different at these frequencies.

C.4.4 Influence of different materials

In Supplementary Figure 4, we consider the intensity of emitted photons induced by vacuum fluctuations in a different material. In particular, we consider the case of thin films of gold of varying thicknesses, whose permittivity we take to be of a Drude form, with parameters from [527]. We find that the emitted power is similar to that of graphene doped to a Fermi energy of 0.5 eV.

C.5 Simultaneous emission of a polariton and a high-energy photon in a fully quantum electrodynamical treatment

Note: In this section, we adopt (SI) natural units in which $\hbar = c = \epsilon_0 = 1$. These constants are restored in the final formulae (Equations (45) and (47)).

In this section, we present additional support for a duality between scattering from fluctuations and two-photon spontaneous emission. To do so, we consider a special case of the general phenomena above: an electron simultaneously emitting two quanta where one is a far-field photon and the other is a plasmon in a two-dimensional electron gas. For simplicity, we assume that the electron is not so relativistic that it emits most of its energy into a single photon. This is a good approximation for electron energies above a fraction of a keV (covering possible experiments in electron microscopes), and stays relevant even for highly

relativistic electrons with energies up to a few GeV (as in accelerator facilities, where the emitted photons carry much higher energies, yet still negligible relative to the electron energy). Having the emitted photon carrying a negligible part of the electron energy (also called the weak-recoil approximation) implies that we can model the interaction Hamiltonian via scalar QED. We now perform the calculations. We note first that the equivalence between the derivation in this section and the derivations of the previous section are not manifest until Equation (44).

The scalar QED Hamiltonian is:

$$H_{int} = \int d^3x \; ieA^\mu(\psi^\dagger \partial_\mu \psi - (\partial_\mu \psi^\dagger)\psi) - e^2 A^\mu A_\mu |\psi|^2. \tag{C.25}$$

Extremely relativistic electrons (> 5 GeV), may lose a significant part of their energy to the emission of a single photon through this process, thereby invalidating the use of scalar QED. In such scenarios, the interaction can be fully accounted for by considering the Dirac interaction Hamiltonian. The corresponding S-matrix, S_{fi} which describes transitions between initial states $|i\rangle$ and $|f\rangle$ is given by

$$S_{fi} = \langle f|\mathrm{T}\exp\left[\int d^4x \; eA^\mu(\psi^\dagger \partial_\mu \psi - (\partial_\mu \psi^\dagger)\psi) + ie^2 A^\mu A_\mu |\psi|^2\right]|i\rangle, \tag{C.26}$$

with T being the time-ordering operator [267], and the metric is taken as $(1, -1, -1, -1)$. A^μ is the quantized vector potential of the plasmons, and ψ is the field operator for the spinless electron of scalar QED. It is written as an expansion over plane waves with four-momentum p in terms of the annihilation operator (c_p) for the electron and the creation operator for its anti-particle ($b_p^\dagger$) as $\psi = \int \frac{d^3p}{(2\pi)^3} \frac{1}{\sqrt{2E_p}} \left(e^{-ipx} c_p + e^{ipx} b_p^\dagger\right)$. Given the strong spatial confinement of the plasmons considered, we approximate its four-potential as a pure scalar potential Φ:

$$A^\mu = (\Phi, 0, 0, 0), \Phi = \sum_{\mathbf{q}} \sqrt{\frac{\omega_{\mathbf{q}}}{4qA}} \left(e^{i\mathbf{q}\cdot(y,z) - q|x|} a_{\mathbf{q}} + \text{h.c.}\right), \tag{C.27}$$

with $\mathbf{q}$ being the plasmon wavevector, q being its magnitude, $\omega_{\mathbf{q}}$ being the wavevector-dependent plasmon frequency, and A being a normalization area.

Taking all terms in the expansion of the time-ordered exponential which are second-order in the electron charge, and plugging in the mode-expanded vector potential describing 2D Drude plasmons, we find that the emission rate Γ of a photon-polariton pair per unit photon solid angle Ω, per photon polarization, per unit plasmon frequency $\omega_{\mathbf{q}}$ and per unit plasmon propagation angle $\chi_{\mathbf{q}}$ is given by

$$\frac{d\Gamma}{d\Omega d\omega_{\mathbf{q}} d\chi_{\mathbf{q}}} = \frac{\alpha^2}{16\pi^3 \bar{\epsilon}_r v_{g\mathbf{q}} (qL)(m\gamma)^2} \times \int_{-\infty}^{\infty} \frac{dQ}{(1+Q^2)^2} \frac{\omega_Q'^2 \left| \hat{\epsilon}_k^\mu \hat{\epsilon}_q^\nu \left[\frac{(2p_\mu - 2q_\mu)(2p_\nu - q_\nu)}{(p-q)^2 - m^2} + \frac{(2p_\mu)(2p_\nu - q_\nu - 2k_\nu)}{(p-k)^2 - m^2} \right] \right|^2}{\beta n_{\mathbf{q}} \cos\chi_{\mathbf{q}} - 1 + \frac{\omega_{\mathbf{q}}}{2m\gamma}(1 - n_{\mathbf{q}}^2(1+Q^2))}, \tag{C.28}$$

where ω_Q' is defined as:

$$\omega_Q' = \omega_{\mathbf{q}} \frac{\beta n_{\mathbf{q}} \cos\chi_{\mathbf{q}} - 1 + \frac{\omega_{\mathbf{q}}}{2m\gamma}(1 - n_{\mathbf{q}}^2(1+Q^2))}{1 - \beta\cos\theta + \frac{\omega_{\mathbf{q}}}{m\gamma}(n_{\mathbf{q}} \cos\chi_{\mathbf{q}} \cos\theta + n_{\mathbf{q}} \sin\chi_{\mathbf{q}} \sin\theta \sin\phi + n_{\mathbf{q}} Q \sin\theta \cos\phi - 1)}. \tag{C.29}$$

In these equations $\alpha = \frac{e^2}{4\pi}$ is the fine-structure constant with e the electron charge, m is the electron mass, β is the electron's initial speed, γ is the corresponding Lorentz factor, ω' is the frequency of the emitted photon, $\bar{\epsilon}_r$ is the average permittivity surrounding the 2D electron gas (which in terms of the substrate permittivity ϵ_s is $\frac{1+\epsilon_s}{2}$), $v_{g\mathbf{q}}$ is the group velocity of the plasmon, $\hat{\epsilon}_k^\mu$ is the polarization of the emitted photon, $\hat{\epsilon}_{\mathbf{q}}^\mu$ is the polarization of the plasmon four-potential, given by $(1,0,0,0)$ as we describe the plasmon by a scalar potential. This corresponds to an electric-field polarization of $\frac{\hat{q}+i\hat{x}}{\sqrt{2}}$ (hats denote unit vectors). Meanwhile, $n_{\mathbf{q}} = \frac{qc}{\omega_{\mathbf{q}}}$ is the confinement factor of effective mode-index of the plasmon, p^μ is the four-momentum of the electron, q^μ is the four-momentum of the plasmon, and k^μ is the four-momentum of the radiated photon. The four-momentum of the plasmon is parameterized as $q^\mu = \omega_{\mathbf{q}}(1, n_{\mathbf{q}}Q, n_{\mathbf{q}} \sin\chi_{\mathbf{q}}, n_{\mathbf{q}} \cos\chi_{\mathbf{q}})$, with Q a dimensionless integration variable proportional to the momentum of the plasmon transverse to the 2D sheet[1]. From this parameterization, $\chi_{\mathbf{q}}$ is the angle of plasmon emission with respect to the projection of the electron's initial velocity vector in the plane of the 2D sheet.

[1]Note that the integration goes only over Q that yield a positive output photon frequency. Denote this maximum possible Q as Q_m. However, the squared Lorentzian in practice gives all of its contributions to the integration at a maximum $Q \ll Q_m$, meaning that we can extend the limits of integration to ∞.

Making a weak recoil approximation by expanding the denominators to lowest non-trivial order in $\frac{\omega_{\mathbf{q}}}{m}$, we find that the Q-integration gives (after summing over photon polarizations)

$$\frac{2\pi n_{\mathbf{q}}^2 \omega_{\mathbf{q}}^2}{(1-\beta\cos\theta)^2(\beta n_{\mathbf{q}}\cos\chi_{\mathbf{q}}-1)} F(\theta,\phi,\chi_{\mathbf{q}}), \tag{C.30}$$

where

$$\begin{aligned} F(\theta,\phi,\chi_{\mathbf{q}}) =& \sin^2\phi + \sin^2\chi_{\mathbf{q}}\cos^2\phi \\ &+ \frac{(\sin\chi_{\mathbf{q}}\sin\phi(\cos\theta-\beta) - \frac{1}{\gamma^2}\sin\theta\cos\chi_{\mathbf{q}})^2 + \cos^2\phi(\cos\theta-\beta)^2}{(1-\beta\cos\theta)^2}. \end{aligned} \tag{C.31}$$

Multiplying by the emitted photon energy ω to get the power emitted, we have that

$$\frac{dP}{d\Omega_k} = \int \frac{d^2q}{(2\pi)^2} \frac{\alpha^2 q\omega_{\mathbf{q}}}{2\bar{\epsilon}_r m^2\gamma^2(1-\beta\cos\theta)^3} \frac{1}{(qL)} F(\theta,\phi,\chi_{\mathbf{q}}), \tag{C.32}$$

We note that the factor $(qL)^{-1}$ is essentially the average over the electron length L of the exponential tail of the plasmon in the limit of $qL \gg 1$. In particular, $\frac{1}{L}\int_{-L/2}^{L/2} dx\, e^{-2q|x|} = \frac{1}{qL}$. As a result, if electron is treated as a point electron centered at transverse distance x_0 away from the plasmonic sheet, the factor $(qL)^{-1}$ is replaced by e^{-2qx_0}. In the case of a Gaussian wavepacket that resembles a point charge one would get a similar result. We now consider this case in order to make close contact with the previous sections of the paper.

C.5.1 Effects of fermionic electrodynamics

In this section, we consider the effect of the fermionic nature of the electron on the radiation spectrum associated with photon-polariton pair emission. The interaction Hamiltonian between a Dirac fermion and the electromagnetic field is given by:

$$H_{int} = e\int d^3x\, \bar{\psi}(x)\gamma_\mu A^\mu(x)\psi(x). \tag{C.33}$$

The fermion field operator ψ is given by [267]:

$$\psi(x) = \int \frac{d^3p}{(2\pi)^3} \sum_{\text{spins},s} \frac{1}{\sqrt{2E_p}} \left(e^{-ip_\mu x^\mu} u_{p,s} c_{p,s} + e^{ip_\mu x^\mu} v_{p,s} b^\dagger_{p,s} \right), \tag{C.34}$$

where, p_μ is a four-momentum, E_p is the energy of a fermion with four-momentum p, $c_{p,s}(b_{p,s})$ is an annihilation operator for the electron (positron), and $u_{p,s}(v_{p,s})$ is the corresponding spinor for the electron (positron). The field operator $\bar{\psi}$ is related to ψ by $\bar{\psi} = \psi^\dagger \gamma^0$ with γ^0 being the time-component of the vector of gamma matrices γ^μ with $\gamma^0 = \text{diag}(1, 1, -1, -1)$ in the particular represention we choose (Dirac representation). The spinors in the representation we choose are given by [528]

$$u^s_p = \begin{pmatrix} \sqrt{E_p + m}\, \eta^s \\ \frac{\mathbf{p}\cdot\sigma}{\sqrt{E_p+m}} \eta^s \end{pmatrix} \tag{C.35}$$

with $\eta^s = (1, 0)$ for spin-up and $(0, 1)$ for spin-down.

To calculate the analogous radiation emission $\frac{d\Gamma}{d\Omega d\omega_{\mathbf{q}} d\chi_{\mathbf{q}}}$ of Equation (28), it is sufficient simply to replace the absolute square in the numerator of the integrand of Equation (28) by

$$\left| \bar{u}_{r,s'} \hat{\epsilon}^\mu_k \hat{\epsilon}^\nu_q \left[\frac{\gamma_\mu (\not{p} - \not{q} + m) \gamma_\nu}{(p-q)^2 - m^2} + \frac{\gamma_\nu (\not{p} - \not{k} + m) \gamma_\mu}{(p-k)^2 - m^2} \right] u_{p,s} \right|^2, \tag{C.36}$$

where we are making use of the Feynman slash notation: $\not{A} = \gamma_\mu A^\mu$.

For low electron energies, such that the radiated photon carries only a small fraction of the electron's energy, the scalar treatment of the electron accurately captures the radiation spectrum. This is shown in Supplementary Figure 5, where we compare the spectrum predicted by fermionic quantum electrodynamics and scalar quantum electrodynamics. In particular, we show $S(\theta, \phi, \omega, \chi) = \frac{dP}{d\Omega d\omega d\chi}$ for spontaneous emission of a photon and a plasmon. The plasmon is taken to have an energy of 0.5 eV, the Fermi level is also taken to be 0.5 eV, and the plasmon is taken to be emitted in the forward direction. We plot the spectrum as a function of the photon polar angle (the azimuthal angle is taken to be zero). The electron is taken to be 5 nm away from the graphene surface. As can be seen from the figure, even for electron energies as high as 300 MeV, corrections due to the fermionic

nature of the electron are weak. The contribution to the radiation spectrum from transitions that conserve the spin of the electron is nearly identical to the radiation spectrum predicted within scalar QED. Moreover, the contribution to the radiation spectrum from transitions that change the electron spin are about 0.1% of the total radiation for electrons of 300 MeV energy. For electrons of 3 GeV energy, as in panel (c), spin-changing contributions become comparable to spin-conserving contributions, but are still significantly weaker. The spin conserving contribution to the spectrum also differs somewhat from the spectrum predicted by scalar QED.

C.5.2 Equivalence to the fluctuational theory

In this section, we demonstrate the equivalence of the fluctuational theory of Sections 3 and 4, and the relativistic quantum field theory of this section.

Consider Equation (15) for the case of a 2D electron gas described by a Drude model. In that case, the imaginary part of the p-polarized reflectivity can be shown [105] to be given by $\text{Im}\, r_p(q,\omega) = \frac{\pi}{\bar{\epsilon}_r} q v_{g\mathbf{q}} \delta(\omega - \omega_{\mathbf{q}})$, where $\omega_{\mathbf{q}} \sim \sqrt{q}$ is the dispersion relation. Plugging this form in, and integrating over the photon frequency ω, one finds that

$$\frac{dP}{d\Omega} = \frac{\alpha^2 \hbar^3}{\bar{\epsilon}_r m^2 \gamma^2 c (1 - \beta \cos\theta)^5} \int \frac{d^2 q}{(2\pi)^2}\, q \omega_{\mathbf{q}} |\mathbf{T} \hat{\epsilon}_\gamma(\chi_{\mathbf{q}})|^2 e^{-2qx_0}. \tag{C.37}$$

Using the equivalence $\frac{1}{2}(1 - \beta\cos\theta)^2 F(\theta,\phi,\chi) = |\mathbf{T}\hat{\epsilon}_\gamma(\chi_{\mathbf{q}})|^2$, it follows immediately that Equations (32) and (37) are equal (note (32) is in natural units), for the case of a point electron, verifying for the specific case of a 2D Drude sheet the equivalence of the fluctuational and quantum field-theoretic derivations of spontaneous emission of a photon-polariton pair. A similar equivalence is going to be found for other structures as well.

C.5.3 Total power emitted

We now integrate over the angular spectrum to retrieve the total power emitted into high-energy photons in this photon-polariton pair emission process. Taking Equation (32) as appropriate for a point electron, and keeping in mind that the integration limits for $\chi_{\mathbf{q}}$ are

$\pm\frac{\pi}{2}$ in the limit of highly confined plasmons, the net power obtained is

$$P = \frac{e^4\gamma^2(4-\beta)^2}{24\pi m^2}\left(\int \frac{dq}{2\pi}\frac{\omega_{\mathbf{q}}q^2}{2\bar{\epsilon}_r}e^{-2qx_0}\right) \tag{C.38}$$

Noting that the remaining integral in parentheses is $\langle 0|\mathbf{E}^2|0\rangle$, the expectation value in the vacuum state of the electric field operator describing the plasmon, one arrives at (now in SI units)

$$P = \frac{e^4\gamma^2(4-\beta^2)}{24\pi\epsilon_0 m^2c^3}\langle 0|\mathbf{E}^2|0\rangle. \tag{C.39}$$

In the relativistic limit, the field which modulates the electron is not precisely $\langle 0|\mathbf{E}^2|0\rangle$ but instead it is $\langle 0|\mathbf{E}_\gamma^2|0\rangle$, which is less than $\langle 0|\mathbf{E}^2|0\rangle$ by a factor of $3/4$ in the relativistic limit. Expressing Equation (39) in the relativistic limit, noting also that $4-\beta^2 \approx 3$, we have that (in SI units)

$$P \approx \frac{e^4\gamma^2}{6\pi\epsilon_0 m^2c^3}\langle 0|\mathbf{E}_\gamma^2|0\rangle. \tag{C.40}$$

See further discussion about this equivalence and its consequences in the main text.

Appendix D

Appendices for: A framework for scintillation in nanophotonics

D.1 Materials and Methods

D.1.1 Experimental

The electron-beam experiments were performed in a modified CamScan CS3200 custom Scanning Electron Microscope (SEM) from Applied Beams (Oregon). The electron emitter is a LaB6 emitter cathode operated with settings producing the highest currents (typically > 20 μA). Measurements are performed at the highest magnification (equivalent to spot mode). The sample is mounted on a 6-axis, fully eucentric stage, at a working distance of about 70 mm.

A Nikon TU Plan Fluor $\times 10$ objective with a numerical aperture (NA) of 0.30 was used to collect light from the area of interest. The spectrometer used was an Acton SP-2360–2300i with a low-noise, deep-cooled PIXIS camera. Monochrome images of the radiation were collected with a Hamamatsu CCD, in order to align the optical setup and spatially resolve the observed radiation.

The objective is mounted on a 5-axis (XYZ, two tilt angles) homemade positioning stage. The focal spot of the objective is aligned with the electron beam focus (and sample surface). Two piezoelectric motors allow the objective to move in a plane parallel to the

sample surface. A compact motorized actuator controls the distance of the objective to the sample surface. Two additional manual adjustment knobs allow control the alignment of the objective focal plane with the sample surface. The current is measured through a Faraday cup in the SEM stage, connected to a Keathley 6485 picoammeter. The picoammeter is triggered to acquire current signals during a time interval corresponding to the optical acquistion time (10 averaged acquisitions of 1 second duration, unless otherwise specified). A calibration measurement is performed with a calibrated light source of known power spectral density to convert the measured spectra to absolute power spectral densities and efficiencies. More information on the experimental setup can be found in the Supplementary Text, Section B. All spectra recorded with the spectrometers were averaged over 10 acquisitions of 1 second each.

The x-ray experiments were carried out inside the enclosure of a ZEISS Xradia 520 Versa micro-CT machine. The same objective (Nikon TU Plan Fluor $\times 10$) was mounted on the detector stage, and positioned to record an image of the surface of the scintillator. The scintillator and specimen were mounted on the same sample stage. Visible filters were taped directly at the back of the objective. In the images shown in Fig. 4 and 5 of the main text, no x-ray filters ("Air" setting) and a narrow bandpass visible filter (AVR Optics FF01-549-15-25) were used. Additional data showing the influence of visible and x-ray filters is given in the Supplementary Text, Section H.

The sample wafer for electron-beam-induced scintillation was purchased from MEMS Material and Engineering, Inc. (Sunnyvale, CA). The wafer was fabricated by a fusion bonding - grinding - polishing process. The wafer is made of a device layer (*p*-doped polished silicon, $\langle 100 \rangle$ orientation, resistivity 1-30 Ω.cm, thickness 0.5 $\pm$ 0.025 μm), on top of an oxide layer (amorphous silica, thickness 1.0 μm $\pm$ 5%), on top of a handle wafer (*p*-doped silicon, $\langle 100 \rangle$ orientation, resistivity 1-30 Ω.cm, thickness 625 $\pm$ 10 μm). The patterning was produced by Dr. Timothy Savas with optical interference lithography. The YAG:Ce crystal used in the x-ray experiment was purchased from Crytur and patterned with a VELION FIB-SEM. Fabrication parameters are given in the Supplementary Text, Section H. One reason we employed the VELION FIB-SEM is that nanofabrication techniques to pattern YAG:Ce are limited. Another reason is that the VELION's FIB field has

astigmatism and distortion corrections, enabling more accurate large-area FIB patterning. Finally, we selected the Au^+ FIB because it conveniently matched the Au later that would subsequently be removed with Au selective etchant.

D.1.2 Fitting to experiments

The experimentally obtained spectra in Fig. 2D of the main text were accounted for based on Eq. 1 of the main text. The red and green peaks of STH were separately fitted (hence, no assumption is made about the relative oscillator strengths of the two peaks). The spectral dependence of $S(\mathbf{r}, \omega)$ was taken as a sum of two Gaussians at the red and green peaks, on account of inhomogeneous broadening of the defect levels. Fits were obtained taking the red and green peak energies to be 1.95 and 2.6 eV respectively, with respective FWHM of 0.25 eV and 1.2 eV. Both the peak energies and widths are consistent with previous experimental measurements of STH spectra (*40*), as well as with our DFT calculations. The function V_{eff}, as defined in Fig. 1 of the main text is calculated using rigorous coupled-wave analysis.

The function $V_{\text{eff}}^{(i)}(\omega, \Omega)$ is calculated through the volume-integrated field enhancement of a plane wave incident from the far-field at angles $\Omega = (\theta, \phi)$ with polarization $i \in \{s, p\}$ and frequency ω. The integration volume (particularly, the effective depth inside silica) is fitted to provide a good agreement with experiment, and accordingly the integrand of V_{eff} is integrated to a depth of 500 nm inside the silica layer, which is within a factor of 2 of the effective depth predicted from CASINO and is within the uncertainty of the incident angle of the electron beam. The theoretically predicted signals are averaged over the numerical aperture of the objective (17.5°) and summed over polarizations. The data is best explained assuming that the samples have a small ($\sim 8°$) misalignment of their normal to the axis of the objective, with the 25 nm sample oppositely oriented from the other samples. The data used for the fit was not normalized by the incident current. Given the moderate variations in currents from sample to sample, similarly good fits can be obtained with the current-normalized data.

For the x-ray experiments: absorption maps are calculated with rigorous coupled-wave

analysis, with geometrical parameters extracted from SEM/AFM measurements. The reported value of the loss in the unpatterned YAG:Ce film is of $\mathrm{Im}(\epsilon) \sim \times 10^{-6}$ (information provided by Crytur). Geometrical parameters are extracted via an atomic force microscopy measurement fitted to as $\sin^2$ profile. Error bars on the predicted enhancements are calculated by varying the geometrical parameters according to the measured error bars from the characterization.

D.1.3 Monte Carlo HEP Energy Loss Simulations

HEP energy loss was calculated for energetic free-electrons impinging on the (unpatterned) silicon-on-insulator wafer using the open source CASINO Monte Carlo software. Calculations of the position-dependent energy loss density, $\frac{dE}{dV}(x, y, z)$ were done for electrons incident at shallow angles of incidence ($\sim 1^\circ$ measured with respect to the substrate plane) by averaging over results from 250,000 incident electrons. The data was used to calculate the marginal electron energy loss distribution per depth $\frac{dE}{dz} = \int dxdy \, \frac{dE}{dV}$ shown in Fig. 2B of the main text. We note that these calculations were also used to model scintillation in patterned samples, thus effectively neglecting the influence of the shallow pattern on the electron energy loss map.

Calculations were also performed to find the energy loss density as a function of the incident electron energy, which was used as input in the fits of Fig. 3E of the main text. Similar calculations were also done for predictions of enhanced luminescence of boron nitride in the Supplementary Text, Section F.

D.1.4 Density Functional Theory (DFT) Calculations

DFT calculations [529, 530] were performed on one bulk and three cluster models of STH. Cluster calculations used the Boese-Martin exchange correlation functional with 42% exact exchange [531] to take into account self-interaction effects. Dangling bonds were passivated with hydrogen atoms to mitigate their effect on the electronic structure. A 20 Hartree plane wave cutoff was used and Coulomb truncation [532] was implemented to mitigate the effects of cluster-cluster interactions. The defect transitions observed were attributed to

localized states at the oxygen atoms – verified by calculations of the spin density.

Bulk models, shown in Fig. 3 of the main text, with constrained 1 Bohr/unit cell magnetization yielded trapped hole defects without the need for hybrid functionals. These models yielded the same transition energies as above but used the PBE exchange correlation functional [533]. Additional details on the various DFT models and calculation results are shown in the Supplementary Text, Section G.

D.1.5 Three-level rate equation model

Based on DFT calculations, a simplified three-level system is designed to model electron pumping and subsequent radiative emission from defect states in silica. The model is pictured in Fig. 3C of the main text, corresponding to calculated energy levels from the DFT model in Fig. 3A. The following rate equations are used to model the system:

$$\begin{cases} \frac{dp_1}{dt} = & -\Gamma_{13}\, p_1(1-p_3) + \Gamma_{31}\, p_3(1-p_1) \\ \frac{dp_2}{dt} = & -\Gamma_{23}\, p_2(1-p_3) + \Gamma_{32}\, p_3(1-p_2) \\ \frac{dp_3}{dt} = & \Gamma_{13}\, p_1(1-p_3) - \Gamma_{31}\, p_3(1-p_1) \\ & +\Gamma_{23}\, p_2(1-p_3) - \Gamma_{32}\, p_3(1-p_2) \end{cases} \tag{D.1}$$

such that the total occupation number is conserved over time $\frac{d\sum_i p_i}{dt} = 0$ with the initial condition $p_1 = p_2 = 1$ and $p_3 = 0$. This set of equations describe a three-level system, where 1 (resp. 2) is the ground state corresponding to green (resp. red) emission, 3 is a shared excited state to which electrons are sent via free-electron pumping. Band electrons can relax from the excited state 3 to one of two ground states 1 and 2, corresponding to the green and red peak emission, respectively.

We can solve the steady-state of Eq. D.1 to estimate the ratio of green to red emission at the steady-state:

$$\eta = \frac{\Gamma_{31}\,(1-p_1)}{\Gamma_{32}\,(1-p_2)}. \tag{D.2}$$

Calculations were performed using the DifferentialEquations.jl package in Julia [534] and fitted using the LsqFit.jl package.

We use this model to gain further microscopic understanding of the observed experimental data, in conjunction with the general nanophotonic scintillator theory described in the main text. We chose η as an experimental observable, since it can be calculated from Eq. D.1 and – assuming green and red peak defects are localized in the same region – the observable is independent of a few experimental unknowns (beam size, number of excited emitters). Electrons in state 3 can then radiatively decay into state 1 or 2.

We assume that Γ is proportional to the electron beam energy deposited in the luminescent material: $\Gamma \propto I \times E \times \eta_{\text{ene}}(E)$ where I is the incident electron current, E its kinetic energy (in keV), and $\eta_{\text{ene}}(E)$ the fraction of energy (normalized to the incident energy E) deposited by an electron in the silica layer, calculated via Monte-Carlo Simulations of electron scattering in the TF sample (see corresponding Methods section above "Monte Carlo HEP Energy Loss Simulations").

In a first numerical experiment shown in Fig. 3E of the main text, we utilized scintillation data measured on the TF sample at various incident voltages and currents. This data was used to estimate the ratio of pumping rates $\Gamma_{13}/\Gamma_{23} = 3.2 \pm 0.09$. This value indicates an intrinsic preference of the system to excite the green defect through electron pumping.

In a second numerical experiment shown in Fig. 3E of the main text, we utilized scintillation data measured on the PhC sample at various incident voltages and currents. This data was used to estimate the ratio of decay rates enhancements Γ_{32}/Γ_{31} and to confirm the value of Γ_{13}/Γ_{23}. When letting both parameters be optimized, we obtain a value of $\Gamma_{13}/\Gamma_{23} = 3.35 \pm 0.13$, similar to the original value. We can also estimate the value of $\left(\frac{\Gamma_{32}}{\Gamma_{31}}\right)_{\text{PhC}} \left(\frac{\Gamma_{32}}{\Gamma_{31}}\right)_{\text{TF}}^{-1} \sim 2.3$ which corresponds to the scintillation rate enhancement of the red defects. This value is in agreement with our calculations and experimental demonstration of V_{eff} scintillation enhancement of the red defects. The relative error of this estimate is of ± 0.4 (uncertainty coming from the first numerical experiment) and of ± 0.9 (uncertainty coming from the second numerical experiment). Therefore, results from the three-level model are a strong indication of the microscopic nature of the observed scintillation spectrum.

We verified the robustness of our fits by trying different differential equation solvers and fitting methods, and did not observe any significant change in the values obtained for

the parameters of interest, which indicates the consistency of our approach. For instance, another local optima of the optimization, which we did not detail for the sake of brevity, had the following parameters: $\Gamma_{13}/\Gamma_{23} = 4.43 \pm 0.94$ (TF data only), $\Gamma_{13}/\Gamma_{23} = 4.42 \pm 0.17$ (PhC data only), and $\left(\frac{\Gamma_{32}}{\Gamma_{31}}\right)_{\text{PhC}} \left(\frac{\Gamma_{32}}{\Gamma_{31}}\right)_{\text{TF}}^{-1} \sim 4.06$, with relative error of this estimate of ± 1.42 (uncertainty coming from the second numerical experiment) and of ± 7.15 (uncertainty coming from the first numerical experiment). Though the error bar in Fig. 3 of the main text only shows the relative model uncertainty with respect to the value of $\frac{\Gamma_{32}}{\Gamma_{31}}$ (which is the main decay rate variable relating to our experimental observables), we observe that the relative error of other parameters is comparable or lower.

D.2 Supplementary Text

D.2.1 End-to-end framework summarized

In this section, we provide additional details about our end-to-end framework to model scintillation in nanophotonics, shown in Fig. D-1, and summarized in Fig. 1G of the main text.

Our framework is fed inputs, which specify the scintillating material, the high energy particle, and the electromagnetic properties of the nanophotonic environment. For example, the scintillating material might be specified by its atomic number and relevant defect/dopant concentrations (if the scintillation is from defects/dopants, as in both cases we consider in the main text). The high-energy particle (HEP) would be specified by the type of particle, as well as its angle of incidence and energy. And the nanophotonic structure is specified by the spatially varying permittivity of the system.

These inputs are transformed into outputs by the following simulation components:

1. **Monte Carlo HEP energy loss** calculations are performed to calculate the three-dimensional energy loss per unit volume (energy loss density) of the HEPs through the structure. Radiative sites may diffuse before emitting, as is typically the case for electron-hole pairs in semiconductors, in which case carrier diffusion may be taken into account at this stage. This energy loss is proportional to the density of excited electrons that ultimately scintillate. This energy loss information can be further combined (as we do in Fig. 3 of the main text) with rate equations to calculate occupation factors of various scintillating levels.

2. **Density Functional Theory (DFT)** is used to calculate the scintillation emitter energy levels and oscillator strengths, which feed into the calculation of the spectral function.

3. **Full-wave nanophotonics simulations** are performed to calculate the position-dependent field enhancement in the nanophotonic structure, where the incident field is taken as a plane wave incident at some given angles, frequency, and polarizations. The field

enhancement is integrated over space, weighted by the position-dependent spectral function (which depends on the spatially-dependent occupation factors).

In principle, these steps are coupled together: the field enhancement is set by the density of excited electrons created by HEPs, and, if their density is high enough, it would change the field solutions relative to the case of no excited electrons. This is because this density of excited electrons can be seen as a change to the permittivity of the scintillator. Thus, the truly *ab initio* method would be to (1) evaluate the position-dependent energy loss density by HEPs, (2) translate this into a density of excited electrons, and (3) calculate the electromagnetic field enhancement of incident plane-waves sent into a material with a permittivity taking these excited electrons into account. In cases we consider, it is adequate to approximate the excited electrons as only weakly changing the permittivity of the scintillator, thus allowing us to decouple the energy-loss and nanophotonic calculations.

Coupled together, results from these three methods allow us to calculate the effective absorption volume (via electromagnetic reciprocity) and the non-equilibrium occupation function. Plugging these two into our theory enables us to calculate the scintillation signal and its polarization, spectral, and angular dependence (as in Eq. 1 from the main text). Alternatively, our framework allows us to calculate the scintillation power density by integrating the spatially-varying effective field enhancement and non-equilibrium occupation over the scintillating volume.

Beyond using this framework to predict the scintillation spectrum, we can also use it to optimize or inverse design the scintillation (e.g., for maximum photon yield, directivity, etc.). This step requires differentiability of the inputs, which for now is only the case for the full-wave nanophotonics, in which case we treat the energy loss as fixed. More details about the inverse design of nanophotonic scintillators, enabled by our framework, can be found in Section E.

D.2.2 General nanophotonic theory of scintillation

In this section, we develop a general quantitative framework for describing scintillation in nanophotonics, providing additional details on the derivation of Equations (1) and (2) of

the main text. Let us consider, as in Fig. 1 of the main text, a material with scintillating centers. Such scintillating centers can be associated with defects or dopants in materials (as in the case of what we consider in the experiments of the main text), electron-hole recombination in semiconductors, excitons, or other mechanisms. Such centers can be generated optically, as in photoluminescence, or via a beam of HEPs, such as electrons (incoherent cathodoluminescence), x-rays, γ-Rays, radioactive particles, and cosmic rays. In all cases, the spontaneous emission associated with these emitters can be considered as a type of non-equilibrium radiation from fluctuating currents of current density $\mathbf{J}(\mathbf{r},\omega)$ in the material. The correlation functions of the current, of the form $\langle J_j(\mathbf{r},\omega)J_k(\mathbf{r}',\omega)\rangle$ (with j,k labeling vector components) are determined by the microscopic structure of the scintillating center (the energy levels and current matrix elements), as well as the non-equilibrium occupation of the various energy levels. These occupation functions depend on the pump strength, and are inferred via a combination of Monte Carlo simulations and a kinetic model of the transition dynamics of the electron between energy levels. As a point of notation, we index the energy levels by the label α, with corresponding energy $E_\alpha \equiv \hbar\omega_\alpha$ and occupation factor f_α.

In what follows, we will take advantage of the fact that in many cases of interest in scintillation, there is a separation of time scales between: (1) the processes that create the excited scintillation centers, and (2) the recombination that leads to radiation. In particular, the process of impact ionization of an electron, followed by relaxation (e.g., by phonons and electron-electron scattering) to the lowest unoccupied states of the system, occurs on timescales much shorter than the spontaneous emission. The spontaneous emission, in many systems, occurs on timescales between microseconds and nanoseconds. As a result of this, we can approximate the scintillating system as being in a non-equilibrium *steady state*, and so the occupation functions $-$ which govern the correlation functions of the fluctuating current $-$ remain well-defined. In that case, the normally-ordered correlation function between different components of the current is given simply as

$$\langle J_j^-(\mathbf{r}_1,\omega)J_k^+(\mathbf{r}_2,\omega)\rangle = 2\pi T\sum_{\alpha,\beta} J_j^{\alpha\beta}(\mathbf{r}_1)J_k^{\beta\alpha}(\mathbf{r}_2)f_\alpha(1-f_\beta)\delta(\omega-\omega_{\alpha\beta}) \equiv 2\pi T S_{jk}(\mathbf{r_1},\mathbf{r}_2,\omega). \tag{D.3}$$

where T a normalization time and $J_k^{\alpha\beta}(\mathbf{r})$ is the matrix element of the k-component of the current density operator between quantum states α and β. Further note that we have taken the correlation function between the negative $(-)$ and positive $(+)$ frequency parts of the current operator, as the far-field flux depends on this combination of current operators. The radiated intensity spectrum in the far-field, along the ith polarization, $\frac{dI^{(i)}(\mathbf{r})}{d\omega}$ which is given in terms of the normally-ordered correlation functions of the electric fields, is (in repeated index notation for j, k)

$$\frac{dI^{(i)}(\mathbf{r})}{d\omega} = \frac{2\mu_0\omega^2}{c}\int d\mathbf{r_1} d\mathbf{r_2}\; G_{ij}^*(\mathbf{r},\mathbf{r}_1,\omega)G_{ik}(\mathbf{r},\mathbf{r}_2,\omega)S_{jk}(\mathbf{r}_1,\mathbf{r}_2,\omega). \tag{D.4}$$

Here, the Green's function $G_{ij}(\mathbf{r},\mathbf{r}_1,\omega)$ is the ith component of the electric field at the position $\mathbf{r}$ created by a dipole at location $\mathbf{r}_1$ and oriented along direction j. What we will now show is that the scintillation spectrum is directly related to the field enhancement in the scintillation volume, which is also proportional to the absorption in the scintillation volume (provided that the absorption is sufficiently weak as to not change the field solutions). Let us focus on the widely applicable case in which the current fluctuations are *local*, so that $S_{jk}(\mathbf{r}_1,\mathbf{r}_2,\omega) = S_{jk}(\mathbf{r}_1,\omega)\delta(\mathbf{r}_1-\mathbf{r}_2)$. We note that in a bulk medium, S would need to be translationally invariant, and this can be taken to be the case either for homogeneously distributed defects or a bulk solid. However, we also note that in cases we consider, due to the spatial non-uniformity of the pump, the occupation factors can depend on position (over a length scale typically much larger than the electronic length-scale), so that $f_{\alpha,\beta} \rightarrow f_{\alpha,\beta}(\mathbf{r})$.

In the case described above, we have

$$\frac{dI^{(i)}(\mathbf{r})}{d\omega} = \frac{2\mu_0\omega^2}{c}\int d\mathbf{r_1}\; G_{ij}^*(\mathbf{r},\mathbf{r}_1,\omega)G_{ik}(\mathbf{r},\mathbf{r}_1,\omega)S_{jk}(\mathbf{r}_1,\omega). \tag{D.5}$$

In reciprocal electromagnetic systems, $G_{ij}(\mathbf{r},\mathbf{r}_1,\omega) = G_{ji}(\mathbf{r}_1,\mathbf{r},\omega)$, thus relating the power to the field emitted by a dipole at position $\mathbf{r}$, which is taken to be in the far-field. Let us define $G_{ji}(\mathbf{r}_1,\mathbf{r},\omega) = \alpha E_j^{(i)}(\mathbf{r}_1,\mathbf{r},\omega)$, with α a proportionality factor, and $E_j^{(i)}(\mathbf{r}_1,\mathbf{r},\omega)$ the electric field along component j at position $\mathbf{r}_1$ created by a dipole located at position $\mathbf{r}$ and polarized along direction i (and at frequency ω). Then, Eq. D.5 can thus be translated into

the i-polarized power spectrum per unit solid angle $\frac{dP^{(i)}}{d\omega d\Omega}$ as:

$$\frac{dP^{(i)}}{d\omega d\Omega} = \frac{\omega^2}{8\pi^2\epsilon_0 c^3}\int d\mathbf{r}' \frac{E_j^{*(i)}(\mathbf{r}', \mathbf{r}, \omega)}{\left|\mathbf{E}_{\text{inc}}^{(i)}(\mathbf{r}', \mathbf{r}, \omega)\right|}\frac{E_k^{(i)}(\mathbf{r}', \mathbf{r}, \omega)}{\left|\mathbf{E}_{\text{inc}}^{(i)}(\mathbf{r}', \mathbf{r}, \omega)\right|}S_{jk}(\mathbf{r}', \omega), \tag{D.6}$$

where we have defined $|\mathbf{E}_{\text{inc}}^{(i)}(\mathbf{r}', \mathbf{r}, \omega)|$ as the magnitude of the field of a dipole with polarization i at frequency ω, emitting from the far-field, which is $|\alpha|/4\pi|\mathbf{r} - \mathbf{r}'|$. The unpolarized spectrum is simply obtained by summing over i. Since the scintillating material is far from the detector, this field is equivalent to a plane wave incident from the far field at an angle set by $\mathbf{r}$. Thus, we may rewrite the various fields more simply as $\mathbf{E}(\mathbf{r}', \mathbf{r}, \omega) \to \mathbf{E}(\mathbf{r}', \omega, \Omega)$, with Ω denoting a direction about which an infinitesimal solid angle $d\Omega$ is centered. While this result is general, to make clear the physics contained within Eq. D.6, we consider the case where the scintillating material is isotropic, so that $S_{jk}(\mathbf{r}', \omega) = \delta_{jk}S(\mathbf{r}', \omega)$. In that case, also using the simplified notation of this paragraph, we have

$$\frac{dP^{(i)}}{d\omega d\Omega} = \frac{\omega^2}{8\pi^2\epsilon_0 c^3}\int d^3\mathbf{r} \frac{\left|\mathbf{E}^{(i)}(\mathbf{r}, \omega, \Omega)\right|^2}{\left|\mathbf{E}_{\text{inc}}^{(i)}(\omega, \Omega)\right|^2}S(\mathbf{r}, \omega). \tag{D.7}$$

Here, we have also taken $\mathbf{r}' \to \mathbf{r}$ in the integration. We have also used the fact that, since the incident field looks like a plane wave in the far-field limit, its norm is position-independent. This equation coincides with Equation (1) of the main text.

From Eq. D.7, one can immediately see that the emitted power is proportional to the field enhancement by a plane wave at frequency ω, direction Ω, and polarization i inside the volume governed by the scintillating material. This is also proportional to the absorbed power of the plane wave. In particular, if instead of S, one had Im ϵ, then Eq. D.7 would be directly proportional to the absorbed power. In fact, the spectral function computed here is proportional to (up to a frequency-dependent factor) the dielectric function corresponding to the material being in a non-equilibrium steady-state with the same occupation functions. As a reminder, the spectral function $S(\mathbf{r}, \omega)$ is set by microscopic properties of the material (energy levels, current/dipole matrix elements), and the properties of the pump beam (current, energy), the latter of which sets the spatial distribution of S through the

occupation functions. Therefore, for a fixed pump, maximizing scintillation corresponds directly to maximization of the absorbed power / field enhancement in the volume set by the distribution of scintillating material.

We note that similar considerations based on electromagnetic reciprocity have been utilized to make predictions in other areas of non-equilibrium radiation,such as thermal radiation, LEDs, and generalizations of the Purcell effect to non-equilibrium bodies (*34, 49–51*).

It is worthwhile to take a few additional simplifying assumptions that lead to an extremely simple formula for scintillation. Consider the case where S is effectively independent of position in the scintillation volume V_S (and its spatial dependence may be dropped so that $S(\mathbf{r},\omega) \to S(\omega)$). In that case, we may write

$$\frac{dP^{(i)}}{d\omega d\Omega} = \frac{\pi}{\epsilon_0 \omega} \times S(\omega) \times (V_{\text{eff}}^{(i)}(\omega,\Omega)/\lambda^3), \tag{D.8}$$

where $V_{\text{eff}}^{(i)}(\omega)$ is the effective volume of absorption or field enhancement (note that it has dimensions of volume) – defined by $V_{\text{eff}}^{(i)}(\omega,\Omega) = \int_{V_S} d\mathbf{r}\ |\mathbf{E}^{(i)}(\mathbf{r},\omega,\Omega)|^2/|\mathbf{E}_{\text{inc}}^{(i)}(\omega,\Omega)|^2$ – and $\lambda = 2\pi c/\omega$. Such an expression states that the scintillation spectrum is a simple product of a microscopic factor, set by the non-equilibrium steady-state distribution function, and an effective absorption volume, which is set only by the (structured) optical medium surrounding the scintillating medium. This expression also allows inference of the microscopic spectral function $S(\omega)$, given the knowledge of V_{eff}, and a measurement of the scintillation spectrum.

As a simple example of V_{eff} which can be calculated even analytically, let us consider V_{eff} for thin film geometries related to the thin film sample of Fig. 2 of the main text. Results are shown in Fig. D-2, assuming that the entire thin film makes up the scintillation volume. The blue curve in Fig. D-2 corresponds to the sample considered in the main text (air - 500 nm Si - 1 μm SiO_2 - Si substrate), while the others differ by removal of the top Si layer (orange) and both Si layers (green). For simplicity, we show just the absorption of light coming at normal incidence (angles of incidence below 15° lead to very small changes in the absorption). Here, V_{eff} may be directly calculated by solving for the E and

H fields induced by solving the Fresnel problem of a plane wave coming from the far field (as expected from reciprocity). The blue curve features somewhat well-defined and sharp resonant peaks corresponding to thin-film resonances associated with the guiding structure formed by silica surrounded by high-index silicon. Even in the case of silica surrounded by air, which in principle is the closest case to an intrinsic system, and provides minimal light-guiding, there is clear nanophotonic shaping that will arise from the etalon fringes: associated with the fact that the silica is a wavelength-scale thin-film. Thus, the observed scintillation spectrum would depart considerably from the singly-peaked Gaussian spectral function of the self-trapped hole (STH) defects in silica (which would represent the bulk spectrum).

D.2.3 Experimental setup

In this section, we describe our general experimental setup. It is based on a modified Scanning Electron Microscope (SEM) is shown in Fig. D-3A. Let us outline a few other elements of the experimental setup. First, the purpose of Element 6 (flat mirror) is to send the optical signal to the visible – near-infrared imaging and spectroscopy system, shown in the right side of Fig. D-3A (Elements 7-15). Second, the polarization-insensitive beamsplitter (Element 8) sends part of the signal to a visible CCD Camera (Hamamatsu). The combination of Elements 4 (objective), 7 (tube lens), and 9 (camera) creates an image of the sample's surface, so the location of the electron beam interaction with the sample can be visualized. This facilitates the alignment of the experimental setup. Third, Elements 16-18 are used to scatter light off from the surface of the sample. Typically, an alignment mark (silver paste dot deposited on a unused sample location) is drawn on the sample surface, to align the imaging and spectroscopy functionalities of the setup. Fourth, a set of two lenses is used (Element 11) to focus the optical signal into the fiber input feeding the spectrometer (Elements 12-15). The spectrometer is comprised of a fiber coupling into a slit, a grating turret (Element 12), and a mirror focusing the signal on a visible CCD (Element 15).

SEM Control

The SEM beam current, voltage, working distance, and stage positioning are controlled in part with the Caesium Software provided by Applied Beams LLC (Oregon). Adjustment knobs outside the SEM chamber allow alignment of the emitter, focusing lenses, stage rotation and tilts.

Objective positioning

The XYZ positioning and tilt angle alignment of the objective (Element 4) is realized with a homemade motorized stage. The three motors are controlled through a computer interface outside the SEM chamber. Each motor is connected to an outside controller through a vacuum-preserving electronic connector.

Calibration measurement

The spectra measurements were converted to power spectral densities after performing a calibration measurement, whose setup is shown in Fig. D-3B. The calibrated source (AVA Light - Element 19) of known power is positioned at the location of the objective / electron beam focus. The conversion relation is a linear mapping from the spectrometer signal to power spectral density:

$$S(\lambda) = P(\lambda)L(\lambda), \tag{D.9}$$

where $S(\lambda)$ is the spectrometer signal, measured in counts per second, $P(\lambda)$ is the signal spectral density measured in W/nm, and $L(\lambda)$ is a spectral loss function accounting for dispersive attenuation through the optical setup. $L(\lambda)$ is measured in (counts/s)/(W/nm). The reconstructed optical dispersive attenuation function $L(\lambda)$ is shown in Fig. D-3C.

Additionally, we performed spectral calibration by measuring emission lines of a lamp with characteristic emission wavelengths (mercury lamp) and used three of those lines to calibrate the spectrometer. There may still be wavelength miscalibration between the lines used for calibration. We accounted for this possible mismatch in our fit with theory.

D.2.4 UV Scintillation shaping in hexagonal boron nitride

In this section, we extend the scope of the general nanophotonic theory of scintillation developed in Section B. In particular, we show how our framework can be used to design highly efficient scintillation sources in the UV. Additionally, we show that our framework can describe how the scintillation spectrum is altered by the presence of gain, enabling for the first time a framework to describe amplification effects in scintillation, potentially enabling description of interesting experimental results such as scintillation-lasing in Watanabe et al. [2]. The perspective of tunable ultraviolet sources is especially exciting given the growing interest in ultraviolet sources for water purification and sanitization. In particular, several wavelengths in the UV-C window have been of interest [535], with some gaining renewed interest in the far-UVC to eliminate airborne human coronaviruses [536].

In this section, we focus primarily on UV scintillation from hBN (hexagonal boron nitride), where Watanabe *et al.* demonstrated efficient UV emission from high-quality hBN substrates pumped by electron beams.

First, let us consider scintillation from a simple thin-film of hBN. For concreteness, we consider an isolated film of BN of thickness 1 μm surrounded by air (mimicking the isolated BN flakes in Watanabe *et al.* [2]. Then we consider the emission per unit area (which is independent of lateral position along the film) for a beam normally incident on it. To calculate the spectrum, we must multiply the intrinsic luminescent spectrum of BN with V_{eff}, which can be readily calculated (by solving for the fields inside the BN resulting from an a plane wave impinging on the air-BN-air system). For the purposes of this section, we are mostly interested in the relative magnitude of the signal between different sample conditions, and not as interested here in the absolute magnitude of the luminescence spectrum, which requires a detailed microscopic understanding of the excitons contributing to the BN signal. Thus, the intrinsic scintillation spectrum for the planar system is taken phenomenologically as the function shown in Fig. D-4(inset), with peak intensity at 216 nm and a width of roughly 5 nm. This function is taken to be in qualitative agreement with the spectrum measured in Ref. [2]. To showcase the kinds of predictions that can be made the formalism of Sec. B, we show the predicted luminescence of hBN as the intrinsic

losses of the BN permittivity are reduced. This is to simulate the effect of gain induced by electron beam pumping. As the loss is reduced, the luminescence spectrum starts to manifest growing and narrowing etalon peaks. This feature is in accord with observations in Ref. [2], which show spectral narrowing and strongly increased intensity as a function of electron-beam pumping of hBN flakes.

Next, we demonstrate control and enhancement of hBN ultraviolet scintillation with nanopatterned structures, shown in Fig. D-5. The structures that are used are shown in Fig. D-5A: a two-dimensional square periodic array of holes etched in hBN (thickness 100 nm) on top of a silica spacer (thickness 200 nm) on top of an aluminium substrate. The period of the structure equates to 180 nm. We compare emission power spectra at various radii (unpatterned structure, $r = 30$ and $r = 50$ nm) and beam locations (shown schematically in Fig. D-5(a,c)).

We assumed that the hBN layer consists of deformed monocrystalline samples similar to the ones in Ref [2, 537]. Such samples, not unlike polycrystalline hBN, exhibit a greater number and variety of scintillating defects. We used for our theory an empirical fit of the spectrum shown in Fig. 6 (blue line) of [537].

The resulting spectra are shown in Fig. D-5(d,e). The peak emission wavelength can be tuned by adjusting the radius and the relative and absolute power of the observed peaks can be controlled by exciting the structures at different locations (which can be realized by operating state-of-the-art SEMs with < 5 nm spatial resolution and beam size in spot mode).

D.2.5 Alternative DFT and rate equation models

Alternative DFT and rate equation models

It is possible to get reasonable agreement with the observed data with an alternative model. Here, we present calculations of energy levels and spectra of a cluster model without hybrid functionals (calculations carried out by Ali Ghorashi). DFT calculations were performed using norm-conserving (SG-15) pseudopotentials, a 30 Hartree plane wave cutoff, and the gga-PBE exchange correlation functional in a 21 atoms cluster to model the STH defect.

The Si-O-Si bonding angle is changed to create a distribution of possible manifestations of the defect, and the excitation spectra and oscillator strengths are obtained through momentum matrix elements. Based on this DFT model, a simplified four-level system is designed to model electron pumping and subsequent radiative emission from defect states in silica. The model is pictured in Fig. D-6B, corresponding to calculated energy levels from the DFT model in Fig. D-6(a, bottom). The following rate equations are used to model the system:

$$\begin{cases} \frac{dp_1}{dt} = & -\Gamma_{41}\, p_1(1-p_4) + \Gamma_{12}\, p_2(1-p_1) + \Gamma_{13}\, p_3(1-p_1) \\ \frac{dp_2}{dt} = & \Gamma_{24}\, p_4(1-p_2) - \Gamma_{12}\, p_2(1-p_1) \\ \frac{dp_3}{dt} = & \Gamma_{34}\, p_4(1-p_3) - \Gamma_{13}\, p_3(1-p_1) \\ \frac{dp_4}{dt} = & \Gamma_{41}\, p_1(1-p_4) - \Gamma_{24}\, p_4(1-p_2) - \Gamma_{34}\, p_4(1-p_3) \end{cases} \tag{D.10}$$

such that the total occupation probability is conserved over time $\frac{d\sum_i p_i}{dt} = 0$ with the initial condition $p_1 = 1$ and $p_{i\neq 1} = 0$. This set of equations describes a four-level system, where 1 is the ground state, 4 is a high-energy state to which electrons are sent via free-electron pumping (since the free-electron energy is much larger than any other energy scale in the bandstructure). Band electrons can relax from the higher-energy state 4 to one of two intermediate states 2 and 3, corresponding to the red and green defect states, respectively.

Since excitation and relaxation mechanisms happen on a much shorter timescale than emission for most scintillating systems, we can assume that $\Gamma_{34}, \Gamma_{24} \gg \Gamma_{13}, \Gamma_{12}$. We can solve the steady-state of Eq. D.10 to estimate the ratio of green to red emission at the steady-state:

$$\eta = \frac{\Gamma_{13}\, p_3}{\Gamma_{12}\, p_2}. \tag{D.11}$$

We use this model to gain further microscopic understanding of the observed experimental data, in conjunction with the general nanophotonic scintillator theory described in the main text. We chose η as an experimental observable, since it can be calculated from Eq. D.10 and – assuming green and red peak defects are localized in the same region – the observable is independent of a few experimental unknowns (beam size, number of excited emitters). Electrons in states 2 and 3 can then radiatively decay into state 1.

In a first numerical experiment shown in Fig. D-6(d, left), we utilized scintillation data measured on the TF sample at various incident voltages and currents. This data was used to estimate the ratio of decay rates $\Gamma_{34}/\Gamma_{24} = 2.45 \pm 0.7$. We assume that Γ_{41} is proportional to the electron beam energy deposited in the luminescent material: $\Gamma_{41} \propto I \times E \times \eta_{\text{ene}}(E)$ where I is the incident electron current, E its kinetic energy (in keV), and $\eta_{\text{ene}}(E)$ the fraction of energy (normalized to the incident energy E) deposited by an electron in the silica layer, calculated via Monte Carlo simulations of electron energy loss in the TF sample.

In a second numerical experiment shown in Fig. D-6(d, right), we utilized scintillation data measured on the PhC sample at various incident voltages and currents. This data was used to estimate the ratio of decay rates enhancements Γ_{13}/Γ_{12} and to confirm the value of Γ_{34}/Γ_{24}. When letting both parameters be optimized, we obtain a value of $\Gamma_{34}/\Gamma_{24} = 2.37 \pm 1.4$, close to the original value. We can also estimate the value of $\left(\frac{\Gamma_{12}}{\Gamma_{13}}\right)_{\text{PhC}} \left(\frac{\Gamma_{12}}{\Gamma_{13}}\right)^{-1}_{\text{thin}} \sim 3.56$ which corresponds to the V_{eff} scintillation enhancement. Therefore, results from the four-level model are a strong indication of the microscopic nature of the observe scintillation spectrum.

We verified the robustness of our fits by trying different values of the ratio Γ_{12}/Γ_{24}, different differential equation solvers, and did not observe any significant change in the values obtained for the parameters of interest, which indicates the consistency of our approach.

D.3 Supplementary Figures

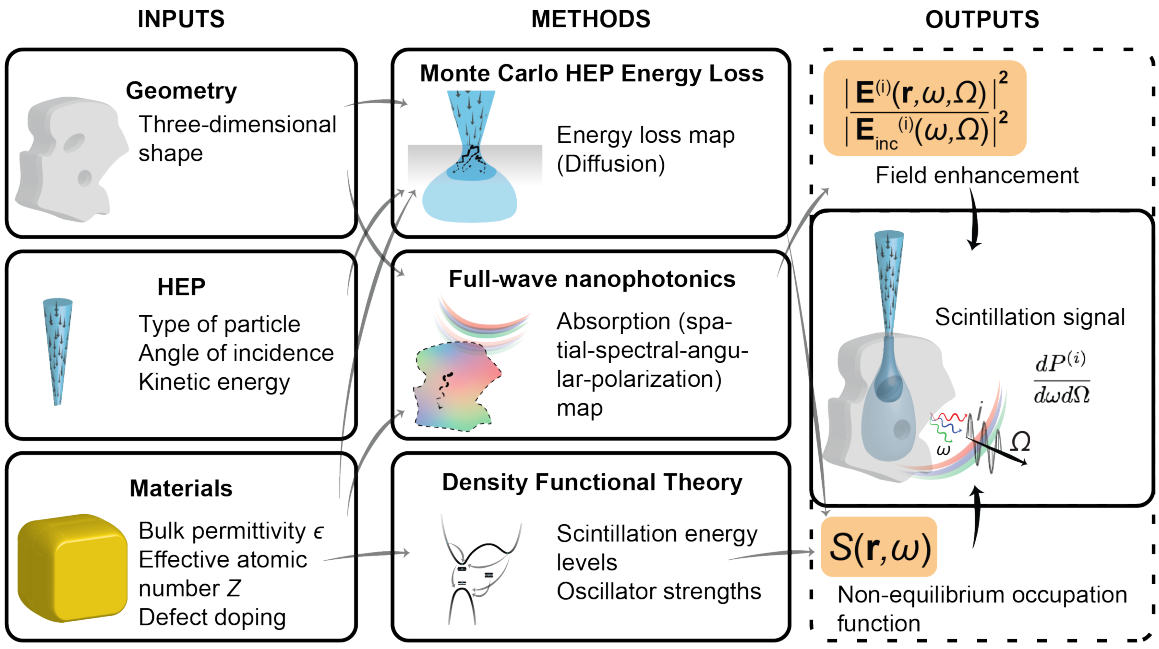

Figure D-1: **End-to-end scintillation framework.** Arrows represent forward flow of information from inputs to outputs through our simulation methods (as an example: geometry information feeds into energy loss calculations, which provides an energy loss map that feeds into the spectral function). HEP: high-energy particle. $dP^{(i)}/d\omega d\Omega$: scintillation spectral-angular power density at polarization i. ω: scintillation frequency, Ω: scintillation angle of emission. $S(\mathbf{r},\omega)$: non-equilibrium steady-state distribution function. $\left|\mathbf{E}^{(i)}(\mathbf{r},\omega,\Omega)\right|^2 / \left|\mathbf{E}^{(i)}_{\text{inc}}(\omega,\Omega)\right|^2$: field enhancement at location $\mathbf{r}$, frequency ω, angle Ω.

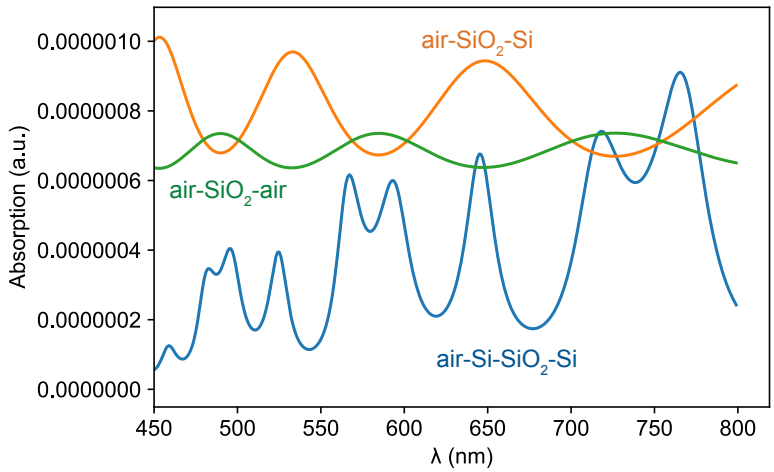

Figure D-2: **Absorbed power (proportional to V_{eff}) at normal incidence as a function of wavelength for a few different thin film geometries.** Thicknesses for blue curve: $\infty - 500$ nm $- 1000$ nm $- 500$ nm $- \infty$. Thicknesses for orange curve: $\infty - 1000$ nm $- \infty$. Thicknesses for green curve: $\infty - 1000$ nm $- \infty$.

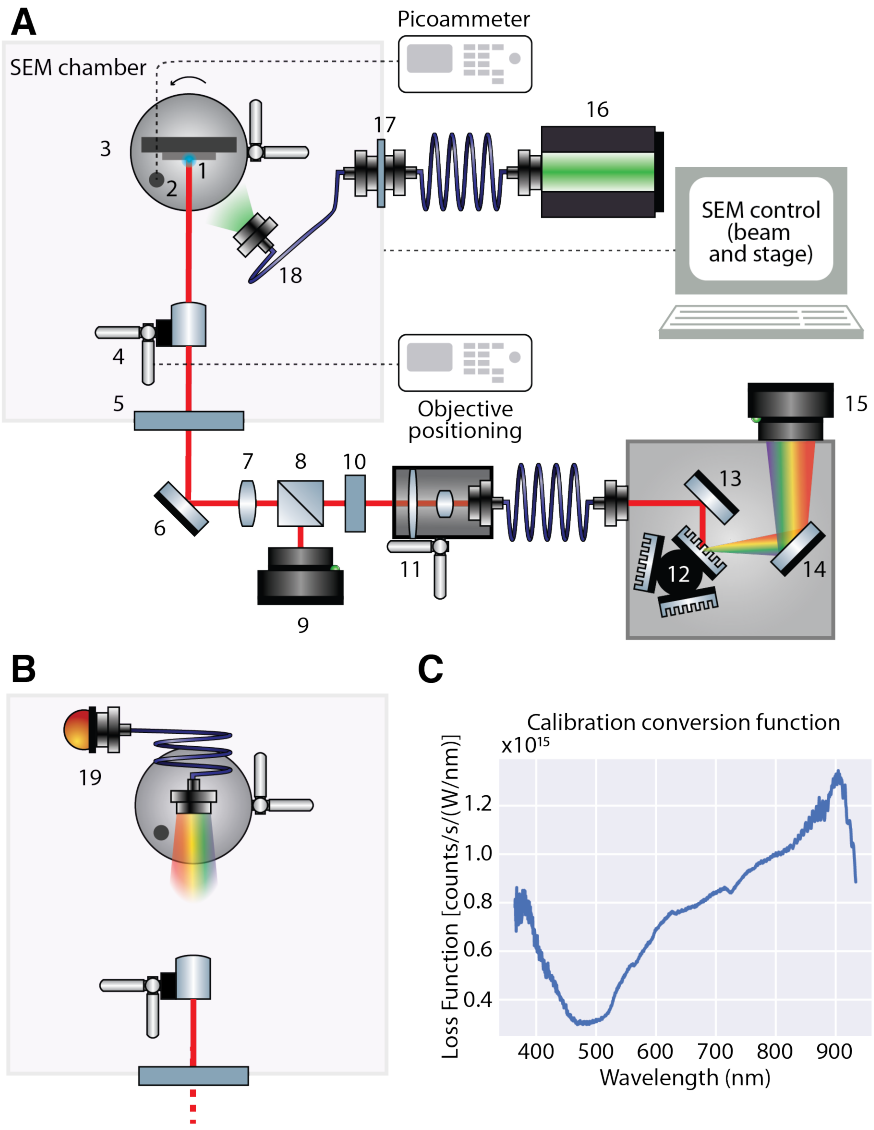

Figure D-3: **Schematic of the experimental setup and calibration measurement.** (**A**) Schematic of the experimental setup. Inside SEM chamber: 1: Electron beam interacting with sample; 2: Faraday cup, connected to external picoammeter, measuring incident current. 3: 6-axis, fully eucentric stage, controlled by SEM control. 4: XYZ objective stage. 5: x-ray blocking window. Outside SEM chamber: 6: Mirror. 7: Tube lens. 8: Beam splitter. 9: CCD Camera, imaging sample surface. 10: polarizer (optional). 11: XYZ cage assembly with two focusing lenses and a fiber-coupling. Inside spectrometer: 12: Grating turret. 13, 14: (Focusing) Mirrors. 15: Spectrometer CCD. Green laser feedthrough alignment arm: 16: Green laser source. 17: Fiber-coupling feedthrough, vacuum compatible. 18: Fiber output illuminating sample. (**B**) Calibration experiment (the rest of the setup is not shown because it is similar to (**A**)). 19: AVA Calibration light source. (**C**) Measured calibration conversion function.

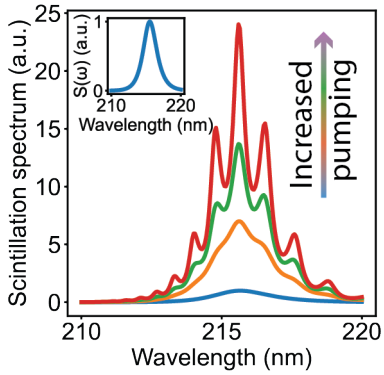

Figure D-4: **Amplified hBN scintillation in hBN flakes.** Inset: Phenomenological intrinsic scintillation spectrum. Parameters used in this plots were chosen in accordance with [2]. As a function of increased pumping, the losses are reduced (as the system moves towards transparency), leading to the spectrum manifesting growing and narrowing etalon peaks associated with thin-film resonances.

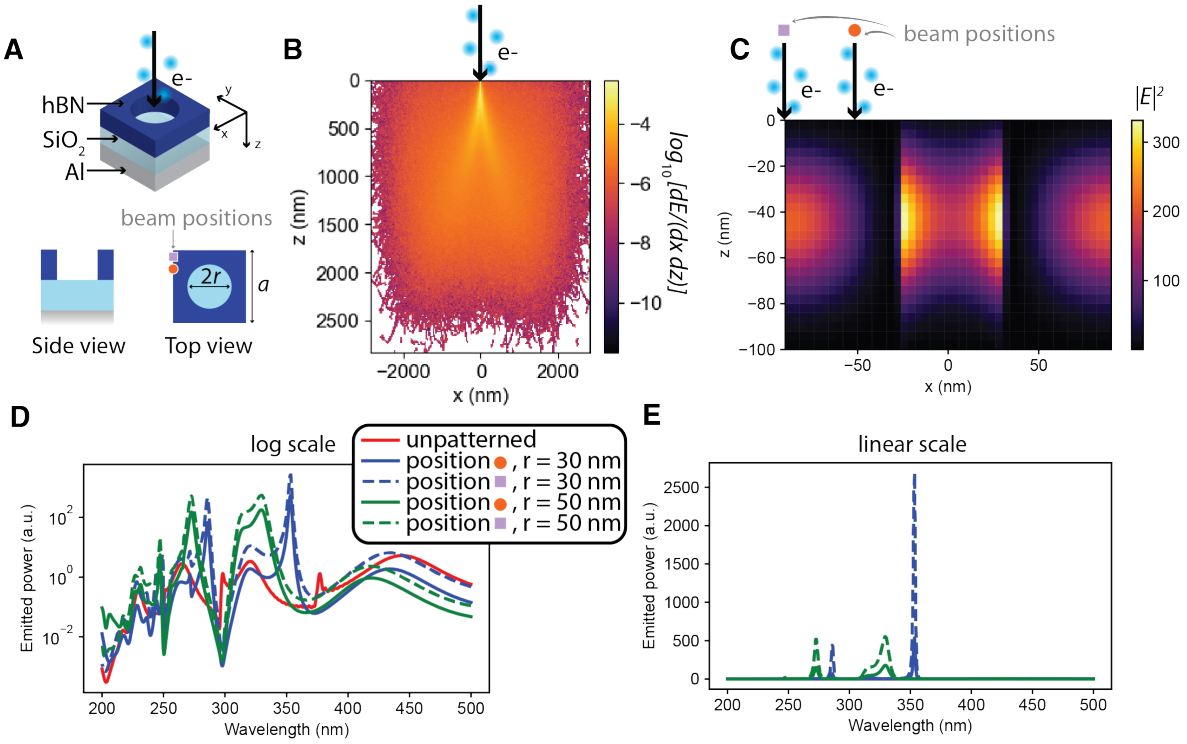

Figure D-5: **Tunable ultraviolet nanophotonic scintillators.** (**A**) Schematic of the design: etched hBN on a silica spacer on an aluminium substrate. (**B**) Marginal (integrated over y) energy loss probability distribution (log scale). (**C**) Total in-plane electric field distribution ($|E_x|^2 + |E_y|^2$) at $\lambda = 350$ nm). Our theory predicts the emitted scintillation power at various locations and etch radii, shown in log (**D**) and linear (**E**) scales.

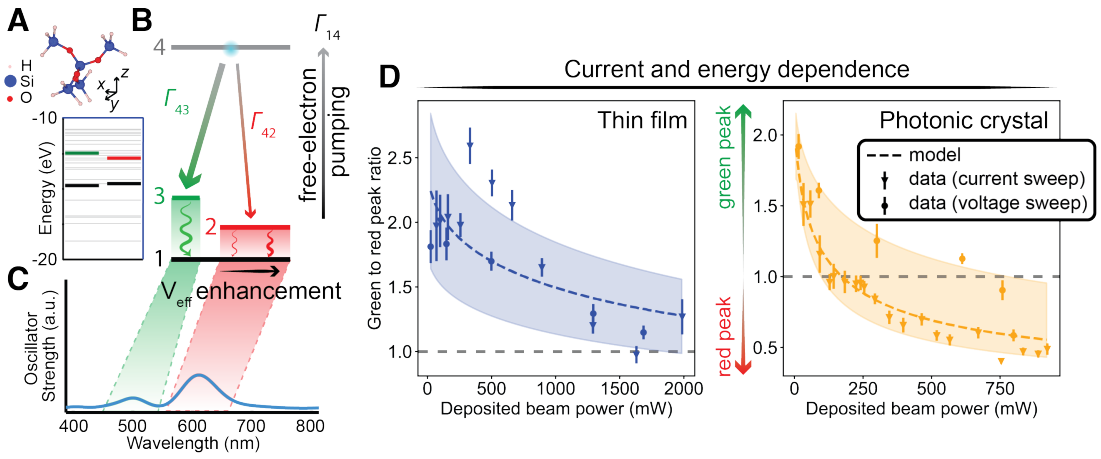

Figure D-6: **Alternative DFT and rate equation models for STH in silica.** (**A**) Top: 3D molecular model of STH defect in silica. Botton: Calculated STH defect energy levels via DFT. (**B**) Simplified four-level system modelling the microscopics of electron scintillation in silica. (**C**) Calculated oscillator strength spectrum. (**D**) TF (left) and PhC (right) scintillation peak ratios as a function of deposited beam powers through electron pumping. The dashed line corresponds to the mean model prediction and the shaded area to the prediction from the model parameters $\pm$ their standard deviation (TF: uncertainty on Γ_{34}/Γ_{24}; PhC: uncertainty on Γ_{12}/Γ_{13}.

Appendix E

Appendices for: Variational theory of nonrelativistic quantum electrodynamics

In this Supplement, we derive a self-consistent extension of the equations describing the ground state of a general quantum electrodynamical system with the effect of correlations included. We derive the equations in the case of a multi-electron system in three spatial dimensions interacting quantum electrodynamically with an arbitrary number of photonic modes. The resulting equations are similar in spirit to the equations of quantum electrodynamical density-functional theory [405, 406] in an optimized-effective potential scheme [414, 411], except that the orbitals used in that scheme are Kohn-Sham orbitals, while ours essentially are mean-field orbitals. We then derive the one-dimensional model used in the main text, as well as describe the parameters used in generating the data of Fig. 2 of the main text. Before doing this, we briefly describe the assumptions made in our framework, regarding our assumptions on gauge, as well as high-frequency free-space modes.

E.0.1 Assumptions behind the Hamiltonian of Equations (1-3)

In writing the Hamiltonian of the main text in the form of Equations (1-3), with the particular form of the field operators, we make a few assumptions. For one, that the interaction of matter with the quantized electromagnetic field is mediated solely by the vector potential.

Moreover, we are assuming that the effect of free-space modes, which an emitter weakly interacts with, is taken into account by renormalization of the electron mass and charge [538]. We focus only on the interaction of the emitter with low-energy cavity modes where strong interaction is possible. For these cavity modes, a natural cutoff emerges based on the transparency of the cavity.

E.0.2 Generalized Coulomb gauge condition of Equation (7) of the main text

In the main text, we arrive at the generalized Coulomb gauge for the modes. The generalized Coulomb gauge, $\nabla \cdot \epsilon(\mathbf{x})\mathbf{A}(\mathbf{x}) = 0$ for some dielectric permittivity $\epsilon(\mathbf{x})$, is the most common gauge for analyzing phenomena in the discipline of macroscopic QED, in which one seeks to analyze the interaction of charges with fields in dielectric media [100]. The reason a particular gauge was chosen was that in the Hamiltonian, we have already assumed that all interaction with the quantized modes is manifested only through the vector potential, and that there is no scalar potential contribution to the interaction: relaxing this assumption allows more general gauge freedom. We also remark that if we performed a frame transformation, for example to the length gauge, the energy would be the same as that of our ansatz in the velocity gauge, although the state would be markedly different, and would be a highly correlated state.

E.1 Self-consistent lamb shift correction to the equations for the quantum electrodynamical ground state

In the derivation of Equations (6) and (7) of the main text, it is notable that the term linear in the vector potential makes no contribution to the expectation value of the Hamiltonian in the ground state. In many quantum electrodynamical problems, this linear term is important. To first order, it leads to spontaneous emission of a single photon. To second order, it leads to Casimir-Polder forces on emitters, which arise from virtual emission and re-absorption of photons. At the same order, the term linear in the vector potential also leads to effective

interactions betweeen distinct emitters. Thus, we must capture the effect of this term. Physically, this term mixes the factorizable ground state of Equation (4) of the main text with states that have virtual excitations of the matter, as well as virtual excitations of the electromagnetic field. The resulting state is now non-factorizable and we thus conclude that the term in the Hamiltonian linear in the vector potential leads to *correlations* in the system, and contributes wholly at lowest order to the *correlation energy* of the quantum electrodynamical ground state.

We capture the effect of correlations perturbatively. In other words, we consider the second-order correction δE to the ground state energy arising from the term in the Hamiltonian linear in the vector potential. That correction is given by

$$\delta E = \frac{e^2\hbar^2}{8m^2\epsilon_0} \sum_{q=1}^{\infty} \sum_{n=N_\sigma+1}^{\infty} \sum_{m=1}^{N_\sigma} \frac{\left| \int d^3x \, \mathbf{F}_q^*(\mathbf{x}) \cdot \mathbf{j}_{nm}(\mathbf{x}) \right|^2}{\omega_q(\omega_{mn} - \lambda_q)}, \tag{E.1}$$

where $\mathbf{j}_{nm} = \psi_n^* \nabla \psi_m - (\nabla \psi_n^*)\psi_m$ are transition current densities, $\omega_{mn} = \omega_m - \omega_n$ are transition frequencies, N_σ is the number of occupied orbitals, the $\mathbf{F}_q$ are the photon mode functions, the ω_q are the photon mode frequencies, and the λ_q are Lagrange multipliers expressing the normalization of each photon mode. We note that the sum over photon modes q is in principle over all modes but can be restricted to either a finite or countably infinite set of photon modes deemed relevant to the system at hand. In a method without self-consistency, the electron and photon orbitals and eigenvalues are those obtained from Equations (6) and (7) of the main text. This non-self-consistent procedure was applied in Fig. 2 of the main text. In what follows, we add this energy correction δE to the expectation value of the energy in the ground state self-consistently, with the orbitals and eigenvalues as variational parameters. As a result, the orbitals and eigenvalues obtained will be different from Equations (6) and (7) of the main text, this difference being small in the case of weak correlations. Strictly speaking, this approach is only justified for weak correlations, but can be applied to systems with strong-correlations as is often done with self-consistent methods.

E.1.1 Physics contained in these equations

As the equations which result from self-consistence are complicated, it is useful to discuss what physics should contained by introducing δE to the Lagrange function to be minimized. From the standpoint of the electrons, the equation for the electron orbitals should differ from Equation (6) of the main text by a potential energy term which corresponds to the spatially dependent Lamb shift that the electrons feel. This Lamb shift is due to virtual emission and re-absorption of photons. We note in passing that the gradient of the Lamb shift with respect to position gives rise to a force called the Casimir-Polder force. It is known that this potential depends on all occupied and unoccupied electron orbitals and the photon orbitals, as well as their respective eigenvalues.

For the photon, the equation will differ from Equation (7) of the main text by the introduction of a term which has the appearance of a source term proportional to a sum over the transition current densities of the electronic system, $\mathbf{j}_{nm}$. These transition currents connect occupied and unoccupied electronic orbitals. The weight of these transition current densities will be proportional to the coupling between the current densities and the photonic modes. In other words, this new term expresses a coupling of the electromagnetic field to fluctuating currents associated with the matter part of the ground state of the QED system.

E.1.2 Equations for the ground state of quantum electrodynamics

Here, we derive the equations implied by the correction to the energy of Equation (1) and confirm the physical understanding presented in the previous two paragraphs.

The derivative of δE with respect to an occupied electron orbital k is given by

$$\frac{\partial \delta E}{\partial \psi_k^*} = \frac{e^2\hbar^2}{8m^2\epsilon_0} \sum_{n=N_\sigma+1}^{\infty} \sum_{q=1}^{\infty} \frac{\int d^3y\ \mathbf{F}_q^*(\mathbf{y}) \cdot \mathbf{j}_{nk}(\mathbf{y})}{\omega_q(\omega_{kn} - \lambda_q)} \int d^3x\ \left(\mathbf{F}_q(\mathbf{x}) \cdot \nabla\psi_n(\mathbf{x}) + \nabla \cdot (\mathbf{F}_q(\mathbf{x})\psi_n(\mathbf{x}))\right) \tag{E.2}$$

A similar equation arises for the derivative with respect to an unoccupied electron orbital, except that the summation should now be over unoccupied electron orbitals.

The derivative of δE with respect to a photonic orbital q is given by

$$\frac{\partial \delta E}{\partial \mathbf{F}_q^*} = \frac{e^2\hbar^2}{8m^2\epsilon_0} \sum_{n=N_\sigma+1}^{\infty} \sum_{m=1}^{N_\sigma} \frac{\int d^3y\, \mathbf{F}_q(\mathbf{y}) \cdot \mathbf{j}_{mn}(\mathbf{y})}{\omega_q(\omega_{mn} - \lambda_q)} \mathbf{j}_{nm}(\mathbf{x}). \tag{E.3}$$

The derivative of δE with respect to a photonic frequency ω_q is given by

$$\frac{\partial \delta E}{\partial \omega_q} = -\frac{e^2\hbar^2}{8m^2\epsilon_0} \sum_{n=N_\sigma+1}^{\infty} \sum_{m=1}^{N_\sigma} \frac{\left| \int d^3x\, \mathbf{F}_q(\mathbf{x}) \cdot \mathbf{j}_{mn}(\mathbf{x}) \right|^2}{\omega_q^2(\omega_{mn} - \lambda_q)} \tag{E.4}$$

Using these derivatives, Equation (6) of the main text is generalized to:

$$\begin{aligned}
&\left(\frac{\mathbf{p}^2}{2m} + v_{ext}(\mathbf{x})\right)\psi_i(\mathbf{x}) + \sum_{j=1}^{N} \int d^3x'\, V(\mathbf{x}-\mathbf{x}') \left(\psi_j^*(\mathbf{x}')\psi_j(\mathbf{x}')\psi_i(\mathbf{x}) - \psi_j^*(\mathbf{x}')\psi_j(\mathbf{x})\psi_i(\mathbf{x}')\right) \\
&+ \frac{\hbar e^2}{4m\epsilon_0} \sum_n \frac{1}{\omega_n} |\mathbf{F}_n(\mathbf{x})|^2 \psi_i(\mathbf{x}) + \\
&\frac{e^2\hbar^2}{8m^2\epsilon_0} \sum_{n=N_\sigma+1}^{\infty} \sum_{q=1}^{\infty} \frac{\int d^3y\, \mathbf{F}_q^*(\mathbf{y}) \cdot \mathbf{j}_{ni}(\mathbf{y})}{\omega_q(\omega_{in} - \lambda_q)} \left(\mathbf{F}_q(\mathbf{x}) \cdot \nabla\psi_n(\mathbf{x}) + \nabla \cdot (\mathbf{F}_q(\mathbf{x})\psi_n(\mathbf{x}))\right) = E_i\psi_i(\mathbf{x}).
\end{aligned} \tag{E.5}$$

Setting the derivative with respect to photonic modes zero gives the equation:

$$\begin{aligned}
&\frac{\hbar}{4}\left(\omega_q \mathbf{F}_q(\mathbf{x}) + \frac{c^2}{\omega_q}\nabla \times \nabla \times \mathbf{F}_q(\mathbf{x})\right) + \frac{\hbar \sum_{m=1}^{N_\sigma} |\psi_m(\mathbf{x})|^2}{4m\epsilon_0\omega_q} \\
&+ \frac{e^2\hbar^2}{8m^2\epsilon_0} \sum_{n=N_\sigma+1}^{\infty} \sum_{m=1}^{N_\sigma} \frac{\int d^3y\, \mathbf{F}_q(\mathbf{y}) \cdot \mathbf{j}_{mn}(\mathbf{y})}{\omega_q(\omega_{mn} - \lambda_q)} \mathbf{j}_{nm}(\mathbf{x}) = \frac{\hbar\lambda_q}{2}\mathbf{F}_q(\mathbf{x})
\end{aligned} \tag{E.6}$$

And setting the derivative with respect to the photonic frequencies to zero gives the equation:

$$\begin{aligned}
&\frac{\hbar}{4}\left(\int d^3x\, |\mathbf{F}_q(\mathbf{x})|^2 - \frac{c^2}{\omega_q^2}\mathbf{F}_q^*(\mathbf{x}) \cdot \nabla \times \nabla \times \mathbf{F}_q(\mathbf{x})\right) - \frac{e^2\hbar}{4m\epsilon_0\omega_q^2} \int d^3x \sum_{m=1}^{N_\sigma} |\psi_m(\mathbf{x})|^2 \\
&- \frac{e^2\hbar^2}{8m^2\epsilon_0} \sum_{n=N_\sigma+1}^{\infty} \sum_{m=1}^{N_\sigma} \frac{\left| \int d^3x\, \mathbf{F}_q(\mathbf{x}) \cdot \mathbf{j}_{mn}(\mathbf{x}) \right|^2}{\omega_q^2(\omega_{mn} - \lambda_q)} = 0
\end{aligned} \tag{E.7}$$

Performing the operation $\frac{1}{\omega_q} \int d^3x \mathbf{F}_q^*(\mathbf{x}) \cdot$ on Equation (6), and adding the result to Equa-

tion (7), gives the result $\lambda_q = \omega_q$, just as before δE was introduced. Using this key simplification, along with the definition of the spatially-dependent plasma frequency as $\omega_p^2(\mathbf{x}) = \frac{e^2}{m\epsilon_0} \sum_{m=1}^{N_\sigma} |\psi_m(\mathbf{x})|^2$, we have that Equation (7) of the main text is generalized to:

$$\left(\nabla \times \nabla \times - \left(1 - \frac{\omega_p^2(\mathbf{x})}{\omega_q^2}\right)\right) \mathbf{F}_q(\mathbf{x}) = -\frac{e^2\hbar}{2m^2\epsilon_0 c^2} \sum_{n=N_\sigma+1}^{\infty} \sum_{m=1}^{N_\sigma} \frac{\int d^3y\, \mathbf{F}_q(\mathbf{y}) \cdot \mathbf{j}_{mn}(\mathbf{y})}{\omega_{mn} - \omega_q} \mathbf{j}_{nm}(\mathbf{x}). \tag{E.8}$$

Equations (5) and (8) represent main results of this work and provide a general starting point for first-principles analysis of ground states of QED systems in the non-perturbative regime.

E.2 Derivation of results for one-dimensional cavity model in the main text

In this section, we provide some additional details on the one-dimensional cavity QED model considered in the main text. Given the Hamiltonian of Equation (9) in the main text describing the coupling of an emitter to a one-dimensional cavity, with the matter being described by the site model of Equations (10) and (11) of the main text, the expectation value of the Hamiltonian according to the ansatz of Equation (4) in the main text is given by

$$\begin{aligned}\langle\Psi|H|\Psi\rangle = \langle\tilde{g}|H_{\text{matter}}|\tilde{g}\rangle + \frac{\hbar}{4}\int dz \sum_{n=1}^{\infty}\left(\omega_n|F_n|^2 - \frac{c^2}{\omega_n}F_n^*\partial_z^2 F_n\right) \\ + \frac{\hbar q^2}{4m\epsilon_0\omega_n}\sum_{n=1}^{\infty}\int dz\, \delta(z-d)|F_n|^2\end{aligned} \tag{E.9}$$

In this equation, $|\tilde{g}\rangle$ is the ground state of the effective matter part of the Hamiltonian, and H_{matter} is the Hamiltonian of Equation (10) of the main text. We impose constraints of matter normalization and photon mode normalization by defining a Lagrange function

$$\mathcal{L}(|\tilde{g}\rangle, \langle\tilde{g}|, \epsilon, \{F_n, F_n^*, \omega_n, \lambda_n\}) \equiv \langle\Psi|H|\Psi\rangle - \epsilon(\langle\tilde{g}|\tilde{g}\rangle - 1) - \sum_{n=1}^{\infty}\frac{\hbar\lambda_n}{2}\left(\int dz\, |F_n|^2 - 1\right). \tag{E.10}$$

To find the ground state, we minimize the Lagrange function with respect to the matter orbital $|\tilde{g}\rangle$ and with respect to the mode functions F_n. The minimization with respect to the matter leads to the trivial equation $H_{\text{matter}}|\tilde{g}\rangle = \epsilon|\tilde{g}\rangle$ which leaves the effective matter ground state as simply the ground state of H_{matter}. On the other hand, the minimization with respect to the photon mode functions leads to the equation

$$\left(\partial_z^2 - \frac{\omega_n^2}{c^2} + 2\frac{\omega_n \lambda_n}{c^2} - \frac{q^2}{m\epsilon_0 c^2}\delta(z-d)\right) F_n = 0. \tag{E.11}$$

We may constrain the λ_n by differentiating the Lagrange function with respect to the ω_n. The equation which follows is:

$$\int dz \, \left(|F_n|^2 + \frac{c^2}{\omega_n^2} F_n^* \partial_z^2 F_n\right) - \frac{q^2}{m\epsilon_0 \omega_n^2} \int dz \, \delta(z-d)|F_n|^2 = 0 \tag{E.12}$$

Performing $\frac{\omega_n^2}{c^2} \int dz \, F_n^*$ on both sides of Equation (11), and adding this equation to Equation (12), one immediately finds that $\lambda_n = \omega_n$ and that

$$\left(\partial_z^2 + \frac{\omega_n^2}{c^2} - \frac{q^2}{m\epsilon_0 c^2}\delta(z-d)\right) F_n = 0. \tag{E.13}$$

This is an ordinary second-order differential equation with the conditions that F_n is continuous at d and that its derivative is discontinuous according to

$$\partial_z F_n\Big|_{z=d^+} - \partial_z F_n\Big|_{z=d^-} = \frac{q^2}{m\epsilon_0 c^2} F_n(d), \tag{E.14}$$

in addition to the usual condition of the modes vanishing at the cavity walls $z = 0$ and $z = L$. It can be shown that the solution to Equation (13) satisfying such boundary conditions

is:

$$\theta(z-d)\left(\frac{\sin\left(\frac{\omega_n L}{c}\right)\sin\left(\frac{\omega_n d}{c}\right)\cos\left(\frac{\omega_n z}{c}\right)}{\sin\left(\frac{\omega_n (L-d)}{c}\right)}-\right)$$
$$-\theta(z-d)\left(\frac{\cos\left(\frac{\omega_n L}{c}\right)\sin\left(\frac{\omega_n d}{c}\right)\sin\left(\frac{\omega_n z}{c}\right)}{\sin\left(\frac{\omega_n (L-d)}{c}\right)}\right)$$
$$+\theta(d-z)\sin\left(\frac{\omega_n z}{c}\right) \tag{E.15}$$

provided that the auxiliary condition

$$\cot\left(\frac{\omega_n}{c}d\right)+\cot\left(\frac{\omega_n}{c}(L-d)\right)=-\frac{q^2}{m\epsilon_0\omega_n c} \tag{E.16}$$

is met. To ensure that the modes are normalized according to the constraint, we have that the solutions of Equation (15) must be multiplied by a normalization factor N_n given by

$$N_n = 2\sqrt{\frac{1}{\frac{c}{\omega_n}\left(\frac{\omega_n L}{c}-\sin\left(\frac{\omega_n L}{c}\right)\right)\left(1+\frac{\sin^2\left(\frac{\omega_n d}{c}\right)}{\sin^2\left(\frac{\omega_n (L-d)}{c}\right)}\right)}}. \tag{E.17}$$

The condition of Equation E.16 determines the resonance frequencies of the photon quasiparticle modes.

Perturbation theory for the one-dimensional cavity model

As discussed in the main text, the variational energies, as well as the energies from numerical diagonalization, are compared against the energies calculated from perturbation theory. We provide additional details on the perturbative calculations here. What we calculate is the energy shift of a state $|a,0\rangle$, where a is any matter state, and 0 denotes the photonic vacuum, according to the perturbation Hamiltonian $\frac{q}{m}Ap+\frac{q^2}{2m}A^2$, where p is the momentum operator for the matter defined in the main text, and A is the vector potential operator of the one-dimensional cavity in the absence of the matter. In particular, $A(z)=\sum_n\sqrt{\frac{\hbar}{\epsilon_0\omega_n L}}\sin\left(\frac{n\pi z}{L}\right)\left(a_n+a_n^\dagger\right)$, with L the length of the cavity and $\omega_n=\frac{n\pi c}{L}$. Upon inspection, it is clear that the A^2 term leads to an energy shift at first-order in perturbation theory, while the $A\cdot p$ term leads to an energy shift at second-order in perturbation

theory. A straightforward application of perturbation theory leads to the following first-order energy shift from the A^2 term:

$$\delta E_a = \frac{q^2}{2m} \sum_{n=1}^{N_p} \frac{\hbar}{\epsilon_0 \omega_n L} \sin^2\left(\frac{n\pi z}{L}\right), \tag{E.18}$$

where z is the location of the matter in the cavity, and N_p is the maximum photon number retained. Note that this value is dependent on the maximum photon number (although somewhat weakly) retained due to the logarithmically diverging nature of the sum, and so to compare variational, numerical, and perturbative calculations, the same number of modes are retained in each. A similarly straightforward application of perturbation theory leads to the energy shift coming from the $A \cdot p$ term being given by:

$$\delta E_a = \frac{q^2}{m^2} \sum_{b \neq a} \sum_{n=1}^{N_p} \frac{\hbar}{\epsilon_0 \omega_n L} \frac{|p_{ba}|^2 \sin^2\left(\frac{n\pi z}{L}\right)}{\hbar(\omega_a - \omega_b - \omega_n)}, \tag{E.19}$$

where b denotes a matter state different from a, and $p_{ba} = \langle b|p|a\rangle$.

In the main text, we also considered expectation values such as $\langle A \cdot p\rangle$ in the ground state within perturbation theory. Calculating the shift of the ground-state wavefunction at first-order in perturbation theory, we immediately find that

$$\langle Ap\rangle = \frac{2q}{m} \mathrm{Re} \sum_{b \neq a} \sum_{n=1}^{N_p} \frac{1}{2\epsilon_0 L} \frac{|p_{ba}|^2 \sin^2\left(\frac{n\pi z}{L}\right)}{\omega_n(\omega_a - \omega_b - \omega_n)}. \tag{E.20}$$

It is also of interest to consider "field-only" observables such as the number of (virtual) photons in the ground state. Calculating the wavefunction of the ground state at first-order in perturbation theory, and calculating the probability of a photon being in the ground state, one finds that

$$\langle N\rangle = \sum_{n=1}^{N_p} \langle a^\dagger_{n,\text{bare}} a_{n,\text{bare}}\rangle = \frac{q^2}{m^2} \sum_{b \neq a} \sum_{n=1}^{N_p} \frac{1}{2\hbar\epsilon_0 L} \frac{|p_{ba}|^2 \sin^2\left(\frac{n\pi z}{L}\right)}{\omega_n(\omega_a - \omega_b - \omega_n)^2}, \tag{E.21}$$

where the "b" or "bare" subscript in the creation and annihilation operators denotes that these are creation and annihilation operators for photon modes in the cavity in the absence

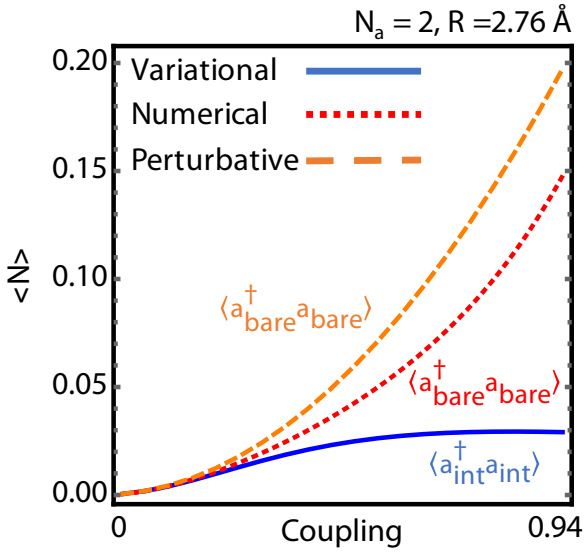

Figure E-1: **Number of virtual photons (bare and interacting) in the ground state calculated variationally, numerically, and through perturbation theory.** Parameters are the same as in Fig. 2 (top panel) of the main text.

of interactions (e.g., the sine modes for the 1D cavity considered here). In Fig. S1, we compare the expectation value of the number of "bare" photons calculated perturbatively, and with exact diagonalization with the variationally calculated number of "interacting" photons, $\sum_{n=1}^{N_p} \langle a^\dagger_{n,\mathrm{int}} a_{n,\mathrm{int}} \rangle$ (e.g., the modes shown in Fig. 2b of the main text). The number of photons in the bare basis differs substantially from the number of photons in the interacting basis.

This behavior does not reflect any inconsistency with the variational method, but is instead a feature which is to be expected. In particular, the physics of the ansatz of Eq. 4 of the main text is that a complicated ground state which has many virtual photons (see numerical diagonalization result) in it should be physically equivalent to a ground state with nearly no virtual photons (see variational result), but with different modes and frequencies. In other words, the reason the number of virtual photons differs is simply because they are being counted in the basis of "interacting modes" shown in Fig. 2b of the main text. That said, our variational theory does not give a prescription to translate the interacting mode operators to the bare mode operators.

We note that in all cases, when calculating these quantities in the variational theory, these expressions are still relevant, with the replacement of the bare photon frequencies

and mode functions replaced by the ones that result from Eq. 7 of the main text.

E.2.1 Model parameters for Figure 2 and details of numerical diagonalization

Here, we note the parameters used in Fig. 2, as well as some details regarding the numerical diagonalization used to assess the validity of the variational approach advanced in the main text.

1. The hopping matrix elements t were taken to be 0.25 eV for the two-, three-, and four-level systems. Meanwhile, the on-site energies were taken to be equal on all sites in the two-, three-, and four-level systems.

2. The cavity length was taken to be 1 micron.

3. The area of the cavity in the transverse direction was taken to be 100 nm^2.

4. The maximum number of cavity modes retained in the calculations was 100. Our results were converged with respect to the number of cavity modes.

5. In the numerical diagonalization results (red lines of Fig. 2 of the main text), the Fock space was truncated such that the number of photons retained was no more than four. For the largest couplings plotted in Fig. 2, this was sufficient. But for higher couplings, more photons in the numerical diagonalization are needed. For four photons and 100 cavity modes coupled to a four-level system, the dimension of the Hilbert space is $4 \times (1 + 100 + 5050 + 171,700 + 4,421,275) = 18,392,504$. The four terms in the parentheses correspond to the dimension of the properly symmetrized zero-, one-, two-, three-, and four-photon Hilbert spaces respectively. Also see Ref. [399] for more details on the exact numerical diagonalization methods for light-matter coupled problems.

6. The largest couplings plotted in Fig. 2 correspond to either a single emitter with a charge of $200e$, or an ensemble of emitters (as is the case in many ultra-strong coupling experiments) in which there are 40,000 emitters in the cavity. The largest

couplings correspond to rather extreme coupling parameters and are shown mostly to demonstrate that our ansatz is quite accurate even in regimes of extremely high coupling.

Regarding the numerical diagonalization, we numerically implement the Hamiltonian of Eq. (9) of the main text by building the matter operators (H_0 and p as defined in the main text) in the basis of states corresponding to the tensor product of any matter state, and any photon state having four photons or less . Details regarding the ordering convention for the properly symmetrized multi-photon states are provided in Ref. [399] for example. Photon operators (a, $a^\dagger$) are constructed in this basis, and used to construct field operators such as A in the basis of bare cavity modes (the usual sine modes). In particular, $A(z) = \sum_n \sqrt{\frac{\hbar}{\epsilon_0 \omega_n L}} \sin\left(\frac{n\pi z}{L}\right)\left(a_n + a_n^\dagger\right)$, with L the length of the cavity and $\omega_n = \frac{n\pi c}{L}$. Diagonalization is performed using standard sparse eigendecomposition routines (such as those implemented in MATLAB).

Appendix F

Appendices for: Nonperturbative quantum nonlinearities and Fock-state lasers based on deep-strong coupling of light and matter

In this Supplement, we derive and extend the results of the main text. Consider a system involving matter coupled to a cavity mode very strongly, so that the system is in the ultra- or deep-strong coupling regime. This system is described by the Rabi Hamiltonian of Eq. (1) of the main text (Hamiltonian and variables re-defined here for self-containedness):

$$H_{\text{Rabi}}/\hbar = \frac{1}{2}\left(\omega_0\sigma_z + \lambda\sigma_x\right) + \omega a^\dagger a + \tilde{g}\sigma_x(a + a^\dagger), \tag{F.1}$$

Here, ω_0 is the transition frequency of the two-level system, $\sigma_{x,z}$ are the x and z Pauli matrices, ω is the cavity frequency, $a^{(\dagger)}$ is the cavity annhilation (creation) operator, and $\tilde{g}$ is the Rabi frequency. We also non-dimensionalize the coupling as $g = \tilde{g}/\omega$.

Let us now transfer energy into this system by means of external emitters, treated as two-level systems of energy ω_0. Let us assume the emitter is primarily interacting with the cavity (as it is too far for direct interactions with the dipole of the matter). Let us then take

the full Hamiltonian describing the coupling of one emitter to the light-matter system as

$$H/\hbar = \frac{\omega_0^{\text{em}}}{2}\sigma_z^{\text{em}} + H_{\text{Rabi}} + \epsilon\sigma_{x,\text{em}}(b + b^\dagger), \tag{F.2}$$

which couples the emitter directly to the DSC photon. We can also consider interactions solely between the emitter and the resonator field, replacing $b \to a$. We consider this case as well, to show that the exact nature of the emitter-qubit dipole-dipole coupling does not qualitatively change our conclusions.

If the emitter is in the excited eigenstate $|e\rangle$, and it is resonant with a transition of the Rabi Hamiltonian, the emitter can transfer energy to the light-matter system. Upon interaction with a second emitter, if the next transition of the Rabi model has nearly the same frequency, the system can get further excited. A key observation is that in the deep-strong coupling regime $g \gg \omega$, the eigenstates are approximately equally spaced, and the excitations are oscillator-like, quite similarly to the zero-coupling case. This should allow the possibility of reaching a very high excitation number in the presence of many emitters, based on stimulated emission of these oscillator modes (we will call them DSC photons). When the coupling is not infinite, as in a realistic case, the levels are no-longer fully equally spaced. This detuning is photon-number dependent, thus acting as a nonlinearity which may qualitatively change the steady-state of this type of laser.

To begin, we need to derive simple forms for the eigenstates of the Rabi Hamiltonian in the deep-strong coupling limit. Then, we will consider their coupling to external emitters, and write a coarse-gained equation of motion for the density matrix of the DSC bosons, and then solve it.

F.0.1 Eigenstates of the Rabi Hamiltonian

In what follows, we will take $\omega_0 = \omega$ (resonant) and $\lambda = 0$. In later subsections, we will analytically and numerically consider the case of a finite λ, which is found to preserve our main findings.

In the deep-strong coupling regime, we can treat the matter term in the Rabi Hamiltonian as a perturbation to the remainder of the Hamiltonian. The remainder of the Hamilto-

nian (divided by $\hbar$), which we call H_{DSC} is

$$H_{\text{DSC}} = \omega a^\dagger a + \tilde{g}\sigma_x(a + a^\dagger) = \omega(a^\dagger + g\sigma_x)(a + g\sigma_x) - \omega g^2, \tag{F.3}$$

where $g \equiv \tilde{g}/\omega$ is a dimensionless measure of the coupling strength. Introducing the displacement operator $D(g\sigma_x) = \exp\left[g\sigma_x(a^\dagger - a)\right]$, where we've taken g real without loss of generality, we have

$$H_{\text{DSC}} = \omega D^\dagger(g\sigma_x)a^\dagger a D(g\sigma_x), \tag{F.4}$$

where we've omitted the overall constant $-\omega g^2$. From here, we can easily see that the eigenstates of this Hamiltonian are of the form $D^\dagger(\pm g)\left|\pm x, n\right\rangle$, where $\left|x\right\rangle$ denotes the x-spin basis, and n is a Fock state. In other words, the eigenstates involve the spin being *x*-polarized (rather than *z*-polarization), and the photon being in a *displaced* Fock state (rather than just a Fock state). Clearly,

$$H_{\text{DSC}}D^\dagger(\pm g)\left|\pm x, n\right\rangle = \omega D^\dagger(\pm g)a^\dagger a D(\pm g)D^\dagger(\pm g)\left|\pm x, n\right\rangle = n\omega D^\dagger(\pm g)\left|\pm x, n\right\rangle. \tag{F.5}$$

Clearly then, in this limit, the eigenstates are evenly spaced, and doubly degenerate. In fact, it can be seen as a system of two non-interacting bosons ("DSC photons"). Introducing $b_\sigma = a + g\sigma_x$ we can write the Hamiltonian as

$$H_{\text{DSC}} = \omega b^\dagger b. \tag{F.6}$$

It can also be easily seen that $[b, b^\dagger] = 1$.

The degeneracy of the DSC Hamiltonian is split by the matter Hamiltonian. We can find the resulting eigenstates and eigenenergies using degenerate first-order perturbation theory. The "good" eigenbasis of the problem is

$$\left|n, \sigma\right\rangle = \frac{1}{\sqrt{2}}\left(D^\dagger\left|+x, n\right\rangle + \sigma D\left|-x, n\right\rangle\right), \tag{F.7}$$

where $\sigma = \pm 1$, and a displacement operator without an argument implies that the argument is g. The energies of the resulting states are

$$\begin{aligned} E_{n\sigma} &= \frac{\omega}{2} \langle n, \sigma | \, \sigma_z \, | n, \sigma \rangle \\ &= \frac{\omega}{4} \left(\langle +x, n | \, D + \sigma \, \langle -x, n | \, D^\dagger \right) \sigma_z \left(D^\dagger \, | +x, n \rangle + \sigma D \, | -x, n \rangle \right) \\ &= \sigma \frac{\omega}{4} \left(\langle n | \, D^2 \, | n \rangle + \langle n | \, D^{\dagger 2} \, | n \rangle \right) \\ &= \sigma \frac{\omega}{2} \langle n | \, D^2 \, | n \rangle \equiv \sigma \frac{\omega}{2} D_n, \end{aligned} \tag{F.8}$$

where $D_n = \langle n | \, D^2(g) \, | n \rangle = \langle n | \, D(2g) \, | n \rangle$. These eigenstates and energies are sufficiently accurate, even for $g = 2$ or $g = 3$.

Evaluation of D_n.

Let us evaluate the D_n. To do so, we write:

$$\begin{aligned} D_n(2z) &= \langle n | \, DD \, | n \rangle = \frac{1}{n!} \langle 0 | \, a^n DDa^{\dagger n} \, | 0 \rangle = \frac{1}{n!} \langle 0 | \, D(D^\dagger a^n D)(Da^{\dagger n} D^\dagger) D \, | 0 \rangle \\ &= \frac{1}{n!} \langle -z | \, (a+z)^n (a^\dagger - z^*)^n \, | z \rangle \, . \end{aligned} \tag{F.9}$$

To proceed, insert a "complete" set of states using the over-completeness of the coherent states. That leaves us with

$$\begin{aligned} D_n(2z) &= \frac{1}{\pi n!} \int d^2\alpha \, \langle -z | \, (a+z)^n \, | \alpha \rangle \, \langle \alpha | \, (a^\dagger - z^*)^n \, | z \rangle \\ &= \frac{1}{\pi n!} \int d^2\alpha (\alpha + z)^n (\alpha^* - z^*)^n \langle \alpha | z \rangle \langle -z | \alpha \rangle. \end{aligned} \tag{F.10}$$

Using the rule for the overlap of two coherent states, we have

$$D_n(2z) = \frac{1}{\pi n!} \int d\alpha d\alpha^* (\alpha + z)^n (\alpha^* - z^*)^n e^{-\alpha\alpha^* - zz^* + \alpha^* z - z^* \alpha}, \tag{F.11}$$

where we have written things this way to emphasize that α and α^* are independent variables. We can now write this as

$$D_n(2z) = \frac{e^{zz^*}}{\pi n!}\int d\alpha d\alpha^*(\alpha+z)^n(\alpha^*-z^*)^n e^{-\alpha\alpha^*+z(\alpha^*-z^*)-z^*(\alpha+z)}. \tag{F.12}$$

Then, we transform variables as $\alpha \to \alpha - z$ and $\alpha^* \to \alpha^* + z^*$ to get

$$D_n(2z) = \frac{e^{zz^*}}{\pi n!}\int d\alpha d\alpha^*\ \alpha^n\alpha^{*n}e^{-(\alpha-z)(\alpha^*+z^*)+z\alpha^*-z^*\alpha} = \frac{e^{2zz^*}}{\pi n!}\int d\alpha d\alpha^*\ \alpha^n\alpha^{*n}e^{-\alpha\alpha^*+2z\alpha^*-2z^*\alpha}. \tag{F.13}$$

This can be generated from simpler integrals by differentiation, as:

$$D_n(2z) = (-1)^n\frac{e^{2zz^*}}{\pi n!}\frac{\partial^{2n}}{\partial^n(2z)\partial^n(2z^*)}\int d\alpha d\alpha^*\ e^{-\alpha\alpha^*+2z\alpha^*-2z^*\alpha}. \tag{F.14}$$

Completing the square in the remaining integral gives

$$\begin{aligned} D_n(2z) &= (-1)^n\frac{e^{2zz^*}}{\pi n!}\frac{\partial^{2n}}{\partial^n(2z)\partial^n(2z^*)}e^{-4zz^*}\int d\alpha d\alpha^*\ e^{-\alpha\alpha^*+2z\alpha^*-2z^*\alpha+4zz^*} \\ &= (-1)^n\frac{e^{2zz^*}}{\pi n!}\frac{\partial^{2n}}{\partial^n(2z)\partial^n(2z^*)}e^{-4zz^*}\int d\alpha d\alpha^*\ e^{-(\alpha-2z)(\alpha^*+2z^*)}. \end{aligned} \tag{F.15}$$

Shifting variables as $\alpha \to \alpha + 2z$ and $\alpha \to \alpha - 2z^*$, and performing the final Gaussian integral, we have

$$D_n = (-1)^n\frac{e^{2zz^*}}{n!}\frac{\partial^{2n}}{\partial(2z)^n\partial(2z^*)^n}e^{-4zz^*}. \tag{F.16}$$

These are related to Laguerre polynomials. To see this, take the derivative with respect to z^*. We will also use the notation $z \to x/2$ and $z^* \to y/2$ for clarity.

$$\begin{aligned} D_n(2z) &= (-1)^n\frac{e^{xy/2}}{n!}\frac{\partial^{2n}}{\partial x^n\partial y^n}e^{-xy} = \frac{e^{xy/2}}{n!}\frac{\partial^n}{\partial(xy)^n}(xy)^n e^{-(xy)} \\ &= e^{-xy/2}\left(\frac{e^{xy}}{n!}\frac{\partial^n}{\partial(xy)^n}(xy)^n e^{-(xy)}\right). \end{aligned} \tag{F.17}$$

From the Rodrigues formula for the Laguerre polynomials, we then have

$$D_n(2z) = e^{-2|z|^2}L_n(4|z|^2). \tag{F.18}$$

Given that the $z = g$, we have then that the the level splitting is given by

$$E_{n\sigma} = n\omega + \sigma\frac{\omega}{2}e^{-2|g|^2}L_n(4|g|^2) \tag{F.19}$$

F.0.2 Time-evolution of the coupled system

With the approximate eigenstates of the Rabi Hamiltonian, we now want to understand the full dynamics of H. We will take advantage of the fact that for a laser, ϵ is small, and in particular, $\epsilon \ll \omega$, so that the rotating-wave approximation is valid. In this system, the rotating wave approximation consists of only considering the dynamics within degenerate subspaces of the unperturbed Hamiltonian

$$H_0 = \frac{\omega_0}{2}\sigma_{z,\text{em}} + H_{\text{Rabi}}. \tag{F.20}$$

The eigenstates of the problem are $|k\rangle\,|n\sigma\rangle$, where now $k = 0, 1$ denotes emitter states (ground is zero, excited is one). The energies of such states are (up to a shift)

$$E_{kn\sigma} = (n + k(1+\delta))\omega + \sigma\frac{\omega}{2}D_n. \tag{F.21}$$

where we have taken $\omega_0 = (1+\delta)\omega$. From here on out, let us assume $\delta \ll \omega$. In that case, it is easy to see that the following four states form our nearly degenerate subspace:

$$\{|1, n-1, +\rangle\,, |0, n, +\rangle\,, |1, n-1, -\rangle\,, |0, n, -\rangle\}. \tag{F.22}$$

We now need to understand the action of the interaction Hamiltonian $V \equiv \epsilon\sigma_{x,\text{em}}(b + b^\dagger)$ on this subspace. First of all,

$$\langle k'n'\sigma'|\,V\,|kn\sigma\rangle = 0 \text{ if } k = k'. \tag{F.23}$$

For $k = -k'$, we have

$$\langle -kn'\sigma'|\,V\,|kn\sigma\rangle = \epsilon\frac{1+\sigma\sigma'}{2}(\sqrt{n}\delta_{n',n-1} + \sqrt{n+1}\delta_{n',n+1}). \tag{F.24}$$

From these matrix elements, we see that: if the pseudo-spin (σ) is conserved, then a non-zero matrix element occurs only when the boson number changes by 1. Noting that $b = a + g\sigma_x$, we can also readily describe interactions using a as $\langle n'\sigma'|a + a^\dagger|n\sigma\rangle = \sqrt{n}\delta_{n',n-1} + \sqrt{n+1}\delta_{n',n+1} - 2g\frac{1-\sigma\sigma'}{2}\delta_{nn'}$, such that: when the pseudo-spin changes, non-zero matrix elements occur only when the boson number is conserved. When the spin is conserved, the matrix elements are the same as for $b + b^\dagger$. Since only states with different photon number differ appreciably in frequency (and in particular, will be resonant with the emitter we introduce), the interactions are effectively the same whether we describe a or b. This is also to say that any modification in the coefficient of the dipole-dipole interaction between emitter and qubit will lead to the same result insofar as DSC photon dynamics are concerned. In Fig. 1, we show the matrix elements of a and b between adjacent states of the same spin, as well as $a^\dagger a$ and $b^\dagger b$. For $n < n_c \sim g^2$, they behave as one might expect for an oscillator.

We should note that beyond n_c, these states and matrix elements that we calculate based on degenerate perturbation theory are expected to change significantly. However, the approximate result turns out to describe the system well because the probabilities to find photon numbers beyond n_c are strongly suppressed in the Fock laser, rendering the description relatively insensitive to these details.

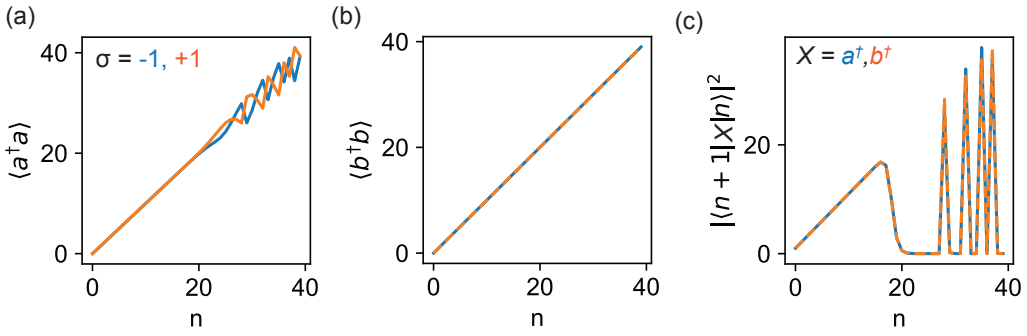

Figure F-1: Matrix elements of $a^\dagger a$, $b^\dagger b$ and a, b, showing that b counts excitations of the DSC system over the full range of eigenstates. However, up to n_c, a and b act similarly.

Based on these considerations, we see that the Hamiltonian in the degenerate subspace

may be written as:

$$\begin{aligned} H = &(\delta\omega + \frac{\omega}{2}D_{n-1})\,|1,n-1,+\rangle\,\langle 1,n-1,+| + (\frac{\omega}{2}D_n)\,|0,n,+\rangle\,\langle 1,n,+| \\ &+ \epsilon\sqrt{n}\,|1,n-1,+\rangle\,\langle 0,n,+| + \text{h.c} \\ &+ (\delta\omega - \frac{\omega}{2}D_{n-1})\,|1,n-1,-\rangle\,\langle 1,n-1,-| + (-\frac{\omega}{2}D_n)\,|0,n,-\rangle\,\langle 0,n,-| \\ &+ \epsilon\sqrt{n}\,|1,n-1,-\rangle\,\langle 0,n,-| + \text{h.c.} \end{aligned} \tag{F.25}$$

As we can see here, there are two independent blocks of the Hamiltonian (for each pseudo-spin) and we can thus study them separately. Let us assume that we're at zero temperature, and so the ground state has the $-$ pseudo-spin, which we assume to be conserved for all times. In that case, we can work with the simple 2x2 Hamiltonian

$$H_{\text{eff}} = \omega(\delta - \frac{1}{2}D_{n-1})\,|1,n-1\rangle\,\langle 1,n-1| - \frac{1}{2}\omega D_n\,|0,n\rangle\,\langle 0,n| + \epsilon\sqrt{n}\,|1,n-1\rangle\,\langle 0,n| + \text{h.c}, \tag{F.26}$$

where the pseudo-spin label has been dropped. This can be written in terms of Pauli matrices as

$$H_n = \frac{\omega}{2}(\delta - \frac{1}{2}(D_{n-1} + D_n))I + \frac{\omega}{2}(\delta - \frac{1}{2}(D_{n-1} - D_n))\sigma_z + \epsilon\sqrt{n}\sigma_x. \tag{F.27}$$

Introducing $E_n = \frac{\omega}{2}(\delta - \frac{1}{2}(D_{n-1} + D_n))$, $\Delta_n = \frac{\omega}{2}(\delta - \frac{1}{2}(D_{n-1} - D_n))$, we have very simply

$$H_n = E_n I + \Delta_n\sigma_z + \epsilon\sqrt{n}\sigma_x. \tag{F.28}$$

As we will see in the next section, we need to know how states of the form $|1,n-1\rangle$ evolve over time. Thus we need

$$e^{-it(\Delta_n\sigma_z + \epsilon\sqrt{n}\sigma_x)} \equiv e^{-i|U_n|t(\hat{U}_n\cdot\sigma)}, \tag{F.29}$$

with $\hat{U}_n = \frac{(\Delta_n, 0, \epsilon\sqrt{n})}{\sqrt{\Delta_n^2 + n\epsilon^2}}$ and $|U_n| = \sqrt{\Delta_n^2 + n\epsilon^2}$. Since $\hat{U}\cdot\sigma = 1$, we have

$$e^{-i|U_n|t(\hat{U}_n\cdot\sigma)} = \cos(|U_n|t) - i(\hat{U}_n\cdot\sigma)\sin(|U_n|t). \tag{F.30}$$

Therefore

$$e^{-iHt/\hbar}\,|1,n-1\rangle = (\cos(|U_n|t) - i\hat{U}_{nz}\sin(|U_n|t))\,|1,n-1\rangle - i\hat{U}_{nx}\sin(|U_n|t)\,|0,n\rangle\,, \tag{F.31}$$

So, the probability of remaining in the same state is

$$P(1,n-1) = \cos^2(|U_n|t) + \frac{\Delta_n^2}{\Delta_n^2+n\epsilon^2}\sin^2(|U_n|t) = 1 - \frac{n\epsilon^2}{\Delta_n^2+n\epsilon^2}\sin^2(|U_n|t), \tag{F.32}$$

while the probability of transitioning is

$$P(0,n) = \frac{n\epsilon^2}{\Delta_n^2+n\epsilon^2}\sin^2(|U_n|t). \tag{F.33}$$

F.1 Equation of motion for DSC photons

Now we consider the description of laser action. To do so, we formulate an equation for how the density matrix of the DSC photon changes due to stimulated emission by the emitter. The method of analysis presented closely follows the coarse-grained density matrix technique used to describe conventional lasers. It is described in many books, such as [433, 426]. Suppose we have our emitter coupled to the light-matter (DSC) system. The emitter unit starts in the state $|i\rangle$ and the DSC system is taken to have a density matrix ρ_{DSC}, so that the initial density matrix of the total system ρ_{tot} is given by $\rho_{\text{tot}}(t) = |i\rangle\langle i|\rho_{\text{DSC}}(t)$. Let us look for an equation describing only the evolution of the DSC system. Assuming the interaction over a time T corresponds to the evolution operator U, we have that

$$\rho_{\text{tot}}(t+T) = U(T)|i\rangle\langle i|\rho_{\text{DSC}}(t)U^\dagger(T). \tag{F.34}$$

Let us express all operators in terms of their matrix elements, writing the above equation as

$$\rho_{\text{tot}}(t+T) = \sum_{ff',mm',nn'} \rho_{\text{DSC},nn'}(t)\langle fm|U(T)|in\rangle\langle in'|U^\dagger(T)|fm'\rangle|fm\rangle\langle f'm'|, \tag{F.35}$$

where $\rho_{\text{DSC},nn'}$ denotes the matrix elements of the DSC system, for a fixed pseudo-spin. More compactly,

$$\rho_{\text{tot}}(t+T) = \sum_{ff',mm',nn'} \rho_{\text{DSC},nn'}(t) U_{fm,in}(T) U^*_{f'm',in'}(T) |fm\rangle\langle f'm'|, \tag{F.36}$$

The DSC photon density matrix, $\rho_{\text{DSC}} = \text{tr}_{\text{em}}\rho_{\text{tot}}$, can then be expressed as

$$\rho_{\text{DSC}}(t+T) = \sum_k \langle k|\rho_{\text{DSC}}(t+T)|k\rangle = \sum_{k,mm',nn'} \rho_{\text{DSC},nn'}(t) U_{km,in}(T) U^*_{km',in'}(T) |m\rangle\langle m'|. \tag{F.37}$$

From here, a number of approaches can be followed. If there is no loss in the system, then the density matrix of the total system upon the next iteration is simply $\rho_{\text{DSC}}(t+T) = |i\rangle\langle i|\rho_{\text{DSC}}(t+T)$ and this procedure can be iterated in a discrete fashion. The evolution can also be seen as continuous if, over time T, the change in the density matrix is small. This doesn't describe the early stages of the evolution, but it can describe later stages once there are many bosons in the system. If there is a steady state, then the continuous evolution must describe the run-up to the steady state, as changes get smaller over time. In such a case, we have

$$\dot{\rho}_{mm'} = r \left(\sum_{k,nn'} U_{km,in}(T) U^*_{km',in'}(T) - \delta_{n,m}\delta_{n',m'} \right) \rho_{nn'}, \tag{F.38}$$

where $r = N/T$ is the number of excited emitters introduced into the system in time T. We have also dropped the "DSC" subscript for the DSC photon for brevity. These terms in the evolution of the density matrix describe the gain in the system. In addition, since there are losses associated with the cavity, the emitter, and the matter coupled to the cavity, we need to describe those. For simplicity, we will assume the emitter has loss, and so does the DSC photon, but not the matter (qualitatively similar results arise if the matter has loss).

F.1.1 Lindblad terms

Here we describe the effect of dissipation of the DSC photon on the equation of motion for its density matrix. Let's assume for simplicity that the cavity loss the primary source of dissipation in the problem. For weak coupling, the standard prescription is to add a

Lindblad term to the Liouvillian which prescribes the evolution of the density matrix. The Lindblad term would be (at zero temperature) $\mathcal{D}[a]\rho \equiv -\frac{\kappa}{2}(a^\dagger a\rho + \rho a^\dagger a - 2a\rho a^\dagger)$. As is well known from studies of dissipation in ultra-strong coupling of light and matter, the use of the standard Lindblad term leads to unphysical excitations (in the energy eigenbasis), even at zero temperature, and zero pumping [539]. Part of the issue is that in the USC regime, the a operator can create excitations in the eigenbasis, clearly not representing dissipation. Framed in terms of the standard derivation, the issue could be said that the interaction picture a operator has negative frequencies, and the use of white noise (with frequencies $-\infty$ to ∞) introduces contributions from these negative frequencies [434, 21]. The issue can be rectified by keeping in mind the positive-frequency nature of the reservoir.

We now use this procedure to describe dissipation in the deep-strong coupling regime. Although the technique has been worked out for ultra-strong coupling, there is a commonly used assumption in the final result that all transitions have different frequencies, which does not necessarily hold in DSC, when the energy ladder is quasi-harmonic. Interestingly, as we will show from a physical dissipator, the issues described above create much less error in the DSC regime, and the use of an operator like a or b produces a similar result to a proper positive-frequency jump operator, as their negative frequency parts get exponentially suppressed.

Let us consider the Lindblad term arising from a system-bath coupling of the form

$$V = J\sum_k (V_k b_k + V_k^* b_k^\dagger), \tag{F.39}$$

where J is a DSC system operator (e.g., $a + a^\dagger$ or $b + b^\dagger$), and the b_k are the bath operators, satisfying $[b_k, b_{k'}^\dagger] = \delta_{kk'}$. The couplings V_k between system and bath are weak. To isolate the positive-frequency parts of J, we express it in its energy eigenbasis as $J = \sum_{n>m} J_{mn}T_{mn} + \sum_{m>n} J_{mn}T_{mn} + \sum_n J_{nn}T_{nn} \equiv J^{(+)} + J^{(-)} + J^0$, with $J_{mn} = \langle m|J|n\rangle$ and $T_{mn} = |m\rangle\langle n|$.

In what follows, we will consider the bath to be concentrated around ω, but broadband enough that the white-noise approximation may be made for any transitions we consider. For example, a bath with a half-bandwidth of 10% of ω would be sufficient for the values of

g, V_k we consider. It would include all active transitions of the form $n \to n+1$, but would not include higher transitions (though the matrix elements for them are small anyway), and in the presence of a λ term, it would also not include transitions that only change spin (for $\lambda = 0$, the two spins are very nearly degenerate and so the argument should be treated with more care). Therefore, we may describe the interaction of Eq. (39) within the rotating wave approximation, instead considering

$$V \approx \sum_k (V_k b_k J^{(+)} + V_k^* b_k^\dagger J^{(-)}). \tag{F.40}$$

We note that it is not necessary to take the RWA at this stage, but it makes the subsequent manipulations simpler.

Thus, we may approximate the evolution of the reduced density matrix of the DSC system (in the interaction picture) to second-order in time-dependent perturbation theory, as:

$$\dot{\rho}_{\text{DSC},I} = -i\text{tr}_b \left([V_I(t), \rho(0)]\right) - \int_0^t dt' \ \text{tr}_b \left([V_I(t), [V_I(t'), \rho_I(t')]]\right), \tag{F.41}$$

where ρ_I is the system-bath density matrix, $\rho_{\text{DSC},I}$ is the system density matrix, V_I is the system-bath coupling in the interaction picture, and tr_b denotes the partial trace with respect to the bath. For simplicity, we will consider the bath at zero temperature. Upon taking the trace with respect to the bath, the term which is linear in V_I will vanish, and the equation of motion becomes

$$\begin{aligned}\dot{\rho}_{\text{DSC},I} = -\int_0^t dt' \ \text{tr}_b(&V_I(t)V_I(t')\rho_I(t') + \rho_I(t')V_I(t')V_I(t) \\ &- V_I(t)\rho_I(t')V_I(t') - V_I(t')\rho_I(t')V_I(t)).\end{aligned} \tag{F.42}$$

The first term may be simplified, taking the trace with respect to the bath variables, as

$$-\int_0^t dt' \int_0^\infty d\omega \ D(\omega)|V(\omega)|^2 e^{i\omega(t'-t)} J_I^{(-)}(t) J_I^{(+)}(t') \rho_{\text{DSC}}(t'), \tag{F.43}$$

where $D(\omega)$ is the density of bath states, and we have replaced the sum over k by an integral

over bath frequencies. Since an operator of the form $J^{(+)}$ is a pure de-excitation operator, no spurious excitations are introduced, and the integration limits may be extended to $-\infty$. Doing so, and making the white noise approximation, one immediately finds that the term evaluates to $-\frac{\kappa}{2} J_I^{(-)}(t) J_I^{(+)}(t) \rho_{\text{DSC}}(t)$, where $\kappa = 2\pi\rho|V|^2$. A similar manipulation for the remaining terms yields that the free dissipation dynamics of the DSC Hamiltonian are governed by

$$\dot{\rho}_{\text{DSC},I} = -\frac{\kappa}{2}\left(J_I^{(-)} J_I^{(+)} \rho_{\text{DSC}} + J_I^{(-)} J_I^{(+)} \rho_{\text{DSC}} - 2 J_I^{(+)} \rho_{\text{DSC}} J_I^{(-)}\right). \tag{F.44}$$

Let us use this to find the contribution of dissipation to the equation of motion for the populations, ρ_{nn}. From here on out, we will suppress the "DSC" subscript. We will ignore the spin degree of freedom (and restrict the dynamics to a single spin ladder). Although this is not rigorous, one expects this to capture well the dynamics of the DSC photon number as, for $\lambda = 0$, one will just expect the nearly degenerate spins to be mixed, with little change of the oscillator quantum numbers. We validate this numerically. For finite λ the spin ladders can be split appreciably, and so they will decouple. Consider a J of the form $b + b^\dagger$. As discussed in the main text, b is a pure de-excitation operator, and $b^\dagger$ is a pure creation operator. Therefore, $J^{(+)} = b$. Using the fact that $\langle n'\sigma|b|n\sigma\rangle = \sqrt{n}\delta_{n',n-1}$ and $b^\dagger b|n\sigma\rangle = n|n\sigma\rangle$, one immediately arrives at

$$\dot{\rho}_{nn} = -\kappa n \rho_{nn} + \kappa(n+1)\rho_{n+1,n+1}, \tag{F.45}$$

which is similar to the form one would expect for damping of a conventional photon. This is perhaps unsurprising in light of the fact that the DSC photon is essentially harmonic up to $n_c \sim g^2$. It is worth noting that the matrix elements derived for a, b in Eq. (24) are based on first-order degenerate perturbation theory. Beyond n_c, these approximations do not hold up and the states and matrix elements change significantly. However, the approximate result turns out to describe the system well because the probabilities to find photon numbers beyond n_c are strongly suppressed. It is also worth noting that if we chose a instead of b as the jump operator, when we neglect spin, the matrix elements are the same. Numerically, we find that whether we choose a or b as the jump operator, negligible levels of excitations

are created in the ground state, and the steady-state of the Fock laser we describe is not qualitatively changed. These numerics are shown in the last section.

Rate equations

We will now obtain a closed set of equations for the diagonals of the DSC density matrix, to get the probability of different Fock state occupations of the DSC photons. Setting $m = m'$, we have

$$\dot{\rho}_{mm} = r \left(\sum_{k,nn'} U_{km,in}(T) U^*_{km,in'}(T) - \delta_{n,m}\delta_{n',m} \right) \rho_{nn'}. \tag{F.46}$$

The set of equations for the coarse grained density matrix is only closed when $U_{km,in}(T)U^*_{km,in'}(T)$ is zero unless $n = n'$. In that case, we have

$$\dot{\rho}_{mm} = r \left(\sum_{k,n} |U_{km,in}(T)|^2 - \delta_{n,m}\delta_{n',m} \right) \rho_{nn'} = r \left(\sum_{k,n} |U_{km,in}(T)|^2 \rho_{nn} - \rho_{mm} \right). \tag{F.47}$$

We can now note the conditions under which the equations for the populations become closed. We require $U_{km,in}(T)U^*_{km,in'}(T)$ is zero unless $n = n'$. This is equivalent to saying that a transition $in \to km$ and $in' \to km$ are not simultaneously possible. Supposing i is also an eigenstate of the light-matter system, and that we are in the RWA, this statement appears to amount to energy conservation, as transitions are assumed to be only efficient if they are resonant, so that $E_i + E_n = E_k + E_m$. Therefore the condition that $U_{km,in}(T)U^*_{km,in'}(T) \neq 0$ for $n \neq n'$ requires $E_n = E_{n'}$, which, for a single oscillator, requires $n = n'$.

In the weak coupling regime then, we have (adding in the photon losses)

$$\dot{\rho}_{mm} = r \sum_{k,n} |U_{km,in}(T)|^2 \rho_{nn} - r\rho_{mm} + \kappa(m+1)\rho_{m+1,m+1} - \kappa m \rho_{mm}. \tag{F.48}$$

Let's now consider the case of the emitter coupled to our light-matter system. Since we inject emitters in the excited state, we have $i = 1$. The state $1n$ couples only to $1n$ and $0(n+1)$. So, the sum over probabilities leaves only the scattering matrix coefficients

$U_{1m,1m}$ and $U_{0m,1(m-1)}$. Therefore, the coarse-grained equation simplifies to:

$$\dot{\rho}_{mm} = r(|U_{0m,1(m-1)}(T)|^2\rho_{m-1,m-1}+|U_{1m,1m}(T)|^2\rho_{mm})-r\rho_{mm}+\kappa(m+1)\rho_{m+1,m+1}-\kappa m\rho_{mm}. \tag{F.49}$$

We found these probability coefficients when studying the dynamics of the Hamiltonian in the degenerate subspace of fixed pseudo-spin. Plugging in the results there, we have [1]

$$\begin{aligned}\dot{\rho}_{nn} =& \frac{rn\epsilon^2}{\Delta_n^2 + n\epsilon^2}\sin^2(|U_n|T)\rho_{n-1,n-1} - \left(\frac{r(n+1)\epsilon^2}{\Delta_{n+1}^2 + (n+1)\epsilon^2}\sin^2(|U_{n+1}|T) + \kappa n\right)\rho_{nn} \\ &+ \kappa(n+1)\rho_{n+1,n+1}.\end{aligned} \tag{F.50}$$

To proceed, we must the emitter loss (T_1 and T_2 decay) into account. Assuming that the emitter loss manifests as exponential decay with rate Γ, the effect is to average the probability coefficients over T with probability distribution $P(T) = \Gamma e^{-\Gamma T}$. Noting that

$$\Gamma\int dT\, e^{-\Gamma T}\sin^2(\alpha T) = \frac{2\alpha^2}{\Gamma^2 + 4\alpha^2}, \tag{F.51}$$

we have

$$\begin{aligned}\dot{\rho}_{nn} =& r\frac{n\epsilon^2}{\Delta_n^2 + n\epsilon^2}\frac{2U_n^2}{\Gamma^2 + 4U_n^2}\rho_{n-1,n-1} \\ &- \left(r\frac{(n+1)\epsilon^2}{\Delta_{n+1}^2 + (n+1)\epsilon^2}\frac{2U_{n+1}^2}{\Gamma^2 + 4U_{n+1}^2} + \kappa n\right)\rho_{nn} \\ &+ \kappa(n+1)\rho_{n+1,n+1}.\end{aligned} \tag{F.52}$$

[1] To check a limiting case, we set the detunings are zero. In that case, $|U_n| = \sqrt{n}\epsilon$, and we have

$$\dot{\rho}_{nn} = r\sin^2(\epsilon T\sqrt{n})\rho_{n-1,n-1} - \left(r\sin^2(\epsilon T\sqrt{n+1}) + \kappa n\right)\rho_{nn} + \kappa(n+1)\rho_{n+1,n+1}$$

This coincides exactly with the equation of motion of the so-called micromaser, which describes the interaction of injected two-level atoms interacting with a cavity (in the perturbative coupling regime $g \ll \omega$). This is quite interesting as the micromaser equations assume $g \ll 1$, while here, we are starting from the limit $g \gg 1$. Moreover, by averaging over decay times as we do in the next subsection, we will find exactly the standard Scully-Lamb master equation for a conventional laser. What's happening here is that in the weak-coupling regime, assuming the emitter is resonant, the detunings also approximately vanish between the nearly degenerate levels. And so we get a similar equation, except that it the conventional case, it is in the photon basis, and here it is in the DSC photon basis.

Noting that $U_n^2 = \Delta_n^2 + n\epsilon^2$, we have

$$\begin{aligned}\dot{\rho}_{nn} = & r\frac{2n\epsilon^2}{\Gamma^2 + 4(\Delta_n^2 + n\epsilon^2)}\rho_{n-1,n-1} \\ & - \left(r\frac{2(n+1)\epsilon^2}{\Gamma^2 + 4(\Delta_{n+1}^2 + (n+1)\epsilon^2)} + \kappa n\right)\rho_{nn} \\ & + \kappa(n+1)\rho_{n+1,n+1}. \end{aligned} \tag{F.53}$$

Assuming resonance between the emitter and the light-matter system, we have finally

$$\dot{\rho}_{nn} = \frac{2rn\epsilon^2}{\Gamma^2 + F(n)}\rho_{n-1,n-1} - \left(\frac{2r(n+1)\epsilon^2}{\Gamma^2 + F(n+1)} + \kappa n\right)\rho_{nn} + \kappa(n+1)\rho_{n+1,n+1}, \tag{F.54}$$

with the nonlinearity, $F(n)$ defined as

$$F(n) = 4n\epsilon^2 + \frac{1}{4}\omega^2 e^{-4g^2}(L_n(4g^2) - L_{n-1}(4g^2))^2. \tag{F.55}$$

Here, we have used $\Delta_n = \frac{\omega}{2}(\delta - \frac{e^{-2g^2}}{2}(L_{n-1}(4g^2) - L_n(4g^2)))$ with $\delta = 0$.

F.1.2 Steady-state dynamics

Perhaps one of the most important results is the steady-state dynamics of the system. Thus we want to solve $\dot{\rho}_n = 0$ with the constraint $\sum_n \rho_n = 1$ (introducing the shorthand $\rho_n = \rho_{nn}$). Writing the steady-state equation as $0 = A_n\rho_{n-1} + B_n\rho_n + C_n\rho_{n+1}$, we have the recursion relation: $\rho_{n+1} = -\frac{B_n\rho_n + A_n\rho_{n-1}}{C_n}$, with $\rho_0 = 1$ and $\rho_{-1} = 0$. Since any scale multiple of ρ also solves this equation, we can normalize the solution at the end to satisfy the normalization constraint.

This equation can be simplified by noting that $B_n = -(A_{n+1} + C_{n-1})$. We thus have $A_n\rho_{n-1} - A_{n+1}\rho_n - C_{n-1}\rho_n + C_n\rho_{n+1} = 0$ or alternatively

$$A_n\rho_{n-1} - C_{n-1}\rho_n = A_{n+1}\rho_n - C_n\rho_{n+1}. \tag{F.56}$$

Defining the difference $S_n = A_n\rho_{n-1} - C_{n-1}\rho_n$, we see that $S_n = S_{n+1}$. Since $S_0 =$

$A_0\rho_{-1} - C_{-1}\rho_0 = 0$, we have that $S_n = 0$ for all n, and thus the simpler recursion relation:

$$\rho_{n+1} = \frac{A_{n+1}}{C_n}\rho_n \implies \rho_n = \left(\prod_{m=1}^{n} \frac{A_m}{C_{m-1}}\right)\rho_0. \tag{F.57}$$

The initial ρ_0 is taken as 1 understanding that we must normalize the probability distribution at the end of the calculation. Plugging in the forms of the A and C coefficients, we have

$$\rho_n = \frac{1}{Z}\prod_{m=1}^{n}\frac{2r\epsilon^2/\kappa}{\Gamma^2 + F(m)} \equiv \frac{1}{Z}\prod_{m=1}^{n}\frac{\alpha}{1+G(m)} = \frac{\alpha^n}{Z}\prod_{m=1}^{n}\frac{1}{1+G(m)}, \tag{F.58}$$

where we have introduced $\alpha = \frac{2r\epsilon^2}{\kappa\Gamma^2}$, $G(m) = F(m)/\Gamma^2$, and $Z = 1 + \sum_{n=1}^{\infty}\left(\prod_{m=1}^{n}\frac{A_m}{C_{m-1}}\right)$, the normalization constant. We note that the factor $\alpha(1+G(n))^{-1}$ essentially "propagates" the probability distribution from n to $n+1$. These results underlie the results of Fig. 2 and Fig. 3 of the main text.

In Fig. 2, we expand upon Fig. 2 of the main text by showing the statistics as a function of pump for different coupling parameters, to give the reader of a clearer sense of the transition from thermal to coherent to Fock statistics.

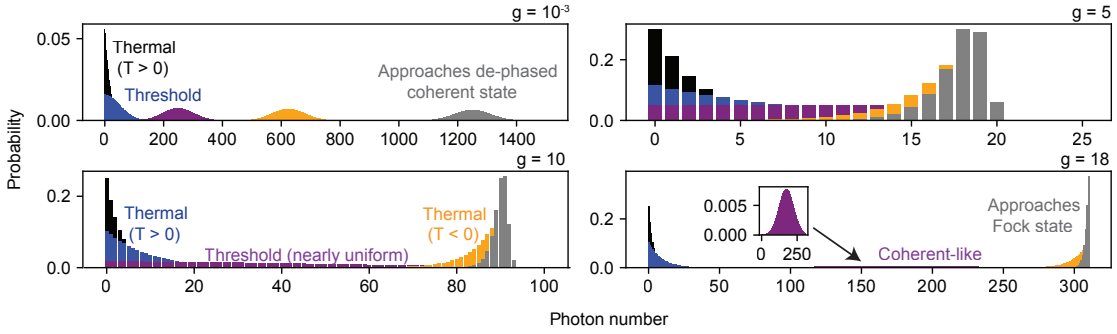

Figure F-2: Evolution of photon statistics with pumping: thermal, coherent, anti-thermal, and Fock states. Photon probability distributions as a function for different pump strengths and different coupling strengths. For weak coupling, the statistics evolve from thermal to coherent with increasing pump. For the largest couplings considered, the state evolves from thermal (for low pump) to coherent (for intermediate pump) to a thermal state of *negative temperature* for higher pump. As the pump increases, the negative temperature state converges effectively to a Fock state. Note that the bottom left panel overlaps with Fig. 2 of the main text.

F.1.3 Summary of changes with $\lambda \neq 0$

In most of the discussion, we have assumed that $\lambda = 0$. However, in many superconducting qubit systems, a nonzero σ_x term is present due to an applied bias field which can tune the system. Our main results of nonperbative nonlinearity, as well as the Fock lasing action in these systems, are robust to the addition of this term. We summarize the main changes here.

We assume that the generalized Rabi Hamiltonian now takes the full form

$$H = \frac{1}{2}(\omega\sigma_z + \lambda\sigma_x) + \omega a^\dagger a + \tilde{g}\sigma_x(a + a^\dagger). \tag{F.59}$$

The spectrum is now approximately given by:

$$E_{n,\sigma} = n\omega + \frac{\sigma}{2}\sqrt{(\omega D_n)^2 + \lambda^2}, \tag{F.60}$$

which corresponds to the eigenstates

$$|n, +\rangle = \cos(\theta/2)D^\dagger(g)\,|+x, n\rangle + \sin(\theta/2)D(g)\,|-x, n\rangle \tag{F.61}$$

$$|n, -\rangle = \sin(\theta/2)D^\dagger(g)\,|+x, n\rangle - \cos(\theta/2)D(g)\,|-x, n\rangle\,, \tag{F.62}$$

where the mixing angle θ is defined by $\tan(\theta) = \omega D_n/\lambda$.

In principles, the modifications to the analysis of the laser action should follow through new additions to the matrix elements which couple these eigenstates. Specifically, we have

$$\langle n', +|(a + a^\dagger)|n, +\rangle = (\sqrt{n}\delta_{n',n-1} + \sqrt{n+1}\delta_{n',n+1}) - 2g\cos\theta\delta_{nn'} \tag{F.63}$$

$$\langle n', -|(a + a^\dagger)|n, -\rangle = (\sqrt{n}\delta_{n',n-1} + \sqrt{n+1}\delta_{n',n+1}) + 2g\cos\theta\delta_{nn'} \tag{F.64}$$

$$\langle n', -|(a + a^\dagger)|n, +\rangle = -2g\sin\theta\delta_{nn'}. \tag{F.65}$$

However, we see that the only new terms are only nonzero when the photon number stays the same. Thus, the only modifications to the equations of motion come from the eigenenergies. This means that the equations of motion derived previously still hold valid, but

with a new nonlinearity:

$$F(n) = 4n\epsilon^2 + \frac{\omega^2}{4}\left(\sqrt{D_n^2 + \lambda^2} - \sqrt{D_{n-1}^2 + \lambda^2}\right)^2. \tag{F.66}$$

F.1.4 Direct method for evolving the density matrix

In the previous section, we treated the emitter-field interaction as if excited two-level systems were being injected into the system at rate r. We also treated the interaction with the emitters as sequential: as if one emitter interacts with the field at any given time, with probability coefficients averaged over the emitter's exponential decay probability. In this section, we provide an alternative treatment of the problem in which we consider the direct evolution of the density matrix in the presence of coherent emitter-field interaction, emitter pumping, emitter decay, and field leakage. This approach, besides being in principle more rigorous, and besides providing further corroboration of our results above, also allows us to consider multi-level emitter systems, such as three- and four-level systems, which are more practical from the standpoint of lasers. This method has been applied to describe conventional lasers (see [433]), but due to its generality, can be used to describe the Fock laser discussed in this paper.

The equation of motion for the density matrix is

$$\dot{\rho} = -i[H/\hbar, \rho] + \sum_i \frac{\gamma_i}{2}\left(2J_i\rho J_i^\dagger - J_i^\dagger J_i\rho - \rho J_i^\dagger J_i\right) \equiv -i[H, \rho] + \sum_i \mathcal{L}_i[\rho], \tag{F.67}$$

where

$$H = H_{\text{Rabi}} + \sum_{i=1}^{N} H_{\text{em,i}} + \hbar\epsilon_i(|a_i\rangle\langle b_i| + |b_i\rangle\langle a_i|)(b + b^\dagger), \tag{F.68}$$

is the Hamiltonian describing N multi-level emitters (with Hamiltonian $H_{\text{em,i}}$) coupled to the electromagnetic field associated with matter strongly coupled to a single electromagnetic field mode with coupling constant ϵ_i. The levels a and b of the ith emitter are coupled to the field and comprise respectively the excited and ground levels of the lasing transition. We have changed $e, g \to a, b$ as in what follows, we will introduce more levels to incorporate realistic decay channels. The terms on the right of the density matrix equation of

motion are Lindblad terms with decay rates γ_i and jump operators J_i. The index i enumerates over the possible decay mechanisms, as well as all of the emitters. In what follows, we review several (standard) simplifications of this equation that render a readily solvable problem.

For simplicity, we will consider the case (as before) where all emitters have the same energy levels (and thus the same $H_{\text{em,i}}$) and coupling constant $\epsilon_i = \epsilon$ (which is the average coupling dictated by the emitter distribution and cavity mode profile). Similarly, the decay constants of all atomic levels are taken as the same. These simplifications do not negate the effects reported here. Beyond these simplifications, a key simplification arises because the emitter-field coupling couples all of the emitters to a single quantum oscillator. In this case, we can consider the problem as effectively a one-emitter problem where

$$H = H_{\text{Rabi}} + \hbar\epsilon(|e\rangle\langle g| + |g\rangle\langle e|)(a + a^\dagger) \equiv H_0 + V, \tag{F.69}$$

and the i in the Lindblad terms enumerates only over decay channels. We have defined for simplicity $H_0 = H_{\text{Rabi}} + H_{\text{em}}$ and $V/\hbar = \epsilon(|e\rangle\langle g| + |g\rangle\langle e|)(a + a^\dagger)$.

To start, we will consider decay channels for the emitter only, and not the field, and include the field decay channels at the end of the calculation. In what follows, we consider an emitter system consisting of lasing levels a, b, ground level g, and "bath levels" c, d for which a and b respectively decay to. The pumping from $g \to a$ occurs with rate r, while the $a \to c$ decay occurs with rate γ_a, the $b \to d$ decay occurs with rate γ_b, the $c \to g$ decay occurs with rate γ_c, and the $d \to g$ decay occurs with rate γ_d. Thus, the density matrix equation of motion may be written as

$$\dot{\rho} = -i[H_0/\hbar, \rho] - i[V/\hbar, \rho] + \sum_{i=g,a,b,c,d} \mathcal{L}_i[\rho], \tag{F.70}$$

where the jump operators for g, a, b, c, d are respectively $|a\rangle\langle g|$, $|c\rangle\langle a|$, $|d\rangle\langle b|$, $|g\rangle\langle c|$, and $|g\rangle\langle d|$ with corresponding rates $r, \gamma_a, \gamma_b, \gamma_c, \gamma_d$.

Let us now write an equation of motion for the matrix elements of the density matrix, $\rho_{\beta n', \alpha n}$, where α, β enumerate over emitter states $g, a - d$ and the n, n' enumerate over

the eigenstates of the Rabi Hamiltonian (e.g., the Fock states of DSC photons). We are considering the Hamiltonian only in one spin projection, as in the previous treatment, since the spins decouple, both in the conventional Rabi model, and the generalized one (with $\lambda \neq 0$). To proceed, we will need the following matrix elements

$$\begin{aligned}
\langle \beta, n' | \left[H_0/\hbar, \rho \right] | \alpha, n \rangle &= (\omega_{\beta n'} - \omega_{\alpha n}) \rho_{\beta n', \alpha n} \\
\langle b, n' | V \rho | \alpha, n \rangle &= V_{b n', a n'-1} \rho_{a n'-1, \alpha n} \\
\langle a, n' | V \rho | \alpha, n \rangle &= V_{a n', b n'+1} \rho_{b n'+1, \alpha n} \\
\langle \beta, n' | \rho V | b, n \rangle &= \rho_{\beta n', a n-1} V_{a n-1, b n} \\
\langle \beta, n' | \rho V | a, n \rangle &= \rho_{\beta n', b n+1} V_{b n+1, a n}.
\end{aligned} \tag{F.71}$$

For matrix elements of $V\rho$ and ρV, we have used the structure of the matrix elements in the section "Time-evolution of the coupled system", where we showed that the effect of the coupling is to change the emitter state, and to change the number of field quanta by one.

We also need the matrix elements of the Lindblad terms. Let us consider a generic Lindblad term of the form

$$\langle \beta, n' | \mathcal{L}_i[\rho] | \alpha, n \rangle = \frac{\gamma_i}{2} \langle \beta, n' | 2 T_{ji} \rho T_{ji}^\dagger - T_{ji}^\dagger T_{ji} \rho - \rho T_{ji}^\dagger T_{ji} | \alpha, n \rangle , \tag{F.72}$$

where $T_{ji} = |j\rangle \langle i|$. T_{ij} is simply J_i with the final-state index j included for clarity. The matrix element follows as

$$\langle \beta, n' | \mathcal{L}_i[\rho] | \alpha, n \rangle = \frac{\gamma_i}{2} (2 \delta_{j\beta} \delta_{j\alpha} \rho_{i n', i n} - \delta_{i\alpha} \rho_{\beta n', i n} - \delta_{i\beta} \rho_{i n', \alpha n}). \tag{F.73}$$

With these matrix elements tabulated, we may write the following set of equations for

the matrix elements of the density matrix:

$$
\begin{aligned}
\dot{\rho}_{an',an} &= -i\omega_{n'n}\rho_{an',an} - \gamma_a\rho_{an',an} + r\rho_{gn',gn} \\
&\quad - i(V_{an',bn'+1}\rho_{bn'+1,an} - \rho_{an',bn+1}V_{bn+1,an}) \\
\dot{\rho}_{bn'+1,an} &= \left[-i(\omega_{bn'+1} - \omega_{an}) - \frac{\gamma_a+\gamma_b}{2}\right]\rho_{bn'+1,an} \\
&\quad - i(V_{bn'+1,an'}\rho_{an',an} - \rho_{bn'+1,bn+1}V_{bn+1,an}) \\
\dot{\rho}_{an',bn+1} &= \left[-i(\omega_{an'} - \omega_{bn+1}) - \frac{\gamma_a+\gamma_b}{2}\right]\rho_{an',bn+1} \\
&\quad - i(V_{an',bn'+1}\rho_{bn'+1,bn+1} - \rho_{an',an}V_{an,bn+1}) \\
\dot{\rho}_{bn'+1,bn+1} &= -i\omega_{n'+1,n+1}\rho_{bn'+1,bn+1} - \gamma_b\rho_{bn'+1,bn+1} \\
&\quad - i(V_{bn'+1,an'}\rho_{an',bn+1} - \rho_{bn'+1,an}V_{an,bn+1}) \\
\dot{\rho}_{cn',cn} &= (-i\omega_{n'n} - \gamma_c)\rho_{cn',cn} + \gamma_a\rho_{an',an} \\
\dot{\rho}_{dn',dn} &= (-i\omega_{n'n} - \gamma_d)\rho_{dn',dn} + \gamma_b\rho_{bn',bn} \\
\dot{\rho}_{gn',gn} &= (-i\omega_{n'n} - r)\rho_{gn',gn} + \gamma_c\rho_{cn',cn} + \gamma_d\rho_{dn',dn}.
\end{aligned}
\tag{F.74}
$$

While these equations can be generally solved, we focus as in the previous treatment on the steady state dynamics. As expected from conventional lasers, the steady state density matrix is diagonal due to decoherence. Numerically, for this laser system, based on deep strong light-matter coupling, we also found that the steady-state (found by the null eigenvector of the Liouvillian (S such that $\dot{\rho} = S\rho$)) is diagonal. Let us thus focus on the steady-state equations for the "photon diagonals" ($n = n'$), which are simply

$$
\begin{aligned}
0 &= r\rho_{gn,gn} - \gamma_a \rho_{bn,an} - i(V^* \rho_{bn+1,an} - \rho_{an,bn+1} V) \\
0 &= \left[i\Delta_{n+1} - \frac{\gamma_a + \gamma_b}{2} \right] \rho_{bn+1,an} - i(V\rho_{an,an} - \rho_{bn+1,bn+1} V) \\
0 &= \left[-i\Delta_{n+1} - \frac{\gamma_a + \gamma_b}{2} \right] \rho_{an,bn+1} - i(V^* \rho_{bn+1,bn+1} - \rho_{an,an} V^*) \\
0 &= -\gamma_b \rho_{bn+1,bn+1} - i(V\rho_{an,bn+1} - \rho_{bn+1,an} V^*) \\
0 &= -\gamma_c \rho_{cn,cn} + \gamma_a \rho_{an,an} \\
0 &= -\gamma_d \rho_{dn,dn} + \gamma_b \rho_{bn,bn} \\
0 &= -r\rho_{gn,gn} + \gamma_c \rho_{cn,cn} + \gamma_d \rho_{dn,dn},
\end{aligned}
\tag{F.75}
$$

where we have defined $\Delta_{n+1} = \omega_{an} - \omega_{bn+1}$.

Immediately, we have $\gamma_a \rho_{an,an} = \gamma_c \rho_{cn,cn}$ and $\gamma_b \rho_{bn,bn} = \gamma_d \rho_{dn,dn}$. The equation for $\rho_{gn,gn}$ then can be written as

$$
r\rho_{gn} = \gamma_a \rho_{an,an} + \gamma_b \rho_{bn,bn}. \tag{F.76}
$$

For simplicity, let us take $\gamma_a = \gamma_b = \Gamma$, so that

$$
r\rho_{gn} = \Gamma(\rho_{an,an} + \rho_{bn,bn}) = \Gamma(\rho_{nn} - \rho_{cn,cn} - \rho_{dn,dn} - \rho_{gn,gn}), \tag{F.77}
$$

where we have defined the photon populations $\rho_{nn} = (\mathrm{tr}_{\mathrm{em}}\rho)_{nn}$ in order to express everything in terms of these populations and arrive at a coarse-grained density matrix for the field. Let us now consider the case where $\gamma_c \gg \gamma_a$ and $\gamma_d \gg \gamma_b$. In this case, we immediately see that $\rho_{cn,cn} \approx 0$ and $\rho_{dn,dn} \approx 0$. This is to say that these levels are depleted immediately after they are populated by the lasing levels. In this case, $\rho_{gn,gn} = \frac{\Gamma}{(r+\Gamma)} \rho_{nn}$.

The steady-state equations then reduce to the simple inhomogeneous equation:

$$\begin{bmatrix} \Gamma & -iV & iV^* & 0 \\ -iV^* & \Gamma + i\Delta_{n+1} & 0 & iV^* \\ iV & 0 & \Gamma - i\Delta_{n+1} & -iV \\ 0 & iV & -iV^* & \Gamma \end{bmatrix} \begin{bmatrix} \rho_{an,an} \\ \rho_{an,bn+1} \\ \rho_{bn+1,an} \\ \rho_{bn+1,bn+1} \end{bmatrix} = \frac{r\Gamma\rho_{nn}}{r+\Gamma} \begin{bmatrix} 1 \\ 0 \\ 0 \\ 0 \end{bmatrix} \equiv r_a\rho_{nn} \begin{bmatrix} 1 \\ 0 \\ 0 \\ 0 \end{bmatrix}, \tag{F.78}$$

whose solution yields $\rho_{an,an}, \rho_{an,bn+1}, \rho_{bn+1,an}, \rho_{bn+1,bn+1}$ in terms of ρ_{nn}. To proceed most efficiently, we now connect these density matrix elements to the equation of motion for the reduced density matrix of the field. This equation of motion is

$$\dot{\rho}_{nn} = -i(\rho_{an-1,bn}V_{bn,an-1} + V_{an,bn+1}\rho_{bn+1,an} - \rho_{bn,an-1}V_{an-1,bn} - V_{bn+1,an}\rho_{an,bn+1}). \tag{F.79}$$

The coherences can be found from the matrix equation above, which for brevity, we denote as $M_nP_n = r_a\rho_{nn}e_1$ so that $P_n = r_a\rho_{nn}(M_n^{-1}e_1)$. We may write this equation in a form similar to that of the equation for the coarse-grained density matrix of the previous treatment, i.e., as

$$0 = A_n\rho_{n-1,n-1} - A_{n+1}\rho_{n,n}, \tag{F.80}$$

where $A_n = -ir_a((e_2^TM_{n-1}^{-1}e_1)V_{bn,an-1} - (e_3^TM_{n-1}^{-1}e_1)V_{an-1,bn})$, and we have looked at the steady-state limit. At this stage, we now add the Lindblad terms corresponding to the cavity leakage. As per the discussion in the section "Lindblad terms", the resulting equation of motion for the field density matrix is

$$\dot{\rho}_{nn} = A_n\rho_{n-1,n-1} - (A_{n+1} + \kappa|\langle n-1|a+a^\dagger|n\rangle|^2)\rho_{n,n} + \kappa|\langle n|a+a^\dagger|n+1\rangle|^2\rho_{n+1,n+1}. \tag{F.81}$$

Defining $B_n = -(A_{n+1} + \kappa|\langle n-1|a+a^\dagger|n\rangle|^2)$ and $C_n = \kappa|\langle n|a+a^\dagger|n+1\rangle|^2$, we have as before $A_{n+1} + B_n + C_{n-1} = 0$, enabling us to immediately write

$$\rho_{n+1} = \frac{A_{n+1}}{C_n}\rho_n \implies \rho_n = \left(\prod_{m=1}^{n} \frac{A_m}{C_{m-1}}\right)\rho_0. \tag{F.82}$$

with the initial ρ_0 is taken as one with the understanding that we must normalize the prob-

ability distribution at the end of the calculation. Upon inversion of the matrix M_n, we immediately find

$$A_n = \frac{2r_a|V_{bn,an-1}|^2}{\Gamma^2 + 4|V_{bn,an-1}|^2 + \Delta_n^2}. \tag{F.83}$$

Noting that $|V_{bn,an-1}|^2 = \epsilon^2|\langle n-1|a+a^\dagger|n\rangle|^2$, we may write the overall equation as

$$\rho_n = \frac{1}{Z}\left(\prod_{m=1}^{n} \frac{2r_a\epsilon^2/\kappa\Gamma^2}{1+(4\epsilon^2|\langle m-1|a+a^\dagger|m\rangle|^2+\Delta_m^2)/\Gamma^2}\right) \equiv \frac{\alpha^n}{Z}\left(\prod_{m=1}^{n}\frac{1}{1+G(m)}\right), \tag{F.84}$$

where $\alpha = 2r_a\epsilon^2/\kappa\gamma^2$ and $Z = 1 + \sum\limits_{n=1}^{\infty}\left(\prod\limits_{m=1}^{n}\frac{A_m}{C_{m-1}}\right)$. Immediately, we see that if we take $|\langle n-1|a+a^\dagger|n\rangle|^2 = n$ and $\Delta_n^2 = \frac{1}{4}\omega^2 e^{-4g^2}(L_n(4g^2) - L_{n-1}(4g^2))^2$ (assuming $\omega_0 = \omega$) that we recover the results of the previous treatment. And it may also be easily seen that this agreement persists if we take the matrix elements and splitting to be governed by the generalized Rabi model (with $\lambda \neq 0$).

F.2 Numerical calculation of the Fock laser steady state

In this section, we numerically validate the analytical developments of the previous sections. Since the analytical calculations make use of many approximations and assumptions, it is important to validate them in terms of a method which is independent of these assumptions. In what follows, we will use a method inspired by the observation that the equation of motion for the laser density matrix effectively describes the interaction of a single gain atom with a cavity, even when the gain medium is composed of many atoms. This is because the atoms only couple to each other through the cavity field, as noted in [433]. Thus, it follows that laser steady states can be understood through the steady state of the Liouvillian operator describing a damped oscillator coupled to a gain atom. By taking the partial trace of the null eigenvector of the Liouvillian, one finds the steady state probability distribution of DSC photons. Applied to conventional lasers, one correctly finds the transition from thermal to coherent state statistics above the laser threshold.

The Hamiltonian part of the Liouvillian is simply the Hamiltonian of Eq. (2). Here, we also consider two different possible interaction terms: $a+a^\dagger$ or $b+b^\dagger$. The steady-states are also insensitive to this. In these calculations, we include a reservoir to describe pumping

of the gain medium, as well as its T_1- and T_2-relaxation (here, $T_2 = 2T_1$). We also include a reservoir to describe the decay of the DSC photon. We take as the jump operator $J^{(+)}$, where $J = a + a^\dagger$ or $b + b^\dagger$ and the $+$ superscript means "positive-frequency", meaning that we project out all negative frequency components. The steady-state is insensitive to whether we use a or b (it changes only slightly), indicating the relative unimportance of the dipole-dipole interaction from the standpoint of the photon probabilities. The overall Liouvillian is then the sum of the Hamiltonian (commutator) part and three dissipators: $\mathcal{D}[\sigma_{\text{em}}^{(-)}], \mathcal{D}[\sigma_{\text{em}}^{(+)}]$ and $\mathcal{D}[J^{(+)}]$ with respective rates r, Γ, and κ, to describe gain pumping, gain decoherence, and DSC photon decay. Note that $\mathcal{D}[O]\rho \equiv O^\dagger O\rho + \rho O^\dagger O - 2O\rho O^\dagger$.

In Fig. 3, we show the probability distribution of DSC photons resulting from one of these steady-state calculations. Because we have largely neglected spin in our analytical discussions, we plot the "unpolarized" photon probability distribution, defined such that $P(n) = P(n,-1) + P(n,1)$. As can be seen, above threshold, the state has very low number fluctuations, in this case, δn = 1, yielding a state very close to a Fock state. Below threshold, a thermal state is found. Around threshold, the quasi-uniform state of Fig. 3 of the main text is found.

These results are insensitive to the presence of a λ-term, as shown in Fig. 4. The presence of a λ term, all else equal, slightly increases the photon noise. This is because the presence of a λ softens the anharmonicity (which can be understood from the term $\sqrt{\lambda^2 + \omega^2 e^{-4g^2} L_n^2(4g^2)}$ in Eq. (60)).

The results are also insensitive to the exact form of interaction and dissipator (provided that the dissipator doesn't create spurious excitations). In Fig. 5, we show the steady-state, computed using interaction terms based on a or b, as well as dissipators based on a or b.

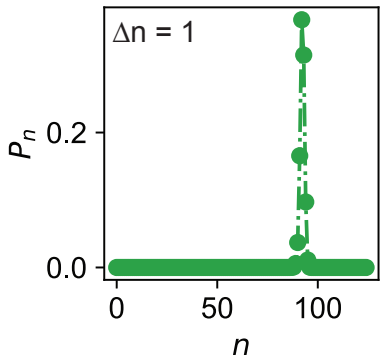

Figure F-3: Steady-state of the Fock laser, calculated numerically, by finding the steady-state of the Liouvillian operator. Plot shows the unpolarized probability distribution for $\lambda = 0$. For $\epsilon = 10^{-5}\omega$, $\kappa = 10^{-8}\omega$, and $r = 10\Gamma$ (such that the population inversion of the gain is about 90%, the resulting state is nearly a Fock state of 100 DSC photons, with a residual uncertainty of 1. This state has noise 99% below the shot noise level. Moreover, this calculation shows that the Hamiltonian of Eq. (3), coupled to damping, supports Fock states as its steady state, from first principles.

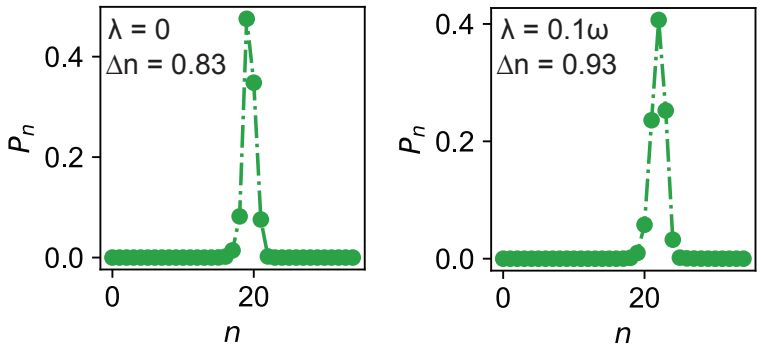

Figure F-4: Steady-state of the Liouvillian of the Fock laser with and without the λ-term of Eq. (1) of the main text. Here, $\lambda = 0.1\omega$ is sufficient to keep the two spin ladders from interchanging, and is not found to alter the steady-state appreciably. ϵ, Γ, κ are the same as in the above figure.

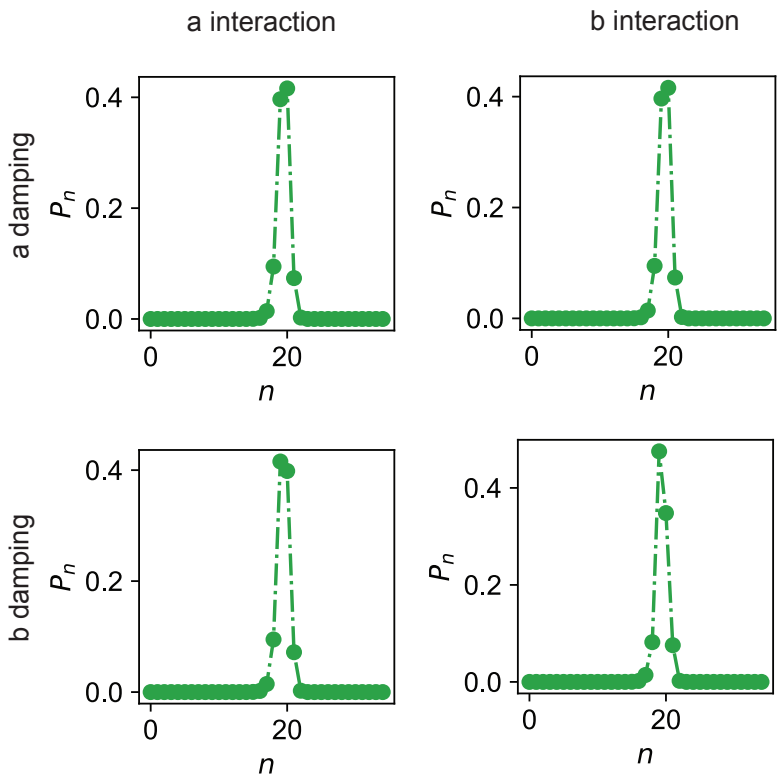

Figure F-5: Steady-state of the Liouvillian of the Fock laser with different choices for the interaction term and dissipator, showing robustness to the exact magnitude of the dipole-dipole interaction between the emitter and the qubit.

Appendix G

Appendices for: Complete condensation of photon noise in nonlinear dissipative systems

In this Supplementary Information (SI), we develop the theory of nonlinear dissipation and amplification in systems with sharp loss (as well as gain). In contrast to the main text, which summarizes the key theoretical results and focuses primarily on applications of the theory, the SI is meant to provide a detailed account of the theory, providing underlying assumptions, as well as derivations.

In the section "Quantum theory of a nonlinear resonator with frequency-dependent loss", we will introduce a nonlinear open system model (and its Hamiltonian, Eq. (1) of the main text) that realizes the sharp loss described in the main text. Then, we develop a master equation (Eq. (2) of main text) to describe dissipation in such systems, showing that it coincides with the type of nonlinear dissipation quoted in the main text (Eqs. (3-5) of main text). From there, we move to derive results related to the statistical dynamics (Eq. (6) of main text)). To close Section I, we develop a quantum Langevin theory of nonlinear dissipation in these systems. The quantum Langevin theory is in correspondence with the density matrix theory, and makes the same predictions as far as the results of the main text are concerned. However, the quantum Langevin approach provides the most convenient starting point for describing fluctuations of lasers. In the Appendix, we develop an

independent derivation of the nonlinear loss developed in this work through the Heisenberg equations for the projection operators of a nonlinear resonator.

In the section "Lasers based on sharply nonlinear loss", we develop the quantum theory of lasers with nonlinear loss. We derive a set of "quantum rate equations" – operator-valued rate equations with fluctuating driving terms (Langevin forces) – to describe inversion and photon number fluctuations of lasers. We then derive amplitude noise spectra describing the photon number fluctuations of the laser cavity to lowest nontrivial order in the mean-field approximation. The treatment provided allows one to account for quantum fluctuations in systems with a wide variety of gain media, including gases, molecular dyes, rare-earth dopants (as in solid-state lasers), and semiconductors.

In the section "Numerical evidence for the effects predicted in the manuscript", we provide numerical validation of the analytical theory developed here. In the first part, we show that the Fock- and sub-Poissonian state-generation effects follow from explicit time-evolution of the master equation corresponding to the Hamiltonian of Eq. (1) of the main text (under a white-noise approximation for the reservoir). In the second part, we provide numerical evidence for the Fock lasing effect. In particular, we show that by modifying the Hamiltonian to include a pumped two-level atom (representing a gain medium), we can create a system that supports steady states (of the Liouvillian) corresponding to low-noise states of light.

In the section "Summary of main results", we summarize the main new theoretical results developed in this work, for ease of quotation. In the section "Potential extensions of the theory", we provide a non-exhaustive list of potential extensions of the work presented here which we believe to be exciting directions of future work. We expect the results derived in the SI to have wider applicability than the Fock- and sub-Poissonian proposals considered in the main text. We believe in particular that the theoretical results concerning the master equations for these dissipative nonlinear systems, as well as the Langevin equations we derive, should provide a useful basis for application to the theory of many more complex optoelectronic device configurations. Finally, in the section "Supplementary figures", we provide additional data, as well as detailed lists of parameters for Figs. 3, 4 of the main text.

G.1 Quantum theory of a nonlinear resonator with frequency-dependent loss

G.1.1 Model and Hamiltonian of a system with nonlinear loss

The starting point in our analysis of loss in a nonlinear resonator with frequency-dependent loss is the specification of the Hamiltonian, which describes the nonlinear cavity, the frequency-dependent end-mirror, and all reservoirs responsible for dissipation of the photon. Let us describe each term in the total Hamiltonian in steps.

Nonlinear cavity. We start by describing the cavity. We will assume in all cases that we are under conditions of single-mode lasing, and can thus consider the electromagnetic field of the cavity as described by a single high-Q resonant mode. In the absence of photon nonlinearity, the Hamiltonian of the cavity would be simply $\hbar\omega a^\dagger a$, with $\hbar$ the reduced Planck constant, ω the frequency of the resonant mode, and a ($a^\dagger$) the annihilation (creation) operator of the cavity mode. Let us consider now what happens when a nonlinear element is introduced into the cavity.

Consider for example the case of a nonlinear crystal embedded in the cavity, leading to Kerr nonlinear shifts of the cavity frequency. The resulting cavity Hamiltonian can be written in the form $H_{\text{Kerr}} = \hbar\omega a^\dagger a + \frac{1}{6}\beta\hbar\omega : (a - a^\dagger)^4 :$ [425], where β is a nonlinear coupling constant, and :: denotes normal ordering. In the rotating-wave approximation (i.e., ignoring terms with unbalanced numbers of creation and annihilation operators), the Kerr nonlinearity takes the more commonly stated form $H_{\text{Kerr}} = \hbar\omega\left((1-\beta)a^\dagger a + \beta(a^\dagger a)^2\right)$ [425, 426]. The cavity eigenstates are Fock states of n photons with energy $E_n \equiv \hbar\omega_n = \hbar\omega\left[(1+\beta)n + \beta n^2\right]$. The Hamiltonian, in the number basis, may alternatively be written as

$$H_{\text{Kerr}} = \sum_{n=0}^{\infty} E_n T_{n,n}, \tag{G.1}$$

with T a projection operator (projector), which is generally defined as: $T_{i,j} \equiv |i\rangle\langle j|$. We have re-written the Hamiltonian in terms of projectors, as they will play an essential role in our theory of nonlinear lasers. Before moving on to the theory of nonlinear lasers, we point out that in this Kerr resonator, the excitation energy from a state with $n-1$ photons,

to a state with n photons, is $\omega_{n,n-1} = \omega(1 + 2\beta n)$. This is equivalent to the statement in classical nonlinear optics that the frequency of a nonlinear cavity shifts by an amount proportional to the intensity [540]. The interaction constant β is governed by the overlap integral between the (normalized) cavity mode $\mathbf{u}(\mathbf{r})$ and the third-order nonlinear susceptibility $\chi^{(3)}(\mathbf{r})$ (taken as a scalar here for simplicity). In particular $\beta = \left(\frac{3\hbar\omega}{8\epsilon_0}\right) \int d^3r\, \chi^{(3)}(\mathbf{r})|\mathbf{u}(\mathbf{r})|^4$. Its characteristic magnitude, for a crystal which fills the cavity, is $\frac{3\hbar\omega}{8\epsilon_0 V}\chi^{(3)}(\mathbf{r})$, with V the mode volume. Before moving on to discuss the other terms in the Hamiltonian, we note that a general *intensity-sensitive* nonlinear cavity will have a Hamiltonian of the form of Eq. (1) with the appropriate photon-number-dependent energies, and so our treatment applies more generally than to the case of Kerr nonlinearities.

Cavity losses. Now we move to a discussion of the terms in the Hamiltonian responsible for the losses of the cavity. For the photon, the reservoirs depend on the exact configuration. In the simplest (and most standard case) the photon is coupled to a single reservoir of far-field modes which convert the cavity photon into the emitted beam. To get the Fock and sub-Poissonian state-generation effect, we must go beyond this single cavity-reservoir coupling. The simplest modification that "does the job" is to introduce two resonances (a, d, as in Fig. 1 of the main text) that are coupled to the same reservoir. This mutual coupling to the same reservoir allows for the Fano-type interferences well-known from classical optics. This approach was recently used to describe the quantum optics of Fano mirrors in [541] (without nonlinearity). Compared to prior work, we consider the case where one of the resonances is nonlinear. In such cases, Fock-state generation is supported under appropriate conditions.

We now set up the Hamiltonian of the "nonlinear Fano resonance." Let us consider a situation in which one mode (labeled by its annihilation operator a, with anharmonic Hamiltonian H_a) is coupled to a second mode (e.g., a Fabry-Perot type mode, or a photonic crystal resonance), of frequency ω_d (labeled by annihilation operator d). In many cases, this second resonance d can be thought of as the resonance of an end-mirror of the cavity, and we will occasionally refer to d as the mirror. We take the d-resonance to be linear, with Hamiltonian $H_{\mathrm{d}} = \hbar\omega_d d^\dagger d$. The two modes in general are coupled by a (beam-splitter) interaction $\hbar(\lambda a d^\dagger + \lambda^* a^\dagger d)$. Both a and d are also coupled to the continuum of far-field

modes b_k outside of the cavity, where k enumerates the continuum of outside modes. For simplicity, we will consider a one-sided cavity, with one wall perfectly reflecting, and one partially reflecting, such that there is only a single input and output "port." Taking g_k and v_k to respectively be the coupling of b_k to a and d , the system-reservoir coupling Hamiltonian may be written as: $H_{\text{res}} = \sum_k \hbar g_k (a b_k^\dagger + a^\dagger b_k) + \sum_k \hbar v_k (d b_k^\dagger + d^\dagger b_k)$. The total Hamiltonian of the system and reservoir may thus be expressed as:

$$H/\hbar = H_a + \omega_d d^\dagger d + (\lambda a d^\dagger + \lambda^* a^\dagger d) + \sum_k \omega_k b_k^\dagger b_k + \sum_k (g_k a b_k^\dagger + g_k^* a^\dagger b_k) + \sum_k (v_k d b_k^\dagger + v_k^* d^\dagger b_k), \tag{G.2}$$

which coincides with Eq. (1) of the main text (defining $H_a = \hbar\Omega(a^\dagger a)$ and $X_k = g_k a + v_k d$). The simpler case of a Fabry-Perot mirror (with a symmetric transmission spectrum) is obtained in the limit where the "direct" coupling of the cavity mode to the far-field can be neglected ($g_k = 0$), so that the cavity must couple through the mirror if it is to escape into the far-field. The other important standard case is that in which the partially reflecting mirror has a frequency independent reflectivity, which corresponds to the case in which the d cavity has a very fast decay. We note that while the parameters λ, g_k, v_k could be in principle be calculated, it is typically impractical to do so, and they may in practice be found by comparing the transmission of the cavity to what is expected from a classical treatment of the cavity transmission (e.g., from temporal coupled mode theory).

G.1.2 Master equation of the nonlinear Fano resonance

In this section, we derive a master equation to describe the damping of a nonlinear resonator (a) due to radiative leakage from a frequency-dependent mirror. The overall Hamiltonian of the system+reservoir (a + d + reservoir) is given by Eq. (2). To simplify notation, we will define

$$H_{ad} \equiv H_a + \omega_d d^\dagger d + \left(\lambda a d^\dagger + \lambda^* a^\dagger d\right). \tag{G.3}$$

Let us now derive an equation of motion for the reduced density matrix of a and d (e.g., tracing out the reservoir). To do so, we define the interaction picture operators $\rho_I = e^{iH_0 t}\rho e^{-iH_0 t}$ and $V_I = e^{iH_0 t} V e^{-iH_0 t}$, with $H_0 = H_{ad} + \sum_k \omega_k b_k^\dagger b_k$ and $V = \sum_k \left(X_k b_k^\dagger + X_k^\dagger b_k\right)$.

Then, the equation of motion for the density matrix becomes $\dot{\rho_I} = -\frac{i}{\hbar}\left[V_I, \rho_I\right]$, admitting the iterative solution:

$$\dot{\rho_I} = -\frac{i}{\hbar}\left[V_I(t), \rho(0)\right] - \frac{1}{\hbar^2}\int_0^t dt' \ \left[V_I(t), \left[V_I(t'), \rho_I(t')\right]\right], \tag{G.4}$$

with $\rho(0) = \rho_I(0)$ being the initial state of the system and reservoir. As we will primarily be interested in the application of this framework at optical frequencies, we will consider the reservoir to be in its vacuum state (i.e., negligible thermal population). The dynamics of the resonator and end-mirror are obtained by taking the partial trace with respect to the bath ($\dot{\rho}_{ad} \equiv \text{tr}_b \rho$), such that

$$\dot{\rho}_{ad,I} = -\frac{i}{\hbar}\text{tr}_b\left(\left[V_I(t), \rho(0)\right]\right) - \frac{1}{\hbar^2}\int_0^t dt' \ \text{tr}_b\left(\left[V_I(t), \left[V_I(t'), \rho_I(t')\right]\right]\right). \tag{G.5}$$

Upon taking the trace with respect to the bath, the term which is linear in V_I will vanish, and the equation of motion becomes

$$\begin{aligned}\dot{\rho}_{ad,I} = -\frac{1}{\hbar^2}\int_0^t dt' \ \text{tr}_b(&V_I(t)V_I(t')\rho_I(t') + \rho_I(t')V_I(t')V_I(t) \\ &- V_I(t)\rho_I(t')V_I(t') - V_I(t')\rho_I(t')V_I(t)).\end{aligned} \tag{G.6}$$

To proceed, we need further approximations. As the coupling of system and reservoir is weak, and the continuum of radiation modes loses memory over a very short timescale (due to its infinite bandwidth), we make the standard Markov approximation. Namely, that ρ factorizes as $\rho_I(t') = \rho_{ad,I}(t')\rho_b(0)$, with ρ_b being the density matrix of the multi-mode vacuum reservoir. Moreover, due to the weak coupling of a and d to the reservoir, the system-reservoir couplings can be approximated as frequency-independent (such that $g_k \approx g$ and $v_k \approx v$). It follows that the first term, under these approximations, evaluates to $X_I(t)X_I^\dagger(t')\rho_{ad}(t')\sum_k e^{i\omega_k(t-t')} = X_I(t)X_I^\dagger(t')\rho_{ad}(t')(2\pi\rho_0\delta(t-t'))$, with ρ_0 the density of states of the far-field continuum (which under these approximations is frequency-independent). Performing the time-integration yields $X_I(t)X_I^\dagger(t)\rho_{ad}(t)$. The other terms

are evaluated in a similar fashion, yielding

$$\dot{\rho}_{ad,I} = -2\pi\rho_0 \left(X_I^\dagger(t) X_I(t) \rho_{ad,I}(t) + \rho_{ad,I}(t) X^\dagger(t) X_I(t) - 2 X_I(t) \rho_{ad,I}(t) X_I^\dagger(t) \right). \tag{G.7}$$

Going back to the Schrodinger picture, one has the equation of motion for the system (a + d):

$$\dot{\rho} = -i[H_{ad}, \rho] - 2\pi\rho_0 \left(X^\dagger X \rho + \rho X^\dagger X - 2 X \rho X^\dagger \right), \tag{G.8}$$

where we have taken $\rho_{ad} \to \rho$ for simplicity of notation (the bath will no longer enter the equations).

Eq. (8) can be taken as the first-principles master equation for the nonlinear Fano resonance, upon which we will make further approximations to analytically isolate the nonlinear loss presented in the main text (e.g., Eqs. (2-4) of the main text). Note that, as compared to standard master-equation descriptions of lossy systems, Eq. (8) is of a similar Lindblad form, except that the jump operator X couples the two modes. In Section III, where we present "exact" numerical evidence for the Fock- and sub-Poissonian state generation effects, we do so by directly solving Eq. (8) in time. Now, we move to simplify Eq. (8) further.

We are mainly interested in the limit in which the d resonance responds instantaneously to changes in the frequency of the cavity mode. In other words, in the limit of $\gamma \equiv 2\pi\rho_0 v^2$ being the fastest timescale of the problem (so for example, $\gamma \gg \kappa \equiv 2\pi\rho_0 g^2$). Physically, thinking of d as the end-mirror, it refers to a situation where the mirror responds to the instantaneous frequency of a (to which the mirror can immediately respond due to its large bandwidth). Under this condition, we may adiabatically eliminate d from the master equation of Eq. (8), getting an equation of motion for a alone.

The adiabatic elimination proceeds along similar lines to the derivation of Eq. (8): we must look at the evolution of the cavity density matrix to second-order in the coupling between a and d. The procedure to arrive at the equation for a is thus similar in spirit to the procedure leading to Eq. (5). A major difference in execution arises from the fact that the free dynamics of d include damping (which is "fast"), and so the interaction-picture transformation must include the effect of damping. Therefore, the Liouvillian to be exponen-

tiated contains a Lindblad term. While interaction picture transformations of Liouvillians with Lindblad terms are a "basic" part of density-matrix theory, they are not as commonplace in the literature ([542] provides a good account). Thus, we shall provide more of the intermediate manipulations than in other sections of the SI.

The equation of motion for the density matrix (in the Schrodinger picture) may be written as

$$\dot{\rho} = (\mathcal{L}_0 + \mathcal{L}_1)\rho, \tag{G.9}$$

where

$$\mathcal{L}_0 \equiv -i[H_a/\hbar + \omega_d d^\dagger d, \cdot] - \gamma(d^\dagger d \cdot + \cdot d^\dagger d - 2d^\dagger \cdot d), \tag{G.10}$$

and

$$\begin{aligned}\mathcal{L}_1 \equiv & -i[\lambda a d^\dagger + \lambda^* a^\dagger d, \cdot] - \kappa(a^\dagger a \cdot + \cdot a^\dagger a - 2a^\dagger \cdot a) \\ & -\sqrt{\kappa\gamma}\left((ad^\dagger + a^\dagger d)\cdot + \cdot (ad^\dagger + a^\dagger d) - 2\left(a \cdot d^\dagger + d \cdot a^\dagger\right)\right).\end{aligned} \tag{G.11}$$

Here, we have introduced the $\cdot$ notation, which indicates how the Liouvillian acts on an operator. For example, for arbitrary operators X, ρ, we have: $(X\cdot)\rho \equiv X\rho$ and $(\cdot X)\rho = \rho X$. Terms of the form $(X \cdot Y)\rho$, for arbitrary X, Y should be understood as $(X\cdot)(\cdot Y)\rho = X\rho Y$. The terms Eq. (11) may also be regrouped to read as:

$$\begin{aligned}\mathcal{L}_1 = & -\kappa(a^\dagger a \cdot + \cdot a^\dagger a - 2a^\dagger \cdot a) \\ & -\left(G_-(ad^\dagger\cdot) + G_-^*(\cdot a^\dagger d)\right) - \left(G_+(a^\dagger d) + G_+(\cdot ad^\dagger)\right) + 2\sqrt{\kappa\gamma}\left(a \cdot d^\dagger + d \cdot a^\dagger\right),\end{aligned} \tag{G.12}$$

with $G_- \equiv i\lambda + \sqrt{\kappa\gamma}$ and $G_+ \equiv i\lambda^* + \sqrt{\kappa\gamma}$. This expression proves more convenient for the manipulations that follow.

We now define the interaction picture density matrix ρ_I as

$$\rho = e^{\mathcal{L}_0 t}\rho_I, \tag{G.13}$$

so that

$$\dot{\rho}_I = e^{-\mathcal{L}_0 t}\mathcal{L}_1 e^{\mathcal{L}_0 t}\rho_I \equiv \mathcal{L}_I(t)\rho_I. \tag{G.14}$$

This equation admits an iterative solution of the form

$$\dot{\rho}_{a,I} = \mathrm{tr}_d\left[\mathcal{L}_I(t)\rho_I(0)\right] + \int^t dt'\ \mathrm{tr}_d\left[\mathcal{L}_I(t)\mathcal{L}_I(t')\rho_I(t')\right]. \tag{G.15}$$

This equation is considerably simplified in the limit where γ is large: in this case, d acts as a broad continuum for a (in other words, as a reservoir). Moreover, d cannot sustain any build-up of excitations, as they damp immediately (on any timescale related to a). It follows that from the perspective of a, d acts as a vacuum reservoir $|0\rangle\langle 0|$, and that the state of the joint system may be written in factorizable form: $\rho_I(t) \approx \rho_{a,I}(t)|0\rangle\langle 0|$. This allows us to write Eq. (15) in the Born-Markov approximation as

$$\dot{\rho}_{a,I} = \mathrm{tr}_d\left[\mathcal{L}_I(t)\rho_a(t)|0\rangle\langle 0|\right] + \int^t dt'\ \mathrm{tr}_d\left[\mathcal{L}_I(t)\mathcal{L}_I(t')\rho_a(t)|0\rangle\langle 0|\right]. \tag{G.16}$$

Here, we have also made an adiabatic approximation, replacing $\rho_a(t')$ with $\rho_a(t)$, since significant contributions to the integrand only arise when t' is within γ^{-1} of t. Over this range of times, the density matrix of d does not vary. To proceed, we must now evaluate the interaction picture Liouvillian operators to second-order, and then evaluate the integrals that arise. The following interaction-picture transformations for d are used heavily in what follows (see [542]):

$$\begin{aligned}
(d\cdot)_I(t) &= e^{-i\omega_d t-\gamma t}(d\cdot)\\
(\cdot d^\dagger)_I(t) &= [(d\cdot)_I(t)]^\dagger = e^{i\omega_d t-\gamma t}(\cdot d^\dagger)\\
(d^\dagger\cdot)_I(t) &= e^{i\omega_d t}\left(e^{\gamma t}(d^\dagger\cdot) + (e^{-\gamma t}-e^{\gamma t})(\cdot d^\dagger)\right)\\
(\cdot d)_I(t) &= [(d^\dagger\cdot)_I(t)]^\dagger = e^{-i\omega_d t}\left(e^{\gamma t}(\cdot d) + (e^{-\gamma t}-e^{\gamma t})(d\cdot)\right).
\end{aligned} \tag{G.17}$$

Similarly, the interaction picture transformations for a are given as

$$(a\cdot)_I(t) = [(\cdot a^\dagger)_I(t)]^\dagger = \sum_{n=0}^{\infty} \sqrt{n} e^{-i\omega_{n,n-1}t}(T_{n-1,n}\cdot)$$
$$(a^\dagger\cdot)_I(t) = [(\cdot a)_I(t)]^\dagger = \sum_{n=0}^{\infty} \sqrt{n+1} e^{i\omega_{n+1,n}t}(T_{n+1,n}\cdot), \tag{G.18}$$

where we have defined the projector $T_{ij} = |i\rangle\langle j|$. Note that due to the polychromatic nature of a (being anharmonic), this is the most convenient way to express the interaction picture operator. With these identities established, we now evaluate the first- and second-order terms of Eq. (12).

As d is in the vacuum state, no terms in $\mathcal{L}_1$ involving d or $d^\dagger$ contribute to the first-order term. Therefore, the first order term is simply $-\kappa(a_I^\dagger a_I \cdot + \cdot a_I^\dagger a_I - 2a_I^\dagger \cdot a_I)$, and in the Schrodinger picture, gives the expected term $-\kappa(a^\dagger a\cdot + \cdot a^\dagger a - 2a^\dagger \cdot a)$. Now we evaluate the second-order term. To proceed, we note that since $\gamma \gg \kappa$, we may neglect contributions of order greater than κ. Hence, we may completely ignore the first line of Eq. (12) for the purposes of evaluating the second-order term. After some algebra, one finds that the second order integrand, under the assumption that d is in the vacuum state, is given by:

$$\begin{aligned}
&-|G_-|^2 \mathrm{tr}_d\left[a_I(t)d_I^\dagger(t)\rho_a(t)|0\rangle\langle 0|a_I^\dagger(t')d_I(t')\right] - G_+G_-\mathrm{tr}_d\left[a_I^\dagger(t)d_I(t)a_I(t')d_I^\dagger(t')\rho_a(t)|0\rangle\langle 0|\right] \\
&-|G_-|^2 \mathrm{tr}_d\left[a_I(t')d_I^\dagger(t')\rho_a(t)|0\rangle\langle 0|a_I^\dagger(t)d_I(t)\right] - (G_+G_-)^*\mathrm{tr}_d\left[\rho_a(t)|0\rangle\langle 0|a_I^\dagger(t')d_I(t')a_I(t)d_I^\dagger(t)\right] \\
&+2\sqrt{\kappa\gamma}\mathrm{tr}_d\left[a_I(t)\rho_a(t)|0\rangle\langle 0|a_I^\dagger(t')d_I(t')d_I^\dagger(t)\right] + 2\sqrt{\kappa\gamma}\mathrm{tr}_d\left[d_I(t)a_I(t')d_I^\dagger(t')\rho_a(t)|0\rangle\langle 0|a_I^\dagger(t)\right].
\end{aligned} \tag{G.19}$$

Plugging in the interaction picture operators of Eqs. (17) and (18), and evaluating the t'-integral, one arrives at the following final result (in the Schrodinger picture):

$$\begin{aligned}
\dot{\rho} = &-\kappa(a^\dagger a\rho + \rho a^\dagger a - 2a\rho a^\dagger) \\
&+ \sum_{n=0}^{\infty} \frac{nG_+G_-}{i(\omega_d - \omega_{n,n-1}) + \gamma} T_{n,n}\rho + \sum_{n=0}^{\infty} \frac{n(G_+G_-)^*}{-i(\omega_d - \omega_{n,n-1}) + \gamma} \rho T_{n,n} \\
&- \sum_{m,n=0}^{\infty} \frac{\sqrt{m(n+1)}(G_+G_-)^*}{-i(\omega_d - \omega_{n+1,n}) + \gamma} T_{m-1,m}\rho T_{n+1,n} - \sum_{m,n=0}^{\infty} \frac{\sqrt{m(n+1)}(G_+G_-)}{i(\omega_d - \omega_{m,m-1}) + \gamma} T_{m-1,m}\rho T_{n+1,n}.
\end{aligned} \tag{G.20}$$

Here, we have taken $\rho_a \rightarrow \rho$, as no further reference will be made to the density operator of d. Eq. (20) could be considered the main theoretical result of this work: it prescribes the dissipation dynamics of an anharmonic oscillator subject to dispersive loss. The equation governs the evolution of the entire density matrix of the anharmonic oscillator: not only the evolution of the populations (which are important for Fock state generation), but also the quantum coherences between different photonic states, which are important for monitoring the build-up and decay of phase and intensity correlations. Eq. (20) also serves as a foundation for the quantum Langevin description of nonlinear loss in systems with the Hamiltonian of Eq. (2). This Langevin description enables us to study the quantum fluctuations of devices that use this nonlinear loss, such as lasers. For all of these reasons, the density matrix equation, Eq. (20) provides the rigorous theoretical foundation for this work.

To make contact with the notations established in the main text (as well as more standard forms of the master equation), we will make the changes of definition $\kappa \rightarrow \kappa/2$ and $\gamma \rightarrow \gamma/2$. Additionally, we define the complex quantity $\mu_n = \frac{1}{2}\kappa - \frac{G_+G_-}{i(\omega_d - \omega_{n,n-1}) + \gamma/2}$. Eq. (20) is then expressed as:

$$\dot{\rho} = -\sum_{n=0}^{\infty} n(\mu_n T_{n,n}\rho + \mu_n^* \rho T_{n,n}) + \sum_{m,n=0}^{\infty} \sqrt{m(n+1)}(\mu_m + \mu_{n+1}^*) T_{m-1,m}\rho T_{n+1,n}, \quad \text{(G.21)}$$

coinciding with Eq. (2) of the main text.

Equation of motion for photon probabilities

The diagonal components of the density matrix $\rho_{n,n}$ correspond to the probability p_n of there being n photons in a. As the main text is primarily focused on realizing Fock and macroscopic sub-Poissonian states of light (with probability distributions more tightly concentrated than Poisson), the equation of motion for the photon probabilities plays a central role. Taking the n, n matrix element of Eq. (21), one immediately finds

$$\dot{\rho}_{n,n} = -2n\text{Re}\ \mu_n \rho_{n,n} + 2(n+1)\text{Re}\ \mu_{n+1}\rho_{n+1,n+1}, \quad \text{(G.22)}$$

which is clearly of the form

$$\dot{p}_n = -L_n p_n + L_{n+1} p_{n+1}, \tag{G.23}$$

with $L_n = 2n\text{Re}\ \mu_n$ found as:

$$L_n = n\left(\frac{\kappa\delta_n^2 + \gamma|\lambda|^2 + 2\sqrt{\kappa\gamma}\delta_n|\lambda|\cos\phi}{\delta_n^2 + \gamma^2/4}\right) \tag{G.24}$$

establishing Eqs. (3-4) of the main text (noting that $p(n) \equiv \rho_{n,n}$).

The solution of Eq. (23) provides the time-dependent probability distribution of a, giving access to all moments of the photon number operator. In many cases, we are primarily only interested in the dynamics mean and the variance. Thus, it is useful to derive an equation of motion for the mean and variance of the probability distribution. We shall do so in the approximation that the uncertainty Δn is small compared to the mean $\bar{n}$, a statement which is almost always valid for states we consider, including Poissonian states (where $\Delta n = \sqrt{\bar{n}} \ll \bar{n}$ provided $\bar{n} \gg 1$). As a result of Eq. (23), a general moment of the distribution $\langle n^k \rangle$ evolves according to

$$\dot{\langle n^k \rangle} = -\sum_{n=0}^{\infty} n^k L_n p_n + \sum_{n=0} n^k L_{n+1} p_{n+1}. \tag{G.25}$$

Shifting the index of the second term from $n+1 \to n$ and making use of the fact that $L_0 = 0$, we find

$$\dot{\langle n^k \rangle} = \langle\Big((n-1)^k - n^k\Big) L(n)\rangle, \tag{G.26}$$

Thus, the mean evolves according to:

$$\dot{\bar{n}} = -\langle L(n)\rangle, \tag{G.27}$$

where we have denoted the mean as $\bar{n}$ to make contact with notations from the main text (other average quantities in this section will not get a bar). The second moment evolves according to:

$$\dot{\langle n^2 \rangle} = -\langle(2n-1)L(n)\rangle. \tag{G.28}$$

The variance satisfies the equation of motion $(\Delta\dot{n})^2 = \langle \dot{n^2} \rangle - 2\bar{n}\dot{\bar{n}}$. To proceed, we will consider distributions for which the distribution is sharply peaked about mean $\bar{n}$ (and is singly-peaked), such that $\Delta n \ll \bar{n}$. In this case, we make a continuous approximation for the probability distribution: $p_n \to p(n)$, with averages given by $\langle f(n) \rangle = \int_0^\infty dn\ f(n)p(n)$. Since the distribution is sharply peaked compared to the scale of variation of $L(n)$, we may Taylor expand the loss about the mean: $L(n) \approx L(\bar{n}) + (n-\bar{n})L'(\bar{n}) + \frac{1}{2}L''(\bar{n})(n-\bar{n})^2$. To lowest order, the mean simply evolves according to

$$\dot{\bar{n}} = -L(\bar{n}). \tag{G.29}$$

Meanwhile, the variance is found as:

$$\begin{aligned}
(\Delta\dot{n})^2 &= -\int_0^\infty dn\ p(n)(2(n-\bar{n})-1)L(n) \\
&= -\int_0^\infty dn\ p(n)(2(n-\bar{n})-1)\left(L(\bar{n}) + (n-\bar{n})L'(\bar{n}) + \frac{1}{2}L''(\bar{n})(n-\bar{n})^2\right) \\
&= L(\bar{n}) - \left(2L'(\bar{n}) - \frac{1}{2}L''(\bar{n})\right)(\Delta n)^2 + O((\Delta n)^3) \\
&\approx L(\bar{n}) - 2L'(\bar{n})(\Delta n)^2.
\end{aligned} \tag{G.30}$$

Here, we have used the simplification that $\langle n - \bar{n} \rangle = 0$. We have also ignored higher order variations in the distribution, and made a somewhat crude approximation that $4L' \gg L''$, which occurs when the distribution varies over a scale large compared to 1 (and hence is not perfectly accurate in the Fock-state regime). Still, the approximate equations capture the dynamics of the first two cumulants fairly well. The approximate equations for the cumulants, Eqs. (29) and (30) correspond to Eq. (6) of the main text.

Equation of motion for field coherences

Although we do not use this result in the main text, we expect that the equation of motion for the off-diagonal terms will play an important role in a theory of phase and higher-order coherence in the presence of nonlinear loss. Hence, we provide an explicit equation of motion for the kth coherence, corresponding to the off-diagonal components of the density

matrix $\rho_{n-k,n}$. The equation of motion follows from Eq. (21) as

$$\dot{\rho}_{n-k,n} = -((n-k)\mu_{n-k}+n\mu_n^*)\rho_{n-k,n}+\sqrt{(n-k+1)(n+1)}(\mu_{n-k+1}+\mu_{n+1}^*)\rho_{n-k+1,n+1}. \tag{G.31}$$

G.1.3 Physical interpretation of the loss terms

Let us now discuss the physical interpretation of the loss found in Eq. (24). We shall take two approaches. In the first, we derive the Heisenberg equations of motion for this system, neglecting nonlinearity, and examine the mean-field limit. We will show that the resulting model coincides with the so-called Friedrich-Wintgen model of two spatially co-located resonances with a common port. This model is known to support bound states in the continuum: modes that, although embedded in a reservoir of continuum states, have zero [472]. This will be due to destructive interference (of the Fano type, between two different leakage pathways). In the second, we show that the loss is what would be expected from a mirror with a frequency dependent Fano reflectivity profile (by comparing to the standard classical model of Fano resonances).

Connection to Fano interference and to bound states in the continuum

We derive a Heisenberg equation of motion for a and d in the absence of nonlinearity. In the Appendix, we derive Heisenberg equations taking into account nonlinearity, and show that in the adiabatic approximation, identical conclusions are drawn (as compared to the density matrix treatment of the previous sections). From the Hamiltonian of Eq. (2), the Heisenberg equations of motion for a, d, b_k are given as:

$$\begin{aligned}
\dot{a} &= -i\omega_a a - i\lambda^* d - i\sum_k g_k^* b_k \\
\dot{d} &= -i\omega_d d - i\lambda a - i\sum_k v_k^* b_k \\
\dot{b}_k &= -i\omega_k b_k - i(g_k a + v_k d).
\end{aligned} \tag{G.32}$$

To proceed, we will eliminate the reservoir. The formal solution to the reservoir equation of motion is given as

$$b_k(t) = b_k(t_0)e^{-i\omega_k(t-t_0)} - i\int_{t_0}^{t} dt'\, e^{-i\omega_k(t-t')}(g_k a(t') + v_k d(t')), \tag{G.33}$$

with t_0 being the initial time (e.g., $t_0 = 0$ or $t_0 = -\infty$). Plugging this into the equation of motion for a and d, and considering a white-noise reservoir $g_k = g$, $v_k = v$ (with both g, v real), we have

$$\begin{pmatrix} \dot{a} \\ \dot{d} \end{pmatrix} = \left[-i\omega_d - \begin{pmatrix} i\delta + \frac{1}{2}\kappa & i\lambda^* + \frac{1}{2}\sqrt{\kappa\gamma} \\ i\lambda + \frac{1}{2}\sqrt{\kappa\gamma} & \frac{1}{2}\gamma \end{pmatrix} \right] \begin{pmatrix} a \\ d \end{pmatrix} + \begin{pmatrix} F_a \\ F_d \end{pmatrix}. \tag{G.34}$$

Here, we have defined $\kappa = 2\pi\rho_0 g^2$ and $\gamma = 2\pi\rho_0 v^2$, with ρ_0 the density of continuum states. The terms F_a and F_d are operator-valued Langevin forces (Langevin forces will be elaborated on in the section "Quantum Langevin theory of the nonlinear Fano resonance"). They have the property that for a vacuum reservoir, $\langle F_{a,d}\rangle = 0$. The non-zero second-order correlators, for a vacuum reservoir, are given as $\langle F_a(t)F_a^\dagger(t')\rangle = \kappa\delta(t-t')$, $\langle F_d(t)F_d^\dagger(t')\rangle = \gamma\delta(t-t')$, and $\langle F_a(t)F_d^\dagger(t')\rangle = \langle F_d(t)F_a^\dagger(t')\rangle = \sqrt{\kappa\gamma}\delta(t-t')$.

As discussed in the main text, much intuition can be built by examining the equation of motion for the mean values of a, d, which we denote as A, D. The equation of motion:

$$\begin{pmatrix} \dot{A} \\ \dot{D} \end{pmatrix} = \left[-i\omega_d - \begin{pmatrix} i\delta + \frac{1}{2}\kappa & i\lambda^* + \frac{1}{2}\sqrt{\kappa\gamma} \\ i\lambda + \frac{1}{2}\sqrt{\kappa\gamma} & \frac{1}{2}\gamma \end{pmatrix} \right] \begin{pmatrix} A \\ D \end{pmatrix}. \tag{G.35}$$

is simply Eq. (5) of the main text. Let us now diagonalize this matrix to isolate the coupled modes of the system. The two eigenvalues are found to differ considerably in overall scale (assuming $\kappa \ll \gamma$), one is $O(\gamma)$, while the other is $O(\kappa)$ (and the corresponding eigenvector is approximately a). The lower loss mode (which is $O(\kappa)$) has eigenvalue

$$z = \frac{1}{4}\left(-\gamma - 2i\delta - \kappa + \sqrt{(\gamma + 2i\delta + \kappa)^2 - 4(2i\gamma\delta - 4i\sqrt{\kappa\gamma}\text{Re }\lambda + 4|\lambda|^2)} \right). \tag{G.36}$$

In the limit of $\kappa, \lambda \ll \gamma$, we find that the real part of the eigenvalue is simply

$$\text{Re } z = -\frac{1}{2}\frac{\kappa\delta^2 + \gamma|\lambda|^2 + 2\sqrt{\kappa\gamma}\delta\text{Re } \lambda}{\delta^2 + \gamma^2/4}. \tag{G.37}$$

The associated temporal loss coefficient of the mode is simply $\kappa = -2\text{Re } z$, which coincides with the loss $L_n = n\kappa(n)$ Eq. (24), except that the detuning is not n-dependent in Eq. (37) (as we have not included nonlinearity). This comparison however makes it clear that the effect of nonlinearity is simply to control the value of δ: stated operationally, the role of nonlinearity is to take $\delta \to \delta_n$.

Now, let us connect this result to the physics of Fano interference and the related phenomenon of bound states in the continuum. For certain values of the parameters $(\kappa, \gamma, \lambda)$ in Eq. (37), the loss can disappear. This is due to destructive interference of (1) a direct pathway for a to leak out and (2) a pathway in which a couples into d before leaking out. To see more explicitly how the loss can vanish, consider the case of no direct coupling ($\lambda = 0$). Such an interference is known as Fano interference, as it can lead to an asymmetric lineshape in the presence of a non-zero λ. In this case, the numerator of Eq. (37) is simply $\kappa\delta^2$, which vanishes for $\delta = 0$ (corresponding to the usual Fano transmission dip to be elaborated on in the next subsection). This mode, which has exactly zero loss, is known as a bound state in the continuum (BIC), which is of much recent interest in photonics (see e.g., [472] for a review of the field). It is referred to as such because the cavity mode is localized (it does not leak), despite the existence of a reservoir of far-field modes for which this cavity mode can couple.

These BICs can be shown to follow from exactly the classical model of Eq. (35) (see Eq. 4 of [472]), which is referred to as the Friedrich-Wintgen model [543], which is known to provide a simple model of BIC formation. Our quantum mechanical treatment of this system (in the linear case, as in Eq. (34)) and in the nonlinear case is thus tantamount to a quantum theory of nonlinear bound states in the continuum, which appear to lead to Fock- and sub-Poissonian state generation. To our knowledge, such a quantum mechanical model, and these conclusions have not been previously reported.

Interpretation of d-mode as a frequency-dependent mirror

To get a further understanding of Eq. (24), let us consider a related problem: the transmission and reflection of classical light scattering from a Fano mirror (a system with a Fano resonance). This problem has been studied by many authors, and is commonly considered in the field of nanophotonics. Consider a wave incident on a Fano mirror surrounded by air (e.g., a photonic crystal mirror). The wave has frequency ω, the Fano mirror has frequency ω_0, and radiative losses governed by the amplitude decay time $2/\gamma$ with γ the energy decay rate. It can be shown [1, 469] that the energy transmission coefficient is then given by

$$T = \frac{|t_d|^2\delta^2 + |r_d|^2\gamma^2/4 \pm |r_d t_d|\gamma\delta}{\delta^2 + \gamma^2/4}, \tag{G.38}$$

with $\delta = \omega - \omega_0$ and r_d, t_d representing reflection and transmission coefficients associated with the *direct* reflection and transmission of the incident light (i.e., without coupling into the internal mode of the mirror). These direct channels interfere with the indirect channel. Here, the $\pm$ denotes the case of an even/odd mode. Comparing this with Eq. (24), we see that the losses are quite similar in form. In fact, we see that by taking Eq. (24) and applying: $\omega \to \omega_{n,n-1}, \gamma \to \gamma, |t_d| \to \sqrt{\frac{2L\kappa}{c}}, |r_d| \to \sqrt{\frac{8L}{c\gamma}}|\lambda|$, with L the length of the cavity supporting mode a, we have:

$$T_n \equiv T(\omega_{n,n-1}) = \frac{2L}{c}\frac{\kappa\delta_n^2 + \gamma|\lambda|^2 \pm 2\sqrt{\kappa\gamma}\delta_n|\lambda|}{\delta_n^2 + \gamma^2/4}, \tag{G.39}$$

which, stated differently, can be written as

$$L_n = n \times \left(\frac{cT_n}{2L}\right), \tag{G.40}$$

for the case of $\phi = 0$ or π. This is Eq. (4) of the main text. Our model also considers more general coupling phases between the direct and indirect channels.

Thus, the physical interpretation is evidently that the loss per photon (L_n/n) is simply the round-trip rate of light propagation in the cavity, multiplied by the cavity transmission. The mode d acts as the resonance associated with a frequency-dependent end-mirror (this viewpoint is also described from a quantum mechanical density matrix model in [541]).

This is largely what one intuitively expects, and is borne out from the density-matrix approach in the adiabatic approximation. This identification however, suggests a generalization to more complicated Fano mirrors, supporting perhaps multiple internal modes: the loss can be specified in terms of the experimental transmission as a function of frequency.

G.1.4 Quantum Langevin theory of the nonlinear Fano resonance

In this section, we develop a complementary perspective on the description of dissipation in a nonlinear resonator with sharply varying loss. In quantum optics, it is well-established that there are two often equivalent ways to describe dissipation. The first is by deriving a master equation for the density-matrix, as we have in the section titled "Master equation of the nonlinear Fano resonance." The second is by deriving quantum Langevin (or Heisenberg-Langevin (HL)) equations for the Heisenberg-picture operators for the system. The quantum Langevin equations resemble classical equations that describe damping, except with operator-valued forces added to the equations to ensure preservation of operator commutation relations at all times. The two methods are complementary to each other, and each presents definite advantages over the other. In the density matrix approach, the equations for the density matrix elements are linear, and it is possible to find the evolution of the density matrix elements in a conceptually straightforward way. The density matrix method is the one which is mostly used in modern quantum engineering, and we have thus made the density-matrix approach the primary method.

On the other hand, the Heisenberg-Langevin equations are generally nonlinear operator equations with quantum stochastic force terms that have no definite numerically implementable representation (though they may be mapped to classical stochastic differential equations which can then be solved). However, the main analytical advantages of the HL approach emerge in situations where quantum fluctuations are small compared to the mean values (as is the case in every system we analyze in the main text). In that case, operator expectation values, even for macroscopic states of light (that cannot be numerically stored as a density matrix, due to sheer dimensionality), can be readily found through a small number of coupled linear differential equations. From a fundamental standpoint, the

Heisenberg-Langevin approach also has the advantage of bearing close similarity to classical equations of motion and thus providing a great deal of intuition. Very often, one may simply take classical equations, add stochastic force terms, and find the correlation functions of the forces through the so-called "Einstein relation" (as described in textbooks such as [544, 545]). The Langevin approach has proven itself to be very useful in the context of laser physics for this reason. From the standpoint of lasers, it is also important because: for many important gain media, such as solid-state and semiconductor gain media, one cannot eliminate the gain from the density matrix, and thus cannot express the dynamics of the photon in terms of a time-local differential equation. Motivated by these advantages, we now develop the Heisenberg-Langevin equations for the photon number operator in a system with the nonlinear loss of Eq. (24).

We follow the general method for deriving Langevin equations for quantum systems presented in Ref. [546] (there, the method is applied to derive Langevin equations for a two-level system). The method allows us to derive a Langevin equation in correspondence with the density matrix equation, Eq. (21). Let us derive a Langevin equation to describe the evolution of the photon number operator, which is related to the photon probabilities, and thus the diagonal components of the density matrix. In the method of Ref. [546], one "Langevinizes" the density matrix equation, e.g., Eq. (23), by assuming an equation of the form

$$\dot{T}_{n,n} = -L_n T_{n,n} + L_{n+1} T_{n+1,n+1} + F_{n,n}, \tag{G.41}$$

where $T_{n,n} = |n\rangle\langle n|$ is a projector whose expectation value is simply p_n. The $F_{n,n}$ are operator valued Langevin forces associated with the quantum fluctuations which are concomitant with nonlinear dissipation. The force is stipulated to have zero mean but finite second-order correlations that are delta-correlated (schematically $\langle F(t)F(t')\rangle = 2D\delta(t-t')$ for some operator-valued "diffusion coefficient" D). Note that Eq. (41) should be thought of as the operator equation in correspondence with Eq. (23): taking the expectation value $\mathrm{tr}[\rho\dot{T}_{n,n}] = \dot{p}_n$ yields $-L_n\rho_{n,n} + L_{n+1}\rho_{n+1,n+1}$ (using the fact that $\langle F_{n,n}\rangle = 0$).

For a general Langevin equation of the form $\dot{A}_\mu = D_\mu + F_\mu$, where A_μ and D_μ are system operators, and F_μ is a Markovian Langevin force of zero mean $-$ quantum me-

chanical consistency (e.g., preservation of commutators) imposes a constraint on the correlation functions between different forces (F_μ, F_ν). In particular, the correlators must satisfy the so-called Einstein relation for the diffusion coefficient $D_{\mu\nu}$, defined such that $\langle F_\mu(t)F_\nu(t')\rangle \equiv 2\langle D_{\mu\nu}\rangle\delta(t-t')$. The Einstein relation reads [545]:

$$2\langle D_{\mu\nu}\rangle = \frac{d}{dt}\langle A_\mu A_\nu\rangle - \langle A_\mu D_\nu\rangle - \langle D_\mu A_\nu\rangle, \tag{G.42}$$

As applied to Eq. (41), the corresponding D_μ is $-L_n T_{n,n} + L_{n+1}T_{n+1,n+1}$ and the corresponding F_μ is $F_{n,n}$.

First, we find the diffusion coefficient $\langle D_{jj,kk}\rangle$, defined such that:

$$\langle F_{j,j}(t)F_{k,k}(t')\rangle = 2\langle D_{jj,kk}\rangle\delta(t-t'). \tag{G.43}$$

It evaluates as:

$$\begin{aligned}
2\langle D_{jj,kk}\rangle &= \delta_{j,k}\langle \dot{T}_{j,j}\rangle - \langle T_{j,j}D_{k,k}\rangle - \langle D_{j,j}T_{k,k}\rangle \\
&= \delta_{j,k}\langle -L_j T_{j,j} + L_{j+1}T_{j+1,j+1}\rangle + \langle (L_k\delta_{jk}T_{j,j} - L_{k+1}\delta_{j,k+1}T_{j,j})\rangle \\
&+ \langle (L_j\delta_{j,k}T_{j,j} - L_{j+1}\delta_{j+1,k}T_{j+1,j+1})\rangle \\
&= \delta_{jk}(L_j\langle T_{j,j}\rangle + L_{j+1}\langle T_{j+1,j+1}\rangle) - \delta_{j,k+1}L_j\langle T_{j,j}\rangle - \delta_{j+1,k}\langle T_{j+1,j+1}\rangle.
\end{aligned} \tag{G.44}$$

As a sanity check on this result, consider the diffusion coefficient $2\langle D_{jj,jj}\rangle$. It evaluates as

$$2\langle D_{jj,jj}\rangle = L_j\langle T_{j,j}\rangle + L_{j+1}\langle T_{j+1,j+1}\rangle = L_j p_j + L_{j+1}p_{j+1}. \tag{G.45}$$

In other words, the diffusion coefficient is the sum of the rate of transitions into and away from the state of j photons. This property is a well-known result in the quantum theory of shot-noise [547], and indicates that the nonlinear loss dynamics can be thought of as associated with a type of *nonlinear shot noise* whose added fluctuations depend on the number of photons present.

The Einstein relation also enables us to specify a Langevin equation for the photon number operator itself (which is more readily measurable than the photon probabilities).

The number operator is expressed in terms of projectors as $n = \sum_{j=0}^{\infty} jT_{j,j}$. Therefore, we have

$$\begin{aligned}\dot{n} &= \sum_{j=0}^{\infty} -jL_jT_{j,j} + jL_{j+1}T_{j+1,j+1} + \sum_{j=0}^{\infty} jF_{j,j} \\ &= \sum_{j=0}^{\infty} -jL_jT_{j,j} + (j-1)L_jT_{j,j} + F_n \\ &= \sum_{j=0}^{\infty} -L_jT_{j,j} + F_n \\ &= -\kappa(n)n + F_n, \end{aligned} \tag{G.46}$$

where $L(n) = n\kappa(n)$ is understood to be a function of the n operator. In this derivation, we have identified $F_n = \sum_{j=0}^{\infty} jF_{j,j}$ and performed index manipulations similar to those used to derive Eq. (26). Eq. (46) is what one would write classically for a system with nonlinear loss, up to the Langevin force term F_n [1].

The corresponding diffusion coefficient for F_n may immediately be found from Eq. (45). In particular:

$$\begin{aligned}2\langle D_{n,n}\rangle &= \sum_{j,k=0}^{\infty} 2jk\langle D_{jj,kk}\rangle \\ &= \sum_{j,k=0}^{\infty} 2jk(\delta_{jk}(L_j\langle T_{j,j}\rangle + L_{j+1}\langle T_{j+1,j+1}\rangle) - \delta_{j,k+1}L_j\langle T_{j,j}\rangle - \delta_{j+1,k}\langle T_{j+1,j+1}\rangle) \\ &= \sum_{j=0}^{\infty} j(L_j\langle T_{j,j}\rangle - L_{j+1}\langle T_{j+1,j+1}\rangle) \\ &= \sum_{j=0}^{\infty} L_j\langle T_{j,j}\rangle = \langle n\kappa(n)\rangle. \end{aligned} \tag{G.47}$$

Eqs. (46) and (47) represent the main result of the Langevin theory of decay of an anharmonic oscillator with intensity-dependent loss of the type resulting from nonlinear dispersive loss introduced in Sec. II. Although we have derived the Langevin equation from the density matrix equation specific to the Hamiltonian of Eq. (2) − the content of Eqs. (46-S47) is more general and are expected to describe photon number fluctuations in

[1] As a somewhat well-known example, such an equation would be used to describe the dynamics of the energy in a resonator with a saturable absorber (with or without Langevin forces [540, 497])

generic systems for which the loss coefficient depends on photon number.

Before moving on to the analysis of lasers employing this sharp loss, we comment on the "Langevinization" procedure. As stated, Eq. (41) appears as an unjustified assumption (regardless of how well it works). We note that such an equation may also be more rigorously derived by considering an explicit reservoir, writing the Heisenberg equations of motion for a and d, and integrating out the reservoirs in the Markov and adiabatic approximations. This is demonstrated in the Appendix, and in some cases provides a cleaner derivation of the nonlinear loss of Eq. (24).

In the next section, we will use this Langevin equation, in conjunction with the standard Langevin equations describing a pumped gain medium, to derive the quantum statistical theory of lasers with sharp intensity-dependent loss. We then show how Fock and macroscopic sub-Poissonian states result.

G.2 Lasers based on sharply nonlinear loss

In this section, we develop the quantum theory of lasers which employ the nonlinear loss leading to Fock- and sub-Poissonian state generation. We shall approach the problem in steps: first, discuss the system purely classically, in terms of rate equations for the population inversion and the cavity photon number. Then we convert these equations into Langevin equations, which will give information about fluctuations in the inversion and the cavity photon number. We derive the amplitude noise spectrum for the cavity, which tells us about frequency-resolved fluctuations in the photon number, as well as the overall photon number uncertainty.

From there, we will discuss a particularly simple limit of the equations in which the inversion relaxation time is fast compared to the cavity decay. In that limit, the gain can be adiabatically eliminated, and a simple equation of motion may be derived for the cavity photon density matrix. Using this, we can derive a simple rule for the photon number fluctuations in terms of the value of the loss and its derivative at the steady-state, justifying Eq. (7) of the main text.

G.2.1 Quantum Langevin theory of photon number fluctuations in a system with sharp loss

As described in the beginning of the section, we start by reminding the reader of the classical analysis of the laser shown in Fig. 3b of the main text. We consider a single-mode cavity with nonlinear loss coefficient $\kappa(n)$ which interacts with a gain medium through emission and absorption. We consider a generic model of a gain medium: e.g., a four-level system in which the upper pumping level and the lower lasing level decay rapidly (through non-radiative processes). Thus, the only relevant populations in the equations are that of the lower pump level (the ground state) and the upper lasing level. Such conditions are well respected in many efficient gain media (as one example: solid-state gain media such as Nd:YAG). We also consider the limit in which the gain is approximately non-depleted, such that most of the population is in the lower pump level (the ground state). Under these conditions, it is very well known that the dynamical evolution (and steady-state) of the photon number and the gain are captured by the canonical rate equations (see any laser textbook, e.g., [548]). Denoting the inversion as N and the photon number as n, we have:

$$\begin{aligned} \dot{n} &= (R_{\text{sp}} N - \kappa(n)) n \\ \dot{N} &= \Lambda - \left(\gamma_{||} + R_{\text{sp}} n\right) N. \end{aligned} \tag{G.48}$$

Here, we have defined R_{sp} as the rate of spontaneous emission of the gain medium into the cavity mode (which, up to a prefactor, satisfies $R_{\text{sp}} = f\sigma_{\text{st}} v/V$ with f the filling fraction of the gain, σ_{st} the stimulated cross section of the gain, $v = c/n_{\text{eff}}$ the speed of light in the cavity, and V the cavity mode volume). We have also defined the pumping rate of the gain medium Λ (sometimes expressed as $\gamma_{||} N_0$ with $\gamma_{||}$ the rate of population decay and N_0 the unsaturated inversion). We have neglected terms related to spontaneous emission in both equations in (48), as they will be negligible (even from a quantum noise perspective).

Steady-state operating condition

To start, it will be useful to find the steady-state operating point of the laser, obtained by setting the left-hand side of Eq. (48) to zero. In that case, we have for the inversion:

$$N = \frac{\Lambda}{\gamma_{||} + R_{\text{sp}} n}, \tag{G.49}$$

and for the photon number:

$$\frac{R_{\text{sp}}\Lambda}{\gamma_{||} + R_{\text{sp}} n} = \frac{R_{\text{sp}} N_0}{1 + n/n_s} = \kappa(n), \tag{G.50}$$

where we have defined the saturation photon number $n_s = \gamma_{||}/R_{\text{sp}}$.

For a generic loss function $\kappa(n)$, the equilibrium condition cannot be solved analytically. However, it is easy to understand graphically, by plotting the saturable gain and the loss and looking for the intersection points, as we have in Figs. 3d and 4b of the main text. From such graphical solutions, it is easy to appreciate that if $\kappa(n_0) = 0$ for some $n_0 \neq 0$, it implies the existence of a solution of the equations for the mean for any non-zero value of Λ. In particular, even if $R_{\text{sp}} N_0 < \kappa(0)$, which means the gain is less than the loss (and thus the system will not lase), a solution will still exist (typically for n not very different from n_0). If the laser instead starts from a state with $n > n_0$ photons, it will move to this steady state.

Eq. (48) can be thought of the lowest-order description of the system in the mean-field approximation (e.g., replacing operators for the inversion and photon number by c-numbers). We now go beyond the mean-field approximation to find the fluctuations.

Quantum fluctuations

Let us now find the quantum statistics of a nonlinear laser with sharp loss. The simplest treatment of quantum fluctuations in lasers proceeds by adding quantum Langevin forces

to Eq. (48) [547]. In particular, we write:

$$\begin{aligned}\dot{n} &= \left(R_{\text{sp}}N - \kappa(n)\right)n + F_n \\ \dot{N} &= \Lambda - \left(\gamma_{||} + R_{\text{sp}}n\right)N + F_N.\end{aligned} \tag{G.51}$$

The diffusion coefficients for the forces are given by:

$$\begin{aligned}2D_{nn} &= \langle\left(R_{\text{sp}}N + \kappa(n)\right)n\rangle \\ 2D_{nN} &= 2D_{Nn} = -\langle R_{\text{sp}}Nn\rangle \\ 2D_{NN} &= \Lambda + \langle\left(\gamma_{||} + R_{\text{sp}}n\right)N\rangle.\end{aligned} \tag{G.52}$$

Compared to previous Langevin treatments of fluctuations in lasers (see as examples [547, 503, 544, 549]), the only difference is the presence of the nonlinear loss $\kappa(n)$. The remarkable statement is that when $\kappa(n)$ takes the form implied by Eq. (24), extremely sub-Poissonian states, approaching Fock states can result (with far lower noise than allowable by the types of low-order nonlinearities studied previously [478, 479, 480, 481]).

We now solve for the photon statistics. We are primarily interested in the cavity photon statistics at the steady-state operating point of the laser (thus we will not consider their evolution in time starting from vacuum). We will quantify the photon statistics primarily by the mean and variance of the cavity photon number (with a variance of zero corresponding to a cavity Fock state). In all cases we consider in this paper (even the noisiest ones), the quantum fluctuations of the photon number and inversion are small compared to the mean values. Thus, we may linearize the Langevin equations (which are nonlinear in n and N) around their mean values as: $n = \bar{n} + \delta n$ and $N = \bar{N} + \delta N$. The quantities $\bar{n}$ and $\bar{N}$ are c-number (mean) values (given by Eqs. (49) and (50)) while δn and δN are operator-valued fluctuations. It follows immediately from the definitions above, and the zero mean-values of the forces, that $\langle n\rangle = \bar{n}$ and $(\Delta n)^2 = \langle(\delta n)^2\rangle$. These fluctuations are of the same order as the Langevin forces F_n and F_N.

The fluctuations of the photon number and inversion satisfy the pair of coupled equa-

tions

$$\begin{pmatrix} \dot{\delta n} \\ \dot{\delta N} \end{pmatrix} = \begin{pmatrix} -\kappa'(\bar{n})\bar{n} & R_{\rm sp}\bar{n} \\ -R_{\rm sp}\bar{N} & -\left(\gamma_{||} + R_{\rm sp}\bar{n}\right) \end{pmatrix} \begin{pmatrix} \delta n \\ \delta N \end{pmatrix} + \begin{pmatrix} F_n \\ F_N \end{pmatrix}. \tag{G.53}$$

Here, we have introduced $\kappa'(n) = d\kappa/dn$, which quantifies the sharpness of the loss. To solve this equation, it is convenient to Fourier transform (defining e.g., $\delta n(t) = \int_{-\infty}^{\infty} \frac{d\omega}{2\pi}\, e^{-i\omega t}\delta n(\omega)$). The uncertainty in the photon number then follows as $(\Delta n)^2 = \int_{-\infty}^{\infty} \frac{d\omega}{2\pi}\, S_{nn}(\omega)$, with $S_{nn}(\omega) = \langle \delta n^\dagger(\omega)\delta n(\omega)\rangle$ being the cavity photon amplitude noise spectrum. The Fourier transformed equations read:

$$\begin{pmatrix} i\omega - \kappa'(\bar{n})\bar{n} & R_{\rm sp}\bar{n} \\ -R_{\rm sp}\bar{N} & i\omega - \left(\gamma_{||} + R_{\rm sp}\bar{n}\right) \end{pmatrix} \begin{pmatrix} \delta n(\omega) \\ \delta N(\omega) \end{pmatrix} = -\begin{pmatrix} F_n(\omega) \\ F_N(\omega) \end{pmatrix}. \tag{G.54}$$

This admits the solution:

$$\begin{pmatrix} \delta n(\omega) \\ \delta N(\omega) \end{pmatrix} = -\frac{1}{(\Omega^2 - \omega^2) - i\omega\eta} \begin{pmatrix} i\omega - \Gamma & -R_{\rm sp}\bar{n} \\ R_{\rm sp}\bar{N} & i\omega - \kappa'(\bar{n})\bar{n} \end{pmatrix} \begin{pmatrix} F_n(\omega) \\ F_N(\omega) \end{pmatrix}, \tag{G.55}$$

where we have defined $\Gamma = \gamma_{||} + R_{\rm sp}\bar{n}$, as well as the "relaxation oscillation frequency"

$$\Omega^2 = \left(\Gamma\kappa'(\bar{n}) + R_{\rm sp}\kappa(\bar{n})\right)\bar{n}, \tag{G.56}$$

and the "relaxation oscillation damping rate"

$$\eta = \Gamma + \kappa'(\bar{n})\bar{n}. \tag{G.57}$$

With these definitions, the photon number spectrum evaluates as:

$$S_{nn}(\omega) = 2\kappa(\bar{n})\bar{n} \times \frac{\omega^2 + \Gamma^2}{(\omega^2 - \Omega^2)^2 + \omega^2\eta^2}. \tag{G.58}$$

Noise spectra of this form are plotted in Fig. 4 of the main text.

G.2.2 Quantum statistics of lasers with sharp loss for fast inversion lasers

While the Langevin framework gives access to the fluctuations of the photon number in the steady-state, it is much less simple to acquire dynamical information regarding the probability distribution of the photon number (as well as higher-order moments of the distribution). It becomes possible to find explicitly a simple, temporally local equation of motion for the density matrix of the cavity photon as a function of time in the limit where the population decay of the gain medium $\gamma_{||}$ is fast compared to the cavity lifetime.

This so-called "class A regime" of laser operation often holds in gain media such as gases and molecular dyes. However, the inequality depends on the cavity lifetime, which can be made large using a long cavity or highly reflective mirrors. Thus in principle, semiconductor gain media can also behave as "class A" systems (for example, in external cavity configurations) – and even rare earth gain media in principle could (using cavities formed via crystalline supermirrors).

In this limit, the gain medium can be fully adiabatically eliminated. The resulting laser theory is called the Lamb-Scully theory of the laser [432, 433]. Let us now write down an equation of motion for the cavity photon density matrix for a system with gain and nonlinear loss. The contribution of the gain medium to the density matrix equation of motion is well-known from the Lamb-Scully theory, and so we merely quote the answer below. The loss terms of Eq. (23) can simply be added to the contributions from the gain, as the photon state (which changes on the cavity time-scale) hardly changes over the time-scale $\gamma_{||}, \gamma_{\perp}$.

The combined effect of the gain-medium and the cavity loss on the equation of motion for the photon probabilities is

$$p_n = A_n p_{n-1} - (A_{n+1} + L_n)p_n + L_{n+1}p_{n+1}, \tag{G.59}$$

where

$$A_n = \frac{An}{1 + n/n_s}, \tag{G.60}$$

with A the linear gain coefficient and n_s the saturation photon number. Here, we have assumed that the gain medium is resonant with the cavity. Few qualitative changes are introduced by including a finite detuning. Note that the value of A which ensures consistency with Eq. (49) is $A = R_{\text{sp}} N_0$.

The steady-state photon statistics are found by setting $\dot{p}_n = 0$ with the normalization constraint $\sum_n p_n = 1$. In steady-state, $\dot{p}_n = 0$ implies

$$A_n p_{n-1} - L_n p_n = A_{n+1} p_n - L_{n+1} p_{n+1}. \tag{G.61}$$

Defining the difference $S_n = A_n p_{n-1} - L_n p_n$, we see that $S_n = S_{n+1}$. Since $S_0 = A_0 p_{-1} - L_0 p_0 = 0$, we have that $S_n = 0$ for all n, and thus the simpler recursion relation:

$$p_{n+1} = \frac{A_{n+1}}{L_{n+1}} p_n \implies p_n = \frac{1}{Z} \left(\prod_{m=1}^{n} \frac{A_m}{L_m} \right) \equiv \frac{1}{Z} \left(\prod_{m=1}^{n} \frac{G_m}{\kappa_m} \right), \tag{G.62}$$

with Z a normalization constant enforcing $\sum_n p_n = 1$. We have also expressed the distribution in terms of the temporal gain coefficient G_n and temporal loss coefficient κ_n. Using this form for the probability distribution, we find an analytical approximation for the photon number uncertainty. We consider distributions which are singly-peaked and vary on a scale large compared to one (making the approximation crude in the Fock state limit, but the resulting approximation is qualitatively predictive, even in that regime). Under these assumptions, we may make a continuum approximation for the probability distribution as follows. Express the probability distribution as

$$p_n = \frac{1}{Z} \exp \left[\sum_{m=1}^{n} \ln r_m \right], \tag{G.63}$$

where $r_m = G_m / \kappa_m$. The peak of the distribution occurs for $\bar{n}$ such that $G_{\bar{n}} = \kappa_{\bar{n}}$. Physically, this is clear because it is the point at which gain balances loss. Mathematically, this is clear because for $m < \bar{n}$, $G > \kappa$ ($r > 1$) and the distribution is increasing (see Fig. 3 of main text for graphical "proof" of this statement). While for $m > \bar{n}$, $G < \kappa$ ($r < 1$) and the distribution is decreasing. Linearizing r about the equilibrium point as $r(n) = 1 + r'(\bar{n})(n - \bar{n})$, such that $\ln r(n) \approx r'(\bar{n})(n - \bar{n})$, and making the continuum

approximation for the distribution, Eq. (63) may be approximated as

$$p_n \approx \frac{1}{Z}\exp\left[\int_{\bar{n}}^{n} dm\, r'(\bar{n})(m-\bar{n})\right] = \frac{1}{Z}\exp\left[-\frac{1}{2}|r'(\bar{n})|(n-\bar{n})^2\right], \tag{G.64}$$

where in the last equality, we have used that $r' < 0$ (otherwise the equilibrium is not stable). From this expression, it immediately follows that the variance in the photon number is given as

$$(\Delta n)^2 = \frac{1}{-\frac{d}{dn}\frac{G(n)}{\kappa(n)}\Big|_{\bar{n}}}. \tag{G.65}$$

This establishes Eq. (7) of the main text. Note that for cases where the loss is sharp compared to the gain, we may ignore the derivative of G and evaluate:

$$(\Delta n)^2 \approx \frac{1}{\frac{G(\bar{n})\kappa'(\bar{n})}{\kappa^2(\bar{n})}} = \frac{1}{\kappa'(\bar{n})/\kappa(\bar{n})}. \tag{G.66}$$

This equation shows that the fluctuations in the photon number are reduced when the loss is sharp compared to its equilibrium value (the latter of which is small near the zero of the loss of Eq. (24)).

G.3 Numerical evidence for the effects predicted in the manuscript

In this section, we provide numerical results based on exact numerical time-dependent solutions, as well as exact numerical steady-states of the Liouvillian, to support the analytical results developed in this SI. The purpose of these numerical demonstrations is to provide a type of "proof" that the simple nonlinear Hamiltonian of Eq. (2) indeed supports Fock-state (or approximate Fock-state generation), and to prove that laser action can indeed generate such unusually low noise states − without resorting to the approximations (e.g., adiabatic elimination) that lead to our analytical theory (which more or less reaches the same conclusions).

G.3.1 Numerical validation of transient noise condensation

To numerically demonstrate that the nonlinear coupled cavity Hamiltonian (Eq. (2)) supports transient noise condensation similar to our analytical theory, we will numerically solve the master equation for the nonlinear Fano resonance (Eq. (8)). Compared to the analytical theory, we do not assume the adiabatic approximation in the numerical solutions. Because we are numerically time-evolving an open system according to a Liouvillian, − which has N^4 elements in its matrix representation (N being the Hilbert space dimension) − it is time-consuming to do simulations for large Fock states. Thus we demonstrate a "toy" example in which a 30-photon optical Fock state results (already such simulations take nearly two hours). The evaluation of the Liouvillian and the solution of the time-dependent equation of motion are performed in a standard numerical quantum optics package: in this case, QuantumOptics in the Julia programming language. Example code is provided [2].

The results are shown in Fig. S1: there is a strong resemblance between Fig. S1(b) and Fig. 2 of the main text. An initially Poisson distribution condenses its noise by orders of magnitude, approaching a near 30-photon Fock state (corresponding with the zero of the loss of Eq. (24)) with near unity probability. At the final time of the simulation, the probability of ending up with an optical 30-photon Fock state is 96%.

There is a somewhat apparent discrepancy when comparing the cumulants (Fig. S1(c)) to Fig. 2 of the main text. The probability distribution at the final time is more sharply peaked around $n = 30$ than at earlier times. But the Fano factor is higher (and in fact, appears to be quite high (about 0.5), indicating a somewhat modest noise reduction). This happens because it appears that a small part of the probability distribution, for lack of a better word, "tunnels" through the zero of the loss. One can see that the probability of being in the vacuum state increases over time (to a small value). In other words, the system displays some signature of bistability: the vast majority of the state is in the 30-photon Fock state while a very small part is in the vacuum state. This bimodality makes the uncertainty a poor indicator of the behavior of the distribution: it is sufficiently clear that the probability

[2] A github repository containing codes used to numerically validate the transient noise condensation and Fock lasing effects is here: https://github.com/nrivera494/photon-noise-condensation.

of generating a large Fock state in this system is quite high.

This bistability is somewhat unsurprising since the loss has zeros in two places (0 and n_0), indicating two valid steady states. We speculate that small (e.g., second-order) corrections away from adiabatic elimination could cause this (but we do not yet conclusively know what terms cause this). Nevertheless, the state already demonstrated through these simulations were mostly intended for "proof purposes," would represent both the highest optical Fock state realized (by over an order of magnitude), and with a very high fidelity. It is likely that changes in parameters can improve this (since we made no attempt to optimize this).

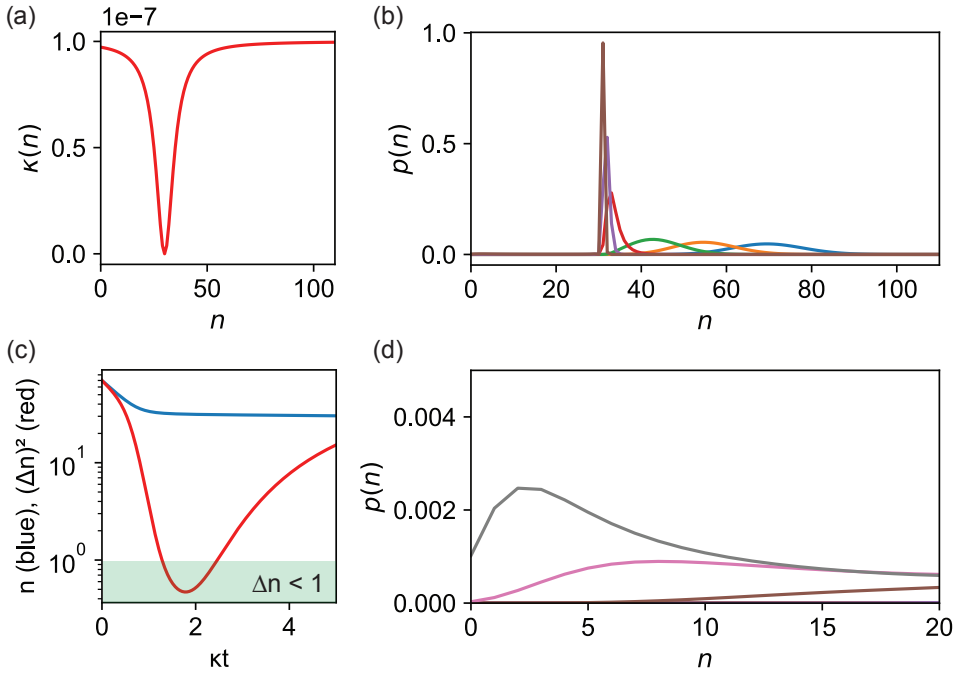

Figure G-1: **Numerical demonstration of transient noise condensation from Eq. (8).** (a) Temporal loss coefficient as a function of photon number. (b) Evolution of the photon statistics in a for different times, assuming an initial Poisson distribution with 70 photons (blue curve). The dynamics largely mirror those presented by the analytical theory in Fig. 2 of the main text. (c) Mean and variance as a function of time, indicating the region where the photon distribution has an uncertainty less than 1. (d) Zoom-in of the small-photon number part of the distribution, showing that part of the distribution moves to smaller photon numbers, somewhat "artificially" diluting the Fano factor. The overall fidelity of generating a 30-photon Fock state in this example is 96%. The parameters for the nonlinear system are $\beta = 5 \times 10^{-4}$, $\kappa = 10^{-7}$, $\gamma = 10^{-2}$, $\lambda = 0$, and $\omega_d = (1 + \delta)\omega_a$ with $\delta = -3\gamma$.

G.3.2 Numerical validation of Fock lasing

In this subsection, we demonstrate numerically (from steady-state solutions of the density matrix equation of motion) that a gain medium, coupled to the nonlinear coupled-resonator system, lases into a heavily sub-Poissonian state, approaching a Fock state. While it is essentially impossible to model from quantum mechanical first principles the interaction of N pumped atoms with a cavity (because the Hilbert space dimension of $N \gg 1$ atoms is simply too large), it is possible to consider a related problem whose solution is representative of a many-body gain medium. In particular, we look at the coupling of a single pumped emitter interacting with the cavity, and look at the photon probability distribution in the steady state. As in the previous subsection, the numerical calculations are performed in Julia's QuantumOptics package. Example code is provided.

Such a system, a single emitter coupled to a cavity (with a suitably rescaled coupling), is capable of correctly modeling the quantum dynamics of a laser, because in a laser, there are negligible inter-atom correlations (although there are implicit correlations in so far as all the atoms couple to the common cavity field that they interact with). As a result, as shown in Ref. [433], the resulting density matrix equations of motion for the system of cavity and gain medium are identical to that arising from the coupling of a single gain atom to the cavity (although of course, a single gain atom provides a much smaller amount of gain).

The type of model considered here, of a single gain atom coupled to a cavity, beyond being useful for modeling purposes, also has a physical "life of its own." In particular, experiments exist demonstrating "one-atom lasing / masing" in which a single pumped atom is sufficient to exceed the threshold of the system (due to the very low losses of the system) [436, 437, 438]. Such one atom lasers have been developed at both optical (with atoms coupled to high-finesse cavities) and microwave frequencies (with superconducting qubits).

The Hamiltonian of a four-level atom (states $1, 2, 3, 4$ with a lasing transition $2 - 3$)

coupled to the nonlinear cavity is given by

$$H_{\text{laser}} = H_{ad} + \sum_{\alpha=1}^{4} E_\alpha |\alpha\rangle\langle\alpha| + \hbar g(\sigma^+ a + a^\dagger \sigma^-), \tag{G.67}$$

with H_{ad} the Hamiltonian of Eq. (3), $\sigma^+ = \sigma_{32} \equiv |3\rangle\langle 2|$, and $\sigma^- = \sigma_{23} = |2\rangle\langle 3|$. The atomic states are labeled in increasing energy order (1 is the ground state, 2 is the lower lasing level, 3 is the upper lasing level, and 4 is the upper pump level). Here, we have not written the reservoir terms corresponding to cavity damping, atomic damping, and atomic pumping. We will consider them as contributing Lindblad terms to the equation of motion for the density matrix.

The Lindblad term for the cavity, according to Eq. (8) is $\mathcal{D}[X]$, with $X = \sqrt{\kappa}a + \sqrt{\gamma}d$ $\mathcal{D}[J] \equiv -\frac{1}{2}(J^\dagger J\rho + \rho J^\dagger J - 2J\rho J^\dagger)$ being the standard dissipator for jump operator J. Defining $\sigma_{ij} = |i\rangle\langle j|$, the atomic damping terms are as follows:

1. The atom is pumped from 1 to 4 at rate Λ, with jump operator σ_{41}.

2. The upper pump level 4 decays to the lower lasing level 3 at rate γ_{34}, with jump operator σ_{34}.

3. The upper lasing level decays to the lower lasing level with relaxation time $\gamma_{||}$, with jump operator $\sigma_{23} = \sigma^-$.

4. The lasing transition is subject to dephasing at rate $\gamma_\perp$ with jump operator $\sigma_z = \sigma_{33} - \sigma_{22}$.

5. The lower lasing level decays to the ground level at rate γ_{12} with jump operator σ_{12}.

The Liouvillian operator $\mathcal{L}$ such that $\dot{\rho} = \mathcal{L}\rho$ is then given as

$$\mathcal{L}\rho = -\frac{i}{\hbar}[H_{\text{laser}}, \rho] + (\mathcal{D}[X] + \Lambda\mathcal{D}[\sigma_{41}] + \gamma_{34}\mathcal{D}[\sigma_{34}] + \gamma_\perp \mathcal{D}[\sigma^-] + \gamma_{||}\mathcal{D}[\sigma_z] + \gamma_{12}\mathcal{D}[\sigma_{12}])\rho. \tag{G.68}$$

The steady state density matrix ρ_{ss} is then found as the null eigenvector of the Liouvillian $\mathcal{L}\rho_{ss} = 0$. Thus, for a given set of parameters describing the laser system, we

numerically implement the Liouvillian and find its zero eigenvalue. The steady-state density matrix is then used to calculated the photon probability distribution of a from which the mean photon number, variance, and Fano factor are calculated. This is done as a function of the pump strength, and the results are presented in Fig. S2.

In Fig. S2a, we plot a gain/loss curve similar to the ones employed in the main text (Figs. 3, 4). This will line-up well with the different regimes of operation (sub-threshold, bistable, near-Fock). Note that the agreement with the analytical theory of the SI is imperfect because at these low photon numbers, spontaneous emission affects the threshold. Nevertheless, the effects shown in the manuscript are all clearly present below (especially the very low-noise steady-states). Namely, we see that: after a threshold, the photon number starts to become significant and the system passes through a series of high-noise states into a low-noise state. The lowest relative noise on the input-output curve of panels (b,c) is just after the threshold, as is the case in Fig. 3 of the main text. In this case, it corresponds to a noise 90% below the coherent-state limit (and much below what standard nonlinear absorbers and low-order nonlinearities provide). The photon uncertainty is about 1.9. The photon number is 35, which is near the approximate zero of the loss at 30 shown in panel (a) (it is higher for reasons that are evident from the gain-loss curves).

Although we do not plot them here, we point out that the atomic populations are what one would expect from a canonical four-level gain: the lowest level is negligibly depleted, the lower lasing and upper pump levels have negligible population, and the small population in the upper lasing level is enough for inversion. Moreover, as in the previous subsection, the d mode has very few photons in it, as expected from $\gamma \gg \kappa -$ validating the assumptions underlying the adiabatic elimination of d in the analytical theory.

G.4 Summary of main results

For ease of quotation, we compile in this section the main new equations derived in this work. **Master equation for a nonlinear resonance and a linear resonance coupled to a common continuum.** In the adiabatic approximation, where the damping rate of the nonlinear resonance is much smaller than that of the linear resonance, the equation of

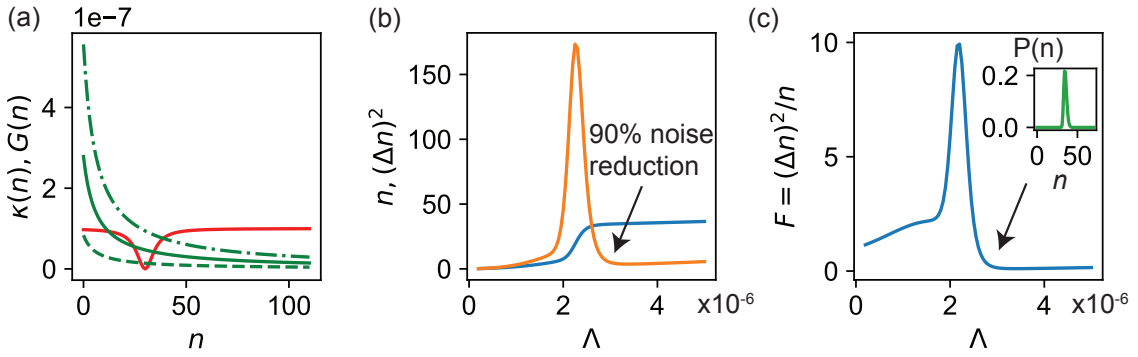

Figure G-2: **Numerical demonstration of Fock lasing from steady state of the Liouvillian.** (a) Loss (red) and gain (green) curves for different values of the pump strength. (b) Mean number of photons in the cavity (blue), as well as variance (orange), as a function of pumping rate from the ground state to the upper pumping level. After a threshold, the photon number increases linearly, before going through a nearly discontinuous jump to a low noise state, with noise here 90% below the coherent state level. (c) Fano factor corresponding to the mean and variance in (b), with inset showing the photon probability distribution at the lowest-relative-noise point. Parameters for the nonlinear cavity are the same as Fig. S1 here. Parameters for the gain are: $g = 3 \times 10^{-4}$, $\gamma_\perp = 10^{-2}, \gamma_{||} = 10^{-4}, \gamma_{12} = 10^{-3}, \gamma_{34} = 1$ (exact value of γ_{34} has little influence insofar as it is much faster than Λ (all units are in units of the frequency of a (e.g., 1.5 eV).

motion ρ for the density matrix of the nonlinear resonance is given by:

$$\dot{\rho} = -\sum_{n=0}^{\infty} n(\mu_n T_{n,n}\rho + \mu_n^* \rho T_{n,n}) + \sum_{m,n=0}^{\infty} \sqrt{m(n+1)}(\mu_m + \mu_{n+1}^*) T_{m-1,m}\rho T_{n+1,n}, \quad \text{(G.69)}$$

with $\mu_n = \frac{1}{2}\kappa - \frac{G_+ G_-}{i(\omega_d - \omega_{n,n-1}) + \gamma/2}$ and $T_{m,n} = |m\rangle\langle n|$. In this equation n indexes over photon number in the nonlinear resonance with annihilation operator a with frequency ω_a, decay constant κ, and Kerr nonlinearity of strength β. The linear mode with annihilation operator d has frequency ω_d and decay constant $\gamma \gg \kappa$. The term $G_+ = i\lambda^* + \frac{1}{2}\sqrt{\kappa\gamma}$ while $G_- = i\lambda + \frac{1}{2}\sqrt{\kappa\gamma}$. The frequency $\omega_{n,n-1} = \omega_a(1 + 2\beta n)$ is the intensity-dependent resonance frequency of the cavity.

Equation of motion for the probabilities. The probability p_n of n photons being in the nonlinear resonance, a, evolve according to:

$$\dot{p}_n = -L_n p_n + L_{n+1} p_{n+1}, \quad \text{(G.70)}$$

with L_n found as:

$$L_n = n\left(\frac{\kappa\delta_n^2 + \gamma|\lambda|^2 + 2\sqrt{\kappa\gamma}\delta_n|\lambda|\cos\phi}{\delta_n^2 + \gamma^2/4}\right), \tag{G.71}$$

with κ, γ, λ being defined above. The term $\delta_n = \omega_{n,n-1} - \omega_d$. We also define the temporal loss coefficient as $\kappa(n) = L_n/n$.

Equation of motion for k-th coherences of the field. The off-diagonal components of the density matrix $\dot{\rho}_{n-k,n}$, with k an integer, evolve according to:

$$\dot{\rho}_{n-k,n} = -((n-k)\mu_{n-k} + n\mu_n^*)\rho_{n-k,n} + \sqrt{(n-k+1)(n+1)}(\mu_{n-k+1} + \mu_{n+1}^*)\rho_{n-k+1,n+1}. \tag{G.72}$$

Langevin equation for a nonlinear resonance. The photon number operator n in a nonlinear cavity with the loss of Eq. (24) evolves according to the Langevin equation

$$\dot{n} = -\kappa(n)n + F_n, \tag{G.73}$$

where $\kappa(n)$ is the temporal loss coefficient defined earlier in this section, and $F_n(t)$ is a quantum Langevin force. The Langevin force has zero mean ($\langle F_n\rangle = 0$), and the diffusion coefficient of F_n (defined so that $\langle F_n(t)F_n(t')\rangle = 2\langle D_{n,n}\rangle\delta(t-t')$) is given by

$$2\langle D_{n,n}\rangle = \langle n\kappa(n)\rangle. \tag{G.74}$$

Noise spectrum of a Fock laser. The spectrum of fluctuations for the cavity photon number, $S_{nn}(\omega)$ is defined such that the photon number variance $(\Delta n)^2 = \int_{-\infty}^{\infty} \frac{d\omega}{2\pi} S_{nn}(\omega)$. The spectrum of fluctuations for a Fock laser $-$ for a four-level gain medium with fast decays of the upper pump and lower lasing level $-$ is given by:

$$S_{nn}(\omega) = 2\kappa(\bar{n})\bar{n} \times \frac{\omega^2 + \Gamma^2}{(\omega^2 - \Omega^2)^2 + \omega^2\eta^2}. \tag{G.75}$$

Here, $\bar{n}$ is the mean photon number in the laser cavity at steady-state, and $\Gamma = \gamma_{||} + R_{\text{sp}}\bar{n}$ with $\gamma_{||}$ the relaxation rate of the upper pump level and R_{sp} the rate of spontaneous emis-

sion into the cavity mode. We have also for simplicity defined the "relaxation oscillation frequency"

$$\Omega^2 = \left(\Gamma\kappa'(\bar{n}) + R_{\text{sp}}\kappa(\bar{n})\right)\bar{n}, \tag{G.76}$$

and the "relaxation oscillation damping rate"

$$\eta = \Gamma + \kappa'(\bar{n})\bar{n}. \tag{G.77}$$

The term $\kappa'(\bar{n})$ is defined as $\left.\frac{d\kappa}{dn}\right|_{\bar{n}}$.

Photon probability distribution of a Fock laser. The probability of n photons being in the laser cavity, in the class A limit (where $\gamma_\perp, \gamma_{||} \gg \kappa$) is given as:

$$p_n = \frac{1}{Z}\left(\prod_{m=1}^{n} \frac{R_{\text{sp}}N_0}{(1+m/n_s)\kappa(m)}\right), \tag{G.78}$$

with Z a normalization constant and $N_0 = \Lambda/\gamma_{||}$ the unsaturated inversion, with Λ the pumping rate of the upper lasing level. We have also defined the saturation photon number $n_s = \gamma_{||}/R_{\text{sp}}$.

Effect of gain and loss sharpness on photon uncertainty in the Fock laser. The uncertainty of the photon number in the cavity, in the class A regime, is given by:

$$(\Delta n)^2 = \frac{1}{\left.-\frac{d}{dn}\frac{G(n)}{\kappa(n)}\right|_{\bar{n}}}, \tag{G.79}$$

with $G(n)$ the intensity-dependent temporal gain coefficient. For cases where the loss varies much more sharply compared to the gain, $(\Delta n)^2$ may be approximated as:

$$(\Delta n)^2 \approx \frac{1}{\frac{G(\bar{n})\kappa'(\bar{n})}{\kappa^2(\bar{n})}} = \frac{1}{\kappa'(\bar{n})/\kappa(\bar{n})}. \tag{G.80}$$

G.5 Potential extensions of the theory

Here, we list some potential theoretical areas of exploration that should be enabled by the results here (experimental directions are discussed in the main text).

1. The equation of motion for the density matrix, Eq. (21), provides a starting point for many investigations of systems with nonlinear frequency-dependent loss. For example, one may use this equation to study statistics under coherent driving.

2. The master equation of Eq. (21), applied to describe coherence, also enables the study of the dynamical evolution of field- ($g^{(1)}(t,t')$), intensity- ($g^{(2)}(t,t')$) and higher-order field correlations ($g^{(k)}(t,t')$). The k-th order correlation functions are connected to the equation of motion for $\rho_{n-k,n}$ by the quantum regression theorem [433].

3. The system introduced in this work, with Hamiltonian given by Eq. (2) is closely related to the physics of optically bistable systems. In particular, removing the d-resonance, one has the canonical model of an optically bistable resonance ([540]).

4. More broadly, the Hamiltonian of Eq. (2) is quite generic, and should apply to open nonlinear systems beyond those considered here. For example, in superconducting qubit systems, nonlinearities can be remarkably high, and there are a great many experimental possibilities for reservoir engineering. Such systems may yield compelling platforms to realize the Fock- and sub-Poissonian state-generation effects discussed here.

5. All results have been provided in the limit $\kappa \ll \gamma$, enabling adiabatic elimination. Generalization of our results beyond this regime is of clear fundamental interest. It is also highly relevant in cases for which the frequency sharpness of the end-mirror becomes sharper than the response time of the cavity mode.

6. As we showed, extremely strong noise reduction can also be obtained in systems with sharply nonlinear gain. The development of practical proposals of systems to realize a sharp nonlinear gain is then of interest as a "competing" platform to realize the Fock- and sub-Poissonian state-generation effects here.

7. We have focused almost exclusively on the quantum statistics of the cavity mode. The statistics of the output beam are also of obvious interest, and are simpler to probe than the cavity statistics. A detailed theoretical exposition of the output field statistics is therefore motivated.

8. The entirety of the manuscript assumes that only a single-mode of the electromagnetic field is relevant. Treatments of Fock-state generation (with or without gain) in the multimode regime are of obvious interest.

G.6 Supplementary figures

Here, we provide additional figures and results, as well as a table of detailed parameters used in Figs. 3, 4 of the main text.

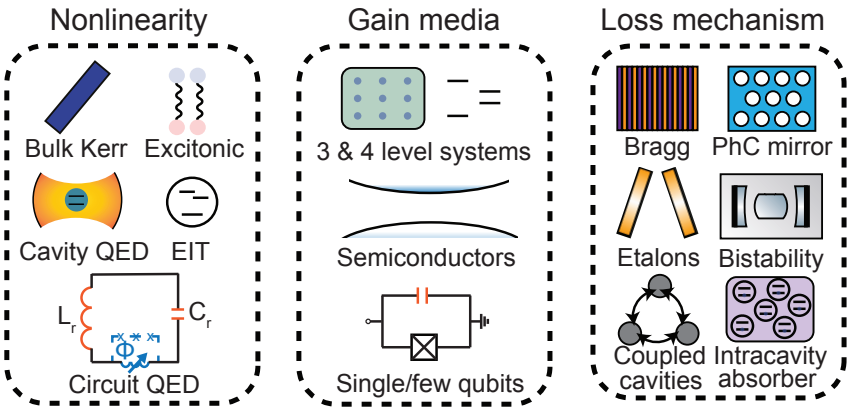

Figure G-3: **Systems which could be explored for Fock lasing.** Many options exist for nonlinearity: circuit and cavity QED systems, atomic gases, excitonic strong coupling, and bulk optical materials. Gain media span solid-state, semiconductors, gases, dyes, artificial atoms, and even single atoms (in one-atom lasers). Sources of sharp loss include absorbers, as well as many systems explored in (nano)photonics: photonic crystals, Fano resonances, bound states in the continuum, bistable systems, and coupled cavities.

In Table S1, we provide detailed parameters for the gain for the examples of Figs. 3, 4 of the main text. The various parameters to be specified are: the gain medium frequency (ω_{gain}), relaxation and decoherence rates $\gamma_{||}, \gamma_{\perp}$, the cross sections for stimulated emission and absorption $(\sigma_{\text{st}}, \sigma_{\text{abs}})$, the density of gain atoms n_{gain}, and the fill fraction f of the gain. The cavity is specified by the cavity length L_{cav}, the cavity waist w_{cav}, the resonance frequency ω_{cav}, and the nonlinear strength per photon β. The lasing mode is taken as a TEM_{00} mode. The Fano mirror is parameterized by its width γ, its direct transmission coefficient t_d (see Eq. (38)), and its frequency $\omega_d = (1+\delta)\omega_a$.

Parameter	Value (Fig. 3)	Value (Fig. 4)
ω_{gain}	1.47 eV	1.17 eV
$\gamma_{\|\|}$	3×10^8 s^{-1}	4.34×10^3 s^{-1}
$\gamma_\perp$	3.1×10^{13} s^{-1}	1×10^{12} s^{-1}
σ_{st}	3×10^{-16} cm^2	2.8×10^{-19} cm^2
σ_{abs}	3×10^{-16} cm^2	7.7×10^{-20} cm^2
n_{gain}	1.7×10^{21} cm^{-3}	1.3×10^{20} cm^{-3}
f	0.5	0.5
L_{cav}	2 μm	1 mm
w_{cav}	1 μm	40 μm
ω_{cav}	ω_{gain}	ω_{gain}
β	$-10^{-5}\omega_{\text{cav}}$	$5 \times 10^{-18}\omega_{\text{cav}}$
γ	$2 \times 10^{-3}\omega_{\text{cav}}$	$10^{-2}\omega_{\text{cav}}$
t_d	0.05	1
δ	20γ	$-10^{-3}\gamma$

Table G.1: Table of gain, cavity, and linear resonance parameters used in Figs. 3, 4 of the main text.

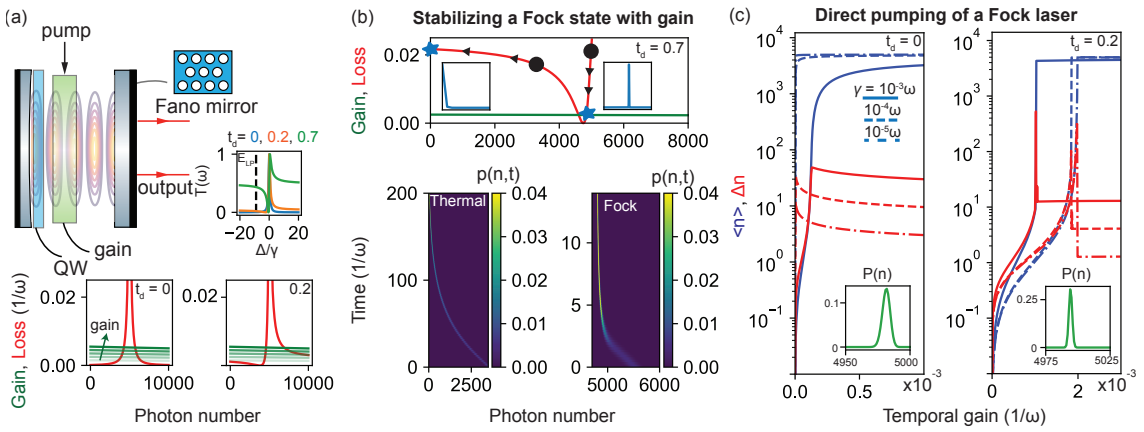

Figure G-4: **Fock lasing in systems with strong optical nonlinearities.** (a) The system of Fig. 3 of the main text is now converted into a "Fock laser" by inclusion of a gain medium. Different transmission profiles for the Fano mirror lead to different losses, and thus different emission-absorption diagrams. Note that t_d is the direct transmission coefficient that controls the Fano lineshape. (b) Evolution of an initial coherent state with different photon numbers (black circles) in the Fock laser. A state to the left of the approximate zero of the loss decays into a thermal state with a very low number of photons, while a state to the right of the zero decays into a steady-state with very low noise, approaching a high-number optical Fock state. (c) Photon number and fluctuations as a function of pump. "S-curves" similar to conventional lasers are observed in the photon number, except they saturate much more strongly, with the photon number hardly changing for increasing pump. Moreover, the photon number fluctuations, rather than increasing according to shot noise, decrease to nearly zero beyond threshold, indicating convergence to a near-Fock state. Different curves indicate different values of the mirror sharpness γ. In this figure, the polaritons have Kerr nonlinear strength $10^{-7}\omega_{\mathrm{LP}}$. The detuning of the mirror from the lower polariton energy (with zero polaritons) is $10^{-3}\omega_0$ and the mirror has a sharpness of $10^{-4}\omega_0$.

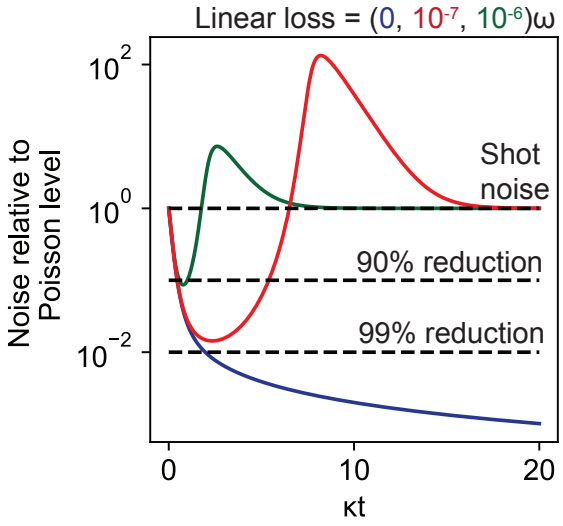

Figure G-5: **Effect of linear loss on transient noise condensation.** Evolution of Fano factor $F = (\Delta n)^2/n$ for the system of Fig. 2 of the main text for different levels of background linear loss. The case of zero linear loss corresponds to the case in which all the loss is nonlinear. For finite linear losses, the noise condensation becomes imperfect, but for realistic values of linear loss (e.g., $Q = 10^6$), the noise condensation can be quite high, corresponding to 10 dB of squeezing.

G.7 Appendix: Deriving the effect of nonlinear loss on probabilities and coherences directly from the Heisenberg picture

In Section II ("Quantum theory of a nonlinear resonator with frequency-dependent loss"), we derived the equation of motion for the photon probabilities from a reservoir theory in which we considered the joint coupling of the cavity and end-mirror to the resonator. We derived a master equation for the density matrix of the cavity and mirror and we then adiabatically eliminated the end mirror. We now provide a potentially simpler and more direct derivation of the result from the Heisenberg equations of motion. This derivation fully agrees with our findings from the density matrix.

G.7.1 General framework

Our goal will be to derive a set of Heisenberg equations of motion to describe the photon in the nonlinear cavity. In a conventional laser theory based on Langevin equations, one writes an equation of motion for a. For the nonlinear laser considered here, this approach is complicated by the polychromatic nature of a nonlinear oscillator. In particular, the operator a can be expressed as $a = \sum_n \sqrt{n}|n-1\rangle\langle n| \equiv \sum_n \sqrt{n} T_{n-1,n}$. In the absence of interactions with gain or reservoirs, the time-evolution of a would simply be $a(t) = \sum_n \sqrt{n} T_{n-1,n}(0) e^{-i\omega_{n,n-1}t}$ with $\omega_{n,n-1} = \omega_n - \omega_{n-1}$. For a linear photon, $\omega_{n,n-1} = n\omega - (n-1)\omega = \omega$, independently of n, recovering the familiar monochromatic evolution $a(t) = a(0)e^{-i\omega t}$.

While the polychromatic nature of a evades solution by conventional methods, the time evolution of the operators $T_{n-1,n}$, and more generally, $T_{n-k,n}$, is quite simple. For example, in the absence of gain or loss, the time-evolution of the operator $T_{n-k,n}$ is given as:

$$\dot{T}_{n-k,n} = \frac{i}{\hbar}\left[\sum_m \hbar\omega_m T_{m,m}, T_{n-k,n}\right] = -i\omega_{n,n-k} T_{n-k,n}, \tag{G.81}$$

so that $T_{n-k,n}(t) = T_{n-k,n}(0)e^{-i\omega_{n,n-k}t}$. Thus, the operators $T_{n-k,n}$ have a simple monochromatic evolution in the absence of interactions. The simplicity of the equation of motion for the projectors then motivates us to formulate our quantum theory of nonlinear loss through the equations of motion for the $T_{n-k,n}$, for each k. Each k corresponds to a quantity with clear physical significance. The case of $k = 0$, which is of primary interest in this work, corresponds to probabilities/populations. In particular, $\langle T_{n,n}\rangle = \mathrm{tr}[\rho T_{n,n}]$ corresponds to the probability of having n photons. The case of k finite correspond to coherences, with $\langle T_{n-1,n}\rangle$ corresponding to first-order (phase) coherence (and the laser linewidth) and $\langle T_{n-2,n}\rangle$ corresponding to second-order (intensity) coherence.

In deriving Eq. (81), we have made use of the fundamental identity of projectors $T_{ij}T_{kl} = \delta_{jk}T_{il}$. We will make heavy use of this identity throughout this section. Beyond

this, the following two identities are also used frequently:

$$[a, T_{n-k,n}] = \sqrt{n-k}T_{n-k-1,n} - \sqrt{n+1}T_{n-k,n+1}, \tag{G.82}$$

$$\left[a^\dagger, T_{n-k,n}\right] = \sqrt{n-k+1}T_{n-k+1,n} - \sqrt{n}T_{n-k,n-1}. \tag{G.83}$$

We have already found the contribution of free evolution to the equation of motion for $T_{n-k,n}$. Now we move to find the contribution from the sharp loss provided by the end mirror.

G.7.2 Loss terms

Now, we derive the contribution of cavity losses to the equation of motion for the kth coherences: defined as $\dot{T}^{(\text{loss})}_{n-k,n}$. We have

$$\begin{aligned}
\dot{T}^{(\text{loss})}_{n-k,n} &= i\left[(\lambda a d^\dagger + \lambda^* a^\dagger d) + \sum_k g_k(a b_k^\dagger + a^\dagger b_k), T_{n-k,n}\right] \\
&= i\sum_k g_k b_k^\dagger(\sqrt{n-k}T_{n-k-1,n} - \sqrt{n+1}T_{n-k,n+1}) \\
&+ i\sum_k g_k(\sqrt{n-k+1}T_{n-k+1,n} - \sqrt{n}T_{n-k,n-1})b_k \\
&+ i\lambda d^\dagger(\sqrt{n-k}T_{n-k-1,n} - \sqrt{n+1}T_{n-k,n+1}) \\
&+ i\lambda^*(\sqrt{n-k+1}T_{n-k+1,n} - \sqrt{n}T_{n-k,n-1})d \\
&\equiv (\text{L1A}) + (\text{L1B}) + (\text{L2A}) + (\text{L2B}).
\end{aligned} \tag{G.84}$$

Here, we have normally ordered the reservoir operators, as we will exclusively consider initial conditions involving no excitations in the far-field or the internal mode of the Fano mirror. Therefore, upon taking expectation values, terms involving the initial values of these operators (Langevin forces) will vanish.

Now, we eliminate the reservoirs from the equations. This is done through the Heisenberg equations of motion for the far-field reservoir and the internal mode of the Fano mirror.

The equation for b_k reads:

$$\dot{b}_k = -i\omega_k b_k - ig_k a - iv_k d, \tag{G.85}$$

admitting the formal solution

$$b_k(t) = b_k(0)e^{-i\omega_k t} - i\int^t dt' \left(g_k a(t') + v_k d(t')\right) e^{-i\omega_k(t-t')}. \tag{G.86}$$

To proceed, let us eliminate b from the equation of motion for d. The equation of motion for d is:

$$\dot{d} = -i\omega_d d - i\lambda a - i\sum_k v_k b_k. \tag{G.87}$$

Plugging in the formal solution for b_k results in:

$$\dot{d} = -i\omega_d d - i\lambda a - i\sum_k v_k \left(b_k(0)e^{-i\omega_k t} - i\int^t dt' \left(g_k a(t') + v_k d(t')\right) e^{-i\omega_k(t-t')} \right). \tag{G.88}$$

Now, we make use of the fact that in laser theory, the coupling between cavity modes and the far-field is well-approximated as a white noise coupling which is independent of frequency, so that $g_k = g$ and $v_k = v$ (Markov approximation). In that case, the sum over k can be carried out. In the continuum limit, $\sum_k \to \int d\omega_k\ \rho_0$, with ρ_0 the (constant) density of (far-field) states, such that the sum yields:

$$\dot{d} = -is_d d - G_- a + F_d. \tag{G.89}$$

Here, we have used $\int dt'\delta(t-t')f(t') = \frac{1}{2}f(t)$ and defined $\gamma = 2\pi\rho v^2$, $\kappa = 2\pi\rho g^2$, $s_d = \omega_d - i\frac{\gamma}{2}$, and $G_- = i\lambda + \frac{1}{2}\sqrt{\kappa\gamma}$. We have also defined the Langevin force on d via $F_d = -i\sum_k v_k b_k(0)e^{-i\omega_k t}$. We may now write the formal solution for d as

$$d(t) = d(0)e^{-is_d t} + \int^t dt' \left(-G_- a(t') + F_d(t')\right) e^{-is_d(t-t')}. \tag{G.90}$$

With the formal solutions for b and d, we may now plug them back into the terms L1A, L1B,

L2A, and L2B. Let us start with L1A and L1B. L1A , under the Markov approximation, is given as:

$$\text{(L1A)} = \left(i \sum_k g_k b_k^\dagger(0) e^{i\omega_k t} - \frac{1}{2}\left(\kappa a^\dagger + \sqrt{\kappa\gamma} d^\dagger\right)\right)(\sqrt{n-k}T_{n-k-1,n} - \sqrt{n+1}T_{n-k,n+1}). \tag{G.91}$$

To proceed, we carry out the following steps (these will be repeated for the terms L1B, L2A, and L2B):

$$\begin{aligned}\text{(L1A)} = &\left(i \sum_k g_k b_k^\dagger(0) e^{i\omega_k t}\right)(\sqrt{n-k}T_{n-k-1,n} - \sqrt{n+1}T_{n-k,n+1}) \\ &- \frac{1}{2}\kappa((n-k)T_{n-k,n} - \sqrt{(n+1)(n-k+1)}T_{n-k+1,n+1}) \\ &+ \frac{1}{2}\sqrt{\kappa\gamma}\int dt' G_-^* a^\dagger(t') e^{is_d^*(t-t')}(\sqrt{n-k}T_{n-k-1,n} - \sqrt{n+1}T_{n-k,n+1}) \\ &- \frac{1}{2}\sqrt{\kappa\gamma}\left(d^\dagger(0)e^{is_d^* t} + \int dt' F_d^\dagger(t') e^{is_d^*(t-t')}\right)(\sqrt{n-k}T_{n-k-1,n} - \sqrt{n+1}T_{n-k,n+1}).\end{aligned} \tag{G.92}$$

In what follows, we consider the limiting case in which the decay of d, set by γ is much faster than the gain dynamics. This is the same adiabatic approximation that was used in the density matrix treatment of the nonlinear Fano resonance. Under those conditions, the third term becomes:

$$\frac{1}{2}\sqrt{\kappa\gamma}G_-^*\left(\frac{n-k}{i(\omega_{n-k,n-k-1} - s_d^*)}T_{n-k,n} - \frac{\sqrt{(n+1)(n-k+1)}}{i(\omega_{n-k+1,n-k} - s_d^*)}T_{n-k+1,n+1}\right). \tag{G.93}$$

This allows us to write L1A as

$$\begin{aligned}(\text{L1A}) = &-\frac{1}{2}\kappa((n-k)T_{n-k,n} - \sqrt{(n+1)(n-k+1)}T_{n-k+1,n+1}) \\ &+\frac{1}{2}\sqrt{\kappa\gamma}G_-^*\left(\frac{n-k}{i(\omega_{n-k,n-k-1}-s_d^*)}T_{n-k,n} - \frac{\sqrt{(n+1)(n-k+1)}}{i(\omega_{n-k+1,n-k}-s_d^*)}T_{n-k+1,n+1}\right). \\ &+\left(i\sum_k g_k b_k^\dagger(0)e^{i\omega_k t}\right)(\sqrt{n-k}T_{n-k-1,n} - \sqrt{n+1}T_{n-k,n+1}) \\ &-\frac{1}{2}\sqrt{\kappa\gamma}\left(d^\dagger(0)e^{is_d^* t} + \int_t dt' F_d^\dagger(t')e^{is_d^*(t-t')}\right)(\sqrt{n-k}T_{n-k-1,n} - \sqrt{n+1}T_{n-k,n+1}).\end{aligned} \tag{G.94}$$

As can be seen, the first two lines, upon taking expectation values, give terms of a similar form to those derived for the density matrix. The remaining lines give zero expectation value when starting in the vacuum of the internal mode and the reservoir, and thus vanish when considering equations of motion for coherences.

Now, let us consider the remaining terms. L1B is quite similar to L1A, and we write

$$(\text{L1B}) = (\sqrt{n-k+1}T_{n-k+1,n} - \sqrt{n}T_{n-k,n-1})\left(i\sum_k g_k b_k(0)e^{-i\omega_k t} + \frac{1}{2}\left(\kappa a + \sqrt{\kappa\gamma}d\right)\right), \tag{G.95}$$

which may be further simplified as

$$\begin{aligned}(\text{L1B}) = &\frac{1}{2}\kappa(\sqrt{(n-k+1)(n+1)}T_{n-k+1,n+1} - nT_{n-k,n}) \\ &-\frac{1}{2}\sqrt{\kappa\gamma}G_-\left(\frac{\sqrt{(n-k+1)(n+1)}}{i(s_d-\omega_{n+1,n})}T_{n-k+1,n+1} - \frac{n}{i(s_d-\omega_{n,n-1})}T_{n-k,n}\right) \\ &+(\sqrt{n-k+1}T_{n-k+1,n} - \sqrt{n}T_{n-k,n-1})\left(i\sum_k g_k b_k(0)e^{-i\omega_k t}\right) \\ &+\frac{1}{2}\sqrt{\kappa\gamma}(\sqrt{n-k+1}T_{n-k+1,n} - \sqrt{n}T_{n-k,n-1})\left(d(0)e^{-is_d t} + \int_t dt' F_d(t')e^{-is_d(t-t')}\right),\end{aligned} \tag{G.96}$$

where we have taken all the same steps as those leading to Eq. (94).

The term L2A is given as:

$$\text{(L2A)} = i\lambda \left(d^\dagger(0) e^{i s_d^* t} + \int^t dt' \left(-G_-^* a^\dagger(t') + F_d^\dagger(t') \right) e^{+i s_d^*(t-t')} \right) (\sqrt{n-k} T_{n-k-1,n} - \sqrt{n+1} T_{n-k,n+1}). \tag{G.97}$$

Under the adiabatic approximation, we may then write:

$$\begin{aligned}\text{(L2A)} = &-i\lambda G_-^* \left(\frac{(n-k)}{i(\omega_{n-k,n-k-1} - s_d^*)} T_{n-k,n} - \frac{\sqrt{(n-k+1)(n+1)}}{i(\omega_{n-k+1,n-k} - s_d^*)} T_{n-k+1,n+1} \right) \\ &+ i\lambda \left(d^\dagger(0) e^{i s_d^* t} + \int^t dt' F_d^\dagger(t') e^{+i s_d^*(t-t')} \right) (\sqrt{n-k} T_{n-k-1,n} - \sqrt{n+1} T_{n-k,n+1}).\end{aligned} \tag{G.98}$$

The term L2B:

$$\text{(L2B)} = i\lambda^* (\sqrt{n-k+1} T_{n-k+1,n} - \sqrt{n} T_{n-k,n-1}) \left(d(0) e^{-i s_d t} + \int^t dt' \left(-G_- a(t') + F_d(t') \right) e^{-i s_d (t-t')} \right), \tag{G.99}$$

similarly follows as:

$$\begin{aligned}\text{(L2B)} = &-i\lambda^* G_- \left(\frac{\sqrt{(n-k+1)(n+1)}}{i(s_d - \omega_{n+1,n})} T_{n-k+1,n+1} - \frac{n}{i(s_d - \omega_{n,n-1})} T_{n-k,n} \right) \\ &+ i\lambda^* (\sqrt{n-k+1} T_{n-k+1,n} - \sqrt{n} T_{n-k,n-1}) \left(d(0) e^{-i s_d t} + \int^t dt' F_d(t') e^{-i s_d (t-t')} \right).\end{aligned} \tag{G.100}$$

Plugging L1A, L1B, L2A, and L2B into the equation for $\dot{T}^{(\text{loss})}_{n-k,n}$, we have

$$\begin{aligned}\dot{T}^{(\text{loss})}_{n-k,n} = &\left(-\frac{1}{2}\kappa(2n-k) + \frac{(n-k)\left(-i\lambda + \frac{1}{2}\sqrt{\kappa\gamma}\right) G_-^*}{i(\omega_{n-k,n-k-1} - s_d^*)} - \frac{n\left(-i\lambda^* - \frac{1}{2}\sqrt{\kappa\gamma}\right) G_-}{i(s_d - \omega_{n,n-1})} \right) T_{n-k,n} \\ &+ \sqrt{(n-k+1)(n+1)} \left(\kappa - \frac{\left(-i\lambda + \frac{1}{2}\sqrt{\kappa\gamma}\right) G_-^*}{i(\omega_{n-k+1,n-k} - s_d^*)} + \frac{\left(-i\lambda^* - \frac{1}{2}\sqrt{\kappa\gamma}\right) G_-}{i(s_d - \omega_{n+1,n})} \right) T_{n-k+1,n+1} \\ &+ F^{(\text{loss})}_{n-k,n},\end{aligned} \tag{G.101}$$

The Langevin force $F^{(\text{loss})}_{n-k,n}$ is given by

$$\begin{aligned}
F^{(\text{loss})}_{n-k,n} = &\left(i\sum_k g_k b_k^\dagger(0)e^{i\omega_k t}\right)\left(\sqrt{n-k}T_{n-k-1,n} - \sqrt{n+1}T_{n-k,n+1}\right) \\
&+ \left(\sqrt{n-k+1}T_{n-k+1,n} - \sqrt{n}T_{n-k,n-1}\right)\left(i\sum_k g_k b_k(0)e^{-i\omega_k t}\right) \\
&+ \left(i\lambda - \frac{1}{2}\sqrt{\kappa\gamma}\right)\left(d^\dagger(0)e^{is_d^* t} + \int^t dt' F_d^\dagger(t')e^{is_d^*(t-t')}\right)\left(\sqrt{n-k}T_{n-k-1,n} - \sqrt{n+1}T_{n-k,n+1}\right) \\
&+ \left(i\lambda^* + \frac{1}{2}\sqrt{\kappa\gamma}\right)\left(\sqrt{n-k+1}T_{n-k+1,n} - \sqrt{n}T_{n-k,n-1}\right)\left(d(0)e^{-is_d t} + \int^t dt' F_d(t')e^{-is_d(t-t')}\right),
\end{aligned} \tag{G.102}$$

and has the important property that $\langle F^{(\text{loss})}_{n-k,n}\rangle = 0$ when the initial state is the vacuum of the reservoirs and the internal mode. Hence, for the systems we will consider here, such terms can be functionally ignored.

G.7.3 Equation of motion for the k-th coherences

Here, we summarize the previous two sections, writing down the total equations of motion for the photon. The equation of motion for the kth coherences are

$$\begin{aligned}
\dot{T}_{n-k,n} = &-i\omega_{n,n-k}T_{n-k,n} \\
&+ \left(-\frac{1}{2}\kappa(2n-k) + \frac{(n-k)(G_+G_-)^*}{i(\omega_{n-k,n-k-1} - s_d^*)} + \frac{nG_+G_-}{i(s_d - \omega_{n,n-1})}\right)T_{n-k,n} \\
&+ \sqrt{(n-k+1)(n+1)}\left(\kappa - \frac{(G_+G_-)^*}{i(\omega_{n-k+1,n-k} - s_d^*)} + \frac{G_+G_-}{i(s_d - \omega_{n+1,n})}\right)T_{n-k+1,n+1} \\
&+ F^{(\text{loss})}_{n-k,n},
\end{aligned} \tag{G.103}$$

where

$$
\begin{aligned}
F^{(\text{loss})}_{n-k,n} = &\left(i \sum_k g_k b_k^\dagger(0) e^{i\omega_k t} \right) \left(\sqrt{n-k}\, T_{n-k-1,n} - \sqrt{n+1}\, T_{n-k,n+1} \right) \\
&+ \left(\sqrt{n-k+1}\, T_{n-k+1,n} - \sqrt{n}\, T_{n-k,n-1} \right) \left(i \sum_k g_k b_k(0) e^{-i\omega_k t} \right) \\
&+ \left(i\lambda - \frac{1}{2}\sqrt{\kappa\gamma} \right) \left(d^\dagger(0) e^{i s_d^* t} + \int^t dt' F_d^\dagger(t') e^{i s_d^* (t-t')} \right) \left(\sqrt{n-k}\, T_{n-k-1,n} - \sqrt{n+1}\, T_{n-k,n+1} \right) \\
&+ \left(i\lambda^* + \frac{1}{2}\sqrt{\kappa\gamma} \right) \left(\sqrt{n-k+1}\, T_{n-k+1,n} - \sqrt{n}\, T_{n-k,n-1} \right) \left(d(0) e^{-i s_d t} + \int^t dt' F_d(t') e^{-i s_d (t-t')} \right).
\end{aligned}
\tag{G.104}
$$

One immediately sees that for $k = 0$, these equations are identical to those from the density matrix description $-$ modulo the explicit form of the Langevin terms here, which resulted from our explicit account of the reservoir in the Heisenberg equations.

Bibliography

[1] Shanhui Fan and John D Joannopoulos. Analysis of guided resonances in photonic crystal slabs. *Physical Review B*, 65(23):235112, 2002.

[2] Kenji Watanabe, Takashi Taniguchi, and Hisao Kanda. Direct-bandgap properties and evidence for ultraviolet lasing of hexagonal boron nitride single crystal. *Nature Materials*, 3(6):404–409, 6 2004.

[3] Paul AM Dirac. The quantum theory of the emission and absorption of radiation. *Proc. R. Soc. Lond. A*, 114(767):243–265, 1927.

[4] Enrico Fermi. Quantum theory of radiation. *Reviews of modern physics*, 4(1):87, 1932.

[5] DN Basov, MM Fogler, and FJ García de Abajo. Polaritons in van der waals materials. *Science*, 354(6309):aag1992, 2016.

[6] Tony Low, Andrey Chaves, Joshua D Caldwell, Anshuman Kumar, Nicholas X Fang, Phaedon Avouris, Tony F Heinz, Francisco Guinea, Luis Martin-Moreno, and Frank Koppens. Polaritons in layered two-dimensional materials. *Nat. Mater.*, 16(2):182, 2017.

[7] Joshua D Caldwell, Igor Aharonovich, Guillaume Cassabois, James H Edgar, Bernard Gil, and DN Basov. Photonics with hexagonal boron nitride. *Nature Reviews Materials*, 4(8):552–567, 2019.

[8] Jianing Chen, Michela Badioli, Pablo Alonso-González, Sukosin Thongrattanasiri, Florian Huth, Johann Osmond, Marko Spasenović, Alba Centeno, Amaia Pesquera, Philippe Godignon, and et al. Optical nano-imaging of gate-tunable graphene plasmons. *Nature*, 487(7405):77, 2012.

[9] Zhe Fei, AS Rodin, GO Andreev, W Bao, AS McLeod, M Wagner, LM Zhang, Z Zhao, M Thiemens, G Dominguez, and et al. Gate-tuning of graphene plasmons revealed by infrared nano-imaging. *Nature*, 487(7405):82, 2012.

[10] S Dai, Z Fei, Q Ma, AS Rodin, M Wagner, AS McLeod, MK Liu, W Gannett, W Regan, K Watanabe, and et al. Tunable phonon polaritons in atomically thin van der Waals crystals of boron nitride. *Science*, 343(6175):1125–1129, 2014.

[11] David Alcaraz Iranzo. Probing the ultimate plasmon confinement limits with a van der Waals heterostructure. *Science*, 360(6386):291–295, 2018.

[12] G. Ni, A.S. McLeod, Z. Sun, L. Wang, L. Xiong, K.W. Post, S.S. Sunku, B.Y. Jiang, J. Hone, C.R. Dean, M.M Fogler, and et al. Fundamental limits to graphene plasmonics. *Nature*, 557(7706):530, 2018.

[13] Rohit Chikkaraddy, Bart de Nijs, Felix Benz, Steven J. Barrow, Oren A. Scherman, Edina Rosta, Angela Demetriadou, Peter Fox, Ortwin Hess, and Jeremy J. Baumberg. Single-molecule strong coupling at room temperature in plasmonic nanocavities. *Nature*, 535(7610):127–130, jun 2016.

[14] F. Benz, M.K. Schmidt, A. Dreismann, R. Chikkaraddy, Y. Zhang, A. Demetriadou, C. Carnegie, H. Ohadi, B. de Nijs, R. Esteban, J. Aizpurua, and et al. Single-molecule optomechanics in "picocavities". *Science*, 354(6313):726–729, 2016.

[15] Jeremy J Baumberg, Javier Aizpurua, Maiken H Mikkelsen, and David R Smith. Extreme nanophotonics from ultrathin metallic gaps. *Nature materials*, 18(7):668–678, 2019.

[16] Giulio Guzzinati, Armand Béché, Hugo Lourenço-Martins, Jérôme Martin, Mathieu Kociak, and Jo Verbeeck. Probing the symmetry of the potential of localized surface plasmon resonances with phase-shaped electron beams. *Nature communications*, 8(1):1–8, 2017.

[17] MS Tame, KR McEnery, ŞK Özdemir, J Lee, SA Maier, and MS Kim. Quantum plasmonics. *Nature Physics*, 9(6):329–340, 2013.

[18] Matthew Pelton. Modified spontaneous emission in nanophotonic structures. *Nature Photonics*, 9(7):427–435, 2015.

[19] P Törmä and William L Barnes. Strong coupling between surface plasmon polaritons and emitters: a review. *Reports on Progress in Physics*, 78(1):013901, 2014.

[20] P Forn-Díaz, L Lamata, E Rico, J Kono, and E Solano. Ultrastrong coupling regimes of light-matter interaction. *Reviews of Modern Physics*, 91(2):025005, 2019.

[21] Anton Frisk Kockum, Adam Miranowicz, Simone De Liberato, Salvatore Savasta, and Franco Nori. Ultrastrong coupling between light and matter. *Nature Reviews Physics*, 1(1):19–40, 2019.

[22] Albert Polman, Mathieu Kociak, and F Javier García de Abajo. Electron-beam spectroscopy for nanophotonics. *Nature Materials*, 18(11):1158–1171, 2019.

[23] Stefan Scheel and Stefan Buhmann. Macroscopic quantum electrodynamics-concepts and applications. *Acta Phys. Slovaca*, 58(5):675–809, 2008.

[24] Vitalii L Ginzburg and Valerii P Frolov. Vacuum in a homogeneous gravitational field and excitation of a uniformly accelerated detector. *Soviet Physics Uspekhi*, 30(12):1073, 1987.

[25] Evgenii Mikhailovich Lifshitz and Lev Petrovich Pitaevskii. *Statistical Physics: Theory of the Condensed State*, volume 9. Elsevier, 2013.

[26] A. Friedman, A. Gover, G. Kurizki, S. Ruschin, and A. Yariv. Spontaneous and stimulated emission from quasifree electrons. *Reviews of Modern Physics*, 60(2):471–535, 4 1988.

[27] F. J. García de Abajo. Optical excitations in electron microscopy. *Rev. Mod. Phys.*, 82(1):209, 2010.

[28] Feliciano Giustino. Electron-phonon interactions from first principles. *Rev. Mod. Phys.*, 89:015003, Feb 2017.

[29] R Hillenbrand, T Taubner, and F Keilmann. Phonon-enhanced light–matter interaction at the nanometre scale. *Nature*, 418(6894):159–162, 2002.

[30] Jean-Jacques Greffet, Rémi Carminati, Karl Joulain, Jean-Philippe Mulet, Stéphane Mainguy, and Yong Chen. Coherent emission of light by thermal sources. *Nature*, 416(6876):61–64, 2002.

[31] Konstantin Y Bliokh, Daria Smirnova, and Franco Nori. Quantum spin hall effect of light. *Science*, 348(6242):1448–1451, 2015.

[32] Peter Lodahl, Sahand Mahmoodian, Søren Stobbe, Arno Rauschenbeutel, Philipp Schneeweiss, Jürgen Volz, Hannes Pichler, and Peter Zoller. Chiral quantum optics. *Nature*, 541(7638):473–480, 2017.

[33] Torsten Karzig, Charles-Edouard Bardyn, Netanel H Lindner, and Gil Refael. Topological polaritons. *Physical Review X*, 5(3):031001, 2015.

[34] S Klembt, TH Harder, OA Egorov, K Winkler, R Ge, MA Bandres, M Emmerling, L Worschech, TCH Liew, M Segev, et al. Exciton-polariton topological insulator. *Nature*, 562(7728):552–556, 2018.

[35] Justin CW Song and Mark S Rudner. Chiral plasmons without magnetic field. *Proceedings of the National Academy of Sciences*, 113(17):4658–4663, 2016.

[36] Dafei Jin, Ling Lu, Zhong Wang, Chen Fang, John D Joannopoulos, Marin Soljačić, Liang Fu, and Nicholas X Fang. Topological magnetoplasmon. *Nature communications*, 7(1):1–10, 2016.

[37] You Zhou, Giovanni Scuri, Dominik S Wild, Alexander A High, Alan Dibos, Luis A Jauregui, Chi Shu, Kristiaan De Greve, Kateryna Pistunova, Andrew Y Joe, et al. Probing dark excitons in atomically thin semiconductors via near-field coupling to surface plasmon polaritons. *Nature nanotechnology*, 12(9):856–860, 2017.

[38] Marinko Jablan, Hrvoje Buljan, and Marin Soljačić. Plasmonics in graphene at infrared frequencies. *Phys. Rev. B*, 80(24):245435, 2009.

[39] Joshua D Caldwell, Andrey V Kretinin, Yiguo Chen, Vincenzo Giannini, Michael M Fogler, Yan Francescato, Chase T Ellis, Joseph G Tischler, Colin R Woods, Alexander J Giles, and et al. Sub-diffractional volume-confined polaritons in the natural hyperbolic material hexagonal boron nitride. *Nat. Commun.*, 5:5221, 2014.

[40] Mark B Lundeberg, Yuanda Gao, Reza Asgari, Cheng Tan, Ben Van Duppen, Marta Autore, Pablo Alonso-González, Achim Woessner, Kenji Watanabe, Takashi Taniguchi, and et al. Tuning quantum nonlocal effects in graphene plasmonics. *Science*, 357:187–191, 2017.

[41] AS McLeod, E Van Heumen, JG Ramirez, S Wang, T Saerbeck, S Guenon, M Goldflam, L Anderegg, P Kelly, A Mueller, et al. Nanotextured phase coexistence in the correlated insulator v2o3. *Nature Physics*, 13(1):80–86, 2017.

[42] Alexander S Mcleod, Jingdi Zhang, MQ Gu, Feng Jin, G Zhang, Kirk W Post, XG Zhao, Andrew J Millis, WB Wu, James M Rondinelli, et al. Multi-messenger nanoprobes of hidden magnetism in a strained manganite. *Nature materials*, 19(4):397–404, 2020.

[43] Daniel Rodrigo, Odeta Limaj, Davide Janner, Dordaneh Etezadi, F Javier García de Abajo, Valerio Pruneri, and Hatice Altug. Mid-infrared plasmonic biosensing with graphene. *Science*, 349(6244):165–168, 2015.

[44] Marta Autore, Peining Li, Irene Dolado, Francisco J Alfaro-Mozaz, Ruben Esteban, Ainhoa Atxabal, Fèlix Casanova, Luis E Hueso, Pablo Alonso-González, Javier Aizpurua, and et al. Boron nitride nanoresonators for phonon-enhanced molecular vibrational spectroscopy at the strong coupling limit. *Light: Sci. Appl.*, 7(4):17172, 2018.

[45] KJ Tielrooij, L Orona, A Ferrier, M Badioli, G Navickaite, S Coop, S Nanot, B Kalinic, T Cesca, L Gaudreau, et al. Electrical control of optical emitter relaxation pathways enabled by graphene. *Nature Physics*, 2015.

[46] Fam Le Kien, VI Balykin, and K Hakuta. Atom trap and waveguide using a two-color evanescent light field around a subwavelength-diameter optical fiber. *Physical Review A*, 70(6):063403, 2004.

[47] Hugen Yan, Tony Low, Wenjuan Zhu, Yanqing Wu, Marcus Freitag, Xuesong Li, Francisco Guinea, Phaedon Avouris, and Fengnian Xia. Damping pathways of mid-infrared plasmons in graphene nanostructures. *Nature Photonics*, 7(5):394–399, 2013.

[48] Christian Junge, Danny O'shea, Jürgen Volz, and Arno Rauschenbeutel. Strong coupling between single atoms and nontransversal photons. *Physical review letters*, 110(21):213604, 2013.

[49] John D Joannopoulos, Steven G Johnson, Joshua N Winn, and Robert D Meade. *Photonic crystals: molding the flow of light*. Princeton university press, 2011.

[50] SM Spillane, TJ Kippenberg, and KJ Vahala. Ultralow-threshold raman laser using a spherical dielectric microcavity. *Nature*, 415(6872):621–623, 2002.

[51] DK Armani, TJ Kippenberg, SM Spillane, and KJ Vahala. Ultra-high-q toroid microcavity on a chip. *Nature*, 421(6926):925–928, 2003.

[52] Kerry J Vahala. Optical microcavities. *nature*, 424(6950):839–846, 2003.

[53] Yoshihiro Akahane, Takashi Asano, Bong-Shik Song, and Susumu Noda. High-q photonic nanocavity in a two-dimensional photonic crystal. *nature*, 425(6961):944–947, 2003.

[54] Bong-Shik Song, Susumu Noda, Takashi Asano, and Yoshihiro Akahane. Ultra-high-q photonic double-heterostructure nanocavity. *Nature materials*, 4(3):207–210, 2005.

[55] Gleb M Akselrod, Christos Argyropoulos, Thang B Hoang, Cristian Ciracì, Chao Fang, Jiani Huang, David R Smith, and Maiken H Mikkelsen. Probing the mechanisms of large purcell enhancement in plasmonic nanoantennas. *Nature Photonics*, 8(11):835–840, 2014.

[56] Kenji Tanaka, Eric Plum, Jun Yu Ou, Takashi Uchino, and Nikolay I Zheludev. Multifold enhancement of quantum dot luminescence in plasmonic metamaterials. *Physical review letters*, 105(22):227403, 2010.

[57] Asaf David, Bergin Gjonaj, Yochai Blau, Shimon Dolev, and Guy Bartal. Nanoscale shaping and focusing of visible light in planar metal–oxide–silicon waveguides. *Optica*, 2(12):1045–1048, 2015.

[58] G Spektor, D Kilbane, AK Mahro, B Frank, S Ristok, L Gal, P Kahl, D Podbiel, S Mathias, H Giessen, et al. Revealing the subfemtosecond dynamics of orbital angular momentum in nanoplasmonic vortices. *Science*, 355(6330):1187–1191, 2017.

[59] G Spektor, D Kilbane, AK Mahro, M Hartelt, E Prinz, M Aeschlimann, and M Orenstein. Mixing the light spin with plasmon orbit by nonlinear light-matter interaction in gold. *Physical Review X*, 9(2):021031, 2019.

[60] Luping Du and Dingyuan Tang. Manipulating propagating graphene plasmons at near field by shaped graphene nano-vacancies. *JOSA A*, 31(4):691–695, 2014.

[61] S Tsesses, E Ostrovsky, K Cohen, B Gjonaj, NH Lindner, and G Bartal. Optical skyrmion lattice in evanescent electromagnetic fields. *Science*, 361(6406):993–996, 2018.

[62] M Babiker, CR Bennett, DL Andrews, and LC Dávila Romero. Orbital angular momentum exchange in the interaction of twisted light with molecules. *Physical review letters*, 89(14):143601, 2002.

[63] Christian T Schmiegelow, Jonas Schulz, Henning Kaufmann, Thomas Ruster, Ulrich G Poschinger, and Ferdinand Schmidt-Kaler. Transfer of optical orbital angular momentum to a bound electron. *Nature communications*, 7(1):1–6, 2016.

[64] Francisco Machado, Nicholas Rivera, Hrvoje Buljan, Marin Soljacic, and Ido Kaminer. Shaping polaritons to reshape selection rules. *ACS Photonics*, 5(8):3064–3072, 2018.

[65] Wei Cai, Ori Reinhardt, Ido Kaminer, and F Javier Garcia de Abajo. Efficient orbital angular momentum transfer between plasmons and free electrons. *Physical Review B*, 98(4):045424, 2018.

[66] Giovanni Maria Vanacore, Gabriele Berruto, Ivan Madan, Enrico Pomarico, P Biagioni, RJ Lamb, D McGrouther, O Reinhardt, I Kaminer, B Barwick, et al. Ultrafast generation and control of an electron vortex beam via chiral plasmonic near fields. *Nature materials*, 18(6):573–579, 2019.

[67] Hui Deng, Gregor Weihs, Charles Santori, Jacqueline Bloch, and Yoshihisa Yamamoto. Condensation of semiconductor microcavity exciton polaritons. *Science*, 298(5591):199–202, 2002.

[68] Jacek Kasprzak, Murielle Richard, S Kundermann, A Baas, P Jeambrun, Jonathan Mark James Keeling, FM Marchetti, MH Szymańska, R André, JL Staehli, et al. Bose–einstein condensation of exciton polaritons. *Nature*, 443(7110):409–414, 2006.

[69] JJ Baumberg, AV Kavokin, S Christopoulos, AJD Grundy, R Butté, G Christmann, DD Solnyshkov, G Malpuech, G Baldassarri Höger von Högersthal, El Feltin, et al. Spontaneous polarization buildup in a room-temperature polariton laser. *Physical Review Letters*, 101(13):136409, 2008.

[70] Hui Deng, Hartmut Haug, and Yoshihisa Yamamoto. Exciton-polariton bose-einstein condensation. *Reviews of modern physics*, 82(2):1489, 2010.

[71] Jan Klaers, Julian Schmitt, Frank Vewinger, and Martin Weitz. Bose–einstein condensation of photons in an optical microcavity. *Nature*, 468(7323):545–548, 2010.

[72] Tim Byrnes, Na Young Kim, and Yoshihisa Yamamoto. Exciton–polariton condensates. *Nature Physics*, 10(11):803–813, 2014.

[73] Sergej O Demokritov, Vladislav E Demidov, Oleksandr Dzyapko, Gennadii A Melkov, Alexandar A Serga, Burkard Hillebrands, and Andrei N Slavin. Bose–einstein condensation of quasi-equilibrium magnons at room temperature under pumping. *Nature*, 443(7110):430–433, 2006.

[74] JJ Baumberg, PG Savvidis, RM Stevenson, AI Tartakovskii, MS Skolnick, DM Whittaker, and JS Roberts. Parametric oscillation in a vertical microcavity: A polariton condensate or micro-optical parametric oscillation. *Physical Review B*, 62(24):R16247, 2000.

[75] Alberto Amo, TCH Liew, Claire Adrados, Romuald Houdré, Elisabeth Giacobino, AV Kavokin, and A Bramati. Exciton–polariton spin switches. *Nature Photonics*, 4(6):361–366, 2010.

[76] Dario Ballarini, Milena De Giorgi, Emiliano Cancellieri, Romuald Houdré, Elisabeth Giacobino, Roberto Cingolani, Alberto Bramati, Giuseppe Gigli, and Daniele Sanvitto. All-optical polariton transistor. *Nature communications*, 4(1):1–8, 2013.

[77] KS Daskalakis, SA Maier, Ray Murray, and Stéphane Kéna-Cohen. Nonlinear interactions in an organic polariton condensate. *Nature materials*, 13(3):271–278, 2014.

[78] Joshua D Caldwell, Lucas Lindsay, Vincenzo Giannini, Igor Vurgaftman, Thomas L Reinecke, Stefan A Maier, and Orest J Glembocki. Low-loss, infrared and terahertz nanophotonics using surface phonon polaritons. *Nanophotonics*, 4(1):44–68, 2015.

[79] Achim Woessner, Mark B Lundeberg, Yuanda Gao, Alessandro Principi, Pablo Alonso-González, Matteo Carrega, Kenji Watanabe, Takashi Taniguchi, Giovanni Vignale, Marco Polini, et al. Highly confined low-loss plasmons in graphene–boron nitride heterostructures. *Nature materials*, 14(4):421–425, 2015.

[80] Peining Li, Martin Lewin, Andrey V Kretinin, Joshua D Caldwell, Kostya S Novoselov, Takashi Taniguchi, Kenji Watanabe, Fabian Gaussmann, and Thomas Taubner. Hyperbolic phonon-polaritons in boron nitride for near-field optical imaging and focusing. *Nat. Commun.*, 6:7507, 2015.

[81] Edward Yoxall, Martin Schnell, Alexey Y Nikitin, Oihana Txoperena, Achim Woessner, Mark B Lundeberg, Félix Casanova, Luis E Hueso, Frank HL Koppens, and Rainer Hillenbrand. Direct observation of ultraslow hyperbolic polariton propagation with negative phase velocity. *Nat. Photonics*, 9:674, 2015.

[82] Alexander J Giles, Siyuan Dai, Igor Vurgaftman, Timothy Hoffman, Song Liu, Lucas Lindsay, Chase T Ellis, Nathanael Assefa, Ioannis Chatzakis, Thomas L Reinecke, et al. Ultralow-loss polaritons in isotopically pure boron nitride. *Nature materials*, 17(2):134–139, 2018.

[83] F Hu, Y Luan, ME Scott, J Yan, DG Mandrus, X Xu, and Z Fei. Imaging exciton–polariton transport in mose 2 waveguides. *Nature Photonics*, 11(6):356–360, 2017.

[84] M Mrejen, L Yadgarov, A Levanon, and H Suchowski. Transient exciton-polariton dynamics in wse2 by ultrafast near-field imaging. *Science advances*, 5(2):eaat9618, 2019.

[85] Peining Li, Xiaosheng Yang, Tobias WW Maß, Julian Hanss, Martin Lewin, Ann-Katrin U Michel, Matthias Wuttig, and Thomas Taubner. Reversible optical switching of highly confined phonon-polaritons with an ultrathin phase-change material. *Nat. Mater.*, 15:870, 2016.

[86] Weiliang Ma, Pablo Alonso-González, Shaojuan Li, Alexey Y Nikitin, Jian Yuan, Javier Martín-Sánchez, Javier Taboada-Gutiérrez, Iban Amenabar, Peining Li, Saül Vélez, and et al. In-plane anisotropic and ultra-low-loss polaritons in a natural van der Waals crystal. *Nature*, 562(7728):557, 2018.

[87] Peining Li, Irene Dolado, Francisco Javier Alfaro-Mozaz, Fèlix Casanova, Luis E Hueso, Song Liu, James H Edgar, Alexey Y Nikitin, Saül Vélez, and Rainer Hillenbrand. Infrared hyperbolic metasurface based on nanostructured van der Waals materials. *Science*, 359(6378):892–896, 2018.

[88] Pablo Alonso-González, A Yu Nikitin, Federico Golmar, A Centeno, A Pesquera, S Vélez, J Chen, G Navickaite, F Koppens, A Zurutuza, et al. Controlling graphene plasmons with resonant metal antennas and spatial conductivity patterns. *Science*, 344(6190):1369–1373, 2014.

[89] Thomas G Folland, Alireza Fali, Samuel T White, Joseph R Matson, Song Liu, Neda A Aghamiri, James H Edgar, Richard F Haglund, Yohannes Abate, and Joshua D Caldwell. Reconfigurable infrared hyperbolic metasurfaces using phase change materials. *Nature communications*, 9(1):1–7, 2018.

[90] Alessandro Principi, Matteo Carrega, Mark B Lundeberg, Achim Woessner, Frank HL Koppens, Giovanni Vignale, and Marco Polini. Plasmon losses due to electron-phonon scattering: The case of graphene encapsulated in hexagonal boron nitride. *Physical Review B*, 90(16):165408, 2014.

[91] Itai Epstein, David Alcaraz, Zhiqin Huang, Varun-Varma Pusapati, Jean-Paul Hugonin, Avinash Kumar, Xander M Deputy, Tymofiy Khodkov, Tatiana G Rappoport, Jin-Yong Hong, et al. Far-field excitation of single graphene plasmon cavities with ultracompressed mode volumes. *Science*, 368(6496):1219–1223, 2020.

[92] Yi Yang, Owen D Miller, Thomas Christensen, John D Joannopoulos, and Marin Soljacic. Low-loss plasmonic dielectric nanoresonators. *Nano letters*, 17(5):3238–3245, 2017.

[93] Yi Yang, Di Zhu, Wei Yan, Akshay Agarwal, Mengjie Zheng, John D Joannopoulos, Philippe Lalanne, Thomas Christensen, Karl K Berggren, and Marin Soljačić. A general theoretical and experimental framework for nanoscale electromagnetism. *Nature*, 576(7786):248–252, 2019.

[94] AV Akimov, A Mukherjee, CL Yu, DE Chang, AS Zibrov, PR Hemmer, H Park, and MD Lukin. Generation of single optical plasmons in metallic nanowires coupled to quantum dots. *Nature*, 450(7168):402–406, 2007.

[95] E Altewischer, MP Van Exter, and JP Woerdman. Plasmon-assisted transmission of entangled photons. *Nature*, 418(6895):304–306, 2002.

[96] James S Fakonas, Hyunseok Lee, Yousif A Kelaita, and Harry A Atwater. Two-plasmon quantum interference. *Nature Photonics*, 8(4):317–320, 2014.

[97] Ludwig Knoll, Stefan Scheel, and Dirk-Gunnar Welsch. Qed in dispersing and absorbing media. *arXiv preprint quant-ph/0006121*, 2000.

[98] Thomas Gerard Philbin. Canonical quantization of macroscopic electromagnetism. *New Journal of Physics*, 12(12):123008, 2010.

[99] L Knöll, W Vogel, and D-G Welsch. Action of passive, lossless optical systems in quantum optics. *Physical Review A*, 36(8):3803, 1987.

[100] Roy J Glauber and M Lewenstein. Quantum optics of dielectric media. *Physical Review A*, 43(1):467, 1991.

[101] Lev Davidovich Landau, JS Bell, MJ Kearsley, LP Pitaevskii, EM Lifshitz, and JB Sykes. *Electrodynamics of continuous media*, volume 8. elsevier, 2013.

[102] Alexandre Archambault, François Marquier, Jean-Jacques Greffet, and Christophe Arnold. Quantum theory of spontaneous and stimulated emission of surface plasmons. *Phys. Rev. B*, 82(3):035411, 2010.

[103] Lev Davidovich Landau and Evgenii Mikhailovich Lifshitz. *Quantum mechanics: non-relativistic theory*, volume 3. Elsevier, 2013.

[104] GS Agarwal. Quantum electrodynamics in the presence of dielectrics and conductors. iv. general theory for spontaneous emission in finite geometries. *Physical Review A*, 12(4):1475, 1975.

[105] Nicholas Rivera, Ido Kaminer, Bo Zhen, John D Joannopoulos, and Marin Soljačić. Shrinking light to allow forbidden transitions on the atomic scale. *Science*, 353(6296):263–269, 2016.

[106] GS Agarwal. Quantum electrodynamics in the presence of dielectrics and conductors. i. electromagnetic-field response functions and black-body fluctuations in finite geometries. *Physical Review A*, 11(1):230, 1975.

[107] GS Agarwal. Quantum electrodynamics in the presence of dielectrics and conductors. ii. theory of dispersion forces. *Physical Review A*, 11(1):243, 1975.

[108] GS Agarwal. Quantum electrodynamics in the presence of dielectrics and conductors. iii. relations among one-photon transition probabilities in stationary and nonstationary fields, density of states, the field-correlation functions, and surface-dependent response functions. *Physical Review A*, 11(1):253, 1975.

[109] Nicholas Rivera, Gilles Rosolen, John D Joannopoulos, Ido Kaminer, and Marin Soljačić. Making two-photon processes dominate one-photon processes using mid-IR phonon polaritons. *Proc. Natl. Acad. Sci. U. S. A.*, 114:13607–13612, 2017.

[110] Yaniv Kurman, Nicholas Rivera, Thomas Christensen, Shai Tsesses, Meir Orenstein, Marin Soljačić, John D Joannopoulos, and Ido Kaminer. Control of semiconductor emitter frequency by increasing polariton momenta. *Nat. Photonics*, 12:423, 2018.

[111] Yaniv Kurman and Ido Kaminer. Tunable bandgap renormalization by nonlocal ultra-strong coupling in nanophotonics. *Nature Physics*, 16(8):868–874, 2020.

[112] Daniel Kleppner. Inhibited spontaneous emission. *Physical review letters*, 47(4):233, 1981.

[113] Eli Yablonovitch. Inhibited spontaneous emission in solid-state physics and electronics. *Physical review letters*, 58(20):2059, 1987.

[114] Sajeev John and Jian Wang. Quantum electrodynamics near a photonic band gap: Photon bound states and dressed atoms. *Physical review letters*, 64(20):2418, 1990.

[115] Sajeev John and Tran Quang. Spontaneous emission near the edge of a photonic band gap. *Physical Review A*, 50(2):1764, 1994.

[116] Shi-Yao Zhu, Yaping Yang, Hong Chen, Hang Zheng, and MS Zubairy. Spontaneous radiation and lamb shift in three-dimensional photonic crystals. *Physical Review Letters*, 84(10):2136, 2000.

[117] Peijun Yao, C Van Vlack, A Reza, M Patterson, MM Dignam, and Stephen Hughes. Ultrahigh purcell factors and lamb shifts in slow-light metamaterial waveguides. *Physical Review B*, 80(19):195106, 2009.

[118] A González-Tudela, PA Huidobro, Luis Martín-Moreno, C Tejedor, and FJ García-Vidal. Theory of strong coupling between quantum emitters and propagating surface plasmons. *Physical review letters*, 110(12):126801, 2013.

[119] Alejandro González-Tudela, PA Huidobro, Luis Martín-Moreno, C Tejedor, and FJ García-Vidal. Reversible dynamics of single quantum emitters near metal-dielectric interfaces. *Physical Review B*, 89(4):041402, 2014.

[120] EA Power and T Thirunamachandran. Quantum electrodynamics in a cavity. *Physical Review A*, 25(5):2473, 1982.

[121] Sofia Ribeiro, Stefan Yoshi Buhmann, Thomas Stielow, and Stefan Scheel. Casimir-polder interaction from exact diagonalization and surface-induced state mixing. *EPL (Europhysics Letters)*, 110(5):51003, 2015.

[122] Stefan Yoshi Buhmann and Dirk-Gunnar Welsch. Dispersion forces in macroscopic quantum electrodynamics. *Progress in quantum electronics*, 31(2):51–130, 2007.

[123] Stefan Yoshi Buhmann and Stefan Scheel. Thermal casimir versus casimir-polder forces: Equilibrium and nonequilibrium forces. *Physical review letters*, 100(25):253201, 2008.

[124] Ido Kaminer, Maor Mutzafi, Amir Levy, Gal Harari, Hanan Herzig Sheinfux, Scott Skirlo, Jonathan Nemirovsky, John D Joannopoulos, Mordechai Segev, and Marin Soljačić. Quantum čerenkov radiation: spectral cutoffs and the role of spin and orbital angular momentum. *Physical Review X*, 6(1):011006, 2016.

[125] Nicholas Rivera, Liang Jie Wong, John D Joannopoulos, Marin Soljačić, and Ido Kaminer. Light emission based on nanophotonic vacuum forces. *Nature Physics*, 15(12):1284–1289, 2019.

[126] Nicholas Rivera, Liang Jie Wong, Marin Soljačić, and Ido Kaminer. Ultrafast multiharmonic plasmon generation by optically dressed electrons. *Physical review letters*, 122(5):053901, 2019.

[127] Lukas Novotny and Bert Hecht. *Principles of Nano-Optics*. Cambridge University Press, 2012.

[128] EM PURCELL. Spontaneous emission probabilities at radio frequencies. *Phys. Rev.*, 69:681, 1946.

[129] Alec Rose, Thang B Hoang, Felicia McGuire, Jack J Mock, Cristian Ciracì, David R Smith, and Maiken H Mikkelsen. Control of radiative processes using tunable plasmonic nanopatch antennas. *Nano letters*, 14(8):4797–4802, 2014.

[130] F. H. L. Koppens, D. E. Chang, and F. J. Garcia de Abajo. Graphene plasmonics: a platform for strong light–matter interactions. *Nano Lett.*, 11(8):3370–3377, 2011.

[131] Joshua D Caldwell, Orest J Glembocki, Yan Francescato, Nicholas Sharac, Vincenzo Giannini, Bezares Francisco, James P Long, Jeffrey C Owrutsky, Igor Vurgaftman, Joseph G Tischler, and et al. Low-loss, extreme subdiffraction photon confinement via silicon carbide localized surface phonon polariton resonators. *Nano Lett.*, 13(8):3690–3697, 2013.

[132] AY Nikitin, P Alonso-González, S Vélez, S Mastel, A Centeno, A Pesquera, A Zurutuza, F Casanova, LE Hueso, FHL Koppens, et al. Real-space mapping of tailored sheet and edge plasmons in graphene nanoresonators. *Nature Photonics*, 10(4):239–243, 2016.

[133] Kevin G Schadler, Carlotta Ciancico, Sofia Pazzagli, Pietro Lombardi, Adrian Bachtold, Costanza Toninelli, Antoine Reserbat-Plantey, and Frank HL Koppens. Electrical control of lifetime-limited quantum emitters using 2d materials. *Nano letters*, 19(6):3789–3795, 2019.

[134] Jorge R Zurita-Sánchez and Lukas Novotny. Multipolar interband absorption in a semiconductor quantum dot. i. electric quadrupole enhancement. *JOSA B*, 19(6):1355–1362, 2002.

[135] Jorge R Zurita-Sánchez and Lukas Novotny. Multipolar interband absorption in a semiconductor quantum dot. ii. magnetic dipole enhancement. *JOSA B*, 19(11):2722–2726, 2002.

[136] AM Kern and Olivier JF Martin. Strong enhancement of forbidden atomic transitions using plasmonic nanostructures. *Phys. Rev. A*, 85(2):022501, 2012.

[137] Prashant K Jain, Debraj Ghosh, Roi Baer, Eran Rabani, and A Paul Alivisatos. Near-field manipulation of spectroscopic selection rules on the nanoscale. *Proc. Natl. Acad. Sci. U. S. A.*, 109(21):8016–8019, 2012.

[138] Mads Lykke Andersen, Søren Stobbe, Anders Søndberg Sørensen, and Peter Lodahl. Strongly modified plasmon–matter interaction with mesoscopic quantum emitters. *Nat. Phys.*, 7(3):215, 2011.

[139] Mai Takase, Hiroshi Ajiki, Yoshihiko Mizumoto, Keiichiro Komeda, Masanobu Nara, Hideki Nabika, Satoshi Yasuda, Hajime Ishihara, and Kei Murakoshi. Selection-rule breakdown in plasmon-induced electronic excitation of an isolated single-walled carbon nanotube. *Nat. Photonics*, 7(7):550, 2013.

[140] Amir Nevet, Nikolai Berkovitch, Alex Hayat, Pavel Ginzburg, Shai Ginzach, Ofir Sorias, and Meir Orenstein. Plasmonic nanoantennas for broad-band enhancement of two-photon emission from semiconductors. *Nano Lett.*, 10(5):1848–1852, 2010.

[141] Annika Melissa Konzelmann, Sjard Ole Krüger, and Harald Giessen. Interaction of orbital angular momentum light with rydberg excitons: Modifying dipole selection rules. *Physical Review B*, 100(11):115308, 2019.

[142] Tomas Neuman, Ruben Esteban, David Casanova, Francisco J García-Vidal, and Javier Aizpurua. Coupling of molecular emitters and plasmonic cavities beyond the point-dipole approximation. *Nano letters*, 18(4):2358–2364, 2018.

[143] A Cuartero-González and AI Fernández-Domínguez. Light-forbidden transitions in plasmon-emitter interactions beyond the weak coupling regime. *ACS Photonics*, 5(8):3415–3420, 2018.

[144] Evgenia Rusak, Jakob Straubel, Piotr Gładysz, Mirko Göddel, Andrzej Kedziorski, Michael Kühn, Florian Weigend, Carsten Rockstuhl, and Karolina Słowik. Enhancement of and interference among higher order multipole transitions in molecules near a plasmonic nanoantenna. *Nature communications*, 10(1):1–8, 2019.

[145] Jamison Sloan, Nicholas Rivera, John D Joannopoulos, Ido Kaminer, and Marin Soljačić. Controlling spins with surface magnon polaritons. *Physical Review B*, 100(23):235453, 2019.

[146] Vasilios D Karanikolas, Cristian A Marocico, Paul R Eastham, and A Louise Bradley. Near-field relaxation of a quantum emitter to two-dimensional semiconductors: Surface dissipation and exciton polaritons. *Physical Review B*, 94(19):195418, 2016.

[147] Vasilios Karanikolas, Ioannis Thanopulos, and Emmanuel Paspalakis. Strong interaction of quantum emitters with a ws 2 layer enhanced by a gold substrate. *Optics Letters*, 44(8):2049–2052, 2019.

[148] PAD Gonçalves, Thomas Christensen, Nicholas Rivera, Antti-Pekka Jauho, N Asger Mortensen, and Marin Soljačić. Plasmon–emitter interactions at the nanoscale. *Nature communications*, 11(1):1–13, 2020.

[149] Stefan Yoshi Buhmann, David T Butcher, and Stefan Scheel. Macroscopic quantum electrodynamics in nonlocal and nonreciprocal media. *New Journal of Physics*, 14(8):083034, 2012.

[150] Peter Schmidt, Fabien Vialla, Simone Latini, Mathieu Massicotte, Klaas-Jan Tielrooij, Stefan Mastel, Gabriele Navickaite, Mark Danovich, David A Ruiz-Tijerina, Celal Yelgel, et al. Nano-imaging of intersubband transitions in van der waals quantum wells. *Nature nanotechnology*, 13(11):1035–1041, 2018.

[151] Jinjiang Zhang, Ruifeng Zhou, Hiro Minamimoto, Satoshi Yasuda, and Kei Murakoshi. Nonzero wavevector excitation of graphene by localized surface plasmons. *Nano letters*, 19(11):7887–7894, 2019.

[152] Eng Aik Chan, Syed Abdullah Aljunid, Giorgio Adamo, Nikolay I Zheludev, Martial Ducloy, and David Wilkowski. Coupling of atomic quadrupole transitions with resonant surface plasmons. *Physical Review A*, 99(6):063801, 2019.

[153] Diane J Roth, Pavel Ginzburg, Liisa M Hirvonen, James A Levitt, Mazhar E Nasir, Klaus Suhling, David Richards, Viktor A Podolskiy, and Anatoly V Zayats. Singlet–triplet transition rate enhancement inside hyperbolic metamaterials. *Laser & Photonics Reviews*, 13(9):1900101, 2019.

[154] Johannes Flick, Nicholas Rivera, and Prineha Narang. Strong light-matter coupling in quantum chemistry and quantum photonics. *Nanophotonics*, 7(9):1479–1501, 2018.

[155] Andreas Wallraff, David I Schuster, Alexandre Blais, Luigi Frunzio, R-S Huang, Johannes Majer, Sameer Kumar, Steven M Girvin, and Robert J Schoelkopf. Strong coupling of a single photon to a superconducting qubit using circuit quantum electrodynamics. *Nature*, 431(7005):162–167, 2004.

[156] J Pelal Reithmaier, G Sek, A Löffler, C Hofmann, S Kuhn, S Reitzenstein, LV Keldysh, VD Kulakovskii, TL Reinecke, and A Forchel. Strong coupling in a single quantum dot–semiconductor microcavity system. *Nature*, 432(7014):197–200, 2004.

[157] Kevin M Birnbaum, Andreea Boca, Russell Miller, Allen D Boozer, Tracy E Northup, and H Jeff Kimble. Photon blockade in an optical cavity with one trapped atom. *Nature*, 436(7047):87–90, 2005.

[158] Takao Aoki, Barak Dayan, Elizabeth Wilcut, Warwick P Bowen, A Scott Parkins, TJ Kippenberg, KJ Vahala, and HJ Kimble. Observation of strong coupling between one atom and a monolithic microresonator. *Nature*, 443(7112):671–674, 2006.

[159] Kotni Santhosh, Ora Bitton, Lev Chuntonov, and Gilad Haran. Vacuum rabi splitting in a plasmonic cavity at the single quantum emitter limit. *Nature communications*, 7(1):1–5, 2016.

[160] Atef Shalabney, Jino George, J a Hutchison, Guido Pupillo, Cyriaque Genet, and Thomas W Ebbesen. Coherent coupling of molecular resonators with a microcavity mode. *Nature communications*, 6(1):1–6, 2015.

[161] James P Long and BS Simpkins. Coherent coupling between a molecular vibration and fabry–perot optical cavity to give hybridized states in the strong coupling limit. *ACS photonics*, 2(1):130–136, 2015.

[162] Jino George, Thibault Chervy, Atef Shalabney, Eloïse Devaux, Hidefumi Hiura, Cyriaque Genet, and Thomas W Ebbesen. Multiple rabi splittings under ultrastrong vibrational coupling. *Physical review letters*, 117(15):153601, 2016.

[163] Wonmi Ahn, Igor Vurgaftman, Adam D Dunkelberger, Jeffrey C Owrutsky, and Blake S Simpkins. Vibrational strong coupling controlled by spatial distribution of molecules within the optical cavity. *ACS Photonics*, 5(1):158–166, 2018.

[164] Anoop Thomas, Lucas Lethuillier-Karl, Kalaivanan Nagarajan, Robrecht MA Vergauwe, Jino George, Thibault Chervy, Atef Shalabney, Eloïse Devaux, Cyriaque Genet, Joseph Moran, et al. Tilting a ground-state reactivity landscape by vibrational strong coupling. *Science*, 363(6427):615–619, 2019.

[165] Evan L Runnerstrom, Kyle P Kelley, Thomas G Folland, J Ryan Nolen, Nader Engheta, Joshua D Caldwell, and Jon-Paul Maria. Polaritonic hybrid-epsilon-near-zero modes: beating the plasmonic confinement vs propagation-length trade-off with doped cadmium oxide bilayers. *Nano letters*, 19(2):948–957, 2018.

[166] Nikolai Christian Passler, Christopher R Gubbin, Thomas Graeme Folland, Ilya Razdolski, D Scott Katzer, David F Storm, Martin Wolf, Simone De Liberato, Joshua D Caldwell, and Alexander Paarmann. Strong coupling of epsilon-near-zero phonon polaritons in polar dielectric heterostructures. *Nano letters*, 18(7):4285–4292, 2018.

[167] P Forn-Díaz, J José García-Ripoll, Borja Peropadre, J-L Orgiazzi, MA Yurtalan, R Belyansky, Christopher M Wilson, and A Lupascu. Ultrastrong coupling of a single artificial atom to an electromagnetic continuum in the nonperturbative regime. *Nature Physics*, 13(1):39–43, 2017.

[168] Fumiki Yoshihara, Tomoko Fuse, Sahel Ashhab, Kosuke Kakuyanagi, Shiro Saito, and Kouichi Semba. Superconducting qubit–oscillator circuit beyond the ultrastrong-coupling regime. *Nature Physics*, 13(1):44–47, 2017.

[169] Cristiano Ciuti, Gérald Bastard, and Iacopo Carusotto. Quantum vacuum properties of the intersubband cavity polariton field. *Physical Review B*, 72(11):115303, 2005.

[170] Christopher M Wilson, Göran Johansson, Arsalan Pourkabirian, Michael Simoen, J Robert Johansson, Tim Duty, Franco Nori, and Per Delsing. Observation of the dynamical casimir effect in a superconducting circuit. *nature*, 479(7373):376–379, 2011.

[171] Simone De Liberato. Light-matter decoupling in the deep strong coupling regime: The breakdown of the purcell effect. *Physical review letters*, 112(1):016401, 2014.

[172] Juan Jose Garcia-Ripoll, Borja Peropadre, and Simone De Liberato. Light-matter decoupling and a2 term detection in superconducting circuits. *Scientific reports*, 5(1):1–8, 2015.

[173] Nicholas Rivera, Johannes Flick, and Prineha Narang. Variational theory of nonrelativistic quantum electrodynamics. *Physical review letters*, 122(19):193603, 2019.

[174] Thomas Niemczyk, F Deppe, H Huebl, EP Menzel, F Hocke, MJ Schwarz, JJ Garcia-Ripoll, D Zueco, T Hümmer, E Solano, et al. Circuit quantum electrodynamics in the ultrastrong-coupling regime. *Nature Physics*, 6(10):772–776, 2010.

[175] Pol Forn-Díaz, Jürgen Lisenfeld, David Marcos, Juan José Garcia-Ripoll, Enrique Solano, CJPM Harmans, and JE Mooij. Observation of the bloch-siegert shift in a qubit-oscillator system in the ultrastrong coupling regime. *Physical review letters*, 105(23):237001, 2010.

[176] VL Ginzburg. Quantum theory of radiation of electron uniformly moving in medium. *Zh. Eksp. Teor. Fiz*, 10:589–600, 1940.

[177] A Sokolow. Quantum theory of cherenkov effect. In *Dokl. Akad. Nauk SSSR*, volume 28, page 415, 1940.

[178] Pavel A Cherenkov. Visible light from clear liquids under the action of gamma radiation. *Dokl. Akad. Nauk SSSR*, 2(8):451–454, 1934.

[179] IE Tamm and IM Frank. Coherent radiation of fast electrons in a medium. In *Dokl. Akad. Nauk SSSR*, volume 14, pages 107–112, 1937.

[180] Chiyan Luo, Mihai Ibanescu, Steven G Johnson, and JD Joannopoulos. Cerenkov radiation in photonic crystals. *science*, 299(5605):368–371, 2003.

[181] Avraham Gover, Reuven Ianconescu, Aharon Friedman, Claudio Emma, Nick Sudar, Pietro Musumeci, and Claudio Pellegrini. Superradiant and stimulated-superradiant emission of bunched electron beams. *Reviews of Modern Physics*, 91(3):035003, 2019.

[182] Viktor G Veselago. Electrodynamics of substances with simultaneously negative and. *Usp. fiz. nauk*, 92(7):517–526, 1967.

[183] Sheng Xi, Hongsheng Chen, Tao Jiang, Lixin Ran, Jiangtao Huangfu, Bae Ian Wu, Jin Au Kong, and Min Chen. Experimental verification of reversed Cherenkov radiation in Left-Handed metamaterial. *Physical Review Letters*, 103(19):194801, 11 2009.

[184] Patrice Genevet, Daniel Wintz, Antonio Ambrosio, Alan She, Romain Blanchard, and Federico Capasso. Controlled steering of cherenkov surface plasmon wakes with a one-dimensional metamaterial. *Nature Nanotechnology*, 10(9):804–809, 2015.

[185] Xiao Lin, Sajan Easo, Yichen Shen, Hongsheng Chen, Baile Zhang, John D Joannopoulos, Marin Soljačić, and Ido Kaminer. Controlling cherenkov angles with resonance transition radiation. *Nature Physics*, 14(8):816–821, 2018.

[186] Riccardo Sapienza, Toon Coenen, Jan Renger, Martin Kuttge, Niek F van Hulst, and A Polman. Deep-subwavelength imaging of the modal dispersion of light. *Nature materials*, 11(9):781–787, 2012.

[187] Siying Peng, Nick J Schilder, Xiang Ni, Jorik Van De Groep, Mark L Brongersma, Andrea Alù, Alexander B Khanikaev, Harry A Atwater, Albert Polman, et al. Probing the band structure of topological silicon photonic lattices in the visible spectrum. *Physical review letters*, 122(11):117401, 2019.

[188] Ido Kaminer, Yaniv Tenenbaum Katan, Hrvoje Buljan, Yichen Shen, Ognjen Ilic, Josué J López, Liang Jie Wong, John D Joannopoulos, and Marin Soljačić. Efficient plasmonic emission by the quantum čerenkov effect from hot carriers in graphene. *Nature communications*, 7(1):1–9, 2016.

[189] Shai Tsesses, Guy Bartal, and Ido Kaminer. Light generation via quantum interaction of electrons with periodic nanostructures. *Physical Review A*, 95(1):013832, 2017.

[190] Roei Remez, Aviv Karnieli, Sivan Trajtenberg-Mills, Niv Shapira, Ido Kaminer, Yossi Lereah, and Ady Arie. Observing the quantum wave nature of free electrons through spontaneous emission. *Physical review letters*, 123(6):060401, 2019.

[191] Liang Jie Wong, Nicholas Rivera, Chitraang Murdia, Thomas Christensen, John D Joannopoulos, Marin Soljačić, and Ido Kaminer. Control of quantum electrodynamical processes by shaping electron wavepackets. *Nature communications*, 12(1):1–10, 2021.

[192] Yiming Pan and Avraham Gover. Spontaneous and stimulated emissions of a preformed quantum free-electron wave function. *Physical Review A*, 99(5):052107, 2019.

[193] F Javier Garcıía de Abajo. Multiple excitation of confined graphene plasmons by single free electrons. *ACS nano*, 7(12):11409–11419, 2013.

[194] Shenggang Liu, Chao Zhang, Min Hu, Xiaoxing Chen, Ping Zhang, Sen Gong, Tao Zhao, and Renbin Zhong. Coherent and tunable terahertz radiation from graphene surface plasmon polaritons excited by an electron beam. *Applied Physics Letters*, 104(20):201104, 2014.

[195] Ravishankar Sundararaman, Prineha Narang, Adam S Jermyn, William A Goddard III, and Harry A Atwater. Theoretical predictions for hot-carrier generation from surface plasmon decay. *Nat. Commun.*, 5:5788, 2014.

[196] Ana M Brown, Ravishankar Sundararaman, Prineha Narang, William A Goddard III, and Harry A Atwater. Nonradiative plasmon decay and hot carrier dynamics: effects of phonons, surfaces, and geometry. *ACS nano*, 10(1):957–966, 2016.

[197] CX Zhao, Wen Xu, and FM Peeters. Cerenkov emission of terahertz acoustic-phonons from graphene. *Applied physics letters*, 102(22):222101, 2013.

[198] Trond I Andersen, Bo L Dwyer, Javier D Sanchez-Yamagishi, Joaquin F Rodriguez-Nieva, Kartiek Agarwal, Kenji Watanabe, Takashi Taniguchi, Eugene A Demler, Philip Kim, Hongkun Park, et al. Electron-phonon instability in graphene revealed by global and local noise probes. *Science*, 364(6436):154–157, 2019.

[199] AB Pippard. Acoustic amplification in semiconductors and metals. *Philosophical Magazine*, 8(85):161–165, 1963.

[200] AR Hutson, JH McFee, and DL White. Ultrasonic amplification in cds. *Physical Review Letters*, 7(6):237, 1961.

[201] FS Hage, DM Kepaptsoglou, QM Ramasse, and LJ Allen. Phonon spectroscopy at atomic resolution. *Physical review letters*, 122(1):016103, 2019.

[202] Kartik Venkatraman, Barnaby DA Levin, Katia March, Peter Rez, and Peter A Crozier. Vibrational spectroscopy at atomic resolution with electron impact scattering. *Nature Physics*, 15(12):1237–1241, 2019.

[203] Jordan A Hachtel, Jingsong Huang, Ilja Popovs, Santa Jansone-Popova, Jong K Keum, Jacek Jakowski, Tracy C Lovejoy, Niklas Dellby, Ondrej L Krivanek, and Juan Carlos Idrobo. Identification of site-specific isotopic labels by vibrational spectroscopy in the electron microscope. *Science*, 363(6426):525–528, 2019.

[204] Vitalii L Ginzburg. Radiation by uniformly moving sources (vavilov–cherenkov effect, transition radiation, and other phenomena). *Physics-Uspekhi*, 39(10):973, 1996.

[205] Stephen Judson Smith and EM Purcell. Visible light from localized surface charges moving across a grating. *Physical Review*, 92(4):1069, 1953.

[206] Yu Ye, Fang Liu, Mengxuan Wang, Lixuan Tai, Kaiyu Cui, Xue Feng, Wei Zhang, and Yidong Huang. Deep-ultraviolet smith–purcell radiation. *Optica*, 6(5):592–597, 2019.

[207] Giorgio Adamo, Kevin F MacDonald, YH Fu, CM Wang, DP Tsai, FJ García De Abajo, and NI Zheludev. Light well: a tunable free-electron light source on a chip. *Physical review letters*, 103(11):113901, 2009.

[208] Ido Kaminer, SE Kooi, R Shiloh, B Zhen, Y Shen, JJ López, R Remez, SA Skirlo, Y Yang, JD Joannopoulos, et al. Spectrally and spatially resolved smith-purcell radiation in plasmonic crystals with short-range disorder. *Physical Review X*, 7(1):011003, 2017.

[209] Brendan P Clarke, Behrad Gholipour, Kevin F MacDonald, and Nikolay I Zheludev. All-dielectric free-electron-driven holographic light sources. *Applied Physics Letters*, 113(24):241902, 2018.

[210] G Doucas, JH Mulvey, M Omori, J Walsh, and MF Kimmitt. First observation of smith-purcell radiation from relativistic electrons. *Physical review letters*, 69(12):1761, 1992.

[211] Charles Roques-Carmes, Steven E Kooi, Yi Yang, Aviram Massuda, Phillip D Keathley, Aun Zaidi, Yujia Yang, John D Joannopoulos, Karl K Berggren, Ido Kaminer, et al. Towards integrated tunable all-silicon free-electron light sources. *Nature communications*, 10(1):1–8, 2019.

[212] Yi Yang, Aviram Massuda, Charles Roques-Carmes, Steven E Kooi, Thomas Christensen, Steven G Johnson, John D Joannopoulos, Owen D Miller, Ido Kaminer, and Marin Soljačić. Maximal spontaneous photon emission and energy loss from free electrons. *Nature Physics*, 14(9):894–899, 2018.

[213] Liang Jie Wong, Ido Kaminer, Ognjen Ilic, John D Joannopoulos, and Marin Soljačić. Towards graphene plasmon-based free-electron infrared to x-ray sources. *Nature Photonics*, 10(1):46–52, 2016.

[214] Gilles Rosolen, Liang Jie Wong, Nicholas Rivera, Bjorn Maes, Marin Soljačić, and Ido Kaminer. Metasurface-based multi-harmonic free-electron light source. *Light: Science & Applications*, 7(1):1–12, 2018.

[215] Andrea Pizzi, Gilles Rosolen, Liang Jie Wong, Rasmus Ischebeck, Marin Soljačić, Thomas Feurer, and Ido Kaminer. Graphene metamaterials for intense, tunable, and compact extreme ultraviolet and x-ray sources. *Advanced science*, 7(1):1901609, 2020.

[216] Ofer Kfir. Entanglements of electrons and cavity photons in the strong-coupling regime. *Physical review letters*, 123(10):103602, 2019.

[217] Valerio Di Giulio, Mathieu Kociak, and F Javier García de Abajo. Probing quantum optical excitations with fast electrons. *Optica*, 6(12):1524–1534, 2019.

[218] Charles Roques-Carmes, Nicholas Rivera, John D Joannopoulos, Marin Soljačić, and Ido Kaminer. Nonperturbative quantum electrodynamics in the cherenkov effect. *Physical Review X*, 8(4):041013, 2018.

[219] G Scalari, C Maissen, D Turčinková, D Hagenmüller, S De Liberato, C Ciuti, C Reichl, D Schuh, W Wegscheider, M Beck, et al. Ultrastrong coupling of the cyclotron transition of a 2d electron gas to a thz metamaterial. *Science*, 335(6074):1323–1326, 2012.

[220] Andreas Bayer, Marcel Pozimski, Simon Schambeck, Dieter Schuh, Rupert Huber, Dominique Bougeard, and Christoph Lange. Terahertz light–matter interaction beyond unity coupling strength. *Nano letters*, 17(10):6340–6344, 2017.

[221] Gian L Paravicini-Bagliani, Felice Appugliese, Eli Richter, Federico Valmorra, Janine Keller, Mattias Beck, Nicola Bartolo, Clemens Rössler, Thomas Ihn, Klaus Ensslin, et al. Magneto-transport controlled by landau polariton states. *Nature Physics*, 15(2):186–190, 2019.

[222] Dimitri Dini, Rüdeger Köhler, Alessandro Tredicucci, Giorgio Biasiol, and Lucia Sorba. Microcavity polariton splitting of intersubband transitions. *Physical review letters*, 90(11):116401, 2003.

[223] Yanko Todorov, Aaron Maxwell Andrews, R Colombelli, Simone De Liberato, Cristiano Ciuti, Pavel Klang, Gottfried Strasser, and Carlo Sirtori. Ultrastrong light-matter coupling regime with polariton dots. *Physical review letters*, 105(19):196402, 2010.

[224] Jacob S Schalch, Kirk Post, Guangwu Duan, Xiaoguang Zhao, Young Duck Kim, James Hone, Michael M Fogler, Xin Zhang, Dmitri N Basov, and Richard D Averitt. Strong metasurface–josephson plasma resonance coupling in superconducting la2-xsrxcuo4. *Advanced Optical Materials*, 7(21):1900712, 2019.

[225] Brett Barwick, David J Flannigan, and Ahmed H Zewail. Photon-induced near-field electron microscopy. *Nature*, 462(7275):902–906, 2009.

[226] Ahmed H Zewail. Four-dimensional electron microscopy. *science*, 328(5975):187–193, 2010.

[227] Armin Feist, Katharina E Echternkamp, Jakob Schauss, Sergey V Yalunin, Sascha Schäfer, and Claus Ropers. Quantum coherent optical phase modulation in an ultrafast transmission electron microscope. *Nature*, 521(7551):200–203, 2015.

[228] Aycan Yurtsever, J Spencer Baskin, and Ahmed H Zewail. Entangled nanoparticles: Discovery by visualization in 4d electron microscopy. *Nano letters*, 12(9):5027–5032, 2012.

[229] Kangpeng Wang, Raphael Dahan, Michael Shentcis, Yaron Kauffmann, Adi Ben Hayun, Ori Reinhardt, Shai Tsesses, and Ido Kaminer. Coherent interaction between free electrons and a photonic cavity. *Nature*, 582(7810):50–54, 2020.

[230] Enrico Pomarico, Ivan Madan, Gabriele Berruto, Giovanni Maria Vanacore, Kangpeng Wang, Ido Kaminer, F Javier García de Abajo, and Fabrizio Carbone. mev

resolution in laser-assisted energy-filtered transmission electron microscopy. *ACS Photonics*, 5(3):759–764, 2017.

[231] Ofer Kfir, Hugo Lourenço-Martins, Gero Storeck, Murat Sivis, Tyler R Harvey, Tobias J Kippenberg, Armin Feist, and Claus Ropers. Controlling free electrons with optical whispering-gallery modes. *Nature*, 582(7810):46–49, 2020.

[232] Tom TA Lummen, Raymond J Lamb, Gabriele Berruto, Thomas LaGrange, Luca Dal Negro, F Javier García de Abajo, Damien McGrouther, Brett Barwick, and Fabrizio Carbone. Imaging and controlling plasmonic interference fields at buried interfaces. *Nature communications*, 7(1):1–9, 2016.

[233] H Petek and S Ogawa. Femtosecond time-resolved two-photon photoemission studies of electron dynamics in metals. *Progress in surface science*, 56(4):239–310, 1997.

[234] Mark I Stockman, Matthias F Kling, Ulf Kleineberg, and Ferenc Krausz. Attosecond nanoplasmonic-field microscope. *Nature Photonics*, 1(9):539–544, 2007.

[235] Timothy J Davis, David Janoschka, Pascal Dreher, Bettina Frank, Frank-J Meyer zu Heringdorf, and Harald Giessen. Ultrafast vector imaging of plasmonic skyrmion dynamics with deep subwavelength resolution. *Science*, 368(6489):eaba6415, 2020.

[236] Naoki Yamamoto. Development of high-resolution cathodoluminescence system for stem and application to plasmonic nanostructures. *Journal of Electron Microscopy*, 65(4):282–295, 2016.

[237] EA Peralta, K Soong, RJ England, ER Colby, Z Wu, B Montazeri, C McGuinness, J McNeur, KJ Leedle, D Walz, et al. Demonstration of electron acceleration in a laser-driven dielectric microstructure. *Nature*, 503(7474):91–94, 2013.

[238] R Joel England, Robert J Noble, Karl Bane, David H Dowell, Cho-Kuen Ng, James E Spencer, Sami Tantawi, Ziran Wu, Robert L Byer, Edgar Peralta, et al. Dielectric laser accelerators. *Reviews of Modern Physics*, 86(4):1337, 2014.

[239] Raphael Dahan, Saar Nehemia, Michael Shentcis, Ori Reinhardt, Yuval Adiv, Xihang Shi, Orr Be'er, Morgan H Lynch, Yaniv Kurman, Kangpeng Wang, et al. Resonant phase-matching between a light wave and a free-electron wavefunction. *Nature Physics*, 16(11):1123–1131, 2020.

[240] Neil V Sapra, Ki Youl Yang, Dries Vercruysse, Kenneth J Leedle, Dylan S Black, R Joel England, Logan Su, Rahul Trivedi, Yu Miao, Olav Solgaard, et al. On-chip integrated laser-driven particle accelerator. *Science*, 367(6473):79–83, 2020.

[241] LUCA Piazza, TTA Lummen, Erik Quinonez, Y Murooka, BW Reed, B Barwick, and F Carbone. Simultaneous observation of the quantization and the interference pattern of a plasmonic near-field. *Nature communications*, 6(1):1–7, 2015.

[242] Giovanni M Vanacore, I Madan, G Berruto, K Wang, E Pomarico, RJ Lamb, D McGrouther, I Kaminer, B Barwick, F Javier García de Abajo, et al. Attosecond coherent control of free-electron wave functions using semi-infinite light fields. *Nature communications*, 9(1):1–11, 2018.

[243] Katharina E Priebe, Christopher Rathje, Sergey V Yalunin, Thorsten Hohage, Armin Feist, Sascha Schäfer, and Claus Ropers. Attosecond electron pulse trains and quantum state reconstruction in ultrafast transmission electron microscopy. *Nature Photonics*, 11(12):793–797, 2017.

[244] Yuya Morimoto and Peter Baum. Diffraction and microscopy with attosecond electron pulse trains. *Nature Physics*, 14(3):252–256, 2018.

[245] Martin Kozák, Norbert Schönenberger, and Peter Hommelhoff. Ponderomotive generation and detection of attosecond free-electron pulse trains. *Physical review letters*, 120(10):103203, 2018.

[246] Konstantin Yu Bliokh, Yury P Bliokh, Sergey Savel'Ev, and Franco Nori. Semiclassical dynamics of electron wave packet states with phase vortices. *Physical Review Letters*, 99(19):190404, 2007.

[247] VN Tsytovich. Macroscopic mass renormalization and energy losses of charged particles in a medium. *Sov. Phys. JETP*, 15(2), 1962.

[248] GX Ni, H Wang, JS Wu, Z Fei, MD Goldflam, F Keilmann, B Özyilmaz, AH Castro Neto, XM Xie, MM Fogler, et al. Plasmons in graphene moiré superlattices. *Nature materials*, 14(12):1217–1222, 2015.

[249] SS Sunku, GuangXin Ni, Bor-Yuan Jiang, Hyobin Yoo, Aaron Sternbach, AS McLeod, T Stauber, Lin Xiong, Takashi Taniguchi, Kenji Watanabe, et al. Photonic crystals for nano-light in moiré graphene superlattices. *Science*, 362(6419):1153–1156, 2018.

[250] Audrey Bienfait, JJ Pla, Yuimaru Kubo, Xin Zhou, Michael Stern, CC Lo, CD Weis, Thomas Schenkel, Denis Vion, Daniel Esteve, et al. Controlling spin relaxation with a cavity. *Nature*, 531(7592):74–77, 2016.

[251] Arisato Kawabata and Ryogo Kubo. Electronic properties of fine metallic particles. ii. plasma resonance absorption. *Journal of the physical society of Japan*, 21(9):1765–1772, 1966.

[252] Dirk Englund, David Fattal, Edo Waks, Glenn Solomon, Bingyang Zhang, Toshihiro Nakaoka, Yasuhiko Arakawa, Yoshihisa Yamamoto, and Jelena Vučković. Controlling the spontaneous emission rate of single quantum dots in a two-dimensional photonic crystal. *Physical review letters*, 95(1):013904, 2005.

[253] Rufus H Ritchie. Plasma losses by fast electrons in thin films. *Physical review*, 106(5):874, 1957.

[254] Hendrik A Kramers and Werner Heisenberg. Über die streuung von strahlung durch atome. *Zeitschrift für Physik*, 31(1):681–708, 1925.

[255] Maria Göppert-Mayer. Über elementarakte mit zwei quantensprüngen. *Ann. Phys.*, 401(3):273–294, 1931.

[256] Willis E Lamb Jr and Robert C Retherford. Fine structure of the hydrogen atom by a microwave method. *Physical Review*, 72(3):241, 1947.

[257] CI Sukenik, MG Boshier, Donghyun Cho, Vahid Sandoghdar, and EA Hinds. Measurement of the casimir-polder force. *Physical review letters*, 70(5):560, 1993.

[258] Oktay Sinanoğlu. *Modern Quantum Chemistry: Action of light and organic crystals*. Academic Press, 1965.

[259] Arthur H Compton. A quantum theory of the scattering of x-rays by light elements. *Physical review*, 21(5):483, 1923.

[260] IM Frank. Optics of light sources moving in refractive media: Vavilov-cherenkov radiation, though interesting, is but an experimental instance of a more general problem. *Science*, 131(3402):702–712, 1960.

[261] Alex Hayat, Pavel Ginzburg, and Meir Orenstein. Observation of two-photon emission from semiconductors. *Nat. Photonics*, 2(4):238, 2008.

[262] Matthew D Schwartz. *Quantum field theory and the standard model*. Cambridge University Press, 2014.

[263] Herbert Fröhlich. Theory of the superconducting state. i. the ground state at the absolute zero of temperature. *Physical Review*, 79(5):845, 1950.

[264] Shambhu Ghimire, Anthony D DiChiara, Emily Sistrunk, Pierre Agostini, Louis F DiMauro, and David A Reis. Observation of high-order harmonic generation in a bulk crystal. *Nature physics*, 7(2):138–141, 2011.

[265] Szu-yuan Chen, Anatoly Maksimchuk, and Donald Umstadter. Experimental observation of relativistic nonlinear thomson scattering. *Nature*, 396(6712):653–655, 1998.

[266] Chandrasekhara Venkata Raman and Kariamanikkam Srinivasa Krishnan. A new type of secondary radiation. *Nature*, 121(3048):501–502, 1928.

[267] Michael Edward Peskin. *An introduction to quantum field theory*. Westview press, 1995.

[268] Claudio L Cesar, Dale G Fried, Thomas C Killian, Adam D Polcyn, Jon C Sandberg, A Yu Ite, Thomas J Greytak, Daniel Kleppner, and John M Doyle. Two-photon spectroscopy of trapped atomic hydrogen. *Physical review letters*, 77(2):255, 1996.

[269] A McPherson, G Gibson, H Jara, U Johann, Ting S Luk, IA McIntyre, Keith Boyer, and Charles K Rhodes. Studies of multiphoton production of vacuum-ultraviolet radiation in the rare gases. *JOSA B*, 4(4):595–601, 1987.

[270] Xiaoji G Xu, Jian-Hua Jiang, Leonid Gilburd, Rachel G Rensing, Kenneth S Burch, Chunyi Zhi, Yoshio Bando, Dmitri Golberg, and Gilbert C Walker. Mid-infrared polaritonic coupling between boron nitride nanotubes and graphene. *ACS Nano*, 8(11):11305–11312, 2014.

[271] Andrea Tomadin, Alessandro Principi, Justin CW Song, Leonid S Levitov, and Marco Polini. Accessing phonon polaritons in hyperbolic crystals by angle-resolved photoemission spectroscopy. *Phys. Rev. Lett.*, 115(8):087401, 2015.

[272] S. Dai, Q. Ma, T. Andersen, A.S. Mcleod, Z. Fei, M.K. Liu, M. Wagner, K. Watanabe, T. Taniguchi, M. Thiemens, F. Keilmann, and et al. Subdiffractional focusing and guiding of polaritonic rays in a natural hyperbolic material. *Nat. Commun.*, 6:6963, 2015.

[273] S. Dai, Q. Ma, M.K. Liu, T. Andersen, Z. Fei, M.D. Goldflam, M. Wagner, K. Watanabe, T. Taniguchi, M. Thiemens, F. Keilmann, and et al. Graphene on hexagonal boron nitride as a tunable hyperbolic metamaterial. *Nat. Nanotechnol.*, 10(8):682–686, 2015.

[274] D. N. Basov, M. M. Fogler, and F. J. García de Abajo. Polaritons in van der Waals materials. *Science*, 354:aag1992, 2016.

[275] DN Basov, RD Averitt, and D Hsieh. Towards properties on demand in quantum materials. *Nat. Mater.*, 16(11):1077, 2017.

[276] A.J. Giles, S. Dai, I. Vurgaftman, T. Hoffman, S. Liu, L. Lindsay, C.T. Ellis, N. Assefa, I. Chatzakis, T.L. Reinecke, J.G Tischler, and et al. Ultralow-loss polaritons in isotopically pure boron nitride. *Nat. Mater.*, 17:134–139, 2018.

[277] Anshuman Kumar, Tony Low, Kin Hung Fung, Phaedon Avouris, and Nicholas X Fang. Tunable light–matter interaction and the role of hyperbolicity in graphene–hbn system. *Nano Lett.*, 15(5):3172–3180, 2015.

[278] Alexander M Dubrovkin, Bo Qiang, Harish NS Krishnamoorthy, Nikolay I Zheludev, and Qi Jie Wang. Ultra-confined surface phonon polaritons in molecular layers of van der Waals dielectrics. *Nat. Commun.*, 9(1):1762, 2018.

[279] Kristian Sommer Thygesen. Calculating excitons, plasmons, and quasiparticles in 2d materials and van der waals heterostructures. *2D Mater.*, 4(2):022004, 2017.

[280] Daniel Sánchez-Portal and Eduardo Hernandez. Vibrational properties of single-wall nanotubes and monolayers of hexagonal bn. *Phys. Rev. B*, 66(23):235415, 2002.

[281] EJ Mele and Petr Král. Electric polarization of heteropolar nanotubes as a geometric phase. *Phys. Rev. Lett.*, 88(5):056803, 2002.

[282] J Serrano, A Bosak, R Arenal, M Krisch, K Watanabe, T Taniguchi, H Kanda, Angel Rubio, and Ludger Wirtz. Vibrational properties of hexagonal boron nitride: inelastic x-ray scattering and ab initio calculations. *Phys. Rev. Lett.*, 98(9):095503, 2007.

[283] Thibault Sohier, Marco Gibertini, Matteo Calandra, Francesco Mauri, and Nicola Marzari. Breakdown of optical phonons' splitting in two-dimensional materials. *Nano Lett.*, 17(6):3758–3763, 2017.

[284] Nicholas Rivera, Jennifer Coulter, Thomas Christensen, and Prineha Narang. Ab initio calculation of phonon polaritons in silicon carbide and boron nitride. *arXiv:1809.00058*, 2018.

[285] Max Born and Kun Huang. *Dynamical Theory of Crystal Lattices*. Clarendon Press, 1954.

[286] Gyaneshwar P Srivastava. *The Physics of Phonons*. CRC Press, 1990.

[287] Thibault Sohier, Matteo Calandra, and Francesco Mauri. Two-dimensional fröhlich interaction in transition-metal dichalcogenide monolayers: Theoretical modeling and first-principles calculations. *Phys. Rev. B*, 94(8):085415, 2016.

[288] Tadaaki Nagao, Torsten Hildebrandt, Martin Henzler, and Shuji Hasegawa. Dispersion and damping of a two-dimensional plasmon in a metallic surface-state band. *Phys. Rev. Lett.*, 86(25):5747, 2001.

[289] Bogdan Diaconescu, Karsten Pohl, Luca Vattuone, Letizia Savio, Philip Hofmann, Vyacheslav M Silkin, Jose M Pitarke, Eugene V Chulkov, Pedro M Echenique, Daniel Farías, and et al. Low-energy acoustic plasmons at metal surfaces. *Nature*, 448(7149):57, 2007.

[290] Alexander A Govyadinov, Andrea Konečná, Andrey Chuvilin, Saül Vélez, Irene Dolado, Alexey Y Nikitin, Sergei Lopatin, Fèlix Casanova, Luis E Hueso, Aizpurua, and et al. Probing low-energy hyperbolic polaritons in van der Waals crystals with an electron microscope. *Nat. Commun.*, 8(1):95, 2017.

[291] Dafei Jin, Thomas Christensen, Marin Soljačić, Nicholas X. Fang, Ling Lu, and Xiang Zhang. Infrared topological plasmons in graphene. *Phys. Rev. Lett.*, 118(24):245301, 2017.

[292] Georgia T Papadakis, Prineha Narang, Ravishankar Sundararaman, Nicholas Rivera, Hrvoje Buljan, Nader Engheta, and Marin Soljačić. Ultralight angstrom-scale optimal optical reflectors. *ACS Photonics*, 5(2):384–389, 2017.

[293] Christopher J Ciccarino, Thomas Christensen, Ravishankar Sundararaman, and Prineha Narang. Dynamics and spin-valley locking effects in monolayer transition metal dichalcogenides. *Nano Lett.*, 18:5709, 2018.

[294] Ning Li, Xiangdong Guo, Xiaoxia Yang, Ruishi Qi, Tianyu Qiao, Yifei Li, Ruochen Shi, Yuehui Li, Kaihui Liu, Zhi Xu, et al. Direct observation of highly confined phonon polaritons in suspended monolayer hexagonal boron nitride. *Nature Materials*, 20(1):43–48, 2021.

[295] EM Lifshitz. The theory of molecular attractive forces between solids. *Sov. Phys. JETP*, 1956.

[296] V Sandoghdar, CI Sukenik, EA Hinds, and Serge Haroche. Direct measurement of the van der waals interaction between an atom and its images in a micron-sized cavity. *Physical Review Letters*, 68(23):3432–3435, 1992.

[297] Ho Bun Chan, Vladimir A Aksyuk, Rafael N Kleiman, David J Bishop, and Federico Capasso. Quantum mechanical actuation of microelectromechanical systems by the casimir force. *Science*, 291(5510):1941–1944, 2001.

[298] JB Pendry. Shearing the vacuum-quantum friction. *Journal of Physics: Condensed Matter*, 9(47):10301–10320, 1997.

[299] J Robert Johansson, Göran Johansson, CM Wilson, and Franco Nori. Dynamical casimir effect in a superconducting coplanar waveguide. *Physical Review Letters*, 103(14):147003, 2009.

[300] PD Nation, JR Johansson, MP Blencowe, and Franco Nori. Colloquium: Stimulating uncertainty: Amplifying the quantum vacuum with superconducting circuits. *Reviews of Modern Physics*, 84(1):1–24, 2012.

[301] Stephen A Fulling. Nonuniqueness of canonical field quantization in riemannian space-time. *Physical Review D*, 7(10):2850–2862, 1973.

[302] Paul CW Davies. Scalar production in schwarzschild and rindler metrics. *Journal of Physics A: Mathematical and General*, 8(4):609–616, 1975.

[303] William G Unruh. Notes on black-hole evaporation. *Physical Review D*, 14(4):870–892, 1976.

[304] JB Pendry. Radiative exchange of heat between nanostructures. *Journal of Physics: Condensed Matter*, 11(35):6621–6633, 1999.

[305] AI Volokitin and Bo NJ Persson. Near-field radiative heat transfer and noncontact friction. *Reviews of Modern Physics*, 79(4):1291–1329, 2007.

[306] MT Homer Reid, Alejandro W Rodriguez, Jacob White, and Steven G Johnson. Efficient computation of casimir interactions between arbitrary 3d objects. *Physical Review Letters*, 103(4):040401, 2009.

[307] Clayton R Otey, Wah Tung Lau, Shanhui Fan, et al. Thermal rectification through vacuum. *Physical Review Letters*, 104(15):154301, 2010.

[308] Alejandro W Rodriguez, Federico Capasso, and Steven G Johnson. The casimir effect in microstructured geometries. *Nature Photonics*, 5(4):211–221, 2011.

[309] Sheng Shen, Arvind Narayanaswamy, and Gang Chen. Surface phonon polaritons mediated energy transfer between nanoscale gaps. *Nano Letters*, 9(8):2909–2913, 2009.

[310] Emmanuel Rousseau, Alessandro Siria, Guillaume Jourdan, Sebastian Volz, Fabio Comin, Joël Chevrier, and Jean-Jacques Greffet. Radiative heat transfer at the nanoscale. *Nature Photonics*, 3(9):514–517, 2009.

[311] Kyeongtae Kim, Bai Song, Víctor Fernández-Hurtado, Woochul Lee, Wonho Jeong, Longji Cui, Dakotah Thompson, Johannes Feist, MT Homer Reid, Francisco J García-Vidal, et al. Radiative heat transfer in the extreme near field. *Nature*, 528(7582):387–391, 2015.

[312] John David Jackson. *Classical Electrodynamics*. Wiley, 1999.

[313] A. Friedman, A. Gover, G. Kurizki, S. Ruschin, and A. Yariv. Spontaneous and stimulated emission from quasifree electrons. *Reviews of modern physics*, 60(2):471–535, 1988.

[314] V.L Ginsburg. *Applications of electrodynamics in theoretical physics and astrophysics*. Routledge, 1989.

[315] C Pellegrini, A Marinelli, and S Reiche. The physics of x-ray free-electron lasers. *Reviews of Modern Physics*, 88(1):015006, 2016.

[316] ID Feranchuk and AV Ivashin. Theoretical investigation of the parametric x-ray features. *Journal de Physique*, 46(11):1981–1986, 1985.

[317] VV Batygin. On the possibility of hard vavilov-cerenkov radiation. *Sov. Phys. JETP*, 21(1):179–180, 1965.

[318] VV Batygin and K Kuz'menko. Quantum theory of vavilov-cerenkov radiation by an electron traveling in vacuum parallel to a dielectric surface. *Sov. Phys. JETP*, 68(88):437–440, 1975.

[319] SM Rytov, Yu A Kravtsov, and VI Tatarskii. *Priniciples of Statistical Radiophysics. 3. Elements of Random Fields.* Springer, 1989.

[320] Stefan Scheel and Stefan Yoshi Buhmann. Macroscopic qed-concepts and applications. *acta physica slovaca*, (5):675–809, 2008.

[321] Joseph I Goldstein, Dale E Newbury, Joseph R Michael, Nicholas WM Ritchie, John Henry J Scott, and David C Joy. *Scanning electron microscopy and X-ray microanalysis*. Springer, 2017.

[322] Ian Blumenfeld, Christopher E Clayton, Franz-Josef Decker, Mark J Hogan, Chengkun Huang, Rasmus Ischebeck, Richard Iverson, Chandrashekhar Joshi, Thomas Katsouleas, Neil Kirby, et al. Energy doubling of 42 gev electrons in a metre-scale plasma wakefield accelerator. *Nature*, 445(7129):741–744, 2007.

[323] Alexandra Boltasseva and Vladimir M. Shalaev. Transdimensional photonics. *ACS Photonics*, 6(1):1–3, 2019.

[324] Gururaj V Naik, Jeremy L Schroeder, Xingjie Ni, Alexander V Kildishev, Timothy D Sands, and Alexandra Boltasseva. Titanium nitride as a plasmonic material for visible and near-infrared wavelengths. *Optical Materials Express*, 2(4):478–489, 2012.

[325] Alejandro W Rodriguez, MT Homer Reid, and Steven G Johnson. Fluctuating-surface-current formulation of radiative heat transfer for arbitrary geometries. *Physical Review B*, 86(22):220302, 2012.

[326] Isaac Freund and BF Levine. Parametric conversion of x-rays. *Physical Review Letters*, 23(15):854–857, 1969.

[327] P Eisenberger and SL McCall. X-ray parametric conversion. *Physical Review Letters*, 26(12):684–688, 1971.

[328] TE Glover, DM Fritz, Marco Cammarata, TK Allison, Sinisa Coh, JM Feldkamp, H Lemke, D Zhu, Y Feng, RN Coffee, et al. X-ray and optical wave mixing. *Nature*, 488(7413):603–608, 2012.

[329] A Gektin and M Korzhik. *Inorganic scintillators for detector systems*. Springer, 2017.

[330] Simon Cherry, James Sorenson, and Michael Phelps. *Physics in Nuclear Medicine*. Wiley, 2012.

[331] Qiushui Chen, Jing Wu, Xiangyu Ou, Bolong Huang, Jawaher Almutlaq, Ayan A. Zhumekenov, Xinwei Guan, Sanyang Han, Liangliang Liang, Zhigao Yi, Juan Li, Xiaoji Xie, Yu Wang, Ying Li, Dianyuan Fan, Daniel B.L. Teh, Angelo H. All, Omar F. Mohammed, Osman M. Bakr, Tom Wu, Marco Bettinelli, Huanghao Yang, Wei Huang, and Xiaogang Liu. All-inorganic perovskite nanocrystal scintillators. *Nature*, 561(7721):88–93, 9 2018.

[332] Yaniv Kurman, Avner Shultzman, Ohad Segal, Adi Pick, and Ido Kaminer. Photonic-Crystal Scintillators: Molding the Flow of Light to Enhance X-Ray and γ-Ray Detection. *Physical Review Letters*, 125(4):040801, 7 2020.

[333] Eli Yablonovitch. Inhibited Spontaneous Emission in Solid-State Physics and Electronics. *Physical Review Letters*, 58(20):2059, 5 1987.

[334] John D. Joannopoulos, Steven G. Johnson, Joshua N. Winn, and Robert D. Meade. *Photonic crystals: Molding the flow of light*. Princeton University Press, 2011.

[335] Matthew Pelton. Modified spontaneous emission in nanophotonic structures. *Nature Photonics 2015 9:7*, 9(7):427–435, 6 2015.

[336] Albert Polman and Harry A. Atwater. Photonic design principles for ultrahigh-efficiency photovoltaics. *Nature Materials*, 11(3):174–177, 3 2012.

[337] Pascal Anger, Palash Bharadwaj, and Lukas Novotny. Enhancement and Quenching of Single-Molecule Fluorescence. *Physical Review Letters*, 96(11):113002, 3 2006.

[338] J. B. Jackson and N. J. Halas. Surface-enhanced Raman scattering on tunable plasmonic nanoparticle substrates. *Proceedings of the National Academy of Sciences*, 101(52):17930–17935, 12 2004.

[339] E. F. Schubert, N. E.J. Hunt, M. Micovic, R. J. Malik, D. L. Sivco, A. Y. Cho, and G. J. Zydzik. Highly efficient light-emitting diodes with microcavities. *Science*, 265(5174):943–945, 1994.

[340] Alexei A. Erchak, Daniel J. Ripin, Shanhui Fan, Peter Rakich, John D. Joannopoulos, Erich P. Ippen, Gale S. Petrich, and Leslie A. Kolodziejski. Enhanced coupling to vertical radiation using a two-dimensional photonic crystal in a semiconductor light-emitting diode. *Applied Physics Letters*, 78(5):563, 1 2001.

[341] Jean-Jacques Greffet, Rémi Carminati, Karl Joulain, Jean-Philippe Mulet, Stéphane Mainguy, and Yong Chen. Coherent emission of light by thermal sources. *Nature 2002 416:6876*, 416(6876):61–64, 3 2002.

[342] Roei Remez, Niv Shapira, Charles Roques-Carmes, Romain Tirole, Yi Yang, Yossi Lereah, Marin Soljačić, Ido Kaminer, and Ady Arie. Spectral and spatial shaping of Smith-Purcell radiation. *Physical Review A*, 96(6):061801, 12 2017.

[343] Yi Yang, Aviram Massuda, Charles Roques-Carmes, Steven E. Kooi, Thomas Christensen, Steven G. Johnson, John D. Joannopoulos, Owen D. Miller, Ido Kaminer, and Marin Soljačić. Maximal spontaneous photon emission and energy loss from free electrons. *Nature Physics*, 14(9):894–899, 9 2018.

[344] I. Kaminer, S. Kooi, R. Shiloh, B. Zhen, Y. Shen, J. López, R. Remez, S. A. Skirlo, Y. Yang, J. D. Joannopoulos, A. Arie, and M. Soljačić. Spectrally and Spatially Resolved Smith-Purcell Radiation in Plasmonic Crystals with Short-Range Disorder. *Physical Review X*, 7(1):011003, 2017.

[345] C; Roques-Carmes, S.E; Kooi, Y; Yang, A; Massuda, P. D; Keathley, A; Zaidi, Y; Yang, J. D; Joannopoulos, K. K; Berggren, I. E; Kaminer, and M Soljačić. Towards integrated tunable all-silicon free-electron light sources. *Nature Communications*, 10(3176), 2019.

[346] Renming Liu, Zhang-Kai Zhou, Yi-Cong Yu, Tengwei Zhang, Hao Wang, Guanghui Liu, Yuming Wei, Huanjun Chen, and Xue-Hua Wang. Strong light-matter interactions in single open plasmonic nanocavities at the quantum optics limit. *Phys. Rev. Lett.*, 118:237401, Jun 2017.

[347] Aviram Massuda, Charles Roques-Carmes, Yujia Yang, Steven E. Kooi, Yi Yang, Chitraang Murdia, Karl K. Berggren, Ido Kaminer, and Marin Soljačić. Smith-Purcell radiation from low-energy electrons. *ACS Photonics*, 5(9), 5 2017.

[348] F. J. García De Abajo. Optical excitations in electron microscopy. *Reviews of Modern Physics*, 82(1):209–275, 2 2010.

[349] Yonghui Li, Shenglai He, Arthur Russakoff, and Kálmán Varga. Accurate time propagation method for the coupled maxwell and kohn-sham equations. *Phys. Rev. E*, 94:023314, Aug 2016.

[350] Clara I. Osorio, Toon Coenen, Benjamin J. M. Brenny, Albert Polman, and A. Femius Koenderink. Angle-Resolved Cathodoluminescence Imaging Polarimetry. *ACS Photonics*, 3(1):147–154, 1 2015.

[351] Yi Yang, Charles Roques-Carmes, Steven E. Kooi, Haoning Tang, Justin Beroz, Eric Mazur, Ido Kaminer, John D. Joannopoulos, and Marin Soljačić. Observation of enhanced free-electron radiation from photonic flatband resonances. *arXiv:2110.03550*, 10 2021.

[352] Bo Liu, Hong Chen, Jingtao Zhu, Jinliang Liu, Liang Chen, Mu Gu, Qiang Wu, Xiaoping Ouyang, Xueye Chen, and Zhichao Zhu. Enhanced light extraction of plastic scintillator using large-area photonic crystal structures fabricated by hot embossing. *Optics Express, Vol. 26, Issue 9, pp. 11438-11446*, 26(9):11438–11446, 4 2018.

[353] Arno Knapitsch, Etiennette Auffray, Christian W. Fabjan, Jean Louis Leclercq, Xavier Letartre, Radoslaw Mazurczyk, and Paul Lecoq. Results of photonic crystal enhanced light extraction on heavy inorganic scintillators. *IEEE Transactions on Nuclear Science*, 59(5 PART 2):2334–2339, 2012.

[354] Arno Knapitsch and Paul Lecoq. Review on photonic crystal coatings for scintillators. *International Journal of Modern Physics A*, 29(30):1430070, 12 2015.

[355] Zhichao Zhu, Shuang Wu, Chaofan Xue, Jun Zhao, Liansheng Wang, Yanqing Wu, Bo Liu, Chuanwei Cheng, Mu Gu, Hong Chen, and Renzhong Tai. Enhanced light extraction of scintillator using large-area photonic crystal structures fabricated by soft-X-ray interference lithography. *Applied Physics Letters*, 106(24):241901, 6 2015.

[356] Bo Liu, H. Smith, Hong Chen, P. Pignalosa, and Yasha Yi. Giant light extraction enhancement of medical imaging scintillation materials using biologically inspired integrated nanostructures. *Optics Letters, Vol. 37, Issue 14, pp. 2808-2810*, 37(14):2808–2810, 7 2012.

[357] Bo Liu, Chi Zhang, Fan Zhang, Huili Tang, Jinliang Liu, Jun Xu, Liang Chen, Mu Gu, Xiaoping Ouyang, Zhichao Zhu, Liang Chen, Jinliang Liu, and Xiaoping Ouyang. Improved light output from thick β-Ga¡sub¿2¡/sub¿O¡sub¿3¡/sub¿ scintillation crystals via graded-refractive-index photonic crystals. *Optics Express, Vol. 29, Issue 12, pp. 18646-18653*, 29(12):18646–18653, 6 2021.

[358] Xiao Ouyang, Bo Liu, Xincheng Xiang, Liang Chen, Mengxuan Xu, Xiaojing Song, Jinlu Ruan, Jinliang Liu, Chuanxiang Chen, Zhichao Zhu, and Yang Li. Enhanced light output of CsI(Na) scintillators by photonic crystals. *Nuclear Instruments and Methods in Physics Research Section A: Accelerators, Spectrometers, Detectors and Associated Equipment*, 969:164007, 7 2020.

[359] Claude A. Klein. Bandgap dependence and related features of radiation ionization energies in semiconductors. *Journal of Applied Physics*, 39(4), 1968.

[360] P. Wurfel. The chemical potential of radiation. *Journal of Physics C: Solid State Physics*, 15(18):3967–3985, 6 1982.

[361] Jean Jacques Greffet, Patrick Bouchon, Giovanni Brucoli, and François Marquier. Light Emission by Nonequilibrium Bodies: Local Kirchhoff Law. *Physical Review X*, 8(2):021008, 4 2018.

[362] David L. C. Chan, Marin Soljačić, and J. D. Joannopoulos. Direct calculation of thermal emission for three-dimensionally periodic photonic crystal slabs. *Physical Review E*, 74(3):036615, 9 2006.

[363] Hendrix Demers, Nicolas Poirier-Demers, Alexandre Réal Couture, Dany Joly, Marc Guilmain, Niels de Jonge, and Dominique Drouin. Three-dimensional electron microscopy simulation with the CASINO Monte Carlo software. *Scanning*, 33(3):135–146, 5 2011.

[364] Sylvain Girard, Antonino Alessi, Nicolas Richard, Layla Martin-Samos, Vincenzo De Michele, Luigi Giacomazzi, Simonpietro Agnello, Diego Di Francesca, Adriana Morana, Blaž Winkler, Imène Reghioua, Philippe Paillet, Marco Cannas, Thierry Robin, Aziz Boukenter, and Youcef Ouerdane. Overview of radiation induced point defects in silica-based optical fibers. *Reviews in Physics*, 4:100032, 11 2019.

[365] Paul Lecoq, Christian Morel, John O Prior, Dimitris Visvikis, Stefan Gundacker, Etiennette Auffray, Peter Križan, Rosana Martinez Turtos, Dominique Thers, Edoardo Charbon, Joao Varela, Christophe de La Taille, Angelo Rivetti, Dominique Breton, Jean-François Pratte, Johan Nuyts, Suleman Surti, Stefaan Vandenberghe, Paul Marsden, Katia Parodi, Jose Maria Benlloch, and Mathieu Benoit. Roadmap toward the 10 ps time-of-flight PET challenge. *Physics in Medicine & Biology*, 65(21):21RM01, 10 2020.

[366] Eli Yablonovitch. Statistical ray optics. *JOSA, Vol. 72, Issue 7, pp. 899-907*, 72(7):899–907, 7 1982.

[367] Patrick Campbell and Martin A. Green. The Limiting Efficiency of Silicon Solar Cells under Concentrated Sunlight. *IEEE Transactions on Electron Devices*, 33(2):234–239, 1986.

[368] Aaswath Raman, Shanhui Fan, and Zongfu Yu. Fundamental limit of light trapping in grating structures. *Optics Express, Vol. 18, Issue S3, pp. A366-A380*, 18(103):A366–A380, 9 2010.

[369] Zongfu Yu, Aaswath Raman, and Shanhui Fan. Fundamental limit of nanophotonic light trapping in solar cells. *Proceedings of the National Academy of Sciences*, 107(41):17491–17496, 10 2010.

[370] A. I. Zhmakin. Enhancement of light extraction from light emitting diodes. *Physics Reports*, 498(4-5):189–241, 2 2011.

[371] S. Derenzo, E. Bourret, C. Frank-Rotsch, S. Hanrahan, and M. Garcia-Sciveres. How silicon and boron dopants govern the cryogenic scintillation properties of N-type GaAs. *Nuclear Instruments and Methods in Physics Research Section A: Accelerators, Spectrometers, Detectors and Associated Equipment*, 989:164957, 2 2021.

[372] Sheng Liu, Aleksandr Vaskin, Sadhvikas Addamane, Benjamin Leung, Miao Chan Tsai, Yuanmu Yang, Polina P. Vabishchevich, Gordon A. Keeler, George Wang, Xiaowei He, Younghee Kim, Nicolai F. Hartmann, Han Htoon, Stephen K. Doorn, Matthias Zilk, Thomas Pertsch, Ganesh Balakrishnan, Michael B. Sinclair, Isabelle Staude, and Igal Brener. Light-Emitting Metasurfaces: Simultaneous Control of Spontaneous Emission and Far-Field Radiation. *Nano Letters*, 18(11):6906–6914, 11 2018.

[373] K. M. Schulz, D. Jalas, A. Y. Petrov, and M. Eich. Reciprocity approach for calculating the Purcell effect for emission into an open optical system. *Optics Express*, 26(15):19247, 3 2018.

[374] Yan Sheng, Wenjie Wang, Roy Shiloh, Vito Roppo, Yongfa Kong, Ady Arie, and Wieslaw Krolikowski. Čerenkov third-harmonic generation in $\chi(2)$ nonlinear photonic crystal. *Applied Physics Letters*, 98(24):241114, 6 2011.

[375] Shuyu Zhang, Emiliano R. Martins, Adel G. Diyaf, John I.B. Wilson, Graham A. Turnbull, and Ifor D.W. Samuel. Calculation of the emission power distribution of microstructured OLEDs using the reciprocity theorem. *Synthetic Metals*, 205:127–133, 7 2015.

[376] Adam C. Overvig, Sander A. Mann, and Andrea Alù. Thermal Metasurfaces: Complete Emission Control by Combining Local and Nonlocal Light-Matter Interactions. *Physical Review X*, 11(2):021050, 6 2021.

[377] Sean Molesky, Zin Lin, Alexander Y. Piggott, Weiliang Jin, Jelena Vucković, and Alejandro W. Rodriguez. Inverse design in nanophotonics. *Nature Photonics*, 12(11):659–670, 11 2018.

[378] Athanasios G. Polimeridis, M. T.H. Reid, Weiliang Jin, Steven G. Johnson, Jacob K. White, and Alejandro W. Rodriguez. Fluctuating volume-current formulation of electromagnetic fluctuations in inhomogeneous media: Incandescence and luminescence in arbitrary geometries. *Physical Review B - Condensed Matter and Materials Physics*, 92(13):134202, 10 2015.

[379] Rasmus E. Christiansen, Jérôme Michon, Mohammed Benzaouia, Ole Sigmund, and Steven G. Johnson. Inverse design of nanoparticles for enhanced Raman scattering. *Optics Express*, 28(4):4444, 2 2020.

[380] Kenji Watanabe, Takashi Taniguchi, Takahiro Niiyama, Kenta Miya, and Masateru Taniguchi. Far-ultraviolet plane-emission handheld device based on hexagonal boron nitride. *Nature Photonics*, 3(10):591–594, 10 2009.

[381] Johannes Flick, Nicholas Rivera, and Prineha Narang. Strong light-matter coupling in quantum chemistry and quantum photonics. *Nanophotonics*, 7(9):1479–1501.

[382] Michael Ruggenthaler, Nicolas Tancogne-Dejean, Johannes Flick, Heiko Appel, and Angel Rubio. From a quantum-electrodynamical light–matter description to novel spectroscopies. *Nature Reviews Chemistry*, 2(3):0118, mar 2018.

[383] P Forn-Díaz, L Lamata, E Rico, J Kono, and E Solano. Ultrastrong coupling regimes of light-matter interaction. *arXiv preprint arXiv:1804.09275*, 2018.

[384] Denis G. Baranov, Martin Wers‰ll, Jorge Cuadra, Tomasz J. Antosiewicz, and Timur Shegai. Novel nanostructures and materials for strong light?matter interactions. *ACS Photonics*, 5(1):24–42, 2018.

[385] Alexandre Blais, Ren-Shou Huang, Andreas Wallraff, S. M. Girvin, and R. J. Schoelkopf. Cavity quantum electrodynamics for superconducting electrical circuits: An architecture for quantum computation. *Phys. Rev. A*, 69:062320, Jun 2004.

[386] A. Wallraff, D. I. Schuster, A. Blais, L. Frunzio, R.-S. Huang, J. Majer, S. Kumar, S. M. Girvin, and R. J. Schoelkopf. Strong coupling of a single photon to a superconducting qubit using circuit quantum electrodynamics. *Nature*, 431(7005):162–167, sep 2004.

[387] James A. Hutchison, Tal Schwartz, Cyriaque Genet, Eloïse Devaux, and Thomas W. Ebbesen. Modifying chemical landscapes by coupling to vacuum fields. *Angewandte Chemie International Edition*, 51(7):1592–1596, 2012.

[388] David M. Coles, Yanshen Yang, Yaya Wang, Richard T. Grant, Robert A. Taylor, Semion K. Saikin, Alán Aspuru-Guzik, David G. Lidzey, Joseph Kuo-Hsiang Tang, and Jason M. Smith. Strong coupling between chlorosomes of photosynthetic bacteria and a confined optical cavity mode. *Nature Communications*, 5:5561, nov 2014.

[389] David M. Coles, Niccolo Somaschi, Paolo Michetti, Caspar Clark, Pavlos G. Lagoudakis, Pavlos G. Savvidis, and David G. Lidzey. Polariton-mediated energy transfer between organic dyes in a strongly coupled optical microcavity. *Nature Materials*, 13(7):712–719, may 2014.

[390] Anoop Thomas, Jino George, Atef Shalabney, Marian Dryzhakov, Sreejith J. Varma, Joseph Moran, Thibault Chervy, Xiaolan Zhong, Eloïse Devaux, Cyriaque Genet, James A. Hutchison, and Thomas W. Ebbesen. Ground-state chemical reactivity

under vibrational coupling to the vacuum electromagnetic field. *Angewandte Chemie International Edition*, 55(38):11462–11466, 2016.

[391] Thomas W. Ebbesen. Hybrid light–matter states in a molecular and material science perspective. *Accounts of Chemical Research*, 49(11):2403–2412, nov 2016.

[392] Kati Stranius, Manuel Hertzog, and Karl Bˆrjesson. Selective manipulation of electronically excited states through strong light–matter interactions. *Nature Communications*, 9(1), jun 2018.

[393] Anoop Thomas, Lucas Lethuillier-Karl, Kalaivanan Nagarajan, Robrecht M. A. Vergauwe, Jino George, Thibault Chervy, Atef Shalabney, EloÔse Devaux, Cyriaque Genet, Joseph Moran, and Thomas W. Ebbesen. Tilting a ground state reactivity landscape by vibrational strong coupling. oct 2018.

[394] Qi Zhang, Minhan Lou, Xinwei Li, John L. Reno, Wei Pan, John D. Watson, Michael J. Manfra, and Junichiro Kono. Collective non-perturbative coupling of 2d electrons with high-quality-factor terahertz cavity photons. *Nature Physics*, 12(11):1005–1011, aug 2016.

[395] Markus Geiser, Fabrizio Castellano, Giacomo Scalari, Mattias Beck, Laurent Nevou, and Jérôme Faist. Ultrastrong coupling regime and plasmon polaritons in parabolic semiconductor quantum wells. *Phys. Rev. Lett.*, 108:106402, Mar 2012.

[396] D. Marković, S. Jezouin, Q. Ficheux, S. Fedortchenko, S. Felicetti, T. Coudreau, P. Milman, Z. Leghtas, and B. Huard. Demonstration of an effective ultrastrong coupling between two oscillators. *Phys. Rev. Lett.*, 121:040505, Jul 2018.

[397] Felix Benz, Mikolaj K. Schmidt, Alexander Dreismann, Rohit Chikkaraddy, Yao Zhang, Angela Demetriadou, Cloudy Carnegie, Hamid Ohadi, Bart de Nijs, Ruben Esteban, Javier Aizpurua, and Jeremy J. Baumberg. Single-molecule optomechanics in "picocavities". *Science*, 354(6313):726–729, nov 2016.

[398] Charles Roques-Carmes, Nicholas Rivera, John D. Joannopoulos, Marin Soljačić, and Ido Kaminer. Nonperturbative quantum electrodynamics in the cherenkov effect. *Phys. Rev. X*, 8:041013, Oct 2018.

[399] Johannes Flick, Michael Ruggenthaler, Heiko Appel, and Angel Rubio. Atoms and molecules in cavities, from weak to strong coupling in quantum-electrodynamics (qed) chemistry. *Proceedings of the National Academy of Sciences*, 114(12):3026–3034, 2017.

[400] Felipe Herrera and Frank C. Spano. Cavity-controlled chemistry in molecular ensembles. *Phys. Rev. Lett.*, 116:238301, Jun 2016.

[401] Johannes Feist, Javier Galego, and Francisco J. Garcia-Vidal. Polaritonic chemistry with organic molecules. *ACS Photonics*, 5(1):205–216, 2018.

[402] Luis A. Martínez-Martínez, Raphael F. Ribeiro, Jorge Campos-González-Angulo, and Joel Yuen-Zhou. Can ultrastrong coupling change ground-state chemical reactions? *ACS Photonics*, 5(1):167–176, 2018.

[403] E. Orgiu, J. George, J. A. Hutchison, E. Devaux, J. F. Dayen, B. Doudin, F. Stellacci, C. Genet, J. Schachenmayer, C. Genes, G. Pupillo, P. Samorì, and T. W. Ebbesen. Conductivity in organic semiconductors hybridized with the vacuum field. *Nat. Mater.*, 14(11):1123–1129, sep 2015.

[404] Anton Frisk Kockum, Adam Miranowicz, Vincenzo Macrì, Salvatore Savasta, and Franco Nori. Deterministic quantum nonlinear optics with single atoms and virtual photons. *Phys. Rev. A*, 95:063849, Jun 2017.

[405] I. V. Tokatly. Time-dependent density functional theory for many-electron systems interacting with cavity photons. *Phys. Rev. Lett.*, 110:233001, Jun 2013.

[406] Michael Ruggenthaler, Johannes Flick, Camilla Pellegrini, Heiko Appel, Ilya V. Tokatly, and Angel Rubio. Quantum-electrodynamical density-functional theory: Bridging quantum optics and electronic-structure theory. *Phys. Rev. A*, 90:012508, Jul 2014.

[407] Johannes Flick, Michael Ruggenthaler, Heiko Appel, and Angel Rubio. Kohn-sham approach to quantum electrodynamical density-functional theory: Exact time-dependent effective potentials in real space. *Proc. Natl. Acad. Sci. U. S. A.*, 112(50):15285–15290, 2015.

[408] Tanja Dimitrov, Johannes Flick, Michael Ruggenthaler, and Angel Rubio. Exact functionals for correlated electron–photon systems. *New Journal of Physics*, 19(11):113036, nov 2017.

[409] Johannes Flick, Davis M Welakuh, Michael Ruggenthaler, Heiko Appel, and Angel Rubio. Light-matter response functions in quantum-electrodynamical density-functional theory: Modifications of spectra and of the maxwell equations. *arXiv preprint arXiv:1803.02519*, 2018.

[410] Johannes Flick and Prineha Narang. Cavity-correlated electron-nuclear dynamics from first principles. *Phys. Rev. Lett.*, 121:113002, Sep 2018.

[411] Johannes Flick, Christian Schäfer, Michael Ruggenthaler, Heiko Appel, and Angel Rubio. Ab initio optimized effective potentials for real molecules in optical cavities: Photon contributions to the molecular ground state. *ACS Photonics*, 5(3):992–1005, 2018.

[412] A. Szabo and N.S. Ostlund. *Modern Quantum Chemistry: Introduction to Advanced Electronic Structure Theory*. Dover Books on Chemistry. Dover Publications, 1989.

[413] C. Cohen-Tannoudji, J. Dupont-Roc, and G. Grynberg. *Atom-photon interactions: basic processes and applications*. Wiley-Interscience publication. J. Wiley, 1992.

[414] Camilla Pellegrini, Johannes Flick, Ilya V. Tokatly, Heiko Appel, and Angel Rubio. Optimized effective potential for quantum electrodynamical time-dependent density functional theory. *Phys. Rev. Lett.*, 115:093001, Aug 2015.

[415] Hendrick BG Casimir. On the attraction between two perfectly conducting plates. In *Proc. Kon. Ned. Akad. Wet.*, volume 51, page 793, 1948.

[416] Daniele De Bernardis, Philipp Pilar, Tuomas Jaako, Simone De Liberato, and Peter Rabl. Breakdown of gauge invariance in ultrastrong-coupling cavity qed. *Phys. Rev. A*, 98:053819, Nov 2018.

[417] Simone De Liberato. Light-matter decoupling in the deep strong coupling regime: The breakdown of the purcell effect. *Phys. Rev. Lett.*, 112:016401, Jan 2014.

[418] James A Hutchison, Tal Schwartz, Cyriaque Genet, Eloïse Devaux, and Thomas W Ebbesen. Modifying chemical landscapes by coupling to vacuum fields. *Angewandte Chemie International Edition*, 51(7):1592–1596, 2012.

[419] Michael Ruggenthaler, Nicolas Tancogne-Dejean, Johannes Flick, Heiko Appel, and Angel Rubio. From a quantum-electrodynamical light–matter description to novel spectroscopies. *Nature Reviews Chemistry*, 2(3):1–16, 2018.

[420] E Orgiu, J George, JA Hutchison, E Devaux, JF Dayen, B Doudin, F Stellacci, C Genet, J Schachenmayer, Claudiu Genes, et al. Conductivity in organic semiconductors hybridized with the vacuum field. *Nature Materials*, 14(11):1123–1129, 2015.

[421] Jorge Casanova, Guillermo Romero, Ion Lizuain, Juan José García-Ripoll, and Enrique Solano. Deep strong coupling regime of the jaynes-cummings model. *Physical review letters*, 105(26):263603, 2010.

[422] Fumiki Yoshihara, Tomoko Fuse, Ziqiao Ao, Sahel Ashhab, Kosuke Kakuyanagi, Shiro Saito, Takao Aoki, Kazuki Koshino, and Kouichi Semba. Inversion of qubit energy levels in qubit-oscillator circuits in the deep-strong-coupling regime. *Physical review letters*, 120(18):183601, 2018.

[423] Nicholas Rivera and Ido Kaminer. Light–matter interactions with photonic quasiparticles. *Nature Reviews Physics*, 2(10):538–561, 2020.

[424] EK Irish. Generalized rotating-wave approximation for arbitrarily large coupling. *Physical review letters*, 99(17):173601, 2007.

[425] PD Drummond and DF Walls. Quantum theory of optical bistability. i. nonlinear polarisability model. *Journal of Physics A: Mathematical and General*, 13(2):725, 1980.

[426] Daniel F Walls and Gerard J Milburn. *Quantum optics*. Springer Science & Business Media, 2007.

[427] Tuomas Jaako, Ze-Liang Xiang, Juan José Garcia-Ripoll, and Peter Rabl. Ultrastrong-coupling phenomena beyond the dicke model. *Physical Review A*, 94(3):033850, 2016.

[428] Daniele De Bernardis, Philipp Pilar, Tuomas Jaako, Simone De Liberato, and Peter Rabl. Breakdown of gauge invariance in ultrastrong-coupling cavity qed. *Physical Review A*, 98(5):053819, 2018.

[429] Daniele De Bernardis, Tuomas Jaako, and Peter Rabl. Cavity quantum electrodynamics in the nonperturbative regime. *Physical Review A*, 97(4):043820, 2018.

[430] Omar Di Stefano, Alessio Settineri, Vincenzo Macrì, Luigi Garziano, Roberto Stassi, Salvatore Savasta, and Franco Nori. Resolution of gauge ambiguities in ultrastrong-coupling cavity quantum electrodynamics. *Nature Physics*, 15(8):803–808, 2019.

[431] Alessio Settineri, Omar Di Stefano, David Zueco, Stephen Hughes, Salvatore Savasta, and Franco Nori. Gauge freedom, quantum measurements, and time-dependent interactions in cavity and circuit qed. *arXiv preprint arXiv:1912.08548*, 2019.

[432] Marlan O Scully and Willis E Lamb Jr. Quantum theory of an optical maser. i. general theory. *Physical Review*, 159(2):208, 1967.

[433] Marlan O Scully and M Suhail Zubairy. Quantum optics, 1999.

[434] Alessandro Ridolfo, Martin Leib, Salvatore Savasta, and Michael J Hartmann. Photon blockade in the ultrastrong coupling regime. *Physical review letters*, 109(19):193602, 2012.

[435] Alexandre Le Boité, Myung-Joong Hwang, Hyunchul Nha, and Martin B Plenio. Fate of photon blockade in the deep strong-coupling regime. *Physical Review A*, 94(3):033827, 2016.

[436] Jason McKeever, Andreea Boca, A David Boozer, Joseph R Buck, and H Jeff Kimble. Experimental realization of a one-atom laser in the regime of strong coupling. *Nature*, 425(6955):268–271, 2003.

[437] Kyungwon An, James J Childs, Ramachandra R Dasari, and Michael S Feld. Microlaser: A laser with one atom in an optical resonator. *Physical review letters*, 73(25):3375, 1994.

[438] Y-Y Liu, J Stehlik, Christopher Eichler, MJ Gullans, Jacob M Taylor, and JR Petta. Semiconductor double quantum dot micromaser. *Science*, 347(6219):285–287, 2015.

[439] J Stehlik, Y-Y Liu, C Eichler, TR Hartke, X Mi, MJ Gullans, JM Taylor, and Jason R Petta. Double quantum dot floquet gain medium. *Physical Review X*, 6(4):041027, 2016.

[440] Guido Burkard, Michael J Gullans, Xiao Mi, and Jason R Petta. Superconductor–semiconductor hybrid-circuit quantum electrodynamics. *Nature Reviews Physics*, 2(3):129–140, 2020.

[441] MH Devoret, Steven Girvin, and Robert Schoelkopf. Circuit-qed: How strong can the coupling between a josephson junction atom and a transmission line resonator be? *Annalen der Physik*, 16(10-11):767–779, 2007.

[442] Nicholas Rivera, Jamison Sloan, Yannick Salamin, and Marin Soljacic. Macroscopic condensation of photon noise in sharply nonlinear dissipative systems. *arXiv preprint arXiv:2111.03099*, 2021.

[443] Daniel F Walls. Squeezed states of light. *nature*, 306(5939):141–146, 1983.

[444] AI Lvovsky, Philippe Grangier, Alexei Ourjoumtsev, Valentina Parigi, Masahide Sasaki, and Rosa Tualle-Brouri. Production and applications of non-gaussian quantum states of light. *arXiv preprint arXiv:2006.16985*, 2020.

[445] Robert Raussendorf, Daniel E Browne, and Hans J Briegel. Measurement-based quantum computation on cluster states. *Physical review A*, 68(2):022312, 2003.

[446] Nicolas C Menicucci, Peter Van Loock, Mile Gu, Christian Weedbrook, Timothy C Ralph, and Michael A Nielsen. Universal quantum computation with continuous-variable cluster states. *Physical review letters*, 97(11):110501, 2006.

[447] Christian Reimer, Stefania Sciara, Piotr Roztocki, Mehedi Islam, Luis Romero Cortés, Yanbing Zhang, Bennet Fischer, Sébastien Loranger, Raman Kashyap, Alfonso Cino, et al. High-dimensional one-way quantum processing implemented on d-level cluster states. *Nature Physics*, 15(2):148–153, 2019.

[448] Mikkel V Larsen, Xueshi Guo, Casper R Breum, Jonas S Neergaard-Nielsen, and Ulrik L Andersen. Deterministic generation of a two-dimensional cluster state. *Science*, 366(6463):369–372, 2019.

[449] Malvin C Teich and Bahaa EA Saleh. Squeezed state of light. *Quantum Optics: Journal of the European Optical Society Part B*, 1(2):153, 1989.

[450] Luiz Davidovich. Sub-poissonian processes in quantum optics. *Reviews of Modern Physics*, 68(1):127, 1996.

[451] Nicholas Thomas-Peter, Brian J Smith, Animesh Datta, Lijian Zhang, Uwe Dorner, and Ian A Walmsley. Real-world quantum sensors: evaluating resources for precision measurement. *Physical review letters*, 107(11):113603, 2011.

[452] Scott Aaronson and Alex Arkhipov. The computational complexity of linear optics. In *Proceedings of the forty-third annual ACM symposium on Theory of computing*, pages 333–342, 2011.

[453] Austin P Lund, Anthony Laing, Saleh Rahimi-Keshari, Terry Rudolph, Jeremy L O'Brien, and Timothy C Ralph. Boson sampling from a gaussian state. *Physical review letters*, 113(10):100502, 2014.

[454] Joonsuk Huh, Gian Giacomo Guerreschi, Borja Peropadre, Jarrod R McClean, and Alán Aspuru-Guzik. Boson sampling for molecular vibronic spectra. *Nature Photonics*, 9(9):615–620, 2015.

[455] Hui Wang, Yu He, Yu-Huai Li, Zu-En Su, Bo Li, He-Liang Huang, Xing Ding, Ming-Cheng Chen, Chang Liu, Jian Qin, et al. High-efficiency multiphoton boson sampling. *Nature Photonics*, 11(6):361–365, 2017.

[456] Craig S Hamilton, Regina Kruse, Linda Sansoni, Sonja Barkhofen, Christine Silberhorn, and Igor Jex. Gaussian boson sampling. *Physical review letters*, 119(17):170501, 2017.

[457] Daniel J Brod, Ernesto F Galvão, Andrea Crespi, Roberto Osellame, Nicolò Spagnolo, and Fabio Sciarrino. Photonic implementation of boson sampling: a review. *Advanced Photonics*, 1(3):034001, 2019.

[458] Han-Sen Zhong, Hui Wang, Yu-Hao Deng, Ming-Cheng Chen, Li-Chao Peng, Yi-Han Luo, Jian Qin, Dian Wu, Xing Ding, Yi Hu, et al. Quantum computational advantage using photons. *Science*, 370(6523):1460–1463, 2020.

[459] Max Hofheinz, EM Weig, M Ansmann, Radoslaw C Bialczak, Erik Lucero, M Neeley, AD O'connell, H Wang, John M Martinis, and AN Cleland. Generation of fock states in a superconducting quantum circuit. *Nature*, 454(7202):310–314, 2008.

[460] H Wang, M Hofheinz, M Ansmann, RC Bialczak, E Lucero, M Neeley, AD O'connell, D Sank, J Wenner, AN Cleland, et al. Measurement of the decay of fock states in a superconducting quantum circuit. *Physical Review Letters*, 101(24):240401, 2008.

[461] Christopher S Wang, Jacob C Curtis, Brian J Lester, Yaxing Zhang, Yvonne Y Gao, Jessica Freeze, Victor S Batista, Patrick H Vaccaro, Isaac L Chuang, Luigi Frunzio, et al. Efficient multiphoton sampling of molecular vibronic spectra on a superconducting bosonic processor. *Physical Review X*, 10(2):021060, 2020.

[462] Gerhard Rempe, F Schmidt-Kaler, and Herbert Walther. Observation of sub-poissonian photon statistics in a micromaser. *Physical review letters*, 64(23):2783, 1990.

[463] Benjamin TH Varcoe, Simon Brattke, Matthias Weidinger, and Herbert Walther. Preparing pure photon number states of the radiation field. *Nature*, 403(6771):743–746, 2000.

[464] Clément Sayrin, Igor Dotsenko, Xingxing Zhou, Bruno Peaudecerf, Théo Rybarczyk, Sébastien Gleyzes, Pierre Rouchon, Mazyar Mirrahimi, Hadis Amini, Michel

Brune, et al. Real-time quantum feedback prepares and stabilizes photon number states. *Nature*, 477(7362):73–77, 2011.

[465] Edo Waks, Eleni Diamanti, Barry C Sanders, Stephen D Bartlett, and Yoshihisa Yamamoto. Direct observation of nonclassical photon statistics in parametric down-conversion. *Physical review letters*, 92(11):113602, 2004.

[466] Merlin Cooper, Laura J Wright, Christoph Söller, and Brian J Smith. Experimental generation of multi-photon fock states. *Optics express*, 21(5):5309–5317, 2013.

[467] M Kitagawa and Y Yamamoto. Number-phase minimum-uncertainty state with reduced number uncertainty in a kerr nonlinear interferometer. *Physical Review A*, 34(5):3974, 1986.

[468] Leonard Mandel and Emil Wolf. *Optical coherence and quantum optics*. Cambridge university press, 1995.

[469] Shanhui Fan, Wonjoo Suh, and John D Joannopoulos. Temporal coupled-mode theory for the fano resonance in optical resonators. *JOSA A*, 20(3):569–572, 2003.

[470] Mikhail F Limonov, Mikhail V Rybin, Alexander N Poddubny, and Yuri S Kivshar. Fano resonances in photonics. *Nature Photonics*, 11(9):543–554, 2017.

[471] Chia Wei Hsu, Bo Zhen, Jeongwon Lee, Song-Liang Chua, Steven G Johnson, John D Joannopoulos, and Marin Soljačić. Observation of trapped light within the radiation continuum. *Nature*, 499(7457):188–191, 2013.

[472] Chia Wei Hsu, Bo Zhen, A Douglas Stone, John D Joannopoulos, and Marin Soljačić. Bound states in the continuum. *Nature Reviews Materials*, 1(9):1–13, 2016.

[473] Michael Fleischhauer, Atac Imamoglu, and Jonathan P Marangos. Electromagnetically induced transparency: Optics in coherent media. *Reviews of modern physics*, 77(2):633, 2005.

[474] Amnon Yariv, Rashit Nabiev, and Kerry Vahala. Self-quenching of fundamental phase and amplitude noise in semiconductor lasers with dispersive loss. *Optics letters*, 15(23):1359–1361, 1990.

[475] J Kitching, R Boyd, A Yariv, and Y Shevy. Amplitude noise reduction in semiconductor lasers with weak, dispersive optical feedback. *Optics letters*, 19(17):1331–1333, 1994.

[476] D Mogilevtsev, A Mikhalychev, VS Shchesnovich, and Natalia Korolkova. Nonlinear dissipation can combat linear loss. *Physical Review A*, 87(6):063847, 2013.

[477] Matthew Thornton, Anton Sakovich, Alexander Mikhalychev, Jesus Diaz Ferrer, Pablo de la Hoz, Natalia Korolkova, and Dmitri Mogilevtsev. Coherent diffusive photon gun for generating nonclassical states. *Physical Review Applied*, 12(6):064051, 2019.

[478] DANIEL F Walls, MJ Collett, and AS Lane. Amplitude-noise reduction in lasers with intracavity nonlinear elements. *Physical Review A*, 42(7):4366, 1990.

[479] H Ritsch. Quantum noise reduction in lasers with nonlinear absorbers. *Quantum Optics: Journal of the European Optical Society Part B*, 2(2):189, 1990.

[480] HM Wiseman and GJ Milburn. Noise reduction in a laser by nonlinear damping. *Physical Review A*, 44(11):7815, 1991.

[481] H Ritsch, MAM Marte, and P Zoller. Quantum noise reduction in raman lasers. *EPL (Europhysics Letters)*, 19(1):7, 1992.

[482] Ulrik L Andersen, Tobias Gehring, Christoph Marquardt, and Gerd Leuchs. 30 years of squeezed light generation. *Physica Scripta*, 91(5):053001, 2016.

[483] Roy S Bondurant and Jeffrey H Shapiro. Squeezed states in phase-sensing interferometers. *Physical Review D*, 30(12):2548, 1984.

[484] Thomas Fink, Anne Schade, Sven Höfling, Christian Schneider, and Ataç Imamoglu. Signatures of a dissipative phase transition in photon correlation measurements. *Nature Physics*, 14(4):365–369, 2018.

[485] Aymeric Delteil, Thomas Fink, Anne Schade, Sven Höfling, Christian Schneider, and Ataç İmamoğlu. Towards polariton blockade of confined exciton–polaritons. *Nature materials*, 18(3):219–222, 2019.

[486] Eric D Black. An introduction to pound–drever–hall laser frequency stabilization. *American journal of physics*, 69(1):79–87, 2001.

[487] Akitoshi Ueda, Noboru Uehara, Katumi Uchisawa, Ken-ichi Ueda, Hisao Sekiguchi, Takayoshi Mitake, Kenji Nakamura, Naoya Kitajima, and Izumi Kataoka. Ultra-high quality cavity with 1.5 ppm loss at 1064 nm. *Optical Review*, 3(5):369–372, 1996.

[488] Martyn D Wheeler, Stuart M Newman, Andrew J Orr-Ewing, and Michael NR Ashfold. Cavity ring-down spectroscopy. *Journal of the Chemical Society, Faraday Transactions*, 94(3):337–351, 1998.

[489] Konstantin E Dorfman, Frank Schlawin, and Shaul Mukamel. Nonlinear optical signals and spectroscopy with quantum light. *Reviews of Modern Physics*, 88(4):045008, 2016.

[490] Shaul Mukamel, Matthias Freyberger, Wolfgang Schleich, Marco Bellini, Alessandro Zavatta, Gerd Leuchs, Christine Silberhorn, Robert W Boyd, Luis Lorenzo Sánchez-Soto, André Stefanov, et al. Roadmap on quantum light spectroscopy. *Journal of Physics B: Atomic, Molecular and Optical Physics*, 53(7):072002, 2020.

[491] YR Shen. Quantum statistics of nonlinear optics. *Physical Review*, 155(3):921, 1967.

[492] Jianming Huang and Prem Kumar. Observation of quantum frequency conversion. *Physical review letters*, 68(14):2153, 1992.

[493] Christian Leefmans, Avik Dutt, James Williams, Luqi Yuan, Midya Parto, Franco Nori, Shanhui Fan, and Alireza Marandi. Topological dissipation in a time-multiplexed photonic resonator network. *Nature Physics*, 2022.

[494] Liang Feng, Ramy El-Ganainy, and Li Ge. Non-hermitian photonics based on parity–time symmetry. *Nature Photonics*, 11(12):752–762, 2017.

[495] Mohammad-Ali Miri and Andrea Alu. Exceptional points in optics and photonics. *Science*, 363(6422), 2019.

[496] Shiqi Xia, Dimitrios Kaltsas, Daohong Song, Ioannis Komis, Jingjun Xu, Alexander Szameit, Hrvoje Buljan, Konstantinos G Makris, and Zhigang Chen. Nonlinear tuning of pt symmetry and non-hermitian topological states. *Science*, 372(6537):72–76, 2021.

[497] Seema Lathi and Yoshihisa Yamamoto. Influence of nonlinear gain and loss on the intensity noise of a multimode semiconductor laser. *Physical Review A*, 59(1):819, 1999.

[498] SR Friberg, S Machida, MJ Werner, A Levanon, and Takaaki Mukai. Observation of optical soliton photon-number squeezing. *Physical review letters*, 77(18):3775, 1996.

[499] Prem Kumar, Giacomo M D'Ariano, Osamu Hirota, et al. *Quantum Communication, Computing and Measurement 2*. Springer, 2002.

[500] Y Yamamoto, S Machida, and O Nilsson. Amplitude squeezing in a pump-noise-suppressed laser oscillator. *Physical Review A*, 34(5):4025, 1986.

[501] S Machida and Y Yamamoto. Observation of sub-poissonian photoelectron statistics in a negative feedback semiconductor laser. *Optics communications*, 57(4):290–296, 1986.

[502] WH Richardson, S Machida, and Y Yamamoto. Squeezed photon-number noise and sub-poissonian electrical partition noise in a semiconductor laser. *Physical review letters*, 66(22):2867, 1991.

[503] Yoshihisa Yamamoto, Susumu Machida, and Wayne H Richardson. Photon number squeezed states in semiconductor lasers. *Science*, 255(5049):1219–1224, 1992.

[504] H Flayac and V Savona. Unconventional photon blockade. *Physical Review A*, 96(5):053810, 2017.

[505] Andrew Lingenfelter, David Roberts, and AA Clerk. Unconditional fock state generation using arbitrarily weak photonic nonlinearities. *arXiv preprint arXiv:2103.12041*, 2021.

[506] Thibault Peyronel, Ofer Firstenberg, Qi-Yu Liang, Sebastian Hofferberth, Alexey V Gorshkov, Thomas Pohl, Mikhail D Lukin, and Vladan Vuletić. Quantum nonlinear optics with single photons enabled by strongly interacting atoms. *Nature*, 488(7409):57–60, 2012.

[507] Philip Krantz, Morten Kjaergaard, Fei Yan, Terry P Orlando, Simon Gustavsson, and William D Oliver. A quantum engineer's guide to superconducting qubits. *Applied Physics Reviews*, 6(2):021318, 2019.

[508] Brahim Lounis and Michel Orrit. Single-photon sources. *Reports on Progress in Physics*, 68(5):1129, 2005.

[509] Marin Soljačić and John D Joannopoulos. Enhancement of nonlinear effects using photonic crystals. *Nature materials*, 3(4):211–219, 2004.

[510] Giuseppe Grosso and Giuseppe Pastori Parravicini. *Solid state physics*. Academic press, 2013.

[511] Tenio Popmintchev, Ming-Chang Chen, Dimitar Popmintchev, Paul Arpin, Susannah Brown, Skirmantas Ališauskas, Giedrius Andriukaitis, Tadas Balčiunas, Oliver D Mücke, Audrius Pugzlys, et al. Bright coherent ultrahigh harmonics in the kev x-ray regime from mid-infrared femtosecond lasers. *Science*, 336(6086):1287–1291, 2012.

[512] Andrea Pizzi, Gilles Rosolen, Liang Jie Wong, Rasmus Ischebeck, Marin Soljačić, Thomas Feurer, and Ido Kaminer. Graphene metamaterials for intense, tunable and compact euv and x-sources. In *CLEO: QELS Fundamental Science*, pages FW4H–7. Optical Society of America, 2018.

[513] WS Graves, FX Kärtner, DE Moncton, and P Piot. Intense superradiant x rays from a compact source using a nanocathode array and emittance exchange. *Physical review letters*, 108(26):263904, 2012.

[514] Emilio A Nanni, William S Graves, and David E Moncton. Nanomodulated electron beams via electron diffraction and emittance exchange for coherent x-ray generation. *Physical Review Accelerators and Beams*, 21(1):014401, 2018.

[515] N Naumova, I Sokolov, J Nees, A Maksimchuk, V Yanovsky, and G Mourou. Attosecond electron bunches. *Physical review letters*, 93(19):195003, 2004.

[516] Jeremy Lim, Yidong Chong, and Liang Jie Wong. Terahertz-optical intensity grating for creating high-charge, attosecond electron bunches. *New Journal of Physics*, 21(3):033020, 2019.

[517] R Brinkmann, Ya Derbenev, and K Flöttmann. A low emittance, flat-beam electron source for linear colliders. *Physical Review Special Topics-Accelerators and Beams*, 4(5):053501, 2001.

[518] Ph Piot, Y-E Sun, and K-J Kim. Photoinjector generation of a flat electron beam with transverse emittance ratio of 100. *Physical Review Special Topics-Accelerators and Beams*, 9(3):031001, 2006.

[519] A Ody, P Musumeci, J Maxson, D Cesar, RJ England, and KP Wootton. Flat electron beam sources for dla accelerators. *Nuclear Instruments and Methods in Physics Research Section A: Accelerators, Spectrometers, Detectors and Associated Equipment*, 865:75–83, 2017.

[520] Chun Hung Lui, Li Liu, Kin Fai Mak, George W Flynn, and Tony F Heinz. Ultraflat graphene. *Nature*, 462(7271):339–341, 2009.

[521] Zhe Fei, AS Rodin, W Gannett, S Dai, W Regan, M Wagner, MK Liu, AS McLeod, G Dominguez, M Thiemens, et al. Electronic and plasmonic phenomena at graphene grain boundaries. *Nature nanotechnology*, 8(11):821–825, 2013.

[522] Shikai Deng and Vikas Berry. Wrinkled, rippled and crumpled graphene: an overview of formation mechanism, electronic properties, and applications. *Materials Today*, 19(4):197–212, 2016.

[523] Wei Sun Leong, Haozhe Wang, Jingjie Yeo, Francisco J Martin-Martinez, Ahmad Zubair, Pin-Chun Shen, Yunwei Mao, Tomas Palacios, Markus J Buehler, Jin-Yong Hong, et al. Paraffin-enabled graphene transfer. *Nature communications*, 10(1):867, 2019.

[524] Lev Davidovich Landau and Evgenii Mikhailovich Lifshitz. *The Classical Theory of Fields*. Pergamon, 1971.

[525] Karl Joulain, Jean-Philippe Mulet, François Marquier, Rémi Carminati, and Jean-Jacques Greffet. Surface electromagnetic waves thermally excited: Radiative heat transfer, coherence properties and casimir forces revisited in the near field. *Surface Science Reports*, 57(3-4):59–112, 2005.

[526] Cyuan-Han Chang, Nicholas Rivera, John D Joannopoulos, Marin Soljacic, and Ido Kaminer. Constructing "designer atoms" via resonant graphene-induced lamb shifts. *ACS Photonics*, 4(12):3098–3105, 2017.

[527] Peter B Johnson and R-W_ Christy. Optical constants of the noble metals. *Physical review B*, 6(12):4370–4379, 1972.

[528] Vladimir Borisovich Berestetskii, Lev Davydovič Landau, Evgenii Mikhailovich Lifshitz, and LP Pitaevskii. *Quantum electrodynamics*, volume 4. Butterworth-Heinemann, 1982.

[529] Ravishankar Sundararaman, Kendra Letchworth-Weaver, Kathleen A. Schwarz, Deniz Gunceler, Yalcin Ozhabes, and T. A. Arias. JDFTx: Software for joint density-functional theory. *SoftwareX*, 6:278–284, 1 2017.

[530] Christoph Freysoldt, Sixten Boeck, and Jörg Neugebauer. Direct minimization technique for metals in density functional theory. *Physical Review B*, 79(24):241103, 6 2009.

[531] A. Daniel Boese and Jan M. L. Martin. Development of density functionals for thermochemical kinetics. *The Journal of Chemical Physics*, 121(8):3405, 8 2004.

[532] Ravishankar Sundararaman and T. A. Arias. Regularization of the Coulomb singularity in exact exchange by Wigner-Seitz truncated interactions: Towards chemical accuracy in nontrivial systems. *Physical Review B - Condensed Matter and Materials Physics*, 87(16), 4 2013.

[533] John P. Perdew, Kieron Burke, and Matthias Ernzerhof. Generalized Gradient Approximation Made Simple. *Physical Review Letters*, 77(18):3865, 10 1996.

[534] Christopher Rackauckas and Qing Nie. DifferentialEquations.jl – A Performant and Feature-Rich Ecosystem for Solving Differential Equations in Julia. *Journal of Open Research Software*, 5(1):15, 5 2017.

[535] Christie Chatterley and Karl Linden. Demonstration and evaluation of germicidal UV-LEDs for point-of-use water disinfection. *Journal of Water and Health*, 8(3):479–486, 9 2010.

[536] Manuela Buonanno, David Welch, Igor Shuryak, and David J. Brenner. Far-UVC light (222 nm) efficiently and safely inactivates airborne human coronaviruses. *Scientific Reports*, 10(1):1–8, 12 2020.

[537] Kenji Watanabe and Takashi Taniguchi. Hexagonal boron nitride as a new ultraviolet luminescent material and its application, 2011.

[538] Peter W Milonni. Semiclassical and quantum-electrodynamical approaches in nonrelativistic radiation theory. *Physics Reports*, 25(1):1–81, 1976.

[539] Félix Beaudoin, Jay M Gambetta, and A Blais. Dissipation and ultrastrong coupling in circuit qed. *Physical Review A*, 84(4):043832, 2011.

[540] Hermann Haus. Waves and fields in optoelectronics. *Prentice-Hall, Inc.*, 1984.

[541] Ondřej Černotík, Aurélien Dantan, and Claudiu Genes. Cavity quantum electrodynamics with frequency-dependent reflectors. *Physical review letters*, 122(24):243601, 2019.

[542] Howard J Carmichael. *Statistical methods in quantum optics 2: Non-classical fields*. Springer Science & Business Media, 2009.

[543] H Friedrich and D Wintgen. Interfering resonances and bound states in the continuum. *Physical Review A*, 32(6):3231, 1985.

[544] Yoshihisa Yamamoto and Atac Imamoglu. Mesoscopic quantum optics. *Mesoscopic Quantum Optics*, 1999.

[545] Weng W Chow, Stephan W Koch, and Murray III Sargent. *Semiconductor-laser physics*. Springer Science & Business Media, 2012.

[546] Hermann Haken. *Waves, photons, atoms*, volume 1. North Holland, 1981.

[547] Melvin Lax. Quantum noise vii: The rate equations and amplitude noise in lasers. *IEEE Journal of Quantum Electronics*, 3(2):37–46, 1967.

[548] A.E. Siegman. *Lasers*. University Science Books, 1986.

[549] NJ Van Druten, Y Lien, C Serrat, SSR Oemrawsingh, MP Van Exter, and JP Woerdman. Laser with thresholdless intensity fluctuations. *Physical Review A*, 62(5):053808, 2000.